The impact of alkali-vanadate(s) in supported vanadia catalysts on the propane oxidation reaction

vorgelegt von
M. Sc.
Ezgi Erdem
ORCID: 0000-0002-6446-8935

an der Fakultät II - Mathematik und Naturwissenschaften
der Technischen Universität Berlin
zur Erlangung des akademischen Grades

Doktor der Ingenieurwissenschaften
Dr.-Ing.

genehmigte Dissertation

Promotionsausschuss:

Vorsitzender: Prof. Dr. Maria Andrea Mroginski (Technische Universität Berlin)
Gutachter: Prof. Dr. Robert Schlögl (Fritz-Haber-Institut der MPG)
Gutachter: Prof. Dr. Reinhard Schomäcker (Technische Universität Berlin)
Gutachter: Prof. Dr. Klaus Rademann (Humboldt-Universität zu Berlin)

Tag der wissenschaftlichen Aussprache: 16. Juni 2022

Berlin 2022

The impact of alkali-vanadate(s) in supported vanadia catalysts on the propane oxidation reaction

Dissertation

for the Doctoral Degree
in Chemical Engineering

Faculty II Mathematics and Natural Sciences
Technical University Berlin

Submitted by
M. Sc.
Ezgi Erdem
ORCID: 0000-0002-6446-8935

Doctoral Committee:

Chair: Prof. Dr. Maria Andrea Mroginski (Technical University Berlin)
First referee: Prof. Dr. Robert Schlögl (Fritz Haber Institute of the MPG)
Second referee: Prof. Dr. Reinhard Schomäcker (Technical University Berlin)
Third referee: Prof. Dr. Klaus Rademann (Humboldt University of Berlin)

Date of oral examination: 16 June 2022

Berlin 2022

The impact of alkali-vanadate(s) in supported vanadia catalysts on the propane oxidation reaction

Ezgi Erdem

FRITZ-HABER-INSTITUT
MAX-PLANCK-GESELLSCHAFT

Berlin 2022

“Dünyada her şey için, uygarlık için, hayat için, başarı için en hakiki mürşit ilimdir; fendir.”

“Science is the most reliable guide for civilization, for life and for success in the world.”

- Mustafa Kemal Atatürk -

(Samsun, 25th Sept. 1924)

Dedicated to today's and tomorrow's kids.

I wish they do much better than this.

Abstract

Introducing additives to supported vanadia catalysts has been intensively studied with the aim to improve catalyst performance in oxidative dehydrogenation of propane. It has been shown that alkali additives influence dispersion of vanadia as well as acid-base and redox properties of supported vanadium oxide species. Possibly formed alkali vanadate(s) can have a melting temperatures in the range of reaction temperatures of propane oxidation (e.g., $K_3V_5O_{14}$ melts at 410°C). However, little is known about the formation of mixed alkali-vanadium oxide compounds and the influence of melting of surface alkali-vanadate phase(s) on the catalytic properties of alkali-containing supported vanadium oxide catalysts.

To investigate the possible impact of melting of alkali-vanadate phase(s), a series of silica supported A/V catalysts (A: alkali, *i.e.*, Li, Na, K, Rb, and Cs) with a systematic variation of A: V ratios were synthesized and tested in propane oxidation reaction. Catalysts were prepared by a fusion of alkali carbonates, V_2O_5 and SiO_2 (by keeping total metal oxide loading as 10 wt. %). Catalyst precursors were in situ activated ($21O_2/79N_2$ at 520°C) and tested in an eight-fold parallel reactor ($C_3H_8/O_2/N_2$=7.5/7.5/85). Fluxing agents such as K-, Rb-, and Cs- decreases melting temperatures of silica supported V_xO_y catalysts to the temperature range where propane oxidation reaction is applied. However Li-, and Na- added catalysts have much higher melting temperatures so that catalysts remain as solid during reaction. Both catalytic test in a fixed bed reactor as well as operando Differential Scanning Calorimetry revealed a drastic change in catalytic performance if melting occurs. Activity drops and selectivity to propylene increases markedly when the supported V-A oxide layer and/or segregated crystalline alkali vanadate phases are melting. Structural reasons behind the drastic change in catalytic properties were investigated based spectroscopic investigations of the materials under operation. Detailed characterization was conducted for silica supported K/V=0.6 catalyst since this catalyst exhibited only one crystalline phase ($K_3V_5O_{14}$) beyond amorphous SiO_2 as detected by XRD.

Operando Raman spectroscopy showed the structural alterations of $K_3V_5O_{14}$ (532 nm laser) due to incongruent melting and how the melting impacts the dispersion of vanadium oxide species (266 nm laser) over the support. Melting initiated the formation of oligomeric vanadium oxide species already in the in situ activation step upon melting of potassium-vanadate. This explained the source of catalytic activity in alkali-containing supported vanadia catalyst. The possible role of melting in propane oxidation was first demonstrated with path-finder experiment (physical mixture of $K_3V_5O_{14}$ and V/SBA-15) in which the activity of supported vanadia catalyst sharply decreased due to the wetting behaviour of the potassium-vanadate. The coverage of active

site(s) by the melt was seen. NAP-NEXAFS was further conducted as a complimentary technique for Raman spectroscopy and as well as to validate the possible role of melting. The spectral features of V L_3-edge NEXAFS of activated K/V=0.6 catalyst varied in terms of the intensity of the peaks at ~516.2 eV and ~517.6 eV upon heating in propane oxidation. The spectra suggests the monomeric/polymeric vanadium oxide species as well as potassium-vanadate exist in activated catalyst which is in agreement with the Raman findings. Based on a fitting model in Athena (Demeter) software, the contribution from alkali-vanadate species increases while the contribution from the dispersed vanadium oxide species decreases upon melting. K L-edge proofed an increase in potassium content over the surface upon heating in propane oxidation. Together with path-finder experiment and spectroscopy techniques, the inhibition effect of melting on the activity of surface vanadium oxide species were explained. Analogous behaviour was found in Rb- and Cs- containing catalysts in terms of at least a change in spectral shape of V L_3-edge.

Overall, the melting correlates with a drop in activity and an increase in selectivity to propylene in the oxidative dehydrogenation of propane. This is a general phenomenon for K-, Rb-, and Cs- containing catalysts, but not for Li- and Na- containing counterparts that do not exhibit melting. The alkali-vanadate phase itself not active for propane oxidation however it has a great impact on reaction kinetics. The mobility of alkali vanadate phase(s) due to melting inhibits the reactivity of surface vanadium oxide species. These results deepen our understanding on the influence of strain on the activity of surface VO_x species in propane oxidation.

Zusammenfassung

Die Zugabe von Additiven zu geträgerten Vanadiumoxid basierten Katalysatoren wurde intensiv mit dem Ziel untersucht, die Katalysatorleistung bei der oxidativen Dehydrierung von Propan zu verbessern. Es hat sich gezeigt, dass Alkalizusätze die Dispersion von Vanadiumoxid sowie die Säure-Base- und Redox-Eigenschaften von Vanadiumoxid-Trägerverbindungen beeinflussen. Gebildete Alkalivanadate können Schmelztemperaturen im Bereich der Reaktionstemperaturen der Propanoxidation aufweisen (z. B. schmilzt $K_3V_5O_{14}$ bei 410 °C). Über die Bildung von gemischten Alkali-Vanadiumoxid-Verbindungen und den Einfluss des Schmelzens der Alkali-Vanadat-Oberflächenphase(n) auf die katalytischen Eigenschaften von alkalihaltigen Vanadiumoxid-Trägerkatalysatoren ist jedoch wenig bekannt.

Um den möglichen Einfluss des Schmelzens der Alkali-Vanadat-Phase(n) zu untersuchen, wurde eine Reihe von A/V-Katalysatoren auf Siliciumdioxidträger (A: Alkali, d.h. Li, Na, K, Rb und Cs), mit einer systematischen Variation des A:V-Verhältnisse, synthetisiert und in der Propan-Oxidationsreaktion getestet. Die Katalysatoren wurden durch Verschmelzung von Alkalicarbonaten, V_2O_5 und SiO_2 hergestellt (wobei der Gesamtgehalt an Metalloxiden bei 10 Gew.-% lag). Die Katalysatorvorläufer wurden in situ aktiviert ($21O_2/79N_2$ bei 520°C) und in einem achtfachen Parallelreaktor getestet ($C_3H_8/O_2/N_2$=7.5/7.5/85). Flussmittel wie K-, Rb- und Cs- senken die Schmelztemperaturen von V_xO_y-Katalysatoren auf Siliziumdioxidträgern in dem Temperaturbereich, in dem die Propanoxidationsreaktion untersucht wurde. Mit Li- und Na- versetzte Katalysatoren haben jedoch viel höhere Schmelztemperaturen, so dass die Katalysatoren während der Reaktion fest bleiben. Sowohl die katalytischen Tests in einem Festbettreaktor als auch die „Differential Scanning Calorimetry“ zeigten eine drastische Veränderung der katalytischen Leistung, wenn es zu einem Schmelzen kommt. Die Aktivität sinkt und die Selektivität steigt deutlich, wenn die geträgerten V-A-Oxidschicht und/oder segregierte kristalline Alkalivanadatphasen schmelzen. Die strukturellen Gründe für die drastische Veränderung der katalytischen Eigenschaften wurden mittels spektroskopischen Untersuchungen an den Materialien unter Reaktionsbedingungen untersucht. Eine detaillierte Charakterisierung wurde für den K/V=0.6-Katalysator auf Siliziumdioxidträger durchgeführt, da dieser Katalysator neben dem amorphen SiO_2 nur eine kristalline Phase ($K_3V_5O_{14}$) aufwies, wie durch XRD festgestellt wurde.

Operando-Raman-Spektroskopie zeigte strukturellen Veränderungen von $K_3V_5O_{14}$ (532-nm-Laser) aufgrund des inkongruenten Schmelzens und die Auswirkung des Schmelzen auf die Dispersion der Vanadiumoxid-Spezies (266-nm-Laser). Das Schmelzen initiierte die Bildung

oligomerer Vanadiumoxid-Spezies bereits in der In-situ-Aktivierungsphase. Spektrale Bestandteile der V L_3-Kante (NEXAFS) des aktivierten K/V=0.6-Katalysators variieren in Bezug auf die Intensität der Peaks bei ~516.2 eV und ~517.6 eV beim Erhitzen in der Propanoxidation. Die Spektren deuten darauf hin, dass im aktivierten Katalysator sowohl monomere/polymere Vanadiumoxid-Spezies als auch Alkalivanadate vorhanden sind, was mit den Raman-Ergebnissen übereinstimmt. Basierend auf einem Fit-Modell in der Software Athena (Demeter), kann gezeigt werden das der Anteil an Alkalivanadat-Spezies zu nimmt, während der Anteil an dispergierten Vanadiumoxid-Spezies beim Schmelzen abnimmt. Mittels „Pathfinder"-Experiment und der angewendeten Spektroskopie konnte die hemmende Wirkung des Schmelzens auf die Aktivität der Vanadiumoxid-Spezies an der Oberfläche aufgeklärt werden. Ein analoges Verhalten wurde bei Rb- und Cs-haltigen Katalysatoren festgestellt, zumindest in Form einer Änderung der spektralen Form der V L_3-Kante.

Insgesamt korreliert das Schmelzen mit einer Abnahme der Aktivität und einer Zunahme der Selektivität gegenüber Propylen bei der oxidativen Dehydrierung von Propan. Dies ist ein allgemeines Phänomen für K-, Rb- und Cs-haltige Katalysatoren, nicht aber für Li- und Na-haltige Gegenstücke, die kein Schmelzen aufweisen. Die Alkali-Vanadat-Phase selbst ist für die Propanoxidation nicht aktiv, hat jedoch aber einen großen Einfluss auf die Reaktionskinetik. Die Mobilität der geschmolzenen Alkalivanadat-Phase(n) hemmt die Reaktivität der Vanadiumoxid-Spezies an der Oberfläche. Es zeigt sich das nicht nur die Bildung einer aktiver Spezies notwendig ist, sondern auch die Umgebung der aktiven Spezies kontrolliert werden muss. Diese Ergebnisse vertiefen unser Verständnis des Einflusses der Verspannung der Oberflächen-VO_x-Spezies auf die Aktivität bei der Propanoxidation.

Acknowledgements

First of all, I express my sincere appreciation to Prof. Dr. Robert Schlögl, director of the Department of Inorganic Chemistry (AC) at the Fritz-Haber Institute of the Max Planck Society for giving me an opportunity to perform my PhD work in his prestigious department. His continuous guidance, support, inspiring talks and lectures, critical but educatory reviews taught me how to be a "good scientist". The way how he has been creating knowledge showed me to "think" and "criticize" every single detail carefully. Thanks to his scientific vision and precious advices throughout my PhD, I consider myself to be extremely privileged to have been one of his students under the department of AC.

I would also like to express my special appreciation and thanks to Dr. Annette Trunschke, group leader of the Catalysis with Oxides who welcomed me to her research group and let me start living almost five years in beautiful Berlin. Dr. Trunschke, you have been a tremendous mentor for me. I benefited enormously for her excellence as a teacher and as a researcher. I thank to her for encouraging my research and for supporting me to grow as a research scientist. Your advices on my research as well as on my future career are precious.

I am also deeply grateful to Dr. Frank Rosowski, a director of the BasCat-UniSysCat BASF Joint Lab at Technical University Berlin, for his supervision, support, and discussions during our BasCat meetings which advanced my work.

I gratefully acknowledge my defense committee members, Prof. Robert Schlögl, Prof. Reinhard Schomäcker, and Prof. Klaus Rademann for reviewing my work and finally letting my defense happens. I also thank to Prof. Maria Andrea Mroginski for leading my defense as a chair.

I particularly thank to Dr. Michael Hävecker for all his time that he spent in teaching and supporting my very first synchrotron experience and discussing the various fundamental aspects of the X-ray absorption techniques. Without his scientific input, this PhD thesis would not be completed in a comprehensive way. I hope to continue doing research with him.

I specially thank to Dr. Pierre Kube for his enormous contribution through my work in terms of introducing me to my "one and only" reactor, *namely*, "Grimsel 2", helping me on catalysis and reaction kinetics as well as overcome with any scientific and technical difficulties. His braveness, problem-solver character, and creative thinking at work widen my scientific view. More than this, I appreciate that he constantly encouraged me to believe in science that I am doing.

I am thankful to Dr. Andrey Tarasov for sharing his expertise on thermoanalytics and helping me on evaluating the experiments. I am also very thankful to Dr. Yuanqing Wang and Dr. Gregory Huff that they introduced me Raman spectroscopy which answered critical questions in this thesis as well as gave me a new skill. I am also deeply grateful for the time and effort done by Dr. Spencer Carey and Dr. Jinhu Dong regarding long Bessy measurements.

I sincerely thank to Dr. Gregor Koch for his support and teaching different experimental setups in chemical laboratory. In addition, I thank to him that he shared the knowledge patiently and willingly, and particularly gave always valuable feedbacks after each of my scientific talks that helped to make it better in next.

I owe a sincere gratitude to my colleagues who conduct routine measurements and support for scientific and technical needs, in alphabetic order: Danail Ivanov, Daniel Brennecke, Frank Girgsdies, Jasmin Allan, Maike Hashagen, Olaf Timpe, and Sven Richter. I also would like to thank our administration team, Sibylle Hartung, Katherina Jäger, and Dorothea Damm for their friendly communication and constant support. Within this, I specially thank to team BasCat and dear Ema for their friendly welcome as well as their scientific inputs during regular BasCat meetings. I would like to also thank to some former colleagues who helped me very much in the very beginning of my PhD: Hamideh, Marie, Elisabeth, Maximilian, and Leon. I also thank to my friends who joined our group lately: Daniel Delgado, Clara, Baris, and Nils for their valuable feedback and support at the final stage of my work. I specially thank to Charles Pare, whom I supervised during his master internship. Thanks to his enthusiasm, I did not only guide him but also I learn from him.

I wish to thank to my PhD fellows that we share the same fate; Giulia, Frederic, Samuel, and Liseth. Thank you for your endless support especially right after each PhD day and as well as for your kind friendship. Without this, the time would not be that pleasant.

I express my endless thanks to one of my former colleague, Rania Hanna, who is more than only a colleague for me. I have not only learned engineering skills from her. I have learned much more than this. I have learned the meaning of strength, faith, justice, respect, and kindness to any living creature. Thank you for teaching me the way how I can protect “the good” inside me independently from the surrounding.

Last but not least I thank to my parents, my brother, and my partner for loving, believing and empowering me. I know they are as excited as I am about my degree. Thank you very much for being there when I need support the most.

List of Contents

List of Figures

List of Tables

List of Supporting Figures

List of Supporting Tables

List of Abbreviations

General

ODH	Oxidative dehydrogenation
ODHP	Oxidative dehydrogenation of propane
A	Alkali (Li, Na, K, Rb, and Cs)

Techniques

XRD	X.-ray Diffraction
XPS	X-ray Photoelectron Spectroscopy
NEXAFS	Near- Edge X.-ray Absorption Fine Structure
NAP	Near ambient pressure
XRF	X-ray Fluorescence
SEM	Scanning Electron Microscopy
STEM/TEM	Scanning Transmission Electron Microscopy
HRTEM	High Resolution Transmission Electron Microscopy
EDX	Energy Dispersive X-ray Spectroscopy
DFT	Density Functional Theory
BET	Brunauer-Emmet- Teller
TG	Thermogravimetric analysis
TA	Thermal analysis
DTA	Differential Thermal Analysis
DSC	Differential Scanning Calorimetry
GC	Gas chromatography
MS	Mass spectroscopy
FID	Flame Ionization Detector
TCD	Thermal Conductivity Detector

Symbols

τ	Contact time ($g \cdot s \cdot ml^{-1}$)
GHSV	Gas hourly space velocity (h^{-1})
β	Ramping rate (Kpm)
C_p	Specific thermal capacity (J/mol·K)
Q	Total heat flow(J)
N	Number of molecules (mol)
ΔH	Reaction enthalpy (J/mol)
HF	Calculated heat flow (J/min/g)
r	Formation rate (mol/min/g)
t	Time
T^{onset}	Onset temperature measured by DSC (°C)

T^{peak}	Peak temperature measured by DSC (°C)
X	Activity (%)
S	Selectivity (%)
λ	Wavelength
m	Mass
F	Flow rate (ml/min)
wt	Weight
at	Atomic
ρ	Density ($g \cdot cm^{-3}$)
W	Catalyst mass (g)
h	Plank's constant (6.63×10^{-34} $m^2 \cdot kg/s$)
v	frequency

CHAPTER 1

1. Introduction

Propylene is one of the most important commodity chemical in the chemical industry since it is used in the production of various chemicals (Figure 1.1). The oxidative dehydrogenation (ODH) of propane to propylene is a promising technology to obtain a high product yield and to avoid the formation of undesired products such as CO and CO_2. This is challenging due to the complexity of the reaction which occurs by a parallel and consecutive reaction scheme.

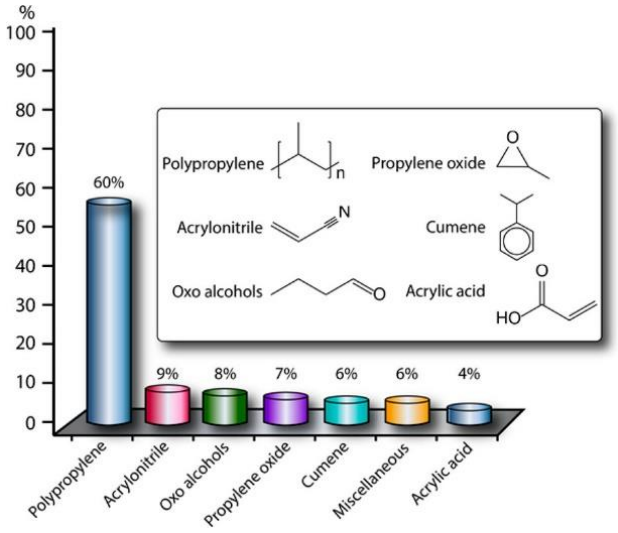

Figure 1.1. Main propylene derivatives (adapted from ref [1])

The effectiveness of the reaction is linked to the effectiveness of the catalyst. The effective catalyst must accelerate the reaction pathway towards the desired product while hindering the nonselective routes [2-4]. The design of such catalyst which is active for alkane conversion and selective for desired product is difficult but the success will ultimately determine the economical actions. There are several issues which limits the understanding of the ODH processes. Since a catalyst is a dynamic system, meaning that the active surface layer may be only formed under operation conditions [3], an individual property of a catalyst cannot predict the catalytic performance. Therefore, experiments under *in situ* and *operando* conditions are applied.

In case of ODH of propane, vanadium oxide-based catalysts are known to be active [5]. The importance of vanadium-containing catalysts in the chemical industry as well as in scientific research is outlined in the next **Section 1.1.** In particular, vanadium oxide species forming extended 2D layers on the surface have been efficiently employed in the ODH of propane [6].

Section 1.2 presents the vanadia catalysts over various supports as they are studied in ODH of propane. This chapter deals with how dependent the structure of vanadia species on the type of support and the loading.

Furthermore, alkali metal additions are known to have a strong influence on the catalytic properties[7] (**Section 1.3**). For instance, alkali metal additives such as Li-, K-, and Rb- on supported V_2O_5 decrease the activity while increases the selectivity to propylene. This is attributed to the modification in redox and acid-base properties[7]. The formation of mixed alkali-vanadium oxide compounds are expected upon alkali adding. It cannot be excluded that alkali vanadate phases formed at least locally whose melting temperatures are in the range of the reaction temperature of propane oxidation. However, there is an only a little known about the formation of these phases. The discussion is in **Section 1.4** in a detail.

This work focuses on the investigation on the impact of the melting of alkali-vanadate phase(s) in oxidative dehydrogenation of propane. Silica supported A/V (A: Li, Na, K, Rb, and Cs) catalysts with various A: V ratio were synthesized and tested. Catalysts were examined by techniques that characterize surface dynamics under operando conditions **(Section 1.5)**.

1.1. Vanadium Oxide Catalysts in Heterogeneous Catalysis

In heterogeneous catalysis, vanadium-containing catalysts have been used as selective oxidation catalysts in the chemical industry as well as for fundamental studies. A great number of scientific research have been conducted to determine the molecular and electronic structures of vanadium oxides and their relationships to catalytic performance. The main key factors in heterogeneous catalysis were discussed based on a “seven pillars” proposed by Robert K. Grasselli [8] which are site isolation, metal-oxygen bond strength, redox properties, host structure, the nature of surface oxygen species, phase cooperation and multifunctionality.

Following chapters present the status of vanadium-containing catalysts used in the industry as well as at the research level.

1.1.1. Vanadium-containing catalysts in the Chemical Industry

Vanadium (V) is a transition metal located in group 5 (group VB) of the periodic table. The metallic form of V has an electron configuration of [Ar] $3d^3$ $4s^2$ which allows for 4 common oxidation states of vanadium: V(II), V(III), V(IV), and V(V) [9]. It is the 5^{th} most abundant transition metal in soil [10]. It is an important component for several technological applications

in *e.g.,* aerospace industry, fabrication of ceramics and manufacturing of smart windows and microelectronic devices [11].

Vanadium oxides are some of the most extensively studied components of oxidation catalysts. Table 1.1 summarizes some important industrial catalytic processes catalyzed efficiently by vanadium-containing oxides. These processes are used in manufacturing important chemicals *e.g.* oxidation of SO_2 to SO_3 for production of sulfuric acid [12], oxidation of benzene and butane to maleic anhydride [13, 14], o-xylene to phthalic anhydride [7], the oxidation of n-pentane to maleic and phthalic anhydride [15]. Moreover, vanadia-based catalysts have been used in selective catalytic reduction (SCR) reaction of nitric oxides by ammonia for removing NO_x pollution. Industrially, both bulk oxides of transition metals (such as vanadium, molybdenum, tungsten) [16-19] or zeolites [17, 20] and metal oxides supported on porous materials (such as titanium oxide, alumina, and silica) have been used as catalyst. Recently, it has been reported that W-substituted vanadium oxide catalysts for NH_3-SCR shows >99% (dry) and >~93% (wet) NO conversion at 150°C [21]. Compared to a conventional titania-supported vanadia, tungsten-substituted vanadia catalyst led to much higher NO conversion. The highest activity was attributed to the increase in number of acid sites and the high redox capability of surface V species.

Table 1.1. Some industrial catalytic processes catalyzed by vanadia-containing catalysts

Main reactant	Reaction	Main product	Catalyst	Reference
SO_2	Oxidation (O_2 or air)	SO_3	V_2O_5 (K)(Na)(Cs)	[12, 22]
Naphthalene		Phthalic anhydride	MoV	[23, 24]
o-xylene		Phthalic anhydride	VTiO	[24, 25]
NO_x	Selective Reduction	$N_2 + H_2O$	V(W)/Ti	[16, 21, 26, 27]
	Chemical Scrubbing	-	V in HNO_3 solution	[27]
Ethane	Selective oxidation	Acetic acid	MoVNbO+Pd/Al_2O_3	[28, 29]
Benzene		Maleic anhydride	V_2O_5 + MoO_3	[30-32]
n-butane		Maleic anhydride	VPO	[32-34]
Ethylene		Acetaldehyde	V_2O_5+$PdCl_2$	[28]
Acrolein		Acrylic acid	MoVWO	[35]
Propane (propylene)	Ammoxidation	Acrylonitrile	VSb(Sn)(Ti)(Al)O	[36-39]
Propylene		Acrylonitrile	FeSbO(Te)(V)(W)	[40]
o-xylene		Phthalonitrile	VSbWCr	[24, 41]
o-xylene	Ammonolysis	Phthalonitrile	$VMoO^{PP}$	[24]

PP: pilot plant

The V_2O_5 catalyst has been industrially used for producing sulfuric acid *via* SO_2 oxidation [42-46], patented by BASF SE [22]. Promoters such as K [42, 43, 47-49], Na [42, 47-49], and Cs

[42, 47, 50] have been used to lower the melting point of the catalyst. With the addition of alkali, alkali pyrosulfate, *i.e.*, $M_2S_2O_7$ (M=alkali) melt is formed, which is a solvent for V_2O_5. This solution has sufficient mobility to allow the catalytic surface to be renewed constantly [43]. Another role of alkali addition*, e.g.,* Cs has been reported as a stabilizing factor on vanadium in its V^V state and preventing V^{IV} formation at low temperature [42]. Different vanadium complexes have been found to be present in the molten active phase of industrial SO_2 oxidation catalysis (Figure 1.2).

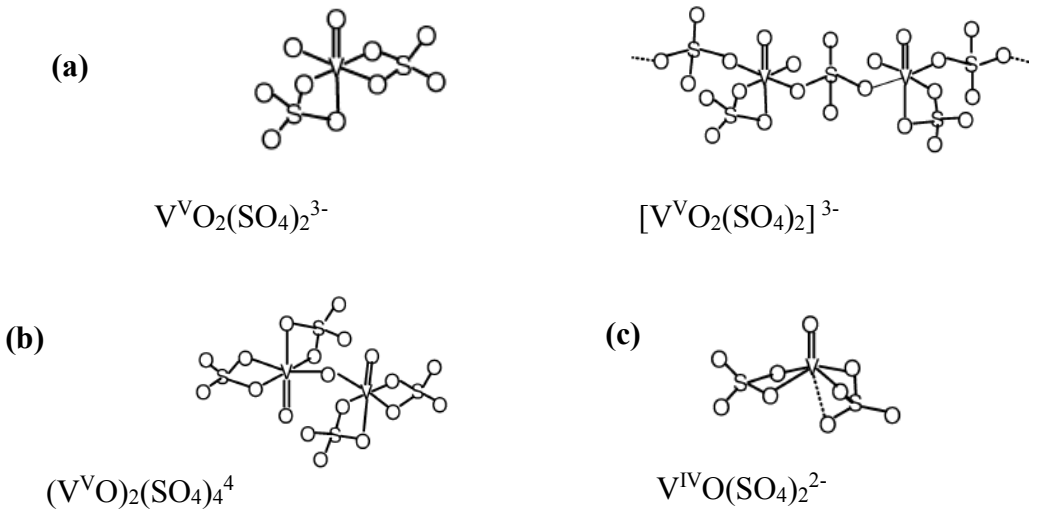

Figure 1.2. Possible molecular structures for the V complexes present in industrial SO_2 oxidation molten salt catalysts [48]

Another important vanadium oxide catalyst is $(VO_2)P_2O_7$ designated as VPO (Vanadium-Phosphorus-Oxide). It has been used for producing maleic anhydride *via* butane partial oxidation [51-54]. Since the VPO precursor systems are composed of several phosphate phases (defined as V (IV), V (V)), the investigation of active sites has always been challenging. A general hypothesis is that vanadyl pyrophosphate (VPP, *i.e.* V (IV)) is a support for some other VPO phase, which is active for butane oxidation [51, 53]. Conte *et al.* [55] showed that the metastable phase ω-$VOPO_4$ is very sensitive to many reactants and products of butane oxidation, which was analyzed by in-situ XRD, Raman and EPR. It has been found out the ω-$VOPO_4$ phase rapidly transforms to δ-$VOPO_4$ in the presence of reactants, hence it is important for the formation of commercial catalysts.

With the aim to enhance selectivity to maleic anhydride, addition of metal promoters were commonly studied in the past [56]. For instance, promoters such as Zn, Bi, Cu, and Li [57] and Co, Cd, and Ni [58] were studied and patented in the 1980s. Guliants *et al*. [59] studied Nb-,

Si-, Ti-, V-, and Zr- promoted bulk VPO systems for *n*-butane oxidation to maleic anhydride. They have shown that the strength of Lewis acidityof the promoter cations impacts the selectivity to maleic anhydride. Moreover, Mo additives have also been considered high-efficient promoters [60, 61]. He *et al*., [62] has shown that Mo-promoted VPP catalysts have much higher activity than those without Mo promoter. The effect was attributed to the existence of different Mo species, which result in higher crystallinity and affect the redox characteristic.

Similar to *n*-butane oxidation, the process of propane ammoxidation has been also challenging. It is an eight electron oxidation reaction which requires a complex catalyst. Many catalysts have been tested and the most effective of them are either antimonates or molybdates. Among antimonite family, VSbM where M can be different dopants such as W, Te, Sn, Bi, and Ti have been frequently studied. The best acrylonitrile yield (40%) was obtained using supported system *i.e.* $VSbWO_x/SiO_2$-Al_2O_3 [63]. The molybdate family is represented as VMoMO where M is mostly Bi or Te. The highest acrylonitrile yield was found on catalyst having the empirical formula $MoV_{0.3}Te_{0.23}Nb_{0.12}O_x$ [64, 65].

Although these vanadium-containing catalysts are widely used in the chemical industry, an intense research is taking place to understand how these catalysts work and to develop better catalysts for the oxidation reactions. The vanadium-containing catalysts in oxidation of light alkanes (C_2-C_4) at research level is presented in the following chapter.

1.1.2. Vanadium-containing Catalysts at Research Level

More recently, the research on V-containing catalysts has been focused more toward the oxidative dehydrogenation (ODH) of lower alkanes (C_2-C_4) into olefins as well as selective oxidation to form oxygenated products (aldehydes, anhydrides, carboxylic acid) [1, 4, 66-72]. Table 1.2 shows some examples of the heterogeneous oxidation reactions catalyzed by vanadia as well as vanadia-including mixed metal oxide catalysts.

In the case of ethane oxidative dehydrogenation for producing ethylene, transition metal oxides (V, Te, Mo, Nb, Sn, Ni, Co, Ti, Ga, and Ta) [73-75], a rare-earth-metal oxides (La_2O, Sm_2O_3, CeO_2, and Pr_6O_{11}) [76-78], supported alkali oxides (Li_2O/MgO) [79], supported alkali chlorides (LiCl, KCl, Li-Na-Cl, Li-K-Cl supported on Dy_2O_3-promoted MgO) [80], and transition-metal-supported zeolites (Ni, Cu and Fe/Y-zeolites) have been extensively studied (Table 2). Among them, Ni-O have been found suitable due to the low operating conditions (300-400°C). NiO itself is very reactive towards ethane, however it exhibits low selectivity to the ethylene. Selectivity have been improved by supporting NiO on an oxide support (Al_2O_3, ZrO2) or

addition of second metal cations such as Nb, Sn, Mo, Mg, Ta and Ga. Another group of interesting catalysts are supported liquid-phase catalysts (SLC) for oxidative dehydrogenation of ethane. As seen in Table 2, Li chlorides supported on Dy_2O_3-promoted MgO (Li-MD) gives 62 % ethylene yield. It is the most active, but less selective compared to Na, and K promoters. However, this requires high reaction temperatures (around 600°C). It is particularly interesting to note that catalysts who show melting have higher selectivity to ethylene. Although these systems are highly active, the main problem is the catalyst stability. The high catalyst performance can be maintained only as long as the halogen is not removed in the form of HCl, from the catalytically active phase.

Vanadium oxide-based catalysts [81-84] and mixed oxides (MoVTeNb) [85-88] have been also studied. However, the ethylene productivity led to be low and considerable amounts of acetic acid, acetaldehyde were possible to be formed [89, 90]. Nieto *et al.* applied a heat treatment at very high temperature (550-750°C) to the hydrothermally synthesized MoVTeNbO catalysts, and they obtained high ethane activity selectivity to ethylene (71% ethylene yield at 400°C) at low temperatures (340-400°C). F- or Cl-doped perovskite-type halo-oxides (La/Sr/Fe/O/(F)(Cl)) were found good and durable (40 h) catalysts for ODH of ethane. Reaction occurred at 660°C and the highest ethylene yield was found as 57.6 % with $La_{0.6}Sr_{0.4}FeO_{3-0.103}Cl_{0.16.}$ A recent review published by Gartner *et al*., summarizes the past and current situation of ethane oxidation [67].

For butane oxidation, only the selective oxidation of n-butane to maleic anhydride over vanadyl pyrophosphate (VPP) has been successfully commercialized (see Table 1). However, there has been long-standing interest in understanding the function of VPP catalysts by research groups seeking to improve VPP catalyst performance or design other alkane oxidation catalysts [34, 55, 91-94]. Hence, several studies have been conducted to understand the working mode of VPP catalyst. For instance, microwave cavity perturbation technique (MCPT) has been applied to probe changes in electronic structure of a working catalyst which is linked to the catalytic function. Eichelbaum *et al*. [95] proved the sensitivity of the MCPT technique as an indicator for the redox stability of catalysts. Complementary techniques such as Raman spectroscopy, in-situ NEXAFS and TPR/O showed that the redox activity of vanadium and the oxygen exchange was restricted to the surface region of the catalyst. Moreover, correlations between the dynamic microwave conductivity and the presence of bulk defects and electronic states in the band gap of α-V_2O_5 were studied by Heine *et al*. [96]. Based on a perfect agreement between the time-dependent response of the absorption at 1.55 eV and the conductivity under oxidizing atmosphere, a correlation between the formation of point defects (and V 3d band gap states)

and the conductivity had been proven. Later Wernbacher *et al.* [97] observed the similar changes in the MCPT conductivity of V_2O_5 supported by in-situ UV-vis which allowed correlations between the catalyst performance for the selective oxidation of n-butane maleic anhydride and the charge carrier dynamics.

Table 1.2. Heterogeneous oxidation reactions catalyzed by vanadia-containing and vanadia-free catalysts at research level

Alkane	Reaction	Products	Catalyst	Yield, % (C_3H_6)	Reference
Ethane	ODH	Ethylene	Ni-Nb-O	46	[74]
			Li_2O/MgO	30	[79]
			Li- Dy_2O_3/MgO	62	[80]
			Li- Na- Dy_2O_3/MgO	40	[80]
			Li-K- Dy_2O_3/MgO	17	[80]
			Ni-W-O	21	[98]
			VMgNi	2.0	[82]
			CoVAPO-5	17.9	[99]
			MgVAPO-5	17.1	[100]
			MoVTeNbO	27	[87]
			MoVTeNbO	71	[101]
			LaSrFeO(F)(Cl)	57.6	[102]
			MoVSbO	38	[103]
			MoV	25	[104]
			V_2O_5/γ-Al	20.0	[105]
			V/Al	24.2	[106]
			VWO/Al	14.4	[107]
	Selective Oxidation	Acetic acid	MoVNb	7.7	[108]
			MoVAlTi	1.2	[109]
			MoVNbO/Ti	1.9	[110]
			PdMoVNbO/Ti	4.0	[110]
			$NbPMoV_{pyr}$	0.8	[111]
		Acetaldehyde	KVO_3/Si	0.4	[112]
			KVO_3/Si	0.8	[113]
			$RbVO_3$/Si	0.5	[113]
			Cs-V/SiO_2	1.3	[114]
Propane	ODH	Propylene	V_2O_5	1.6	[115]
			V_2O_5	4.0	[116]
			V-Mg-O	11.3[116]	[116-120]
			V-Mg-O	13.8	[121]
			V-Ga-O	7.7	[121]
			Li-MD	14	[80]
			Li-Na-MD	10.4	[80]
			Li-K-MD	5	[80]
			V-Nb-O	2.0	[122]
			V_2O_5/Nb_2O_5	3.6	[122]
			MgAlVO (LDH)	6.0	[123, 124]
			MoVTe	2.6	[125]

Table 1.2. (cont.)

			MoV	1.6	[125]
			VMgGa (Mo)(Fe)	8.0	[121]
			V/Zr	12.1	[126]
			VSb/Ti	10.4	[127]
			VSb/Zr	10.0	[128]
			MoNbO	5.0	[129]
			VNbO	4.3	[129]
			Co-POV	1.1	[130]
			BiVMoO	0.9	[72]
			CsHPVMoO	9.3	[131]
	Selective Oxidation	Propylene and acrylic acid	VPP	34.3	[92]
		Acrylic acid	MoVTeNbO	2.1	[132]
			MoVTeO	17.9	[133]
			MoVTeO	12.6	[125]
			MoVTeO	16.8	[134]
			MoVTeNbO	20.8	[134]
			MoVTeNbO	18.0	[135]
			MoVTeNbO	20.8	[136]
		Acetic acid	MoV	5.5	[134]
			MoVTeO	5.1	[136]
	Ammoxidation	Acrylonitrile	MoVTeNbO	-	[137]
			VSb(Sn)O	12.0	[28, 138]
			V(Cr)NbSnSbO	5.0	[139-141]
***n*-butane**	ODH	Butylene	V-Mg-O	15.7	[81, 142-146]
			Ni-V-SbO	16.4	[147]
			Sn-V-Sb	13.6	[147]
			MoV	8.0	[147]
			LaV (Ti)	2.5	[148]
		1,3-butadiene	Mo-VMgO	30	[143]
			V/Al	1.1	[149]
	Selective oxidation	Maleic anhydride	MoVTeNbO	20.1	[150]
			MoTeNb	13.9	[150]
			$VWOPO_4$	14.0	[94]
			VPO	38.8	[150]
			(Co)VPO	28.0	[91, 151]
			VPO	24.0	[152]

It is known that VPP is very dynamic material and can form different metastable phases under reaction conditions as mentioned before. Heine *et al.* [93] studied the changes in the surface structure and the function of each component in the reaction with the near-edge X-ray absorption fine structure (NEXAFS) setup. The authors investigated the vanadium L-edges of polycrystalline VPP in the soft- X-ray range at pressures up to 1 bar and temperatures up to 400°C. Results obtained at different temperatures showed that the oxidation state of vanadium ions on the surface were changing. However, the general shapes of V L_3-edge spectra were similar, which indicated that the vanadium coordination and hence the geometric structure was

not affected by the total pressure. More interestingly, the regeneration of V=O species after transformation into V-OH groups is found to be critical for maintaining catalytic cycle. Consequently, this was a limiting factor for re-oxidation kinetics.

In the oxidative dehydrogenation of propane using vanadia-including catalysts the propylene yield varies in between 1 and 20% (Table 2). In general, higher propylene yield was obtained using an oxide support (Al_2O_3, ZrO_2, TiO_2 and etc.). While V_2O_5 itself was found not to be a good catalytic system for ODH of propane [153], mesoporous V-Mg-O mixed oxides have yielded better olefin selectivity in ODH of propane [7, 117, 119, 121, 154]. Balderas-Tapia *et al.*[117] found that magnesium incorporation with vanadium inhibits the formation of V_2O_5. Moreover TPR results showed that an $Mg_3V_2O_8$ phase containing isolated VO_4 tetrahedral species was formed with greater reducibility which may favor enhancement of the catalytic activity of propane dehydrogenation. More recently, Valverde *et al.*[120] studied V-Mg-Al catalysts derived from hydrotalcite for oxidative dehydrogenation of propane and they found high propylene yield in particularly with $Mg_2V_2O_7$, $MgV_xSb_yO_z$, or orthovanadate on hydrotalcite catalysts. The catalysts reached up to 80% selectivity to propylene at 400°C with an excess of oxygen. Although the system does not contain vanadium, it is noteworthy to mention that molten alkali metal (Li, Na, K) chlorides supported on Dy_2O_3/MgO showed promising results for the oxidative dehydrogenation of propane (as well as ethane) [80]. Especially molten LiCl supported on Dy_2O_3/MgO (Li-MD) was found as exceptional catalyst (70% propylene selectivity). Authors postulated that the low concentration of accessible Lewis acid sites (due to alkali) and the high mobility of cations and anions within the melt were main reasons which contributes to the high selectivity to olefins.

For selective oxidation of propane, Mo-V-O based complex mixed metal oxides have been extensively studied. Ueda *et al.* [125, 134] studied the hydrothermally synthesized MoV-(Te)(Nb) oxides for selective oxidation of propane for producing acrylic acid, acetone and acetic acid. For instance, at low temperature (380°C), the MoVTeNbO catalyst yielded in 33.4 % propane conversion and 62.4 % selectivity to acrylic acid [134].

Mo-V-Te-Nb M1 oxide (multi-oxide system) is widely studied mixed metal oxide catalyst system in oxidation reactions. The catalyst developed by Mitsubishi Chemicals can achieve 50% acrylic acid yield [155]. A significant amount of work has been reported about these multi-oxide system. The impact of preparation methods, the calcination conditions, reaction mechanism and kinetics, a role of each element and their compositions have been discussed to improve catalytic performance [122, 132, 133, 135, 136, 156-159]. The process of direct

conversion of propane to acrylic acid needs transfer of eight electrons and different quality of oxygen species [71]. Therefore multiple oxidation functionalities of M1 structure [160] provide a suitable base to solve structure-function relationships in a complex oxidation reaction. Recently, Hävecker *et al.* [161] found that the chemical composition of M1 surface substantially changes under reaction conditions. The changes were analyzed by high pressure *in-situ* XPS and correlated with acrylic acid formation. It has been seen that depletion of the catalyst surface in Mo^{6+} and the enrichment in V^{5+} leads to acrylic acid formation. Although there is still a lack of information on identification of multiple active sites, it has been generally accepted that the V is the key element for the propane activation [162] whereas incorporation of Nb and Te seems to be more responsible for acrylic acid formation [135, 163]. Trunschke *et al.* [159] later reported the unnecessity of Te for selective oxygen insertion based on the observation of significant acrylic acid formation over Te-free M1. However, in this study the reaction temperature was kept low (<300°C).

In oxidation reactions of light alkanes as outlined above, vanadium-containing mixed metal oxides (*e.g*. MoV oxides) have generally resulted in better yield towards oxygenates such as acrolein, acrylic, acid and maleic anhydride whereas supported vanadium-containing catalysts have been more promising for olefin formation.

Overall, all these studies show that there is a large effort done by researchers to improve oxidation reactions, mainly to provide better selectivity. Figure 1.3 clearly shows that studies which focuses on vanadium oxide catalysts have been always in interest in last 25 years. However, specifically for ODH of propane, the best yields obtained are still far from being interesting for industrial implementation.

Nevertheless, catalytic oxidation is a scientific area in which recent advances will have an impact towards improvements in the chemical industry. Based on the studies presented above, without a doubt, vanadia-based catalysts hold great potential for applications in oxidation catalysis.

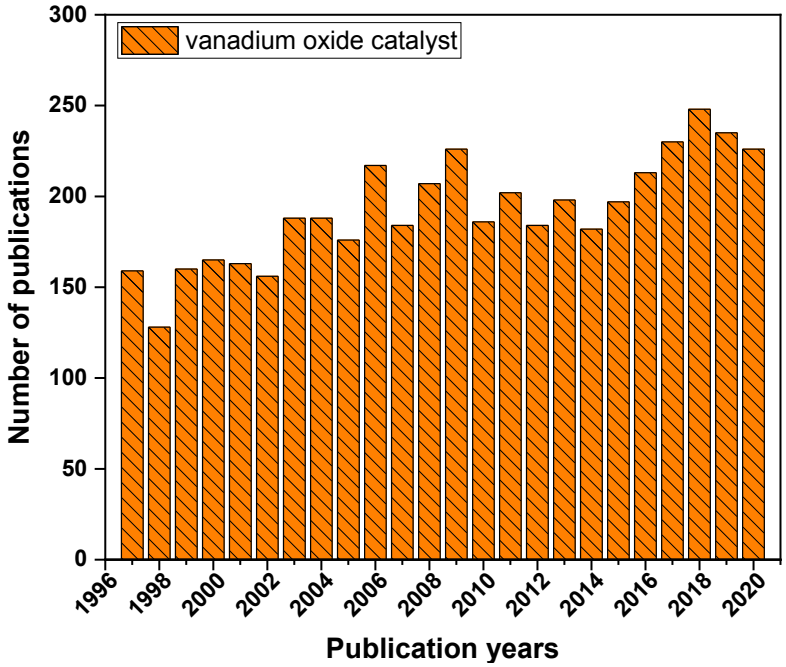

Figure 1.3. Number of publications by year during the last 24 years with "vanadium oxide catalysts" (Note: Records for Topic including vanadium oxide catalyst according to Web of Science) [164]

1.2. Supported Vanadium Oxide Catalysts in Propane Oxidation

Propylene is a very important building block for the petrochemical industry [165]. It is used to produce a wide variety of chemicals including, but not limited to polypropylene, acrylonitrile, and propylene oxide derivatives [165, 166].

Propylene has been primarily manufactured by two methods for many years: (i) steam cracking of naphtha and (ii) catalytic cracking of oil [66, 153, 167]. During these processes, ethylene is also produced in large amounts. Since the demand for propylene has always been higher than the demand for ethylene, research and development has been focused on new production methods for producing propylene while minimizing ethylene production. Now on-purpose-propylene technologies exist for propylene production – including methanol to olefins (MTO) [168], propane dehydrogenation (PDH) [169, 170], and reaction between butylene and ethylene (metathesis, MT) processes [171].

Among these latter processes, catalytic propane dehydrogenation (PDH) is the most direct and selective way for producing propylene if pure propane is available, with hydrogen as an additional valuable product. However, due to the endothermic nature of the reaction, a temperature above 600°C is required. Moreover, a high alkane partial pressure is needed [172-175]. Further difficulties with coke deposition and the associated catalyst deactivation must

also be overcome. The oxidative dehydrogenation (ODH) of propane has been investigated as a promising alternative method over existing technologies. It has many advantages for example, it is exothermic, irreversible, thermodynamically unrestricted, and it minimizes coke deposition and ensures long-term stability of a catalyst [66, 69, 153]. Here, however, total oxidation of propane to CO_2 is a difficult problem to get under control.

Table 1.3 reports the various reaction conditions and experimental results using vanadia catalysts on different supports in propane oxidation. Previously it has been shown that vanadium-containing catalysts are one of the most important catalysts for ODH of light alkanes due to their physical and chemical properties [11, 23]. The ability to change in oxidation state from between V^{3+} and V^{5+} makes vanadium-containing catalysts promising for redox reactions in general. Recently, the research on vanadia catalysts has been focused more to the oxidation of light alkanes (C_2 to C_4) to corresponding olefins and oxygenates [66, 176-178]. In many cases, the properties of vanadia catalysts have been improved by deposition on a support. Based on several different characterization techniques such as Raman, FT-IR, XRD, and UV-vis spectroscopy, four different types of vanadium containing species have been identified in supported vanadia catalysts [179]: (i) isolated surface VO_4 species, (ii) polymeric surface V_xO_y species, (iii) nano-crystalline V_2O_5, and (iv) compounds forming mixed oxides with the support (*e.g.* $Mg_3(VO_4)_2$, $AlVO_4$) or with additives [180-182]. In general, isolated monovanadate species are formed at low V loadings first, later they become oligomeric species and finally they are polymerized up to a monolayer with progressive increasing of V concentration [183]. In ODH of propane, higher propylene productivity has been found with two-dimensional dispersion of vanadate species, while lower propylene productivity has been associated with the existence of three- dimensional vanadate species *e.g.,* bulk V_2O_5 [180, 182, 184, 185]. So the target in the ODH field is to develop oligomeric V_xO_y (2D) species rather than V_2O_5 nanoparticles (3D).While isolated VO_x sites are known to be beneficial for propylene selectivity when vanadia loading is low [179, 186-189], complete coverage of the support surface with high dispersion of vanadia becomes untenable. A high selectivity to propylene can be obtained by fully covering the support with well-dispersed vanadia species. Although there is no general agreement on exactly which species are more active and selective, factors which affect the reactivity of supported vanadia catalysts in ODH of propane are well agreed as follows [66, 187, 190]:

(i) The coordination and dispersion of vanadium oxide species with different cluster sizes, which determine the nature of reaction products.

(ii) The redox properties of a catalyst, which is influenced by the nature of the metal oxide support and the promoters.

(iii) The acid-base character of a catalyst, which strongly influences the adsorption of reactants and desorption of partial oxidation products, thereby shifting the selectivity towards the desired product.

All these factors depend upon the nature of the support, as well as the vanadia loading [191-196]. Therefore, the choice of support is consequently crucial. Supports such as Al_2O_3, ZrO_2, CeO_2, SiO_2, and TiO_2 have been commonly used as oxide supports [106, 126, 185, 197-202]. Obviously, silica supported vanadia catalysts are the most explored among supported vanadia catalysts in oxidative dehydrogenation of propane. Recently, the impact of different synthesis strategies on control of VO_x species on the silica surface investigated by Barman *et al.* [203]. They prepared SiO_2 (Aerosil 200)-supported vanadia catalysts using [V_2O_4 (acac) $_2$] *via* two methods: (i) surface organometallic chemistry (SOMC), and (ii) incipient wetness impregnation (IWI). The catalysts prepared via IWI showed a significant drop in selectivity to propylene from 80 % to 62 by 13% propane conversion with increasing flow, however the propylene selectivity of the catalyst prepared via SOMC is observed to remain constant (66%) up to 12% propane conversion and it slightly drops. Overall, the protocol SOMC offered a high degree of control in the isolation of monomeric VO_x species which yields in higher ODHP performance compared to the catalyst prepared *via* IWI method at comparable vanadia loading. Yield reached as 11% is clearly a breed apart from the majority of SiO_2- supported vanadia catalysts.

The enhancement of catalyst performance has also been achieved on SiO_2 supported vanadia catalyst by diluting the vanadia with an addition of second metal oxide. Zhang *et al.* [204] studied the V-Sb-O/SiO_2 catalyst prepared *via* two step impregnation in ODH of propane. The aim with two step impregnation was to generate highly monomeric VO_x species isolated by Sb atoms. From the comparison of UV-Vis and Raman spectra of VO_x/SiO_2 and V-Sb-O/SiO_2 catalyst, the authors postulated that the amount of aggregated VO_x species in VO_x/SiO_2 catalyst was much higher than that in V-Sb-O/SiO_2 catalyst. Due to the O-Sb-O-V-O-Sb frameworks of V-Sb-O/SiO_2 catalyst, more monomeric VO_x species which are isolated by Sb atoms were obtained. This gives higher activity and selectivity to propylene than that of ODH of propane catalyzed by V/SBA-15, V/MCM-4 and V/MCM-48. With the aim to determining the nature of active sites e.g., for propane ammoxidation, spectroscopic studies (operando-Raman-GC) on V-Sb-O catalysts were conducted by Guerrero-Pérez *et al*. [205] $VSbO_4$ sites were found highly redox active compared to SbO_x and VO_x sites [205, 206]. Fu *et al.* [207] studied the MoV on mesoporous SBA-15 in propane oxidation. In this study, authors observed less activity by

diluting silica supported vanadium oxide species by Mo (*i.e.* $(Si\text{-}O\text{-})_2Mo(=O)_2$). The addition of MoO_x prevented the formation of V-O-V bond in favour of isolated VO_x species. The latter species were found less active than their oligomeric counterparts which is in agreement with the literature where activity of VO_x/SiO_2 increases with increasing V loading [66].

Hamilton *et al.* [208] studied the V-Ti/SBA-15 catalysts and obtained a considerably high productivity which varies between 6 and 9 g propylene per g catalyst at different temperatures. This seems so far the highest propylene productivity met in literature (obtained with the catalyst 4V-13Ti/SBA-15). Authors here took the advantage of highly dispersed, two-dimensional titania species rather than bulk titania. The highly dispersed titania promoted the dispersion of surface vanadia species up to monolayer concentration. The resulting V-Ti mixed monolayer catalyst is found to give maximum propylene productivity which was attributed to the enhanced abundance of V-O-Ti bonds come from VO_x islands that are embedded in a matrix of dispersed titania species as analyzed by UV-Vis, Raman and NEXAFS spectroscopy [208, 209]. More structured supports such as monolith, MCM, MCF, and SBA-15 have been also extensively studied due to their excellent stabilization on active sites [209-213]. Among them, vanadia catalysts supported on mesocellular silica foams (MCF) show much better performance than that of its conventional hexagonally ordered counterparts such as SBA-15, MCM-41 and as well as nonporous silica gel in the ODH of propane. Liu *et al*. [212] reported that V/MCF catalysts are highly active and selective for the ODH of propane. The reason was attributed to the well-defined 3D mesoporous systems and the much large pore diameters of the MCF materials resulting in more favorable conditions for mass transfer in the ODH of propane. That means apart from the active redox sites, internal molecular transport of the catalyst is also important in the gas-phase selective oxidations. Moreover, based on spectroscopic findings by Raman and UV-Vis, vanadium was found to exist mainly in tetrahedral environment within V-MCF catalysts when V content < 4.2 wt. %, indicating a very high surface concentration of isolated or low-polymeric VO_x species could be achieved.

V_2O_5 supported on TiO_2 is one of the most efficient catalysts used in the oxidative dehydrogenation of propane. From Table 1.3, it is seen that the majority of the vanadia supported on TiO_2 catalysts give propylene yield between 5 and 7%. Recently, Kazerooni *et al.*[214] achieved higher propylene yield (7.3%) than previous studies using vanadia/TiO_2 catalyst synthesized *via* atomic layer deposition (ALD) of vanadyl acetylacetonate ($VO(acac)_2$). Compared to the catalysts prepared *via* incipient wetness impregnation (IMP), ALD-prepared catalysts showed superior performance for the low temperature (300°C) ODH of propane. The reason was attributed to the formation of monovanadate sites due to better dispersion of active

phase on support in the ALD catalysts as investigated by O_2-chemisorption and H_2-TPR. However, a difference in the BET surface areas of catalysts prepared via two different synthesis methods have not been discussed ($SA^{ALD} > SA^{IMP}$).

The improved performance was also obtained by utilizing VO_x/TiO_2 catalysts deposited on stainless steel plates and foams in the oxidative dehydrogenation of propane [215, 216]. Löfberg *et al.* [216] investigated the catalytic properties of VO_x/TiO_2 when coated as a thin layer on stainless steel in the ODH of propane. The method simply is to obtain mechanically stable as well as catalytically active and selective coatings prepared by dip-coating plates in titanium oxide suspension followed by grafting of oxovanadium precursor specie. The catalysts prepared by this method showed very similar textural and structural properties compared to the VO_x/TiO_2 powder catalysts. However, the lower activity of plates compared to powders were obtained for the same vanadia composition and the amount of active phase which was probably due to the iron diffusing towards surface and this caused poisoning of vanadate specie. A year later, Essakhi *et al.* [215] improved the system by adding SiO_2 to anchor the active site and to act as a barrier between stainless steel plate and TiO_2 support (*i.e.* $VO_x/TiO_2/SiO_2$ foam). With this, they obtained 10% higher selectivity to propylene on silica-protected VO_x/TiO_2 foam than in the absence of silica and higher by more than 20% than VO_x/SiO_2 powders at any conversion. The authors here underlined the impact of enhanced heat transfer, mass transfer (due to the structured foams) and the amount of loaded catalysts. The thinner the catalyst layer deposited, the higher the catalytic performance was obtained.

Magnesia promoted vanadia catalyst on titania support exhibits one of the most interesting results in terms of propylene yield. Machli *et al.* [217] obtained very promising results with the 5 wt. % of vanadia on titania catalyst promoted with 1.9 wt. % MgO in oxidative dehydrogenation of propane. Compared to the un-promoted catalyst, almost doubled selectivity to propylene was observed. It is known from the literature that alkali or alkaline earth metal addition favors propylene desorption and prevents over oxidation of propylene to undesired carbon oxides [7, 218]. From this point, the changes in acid-base character due to Mg promoter have been consequently correlated with the enhanced selectivity. The authors found out the catalyst 5V-1.9Mg-Ti achieved a propylene productivity at 500°C amounts to 2 g C_3H_6 per g catalyst. The reason was explained as higher acidity (µmol NH_3 ads. /g cat.) and ease of vanadium reduction was attributed to the different vanadia dispersion and stronger vanadia interaction with magnesia and titania. However, the change in acid-base character cannot explain the similar selectivity for catalysts with different magnesia loading. Other structural

properties which occurs due to the difference in deposition sequence and Mg loading may control the selectivity to desired product.

Utilizing a hybrid support where two different oxide supports are used is a promising approach towards the improvement of propylene productivity in ODH of propane. Kazemeini *et al.* [219] deposited V_2O_5 onto the hybrid of the nano-TiO_2 and γ–Al_2O_3 (hydrothermally) and tested for ODH of propane. Propylene, ethylene and CO_x were detected as products. Authors obtained very high activity (35.53%) and propylene selectivity (23.88%) at 500°C. Compared to previous studies where supported vanadia are used, they obtained high propylene yield (10.76 %). The XRD pattern of catalyst showed the rutile and anatase phases which is expected. However, a bulk of the V_2O_5 was formed which is normally not reported as selective for propylene. The existence of V_2O_5 was also confirmed by H_2-TPR where three reduction temperature were detected.

Table 1.3. Supported vanadia catalysts used for ODH of propane

Catalyst	T (°C)	V loading (wt.%)	Feed C_3/O_2/inert	τ (g s ml^{-1})	Productivity (g C_3H_6/ (g_{cat} h))	C_3H_6 yield (%)	Ref.
V_2O_5	500	-	40/20/40	0.12	-	1.69	[115]
Silica supported systems							
V/SiO_2-IWI	525	0.98	15/7.5/77.5	0.3	-	8.4	[203]
V/SiO_2-SOMC	525	1.04	15/7.5/77.5	0.3	-	11	[203]
V/*pro*-SiO_2	490	7	30/15/55	0.11	0.5	2.5	[220]
V/18Ta/*pro*-SiO_2	490	4.5	30/15/55	0.06	1.2	5.4	[220]
V/SiO_2	450	~2.0	30/10/60	1.5	0.16	-	[200]
V/SiO_2	525	10	20/20/60	0.65	0.2	-	[179]
V/SiO_2	550	15	20/20/60	0.1	-	7.8	[177]
V/SiO_2	550	1.8	10/10/80	0.05	0.99	7.3	[212]
V/SiO_2-PEG	450	2.0	1:4	2.4	-	2.8	[176]
V/MCM-41	500	5.3	2:1	0.01-0.04	-	5.8	[221]
V/MCM-41	500	3.1	40/40/20	0.02	-	3.5	[211]
V/MCM-41	500	5.3	40/20/40	0.1	-	3.2	[222]
V/MCM-41	500	2.8	40/20/40	0.04	-	14.9	[223]
V/MCM-41	520	4.63	5/5/90	0.11	-	8.34	[224]
V/MCM-41	550	4.5	10/10/80	0.05	1.81	13.4	[212]
V/MCM-48	500	0.08	40/20/40	0.08	-	17.4	[223]
V/MCF	550	2.8-4.2	10/10/80	0.05	3.77	27.9	[212]
V/MCF	520	4.6	5/5/90	0.11	-	6.37	[224]
V/SBA-15	600	11	2:1	0.8	-	8.2	[225]
V/SBA-15	550	2.8	10/10/80	0.05	2.15	15.9	[212]
V/SBA-15	520	4.18	5/5/90	0.11	-	6.7	[224]
V/SBA-15	500	4.0	2:1	0.01-0.04	-	5.6	[221]
V/SBA-15	400	6.0	10/5/85	1.34	-	3.0	[157]

Table 1.3. (cont.)

V/HMS-3	520	4.43	5/5/90	0.11	-	10.14	[224]
V/silicalite	520	4.23	5/5/90	0.11	-	5.14	[224]
Sb-V/SiO_2	600	5.7	10/10/80	-	-	26.3	[204]
Mo-V/SiO2	460	3.3	10/5/85	0.6	-	4.5	[207]
Nb-V/SiO_2	600	4.91	10/5/85	-	-	17.1	[226]
TiO_2 supported systems							
V/TiO_2	500	3.87	10/10/80	-	1.43	6.93	[227]
V/TiO_2-ALD	300	6.2	-	0.06	-	7.3	[214]
V/TiO_2-IMP	300	6.2	-	0.06	-	1.15	[214]
V/TiO_2-SS	400	7.0	5/2.5/92.5	0.12	-	6.0	[216]
V/TiO_2-foam	500	7.0	5/2.5/92.5	0.12	-	5.7	[215]
V/TiO_2	500	7.0	5/2.5/92.5	0.12	-	1.96	[215]
VOP/TiO_2	450	2.7	2:1	0.01-0.03	-	5.8	[228]
VMgO/TiO_2	500	5.0	5/5/90	0.06	2.0	12.5	[217]
VSbO/TiO_2	500	10	40/20/40	0.15	1.81	10.4	[127]
Mixed oxide supported systems							
V/13Ti/SBA-15	500	4.0	2:1	0.01-0.03	6-9	1.46	[209]
V-Ti/Al_2O_3	500	-	1:1.6	0.33	-	10.7	[219]
V-Sb/$SiZrO_2$	550	-	13/36/51	0.1	-	7.5	[128]
Al_2O_3 supported systems							
V/Al_2O_3	500	4.0	10/10/80	-	0.40	8.07	[227]
V/Al_2O_3	440-480	3.0	5/25/70	0.02-0.12	0.78	11.1	[229]
V/Al_2O_3	420	7.0	9/3/38	0.04	-	4.0	[230]
V/γ-Al_2O_3	500	3	-	-	-	9.48	[231]
VOP/Al_2O_3	450	1.8	2:1	0.01-0.03	-	6.2	[228]
V-MgO/Al_2O_3	500	6.5	5/5/90	0.015	-	5.36	[232]
V-MgO/Al_2O_3	500	11.0	5/5/90	0.06	-	3.85	[178]
V-W/ Al_2O_3	380	7.0	9/3/38	0.04	-	3.5	[230]
V-Cr/ Al_2O_3	380	7.0	9/3/38	0.04	-	7.0	[230]
V-Mo/ Al_2O_3	380	7.0	9/3/38	0.04	-	3.1	[230]
V-Mo/ Al_2O_3	320	-	5/57/38	0.13	-	2.8	[233]
Other systems							
V/ZrO_2	500	3.96	10/10/80	-	0.28	5.6	[227]
V/ZrO_2	425	7.4	4/4/92	0.1	-	12.1	[126]
V/CeO_2	400	6.0	5/15/80	0.24	0.05	4.2	[197]
V/MgO	450	7.05	-	0.2-1	-	4.5	[234]
V-A-G	500	-	1:2	0.5	-	26.27	[235]
V-DDA	500	-	1:2	0.5	-	20.69	[235]
V-SAC	380	3-20	13/18/69	0.54	-	10.0	[236]
V/MgO-AP	550	10	5/5/90	0.3	-	8.4	[237]
V/Siβ	470	0.2-4.7	7:1	0.5	0.06	4.2	[238]
V/nano-ZSM-5	600	10	2:1	-	-	19.5	[239]
V/nano-ZSM-5	600	2	2:1	-	-	18.6	[239]

Besides amorphous oxide supports and zeolites, carbon-based materials have been used as an alternative which also catalyzes VO_x in oxidative dehydrogenation of propane [235, 239, 240].

For instance, the graphene nanosheets have been used as a suitable support material for the ODH of propane. Fattahi *et al*. [235] investigated the bulk catalyst of V_2O_5 on graphene (V-DDA) and hybrid catalyst which is a composite of vanadium and graphene with aniline (V-A-G) in oxidative dehydrogenation of propane. The ODH of propane measured for V_2O_5 supported on graphene catalysts (V-DDA) resulted in 50.44 % selectivity to propylene at 41.02 % propane conversion. The synthesized hybrid catalyst (V-A-G) also displayed higher conversion (53.93%) and selectivity to propylene (47.02%). 6 h of catalyst stability was monitored after propane injection. Although the higher yield was obtained using graphene, the reason has not discovered yet by authors. Based on previous studies, inertness of carbon support which is a general outcome in the literature was postulated as one of the reasons which minimizes the CO_x formation. More recently, activated carbon (AC) derived from sugarcane straw was also used as a support material [236] for vanadium-based catalyst. In that case authors utilized phosphorus as a chemical activation agent for the support and this improves the dispersion of the active VO_x species. The well-dispersed AC-supported vanadium catalyst exhibited propane conversion of 30% and 10% propylene yield (V-SAC). However, a sharp decline in activity occurred after 3 h of stable performance due to the carbonization which caused the structure to collapse.

Findings show that highly dispersed surface vanadia species seems to be the most selective to propylene [66, 182, 224, 241]. Within the oxide supports, isolated VO_x species have been found on SiO_2 support up to *ca*. 2V/nm^2 surface density whereas for Al_2O_3 and TiO_2 supported vanadia catalysts showed higher surface density (7-8 V/nm^2) which is corresponded to more polymeric vanadyl species. That means isolated vanadyls so far have only been detected with vanadia catalysts supported on SiO_2 [179, 180]. The extent of this polymerization follows the trend $Al_2O_3 > ZrO_2 >> SiO_2$ for the same surface vanadia density [179, 180]. The high dispersion of vanadia was also successful with latter catalysts however the necessity to lowering the vanadia loading must be noted. Dispersion of surface vanadium oxide species may depend on silica materials whose structures are different than one another. Chlosta *et al.*[242] investigated the impact of differently structured silica supports (Aerosil 300 and SBA-15) on dispersion of surface vanadium oxide species at comparable vanadium density. Based on XPS analysis, the use of higher surface area support (SBA-15) leads to a higher dispersion as compared to Aerosil 300. Using an acidic support such as γ-Al_2O_3 may favor the formation of polymerized VO_x and a less active V_2O_5 crystalline phase (> 4.5 wt.%) [182]. In a contrast, due to the strong interaction of V_2O_5 and basic MgO may result in formation of highly dispersed VO_x species

[243]. However, independently from V-loading, bulk MgV_xO_y (*e.g.* MgV_2O_6 at high V-loading) [243] compounds may also be formed.

The redox properties of supported vanadium oxide is influenced by the electronic structure of the support [1, 244]. As the reaction occurs by a redox mechanism, any change in redox potential of the surface vanadium oxide species becomes crucial. The following trend for reducibility of the different supported vanadia species has been reported: polymeric surface VO_x > isolated surface VO_x > crystalline V_2O_5 nanoparticles [69, 196, 245]. The support, which can be considered as a ligand, has an impact on the extent of the reducibility of supported vanadium oxide species *via* the V-O-support bridging bond [1]. The reducibility of supported vanadia species depends on the strength of the V-O-support bridging bond (ZrO_2 >TiO_2> Al_2O_3> SiO_2) [1]. Gao *et al*., previously showed that TOF of supported VO_x catalysts increases in the order of VO_x /SiO_2 < VO_x /Al_2O_3 < VO_x/ZrO_2 [246, 247]. On the other hand, reducibility of supported V^{5+} structures increases in the same order. However, propylene yield decreased in the following order VO_x /SiO_2 > VO_x /Al_2O_3 >VO_x/TiO_2 and VO_x/ZrO_2 catalysts [176]. Therefore, it can be generally stated that the type of support impacts the reducibility character of surface vanadium oxide species which further determines reactivity in ODH of propane.

The last factor which has been discussed within supported vanadia catalysts but definitely in an agreement among most in this field is surface acidity/basicity. The acid-base character of catalysts may contribute in terms of: (i) dispersion of vanadia species, (ii) C-H bond activation, (iii) the rate of adsorption and desorption of reactants and products [248]. For instance, in nano-ZSM-5 supported vanadia catalysts, the acidity of catalyst is high due to the nature of acidic support [239]. The impact of acidity compensated the impact of isolated VO_x species and finally caused more CO_x formation. The same also occurs on alumina supports on where intermediate products are adsorbed, thereby leading to produce more CO_x. Thus, acidity/basicity of support materials are important. However, the surface acidity/basicity can be controlled by doping the catalyst with alkali metals such as K, Li, and Na [7, 244, 249]. Doping causes drastic changes in olefin desorption/adsorption rates and/or reactivity of the actives sites which further results in an increase in selectivity to desired olefins *i.e.* propylene [7, 192, 198, 244, 249, 250]. For instance, the comparison between K- doped V/Al_2O_3 and un-doped catalyst in ODH of alkanes showed a significant increase in selectivity to C_3- and C_4-olefins with only an addition of small amounts of potassium [106]. This occurs by reducing acidity with K-addition which allows easy desorption of olefins from the surface of a catalyst. Moreover, modification of catalyst with *e.g.* potassium especially at lower loadings of vanadium is beneficial for formation of isolated VO_x species [251]. However, a significant decrease in the pore diameter resulted in loss of

accessibility of active sites on the support. The impact of addition of alkali metal oxide on the reactivity of supported vanadia catalysts will be discussed in the following chapter in detail (Section 1.3).

More recently, oxidative dehydrogenation of propane have been operated under oxygen-free atmosphere where the reaction is facilitated by the catalyst lattice oxygen instead of gas-phase O_2. This approach is known as chemical looping oxidative dehydrogenation of propane (CL-ODHP). Typical examples of catalysts for propane CL- ODH are listed in Table 4. It is clearly seen that VO_x on alkaline-oxide-modified θ-Al_2O_3 catalysts displays the highest olefin yields (49 %) among all catalysts presented here. The critical thing in this method is inefficient with long time-on-stream since the amount of lattice oxygen is increasingly depleted with more stoichiometric cycles. It is also worth mentioning that the reaction takes place at specified time *e.g.* 30 s. Thus catalyst regeneration in hot air is needed. Despite the fact that the method is limiting the parallel propane combustion and consecutive propylene oxidation, the main challenge remains in the design of a lattice-oxygen rich catalyst with high activity and selectivity.

Table 1.4. Supported vanadia catalysts used for chemical looping oxidative dehydrogenation of propane (CL-ODHP)

Catalyst	T (°C)	Feed C_3/O_2/inert	τ (g s ml^{-1})	C_3H_6 yield (%)	Ref.
V/θ-Al_2O_3	625	10 ml C_3H_8 injection (×20)	30*	38	[252]
V-θ-Al_2O_3/ MgO	625	10 ml C_3H_8 injection (×20)	30*	32	[252]
V-θ-Al_2O_3/ CaO	625	10 ml C_3H_8 injection (×20)	30*	39	[252]
V-θ-Al_2O_3/ BaO	625	10 ml C_3H_8 injection (×20)	30*	49	[252]
V-θ-Al_2O_3/ ZrO_2	550	10 ml C_3H_8 injection (×20)	1.52	23.5	[253]

*reaction time (s)

Therefore, ODH is still a more viable method for producing propylene but the main difficulty with ODH of propane using vanadia-based catalysts, as with most oxidative catalytic processes, is control of selectivity. The formation of electrophilic surface oxygen species such as O_2*, O, O_2^-, and O_2^{2-} is discussed by several researchers as one of the possible reasons for limited selectivity [186, 254-256]. It is known that electrophilic oxygens are highly reactive for combustion of the alkane to CO_x while nucleophilic oxygens are more associated with selective reaction pathway [187, 256, 257]. For instance, Heracleous and Lemonidou obtained the enhanced selectivity towards ethylene by adding Nb to NiO catalysts [74]. Those authors reported that the incorporation of Nb allowed an elimination of the electrophilic oxygen sites. However, electrophilic oxygen sites are needed for the activation of strong C-H bonds in CH_4

[258]. Low selectivity can be caused by consecutive oxidation of the desired alkene product, which results in formation of carbon oxides [66, 192, 259]. Overall, the reactivity of the reactant and the stability of the partial oxidation products are crucial in determining selectivity. Under these limitations, the propylene yields using currently available catalysts still do not satisfy economic demands.

Recently, Kube *et al.*,[157] showed the complexity of the reaction network over M1 (Mo-V-Te-Nb-O_x) and 6V/SBA-15 catalysts in propane oxidation (Figure 1.4). Therein 11 different products were formed and a possible reaction network was proposed based on the observed intermediates and/or side products.

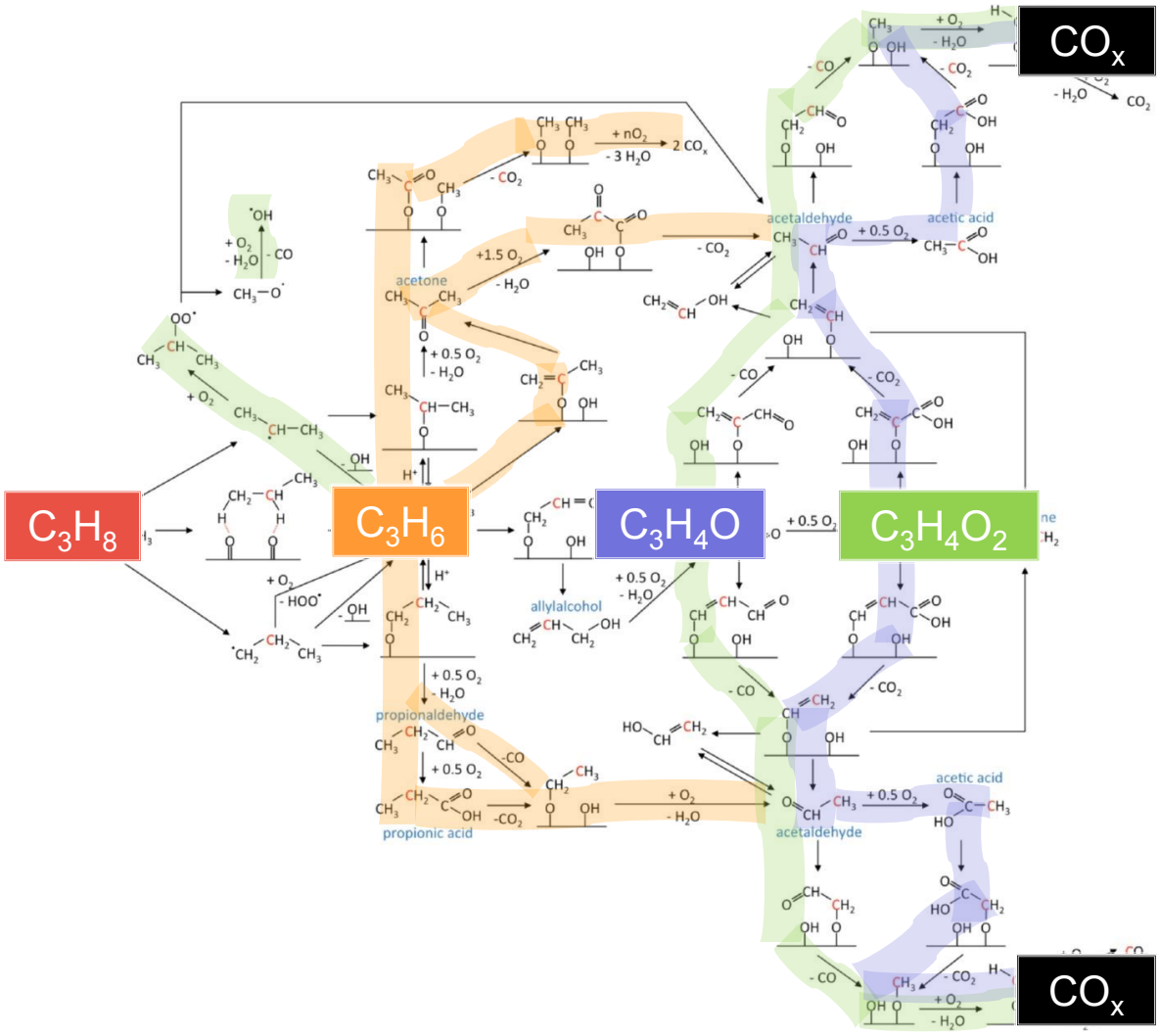

Figure 1.4. Reaction network in propane oxidation outlined based on intermediate products over M1 and 6V/SBA-15 catalysts [157]

The measurements of kinetic isotope effects in propane oxidation at reaction temperature revealed that the abstraction of the first hydrogen atom at the methylene group of the propane

molecule is kinetically relevant for the overall rate on silica-supported vanadium oxide. The activation of this C-H bond necessitates nucleophilic oxygen, of which the vanadyl oxygen has been found to be the most active. The mechanism defined by Kube *et al*.[157] was found to be followed by oxyhydration/oxidation to acetone or allylic oxidation to acrolein. Carbon oxides were mainly formed by decomposition of the main selective oxidation products like acrolein and acrylic acid. Acrolein was also found to be formed at low temperature, probably due to the attack of electrophilic oxygen species which are abundant on the surface.

Many researchers agree that it is necessary to understand all of the elementary steps in the complex reaction network, which is a challenging task. Thus, no significant progress in the development of V-containing catalysts has been achieved for ODH of propane. Important reviews which summarizes the developments until 2008 can be found in reference [66] and more recent situation of vanadium oxide catalysts in ODH of propane in following studies [1, 187, 260]. Notably, there are several factors needs to be taken into account for producing propylene using supported vanadia catalysts. The main properties discussed here included the role of supports results in modulation of vanadia dispersion, surface acidity/basicity and surface oxide reducibility, thereby significantly impacting on the catalyst performance. As such, crucial metal oxide-support interaction is important in the creation of better catalysts which favor initial oxidation to form the desired alkene, while further oxidation towards carbon oxides is inhibited.

1.3. Alkali Added Silica Supported Vanadium Oxide Catalysts in Propane Oxidation

The catalytic activity of supported metal oxide catalysts can be modified with additives. P, Cs, Mg, Li, Na, Rb, and K have been used as typical additives [154, 218, 234, 244, 249, 261]. The additives have an impact on the structure, acid-base properties and the reducibility of a catalyst which further influence the activity and the selectivity to olefins.

1.3.1. The effect of additives on ODHP

Table 1.5 summarizes the studies include non-promoted and alkali-promoted supported vanadium oxide catalysts used for propane oxidation. It has been found out that the additives enhances the yield to desired product. In 1995, Grabowski et al. [218] studied the oxidative dehydrogenation of propane on V_2O_5/TiO_2 catalysts promoted with Li, K and Rb cations. Catalytic activity measurements in the temperature range 150-450^oC show that the total activity in oxidative dehydrogenation of propane decreased for promoted catalysts in the order: non-

promoted ≥ Li ≥ K ≥ Rb-promoted catalyst. The propene yields and selectivies at equal conversion increased in the same order. The authors proposed that the decrease in activity could be due to a poisoning effect of the alkaline cations on the centres for hydrocarbon activation. This poisoning effect of alkali increased with increasing radius of the cations: Li (0.68 Å) < K(1.33 Å) < Rb (1.48 Å). In addition, XPS suggested an increase in the dispersion of the supported vanadium oxide species at high loadings under the influence of the alkali ions.

Courcot *et al.* [262] explained the different catalytic behavior in terms of existence of different VO_x species, as shown by NMR and Raman findings. For pure (VTi) and K-doped samples (KVTi), monomeric and polymeric VO_x species and V_2O_5 were detected whereas for K-doped samples the polymeric species were observed only at high V content and tetrahedral VOx species and traces of potassium vanadate (i.e. KVO_3) in the monolayer content when the K/V ratio is high. They found out that potassium hinders the reduction of vanadium which results in decrease in activity as compared to un-doped catalyst. In the following year, Courcot *et al*. [250] investigated the impact of sequence of the potassium introduction to V_2O_5/TiO_2 catalysts on their performance in oxidative dehydrogenation of propane at 350°C and 400°C. The sample in which vanadia was first introduced is denoted by TiVK, whereas the sample in which potassium was first introduced is denoted by TiKV. The sequence of impregnation is reflected in the type of V-containing species present after calcination as evidenced by ^{51}V MAS NMR. TiKV catalysts contain polymeric [V-O-V] species and segregated V_2O_5, wheras potassium trivanadate, *i.e.*, KV_3O_8 was detected in TiVK catalysts. TiVK catalysts were found more active and selective in the ODH of propane compared to TiKV ones.

In 2000, Lemonidou *et al.*[244] performed the oxidative dehydrogenation of propane using vanadia supported on Al_2O_3, TiO_2, ZrO_2, MgO as well as V/Al_2O_3 catalysts doped with alkali ions such as Li, Na and K. Furthermore, in analogy to the previous studies, the authors found significantly increased propylene selectivity whereas decrease in activity in the presence of alkali. The most drastic decrease in activity was seen with K addition. The catalytic activity decreased in the following order: non-doped > Li > Na > K. The propylene selectivity increased, irrespective of the alkali used. Therefore, very well dispersion of vanadia species due to alkali existence (the absence of V_2O_5 by XRD) were postulated as a main reason of promoting effect of alkali. However, it has not been clarified how the alkali metals affect the propylene selectivity either by blocking unselective acid sites which favor CO_x formation and/or by facilitating the quicker desorption of propylene from the surface.

Table 1.5. Comparison of non-promoted and promoted vanadium oxide catalysts on different supports in the literature for ODH of propane to propylene

Support	Additive (A)	V_2O_5 loading (wt. %)	A_2O loading (wt. %)	A/V	T °C	τ (g s ml^{-1})	Productivity (g C_3H_6/ (g_{cat} h))	C_3H_6 yield (%)	Ref.
SiO_2	-	28.4	-		450	-	-	2.6	[261]
	P		-	0.2	450		-	2.8	
	K		-	0.1	500		-	6.3	
	Cr		-	0.3	450		-	3.8	
	Ni		-	0.1	450		-	3.2	
	Mo		-	0.2	450		-	3.1	
SiO_2	-	28.4	-	-	450	0.5	-	2.7	[234]
	K	28.0	1.2	0.2	470		-	6.7	
	Cr	27.5	3.2		450		-	3.5	
	Nb	26.8	5.5		450		-	3.0	
	P	27.9	1.9		450		-	2.5	
	Mo	26.8	5.7		450		-	3.3	
	Ni	27.4	3.5		450		-	3.2	
SiO_2	-	2.0	-	-	450	1.5	0.16	3.01	
	Na	2.0	-	0.6	450	1.5	0.41	3.2	[200]
pro-SiO_2	-	7.0	-	-	490	0.11	0.5	2.5	[185]
	Na	6.2	<0.4	<0.25	490	0.11	-	4.3	
KIT	K-free	0.5*	-	-	550	0.15	-	7.5	[251]
		1.8*	-	-	550	0.15	-	29.8	
	K	-	-	0.02	550	0.15	-	18.7	
		-	-	0.1	550	0.15	-	17.0	
		-	-	0.2	550	0.15	-	18.0	
		-	-	0.27	550	0.15	-	2.0	
MgO	-	14.1	-	-	450	0.5	-	3.0	[234]
	K	14.0	0.6	0.2	450		-	2.0	
	Ni	13.8	1.8		450		-	4.2	
	Cr	13.9	1.6		450		-	3.5	
	Nb	13.7	2.8		450		-	3.2	
	P	13.8	1.0		450		-	2.8	
	Mo	13.7	2.9		450		-	3.0	
Al_2O_3	-	4.00	-	-	500	-	0.40	8.0	[244]
TiO_2	-	3.87	-	-	500	-	1.43	6.9	
ZrO_2	-	3.96	-	-	500	-	0.28	5.6	
MgO	-	3.85	-	-	500	-	0.15	6.3	
Al_2O_3	Li	4.05	0.16	0.25	450	-	-	5.5	
					500	-	-	11.8	
	Na	4.13	0.3	0.22	450	-	-	4.8	
					500	-	-	10.2	
	K	4.10	0.5	0.24	450	-	-	4.5	
					500	-	-	9.6	
γ-Al_2O_3	-	12.0	-	-	500	0.33	-	5.9	[263]
	-	12.0	-	-	500	0.16	-	3.5	
	K	12.0	6.0	0.9	500	0.33	-	2.4	

Table 1.5. (cont.)

		12.0	6.0	0.9	450	0.16	-	2.6	
Al_2O_3	-	15.8	-	-	380	-	-	0.4	[249]
	K	15.0	0.8	0.10	400	-	-	0.4	
		16.1	0.7	0.08	400	-	-	0.58	
		14.5	0.9	0.12	450	-	-	0.6	
		14.6	0.8	0.10	450	-	-	0.7	
		14.9	1.0	0.13	450	-	-	0.78	
		16.1	0.8	0.096	400	-	-	0.68	
		14.4	1.9	0.25	500	-	-	0.4	
		14.6	1.7	0.22	500	-	-	0.7	
		14.9	1.5	0.20	500	-	-	0.3	
TiO_2	-	6.7	-	-	210	1.0	-	3.3	[218]
	Li	6.7	0.05	0.04	190	1.0	-	4.2	
		26.6	0.6	0.13	230	1.0	-	3.9	
	K	6.7	0.03	0.01	250	1.0	-	4.5	
		26.3	1.13	0.08	365	1.0	-	5.4	
	Rb	6.7	0.05	0.01	335	1.0	-	5.3	
		26.0	2.44	0.09	400	1.0	-	5.5	
TiO_2	-				558	0.1	-	1.8	[264]
	Rb	6.7	-	1	603	0.25	-	2.4	
					603	0.25	-	4.5	
					603	0.5	-	5.4	
					603	1.0	-	5.2	
					603	1.2	-	5.1	
TiO_2	-	$10^{\perp}$	-	-	400	1.0	-	0.5	[250]
	K	$10^{\perp}$	$2.5^{\perp}$	0.3	400	1.0	-	2.8	
		$10^{\perp}$	$2.5^{\perp}$	0.36	400	1.0	-	3.8	
		$20^{\perp}$	$2.5^{\perp}$	0.25	400	1.0	-	3.4	
		$20^{\perp}$	$2.5^{\perp}$	0.28	400	1.0	-	3.9	
TiO_2	-	$2.4^{\perp}$	-	-	400	1.0	-	1.75	[262]
	K	$3.6^{\perp}$	$1.2^{\perp}$	-	400	1.0	-	3.75	
		$3.6^{\perp}$	$1.2^{\perp}$	-	450	1.0	-	4.5	
		$10^{\perp}$	$2.5^{\perp}$	-	400	1.0	-	2.4	
		$10^{\perp}$	$2.5^{\perp}$	-	450	1.0	-	4.0	
TiO_2	P	-	-	1.0	500	0.01	-	4.5	[228]
ZrO_2	P	-	-	1.4	500	0.01	-	10.0	[228]

*number of V atoms nm^{-2} on the SiO_2 support
$^{\perp}$number of K or V atoms nm^{-2} on the TiO_2 support

Cortez *et al*.[249] also studied the influence of potassium loading on the structure and properties of alumina-supported vanadium oxide catalysts by applying different preparation methods such as sequential impregnation (xK/VAl and V/xKAl) and co-impregnation (xKV/Al). Catalytic activity measurements for propane oxidation performed at 300ºC and 500ºC showed that the effect of preparation method was not significant at low and medium K loadings (between 1-3 wt. % K_2O). The best catalytic results were obtained by the samples with ~ 1 wt. % K_2O at 450°C. In this case, the Raman spectra shows a weakening of the terminal V=O (1027 cm^{-1}) bond with K-doping. This change was correlated with the change in catalytic activity.

In addition to catalytic measurements, the influence of alkali-addition on the different steps of propane ODH was investigated. Grabowski [264] carried out an experiment by measuring conversion and selectivities over VRbTi catalyst for various feed compositions at various contact times and temperatures. Langmuir-Hinshelwood (LH) and Eley-Rideal (ER)-Steady State Adsorption Model (SSAM) were tried and the Eley-Rideal-SSAM model was found more appropriate for the description of the propane ODH. Generally in the frame of ER-SSAM model, it was found that rubidium additive leads to decrease of all the pre-exponential factors for rate constants which describes why rubidium doped catalyst had a lower activity. The same impact was observed for other alkali metals (Li and K) in the ODH of propane on the VTiO catalyst [265]. In that study, the ODH of propane decreased in the order VTi > LiVTi > KVTi > RbVTi which is in an agreement with previous studies.

The improved selectivity to propylene was obtained by utilizing alkali (K, P) as well as transition metals (Ni, Cr, Mo) as an additive to VO_x/SiO_2 catalysts. Klisińska *et al.* [261], investigated the impact of these additives on the reactivity of VO_x/SiO_2 catalysts *via* experimental and theoretical studies. Experimental findings showed that the propylene selectivity in ODH of propane found decreasing in the order VK > VCr > V Mo=VNi > VP > V. Quantum mechanical calculations by modelling a cluster of only V and O atoms (two oxygen atoms) and adding additives revealed that out of all additives K was capable to interact with many oxygen atoms and to transfer its electrons to the nearest oxygen. Results of the calculations confirmed the exceptional behavior of the potassium (the most effective additive in terms of selectivity to propylene, 63 % selectivity at 10% propane conversion). Recently, Calatayud and Minot [266] studied the role of alkali (Li, Na, K) in vanadia/titania catalyst model based on DFT (Density Functional Theory) calculations. They have also found out that vanadyl V=O groups were affected by the presence of alkali. Both vanadia and support interacts with alkali and a physical effect of alkali was suggested as the easier dispersion of the V_2O_5 units due to the stabilizing role of alkali in the interphase between support and active phase.

Klisińska *et al.* [82] further investigated the impact of same additives on the propane ODH over V_2O_5/SiO_2 and V_2O_5/MgO catalysts. Considerably increase in selectivity to propylene in ODH of propane was found for K-doped VSiO catalysts whereas decrease for K-doped VMgO catalysts. In terms of activity, they have found increase in the specific activity (except K) for VSiO and decrease for VMgO catalysts. The following trend for the specific activity at 450°C for VSiO series has been reposted as a following sequence: VSiK << VSi = VSiNi = VSiCr < VSiNb < VSiMo << VSiP. This shows all additives except for K, increase the total activity of VSiO catalysts. For VMgO series, the sequence of the activities was: VMgK << VMgMo =

VMgNb = VMgP < VMgNi = VMgCr < VMg meaning all the additives decrease the total activity of the VMgO catalysts.

More recently, Grant *et al.* [185] showed that promoting amorphous silica with low amount of sodium (0.4 wt.% Na^+) significantly enhance the rate of propane consumption while maintaining high propylene selectivity. This is in a contrast with a study done by Lemonidou *et al.* [244] where authors showed that Na decreases the catalytic activity. Although Grant *et al.* [185] postulated that this contrast might be due to the low molar ratios of Na^+ used in their study compared to previous works, it must be noted that Lemonidou *et al.* [244] also studied very low loading of Na_2O (0.3 wt.%) as well as the same Na to vanadium ratio (~ Na/V =0.25). However, authors proposed that Na^+ enhances 2D metal oxide dispersion on SiO_2.The working role of Na^+ was to ion-exchange with surface silanols to form more reactive $Si\text{-}O^-Na^+$ anchoring sites. This made silanol groups have an ability to function as an anchoring sites toward metal oxide precursor. The existence of 2D vanadia species (tetrahedral and monomeric species) on Na^+-promoted V/SiO_2 was shown by Raman and ^{51}V MAS NMR spectroscopy. No indication for polymeric species could be observed. The hypothesis was supported by IR spectroscopy where it was seen sodium addition reduces the amount of silanol groups (features between 3745 and 3660 cm^{-1}).

A research done by Liu *et al.* [251] on the potassium-modified vanadium incorporated mesoporous silica catalyst (KIT) for ODH of propane showed that K- modification can promote the formation of isolated VO_x species at low V content. In contrast to previous works [244, 249], it shows a positive effect on the conversion of propane. In addition, it increases the selectivity to propylene which is in an agreement with previous studies. UV-Vis DRS spectra of K-modified V/KIT catalysts indicated that the transformation of VO_x species from oligomeric into monomeric units occurs with the increasing K-loading (decrease on band intensity at 35 cm^{-1}). Compared results of K-modified V/KIT and K-free catalysts indicated that K interacts with the vanadia species and promotes the dispersion of vanadia. Moreover, Raman spectroscopy showed isolated VO_4 species exist at low K-loading (<0.5% molar ratio). However, when the K-loading reaches 0.5 % (K:Si molar ratio), a Raman band at 934 cm^{-1} which is associated with the bridging V-O-V bonds of the polymeric surface vanadate species was found. At this point, authors postulated the due to the reaction between K^+ and VO_x species, potassium vanadate phase/s may form. Since these catalysts (*e.g.* K/V=0.27) shows less activity, the formation of KVO_x species was suggested as species which may be unfavorable for oxidative dehydrogenation of propane.

A positive effect of Na addition was very recently reported by Nadjafi *et al.* [200]. Those authors studied the case of sodium decavanadate, namely, $Na_6V_{10}O_{28}$ /SiO_2 in ODH of propane. The productivity per gr C_3H_6 per h was increased from 0.16 to 0.41 with addition of Na. In agreement with Grant *et al.* [185], they have found enhanced catalytic activity in ODH of propane. It has been shown that the calcination of $Na_6V_{10}O_{28}$ on SiO_2 yields in a metastable β-$NaVO_3$ and $Na_{1+x}V_3O_8$ interacting with silica. The activity of the catalyst itself was found much more than blank, VO_4/SiO_2 and $NaVO_3/SiO_2$ catalysts. Under oxidative environment of ODP conditions, larges crystallites of $Na_{1+x}V_3O_8$ (in-situ TEM and Raman spectroscopy-mapping) were found. During reaction (ca. 3h) the re-dispersion of these crystallites on the support was seen which indicates the increasing number of active sites and enhancing catalytic activity. However, no catalytic test of Na-added VO_x/SiO_2 has been conducted in ODH of propane.

In summary, two main effects on a catalyst performance of vanadium oxide catalysts have been discussed. The identity of the type of support chosen to immobilize a reactive metal oxide active site has a great influence on the observed catalytic activity. Moreover, alkali addition influences the catalytic properties. Briefly, a general trend of changes in activity and selectivity to propylene (decrease in activity whereas increasing in selectivity to propylene) with the alkali addition is the same, but some discrepancies in propane consumption exist with K and Na addition. However, the selectivity to propylene was found always enhanced with alkali promotion. These two factor are interrelated in a way to modify the surface characteristics, by changing acid-base and redox properties, hence improving catalytic properties. This study concentrates on the impact of alkali addition of SiO_2-supported VO_x catalysts in propane oxidation. Therefore, the main changes in catalyst properties (i.e., acid-base and redox properties) due to alkali addition will be discussed in the following chapter.

1.3.2. The effect of additives on acidity

The acid-base properties are always important factor in controlling selectivity. Therefore, the impact of alkali additives on reactivity of catalysts within the context of an acid-base properties have been extensively studied. Some examples regarding to the different methods used to determine acid-phase properties of catalysts in a literature have been summarized in Table 1.6.

Grabowski *et al.* [218] applied an isopropanol decomposition reaction as a test reaction to investigate how acid-base properties of V_2O_5/TiO_2 catalysts change with the addition of Li, K and Rb cations. Isopropanol is converted to propylene over acid sites and to acetone over acid-base pairs. They found that the rate of acetone formation increases and the rate of propane

formation decreases in the order; non-promoted > Li > K > Rb. The results of the ispropanol decomposition correlated between the acid-base properties and the selectivity to propylene in ODH of propane. That means selectivity was obtained increased with decreased in acidity and the increase in basicity of the catalysts. The decrease in acidity was explained due to the elimination of Brønsted acid centers by replacing surface protons with alkaline cation. This suggested as a factor reduces the nonselective route of oxidation at which involves formation of carbocation to further oxidation to carbon oxides [250, 262].

Isopropanol decomposition was studied as a test reaction also by Courcot *et al.* [250] where the impact of the sequence of potassium introduction to V_2O_5/TiO_2 catalysts was investigated. TiVK catalysts (in which vanadium introduced first) were found more active and selective in the ODH of propane compared to TiKV catalysts (in which potassium introduced first). The TiVK catalysts were also more active for dehydrogenation of isopropanol to acetone which had higher basicity.

Lemonidou *et al.* [244] correlated the acid-base character of the catalysts in the reducibility of surface V species by measuring H_2-TPR. They have found a slight shift in T_{max} from 585°C to 600-604°C upon alkali addition (K, Na, and Li-V/Al_2O_3). This shift indicated a stronger interaction between V and basic alkalies which was in analogy with the activity of the catalysts in ODH of propane. More recently, the impact of Na-addition on surface acidity was investigated over VO_x/CeO_2 catalysts for oxidative dehydrogenation of methanol [267]. Pyridine DRIFTS was used as a test reaction. The sodium-free catalysts (VO_x/CeO_2) exhibited both Brønsted (1540 cm^{-1}) and Lewis acidity (1440 cm^{-1}). Upon sodium addition, diminishing of Brønsted acidity was seen. The band at 1540 cm^{-1} was barely detectable. Again, the complete elimination of acidity was obtained. However in this case since the target reaction was ODH of methanol, the elimination of acid sites (increased surface basicity) caused decrease in formaldehyde selectivity. The negative impact of the increased surface basicity was also observed by Kustiv *et al.* [268] where they have reported that K-modified V_2O_5/TiO_2 catalyst was inactive in NO SCR with ammonia. It was due to the fact that Brønsted acid sites were essential for the reaction however they were completely poisoned by potassium.

Cortez *et al.* [249] performed methanol chemisorption and its temperature programmed surface reaction (TPSR) over potassium added alumina-supported vanadia catalysts to study acid-base sites. Methanol chemisorption experiments showed that the potassium addition reduces the quantity of methanol chemisorbed over K-V/Al_2O_3 catalysts. Together with the TPSR profiles (decrease of DME (acidic) formation with K –loading), it was obtained that there was a

replacement of acid sites by basic ones. That was parallel to the decrease in catalytic performance. Similarly with the previous studies, potassium decreased the acidic character of surface vanadia which resulted in better selectivity in ODH of propane due to a variation in the interaction between intermediates and the surface. More clearly, decrease in acidity allowed easier desorption of propylene from the less acidic surface which prevents further consecutive total combustion of propylene to CO_x [269].

Klisińska *et al.* [261] discussed the impact of potassium on the changes of atomic charge of vanadium by DFT calculations. Calculations via cluster modelling (one vanadium, two oxygen) showed that the positive charge on V atom changes in the presence of K. The positive charge of vanadium was considerably lower for cluster substituted with K (positive charge decreases from q= 0.66 to 0.33). However no correlation was found between the selectivity to propylene and acidity of vanadium center.

Table 1.6. The effect of alkali metals on acidity of supported vanadia catalyst

Catalyst	Alkali Metal	Method	Effect of Alkali Metal	Ref.
VO_x/TiO_2	K	FTIR(NH_3)	Decrease of number and strength of Brønsted and Lewis sites	[270]
VO_x/Al_2O_3	K	FTIR(Py)	Decrease of number of Brønsted and Lewis sites on VO_x and on Al_2O_3	[192]
VO_x/TiO_2	Na, K, Rb, Cs	Cumene cracking	Decrease of number of acid sites	[271]
VO_x/TiO_2	Li, K, Rb	Isopropanol Decomposition	Decrease of number and strength of acid sites	[218]
VO_x/TiO_2	K	Isopropanol Decomposition	Decrease of number and strength of acid sites	[250]
CsHPVMoO*	Cs	NH_3-TPD and FTIR (Py)	Significant decrease of number of Brønsted and Lewis sites	[131]
VO_x/SiO_2	K	Calculating atomic charge (DFT)	Positive charge of V atom decreases	[261]
VO_x/CeO_2	Na	H_2-TPR and DRIFTS (Py)	Neutralizes the Brønsted acidic sites, increased surface basicity	[267]

*Keggin-type polyoxometalates

Studies shows that the catalytic properties of supported vanadia for oxidative dehydrogenation of propane are strongly influenced by change in acid-base properties upon alkali addition. The acid-base properties may determine the nature of active vanadium species and the reactivity. In general, it can be concluded that alkali metals decreases the surface acidity increases basicity. It is known that this allows easy desorption of propylene from the surface thus inhibits secondary reactions [244]. However, direct correlation between acid-base character and activity/selectivity cannot be drawn. Some other factors such as alkali loading, preparation method, and type of support always important which determine surface properties of catalysts.

1.3.3. The effect of additives on reducibility

The redox character of catalysts as important as acid-base character which affect the performance of selective oxidation catalysts. There is, in fact, a close relation between the catalyst reducibility and the nature of VO_x species on a given oxide support. The following trend for reducibility of the different supported vanadia species has been reported: polymeric surface VO_x > isolated surface VO_x > bulk-like V_2O_5 crystallites [69, 196, 245]. The addition of alkali (as well as support) affects the redox properties of a catalyst [192, 272, 273]

Generally, the M-O-V bonds (M is the cation of the support or alkali metal) are assumed to be crucial to the catalyst reducibility which is in analogy with the activity of the catalysts, *i.e.* the higher the reducibility of V species, the higher is the activity of the catalysts in ODH of propane [188, 227, 274]. Lemonidou *et al.* [227] showed the reducibility of V_2O_5 was affected by the type of supports as measured by H_2-TPR. This has been studied both experimentally (H_2-TPR) [188, 275-278] and theoretically (DFT calculations and statistical thermodynamics) [279, 280] by many researchers in this field. Results from the H_2-TPR experiments by Lemonidou *et al.* [227] showed that the lowest temperature is needed for the reduction of V on TiO_2 whereas the significantly higher temperature is needed for V on MgO catalysts. Since it is accepted that low H_2-reduction temperatures correspond to a high degree of V dispersion [277, 281-283], authors concluded that a parallelism between catalytic activity and reducibility occurs. However the hypothesis failed to explain the propylene selectivity. When strong basic alkali metals were added (Li, Na, and K), a decrease in reducibility of V species (shift to higher temperature of H_2 consumption) was reported. The dramatic effect in activity becomes more pronounced as the ionic radius of the promoter increases. Therefore, authors postulated that alkali metal ions blocked the propane adsorption centers. Galli *et al.* observed the same impact of potassium incorporation (decrease in reducibility of surface vanadium species) over Al_2O_3 supported vanadia catalysts on the selective oxidation of n-butane [106].

Cortez *et al*. [249] measured an increase in the reduction temperature with increasing K loading by H_2-TPR, irrespective of the preparation method (sequential impregnation, and co-impregnation). Methanol chemisorption and its temperature programmed surface reaction (TPSR) were applied as probe reaction to investigate redox properties of the K-V-Al_2O_3 catalysts. When K is added to VAl, formaldehyde production presents a shift of its production maximum from 230 to 258^{o}C in the V-KAl series. Similar shifts were also observed in K-VAl (from 239 to 292^{o}C) and the co-impregnated KV-Al series (from 234 to 285^{o}C). The shifts of the maximum temperature in the formaldehyde formation and methanol desorption were in

accordance with the increase in the reduction temperature observed by H_2-TPR. Interestingly the Raman spectra showed a weakening of the V=O bond (shift to lower wavenumbers) with K-doping. Together with TPR profiles and Raman spectra showed that interaction between surface vanadia with K oxides decreases the reducibility of the surface vanadium oxide species which was further parallel to the decrease in the catalytic performance.

Recently, Nadjafi *et al.* [200] discussed the key roles of dispersion and reducibility based on a supported sodium decavanadate catalyst ($Na_6V_{10}O_{28}$ /SiO_2) for ODH of propane. The catalyst, $Na_6V_{10}O_{28}$ on SiO_2, yielded in a metastable β-$NaVO_3$ and $Na_{1+x}V_3O_8$ interacting with silica upon calcination. The recovery in activity found via fast re-oxidation of α'-NaV_2O_5 (reduced phase) to $Na_{1+x}V_3O_8$/SiO_2 and β-$NaVO_3$ (*in-situ* Raman). H_2-TPR analysis showed that the maximum H_2-TPR temperature of α'-NaV_2O_5 was much lower than the catalyst itself. Hence the activity trend correlated with the higher reducibility of $Na_6V_{10}O_{28}$ /SiO_2 as it readily converts to the reduced phase α'-NaV_2O_5. In a summary, the variation of alkali (as well as type of support) affects the extent reducibility of supported vanadium oxides. One can conclude that the reducibility of catalysts are significantly affected by the properties of support, type of alkali and loading (both alkali and vanadium).

1.4. Discussion

On the whole, the production of olefins (ethylene, butane, and propylene) and oxygenates (acetaldehyde, acrolein, acetic acid, maleic anhydride, and acrylic acid) are key pillars of the chemical industry. The catalysts of choice for oxidation processes are mostly vanadia-containing metal and mixed metal oxides. Specifically, supported VO_x catalysts are highly active and selective for oxidative dehydrogenation of propane to propylene. Various studies have been carried out to improve their activity and selectivity as well as stability. The type of support and alkali promoter have been varied to investigate their effects on catalytic performance and the structure of supported vanadium oxide species.

The role of support has been known as: (i) provides high surface area, (ii) establishes strong contact with active species, and (iii) affects structure of active species and subsequently their catalytic performance [181, 187, 260]. The catalytic properties of supported vanadia catalysts are strongly influenced by the alkali addition such as Li, Na, and K. Numerous works as outlined above reported the poisoning effect of alkali metals on activity in oxidation reactions, although also their positive contribution on the selectivity to olefins. Generally in oxidative dehydrogenation of propane, the decrease in activity whereas increase in selectivity to

propylene have been observed on supported vanadium oxide catalysts with Li, and Rb addition. However, some discrepancies exist with K and Na addition. The phenomena observed in catalysis have been generally attributed to the modifications on the redox and acid-base properties of supported vanadium oxide catalysts upon alkali addition. However the impact is not limited to this. For instance, alkali metals located on the surface of the active phase may block the access of reacting molecule to the active vanadia centers which is purely geometric affect [7]. In addition, *e.g.,* potassium increases a local electrostatic potential over a distance about 4 Å radius that subsequently affects at least two vanadium ions [284]. Thus, it can be concluded that the additive may possess a multiple effect (Figure 1.5). These effects are [7]:

- Geometrical blockage of the active centers,
- A decrease in acidity, increase in basicity which results in increase in selectivity to propylene (additives whose electronegativity lower than that of the main oxide cation decreases the acidity whereas additives of higher electronegativity increases the acidity),
- An impact on catalyst reducibility,
- An impact on the amount of electrophilic (non-selective for propylene) oxygen species due to the decrease in electron work function of the catalyst [218, 285, 286],
- It may favor the formation of alkali-vanadates (*e.g.,* KVO_3) [250] whose reactivity needs to be investigated in an applied reaction,
- It may increase the dispersion of supported metal oxide phase, or introduce point defects into the bulk of a catalyst [287].

However, a description of the interaction between vanadium oxide species and the alkali additive at a molecular level is still missing. The role of alkali on the structure of active component is not fully understood. The impact of Cs as a dopant has not been investigated yet in propane oxidation.

The one study in which Cs-addition studied was conducted by Zhao *et al.* [83, 288, 289]. Those authors studied the impact of Cs on V_2O_5/SiO_2 catalysts for selective oxidation of ethane to acetaldehyde and acrolein [83]. Several different impacts of cesium were observed. For instance, the addition of Cs to the low V-loading catalysts (V: Si=0.02-0.1 at. %) enhances the reaction rate by about 50 times as well as the selectivity to acetaldehyde and acrolein. However, the addition of Cs to high V-loading catalysts caused reducing the ODH of ethane by facilitating combustion. The study on how the acid-base and redox properties are affected by Cs-addition was conducted later [84]. At low vanadia loadings (V: Si=0.02-0.1 at. %), H_2-TPR experiments showed that the maximum reduction temperature slightly increased (from 683°C to 711°C).

However, significant decreased, *e.g.*, from 681°C to 503°C in the maximum reduction temperature was seen at higher vanadia loadings (V: Si=2-10:100 at. %). In this case, it was concluded that the reduction extent increases with the increasing vanadia loading. Moreover, Cs enhances the reduction extent in where the oxygen mobility was very high, therefore deep oxidation of ethane occurred.

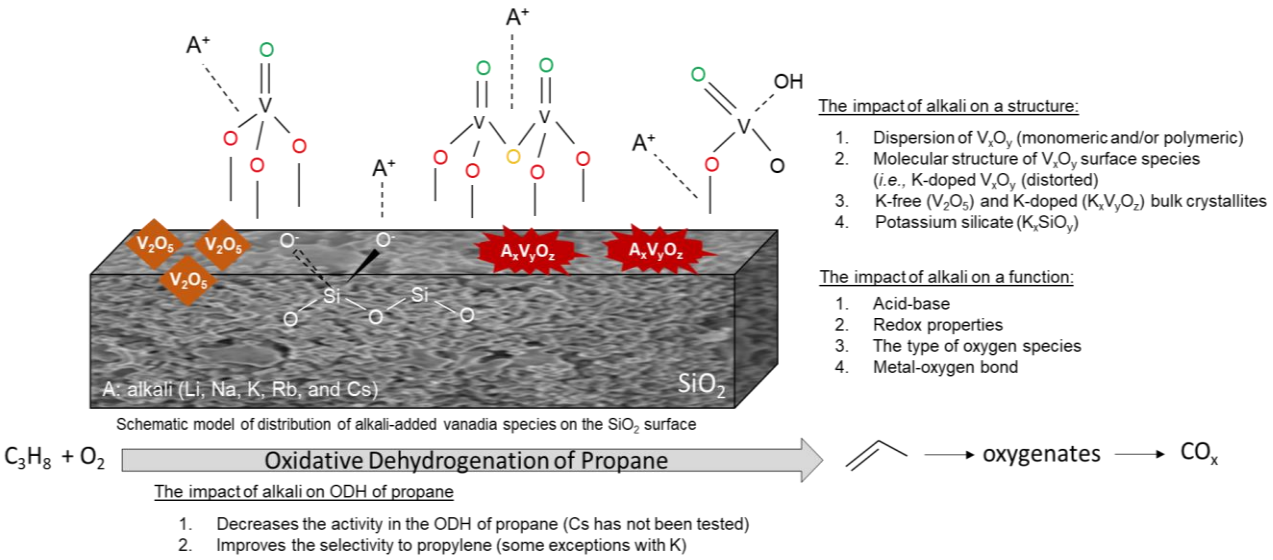

Figure 1.5. The influencing factors of alkali addition to supported vanadium oxide catalyst on the catalytic performance in ODH of propane

Later in 2006, Zhao *et al*. [290] studied the same catalysts in the selective oxidation of ethane the complete oxidation of diesel soot. The A/V ratios were varied (A: V: Si= x: 10:100, x=1, 5, 10, 20, 50, A: Li, Na, K, Rb, and Cs). For Cs, the loadings of 0.1, 0.5, 1.0, 2.0, 5.0, and 10.0 at. % were studied. Catalytic activity measurements showed that the ethane conversion increased with the increasing Cs loading and it reached a maximum value at Cs loading of 5 at. %. Afterwards it decreased with further increase of Cs loading. On the other hand, the total selectivity to aldehydes was not enhanced when Cs loading was equal to 0.1% while it was significantly enhanced when Cs loading was equal to or more than 0.5%. These results indicated that the concentration of Cs plays an important role in obtaining both high activity and selectivity to aldehydes. Different types of cesium vanadate compounds were detected by Raman spectroscopy and their structures depend on the V-loading when cesium content kept constant (Cs: Si = 1:100). Differently from previous studies the authors further analyzed the influence of alkali metal on the melting point. TG-DTA analysis indicated that the melting points of the supported phase were lowered by modification of the catalyst with alkali ions. CO_2-TPD results of alkali-V_2O_5/SiO_2 catalysts (alkali= Li, Na, K, Rb and Cs) showed that the

acidity and basicity was altered by addition of alkali. Ethane conversion and selectivity to aldehydes increased with increasing radius of the alkali ion. It was found that addition of alkali metals neutralizes the acidic sites and thus enhances the basicity of SiO_2-supported vanadium catalysts. On the other hand, the extent of the effect of alkali addition on the basicity of the modified V_2O_5/SiO_2 catalysts is highly dependent upon the amounts and types of alkali added as well as the vanadium loading. The H_2-TPR profiles of alkali modified catalysts showed that the reduction temperature was obviously shifted towards lower values and this indicated that doping vanadium oxide catalysts with alkali ions facilitated reduction of vanadia with hydrogen, which is in contrast to previously reported results of alumina and titania supported vanadium oxide catalysts. Although it is known that the coordination environment of vanadium can change during the phase transition which can also happen in reaction conditions where melting happens, the presence of possibly formed alkali vanadate phases and their phase transition effect on the catalytic performance of supported vanadia catalysts have not been investigated so far.

In none of the studies melting was discussed as a possible reason for the changes in the catalytic properties although in some cases the alkali content allows at least partial melting at reaction temperature according to the phase diagram and in all cases local melting is possible.

Recently, Ahi [291] studied the effect of phase transition of silica-supported vanadium-potassium oxides from solid to liquid on their catalytic performances. Oxidative dehydrogenation of propane was performed and catalytic performance was compared before and after melting of potassium vanadate. In Figure 1.6(A) it can be seen that the conversion dropped suddenly in the temperature range of melting. When the reaction temperature was increased further, the conversion increased again and similar conversions were achieved at higher temperatures. Figure 1.6(B) shows that the selectivity towards propylene at comparable conversion was increased after phase transition from solid to liquid.

The experiments indicate that there is a significant effect of phase transition from solid to liquid on selectivity to propylene. UV-vis spectroscopy under operation conditions suggested structural changes in the first coordination sphere of vanadium during melting, however, an explanation of the observed effect in catalysis requires further investigations.

Although it is known that the catalytic properties in alkane oxidation depend on many factors, such as the nature of the support, the interaction of vanadia with the support, the vanadia loading and the resulting degree of oligomerization, an explanation of the effect of alkali additives on an atomistic level has not been provided. Mainly the acid-base properties have been studied and

discussed. Often, a change in the reducibility was observed. The change in reducibility might be caused by changes in the vanadia dispersion, which was studied only in some cases and not in connection with the reducibility. None of the effects have been systematically analyzed so that no clear correlation results from the literature. Furthermore, the impact of the formation of liquid phases on the surface of oxidation catalysts at reaction temperature is not completely understood.

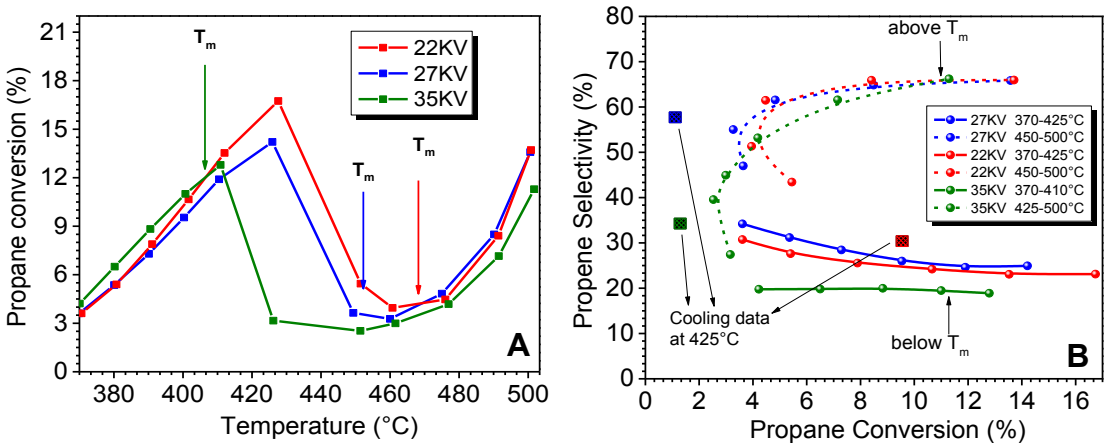

Figure 1.6. (A) Conversion of propane in the oxidative dehydrogenation of propane with increasing temperature, and **(B)** propene selectivity as a function of propane conversion in the temperature range below and above the conversion drop over the catalysts indicated in the legend [291]

In this thesis, a systematic study of doping silica supported vanadium oxide with all types of alkali elements (*i.e.* Li, Na, K, Rb, and Cs). A reproducible synthesis of alkali added silica supported vanadium oxide catalysts were achieved and the melting temperatures of formed alkali vanadate phase(s) were determined. To the best of our knowledge, for the first time the effect phase transition of alkali vanadate phases from solid to liquid has been studied in propane oxidation. The impact of melting on the surface dynamics catalysts have been further investigated with *operando* spectroscopy techniques.

1.5. Aims and Outline of the Thesis

Brief review on the importance of vanadia-based catalysts in oxidative dehydrogenation of propane has been presented above in the Sections 1.1-1.4. On the one hand, the factor of support is recognized as being important for obtaining higher selectivity to propylene. On the other hand, further improvement has been possible with alkali addition such as Li, Na, and K. Generally saying, alkali addition increases selectivity to propylene and decreases the

conversion of propane (exceptions exist with K). The decrease in activity was attributed to the decrease in reducibility of vanadia by adding an alkali. Whereas the enhancement in selectivity to propylene was due to the increased basicity which allows easy desorption of propylene from the surface. The presence of promoters or additives, enrichment of catalyst components on the surface due to specific preparation procedures, or the chemical gradient generated by interaction of the catalyst with the gas phase may cause lowering melting points and partial/or complete melting of a surface layer. Therefore, under reaction conditions of propane oxidation, molten or glassy surface phases cannot be excluded.

The present thesis focuses on the investigating the role of alkali metal addition on the phase composition of supported vanadium oxide layers. For this purpose, silica supported A/V (A: Li, Na, K, Rb, and Cs) catalysts with various A: V (at.) ratios were synthesized. The physical and chemical properties of silica supported A/V catalysts were analyzed using several basic characterization techniques. The melting temperatures of catalysts were measured by Differential Scanning Calorimetry (DSC). Catalysts were tested in oxidative dehydrogenation of propane in a temperature range between 350 and 520°C. In addition, *in-situ* and *operando* characterization including calorimetric and spectroscopic techniques were applied to detect surface dynamic changes under applied reaction conditions. The methodology regarding all characterization methods used in this study including ex situ, in situ and operando as well as catalytic testing protocol are presented in Chapter 2.

The results and discussion of synthesis and basic characterization of silica supported A/V catalysts are presented in a detail in Chapter 3. The alkali addition caused a formation of some alkali vanadates on the surface of the catalyst. With the addition of K, Rb, and Cs, melting of the surface phases is expected under applied reaction conditions whereas catalysts modified with Li and Na are expected to show no melting. In this chapter, two groups of catalysts are introduced which differed based on melting temperatures of surface A-V phase(s).

Chapter 3 also includes detailed characterization of support-free bulk-crystalline material, *namely*, $K_3V_5O_{14}$. This is a material which was in-house synthesized and used as a reference material to demonstrate and understand how the melting phenomenon occurs over supported catalyst. This section shows the thermal stability/instability of alkali-vanadates as measured by DSC as well as the behavior of the melting (*i.e.*, wetting, non-wetting, or droplet formation).

The catalytic performance of silica supported A/V catalysts were tested in ODH of propane and presented in Chapter 4. The activity, selectivity to propylene as well as activation energies are also presented. Catalysts which show melting (*i.e.,* K, Rb and Cs-containing) under applied

reaction conditions showed a peculiar catalysis profile. Activity drops and selectivity to propylene increases crossing the temperature of alkali-vanadate phase(s). In this chapter, the great impact of phase transition from solid to liquid is introduced. However, Li, and Na-containing silica supported vanadium oxide catalysts show typical catalysis profile *i.e.*, selectivity to propylene decreases with increasing conversion upon increasing temperature, which occurs over many oxidation catalysts. This is an expected phenomenon since the alkali-vanadate phases formed in these group of catalysts have higher melting temperatures than applied reaction conditions. The reproducibility of the catalytic profile and chemical, compositional and thermal properties of spent catalysts are also included in Chapter 4.

The great effect of alkali addition due to lowering melting temperatures on a catalyst performance was observed with catalysts which show melting (*i.e.,* K, Rb and Cs). However, melting points of these catalysts measured by DSC under dynamic flow ($21O_2/79N_2$) cannot be associated with the impact on catalytic activity since reaction feed may have a different influence on melting. It is known in the literature that the environment has an influence on the melting points of compounds [292]. Based on our experience, it has been also seen that the melting of a component is dependent on the feed. Therefore, the impact of the melting of surface alkali vanadates on a catalyst performance was validated by applying *operando* Differential Scanning Calorimetry (*operando*- DSC). In order to demonstrate the impact of melting on a reactivity, a model experiment that contains a physical mixture of V/SBA-15 and $K_3V_5O_{14}$ were measured in temperature-programmed reaction of propane oxidation. This experiment gave us a first idea on the possible role of molten layer on the activity of active specie(s).

Raman spectroscopy was used to probe molecular-level information about catalyst surface (*e.g.* 2D vanadia, 3D vanadia, alkali vanadates and reactive surface species under reaction conditions. For this, silica supported K/V=0.6 catalyst was used since this catalyst contains only one crystalline phase which is $K_3V_5O_{14}$ as detected by XRD. The changes in the surface structure of the catalyst under reaction conditions were detected with two different lasers, which are 532 and 266 nm. With the same aim, operando near-edge X-ray absorption fine structure (NEXAFS) was applied. NEXAFS spectroscopy was used to deeply study the changes in geometric and electronic structure of the surface vanadium oxide species due to melting. Reference spectra of several different alkali vanadates (support-free) were measured for spectra fitting. The spectra fitting was conducted in ATHENA (Demeter)[293] software. The NEXAFS measurements were complemented by *in situ* X-ray photoelectron spectroscopy (XPS).

The results of the *operando* studies including DSC, Raman, and NAP- NEXAFS are discussed in Chapter 5. First of all, this chapter confirms that a drastic change in catalytic profile is associated with melting. Further, spectroscopic techniques allows to identify active specie(s) over alkali-containing supported vanadia catalysts and the impact of melting on changes in distribution of active species. Observations indicates that the surrounding environment of the active phase is a critical issue that needs to be controlled.

The overall conclusion obtained in the thesis are presented in Chapter 6.

CHAPTER 2

2. Experimental Techniques

2.1. Chemicals

Li_2CO_3 (>99.99%, Alfa Aesar), Na_2CO_3 (>99.99%, Merck), K_2CO_3 (>99%, Sigma Aldrich (Fluka)), Cs_2CO_3 (>99%, Alfa Aesar), Rb_2CO_3 (>99%, Alfa Aesar) V_2O_5 (>99%, BASF), KOH (>99, 97%, Sigma Aldrich) and conventional amorphous silica (Aerosil 300, Degussa; 285 $m^2\ g^{-1}$) were used as starting materials. All chemicals were dried overnight at 80°C before using. Millipore® water was used as solvent. Propane with a purity of 99.95% was purchased from Westfalen AG for the catalytic reaction. The purity of nitrogen, oxygen and argon was 99.999%.

2.2. Synthesis

Alkali-containing (Alkali: Li, Na, K, Rb, and Cs) silica supported vanadium oxide catalysts were the main catalyst group in this thesis. Support-free alkali vanadate(s) were also synthesized as reference catalysts.

2.2.1. Silica supported A/V catalysts (A: Li, Na, K, Rb, and Cs)

The silica supported A/V catalysts were prepared using a spray dryer. The details of the synthetic procedure are as follows, a 1 gr mixture of A_2CO_3 and V_2O_5 was added to the suspension of SiO_2 (9 gr) in distilled water (350 ml) and stirred for 2 h at room temperature. The resulting slurry was spray-dried with the following parameters; T_{inlet}=200°C, T_{outlet}=130°C, Aspirator=100%, Nozzle Cleaner=1, Pump rate=15%. The obtained fine powder was immediately transferred into a rotating quartz tube for calcination under synthetic air (21 vol. % O_2 in N_2), using a flow rate of 10 $mlmin^{-1}$, ramping with 2 $Kmin^{-1}$ to 620 °C, and holding for 16 h. After cooling down to room temperature, 6 g of each catalyst was obtained (Figure 2.1). The nominal loading of total metal oxide for all catalysts was kept at 10 wt. %. By keeping the total metal oxide loading the same (10 wt. %), the content of alkali and vanadium were systematically varied. The properties of the catalysts are summarized in Table 3.1-3.5.

2.2.2. Support-free alkali-vanadates (K, Rb, Cs-containing)

The support-free bulk phase *i.e.*, $K_3V_5O_{14}$ was prepared using the conventional solid-state method which is explained elsewhere[294]. 3 gr of K_2CO_3 and 6 gr of V_2O_5 were mixed and ground in a mortar. The solid mixture was pressed into pellets (3 cm diameter) with 2 tons for 1 min. Prepared pellets were transferred into a tube furnace (Carbolite), and heated to 380°C (heating rate 10 K min^{-1}) in flowing 21 vol. % O_2 in Ar. After heating, the pellets were held there for 4 days then allowed to cool down to room temperature at the natural rate of cooling of the tube furnace. The procedure was repeated several times until the target phase was reached (internal ID, 31564).

The reaction equation is as follow:

$$3K_2CO_3 + 5V_2O_5 = 2K_3V_5O_{14} + 3CO_2 \uparrow$$

The possible decomposition product of $K_3V_5O_{14}$, namely, support-free KV_3O_8 was synthesized using a hydrothermal method explained elsewhere[295]. Specifically, 0.9 g V_2O_5 was dissolved in 40 mL deionized water and 0.28 g KOH was added to the solution during stirring. The prepared solution of KOH + V_2O_5 was continuously stirred at 80°C for 30 min. While holding for 30 min, the color change of the solution from orange to dark brown was observed. The solution was later transferred to 50 mL Teflon-lined stainless steel autoclave. The autoclave was sealed and heated in a muffle furnace to 180°C and kept at this temperature for 48 h. After it was cooled to room temperature naturally, the product was obtained. First the solution was washed three times with deionized water and the precipitates were collected by vacuum filtration. The obtained precipitates were dried overnight at 80°C (internal ID, 32008).

Synthesis of target rubidium and cesium-vanadates which exist on supported Rb/V catalysts, (*i.e.* $Rb_3V_5O_{14}$ and $Cs_2V_4O_{11}$) could not been achieved even though several calcination steps were conducted. However, the synthesis of alkali- metavanadate phases, namely, $RbVO_3$ and $CsVO_3$, were successful. The properties of support-free alkali-vanadate catalysts are summarized in Table 3.6.

2.2.3. Reduced support-free potassium vanadate(s)

It was previously mentioned that a possible decomposition product of $K_3V_5O_{14}$ was determined as KV_3O_8. However, the diffraction pattern of the decomposed structure was found with a stoichiometric ratio of potassium to vanadium equal to 1:2.5. Therefore, syntheses were performed starting from K: V=1: 3 as the potassium content was systematically reduced.

The reduced $K_xV_yO_z$ catalysts were synthesized *via* a sol-gel route. For this, 80 mL of distilled water was heated to 70°C and a mixture of 2.4 g of V_2O_5 and 5 g of oxalic acid dehydrate was added to the hot water during stirring. The solution was stirred continuously for 3 h. Later, 0.3 gr of KNO_3 was added at 70°C and stirring continued for an additional hour. With addition of KNO_3, a color change from orange to black occurred, as well as gelation was. The observed viscosity of the gel varied depending on the KNO_3 content. The obtained product was dried at 80°C overnight. The residue was calcined at 400°C for 4 h in a muffle furnace to get final product. The properties of the reduced potassium-vanadate phases can be seen in Table 3.7.

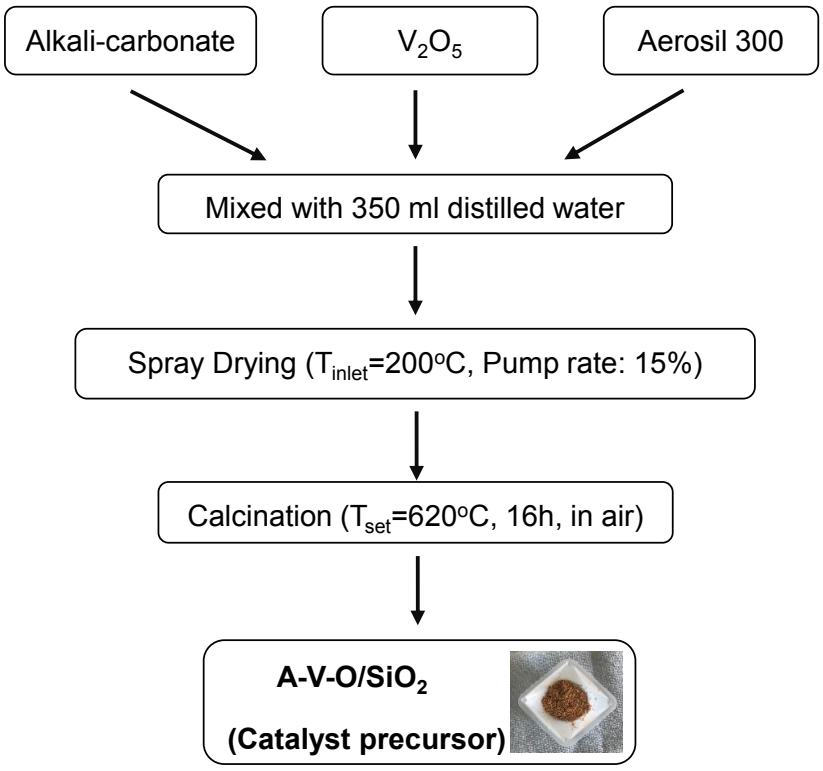

Figure 2.1. Experimental procedure of synthesis of alkali-containing vanadium oxides on silica support

2.3. Basic Characterization

2.3.1. Brunauer-Emmet-Teller (BET) method

The BET surface area of the catalysts was measured using an Autosorb AS-6B, Quantachrome apparatus by measurement of N_2 adsorption-desorption isotherms at 77 K. The sample was degassed in dynamic vacuum at a temperature of 150°C for 2 h prior to adsorption. 11-point adsorption isotherms were measured. The linear range of adsorption isotherm (p/p_0=0.046) was considered for calculation of the surface area according to the BET method.

2.3.2. X-ray Diffraction (XRD) analysis

The crystalline phase of the catalysts was identified by XRD analysis using a Bruker D8 Advance II Bragg-Brentano Theta/Theta diffractometer using Ni-filtered Cu Kα radiation and a position sensitive energy dispersive LynxEye silicon strip detector. The sample powder was filled into the recess of a cup-shaped sample holder, the surface of the powder bed being flushed with the sample holder edge. Diffraction patterns were recorded in the range 20-90° with a step size of 0.02° and an accumulation time of 15 s/step. The XRD data were analyzed by full pattern fitting according to the Rietveld refinement as implemented in the TOPAS software (TOPAS, version 6, copyright 1999-2017 Bruker AXS).

2.3.3. X-ray Fluorescence (XRF) analysis

The content of alkali and vanadium in the catalysts were determined by X-ray Florescence using the Pioneer S4 (Bruker AXS GmbH) spectrometer. For sample preparation, a mixture of 0.05 g catalyst and 8.9 g lithium tetraborate (>99.995%, Aldrich) was fused into a disk using an automated fusion machine (Vulcan 2 MA, Fluxana). For Li, and Na-containing catalysts, ICP-OES (inductively coupled plasma –optical emission spectrometry) technique was used. The concentrations were determined after digesting samples (about 25 mg) in 5.0 ml (HNO_3), 1.0 ml HF (40%), 50 ml H2O and heating to 230°C at 60 bar in a microwave autoclave.

2.3.4. Thermo-gravimetric Analysis (TG-DTA-MS)

Thermo-gravimetric analysis (TG-DTA-MS) of freshly prepared catalyst precursors were performed on a Netzsch STA449 Jupiter thermo-analyzer using 60 mg of sample placed into a Netzsch® alumina crucible (200 µl) without lid. Evolution of the gas phase was monitored with a quadrupole mass spectrometer (Pfeiffer, QMS Omnistar). The thermal decomposition was checked from room temperature to 600°C, with a heating ramp of 10 Kpm under 70 ml min^{-1} flow of Ar. The same TG-MS protocol was applied to the activated silica supported K/V=0.6 catalyst (activation: heating in 21% O_2 in Ar at 620°C and held there for 2h).

2.3.5. Scanning Electron Microscope and Energy Dispersive X-ray Analysis (SEM-EDX)

The textural images of catalysts were captured using a Hitachi S-4800 Field Emission Scanning Electron Microscope (SEM), working in the kV range 0.1 to 30. The SEM images were undertaken at a voltage of 1.5 kV and a relatively close working distance of 3 mm. The Energy Dispersive X-ray Analysis Data were detected with a Bruker EDX System using a SDD (silicon

drift detector). The working distance for detecting X-rays was, in this case, optimized to 10 mm. Images based on backscatter electrons (BSE) were captured using an yttrium aluminum garnet (YAG) detector. Use of the YAG BSE detector allows for improved visualization of the surface topography of the catalyst.

2.3.6. Transmission Electron Microscopy (TEM) Analysis

The chemical composition of selected sample regions was studied by STEM-EDS analysis on the double-corrected JEOL JEM-ARM 200 CF transmission electron microscope equipped with a large-angle SDD EDS detector with a solid angle of 0.7 sr. Emission current was set to 10 μA and spot size 5C.

2.3.7. Optical Microscope

The visualization of melting was conducted in an optical microscope (Keyence –VHX-5000) motorized XY stage and height (Z) adjustment (magnification from 20x to 5000x). The high resolution HDR-images of samples and video of melting phenomena were recorded (50 frames per second).

2.3.8. Raman Spectroscopy

Raman measurements were performed using an S&I TriVista Raman microscope system consisting of a triple grating spectrograph (Princeton Instruments TriVista 557) equipped with a liquid N_2-cooled CCD camera (Princeton Instruments, PyLoN 2KBUV), and Olympus microscope (BX51) and a series of continuous wave-lasers. These measurements utilized a single spectrograph stage (750 mm focal length, f/9.7, 100μm slit) along with two lasers, namely, 266 (CryLas) and 532 nm (Cobolt) and matching long-pass filters to decrease the intensity of Rayleigh scattered light. A spectral resolution of about 7 cm^{-1} was achieved using 2400 and 600 groove/mm gratings for the 266 nm and 532 nm measurements, respectively. A 15x microscope objective was used for the 266 nm measurements, while the 532 nm measurements used a 10x objective. Laser powers were reduced to 1 mW and 2 mW at 266 and 532 nm, respectively, using neutral density filters. Under these conditions, no beam damage was observed. The temperature dependent experiments were conducted in a Linkam CCR1000 (Linkam Scientific, Tadworth, UK) cell under the flow of 1 $mlmin^{-1}$ gas mixture of 7.5 % C_3H_8 and 7.5% O_2 diluted in nitrogen in a temperature range between 350°C and 520°C.

2.3.9. Differential Scanning Calorimetry (DSC)

The analysis of the thermal behavior of the catalysts regarding phase transitions was carried out on a heat flux differential scanning calorimeter (Mettler-Toledo HP DSC 827) with a star shaped, layered Au-AuPd sensor (one layer 56 thermocouples). Measurements for supported catalysts were done with 5 mg, while 1 mg was used for support-free catalysts in a Netzsch® alumina 85 µl crucible with lid under a dynamic atmosphere 21 % O_2 / 79 % Ar (50 $ml_n\,min^{-1}$) with 10 $Kmin^{-1}$ as heating and 5 K min^{-1} as cooling rate. Three cycles of heating and cooling was applied to ensure the reversibility of the endothermic events. Temperatures and heat flow were calibrated by measuring the melting points of In (indium) and Zn (zinc).

2.4. Catalytic Testing

Catalytic activity of each silica supported A/V catalyst for propane oxidation was measured in a commercial parallel reactor setup "Grimsel 2" (Premex GmbH, Berlin DE) composed of two reactor blocks with 8 fixed-bed reactors at atmospheric pressure (Figure 2.2). Temperatures for propane oxidation measurements were varied between 350°C and 520°C. The catalysts were pressed under 0.0196 MPa and sieved into a particle size of 250-355 µm. Quartz wool was placed at the tapering point of the empty reactor in order to hold the catalyst. 350 mg of catalyst was loaded into the reactors. The thermocouple for temperature measurements was placed coaxially in the catalyst bed. An empty reactor with bare SiO_2 (Aerosil 300, particle size: 250-355 µm) was used to confirm the inertness of the support. All catalysts were "activated" in an oxidative atmosphere (21vol. %O_2, rest N_2) at 520°C (heating rate 2 $Kmin^{-1}$) for 2 h, and cooled to 50°C. Then the catalysts were exposed to the reaction mixture containing C_3H_8, O_2 and N_2 with a ratio of 7.5:7.5:85 vol. %. A precise total gas flow of 10 mL min^{-1} was fed to start the reaction. Analysis of the amount of product and unreacted propane were performed with an Agilent 7890A GC system equipped with thermal conductivity (TCD) and flame ionization detector (FID). A combination of Plot-Q (length 30 m, 0.53 mm internal diameter, 40µm film thickness) and Plot-MoleSieve 5A columns (30m length, 0.53 mm internal diameter, 50µm film thickness), connected to a thermal conductivity detector (TCD), was used to analyze the permanent gases CO, CO_2, N_2, O_2, and CH_4. A system consisting of an FFAP (length 30 m, 0.53 mm internal diameter, 1 µm film thickness) and a Plot-Q column (length 30 m, 0.53 mm internal diameter, 40 µm film thickness), connected to a flame ionization detector (FID), was used to analyze C_2-C_3 hydrocarbons and oxygenates.

Catalysts were kept at each temperature for 24 h until having a constant value of propane conversion and the yields of the product were obtained. Propylene and carbon oxides (CO and CO_2) were found as main reaction products. The C_2 products and oxygenates (acrolein, acrylic acid and propionaldehyde) were below 2 % of the total amount of products. Pure SiO_2 was found to be inactive under the reaction conditions, since the conversion of propane at the highest temperature (*i.e.* 520°C) was found to be 1.7 %. The catalyst testing was repeated two times to evaluate the reproducibility of the catalyst performance. Catalysts were cooled down in the reaction feed to room temperature. Characterization of all catalysts was repeated after catalytic testing.

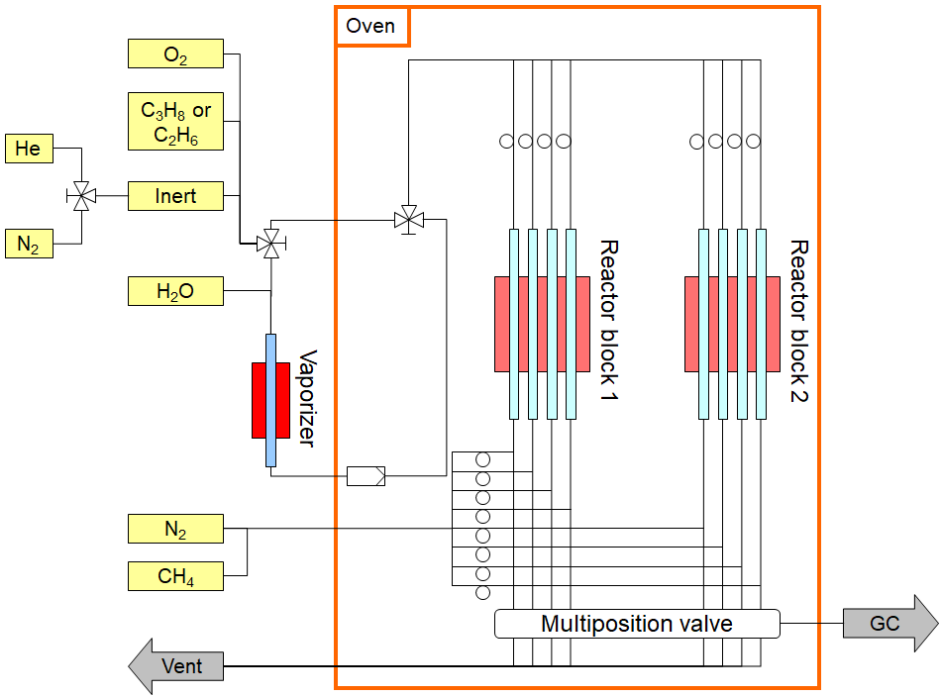

Figure 2.2. Flowchart depicting the Grimsel 2 reactor [296]

Temperature-programmed reaction of propane oxidation of support-free $K_3V_5O_{14}$ and KV_3O_8 catalysts were conducted in a self-constructed single tube reactor setup. Details of the reactor was described elsewhere[157]. The catalyst was directly exposed to the reaction mixture containing C_3H_8, O_2 and N_2 with a ratio of 7.5:7.5:85 vol. %. A precise total gas flow of 10 mL min^{-1} was fed to start the reaction. Analysis of the amount of product and unreacted propane were performed with an online gas chromatography (Agilent 7890) system equipped with thermal conductivity (TCD) and flame ionization detector (FID). Catalysts were loaded into a reactor where quartz was inserted first to protect the reactor from the flowing of the melt downward. 150 mg of support-free catalyst was used which is five times higher than loading of total metal oxide in supported catalyst. Similarly to the supported catalysts, each catalyst profile

was measured in a temperature range between 350°C and 520°C (3 K min^{-1} heating rate, 10 min holding in each temperature). Two cycles of TPR of propane oxidation were performed.

The conversion of propane X and selectivity to product j S_j were calculated based on the sum of products according to eqn (2.1)-(2.2):

$$X = \frac{\sum_{j=1}^{n} N_j c_j}{N_{alkane} c_{alkane,0}} \times 100 \quad (2.1)$$

$$S_j = \frac{\frac{N_j}{N_{alkane}} c_j}{\sum_{j=1}^{n} \frac{N_j}{N_{alkane}} c_j} \times 100 \quad (2.2)$$

where N_j is the number of carbon atoms in the product j, c_j is the concentration of product j in the reactor exit gas, N_{alkane} is the number of carbon atoms in the alkane, $c_{alkane,0}$ is the concentration of the alkane in the reactant feed.

Reaction rates for propane consumption and propylene formation were determined using the following eqn (2.3):

$$\frac{d(n_i)}{d(W/F)}) = \vartheta_i r_i \quad (2.3)$$

where n_i is the number of alkane at the reactor exit, W is the mass of the catalyst in g, F is the total flow rate of the inlet gas stream, and ϑ_i is the stoichiometric coefficient of alkane. The rates are normalized to V content in g and provided in the unit [$mol\ g^{-1}Vs^{-1}$].

The yield of product j Y_j was calculated based on eqn (2.4):

$$Y_j = S_j X \quad (2.4)$$

where S_j is the product selectivity and X is the alkane conversion. Data regarding the conversion, selectivity and yield are provided in vol. %.

The apparent activation energies of alkane consumption was determined based on the rates determined at minimum three different reaction temperatures and provided in the unit [$kJ\ mol^{-1}$].

2.5. Operando Characterizations

2.5.1. Operando Differential Scanning Calorimetry (DSC)

2.5.1.1. Introduction

Differential scanning calorimetry (DSC) is well-established technique to study the change in properties of a material along with temperature against time [297, 298]. The method provides quantitative information such as melting, crystallization, heat of fusion, heat capacity, and heat of reaction. The method is widely used in chemistry [299-302], biology and nanoscience [303], biochemistry [303, 304], electrochemistry [305], pharmacology [306, 307], food [308], and others. In recent decades, several different DSC-based techniques have been developed. Although they are named differently such as conventional-DSC [309], high-speed DSC (Hyper-DSC^{TM}) [310], infrared (IR)-heated DSC [311], pressure perturbation calorimetry (PPC) [312], the working principle of each of them is always either power compensation type DSC or the heat flux type DSC [313, 314]. A heat flux type DSC consist of a cell composed of reference and sample holders. The two holders are subjected to the same temperature program. If during heating (or cooling) a thermal symmetry or asymmetry occurs, a temperature difference is detected. This difference is used to calculate the thermal properties of the material. Power consumption DSC consists of two micro-furnaces which contains a temperature sensor and a heating resistor. The same power is applied during heating (and cooling). If an asymmetry occurs due to the phase transition, a control circuit attempt to stabilize it by increasing or decreasing the heating power. This compensating heating is proportional to the heat consumed or evolved. The difference in power can be used for further investigation of thermal properties of material[315].

In the present work, the DSC technique is aimed towards use during propane oxidation. The detection of endothermic events from melting in spite of the exothermicity of propane oxidation was challenging, but possible with *operando*- DSC technique. The method allows for simultaneous measurement of thermal effects (heat evolution and consumption) in an extended range of temperatures during the course of chemical reactions and phase transitions. Calvet-type DSC[316] was chosen as the basis technique. In this case, the heat fluxes into a substance and a reference are measured outside of the sample assuming that it is proportional to the ΔT (temperature difference between inner and outer cylindrical surface) while the sample is subjected to a controlled temperature program. In contrast to other calorimetric techniques, Calvet-type DSC is more efficient in terms of capturing of heat fluxes from/to sample. Moreover, the sensitivity is not drastically affected by the type of gas and the flow rate[317].

Generally two methods have been used to calculate measured heat signal and the thermal effects (consumed or produced heat) during reaction. These methods are: Tian equation[313, 318] and the convolution integral method[313].Data from a Calvet type DSC is analyzed using the Tian equation[318], which is a macroscopic description of experimental output. The equation is shown here:

$$q = K.\Delta T + C.\frac{\partial T}{\partial t} \approx K\left[\Delta T + \tau\left(\frac{d\Delta T}{dt}\right)\right] \tag{2.5}$$

where q is the heat flux at every moment of time, K is the specific thermal conductivity, C is the specific thermal capacity and τ is the characteristic time constant K/C.

In this study, a Calvet type in situ calorimeter with plug-flow geometry "Sensys Evo" developed by Setaram[319] was used (Figure 2.3). The equipment provides improved productivity and higher temporal resolution. Particularly the 3D sensor of Calvet-type DSC is truly a breed apart from the classical thermal analysis methods which use 2D sensor technology. This way, all heat convection, conduction and radiation is measured, while only heat conducted directly through the bottom of the vessel is measurable with 2D sensing technologies.

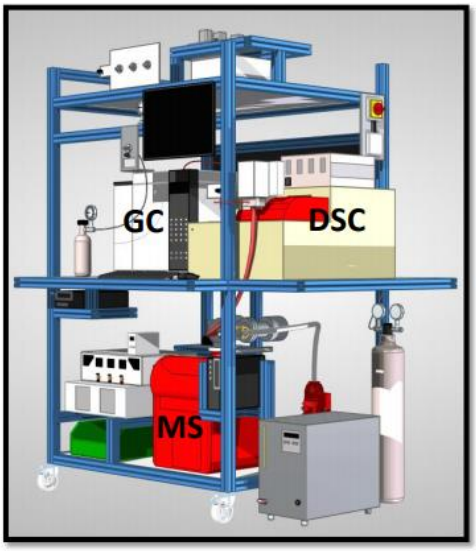

Figure 2.3. Calvet-type *in-situ* calorimeter with plug-flow geometry Sensys Evo (Setaram) (adopted from[320])

The compared scheme of the 3D Calvet-sensor with 2D sensor can be seen in Figure 2.4. The sensor is composed of 2 cylindrical thermopiles, each has 10 rings which contains 12 thermocouples each. Each thermopile totally surrounds either the sample or the reference zone to measure heat in all directions.

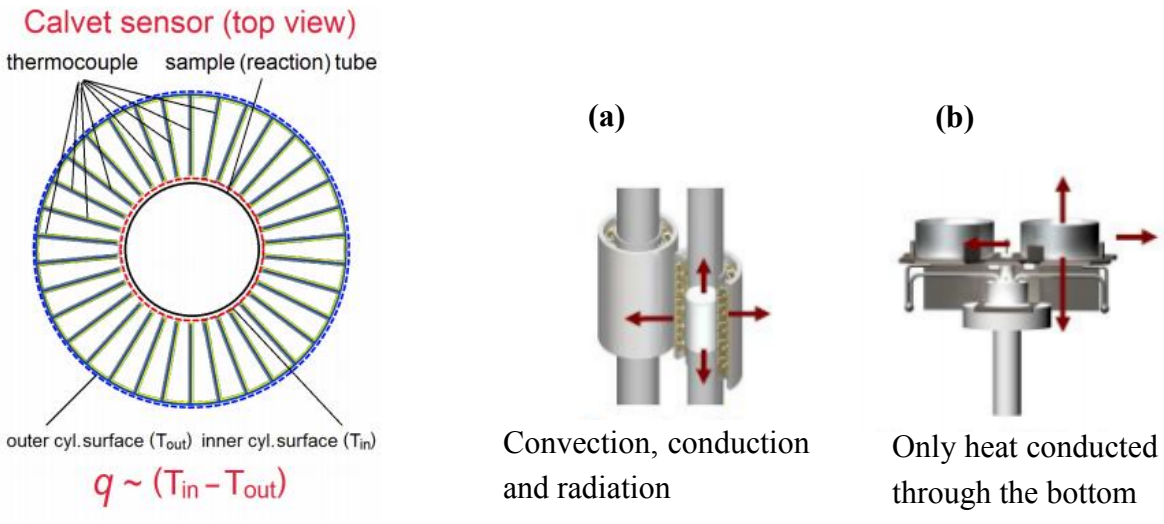

Figure 2.4. (a) 3D sensor, (b) plate-shape 2D DSC sensor [320]

Using the technology explained above, various information either from the gas phase or the catalyst's surface can be extracted. In the case of a gas phase exothermic process, information on reaction kinetics (E_a), and adsorption-desorption enthalpies can be calculated. Furthermore, redox dynamics, the impact of oxygen diffusion into subsurface, oxygen binding energies, and thermochemistry of defects formation on the catalyst surface can be investigated for transformations in the solid state[320]. In the next section, the experimental protocol during propane oxidation will be explained.

2.5.1.2. Experimental protocol

Operando thermal analysis was studied using a Calvet type[316] *in situ* calorimeter with plug-flow geometry Sensys Evo (Setaram) coupled with a gas chromatograph (Agilent 7890B) and custom-designed mass-spectrometer (Figure 2.3). The (PtRh-Pt) Calvet type sensor was calibrated at the production site with contact free Ohm resistance and verified against melting enthalpy of certified indium standard. Around 125 µl of each catalyst was pressed under 0.0196 MPa and sieved in a particle size of 100-250 µm. ~50 mg of each sample was loaded into a 150 mm long quartz tubes with an inner diameter of 4 mm. The catalyst was placed in the quartz tube reactor on a sintered glass substrate covered with thin layer of quartz wool (10 mm batch length, 125 µl batch volume). The measurement quartz reactor tube containing the sample was placed directly into the center of the measurement zone. An identical reactor was used on the reference side of calorimeter. The reference reactor was filled with quartz wool and kept under continuous N_2 flow equal to the total flow on the sample side. The schematic representation of the reactor block and the catalyst location are demonstrated in Figure 2.5.

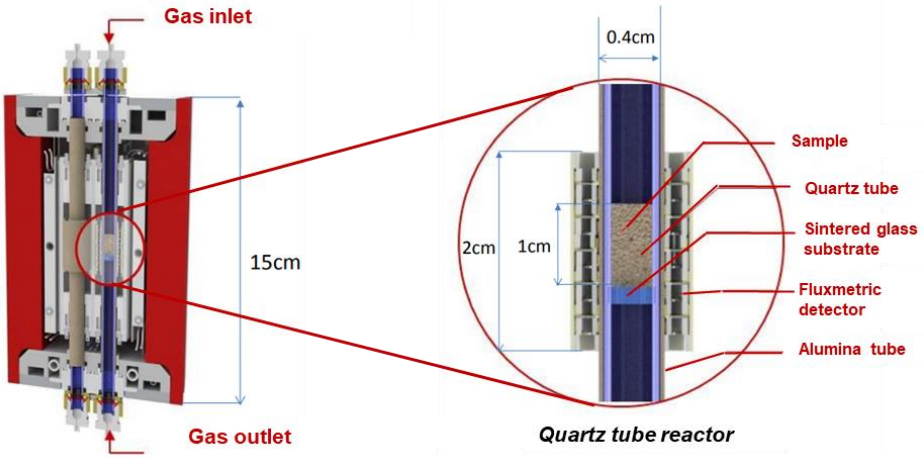

Figure 2.5. The reactor block of the *in-situ* DSC and the catalyst location[320]

The gas-chromatograph was coupled with the calorimeter downstream of the reactor. Once injected through the preheated inlet, the solute is split and introduced into two channels: a thermal conductivity detector (TCD) for the analysis of CO, CO_2, Ar, O_2 via HP Plot Q (30 m, 0.53 mm I.D., 40 µm) and HP Molsieve 5A (30 m, 0.53 mm I.D., 50 µm) capillary columns, and a flame ionization detector (FID) for detecting C_3H_8 and C_3H_6 via HP Plot Q and HP FFAP (30 m x 0.53 mm x 1.0 µm) columns. The complete separation run last 22 min. Thus, to acquire the product concentration at every 10°C a heating rate of 0.42 Kpm was used for the DSC experiment. All connection lines were permanently held at 120°C to avoid condensation. Quantitative calibration was performed for CO_2 with multiple concentrations (0.25-20%). Each calibration test had 5 repetitions which were consequently averaged. Excellent linearity in the analyzed concentration range was achieved with 5 points. For calibration of C_3H_6, C_3H_8, CO, O_2 certified calibration mixtures containing gas concentrations of 2%, 5%, 1%, and 1%, respectively were used. The controlled gas flow was maintained with El-Flow mass flow controllers from Bronkhorst, which were additionally calibrated with a Definer 220 flowmeter.

Catalysts were activated in an oxidative environment with 9 mL min^{-1} total flow (21vol. % O_2, rest N_2) at 620°C (heating rate=10 K min^{-1}) for 2 h then completely cooled down with 10Kpm in the same gas feed. For the reaction, a total flow of 9 mL min^{-1}, $C_3H_8/O_2/N_2$-7.5/7.5/85 (M_{cat}/F_{total} =0.34 g·s·ml^{-1}, GHSV ≈4300 h^{-1}) was set and a temperature ramp (β=0.42 Kpm) started.

A flowchart showing an *in-situ* DSC experiment is in Figure 2.6. Owing to the heat capacity *(C_p)* of the sample, a temperature difference between the heat transferred to the sample and the reference reactor is expected. The difference is measured by the thermocouples and represented

as *dQ/dt.* The change in the number of molecules in the outlet stream is recorded by the GC and represented as *dN/dt*.

The general equation of heat flow for a sample is as follows (eqn 2.6)

$$q = \left(\frac{dQ}{dt}\right) / \left(\frac{dN}{dt}\right) \tag{2.6}$$

where *dQ/dt* is the total heat flow and *dN/dt* is the change in number of molecules at the reactor exit.

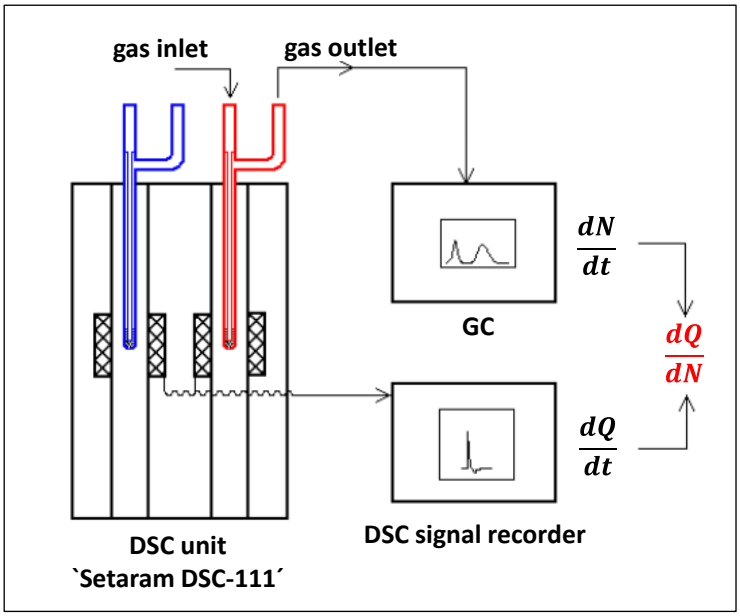

Figure 2.6. Experimental setup for an *in-situ* DSC experiment [321]

Calculation of the heat flow generated by the reaction was calculated on the basis of the rates of C_3H_6 and CO_x formation and standard reaction enthalpies calculated for stoichiometric reaction per mol of propane. The calculated heat flow (HF) in *J/min/g* is defined as follows:

$$-HF = r_{C_3H_6} \times \Delta H^0_{r(C_3H_6)} + r_{CO_2} \times \Delta H^0_{r(CO_2)} + r_{CO} \times \Delta H^0_{r(CO)} \tag{2.7}$$

where r_i are formation rates in *mol/min/g* and $\Delta H^0_{r(i)}$ is a reaction enthalpy form tabulated enthalpies of formation in *J/mol* (C_3H_8).

Temperature effect on enthalpies were neglected.

$$C_3H_8 + 0.5O_2 \rightarrow C_3H_6 + H_2O \quad \Delta H^0_{r(C_3H_6)} = -116.7 kJ/mol(C_3H_8)$$

$$C_3H_8 + 5O_2 \rightarrow 3CO_2 + 4H_2O \quad \Delta H^0_{r(CO_2)} = -2043 kJ/mol(C_3H_8)$$

$$C_3H_8 + 3.5O_2 \rightarrow 3CO + 4H_2O \quad \Delta H^0_{r(CO)} = -1194 kJ/mol(C_3H_8)$$

2.5.2. Operando Raman Spectroscopy

2.5.2.1. Introduction

The term Raman scattering was named after one of its discoverers, the Indian scientist Sir C.V. Raman (Nobel Prize Laureate in Physics in 1930) who observed the effect by means of sunlight in 1928[322]. The Raman spectroscopy detects certain interactions of light with matter in particular it uses the existence of Stokes Raman scattering (where the energy of a scattered photon is lower than the incident photon) and anti-Stokes Raman scattering (where the energy of a scattered photon is higher than the incident photon) to examine molecular structure[323]. Detailed information regarding the fundamental on Raman theory can be found elsewhere [323-326]. A Raman spectrum is a plot of the intensity of Raman scattered light as a function of Raman shift which is the difference in frequency between incident laser light and the scattered light in wavenumbers (cm^{-1})[323].

Numerous applications of Raman spectroscopy can be found to study minerals, ceramics and glasses[327, 328], Li-batteries[323], phase transition mechanisms[329, 330], and catalysis[331, 332]. Presently, *in situ* Raman spectroscopy studies are extensively applied to heterogeneous catalysis [206, 324, 333, 334] to determine the molecular and electronic structures of the surface metal oxide catalysts [6, 335]. By investigating the surface chemistry, structure-function relationships can be better understood. With this aim, modern in-situ characterization techniques such as Raman, IR, UV-Vis, XANES, and NAP-NEXAFS have been applied [6, 209, 247, 335-338]. Among these, Raman spectroscopy is unique because of its ability to directly provide molecular level information that allows discrimination in spite of different catalytic active sites which might be present in oxidation catalysis[334, 339]. It has been used to examine many types of catalytic materials including bulk and supported metals[338, 340], bulk mixed metal oxides[341, 342], supported metal oxides[207], zeolites[343] and even enzymes[344].

Many studies have investigated vanadium oxide catalysts during ODH of propane utilizing the in situ capabilities of Raman spectroscopy [207, 345-348]. It has been aimed at exploration of catalytically active sites and surface reaction intermediates during catalytic reactions. Therefore, a molecular level of understanding on a structure/activity-selectivity relationships of the various vanadium oxide entities in the catalyst have been determined[331].

Based on a loading, type of precursor, calcination temperature, and synthesis method, the molecular structure of vanadium oxides over support can result in different types: (i) isolated vanadium ions, (ii) dimeric and polymeric species, (iii) chains of vanadium ions building up a

two-dimensional over-layer of supported vanadium oxides, (iv) three-dimensional vanadium oxides (e.g., V_2O_5) bulk-crystalline or not, (v) mixed metal oxide phases with support (e.g. ZrV_2O_7)[332] (Figure 2.7). At low loadings below monolayer coverage, the supported vanadium oxides exhibits as isolated VO_4 units which contains one terminal V=O bond and three bridging vanadium-oxygen-support bond with symmetry C_{3v}. With increasing surface vanadium oxide loading, the amount of dimeric and polymeric chains of VO_4 gradually increases. The polymeric vanadium oxide species consist of a one terminal V=O bond with one V-O-support and two bridging V-O-V bonds. In summary, VO_4 species possess three different bonds which are V=O, V-O-V and V-O-support (Figure 2.7). Raman spectroscopy detects the frequency of these bonds and hence provides information about the possible presence of multiple molecular structure.

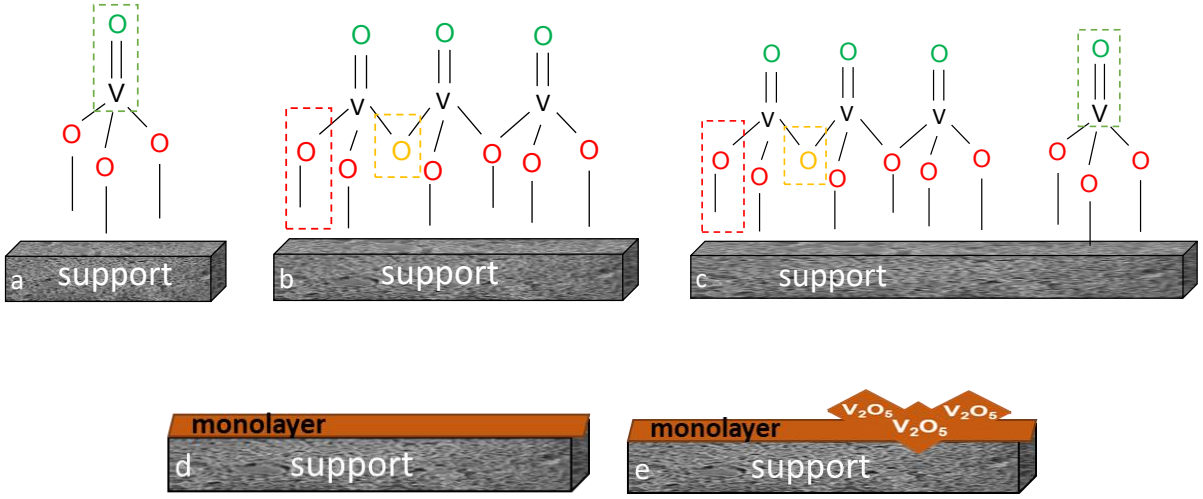

Figure 2.7. Three possible V-O bonds in supported vanadium oxide catalysts formed below monolayer (a-c), and monolayer (d) and above monolayer coverage (e)

The surface VO_4 species give Raman band frequencies between 800 and 1200 cm^{-1} due to the stretching vibrations [1]. The vibrations between 400-700 cm^{-1} appears due to the bending/vibrations of short V-O bonds [335, 337, 349]. The four bands at about 900, 1020, 1040, and 1060 cm^{-1} have been extensively discussed for clarification. For instance, a band at 1027-1040 cm^{-1} observed in the visible Raman spectrum of dehydrated VO_x/SiO_2 (below monolayer) is assigned exclusively to vanadyl bond (V=O)[350]. Wu *et al.*[349] indicated that two different monomeric surface VO_x species exist on dehydrated SiO_2 whose Raman frequencies are at 1032 and 1040 cm^{-1}. The band at 1060 cm^{-1} has been assigned to V-O-Si stretching vibrations by several researches [349, 351, 352]. Several different assignments have been proposed for the Raman band at ca. 900-940 cm^{-1} including assignments of V-O-V[348, 353], O-O[354], and V-O-support [351, 355, 356] vibrations. Traditional assignment of this

band is mostly to V-O-V bending vibrations. However, recently it was reported [351, 356] that V-O-V bonds were found between 840 and 770 cm^{-1}, and not in the 940-990 cm^{-1} as assumed earlier. On the other hand, Wu *et al.*[349] proposed the assignment of 920 cm^{-1} band to V-O-Si vibrations supported by DFT calculations as well. So some discrepancies exist on assignment of Raman bands for ca. 800-900 cm^{-1}. It is also known that there is a strong vibrational coupling between the vanadia species and the support which makes the interpretation of the spectra difficult.

Nonetheless, Raman is an extremely powerful technique for characterizing supported vanadium oxide catalysts. Yet, Raman alone is not sufficient to discriminating between these different V-O bonds. The combinatorial approach of multiple spectroscopy techniques (such as IR, X-ray absorption spectroscopy, UV-vis) gives a successful characterization.

2.5.2.2. Experimental protocol

Operando Raman spectra were collected in a TriVista Raman Microscope System, which was defined previously (2.3.8). The experimental set-up is shown in Figure 2.8. The spectra acquisition consisted of 10 accumulations of 60 seconds (Δt= 10 min) for the 532 *nm* laser whereas 30 accumulations of 60 seconds (Δt= 30 min) for the 266 nm laser. The gas flows from top to the bottom of the cell, passing through the powder sample that is supported by a ceramic fiber filter on a ceramic sample holder. The out flowing gas is connected to the micro-GC (490 Micro GC, Agilent) which performs on-line gas product analysis. There are two thermocouples in this reaction chamber. One is located in the inner wall of the sample holder for temperature control. The second thermocouple was inserted into the sample to measure the actual temperature for calibration, but was removed to eliminate its contribution to the propane oxidation reaction.

Instead of inserting second thermocouple, temperature calibration in the cell was done by measuring the melting point of potassium pentavanadate crystals ($K_3V_5O_{14}$) under 10 $mlmin^{-1}$ flow of static air. The same protocol of propane oxidation in a reactor was followed during *operando*- Raman experiments. Therefore, the sample was first activated in a flow of synthetic air (21 vol. % O_2, rest Ar) at 520°*C*, holding for 2 h and cooled down to room temperature. Propane oxidation ($C_3H_8/O_2/N_2$=7.5/7.5/85 vol. %) was performed with a total flow rate of 1 $mlmin^{-1}$ and 20 mg of catalyst. To overcome the difficulty in keeping gas flow stable, one gas bottle which contains the reaction mixture was used. During the operando Raman-GC study, the catalyst structure was analyzed every 10 min for the 532 nm laser, or

every 30 min for the 266 nm laser and the performance was analyzed in every 2 minutes with the micro-GC.

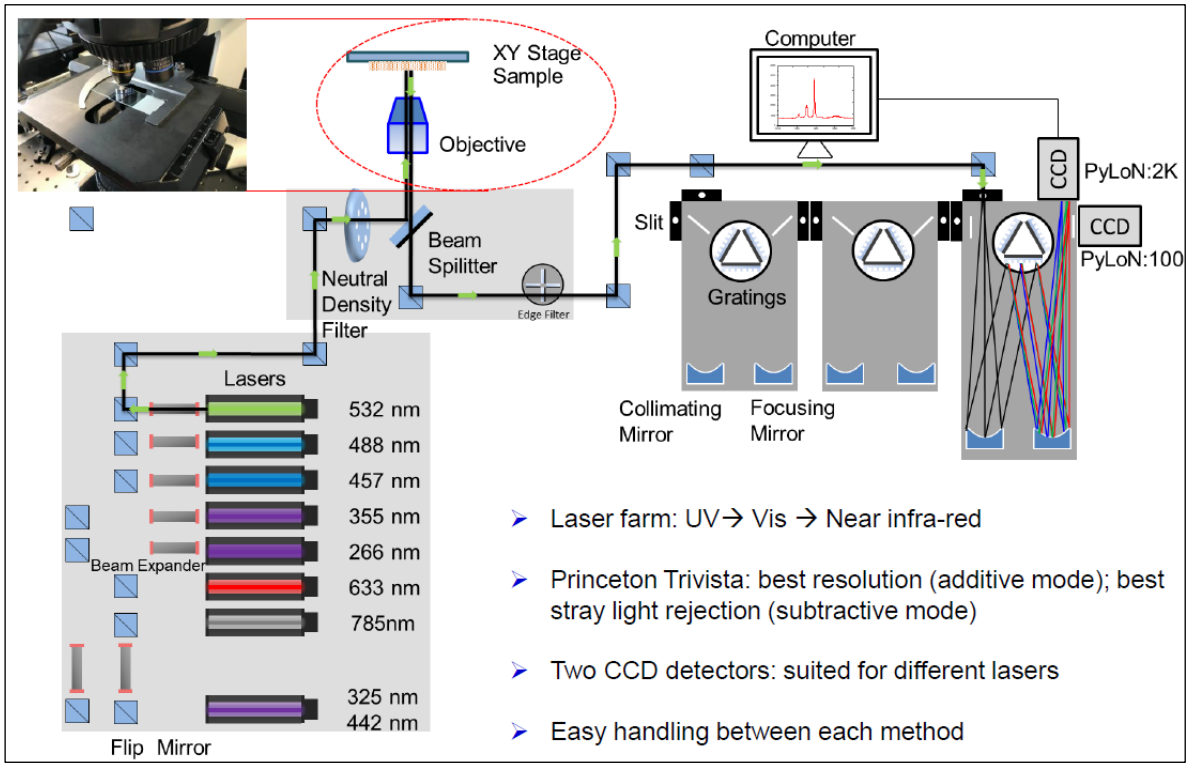

Figure 2.8. Sketch of Trivista Raman set-up[357]

2.5.2.3. Temperature calibration of the commercial/in situ operando cell

Raman spectroscopy experiments under in situ and operando conditions were conducted in Linkam CCR1000 cell (Figure 2.9). This cell allows temperature up to 1000°C. Temperature is accurately controlled by the Linkam T96.S controller (via the S-type platinum/rhodium thermocouple) which can heat samples at a rate of up to an impressive 200°C/min. Water cooling is used to keep stage body at safe temperature. The gas mixture enters the reactor via a 1/16" tube and is heated while rising up inside the cell. The heating filament is positioned spirally inside a ceramic casing. An integrated thermocouple is directly underneath the sample holder. The sample holder has a height of approximately 2 cm. Samples are loaded on ceramic fabric filters which sits on the first 1 cm of the sample holder. The stage lid has to be slightly pressed onto the quartz transparent window to guarantee a leak free operation.

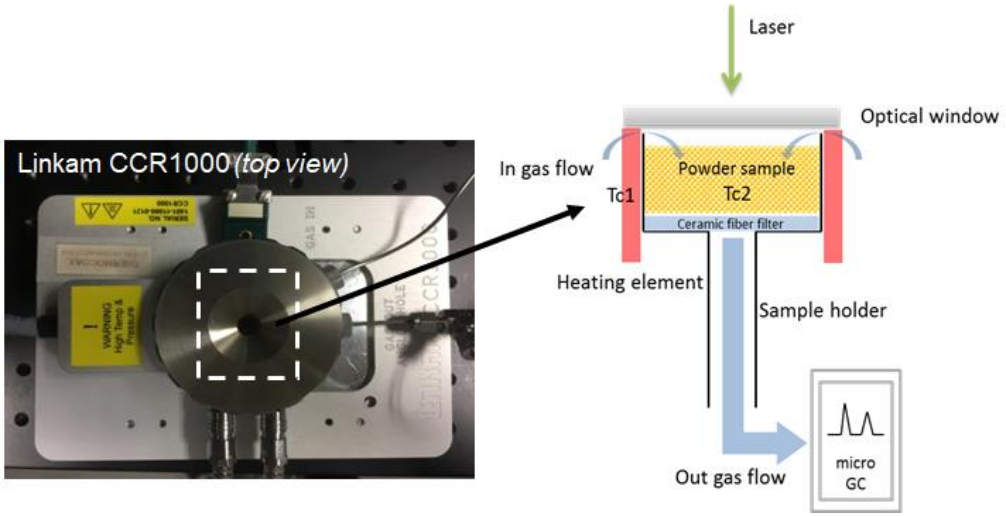

Figure 2.9. Detailed sketch of Linkam CCR1000 reaction cell

However, the design of Linkam's cell causes a temperature gradient through the sample holder, including catalyst bed. Since a thermocouple is located in its proximity, the actual sample temperature differs from the set controller temperature. Therefore, temperature calibration is always needed prior to the in situ/operando experiments. Temperature calibration was done by observing the melting of support-free $K_3V_5O_{14}$ in Linkam cell and calibrating this temperature with respect to the melting temperature measured by DSC (*i.e.* T^{peak}=414°C). With this, the contribution from the thermocouple to the reaction was also eliminated. Calibration parameters are in Table 2.1.

Table 2.1. Temperature calibration in the Linkam cell by correlating melting temperature of support-free $K_3V_5O_{14}$ with measured temperature by DSC

Cell type	**[a]Observed melting / °C ($21O_2$/79Ar 10 mlmin^{-1})**	**[b]T^{peak} / °C ($21O_2$/79Ar 50 mlmin^{-1})**	**$T_{calibration\ factor}$**
Linkam	393	414	1.05

[a]Melting observed by light microscope in Raman set-up
[b]Measured melting point by DSC (Figure 3.17)

2.5.3. Operando NAP-XPS and NAP-NEXAFS

2.5.3.1. Introduction

Previously it was concluded that Raman spectroscopy itself is not sufficient to draw a conclusion on active species and changes in active species under reaction conditions. Therefore, complimentary techniques such as IR, UV-vis, and X-ray absorption spectroscopy are needed. Soft X-rays are valuable probe for studying electronic and structural information of metal oxides. The "near-edge absorption fine-structure spectroscopy" (NEXAFS) and "X-ray absorption spectroscopy" (XPS) techniques enable analysis of sample surfaces using synchrotron radiation which probes only a limited sample depth (up to a few 100 nm)[358].

NEXAFS is a powerful method due to its atom specificity and is used as a probe of the unoccupied band structure of a material[359]. It allows one to study electronic and geometric structures of materials by providing information about *e.g.* valence band, coordination environment, and oxidation state. In addition, XPS is a highly surface sensitive technique due to photoelectron detection[358] and it gives elemental and chemical information of both catalysts and adsorbates[360].

One of the most challenging limitations with soft x-ray spectroscopy is that the experiments generally must be performed under ultra-high vacuum, which clashes with the desire to study catalytic reactions under ambient pressure. Nevertheless, the analysis of surfaces by X-ray techniques can give important information on the chemical processes of heterogeneous catalysts. A satisfying balance between soft x-ray and *in situ* measurements under realistic conditions was achieved by Knop-Gericke in late 1990s [361, 362]. The near- ambient pressure (NAP) spectroscopies XPS and NEXAFS enable researches to observe dynamic changes on catalyst surface at elevated pressures.

In- situ NAP XPS has been applied to several different reactions to clarify the changes in the chemical state of catalytically active surface under NAP conditions. For instance, CO[363, 364] and NO oxidation[365] on platinum group metals, ethylene epoxidation on Ag[366], and alkyne hydrogenation over Pd[367] have been deeply studied using NAP-XPS techniques. The NAP-NEXAFS technique is based on the total electron yield (TEY) method where Auger electrons and secondary electrons are collected with electrodes near the sample[361]. This technique was first applied to the Cu catalyst for methanol oxidation under reaction conditions[368]. Later the technique was improved by combining Auger electron yields (AEY) and TEY modes with a NAP-XPS electron analyzer and positively biased wire. The upgraded NAP-NEXAFS schematics can be seen in Figure 2.10. Since Auger electrons are significantly influenced by

inelastic scattering in the catalyst, applying a lower kinetic energy window to the AEY enabled maximization of surface related signals[359]. However, on the TEY mode, the gas-phase related signal is also obtained with the wire electrode. Therefore AEY is more surface sensitive than TEY (near-surface sensitive) since TEY detects all electrons [369]. However by applying a correction in which the gas phase O_2 transmission spectrum is measured and the spectrum is reconstructed, the impact from the gas-phase absorption can be successfully eliminated. The details of the methodology on reconstruction of the NEXAFS-spectrum was described by Hävecker *et al*.[359].

With all these developments, the combined technique of NAP-XPS and NEXAFS became a very powerful tool for identifying surface species under NAP conditions. In particular the knowledge in oxidation catalysis regarding the electronic structure of catalytically active surfaces have been broadened. For instance, selective oxidation of propane to acrylic acid over M1 MoVTeNb oxide catalyst [161, 370], n-butane oxidation to maleic anhydride over VPP [95, 371] and silica (SBA-15) supported vanadia during propane oxidation [336, 359, 372] have been studied by combined NAP-XPS and NEXAFS techniques. In addition, studies on supported vanadia during propane oxidation which aimed to understand the molecular structure of dehydrated surface VO_x species, *i.e,* to distinguish whether vanadia structures are monomer or polymer have also been conducted. Hävecker *et al*.[336] studied vanadium L- and oxygen K-edges of vanadia catalysts supported on SBA-15 with a various loadings of vanadia (2-14 wt. %) as well as the evolution of vanadium oxide species under reaction conditions. The interpretation of *in situ* V L-edge and O K-edge spectra of vanadium oxides have been improved with the aid of *ab initio* Density Functional Theory (DFT) cluster calculations[372]. With this, the authors were able to define vanadium oxide species on the surface of dehydrated catalysts. For instance, the NEXAFS spectra of catalysts with V loading below 8 wt. % on SBA-15 suggested the presence of both monomeric and polymeric species. The spectra of catalysts with metal loading equal and above 12 wt. % were assigned to three-dimensional character of V species. Moreover, it has been shown that significant structural surface reconstruction of vanadia occurs under reaction conditions. Overall, using experimental and theoretical methods together gives insight into the local geometric and electronic structures of the active species in the surface and correlates structures with their catalytic performance [241, 372, 373].

In the present study, the aim of the NAP-XPS and NEXAFS studies was to perform structural characterization of alkali-containing silica supported vanadium oxide catalysts. In addition, dynamic changes in the electronic structure of vanadium due to phase transition from solid to

liquid occurs under reaction conditions, was critically important to investigate. The experimental protocol is explained in the following.

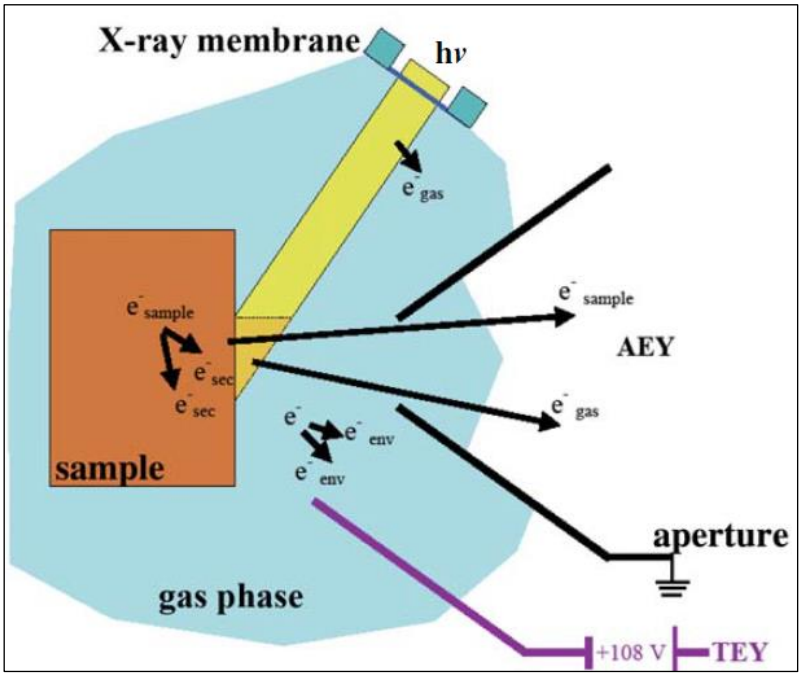

Figure 2.10. Sketch of the NAP-NEXAFS technique based on combined AEY and TEY modes (adopted from[359])

2.5.3.2. Experimental protocol

Operando near-edge X-ray absorption fine structure (NEXAFS) measurements and *operando* near-ambient pressure X-ray photoelectron spectroscopy (NAP-XPS) were carried out at the BElChem (Berlin joint lab for electrochemical interfaces) beamline at the synchrotron radiation source BESSY II in Berlin, Germany. The beamline is equipped with UE56/2 elliptical undulator and combines a high photon flux at low photon energies with an AP-XPS spectrometer without a wide angle acceptance lens but with a high, robust transmission at low kinetic energies and a powerful differential pumping of the electrostatic lens. The setup also allows for superior performance in valence band studies and direct in-situ determination of a material's work function by evaluating the position of the secondary electron cut-off [374].

A pressed powder pellet (1 ton, 8 mm diameter) of about 15 mg supported catalysts on a SiC plate and a sapphire sample holder was first activated, *i.e.*, heated under dynamic flow (21 O_2, rest N_2) at 10 K/min to 520°C and held there for 2 h. The measurements for propane oxidation were carried out at temperature range between 350 and 520°C and 250 Pa in 1:1 (7.5 $mlmin^{-1}$, 7.5 $mlmin^{-1}$) mixtures of propane and oxygen (C_3H_8/O_2, rest N_2).

NEXAFS measurements were carried out in the total electron yield (TEY) and Auger electron yield mode (AEY) with the kinetic energies set to 385 eV for K, Rb, and Cs-V-O/SiO_2 while 285 eV for Li-V-O/SiO_2 and 185 eV for Na-V-O/SiO_2 catalysts with a pass energy of 100 eV as a X-ray absorption spectroscopy (XAS) detector to minimize contributions from the gas phase spectra. O K-edge spectra of the sample surface were reconstructed applying a correction for the variation in photon flux at the sample position by using a gas phase O_2 TEY spectrum based on a methodology explained elsewhere[359].

Using insulating supports like SiO_2 inhibits the spectral quality due to differential charging. Fortunately, the unfavorable effect of differential charging decreases with increasing temperature. In this work, the loading of vanadium was sufficient to obtain a high quality of near-edge structure of the X-ray absorption spectra (NEXAFS). However XPS data were only reliable at the highest temperature (520°C) due to charging. Therefore, change in oxidation state of vanadium could not be discussed based on XPS data.

V L_3 and L_2- X-ray absorption spectra of catalysts were measured in the photon energy range between 512 and 528 eV. The V L_3- edge (corresponding to transition from V 2p to 3d orbitals) is sensitive to changes in the stoichiometry of the vanadium oxide therefore it can be used for identification of coordination environment of vanadium. However V L_2-edge is less important for the analysis due to its broadened structure along Coster-Kronig decay of the $2p_{1/2}$ hole[375, 376]. The oxygen K-edge (transition from O 1s to O 2p) above 528 eV was also measured. The energy range between 528 and 534 eV are defined by the pecularities of the V-O bonding while resonances at photon energy above ca. 534 eV reflect mainly the O 1s excitations of Si-O-Si bonds [336, 372]. A recent review gives the comprehensive information on oxygen K-edge X-ray absorption spectra of both molecules and solids [377].

The interpretation of NEXAFS spectra is challenging. Therefore, NAP-XPS and NEXAFS spectra of support-free alkali-vanadates were also measured as references for supported systems. In addition, fitting of V L-edges was conducted in ATHENA (Demeter)[293] software for quantitative analysis.

Si 2p, O 1s and V 2p XPS core level spectra were collected by setting the pass energy of the spectrometer to 20 eV. The excitation energy was 680 eV for O1s/V 2p spectra and 260 eV for Si 2p spectra. XPS core level spectra of K 2p, Cs 3d, Rb 3d, and Na 2p were also collected with photon energies of 440, 880, 260, and 180 eV, respectively. Quantitative elemental abundance of O 1s and the V $2p_{1/2}$ and V $2p_{3/2}$ core levels were determined using atomic subshell photo-ionization cross sections [378, 379]. The peaks were fitted with Gaussian-Lorentzian functions

after a Shirley background correction within CASA data analysis software [380]. The total peak areas of the respective core levels after a Shirley background correction were taken for calculation of the average oxidation state. For vanadium, the sum of V $2p_{1/2}$ and V $2p_{3/2}$ areas was used.

CHAPTER 3

3. Catalyst Synthesis and Basic Characterization

3.1. Freshly prepared catalyst precursors

The silica supported A/V catalysts were synthesized via spray dryer which is explained in detail in Section 2.2.1. The atomic ratio between Alkali (A): V was varied between 0.3 and 0.7 by keeping the total metal oxide loading constant at 10 wt. % ($A_2O+V_2O_5$). The range of A: V was selected based on an original phase diagram of A_2O and V_2O_5. With this, the impact of phase transitions under applied reaction conditions is aimed to be studied.

Phase composition, chemical composition and surface areas of freshly prepared catalyst precursors were measured by XRD, XRF, and BET techniques. Results obtained for supported A/V catalysts (A: Li, Na, K, Rb, and Cs) of varying A: V ratio are shown in Table 2-6, respective to the order of alkali element. Catalysts are denoted by atomic ratio of A/V, *i.e.* catalyst Li/V=0.3 has an analytical Li: V atomic ratio of 22: 78 as determined by XRF.

Table 3.1. Chemical composition, phase composition and surface area of silica supported Li/V catalysts with a different ratio of Li: V

ID#	Li/V (at.)	V_2O_5 wt.%	Total loading* (wt. %)	V (at. %)	Li (at. %)	XRD (expected phase)	XRD (observed phase)	BET (m^2/g)
30211	0.2	7.6	7.8	84	16	$Li_4V_{34}O_{87}$, $Li_4V_{10}O_{27}$	$Li_{1.5}V_3O_8$	120
30306	0.25	8.7	9.1	80	20	$Li_4V_{34}O_{87}$, $Li_4V_{10}O_{27}$	$Li_{1.5}V_3O_8$	101
30084	0.3	8.4	8.8	78	22	$Li_4V_{34}O_{87}$, $Li_4V_{10}O_{27}$	$Li_{1.5}V_3O_8$	110
30379	0.35	8.6	9.1	75	25	$Li_4V_{34}O_{87}$, $Li_4V_{10}O_{27}$	$Li_{1.1}V_3O_8$	96
30696	0.4	8.0	8.5	72	28	$Li_4V_{34}O_{87}$, $Li_4V_{10}O_{27}$	$Li_{1.1}V_3O_8$	87
30072	0.45	5.8	6.2	70	30	$Li_4V_{10}O_{27}$, $Li_2V_2O_6$	$Li_{1.5}V_3O_8$	100
30264	0.5	7.2	7.8	65	35	$Li_4V_{10}O_{27}$, $Li_2V_2O_6$	Opal, $LiVO_3$	25

*Analyzed by ICP-OES, based on $Li_2O+V_2O_5$

Table 3.2. Chemical composition, phase composition and surface area of silica supported Na/V catalysts with a different ratio of Na: V

ID#	Na/V (at.)	V_2O_5 wt.%	Total loading* (wt. %)	V (at. %)	Na (at. %)	XRD (expected phase)	XRD (observed phase)	BET (m^2/g)
31187	0.3	8.0	8.8	78	22	NaV_6O_{15}, $Na_3V_{24}O_{63}$	$Na_{1.16}V_3O_8$, $Na_{0.2}V_2O_5$	74
31267	0.35	8.0	9.0	74	26	$Na_3V_{24}O_{63}$	$Na_{1.16}V_3O_8$	40
30689	0.5	5.4	6.3	66	34	$Na_3V_{24}O_{63}$, $NaVO_3$	$Na_{1.16}V_3O_8$	62
31278	0.6	5.2	6.3	63	37	$Na_3V_{24}O_{63}$, $NaVO_3$	$Na_{1.16}V_3O_8$	41
30697	0.7	5.7	7.1	59	41	$Na_3V_{24}O_{63}$, $NaVO_3$	$Na_{1.16}V_3O_8$	44
30961	0.8	5.7	7.2	56	44	$Na_3V_{24}O_{63}$, $NaVO_3$	$Na_{1.16}V_3O_8$	27
30989	0.9	5.4	7.2	52	48	$NaVO_3$	$Na_{0.56}V_2O_5$	17

*Analyzed by ICP-OES, based on $Na_2O+V_2O_5$

Table 3.3. Chemical composition, phase composition and surface area of silica supported K/V catalysts with a different ratio of K: V

ID#	K/V (at.)	V_2O_5 wt.%	Total loading* (wt. %)	V (at. %)	K (at. %)	XRD (expected phase)	XRD (observed phase)	BET (m^2/g)
28594	0.3	7.8	8.9	78	21	$K_2V_8O_{21}$	$K_2V_8O_{21}$ $K_2V_2O_{16}1.5H_2O$	38
28772	0.4	7.7	9.2	73	26	$K_2V_8O_{21}$, $K_2V_2O_6$	$K_3V_5O_{14}$, $K_2V_2O_{16}1.5H_2O$	33
28645	0.5	7.1	9.1	66	34	$K_2V_8O_{21}$, $K_2V_2O_6$	$K_3V_5O_{14}$, $K_2V_2O_{16}1.5H_2O$	34
28654	0.6	6.4	8.5	62	37	$K_2V_8O_{21}$, $K_2V_2O_6$	$K_3V_5O_{14}$	24
28667	0.7	6.0	8.3	56	43	$K_2V_8O_{21_1}$, $K_2V_2O_6$	SiO_2	82

*Analyzed by XRF, based on $K_2O+V_2O_5$

Table 3.4. Chemical composition, phase composition and surface area of silica supported Rb/V catalysts with a different ratio of Rb: V

ID#	Rb/V (at.)	V_2O_5 wt.%	Total loading* (wt. %)	V (at. %)	Rb (at. %)	XRD (expected phase)	XRD (observed phase)	BET (m^2/g)
#29672	0.3	6.6	8.9	77	23	V_2O_5 + RbV_3O_8	$Rb_2V_6O_6$ $1.5H_2O$, $Rb_3V_5O_{14}$	20
#30184	0.35	6.4	9.0	74	25	RbV_3O_8	$Rb_2V_6O_6$ $1.5H_2O$, $Rb_3V_5O_{14}$, $Rb_2V_4O_{11}$,	53
#30182	0.4	6.0	8.9	70	30	RbV_2O_8, RbV_3O_8	$Rb_2V_4O_{11}$, $Rb_3V_5O_{14}$	78
#29680	0.5	5.8	9.0	65	35	RbV_2O_8, RbV_3O_8, $Rb_2V_4O_{11}$	$Rb_2V_4O_{11}$, $Rb_3V_5O_{14}$	55
#30151	0.6	5.7	9.1	63	37	RbV_2O_8, RbV_3O_8, $Rb_3V_5O_{14}$	$Rb_2V_4O_{11}$, $Rb_3V_5O_{14}$	86
#30178	0.65	5.6	9.5	60	40	RbV_2O_8, RbV_3O_8	$Rb_2V_4O_{11}$	83
#29697	0.7	5.2	9.0	58	42	RbV_2O_8, RbV_3O_8	$Rb_2V_4O_{11}$, $Rb_3V_5O_{14}$	99

*Analyzed by XRF, based on $Rb_2O+V_2O_5$

Table 3.5. Chemical composition, phase composition and surface area of silica supported Cs/V catalysts with a different ratio of Cs: V

ID#	Cs/V (at.)	V_2O_5 wt.%	Total loading* (wt.%)	V (at. %)	Cs (at. %)	XRD (expected phase)	XRD (observed phase)	BET (m^2/g)
28823	0.25	6.1	8.7	79	21	V_2O_5, $Cs_2V_6O_{16}$	CsV_2O_5	20
28913	0.3	5.6	6.0	76	24	$Cs_2V_6O_{16}$	CsV_2O_5	77
28845	0.4	5.5	9.0	72	28	$Cs_2V_4O_{11}$	CsV_2O_5	89
28857	0.5	5.4	9.4	68	32	$Cs_2V_6O_{16}$, $Cs_2V_4O_{11}$, $Cs_2V_2O_6$	CsV_2O_5	67
28862	0.6	4.6	9.0	62	38	$Cs_2V_6O_{16}$, $Cs_2V_2O_6$	CsV_2O_5	142
28897	0.8	4.3	9.7	56	44	$Cs_2V_6O_{16}$, $Cs_2V_2O_6$	CsV_2O_5	139

*Analyzed by XRF, based on $Cs_2O+V_2O_5$

3.2. Reference catalysts (supported and support-free alkali vanadate)

Supported alkali and supported vanadium oxide catalysts as well as the support itself were included as references. The properties of the supported reference catalysts measured by XRD, XRF, and BET are presented in Table 3.6. The chemical and phase composition of alkali vanadate (stoichiometric and reduced) phases are summarized in Table 3.7.

Table 3.6. Chemical composition, phase composition and surface area of reference catalysts (SiO_2-supported)

ID#	A/V (at.)	V_2O_5 wt.%	Total loading* (wt. %)	V (at. %)	A (at. %)	XRD (expected phase)	XRD (observed phase)	BET (m^2/g)
Li/SiO_2 #30462	1	-	0.2	-	100	-	SiO_2	227
Na/SiO_2 #31042	1	-	0.42	-	100	-	SiO_2	98
K/SiO_2 #28690	1	0	6.0	0	100	-	SiO_2	113
Rb/SiO_2 #29711	1	0	10.0	0	100	-	SiO_2	79
Cs/SiO_2 #28911	1	0	13.1	0	100	-	SiO_2	108
V/SiO_2 #28683	0	8.8	8.8	100	0	V_2O_5	V_2O_5	206
SiO_2 #28958	0	0	0	0	0	SiO_2	SiO_2	285

*Analyzed by XRF, based on $A_2O+V_2O_5$ (ICP-OES for Li and Na)

Table 3.7. Chemical composition and phase composition of reference catalysts (support-free)

ID#	Name	A: V (at. %)$^{\perp}$	XRD
31564	$K_3V_5O_{14}$	3: 5	$K_3V_5O_{14}$
32008	KV_3O_8	1: 3	KV_3O_8
29584	$K_2V_8O_{21}$	1: 4	$K_2V_8O_{21}$ [291]
30216	KVO_3*	1:1	KVO_3
32579	$K_xV_yO_z$	1.06: 3	$K_2V_8O_{21} + KV_3O_8 + K_{0.48}V_2O_5$
32648	$K_xV_yO_z$	0.8: 3	$K_2V_8O_{21} + KV_3O_8 + K_2V_6O_{16}.1.5H_2O$
32741	$K_xV_yO_z$	0.7:3	$K_2V_8O_{21} + K_{0.25}V_2O_5 + K_xV_2O_5$
32812	$K_xV_yO_z$	0.5:3	$K_{0.75}V_6O_{16} + K_{0.25}V_2O_5 + KV_3O_8$
32815	$K_xV_yO_z$	0.4: 3	$K_xV_6O_{16}, K_xV_2O_5$
33753	$K_xV_yO_z$	0:3: 3	$K_{0.71}V_6O_6$
32835	$K_xV_yO_z$	0.3:3	$K_{0.75}V_6O_6 + K_xV_2O_5$
32836	$K_xV_yO_z$	0.2: 3	$K_{0.75}V_6O_{16} + V_2O_5$
32841	$K_xV_yO_z$	0.1:3	$K_{0.75}V_6O_6 + V_2O_5$
32836	$Rb_xV_yO_z$	3: 5	$Rb_2V_4O_{11} + RbV_2O_5$
32285	$Rb_xV_yO_z$	1: 2	$Cs_2V_4O_{11} + CsV_2O_5$
32135	$CsVO_3$	1: 1	$CsVO_3$
32154	$RbVO_3$	1: 1	$RbVO_3$

$^{\perp}$Analyzed by XRF, based on $A_2O+V_2O_5$ *commercial

3.3. Characterization of freshly prepared catalyst precursors

3.3.1. Chemical composition

The chemical composition of the catalysts was analyzed by XRF (Table 3.1-3.7). The total metal oxide loading (A_2O+ V_2O_5) had been achieved as ~10 wt. %. Since the vanadium introduction is higher than 5 wt. %, the monolayer coverage is expected [381-383]. By keeping the total metal oxide loading constant, the atomic ratio of alkali to vanadium was varied between 0.2 and 0.9 based on the phase diagram of A_2O-V_2O_5 systems (Figure 3.1).

For Li/V and Na/V catalysts, the loading of V_2O_5 was found to be accumulated around 6-8 wt. %. By keeping the total metal oxide loading constant, the atomic ratio of lithium to vanadium was altered between 0.2 and 0.5. For Na/V catalysts, the atomic ratio of sodium to vanadium was altered between 0.3-0.9.

According to the phase diagram of Li_2O-V_2O_5[384], and Na_2O-V_2O_5[385] systems, no phase transitions are expected in the regions of interest (Figure 3.1A-3.1B). However, the atomic ratio of potassium to vanadium was altered between 0.3-0.7, where the phase transition of potassium-vanadate phase occurs[386] (Figure 3.1C). The same approach was applied for Rb (Figure 3.1D), and Cs added vanadia catalysts (Figure 3.1E) as well. For Cs/V catalysts, the loading of V_2O_5 accumulated around 4-6 wt. % and Cs: V was varied between 0.2-0.8 [387]. Rb: V was varied between 0.2-0.5 with the loading of V_2O_5 between 5-6 wt. %[388]. The regions studied for K/V, Rb/V, and Cs/V catalysts were chosen to investigate the effect of melting in propane oxidation based on their corresponding A_2O-V_2O_5 phase diagrams (Figure 3.1).

3.3.2. Phase composition

Powder XRD patterns of silica supported A/V catalysts (Table 2-6) indicated that the catalysts contained some crystalline alkali vanadate phases. The phases detected by XRD are in accordance with the A/V ratio determined by XRF. However, the identified phases by XRD differ from the phase diagrams, probably because either thermodynamic equilibrium was not reached or support has an impact on phase formation. No binary metal oxide phase/s were observed. For supported Li/V catalysts (Table 3.1), the formation of $Li_4V_{34}O_{87}$, $Li_4V_{10}O_{27}$, and $Li_2V_2O_6$ phases are expected for the range between 0.2- 0.7 (Li/V at.)[384]. All diffraction patterns were found possibly to be corresponded to some $Li_xV_3O_8$ structures: $Li_{1.5}V_3O_8$ and $Li_{1.1}V_3O_8$ (ICSD No. 55717)[389].

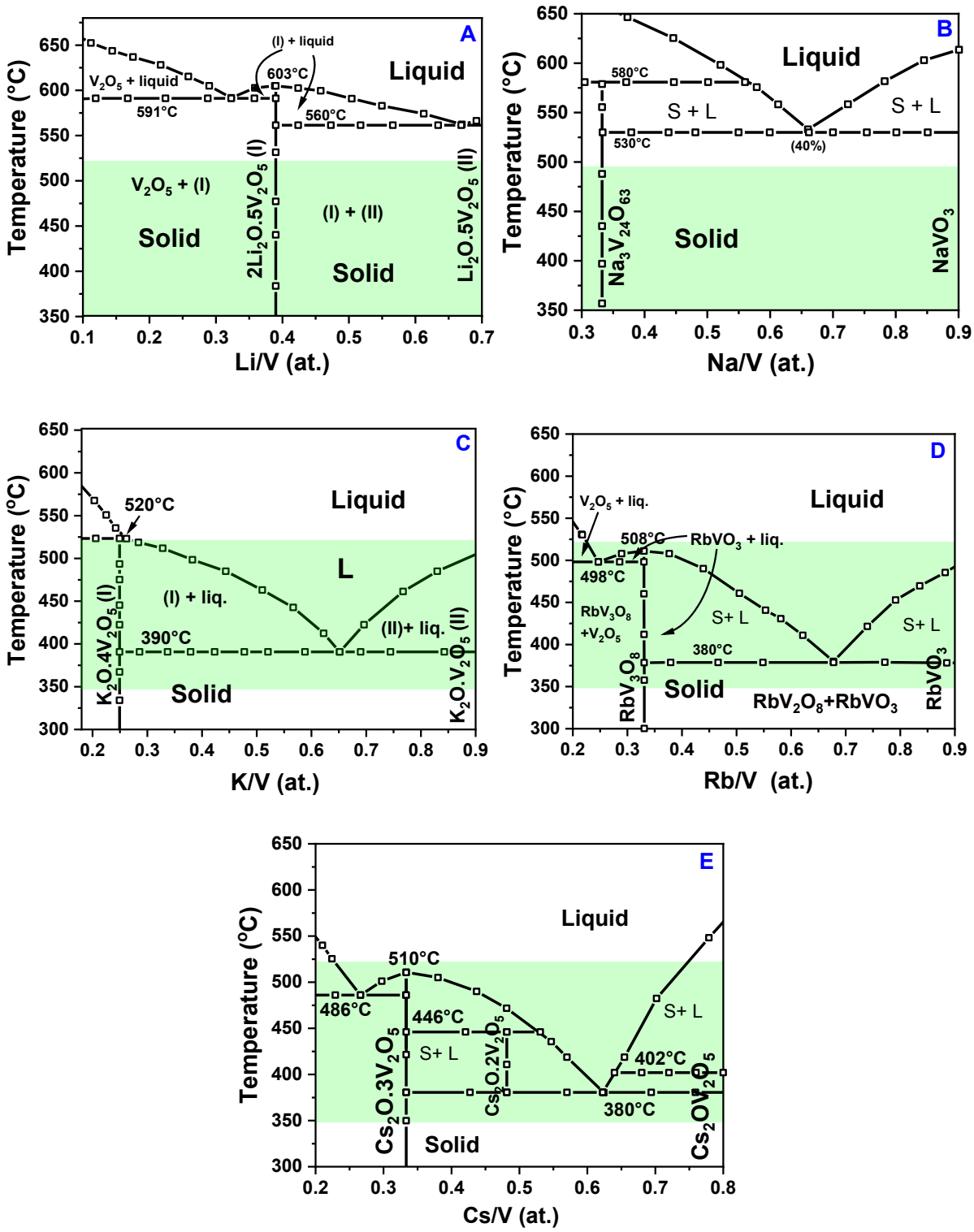

Figure 3.1. Phase diagrams of **(A)** Li_2O-V_2O_5 system[384]; **(B)** Na_2O-V_2O_5 system[385]; **(C)** K_2CO_3-V_2O_5 system[386]; **(D)** Rb_2O-V_2O_5 system[388]; **(E)** Cs_2CO_3-V_2O_5 system[387] (green rectangle indicates the applied reaction temperature range in this study, *i.e.*, 350- 520°C)

As seen upon lithium addition, the formation of $Na_xV_3O_8$ was detected for Na/V catalysts (Table 3.2). It has to be underlined that very low crystallinities were observed for both Li/V and Na/V catalysts. Na/V catalysts have slightly higher crystallinity than Li/V catalysts. This is because

calcination temperature (620°C) presumably was not sufficient for complete liquefaction to form crystalline alkali-vanadates since complete liquefaction for Li/V and Na/ V catalysts is expected to occur at temperatures higher than 550°C according to phase diagrams (Figure 3.1A, and Figure 3.1B). This temperature is much higher compared to the rest of the alkali metals (K, Rb, and Cs).

$K_2V_2O_6$ and $K_2V_8O_{21}$ phases are expected based on the phase diagram of K_2O-V_2O_5[386] (Table 3.3) for the range between 0.3- 0.7 (K/V at.). For K/V=0.6, potassium pentavanadate ($K_3V_5O_{14}$) (ICSD No. 24068) [294, 390] was the only crystalline phase detected beyond the amorphous support. The remaining catalysts consist of a mixture of potassium vanadium oxides. For K/V=0.3, mixed potassium vanadate phases were identified, including potassium octavanadate ($K_2V_8O_{21}$) (ICSD No. 154164)[391] and potassium hexavanadate ($K_2V_2O_{16}1.5H_2O$)[392]. In the case of K/V=0.4 and K/V=0.5 catalysts, the $K_2V_2O_{16}1.5H_2O$ phase and $K_3V_5O_{14}$ were observed. Whilst for K/V=0.7 no crystalline phase was identified.

For supported Rb/V catalysts (Table 3.4), the formation of RbV_3O_8, RbV_2O_8, $Rb_2V_4O_{11}$ and $Rb_3V_5O_{14}$ phases are expected for the range between 0.3- 0.7 (Rb/V at.)[393]. For Rb/V=0.3 and Rb/V=0.35 catalysts, $Rb_2V_6O_6$ $1.5H_2O$, $Rb_3V_5O_{14}$ (ICSD No. 420851)[394] and $Rb_2V_4O_{11}$ were identified. Catalysts for Rb/V ≥0.4, a mixture of two rubidium vanadium oxide phases was identified, these were $Rb_2V_4O_{11}$ and $Rb_3V_5O_{14}$.

For supported Cs/V catalysts (Table 3.5), $Cs_2V_6O_{16}$, $Cs_2V_4O_{11}$ (ICSD No. 85005)[395], and $Cs_2V_2O_6$ phases are expected for the range between 0.25-0.8 (Cs/V at.)[387]. Independent of the cesium and vanadium content, the XRD pattern of CsV_2O_5 (ICSD No. 850)[396] wasobserved for all Cs/V catalysts.

The total metal oxide loading of reference catalysts were comparable with supported catalysts which varies between 6 and 13 wt. % (Table 3.6). However, the total metal oxide loading of Li/SiO_2 and Na/SiO_2 catalysts obtained very low (*i.e.* 0.2-0.4 wt. %) possibly due to the higher volatility of these alkali metals.

The VO_x/SiO_2 sample appears orange after calcination, while catalysts with alkali modifications change color after calcination which varies from yellow through dark salmon. According to Erdöhelyi and Solymosi[113], colored compounds are probably polyvanadates where A_2O content is less than that of V_2O_5. In this study, catalysts with A/V < 0.5 appeared in a dark-salmon color while A/V >0.5 was beige orange-yellowish color, which further indicates the formation of alkali vanadate species. In general, the color of A/V catalysts varies from dark

salmon to light yellow with increasing alkali content. The variety of catalyst colors further indicates that either crystalline or amorphous alkali vanadium oxide phases are formed (Figure S1.1).

3.3.3. Specific surface areas of the calcined catalysts

The specific surface area of SiO_2 (Aerosil 300) reduced from 285 m^2 g^{-1} to 206 m^2 g^{-1} upon adding vanadium (Table 3.6). This is simply due to the channel blocking upon vanadium oxide deposition [242, 397]. In addition, alkali additives led to the further decrease of surface area of catalysts (Table 3.1-3.3.5) which has been reported in the literature as well [198, 249, 398, 399]. In general, the surface area of catalysts change based on either the loading of vanadium[83] or the loading of alkali metals[249].

The surface areas of the supported Li/V catalysts (Table 3.1) were relatively similar, varying between 87 and 120 m^2 g^{-1}, except for the catalyst Li/V=0.5, for which a surface area of 25 m^2 g^{-1} surface obtained. The BET surface area of the catalysts decrease in the following order: Li/V=0.2 > Li/V=0.3 > Li/V=0.25 > Li/V=0.45 > Li/V=0.3> Li/V=0.4.

Compared to the Li/V catalysts, the addition of Na lowered the surface area more drastically. The surface areas of the supported Na/V catalysts (Table 3.2) vary between 41 and 74 m^2 g^{-1}. For Na/V=0.8, and Na/V=0.9 catalysts, even lower surface areas were obtained which are 27 and 17 m^2 g^{-1}, respectively. The BET surface area of the Na/V catalysts decrease in the following order: Na/V=0.3 > Na/V=0.5 > Na/V=0.7 > Na/V=0.6 > Na/V=0.35 > Na/V=0.8 > Na/V=0.9.

The decrease in surface area of catalysts was further decreased upon K-addition (Table 3.3). The surface area of most catalysts was similar, varying between 24 and 38 m^2 g^{-1}. However, the surface area of the catalyst K/V=0.7 was larger than all, which is 82 m^2 g^{-1}. The most dramatic effect within catalysts is seen for the catalyst K/V=0.6 in which only $K_3V_5O_{14}$ was detected.

The surface area of the supported Rb/V catalysts were higher compared to supported K/V catalysts. The surface area of the catalysts varies between 20 and 99 m^2 g^{-1} (Table 3.4). The lowest surface was determined for Rb/V=0.3 catalyst. Generally, the BET surface area of catalysts decreases in the order Rb/V=0.7 > Rb/V=0.6 > Rb/V=0.4 >Rb/V=0.5 >Rb/V=0.3.

The surface area of supported Cs/V catalysts (Table 3.5) was varied within the similar extent of supported Rb/V catalysts. The surface areas of the catalysts were diverse, varying with a similar extent of surface area as supported Rb/V catalysts between 20 to 142 m^2 g^{-1}. The lowest

BET surface area was determined for the lowest Cs-loaded catalyst (*i.e.* Cs/V=0.2) whereas the highest BET surface area was determined for one of the highest Cs-loaded catalyst (*i.e.* Cs/V=0.6). The BET surface areas of the catalysts decrease in the order Cs/V=0.6 > Cs/V=0.8 > Cs/V=0.4 > Cs/V=0.3 > Cs/V=0.5 > Cs/V =0.25.

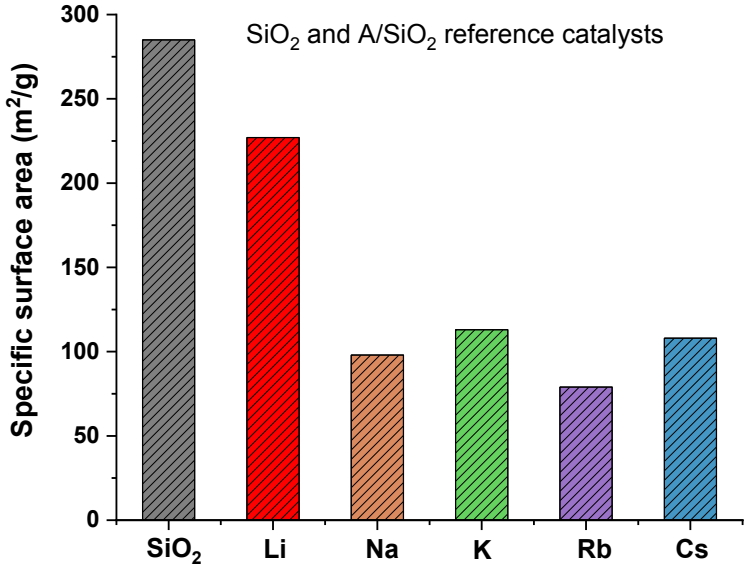

Figure 3.2. The specific surface areas of alkali-containing SiO_2 catalysts compared to SiO_2

The comparison of surface areas of the catalysts as a function of A: V ratio (at.) is shown in Figure (3.3). First of all, a significant decrease in surface areas upon alkali addition is noticeable (Figure 3.2). Although the Li-loading seems to have no impact on surface area of VO_x/SiO_2 catalysts, a very low loading of Li_2O which is 0.2 wt. % must be noted. Within the A/V catalysts, the Li/V, Na/V and K/V catalysts shows roughly a decreasing trend with increasing alkali-content. However, Rb/V and Cs/V catalysts show an increasing trend in surface areas with increasing alkali content until A/ V equal to 0.5 (at.). This is the ratio where surface areas of all A/V catalysts decrease. Above 0.5, increasing behavior in surface areas (except for Na/V) was obtained.

Overall, the surface areas of catalysts decreases upon alkali addition. Not only the addition of a second component was the reason, but also synergistic effect between vanadia and alkali additives lead to the sintering of the support by forming some crystalline alkali- vanadates (as detected by XRD) and/or some amorphous phases (will be discussed further at DSC analysis). No clear correlation is seen on the BET surface area as a function of the content of metal oxides.

The highest surface area was obtained for Li addition and decrease according to the following order:

Si< VSi< LiVSi< CsVSi< RbVSi< NaVSi< KVSi

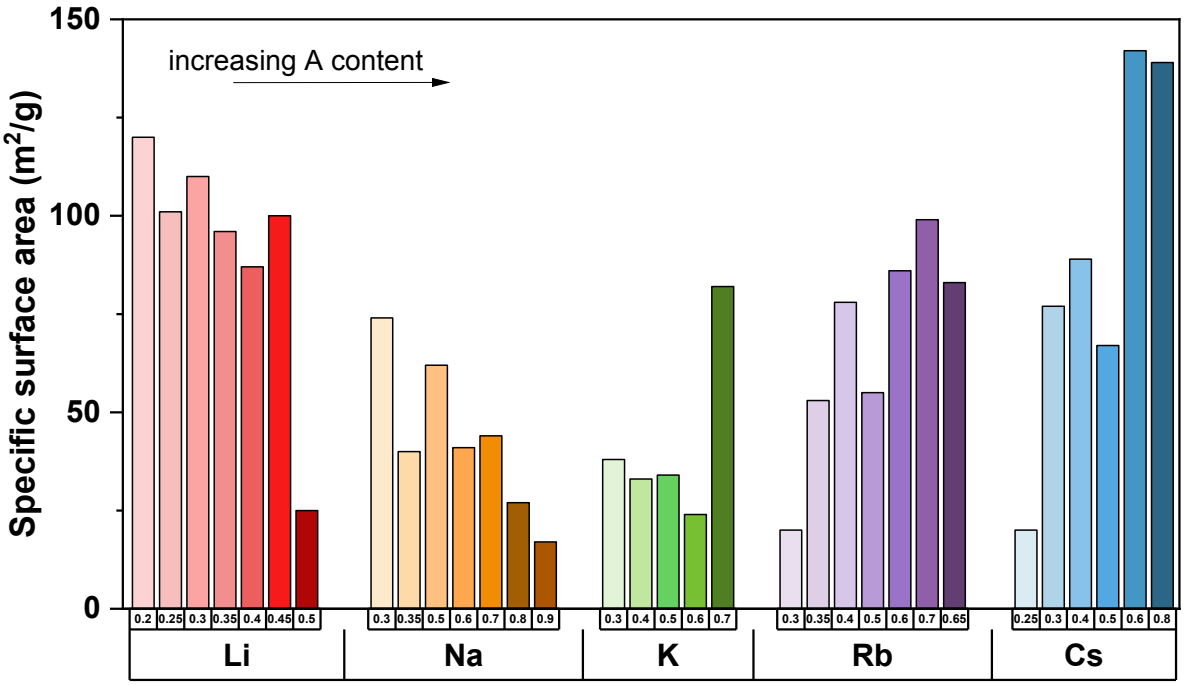

Figure 3.3. The specific surface areas of A/V catalysts with a different ratio of A: V (A: Li, Na, K, Rb, and Cs)

3.3.4. Raman spectroscopy (ex situ)

All *ex-situ* Raman measurements for silica supported A/V catalysts were conducted with 532 nm laser. The Raman spectra of silica supported Li/V catalysts are presented in Figure 3.4A. The Raman spectrum of Li/V catalysts revealed several main peaks that were noticeable at 477, 759, 995 cm^{-1}, and broad peak at 578 cm^{-1}. Peak intensities do not change with Li-loading except for the catalyst Li/V=0.5 whose peak intensity at 750 cm^{-1} reduced significantly. For catalysts Li/V=0.4 and Li/V=0.5, three minor but distinguishable peaks located at 969, 984, and 1007 cm^{-1} were found. Raman spectra of Li/V catalysts were compared with the Raman spectrum of LiV_3O_8 which was intensively studied in the literature. Zorkipli *et al.*[400] had previously reported that the Raman band at 777 cm^{-1} corresponded to the corner-sharing oxygen atomic motions of between the polyhedral VO_5, VO_6, and LiO_6. Moreover, the peaks between 966 and 1099 cm^{-1} were derived from the V-O stretching vibrations of VO_5.

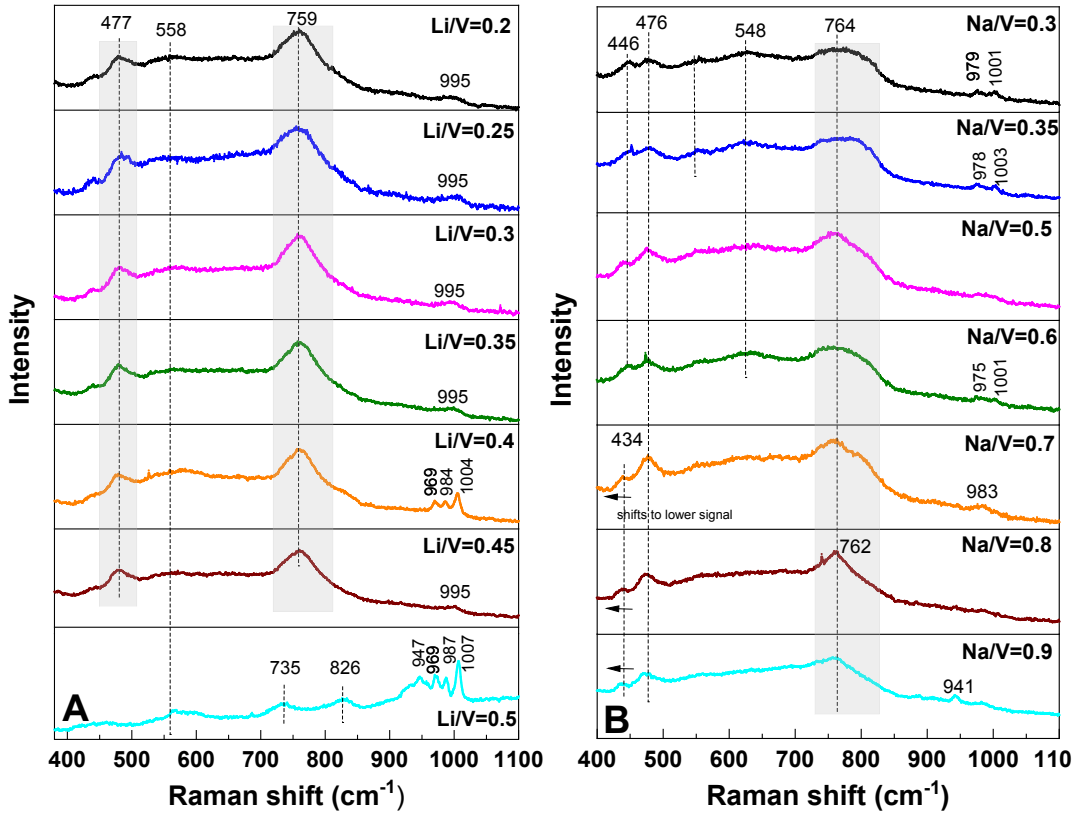

Figure 3.4. Ex-situ Raman spectra of calcined supported **(A)** Li/V and **(B)** Na/V catalysts (λ_{exc} =532 nm)

The Raman spectrum of supported Na/V catalysts (Figure 3.4B) revealed several main peaks which were broad but distinguishable at 446, 477, 548, 626, 764, and minor peaks at about 990 cm^{-1}. The Raman spectra of Na/V catalysts very much resemble the spectra of Li/V catalysts. The only difference is the intensity of the peak at 764 cm^{-1} which appears much broader in Na/V catalysts. This is in agreement with the literature report wherein the broader mode at about 650-700 cm^{-1} were assigned to V-O_2 stretching vibrations of NaV_2O_5 system[401]. In the same study, Raman modes at lower frequency between ca. 440-460 cm^{-1} were assigned as V-O_3-O bending vibrations. The peak at 764 cm^{-1} gets sharper upon increased Na-loading.

The ex-situ Raman spectra of silica supported K/V catalysts are presented in Figure 3.5. The Raman spectrum of the K/V=0.3 catalyst showed relatively few active bands which are broad. Based on XRD analysis result, the Raman spectrum of K/V=0.3 was compared with the room temperature Raman spectrum of $K_2V_8O_{21}$ which was previously recorded by Krasilńikov *et al.* [402]. In addition, the spectra of support-free $K_2V_8O_{21}$ (synthesized *via* solid-state method[291]) was measured and compared to the spectra of K/V=0.3 (Figure 3.6). Based on these, terminal V-O bonds appeared at 955 cm^{-1} and the highest intensities was characterized of the Raman lines peaking at 800-700 cm^{-1} associated with the vibrations of bridging bonds.

In a similar trend, the most intense band in the spectrum of K/V=0.3 was at 736 and 789 cm^{-1}, with much less intense features at 988 cm^{-1}.

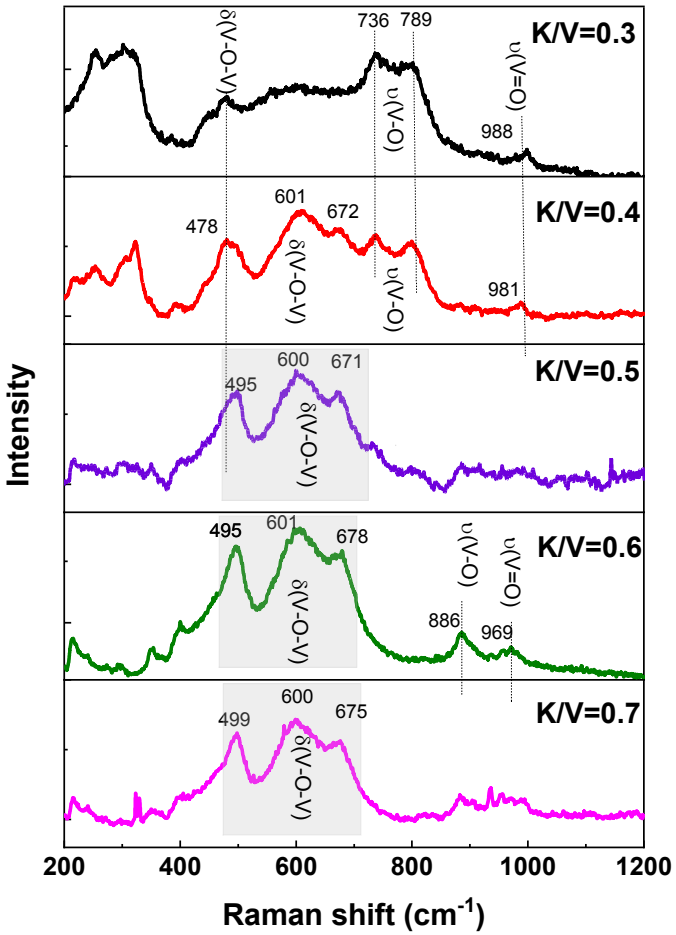

Figure 3.5. Ex-situ Raman spectra of calcined silica supported K/V catalysts (λ_{exc} =532 nm)

The spectrum of catalyst K/V=0.4 showed increasing vibrational bands at 478, 601 and 672 cm^{-1} in addition to vibrations of terminal V-O bonds. These bands are similar features of vibrations of V-O-V bridging bonds calculated and measured for appropriate reference compound, *i.e.* $K_3V_5O_{14}$. Moreover, the bands between 730-790 cm^{-1} were also detected which is similar to the stretching vibrations of V-O from the alterations of $K_2V_8O_{21}$ (Figure 3.6). The detailed assignment of the Raman bands for catalysts K/V=0.3, 0.4 and 0.5 were difficult as there is little previous Raman data on potassium vanadate systems. However, it is still seen that the Raman spectra of catalysts resemble the Raman spectrum of $K_3V_5O_{14}$ with an increasing K content, which is in an agreement with XRD results. In the case of the catalyst K/V=0.6, the Raman bands were confirmed as alterations of $K_3V_5O_{14}$, which is in a good agreement with the result obtained by XRD.

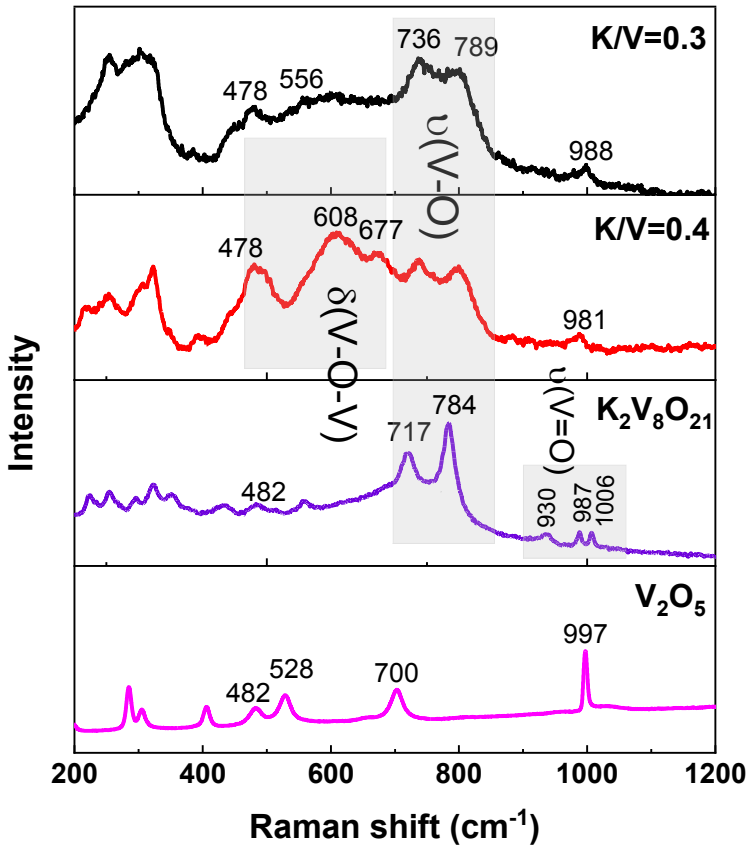

Figure 3.6. Ex-situ Raman spectra of silica supported K/V=0.3 and K/V=0.4 catalysts compared to the reference spectra of $K_2V_8O_{21}$ and V_2O_5 (λ_{exc} =532 nm)

General assignment regarding to the $K_3V_5O_{14}$ was made by measuring support-free $K_3V_5O_{14}$ as reference material and calculating vibrational modes of $K_3V_5O_{14}$ with DFT [291] (Figure 3.7). Detailed characterization of $K_3V_5O_{14}$ can be found in Section 3.4. By following the unit-cell structure of the $K_3V_5O_{14}$ (Figure 3.23), it can be seen that K cation is surrounded by five polyhedral which are three square pyramid [VO_5] and two tetrahedral [VO_4] units. According to spectra measured with 532 nm laser (Figure 3.7), the support-free $K_3V_5O_{14}$ has Raman modes at 215, 351, 427, 566, 501, 602, 680, 884, and 989 cm^{-1}. By combining the unit-cell structure of $K_3V_5O_{14}$ with its DFT calculation (Figure 3.7), it can be stated that the most intense bands in range of 450-700 cm^{-1} are due to the bending vibrational modes (V-O-V) between units whereas bands between 850 and 990 cm^{-1} are due to the stretching modes within [VO_4] and [VO_5] units. The Raman spectrum of silica-supported K/V=0.6 matches very-well with the spectra of $K_3V_5O_{14}$ as measured by 532 nm laser.

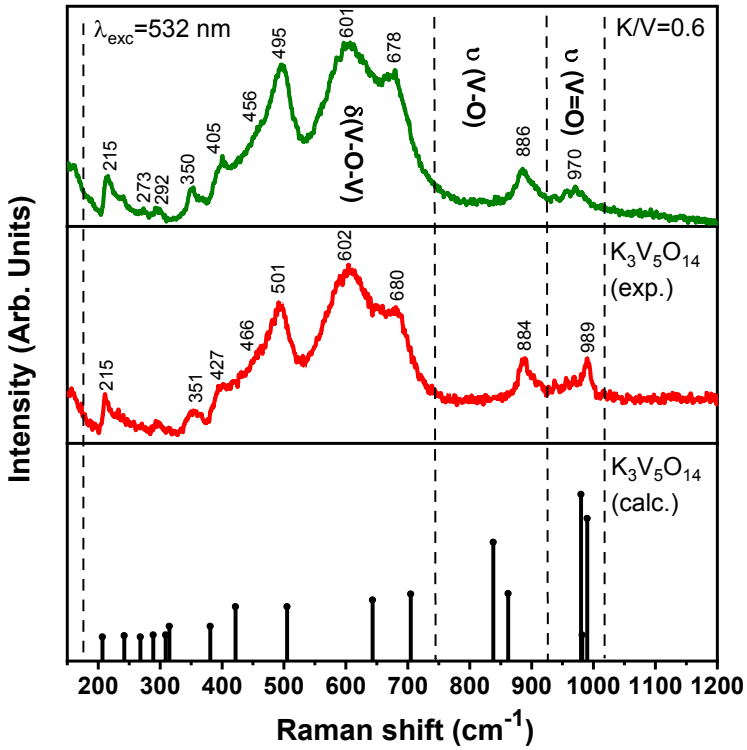

Figure 3.7. Ex-situ Raman spectrum of silica supported K/V=0.6 catalyst compared to experimental and calculated Raman spectra of $K_3V_5O_{14}$ (λ_{exc} =532 nm)

The Raman spectrum of silica-supported Rb/V catalysts are presented in Figure 3.8. The Raman spectra of catalysts Rb/V=0.3 and Rb/V=0.35 showed few bands which are broad. The most intense band in the spectrum was at 733 and 785 cm^{-1}. The remaining catalysts showed increased intensity in vibrational bands at 495, 602 and 675 cm^{-1}. These bands are similar features of vibrations of V-O-V bridging bonds. It can further be seen that the spectra of catalysts between Rb/V=0.4 and Rb/V =0.65 is very much similar to the spectra of K/V=0.6. This is because $Rb_3V_5O_{14}$ (rubidium pentavanadate) has the same crystal structure of $K_3V_5O_{14}$. However due to the mixture of, $Rb_2V_4O_{11}$ (rubidium tetravanadate) and $Rb_3V_5O_{14}$ phases, the relative intensities between the band at 670 cm^{-1} and the band at 602 cm^{-1} are different. The other bands at about 878, 953 and 991 cm^{-1} originate from the stretching vibrations from a short V-O and V=O (vanadyl group) bond.

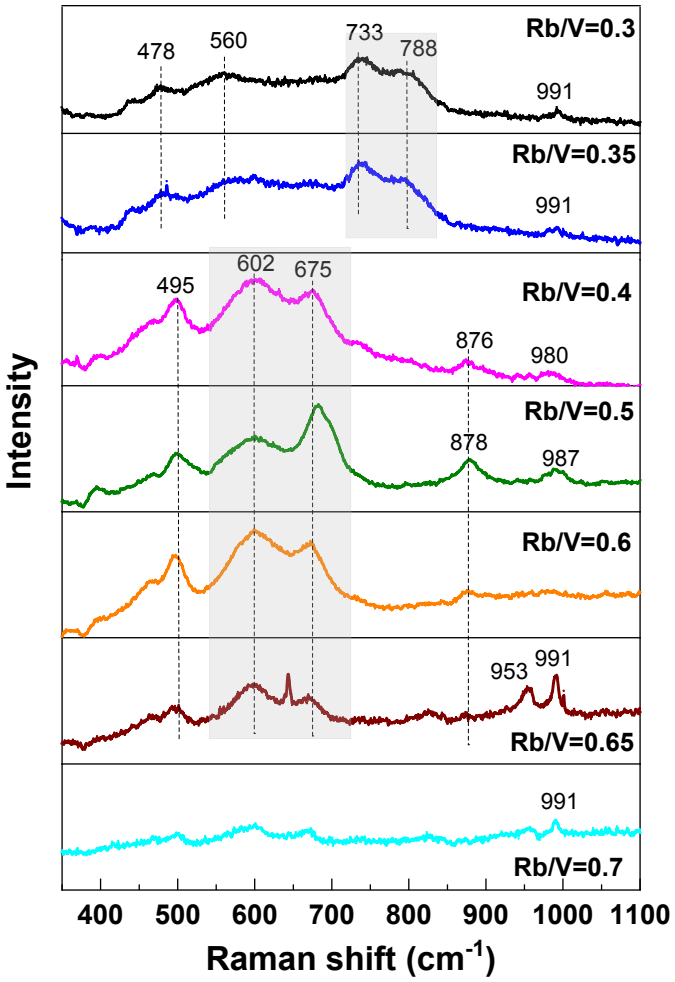

Figure 3.8. Ex-situ Raman spectra of calcined silica supported Rb/V catalysts (λ_{exc} =532 nm)

The Raman spectrum of some of the supported Cs/V catalysts are presented in Figure 3.9. The measurement of Raman spectroscopy of supported Cs/V catalysts were not successful for some compositions due to fluorescence. Therefore, only catalysts Cs/V=0.3, 0.4 and 0.5 were presented. Raman modes of supported Cs/V catalysts are grouped into two spectral regions, one is at about 700 cm^{-1} and the other is at 800-900 cm^{-1}. The assignment was done based on Raman modes of CsV_2O_5 since it was the only phase detected beyond amorphous SiO_2 by XRD.

The spectrum of catalyst Cs/V=0.3 showed some Raman active bands at 674, 710, 874, and 994 cm-^{1}. These bands become more pronounced with increasing Cs-content. According to the Raman spectroscopy of CsV_2O_5 in the literature as measured with 448 nm laser [401], the modes between 500 and 700 cm^{-1} were represented as the vibration of VO_5 pyramid. The modes between 750 and 950 cm^{-1} originated from V-O stretching vibrations of the corresponding bonds of VO_4 tetrahedra. Similarly with the previous alkali-containing measurements, stretching vibrations from short V-O (planar) and V=O (terminal) vanadyl group at 874 and 994 cm^{-1} were also detected.

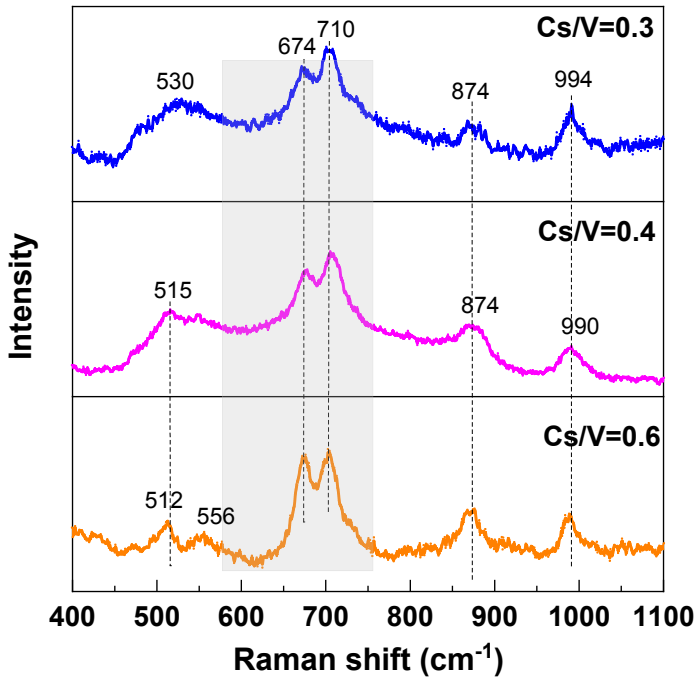

Figure 3.9. Ex-situ Raman spectra of calcined silica supported Cs/V catalysts (λ_{exc} =532 nm)

3.3.5. Morphology of the calcined catalysts

Representative SEM images of some A/V catalysts are displayed in Figure 3.10. It must be remembered that the catalysts were calcined at 620°C. This is the temperature where melting is expected based on phase diagrams (Figure 3.1). After calcination at elevated temperature, A-V/SiO_2 catalysts are composed of two individual structures: (i) distinguishable silica spheres and (ii) a glassy structure of alkali-vanadate phases on the surface of silica spheres. This structure can be seen in Figure 3.11 in a higher magnification. This is a common feature which is seen in each different type of silica supported alkali-added vanadium oxide catalysts (Figure S1.2-S1.6).

Note that although the calcination temperature (620°C) was thought insufficient for melting of Li and Na-containing vanadates based on the phase diagram, glassy structures are still distinguishable with subsequent solidification after calcination (Figure 3.10A, 3.10B). This indicates that amorphous surface alkali-vanadate phases were formed since the thermal equilibrium not being reached, which results in very low crystallinity as detected by XRD and Raman spectroscopy as well.

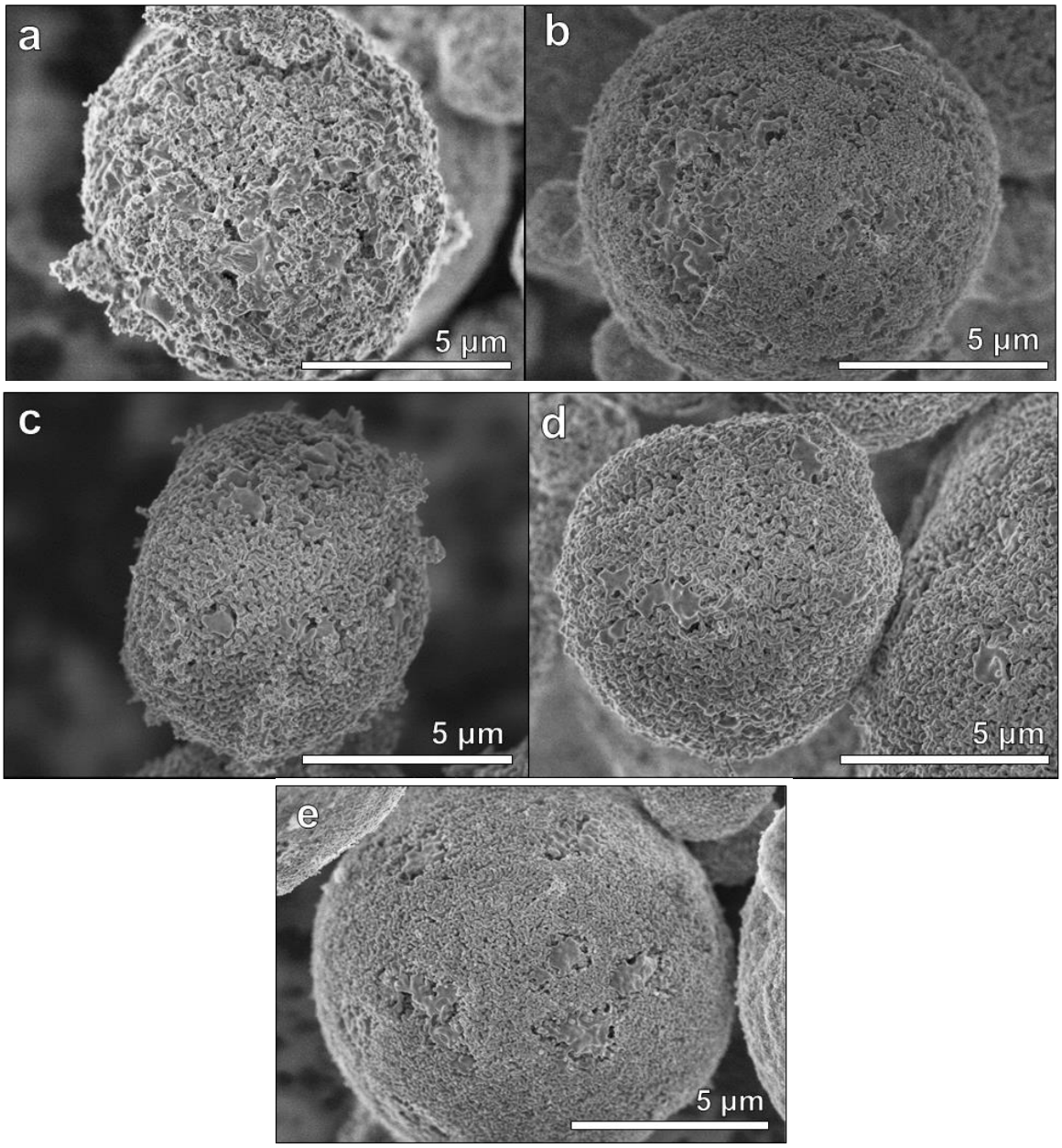

Figure 3.10. SEM image of silica supported A/V catalysts **(a)** Li/V=0.3 (ID=#30084), **(b)** Na/V=0.5 (ID=#30689), **(c)** Rb/V=0.3 (ID=#29672), **(d)** K/V=0.4 (ID=#28772), and **(e)** Cs/V=0.5 (ID=#28857)

The dispersion of K and V species over K/V=0.4 catalyst was monitored with a YAG BSE detector (Figure S1.7) of SEM. It is seen that YAG BSE detector permits clear identification of molten areas on the surface of the support. Areas indicated as ‘a’ and ‘b’ contain potassium and vanadium, measured by EDX as well (Figure S1.7). This further indicates that our synthesis method is successful in forming alkali vanadate on the surface of the support.

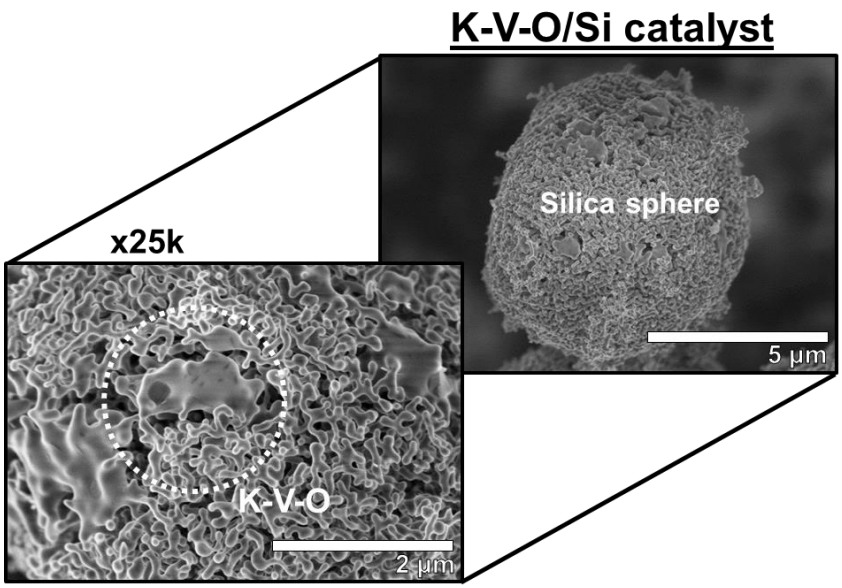

Figure 3.11. Representative SEM image of catalyst K/V=0.4 (internal ID=#28772)

Direct analysis of chemical composition on the melt was conducted for the phase pure catalyst K/V=0.6 (as detected by XRD) to confirm the formation of the alkali- vanadate phase. From the STEM-EDS analysis it can be seen that elements K, V, and O are unequally distributed over the support (Figure 3.12).

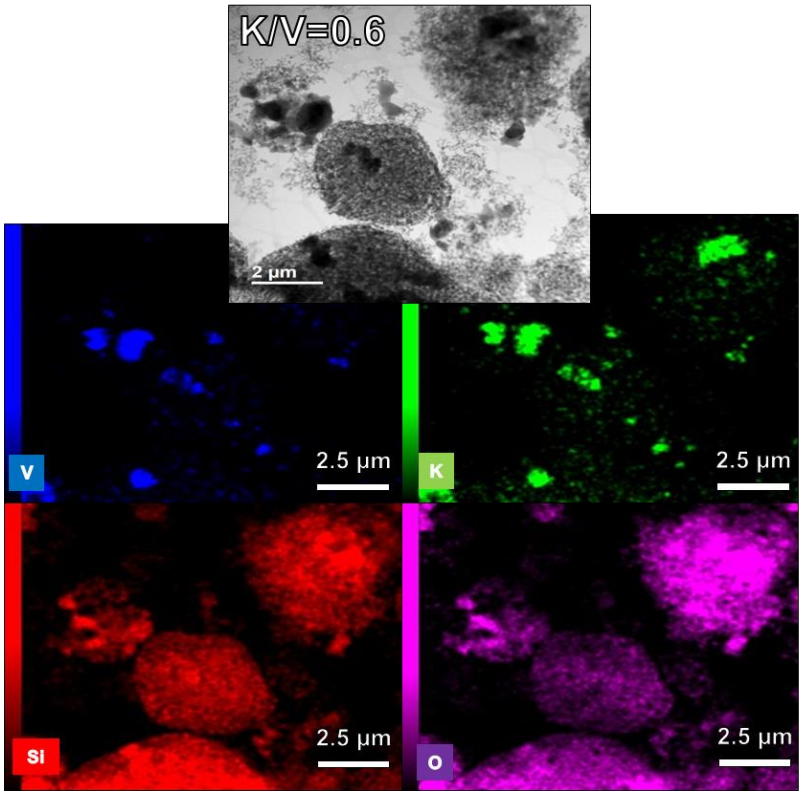

Figure 3.12. STEM-EDS image of K/V=0.6 catalyst

The bulk metal composition corresponds to 10.39 at. % of V and 6.18 at. % of K, which gives K/V ratio 0.58 in agreement with XRF (Table 3.3). EDS analysis also showed that the molten areas are not phase pure K-V-O phase but there is also presence of K-SiO_2 phase as is expected due to the reaction of potassium with silica and V-enrichment on the surface (Figure 3.13). Overall the analysis suggests the formation of alkali-vanadate phases occurred on the surface which supports the results obtained from XRD and Raman spectroscopy.

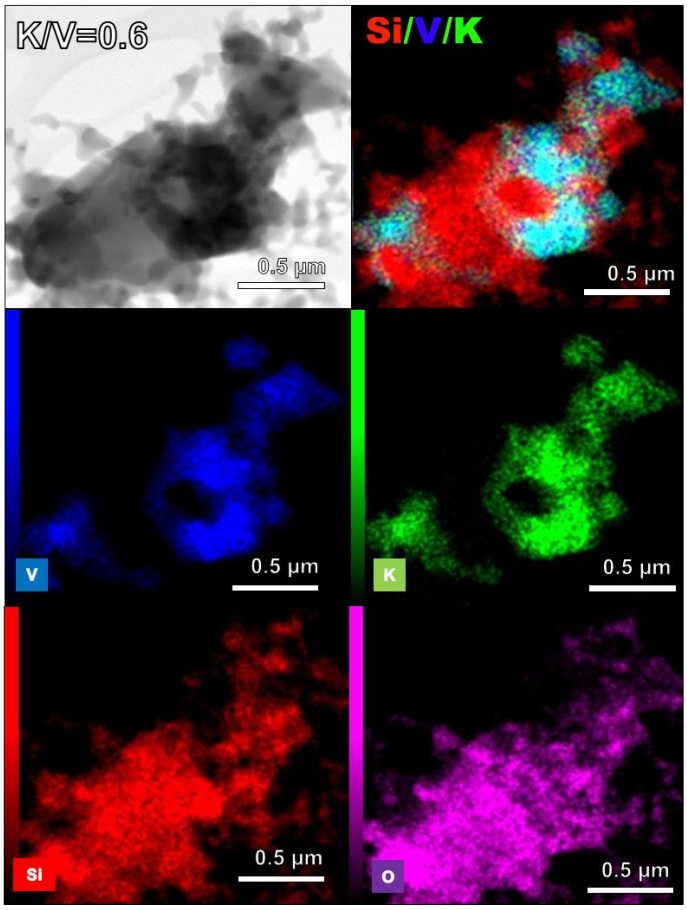

Figure 3.13. STEM-EDS image of K/V=0.6 catalyst

3.3.6. Thermal behavior of the calcined catalysts

Melting temperatures of catalysts were measured under synthetic air by DSC. The reversibility of melting was determined by three heating and cooling cycles. (Figure S8-S12).DSC onset and peak temperatures as well as the peak areas are presented in Table S1.1-S1.5. Reversible melting and cooling (no crystallization peak when Li/V≥ 0.4) can be seen. Although the same melting temperatures were obtained, peak areas were different. This indicates either phase changes upon melting or lithium reacts with SiO_2 further which yields in a decrease in the amount of lithium vanadate phase.

Two cycles of heating and cooling data of silica supported Li/V catalysts are shown in Figure S1.8 (Peak areas are in Table S1.1).The DSC results of Li/V catalysts from the first heating are shown in Figure 3.14. Compared to the thermal behavior of V/SiO_2 (T^{onset}= 667°C), much lower melting points were detected. The endothermic peaks were found to be generally located between 530 and 600°C. Catalysts Li/V=0.2 and Li/V=0.25 showed slight endothermic peaks at 560 and 600°C. The peak at 560°C become noticeable with increasing Li-loading as seen for Li/V=0.3 and Li/V=0.4. Another peak at 528°C was detected for Li/V=0.4 and Li/V=0.45 catalysts. These are the catalysts which show the highest effect on reducing melting points. Catalyst which contains the maximum Li-loading, Li/V=0.5, has two slight but still noticeable endothermic peaks at 545 and 592°C which are different than the remaining catalysts. Although only one crystalline phase with low crystallinity is defined for each different Li/V catalyst by XRD, DSC analysis indicates that the catalysts contain various amorphous surface phases which show melting between 530-600°C.

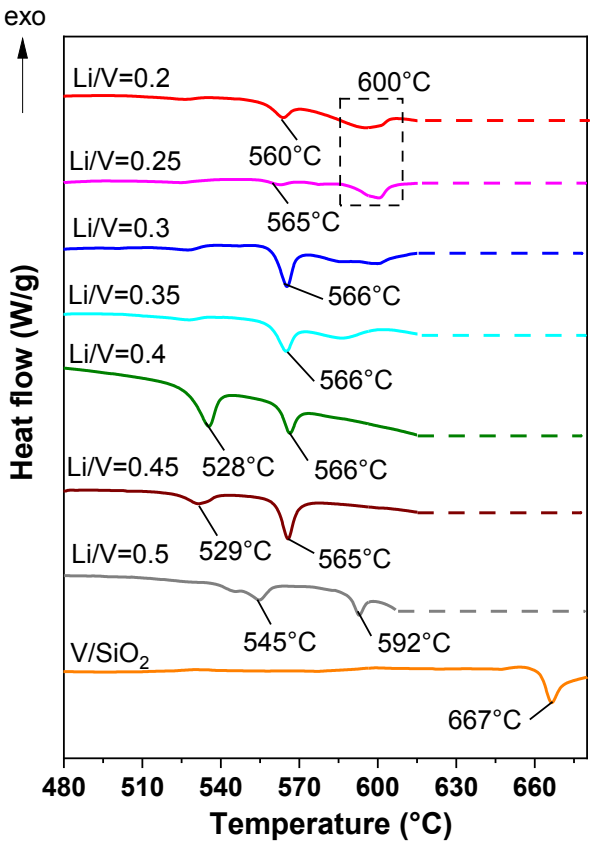

Figure 3.14. DSC profiles of Li/V catalysts under 21%O_2/ 79% Ar with a flow of 50 ml min^{-1}, heating rate: 10 Kpm, cooling rate: 5 Kpm in an alumina crucible with lid.

Two cycles of heating and cooling data of silica supported Na/V catalysts are shown in Figure S1.9 (Peak areas are in Table S1.2). DSC onset and peak temperatures as well as peak areas are presented in detail in Table S2. Reproducible melting and recrystallization were observed. The

onset of endothermic peaks was generally between 510 and 575°C (Figure 3.15). Na/V=0.3 and Na/V=0.35 catalysts showed one broad endothermic peak at 575°C. By increasing Na-content, endothermic peaks were lowered further. A peak at 566 °C was detected for catalysts Na/V=0.6 and Na/V=0.7, and 510°C was measured for catalysts with much higher Na-content (*i.e.* Na/V=0.8 and Na/V=0.9). Therefore, it can be stated that increasing Na-content leads to a decrease in the melting temperatures of the catalysts. The endothermic peaks of Na/V catalysts are typically not sharp, but rather broad. This indicates that catalysts contain various amorphous surface phase/s which shows melting between 560-570°C.

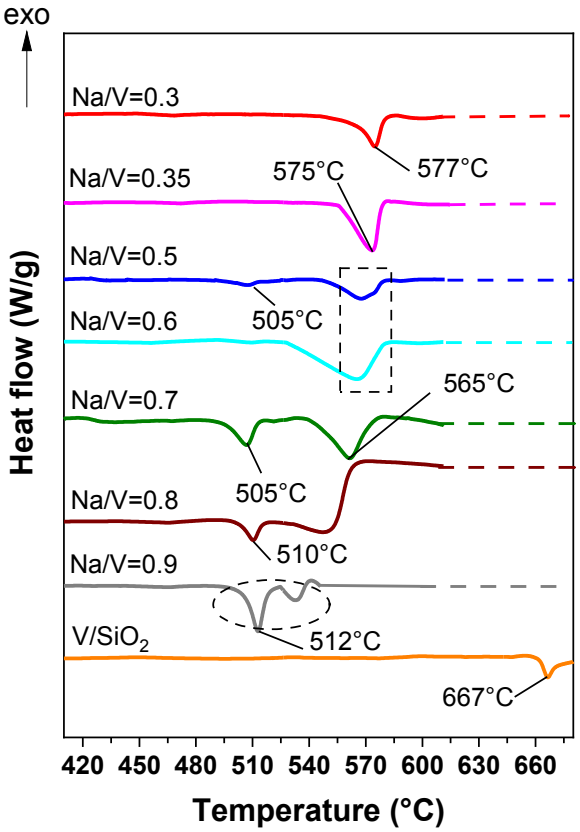

Figure 3.15. DSC profiles of Na/V catalysts under 21%O_2/ 79% Ar with a flow of 50 ml min^{-1}, heating rate: 10 Kpm, cooling rate: 5 Kpm in an alumina crucible with lid.

The DSC results of silica supported K/V samples from the 1st heating are shown in Figure 3.16. Three cycles of heating and cooling are presented in Figure S1.10. DSC peak and onset temperatures as well as the peak areas of heating cycles are in Table S1.3. Generally speaking, reversible heating and cooling were obtained. However, a decrease in endothermic peak areas and slight shift of melting to lower temperatures in the second heating has to be mentioned. This tells us that silicon dioxide leaches the potassium out which results in a loss of crystalline phase.

In Figure 3.16, it can be seen that generally endothermic peaks were located at 410, 477, and 525°C. Silica supported vanadium oxide catalyst showed one endothermic peak at 667°C. These results reveal that the melting points are lowered with additional K. This is valid also for Li and Na addition. Since catalysts K/V < 0.5 contain more than one phase, there are second events contribute to the melting. For catalyst K/V=0.3, two endothermic peaks were observed, one at 477°C and one weaker peak at 525°C. Melting at 525°C corresponds to the melting of $K_2V_8O_{21}$ (potassium octavanadate),[291] which was later confirmed with spent catalyst as well.

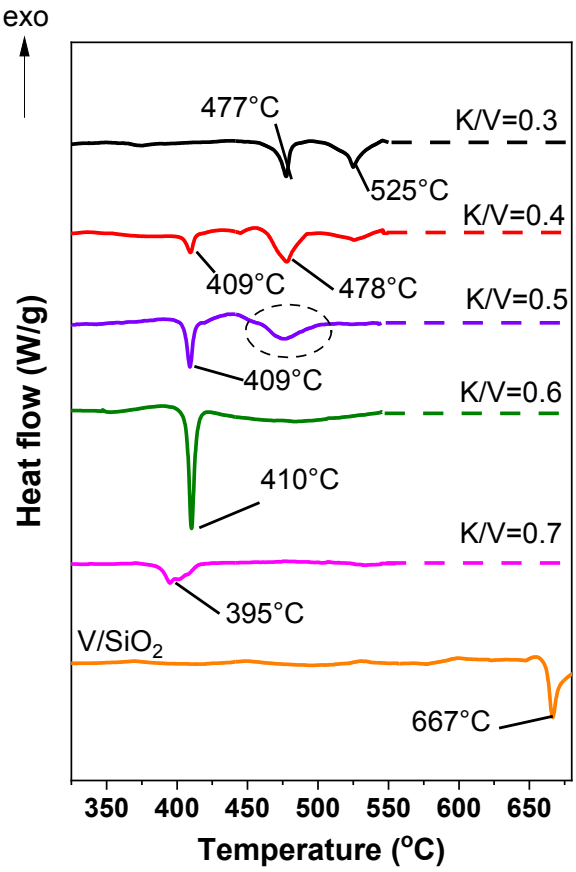

Figure 3.16. DSC profiles of K/V catalysts under 21%O_2/ 79% Ar with a flow of 50 ml min^{-1}, heating rate: 10 Kpm, cooling rate: 5 Kpm in an alumina crucible with lid.

Catalysts K/V=0.4 and K/V=0.5 show two endothermic peaks at 409 and 478°C. Since these catalysts contain $K_2V_2O_{16}1.5H_2O$ and $K_3V_5O_{14}$, these two endothermic peaks could be corresponded to the melting of each phase. The phase-pure catalyst, K/V=0.6, shows only one clear endothermic peak at 410°C, which was confirmed as a melting of the $K_3V_5O_{14}$ phase itself *(will be discussed later in detail)*. Although the catalyst with highest loading of potassium (K/V=0.7) has no crystalline phase, it shows a very weak endothermic signal at 395°C. It can be stated that this is a melting of amorphous phase due to the broader peak shape of the endothermic event as well.

The sample K/V=0.6 with only one crystalline phase of $K_3V_5O_{14}$ shows melting at 410°C. This result has been confirmed by measuring the melting point of support-free $K_3V_5O_{14}$, which was prepared as a reference material. As seen in Figure 3.17, both support-free $K_3V_5O_{14}$ (Figure 3.17A), which was synthesized in this study and data published in literature (Figure 3.17D) [403] have the same endothermic event at about 412°C. Silica supported $K_3V_5O_{14}$ (Figure 3.17B) and physical mixture of $K_3V_5O_{14}$ and silica (Figure 3.17C) have slightly lower melting points as compared to its support-free counterpart at 409°C. This slight shift can be expected because of the silica impact on the heat conductivity over the catalyst.

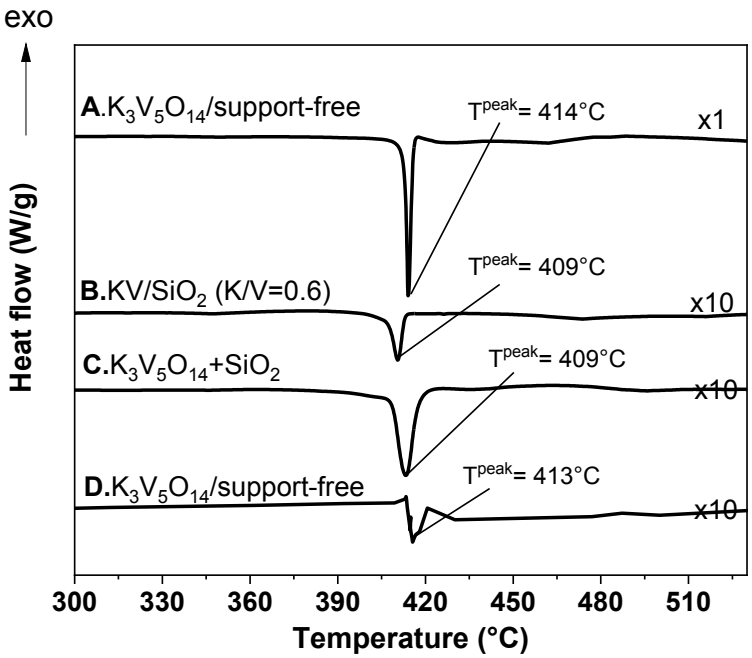

Figure 3.17. DSC profile of potassium vanadate systems measured under synthetic air **(A)** Support-free $K_3V_5O_{14}$ synthesized via conventional synthesis method (Internal ID: #31564); **(B)** K-containing silica supported vanadium oxide catalyst (K/V=0.6); **(C)** Physical mixture of $K_3V_5O_{14}$ and Aerosil 300; **(D)** Support-free $K_3V_5O_{14}$ published data [403]

Three cycles of heating and cooling of Rb/V catalysts are presented in Figure S1.11. DSC peak and onset temperatures as well as the peak areas of heating cycles are in Table S1.4. The DSC results of silica supported Rb/V catalysts from the 1st heating are shown in Figure 3.18. The endothermic peaks were generally located between 380 and 450°C. Catalyst Rb/V=0.3 showed one clear endothermic peak at 442°C. For catalyst Rb/V = 0.35, one clear endothermic peak at 438°C and two weaker peaks at 387 and 508°C were measured. The remaining catalysts has two endothermic peaks at 390 and 438°C.

Since Rb/V catalysts contain more than one phase, there are always second event contributes to the melting. When Rb-content increases, the peak at 390°C becomes pronounced and reaches

the maxima with Rb/V=0.5 catalyst. This peak at 390°C could be assigned to the melting of $Rb_2V_4O_{11}$ as identified by XRD. The second broader event at 438°C is attributed to the endothermic event due to the thermal instability of the $Rb_3V_5O_{14}$ (*i.e.,* incongruent melting) which was reported in the literature as well [403, 404].

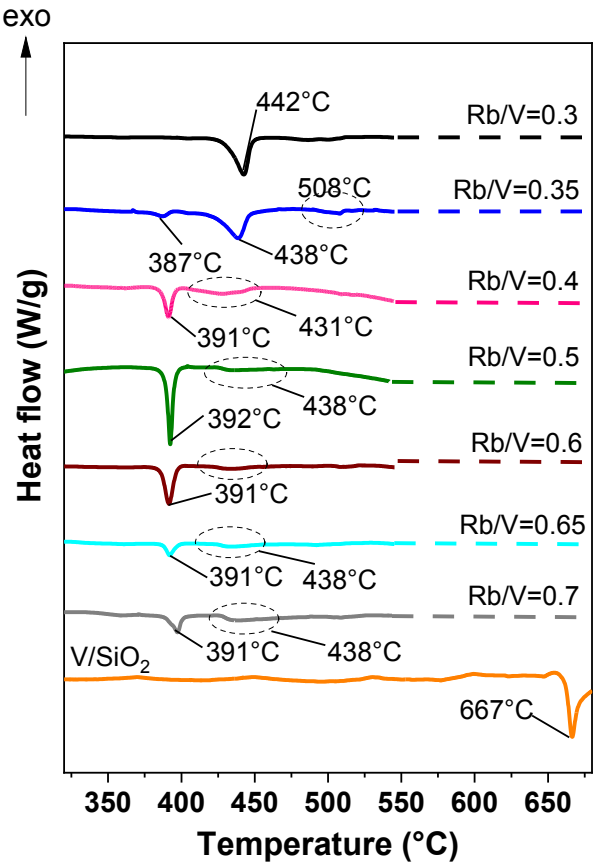

Figure 3.18. DSC profiles of Rb/V catalysts under 21%O_2/ 79% Ar with a flow of 50 ml min^{-1}, heating rate: 10 Kpm, cooling rate: 5 Kpm in an alumina crucible with lid.

Three cycles of heating and cooling of Cs /V catalysts are presented in Figure S1.12. DSC peak and onset temperatures as well as the peak areas of heating cycles are in Table S1.5. Although reversible melting temperatures were obtained in each cycle, the amount of phase which is melting decreased from 1st heating to 2nd heating. Figure 3.19 shows the DSC results of silica supported Cs/V catalysts from the 1st heating are shown in Figure 15. For Cs/V catalysts, the endothermic peaks were detected between 430 and 450°C. Catalysts Cs/V=0.25 and Cs/V=0.3 showed one endothermic peak at 428°C. For Cs/V =0.5, endothermic peak at 428°C become broader and relied between 430-450°C. Peaks between 430-450°C are individually noticeable with increasing Cs-loading. Although only CsV_2O_5 is identified by XRD, broad endothermic range is an indicator for that catalyst contains various amorphous surface phase(s). The remaining catalysts has two endothermic peaks at 390 and 438°C.

As seen above, the melting temperature of silica supported vanadium oxide catalysts are lowered by the addition of alkali element. This is known in the literature due to the low melting points of alkali metal oxides [399]. Also in the present work, the melting temperatures of supported vanadium oxide catalysts have been reduced but this is defined as due to the formation of alkali vanadate phases with low melting temperatures. The study differs from the previous studies because the impact of the melting of alkali-vanadate phases was included. Up to now, the formation of alkali vanadate phases was detected by XRD, and Raman spectroscopy and melting temperatures of the corresponding phases were measured by DSC.

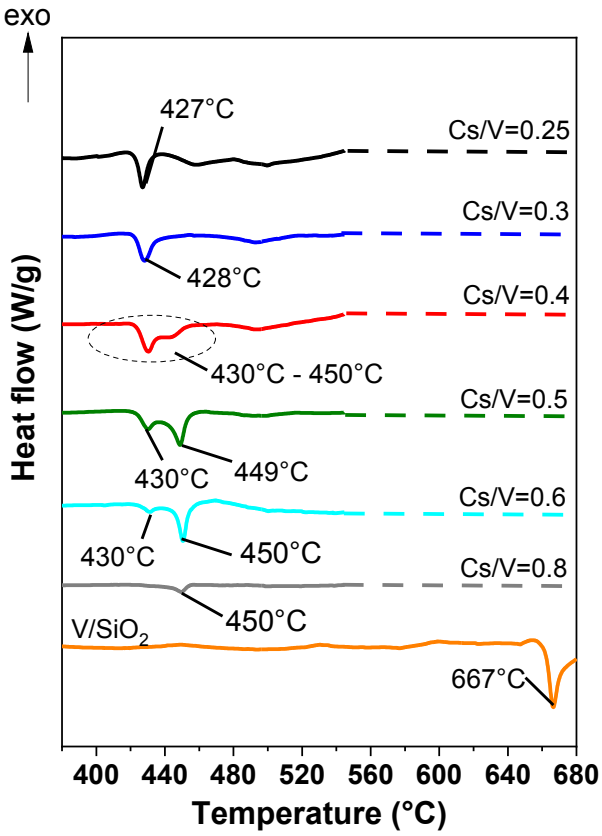

Figure 3.19. DSC profiles of Cs/V catalysts under 21%O_2/ 79% Ar with a flow of ml min^{-1}, heating rate: 10 Kpm, cooling rate: 5 Kpm in an alumina crucible with lid.

Based on this, the catalysts can be grouped into two classes, which are catalysts show melting in the region of interest for propane oxidation (350°C-520°C), including K/V, Rb/V and Cs/V and those, which shows no melting under applied propane oxidation conditions, including Li/V and Na/V catalysts. The impact of the phase transition from solid to liquid due to the low melting temperatures of alkali vanadate(s) on the reaction kinetics on supported vanadium oxide catalysts will be presented and explained in a detail.

(i) Catalysts show no melting under applied reaction conditions

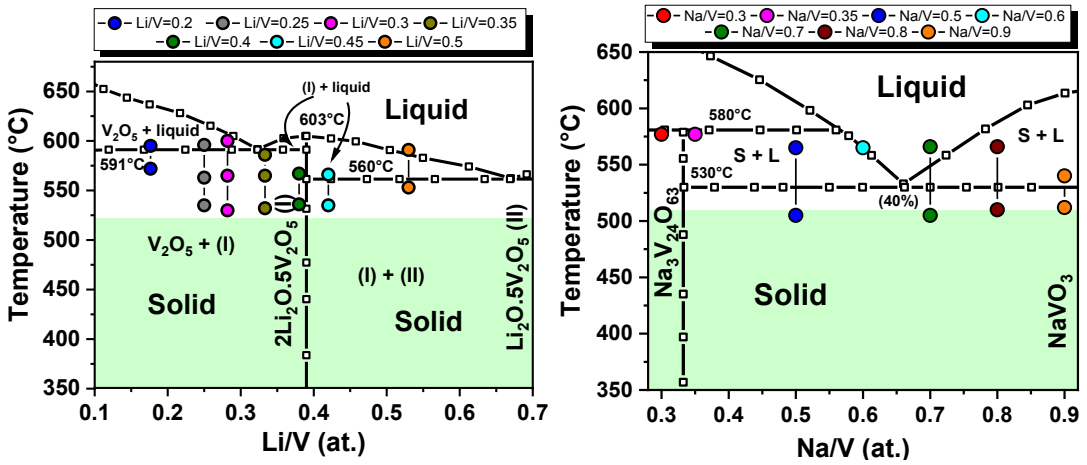

(ii) Catalysts show melting under applied reaction conditions

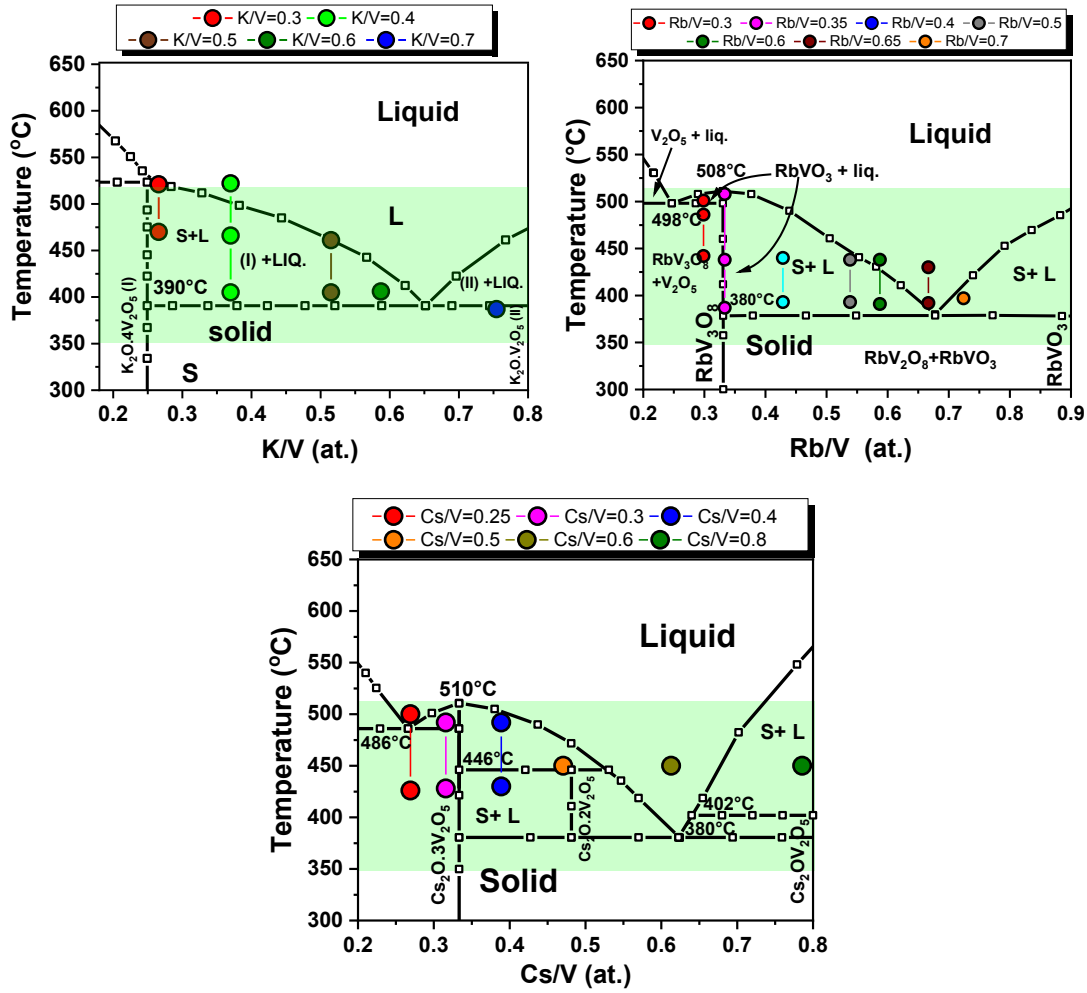

Figure 3.20. Melting temperatures of silica supported A/V catalysts with various A: V ratios on published phase diagrams of A_2O-V_2O_5 systems (A: Li, Na, K, Rb and Cs) (i) catalysts show no melting under applied reaction conditions, (ii) catalysts show melting under applied reaction conditions (applied reaction temperature range is in green rectangle)

Figure 3.20 shows the original phase diagrams of A_2O- V_2O_5 systems (A: Li, Na, K, Rb, and Cs) coupled with melting temperatures of alkali-vanadate phases measured by DSC in synthetic air. Applied temperature range of propane oxidation reaction is marked with green rectangle (350- 520°C). It is seen that Li, and Na-containing catalysts show melting in temperatures above the applied reaction temperature range. However, K, Rb, and Cs added catalysts have much lower melting temperatures which is in the applied reaction conditions. The impact of the melting of surface phases in propane oxidation will be presented in related chapter further based on the catalytic performance of these two groups.

3.4. Characterization of support-free $K_3V_5O_{14}$

Silica supported K/V=0.6 catalyst contained only one crystal phase which was detectable by XRD, *namely*, $K_3V_5O_{14}$ (Table 3.3) (Figure 3.21). Therefore, support-free $K_3V_5O_{14}$ (#31564) was synthesized (Table 3.7) to be used as a reference material for understanding the supported system. Material properties including structural and thermal information of the $K_3V_5O_{14}$ will be presented here in this section.

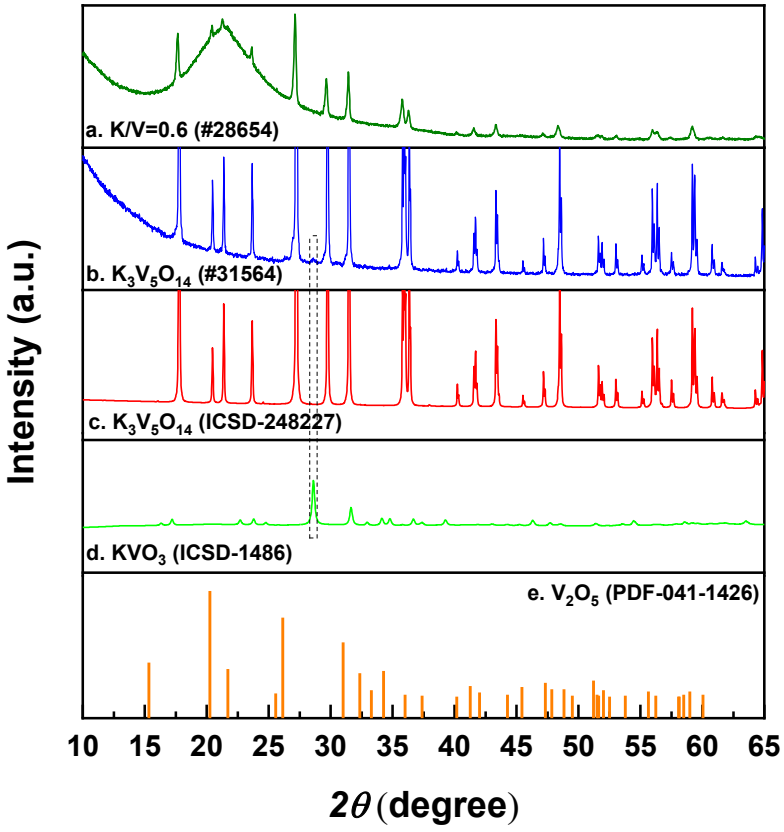

Figure 3.21. Powder XRD patterns of **(a)** silica supported K/V= 0.6 catalyst, **(b)** support-free $K_3V_5O_{14}$, **(c)** $K_3V_5O_{14}$ (ICSD-248227), **(d)** KVO_3 (ICSD-1486), and V_2O_5 (PDF 00-041-1426)

3.4.1. Crystal structure

Powder XRD pattern of the sample indicated that the $K_3V_5O_{14}$ via solid-state method has high purity with a minor bi-phase of KVO_3 (<2%) (Figure 3.22). The material exhibit tungsten bronze (TTB) topology where cation 'K' is surrounded by five polyhedra, three VO_5 square pyramids and two VO_4 tetrahedra[294]. Howard and Evans[390] reported the crystal structure of $K_3V_5O_{14}$ as follows; the point group symmetry is ditrigonal pyramidal C_{3v}, belongs to *P*31m space group (No.157) with unit cell parameters as a=8.6899(6) Å, c=5.0028(6) Å, V=327.17(5) Å, and ρ=3.01 g cm^{-3}.

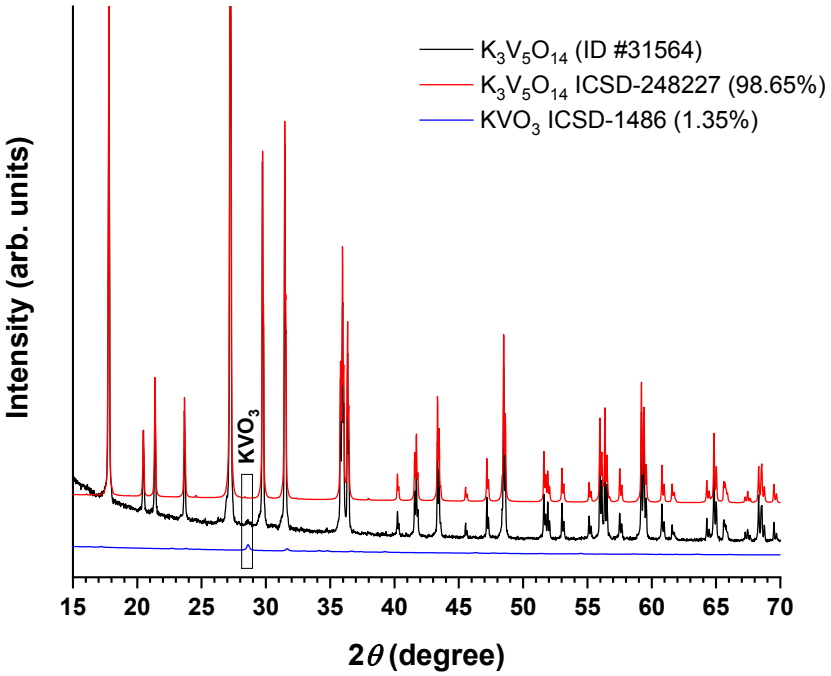

Figure 3.22. Rietveld refinement of $K_3V_5O_{14}$ (internal ID #31564)

A polyhedral view of the $K_3V_5O_{14}$ structure is shown in Figure 3.23. The structure exhibits two-dimensional (2D) cationic layers of $(V_5O_{14})^{3+}$ which are composed of corner-linked VO_4 tetrahedra and VO_5 square pyramids. 14 oxygen atoms are bound to the vanadium which form trigonal pyramids around V1 and square pyramids around V2 atom. The potassium atom sits in the hollow resulting from five-ring configuration and surrounded by 10 oxygen atoms, five from oxygen in the polyhedra and the five from the basal corner of polyhedra in the upper layer[291, 405].

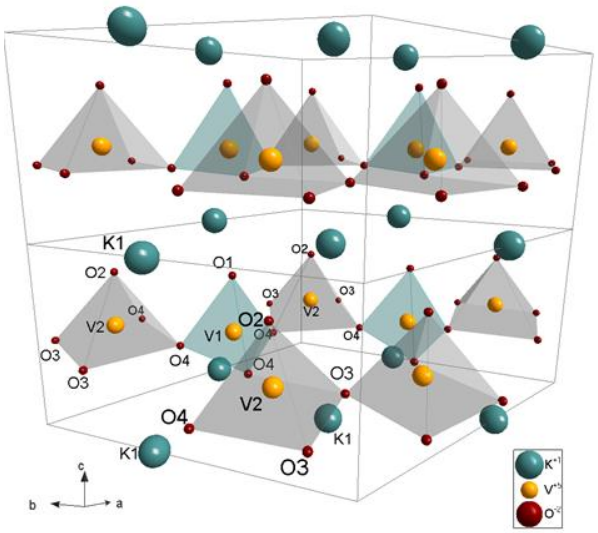

Figure 3.23. Polyhedral diagram of $K_3V_5O_{14}$[291]

3.4.2. Melting behavior of $K_3V_5O_{14}$

In the literature, the thermal properties of $K_3V_5O_{14}$ have been reported by several groups. Gáplovská and Žůrková studied the thermal stability of several pentavanadates including $K_3V_5O_{14}$, $Rb_3V_5O_{14}$, and $Tl_3V_5O_{14}$ [403] They prepared 120 mg of a sample and heated to 1000°C with 5°C/ min in a Pt crucible under a flow of air. Products obtained after cooling down to room temperature (no cooling rate is reported) were analyzed using IR- spectroscopy and XRD. The DTA curve of $K_3V_5O_{14}$ showed an endothermic event at 440°C as a peak maximum. This was assigned as a melting of $K_3V_5O_{14}$. Further they interrupted the DTA at 410°C, 505°C, and 1000°C. The compound obtained at 410°C was $K_3V_5O_{14}$ however the product formed at 505°C by crystallization of the melt was $K_3V_5O_{14}$ with KV_6O_{16} as admixture. The same product was obtained at 1000°C, which was attributed to thermal instability of the material. However, either the decomposition was driven by the melting or decomposition occurred after melting due to high temperature was not reported. Li *et al.* [405] found the melting of $K_3V_5O_{14}$ is about 412°C and decomposition is at 1100°C due to a high weight loss from the TGA measurement which occurred at temperatures higher than 1100°C. In 2010, Yeon *et al.*[294] have investigated the structural and functional properties of $K_3V_5O_{14}$. The DSC data indicated that $K_3V_5O_{14}$ melts congruently at 418°C. A year later, Ye-Qing *et al.* reported the same which is congruent melting of $K_3V_5O_{14}$ at 412°C. Evans *et al.*[390] also studied the thermal behavior of the material with a heating powder camera over the temperature range 25- 550°C. It has been reported that the sample melts incongruently at 400°C to a liquid and an unidentified phase which further melts at 520°C. Until the temperature below melting point, no thermal anomalies were observed. It is seen that discrepancies exist regarding to the thermal stability of $K_3V_5O_{14}$.

Clear experimental proof of its stability has not been presented yet. Therefore, this part of the work is aimed to investigate the thermal stability of $K_3V_5O_{14}$.

Figure 3.24 shows the thermal behavior of bulk crystalline $K_3V_5O_{14}$ measured by DSC in dynamic air flow. The DSC curve of $K_3V_5O_{14}$ is characterized by a marked endothermic peak at 412°C which corresponds to the melting of the compound (three heating and cooling cycles can be seen in Figure S1.13). From the 3 cycles of heating and cooling experiment, it is seen that the support-free $K_3V_5O_{14}$ melts at 412°C (T^{onset}) (Figure 3.24A). However, melting is incongruent as it is seen in the 2nd and 3rd heating. (Figure 3.24A). Since heating cycles are in between 30°C and 550°C, it may not be known in which temperature the phase decomposes. In order to investigate whether the decomposition is driven by the melting or not step by step heating and cooling was applied. With this, the material was first heated to 400°C which is below the melting temperature, then cooled down to 50°C. Then the material was heated to the melting temperature, *i.e.*, 410°C and cooled down. This protocol was continued up to 480°C with 10°C increments. Herein Figure 3.24B, it is seen that there is no thermal anomaly in the temperature range 30-400°C. However, passing melting (3rd heating, 420°C) causes thermal decomposition. After cooling down to 50°C and heating again to 430°C, two separated endothermic peaks were clearly seen which indicates that the material is already decomposed during melting between 410°C and 420°C. This confirms that the $K_3V_5O_{14}$ melts incongruently at or above 412°C (T^{onset}).

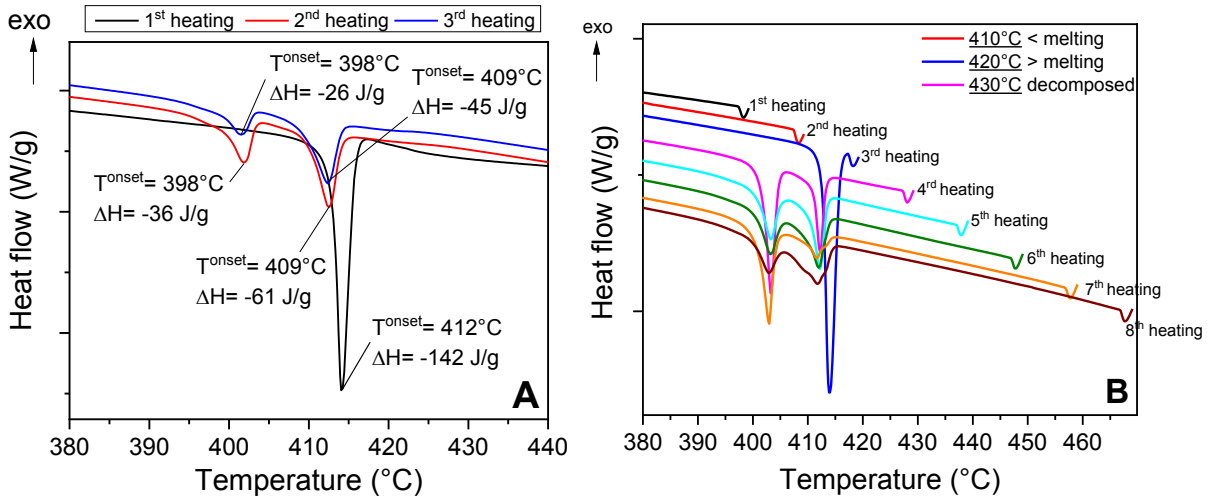

Figure 3.24. (A) DSC heating profile of support-free $K_3V_5O_{14}$ (#31564) during 3 cycles in a dynamic flow in a platinum crucible (30°C-550°C); **(B)** DSC heating profile of support-free $K_3V_5O_{14}$ with step-by-step heating and cooling

3.4.3. Light microscope experiments: visualization of melting

Moreover, the visualization of the melting behavior was conducted in an optical microscope. $K_3V_5O_{14}$ was placed on an alumina crucible and inserted to an operando cell (Harrick cell[406]).The catalyst was heated from 30°C to 550°C under the flow of air. The catalyst became darker and softer upon heating (Figure 3.25). When the temperature reached the melting temperature of the phase as measured by DSC, the compound melted and wetted the crucible. However, the formation of unknown crystals during melting was also observed. This proofs that the melting of $K_3V_5O_{14}$ is incongruent which supports past studies [390, 403].

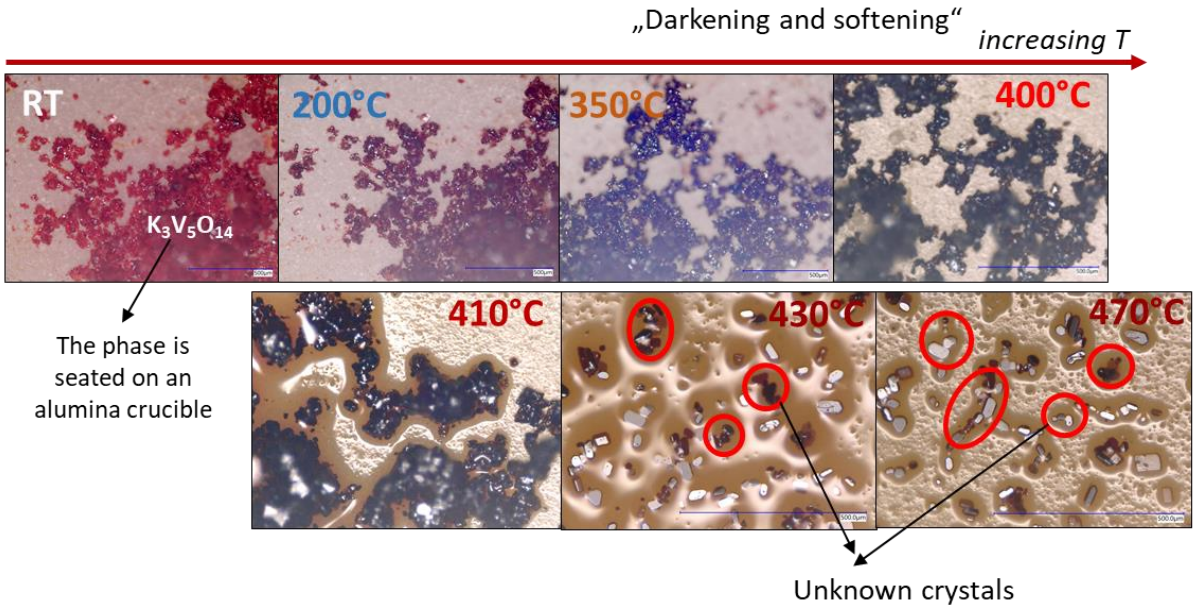

Figure 3.25. Melting behavior of $K_3V_5O_{14}$ on an alumina crucible conducted by light microscope

To see how silica impacts the melting pathway of the $K_3V_5O_{14}$, the physical mixture of $K_3V_5O_{14}$ and SiO_2 was investigated by light microscope as well (Figure 3.26). To do so, the one half of alumina crucible was filled with SiO_2 while the other half was filled with $K_3V_5O_{14}$. The images recorded upon heating are shown in Figure 3.26. Again, the crystals became darker and softer upon heating. At about melting temperature, the mobility of $K_3V_5O_{14}$ towards silica was observed. The formation of unknown crystals once again was observed on the surface of silica chunks as In addition, orange crystals on the surface of $K_3V_5O_{14}$-covered silica chunks were formed. This experiment further highlights decomposition occurs during interaction with silica as well however the silica support presumably influences the decomposition pathway of $K_3V_5O_{14}$.

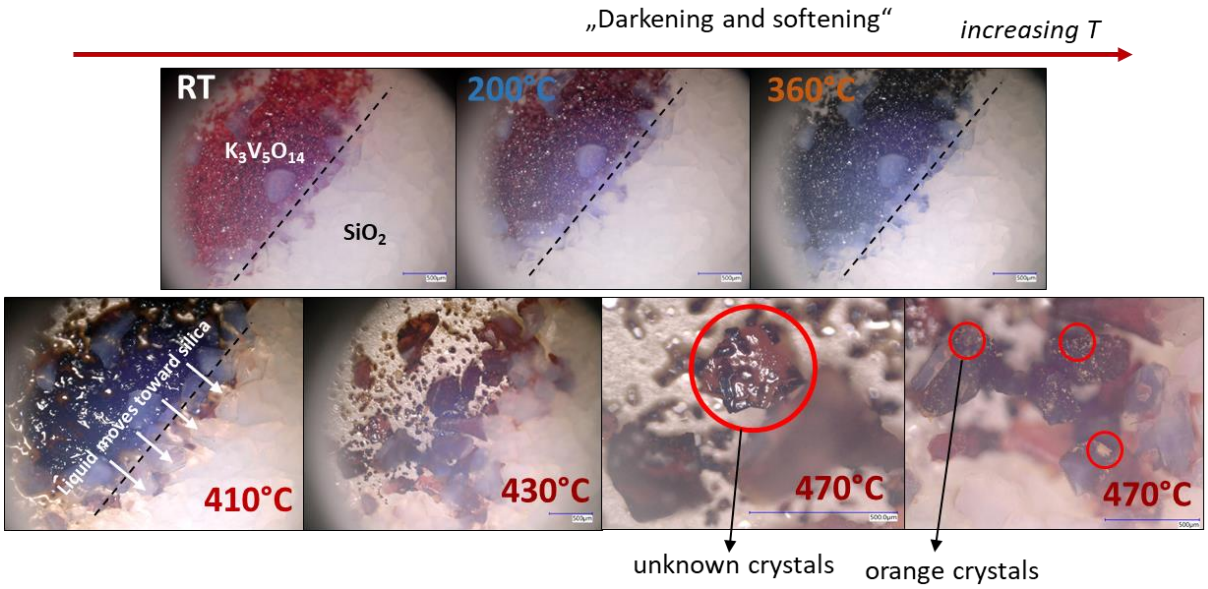

Figure 3.26. The interaction between silica (Aerosil 300) and $K_3V_5O_{14}$ during melting

In silica supported K/V=0.6, the melting could not be observed due to the low metal loading (~10 wt. %). Only color change from dark salmon to light yellow was seen temperature above melting (Figure 3.27) which indicates a change in oxidation state of vanadium (V^{4+}).

Figure 3.27. Melting visualization of supported K/V=0.6 catalyst with light microscope

Three different system have been presented so far. These are in a summary, (i) support-free $K_3V_5O_{14}$, (ii) physical mixture of $K_3V_5O_{14}$ and SiO_2 and (iii) silica supported K/V=0.6 ($K_3V_5O_{14}/SiO_2$) allowed to investigate possible decomposition of the phase. The comparison of the thermal behavior of these three systems measured by DSC is shown in Figure 3.28. In general there are similarities exist in the observations with each system. For support-free $K_3V_5O_{14}$, a decomposition occurs in the first heating. In the second heating, the melting of unknown decomposition phase at 398°C and a shift in the main peak at 412°C to lower temperature *i.e.*, 409°C, was seen (Figure 3.28A). A physical mixture of SiO_2 and $K_3V_5O_{14}$ gives an insight on how melting occurs on silica supported system. The melting of unknown phase at 398°C is weak, but still distinguishable in the second heating.

In the physical mixture, the first melting is measured at 409°C instead 412°C due to the silica impact on the heat conductivity (Figure 3.28B). In the second heating, a noticeable shift in the melting to 10°C lower temperature (400°C) is obtained.

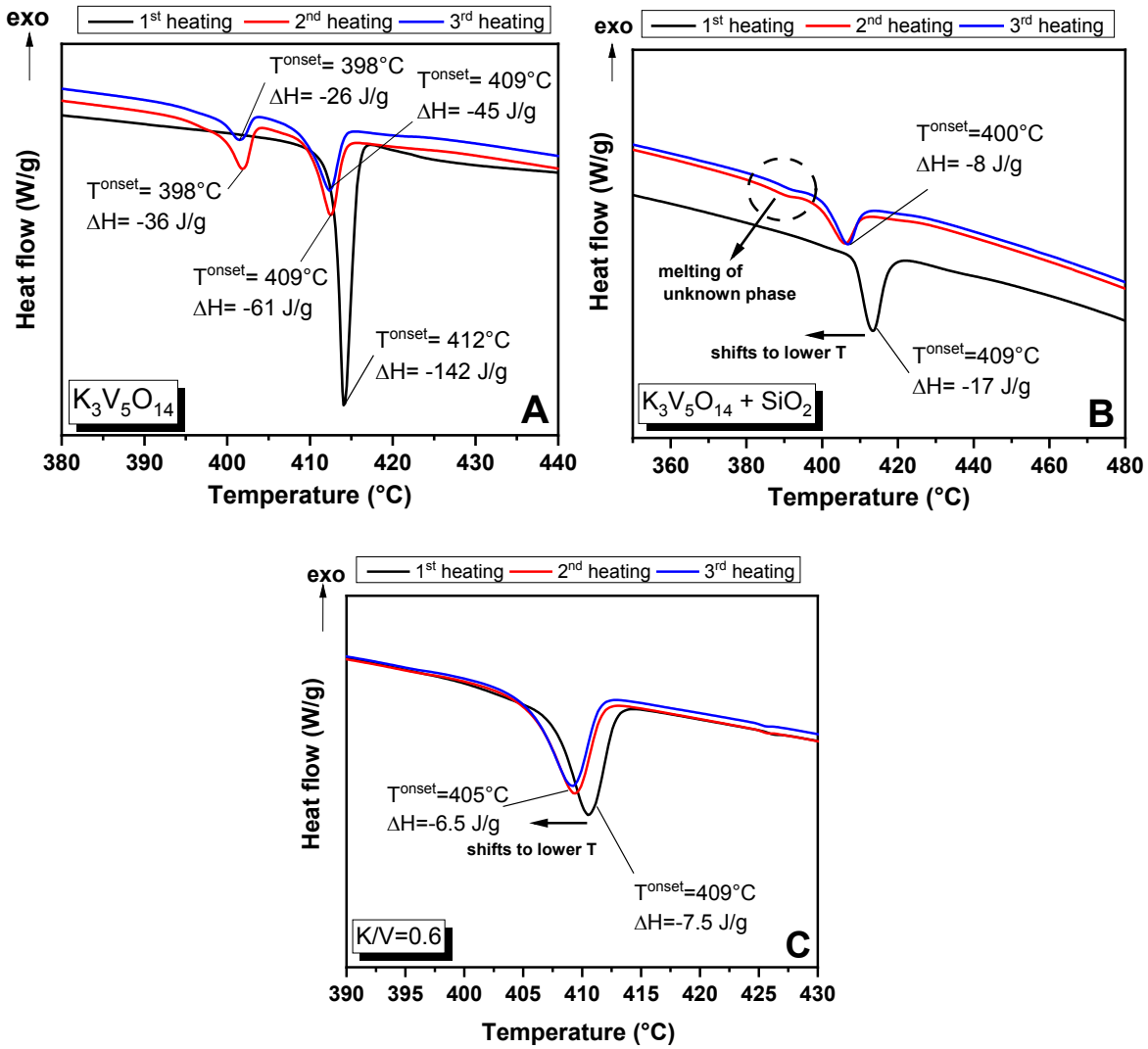

Figure 3.28. DSC profiles of systems from bulk to supported catalyst measured under 21%O_2/ 79% Ar with a flow of 70 ml/min, heating rate: 10 Kpm, cooling rate: 5 Kpm in a Pt crucible with lid; **(A)** support-free $K_3V_5O_{14}$ (#31564), **(B)** A physical mixture: $K_3V_5O_{14}$-SiO_2, **(C)** Silica supported K/V=0.6 (#28654, $K_3V_5O_{14}/SiO_2$)

In the supported K/V=0.6 system (Figure 3.28C), a second peak at lower temperature which is a melting of decomposition product is not seen. However, the same shift in the melting temperature to 405°C was apparently observed. In addition, decrease in the enthalpy of the peak indicates that the amount of phase which is melting decreased. This is expected since potassium reacts with silica. It must be noted that in each case, the decrease in the amount phase was observed due to the incongruent melting. Therefore, melting in the second cycle can be attributed to the melting of mixture of potassium-vanadate(s) rather than a pure $K_3V_5O_{14}$. The

loading of the crystalline phase of the supported K/V 0.6 (internal ID: 28654) sample was determined using the melting enthalpy of support-free $K_3V_5O_{14}$ (internal ID: 31564) as following: $m = \frac{dQ(supported\ K3V5O14)}{dQ\ (K3V5O14)}$ From the ratio of DSC peak areas of supported and support-free pentavanadate, the loading of the crystalline $K_3V_5O_{14}$ on silica was assessed as 5.2 wt. %. Hence, the detection of melting over silica support was not possible due to the low loading of $K_3V_5O_{14}$.

Overall, the experiment further proofs the instability of $K_3V_5O_{14}$ (either bulk or as silica supported) which results in a decomposition to an unknown product whose melting temperature is at about 400°C.

Identification of the product of melting was impossible since melt solidifies on the inner surface of the crucible. Sample removal was only possible by washing the Pt crucible in hot nitric acid bath for 2-3 hours. The spent sample of the physical mixture of $K_3V_5O_{14}$ and SiO_2 from DSC experiment (Figure 3.28B) was neither able to be properly analyzed by XRD since the pattern was strongly dominated by SiO_2 (<1 mg $K_3V_5O_{14}$ loaded). However, the spent catalyst from catalytic measurement of support-free $K_3V_5O_{14}$ was analyzed, will be presented in Section 3.4.5.

3.4.4. In situ Raman spectroscopy

The Raman spectra of support- free $K_3V_5O_{14}$ was recorded in 21 % O_2 in Ar from 30°C to melting temperature, *i.e.*, 410°C. Raman features of support- free $K_3V_5O_{14}$ appears at 466, 501, 602, 656, 696, 886, 938, and 955 cm^{-1} at room temperature under flow of static air (Figure 3.29). The assignment of these bands was done based on DFT calculation of $K_3V_5O_{14}$ unit-cell (Figure 3.23). The calculated vibrational modes are listed in Table 3.8.

The most intense bands in range of 450-700 cm^{-1} are specified as bending vibrational modes whereas bands between 850 and 990 cm^{-1} are defined as stretching modes. By following the unit-cell structure of $K_3V_5O_{14}$ (Figure 3.23), the strong sharp band at 501 cm^{-1} is assigned as corresponded to V1-O4-V2 bending whereas the two at 602 and 656 cm^{-1} are corresponded to bending modes of O3-V2-O3 and V2-O3-V2. Furthermore the one at 696 cm^{-1} is due to O3-V2-O4 and V2-O4–V1 bending. The other bands between 880 and 990 cm^{-1} are due to stretching vibrations. The Raman band at 886 cm^{-1} is attributed to the vibrational stretching modes of O4-V2-O4 and O4-V1-O4 in the VO_4 tetrahedral units. The weaker band at 938 cm^{-1} is due to stretching modes in VO_4 tetrahedral and VO_5 square pyramids. The last one at

955 cm^{-1} is assigned as V=O stretching in shorty V1-O1 and V2-O2 bands. In situ Raman spectroscopy of support-free $K_3V_5O_{14}$ showed substantial changes by increasing temperature under the flow of synthetic air (Figure 3.30).

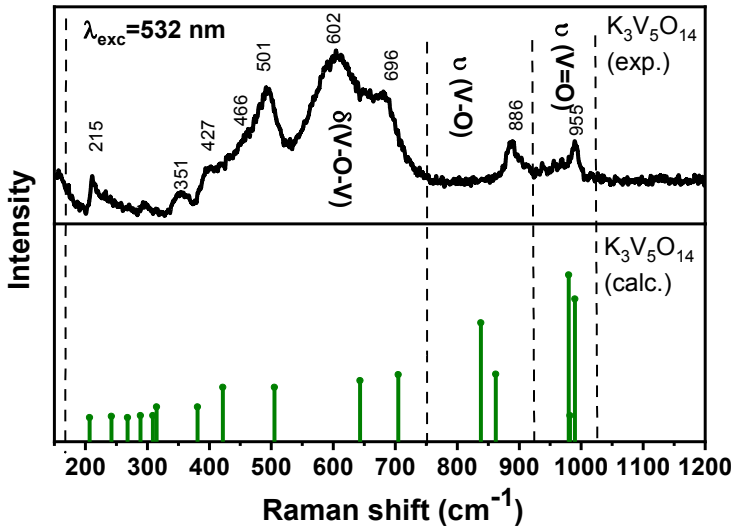

Figure 3.29. Ex-situ Raman spectrum of support-free $K_3V_5O_{14}$ (top) and its calculated Raman spectra by DFT (bottom) [291]

Generally, a significant loss of band intensity and band broadening were observed during heating. Merging three bands together at 602, 656, and 696 cm^{-1} and turn to a single and broad band which was centered at 656 cm^{-1} was clearly seen. Change in relative intensity of a band to another indicates a structural alteration. That means $K_3V_5O_{14}$ structure was alternated before melting temperature was reached. Further increase in temperature to 310°C showed that a new component at 985 cm^{-1} appeared, which continuously increases in intensity without any shift in peak position.

Normally V=O stretching of bulk V_2O_5 exhibits at 997 cm^{-1}[407], however a slight shift to lower Raman band is expected upon adding potassium or other alkali additives[401, 408, 409]. Therefore this Raman mode at 985 cm^{-1} is attributed to the formation of bulk-like V_2O_5 or K-distorted V_xO_y species upon melting.

At 410°C where melting occurs, the V-O-V bending modes (450-700 cm^{-1}) completely disappeared. This can be understood by breaking of bridging bonds between VO_4 and VO_5 units after melting in which strain was lost. The modes at 938 cm^{-1} and 955 cm^{-1} remain unchanged in frequency, but the relative intensities changed. Conversely, the 886 cm^{-1} band progressively shifts toward lower wavenumbers, up to 869 cm^{-1}.

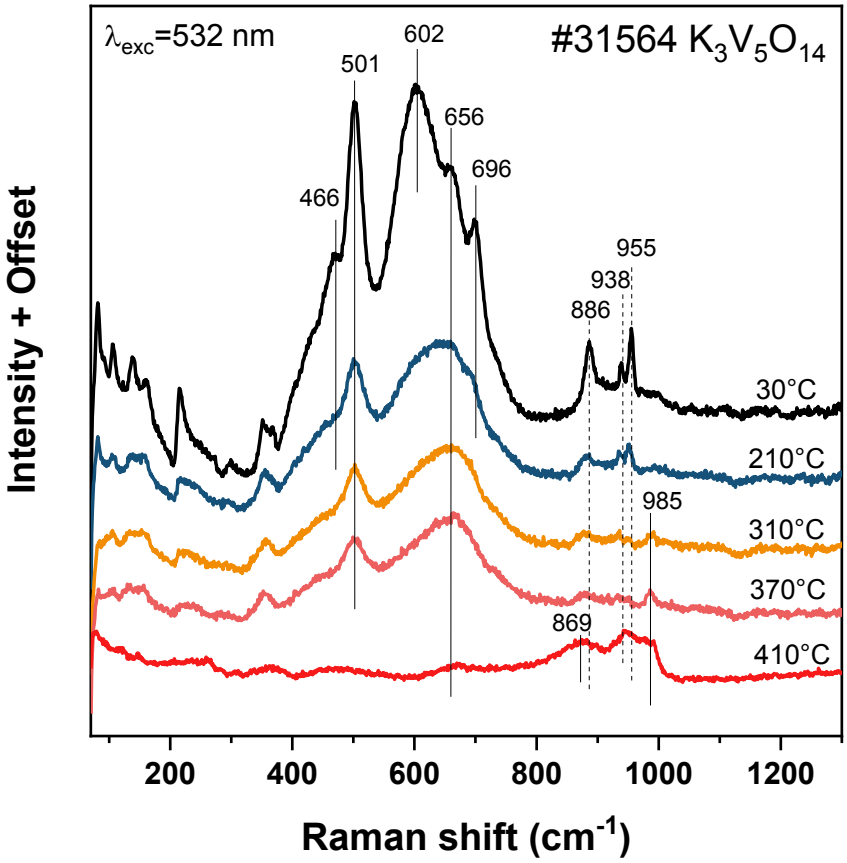

Figure 3.30. Temperature-dependent spectra of support-free $K_3V_5O_{14}$ measured in 21 % O_2 in Ar with a flow of 10 mlmin^{-1}

Table 3.8. The assignment of vibrational modes of $K_3V_5O_{14}$ based on phonon calculation (acoustic modes are not included) [291]

Phonon Mode No.	Symmetry	$\upsilon_{calculated}$	Assignment
4,5	E	57	
6	A_1	58	
7	A_2	63	
8,9	E	81	
10	A_2	92	
11,12	E	96	
13,14	E	104	
15	A_1	105	
16	A_1	114	
17	A_2	118	
18,19	E	128	
20,21	E	139	
22,23	E	149	
24	A_2	154	
25,26	E	179	
27	A_1	199	
28,29	E	207	
30	A_1	215	
31,32	E	242	
33,34	E	268	
35,36	E	289	
37	A_1	306	
38	A_2	307	
39,40	E	309	
41,42	E	315	
43	A_1	345	
44,45	E	381	
46	A_1	422	
47	A_2	437	
48,49	E	505	V1-O4-V2 bending mode
50	A_2	571	
51,52	E	642	O3-V2-O4 bending mode
53	A_1	653	
54,55	E	705	O3-V2-O4 bending, V2-O4-V1 bending mode
56	A_2	765	
57	A_1	838	VO4 tetrahedral bending, bending of V2 in V2-O3 ring
58,59	E	862	O4-V2-O4 stretching, O4-V1-O4 stretching
60,61	E	942	VO_4 tetrahedral and VO_5 square pyramids stretching
62	A_1	975	V1-O1, V2-O2 stretching
63	A_2	980	
64,65	E	982	
66	A_1	990	V1-O1, V2-O2 bending

3.4.5. Catalytic activity

$K_3V_5O_{14}$ was tested in propane oxidation by temperature-programmed reaction in a single-tube reactor. $K_3V_5O_{14}$ was loaded on a reactor in where quartz was inserted first to protect the reactor from the flowing of the melt downwards. A quartz wool was used to secure the catalyst bed in place. 150 mg of $K_3V_5O_{14}$ was used and the reaction was performed between 350-520°C. After the first run, the reactor cooled down to 30°C and the second cycle was performed. Applying 2 cycles aimed to investigate both the activity of $K_3V_5O_{14}$ and its possible decomposition product in propane oxidation. Based on the results from Figure 3.31, it can be concluded that both $K_3V_5O_{14}$ and its decomposition product have no activity in propane oxidation. Based on XRD analysis on spent catalyst, minor reflections of KVO_3 and unknown phase were found beside SiO_2 and $K_3V_5O_{14}$ (Figure S1.14).

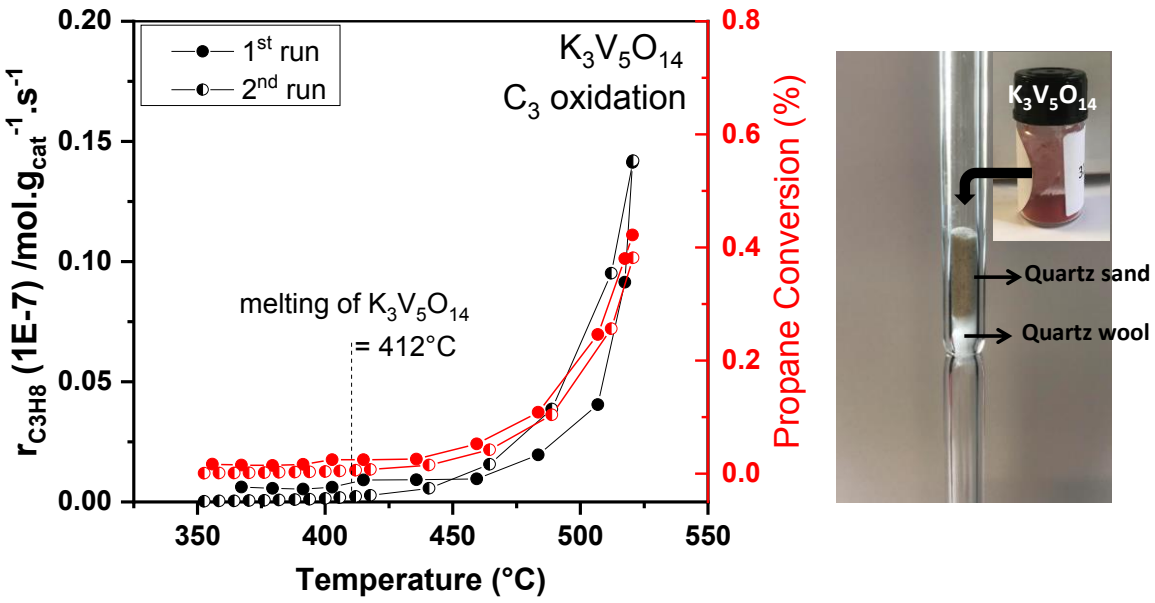

Figure 3.31. Rate of propane consumption with increasing temperature of $K_3V_5O_{14}$ measured in propane oxidation (Conditions: T=350°C-520°C, feed $C_3H_8/O_2/N_2$=7.5/7.5/85 vol. % W/F=0.9 g s ml^{-1})

CHAPTER 4

4. Catalytic properties of alkali-containing silica supported vanadia catalysts in propane oxidation

Catalytic performance of silica supported A/V catalysts were investigated in the gas-phase propane oxidation with a reaction temperature between 350 and 520°C, in a feed of $C_3H_8/O_2/N_2$=7.5/7.5/85 vol. %, using a catalyst mass of 350 mg, and applying a contact time of W/F= 1.8 g s ml^{-1}. Prior to the catalytic measurement, catalysts were in situ "activated" at 520°C under the flow of synthetic air and held there for 2 h. After 2 h, catalysts were cooled down to 50°C (synthetic air) and exposed to the reaction mixture. During propane oxidation, catalysts were kept at each given temperature for 24 h to reach steady-state. The only major reaction products were C_3H_6, CO and CO_2. C_2H_4 (2% selectivity), acetone (~10% selectivity), acrolein and propionaldehyde (both <1% selectivity) were observed in minor amounts (Figure S2.1-2.5).

4.1. Silica supported Li/V catalysts with various ratios of Li: V

Figure 4.1 shows that the catalytic activities of all Li/V catalysts were lower than VO_x/SiO_2 however selectivity to propylene was found much higher. Propane conversion increases with increasing temperature as a function of Li-content. Lower the Li-content higher the conversion was obtained (Figure 4.1A). On the other hand, higher the Li-content, higher the selectivity to propylene was reached (Figure 4.1B). The most selective catalyst to propylene was found as Li/V=0.4 with 74% selectivity at 5% propane conversion. Product distribution including CO, CO_2, C_2H_4 (2% selectivity), acetone (<1%), acrolein, and propionaldehyde with around 2% selectivity can be found in Figure S2.1.

In order to compare the rate and activation energies within the different type of alkali, two temperatures were selected. One temperature was selected as 370°C in which all catalysts are in solid state and none of the catalysts show phase transition while the other temperature was selected as about 450°C in which some type of alkali are expected to show melting. Therefore the second temperature represents the state after melting for K, Rb, and Cs catalysts. However, it must be noted that Li and Na- containing catalysts remain solid in both temperature.

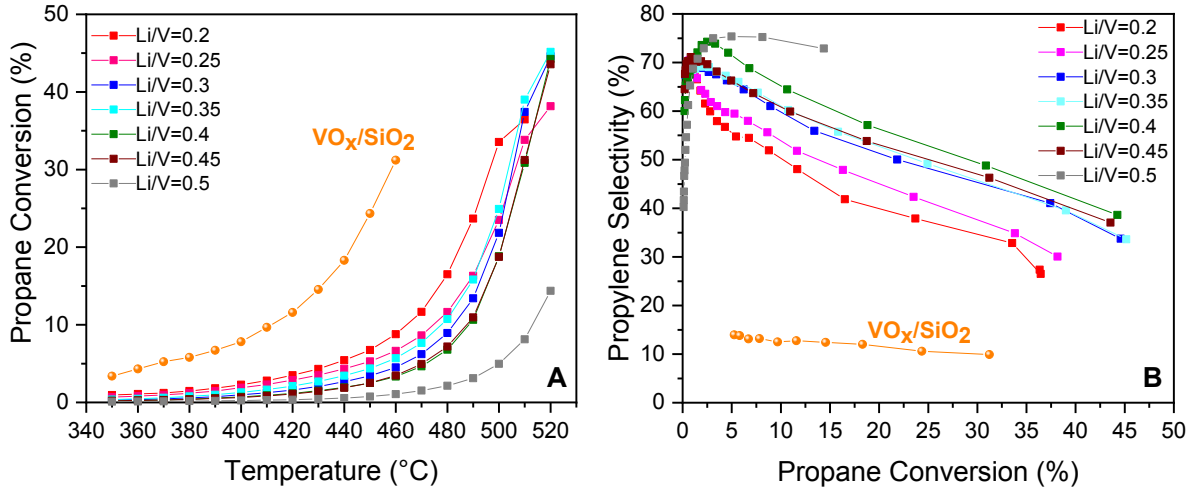

Figure 4.1. (A) Conversion of propane in propane oxidation over silica supported Li/V catalysts with increasing temperature, and **(B)** propylene selectivity as a function of propane conversion (Conditions: T=350°C-520°C, feed $C_3H_8/O_2/N_2$=7.5/7.5/85 vol. %, W/F= 1.8 g s ml^{-1}).

Table 4.1 summarizes the reactivity and apparent activation energies of catalysts at 370°C.The propane consumption rate normalized to vanadium mass (in gr) measured over Li/V catalysts differ by order of magnitude. Catalyst Li/V=0.2 exposes the highest propane consumption rate, combined with the lowest activation energy within Li/V catalysts. The propane consumption rate correlates with the Li-loading and it decreases in the order Li/V=0.2 > Li/V=0.25 > Li/V=0.35 > Li/V=0.3 > Li/V=0.4 > Li/V=0.45 > Li/V=0.5. However, propylene formation rate increases in the same order.

Table 4.1. Consumption rate of propane, activation energy and propylene formation rate measured over silica supported Li/V catalysts in the propane oxidation, applying a feed composition of $C_3H_8/O_2/N_2$=7.5/7.5/85 vol. %, and a contact time of 1.8 g s ml^{-1}

Catalyst	r(C_3H_8)[a] ($mol.g^{-1}$ $V.s^{-1}$)	Activation energy [b] (kJ/mol)	r(C_3H_6)[a] ($mol.g^{-1}$ $V.s^{-1}$)
Li/V=0.2	5.15	63.4	3.51
Li/V=0.25	3.50	75.2	2.43
Li/V=0.3	1.73	86.8	1.20
Li/V=0.35	2.20	89.5	1.49
Li/V=0.4	1.27	91.4	0.83
Li/V=0.45	1.72	85.7	1.17
Li/V=0.5	0.62	63.8	0.27
VO_x/SiO_2	19.1	59.0	2.67

[a]At a temperature 370°C (divided by 1E-7)
[b]Calculated in a temperature range between 350°C and 420°C.

Table 4.2 summarizes the reactivity and apparent activation energies of catalysts at high temperature (460°C). The propane consumption rate decreases with increasing Li-content in

the order: Li/V=0.2 > Li/V=0.25 > Li/V=0.35 > Li/V=0.45 > Li/V=0.3. The apparent activation energies slightly higher than that of measured at 370°C. The highest propylene formation was obtained for the lowest Li-containing catalyst (Li/V=0.2).

Table 4.2. Consumption rate of propane, activation energy and propylene formation rate measured over silica supported Li/V catalysts in the propane oxidation, applying a feed composition of $C_3H_8/O_2/N_2$=7.5/7.5/85 vol. %, and a contact time of 1.8 g s ml^{-1}

Catalyst	r(C_3H_8)[a] ($mol.g^{-1}$ $V.s^{-1}$)	Activation energy [b] (kJ/mol)	r(C_3H_6)[a] ($mol.g^{-1}$ $V.s^{-1}$)
Li/V=0.2	36.9	104.0	19.1
Li/V=0.25	24.2	92.3	14.0
Li/V=0.3	17.1	114.6	11.3
Li/V=0.35	21.0	108.2	13.8
Li/V=0.4	13.2	117.0	9.76
Li/V=0.45	19.0	132.9	12.9
Li/V=0.5	4.73	137.2	3.25
VO_x/SiO_2	114.0	116.1	11.28

[a]At a temperature 460°C (divided by 1E-7)
[b]Calculated in a temperature range between 440°C and 460°C.

4.1.1. Reproducibility of catalytic activity

After reaction was completed, reactors were completely cooled down (50°C) under the flow of reaction feed. The same catalytic measurement protocol was performed to check the reproducibility of the catalytic data. Figure 4.2 shows the comparison of reactivity data from 1st and 2nd measurement in propane oxidation over silica supported Li/V catalysts.

Slightly lower selectivity to propylene and propane conversion were obtained for Li/V=0.2 and Li/V=0.25 catalysts. For other catalysts, similar selectivity to propylene and propane conversion were able to be reached. However, higher reaction temperature were needed. This indicates that catalysts were not stable. A change in phase and textural properties are discussed in the following section.

4.1.2. Properties of spent Li/V catalysts

The change in phase composition and surface area was analyzed after applying two reaction cycles in propane oxidation. XRD and BET results of spent Li/V catalysts was compared with fresh Li/V catalysts (Table 4.3). Phase separation and Li-deficiency by chemical analysis was seen for all Li/V catalysts after catalysis. Phases which are formed due to phase separation were found in much higher in crystallinity.

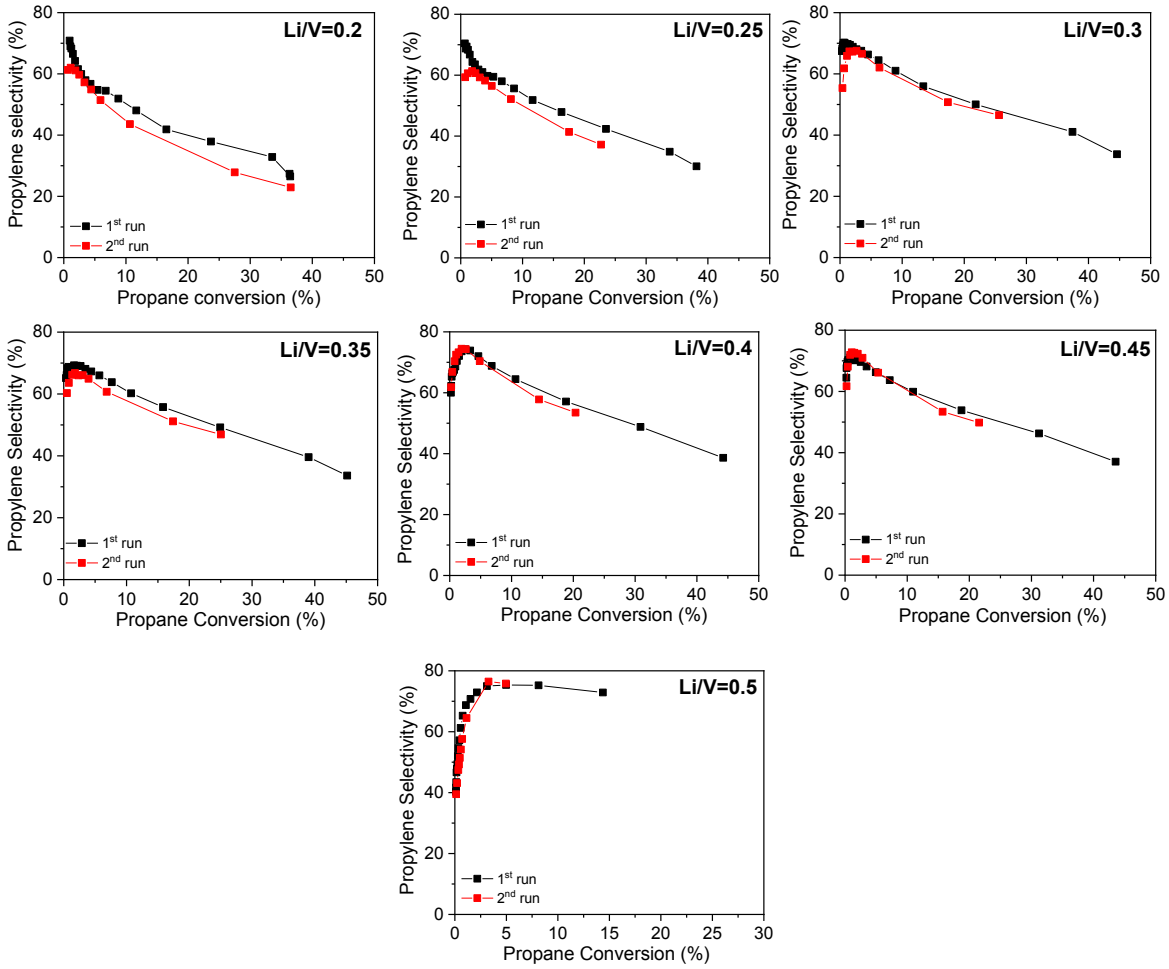

Figure 4.2. Catalytic activity results of silica supported Li/V catalysts obtained from1st and 2nd measurement in propane oxidation reaction (black: 1st run, red: 2nd run)

BET surface area of catalysts after reaction were found to be reduced about 40-50%. The decrease in surface area is attributed to the formation of other lithium –vanadate(s) due to the chemical reaction.

Table 4.3. Properties of spent silica supported Li/V catalysts compared to fresh catalysts

ID#	Li/V	XRD (fresh)	XRD (spent)	BET (fresh) (m^2/g)	BET (spent) (m^2/g)
31045	0.1	$Li_{1.5}V_3O_8$	LiV_3O_8, $Li_4V_{10}O_{27}$	120	57
31044	0.2	$Li_{1.5}V_3O_8$	$Li_{1.5}V_3O_8$, $Li_4V_{10}O_{27}$	101	65
31046	0.3	$Li_{1.5}V_3O_8$	LiV_3O_8, $LiVO_3$	110	63
31047	0.35	$Li_{1.1}V_3O_8$	$Li_{1.5}V_3O_8$, $Li_4V_{10}O_{27}$, $LiVO_3$	96	56
31048	0.4	$Li_{1.1}V_3O_8$	LiV_3O_8, $LiVO_3$	87	54
31049	0.45	$Li_{1.5}V_3O_8$	$Li_{1.5}V_3O_8$, $LiVO_3$	100	62
31050	0.5	Opal, $LiVO_3$	Opal, $LiVO_3$	25	21

DSC profiles of spent silica supported Li/V catalysts are shown in Figure 4.3. The melting occurred at 566°C for fresh catalysts become much less pronounced but still detectable after catalysis. Moreover the melting at 530°C seems disappeared. Overall these changes supports the phase change which yields in unreproducible catalytic data measured for the same temperatures in each cycle.

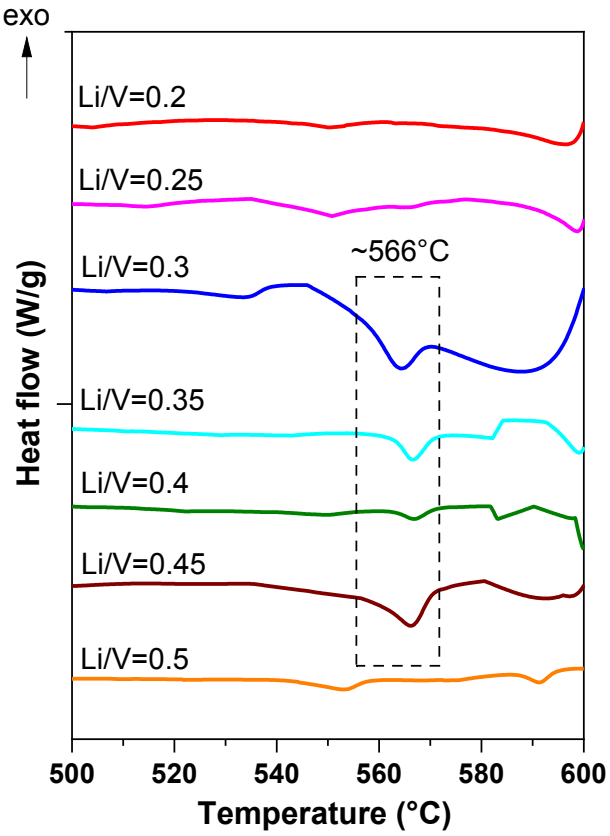

Figure 4.3. DSC profiles of spent Li/V catalysts under 21%O_2/ 79% Ar with a flow of 70 ml/min, heating rate: 10 Kpm, cooling rate: 5 Kpm in an alumina crucible with lid.

4.2. Silica supported Na/V catalysts with various ratios of Na: V

The catalytic performance of silica supported Na/V catalysts in propane oxidation are shown in Figure 4.4. Product distribution including CO, CO_2, C_2H_4 (10% selectivity), acetone (~2% selectivity), acrolein, and propionaldehyde (both <1% selectivity) is presented in Figure S2.2.

Na/V catalysts were all active for propane oxidation to propylene in varying degrees. An increase of propane conversion with increasing temperature is obtained for all catalysts (Figure 4.4A). Increase in conversion was accompanied by the decrease in the selectivity to propylene (Figure 4.4B).

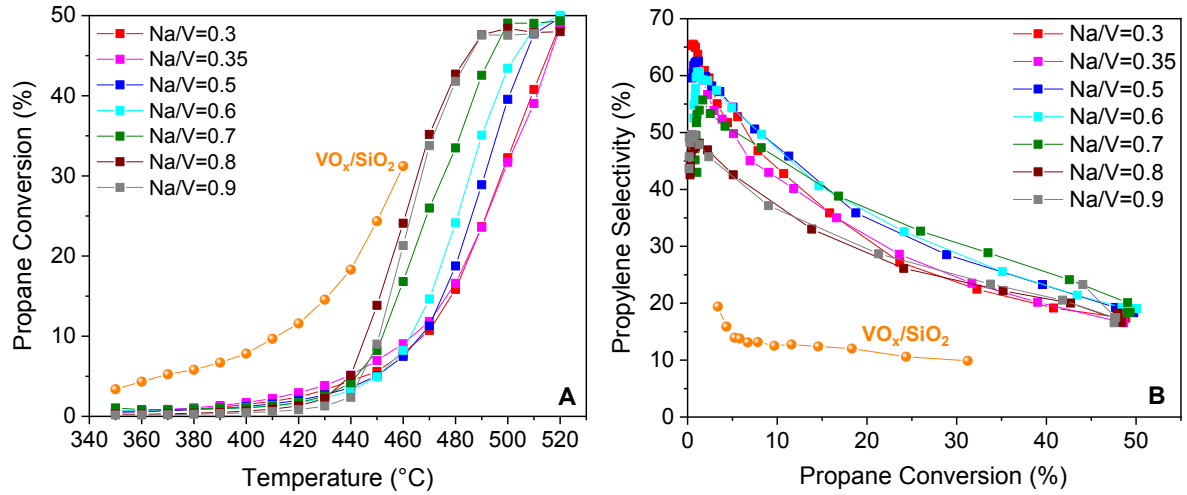

Figure 4.4. (A) Conversion of propane in propane oxidation over silica supported Na/V catalysts with increasing temperature, and **(B)** propylene selectivity as a function of propane conversion (Conditions: T=350°C-520°C, feed $C_3H_8/O_2/N_2$=7.5/7.5/85 vol. %, W/F= 1.8 g s ml^{-1}).

There is no significant difference in activity based on a Na-content until 450°C. Selectivity to propylene were similar over each catalyst. From this perspective, no clear correlation can be done in the change in activity with Na-content in contrast to Li/V catalysts. However, conversion changes as a function of sodium-loading after 450°C. This is a critical temperature in which homogeneous gas-phase reactions are dominant. After crossing 450°C, the same conversion can be reached at lower temperature with catalyst including higher sodium content. However the selectivity systematically decreases with increasing conversion. The most selective catalyst to propylene was found as Na/V=0.5 with 55% selectivity to propylene at 5% propane conversion.

Table 4.4 summarizes the reactivity and apparent activation energies of catalysts at 370°C. The propane consumption rate normalized to vanadium mass (in gr) measured over Na/V catalysts differ by order of magnitude. At 370°C, catalyst Na/V=0.6 exposes the highest propane consumption rate. The propane consumption rate decreases in the order Na/V=0.6 > Na/V=0.7 > Na/V=0.5 > Na/V=0.35 > Na/V=0.3 > Na/V=0.8 > Na/V=0.9. The propylene formation rate was found higher with catalysts containing lower Na-content. The optimal reactivity in terms of higher propane conversion and higher in propylene formation was found over Na/V=0.5 and Na/V=0.6 catalysts.

Table 4.4. Consumption rate of propane, activation energy and propylene formation rate measured over silica supported Na/V catalysts in the propane oxidation, applying a feed composition of $C_3H_8/O_2/N_2$=7.5/7.5/85 vol. %, and a contact time of 1.8 g s ml^{-1}

Sample	r(C_3H_8)[a] ($mol.g^{-1}$ $V.s^{-1}$)	Activation energy [b] (kJ/mol)	r(C_3H_6)[a] ($mol.g^{-1}$ $V.s^{-1}$)
Na/V=0.3	2.9	80.6	1.89
Na/V=0.35	3.4	78.8	2.11
Na/V=0.5	4.2	67.1	2.64
Na/V=0.6	5.1	42.6	2.86
Na/V=0.7	4.5	26.9	2.14
Na/V=0.8	1.7	83.1	0.74
Na/V=0.9	1.1	85.4	0.55
VO_x/SiO_2	19.1	59.0	2.67

[a]At a temperature 370°C (divided by 1E-7)
[b]Calculated in a temperature range between 350°C and 420°C.

Table 4.5 summarizes the reactivity and apparent activation energies of catalysts at 460°C. The order in propane consumption rate had been reversed and decreases in the following order: Na/V=0.8 > Na/V=0.9 > Na/V=0.7 > Na/V=0.6 > Na/V=0.5 > Na/V=0.35 > Na/V=0.3. Apparent activation energies extremely higher than that of measured at 370°C. Propylene formation rate was increased as well with increasing Na -content. The highest propylene formation rate was measured for Na/V= 0.9 catalyst.

Table 4.5. Consumption rate of propane, activation energy and propylene formation rate measured over silica supported Na/V catalysts in the propane oxidation, applying a feed composition of $C_3H_8/O_2/N_2$=7.5/7.5/85 vol. %, and a contact time of 1.8 g s ml^{-1}

Catalyst	r(C_3H_8)[a] ($mol.g^{-1}$ $V.s^{-1}$)	Activation energy [b] (kJ/mol)	r(C_3H_6)[a] ($mol.g^{-1}$ $V.s^{-1}$)
Na/V=0.3	31.46	123.4	14.7
Na/V=0.35	35.9	124.5	15.4
Na/V=0.5	44.4	158.9	22.5
Na/V=0.6	50.1	203.2	24.9
Na/V=0.7	93.6	302.9	36.3
Na/V=0.8	134.1	338.1	35.0
Na/V=0.9	124.6	477.2	35.7
VO_x/SiO_2	114.0	116.1	11.28

[a]At a temperature 460°C (divided by 1E-7)
[b]Calculated in a temperature range between 440°C and 460°C.

In general, based on temperature, catalysts behave different. Higher Na-content yields in higher propylene selectivity at 460°C whereas lower Na-loading yields in better performance at 370°C.

4.2.1. Reproducibility of catalytic activity

Figure 4.5 shows the comparison of reactivity data from 1st and 2nd measurement in propane oxidation over silica supported Na/V catalysts.

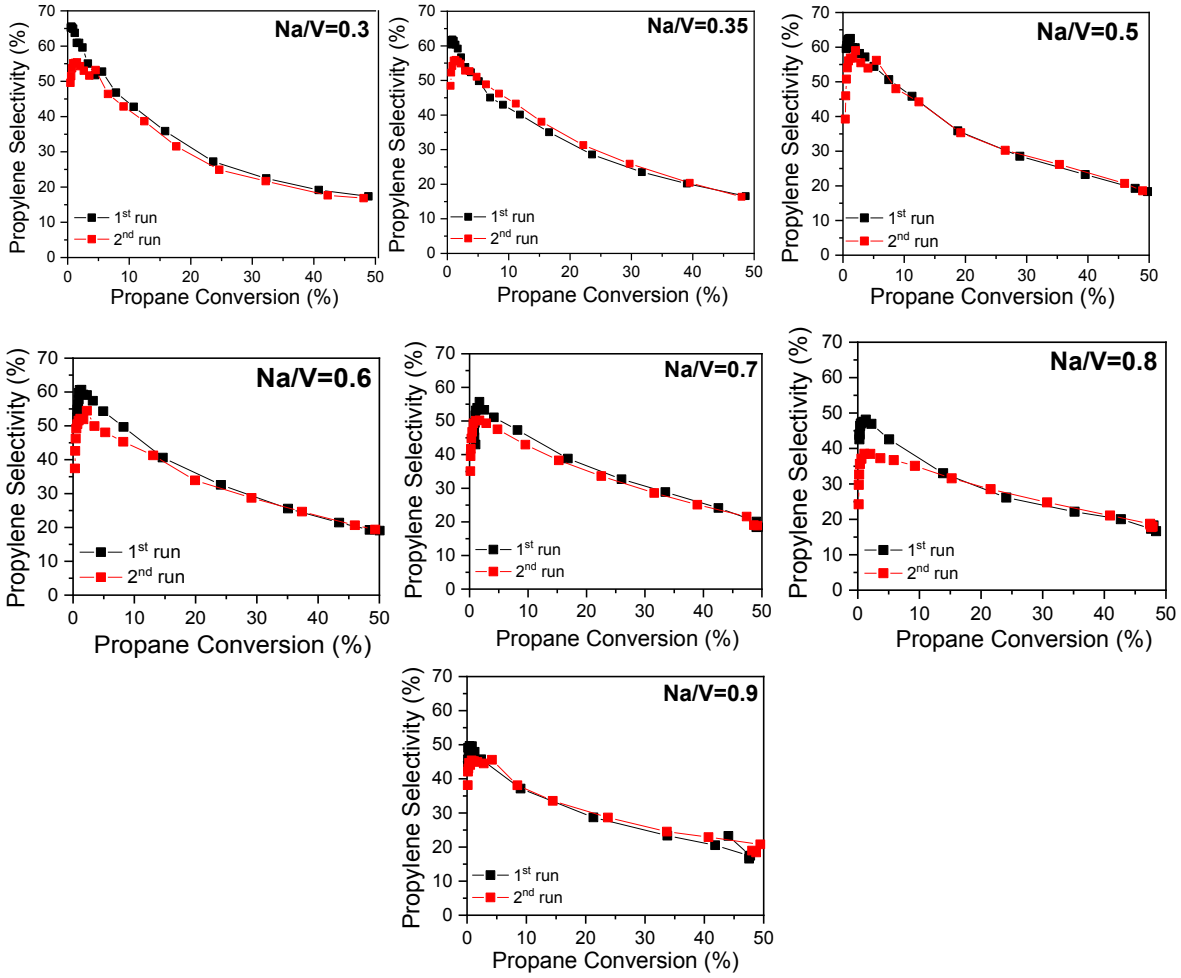

Figure 4.5. Catalytic activity results of silica supported Na/V catalysts obtained from1st and 2nd measurement in propane oxidation reaction (black: 1st run, red: 2nd run)

Compared to silica supported Li/V catalysts (Figure 4.2), the catalytic reproducibility was found better over silica supported Na/V catalysts in propane oxidation. Similar conversion and selectivity were reached at similar temperatures. Therefore silica supported Na/V catalysts can be evaluated as more stable than Li/V catalysts. Following the structural properties of fresh and spent catalysts are compared.

4.2.2. Properties of spent Na/V catalysts

The XRD and BET analysis of spent catalysts of supported Na/V catalysts was analyzed and compared with fresh Na/V catalysts (Table 4.6). No phase change but higher crystallinity was

observed for Na/V=0.35, Na/V=0.5, and Na/V=0.6 catalysts. Na/V=0.7, Na/V=0.8, and Na/V=0.9 catalysts showed a phase change.

Table 4.6. Properties of spent silica supported Na/V catalysts compared to fresh catalysts

ID#	Na/V	XRD (fresh)	XRD (spent)	BET (fresh) (m^2/g)	BET (spent) (m^2/g)
32515	0.3	$Na_{1.16}V_3O_8$, $Na_{0.2}V_2O_5$	$Na_{1.16}V_3O_8$, $Na_{0.33}V_2O_5$	74	54
32516	0.35	$Na_{1.16}V_3O_8$	$Na_{1.16}V_3O_8$	40	36
32517	0.5	$Na_{1.16}V_3O_8$	$Na_{1.16}V_3O_8$	62	45
32518	0.6	$Na_{1.16}V_3O_8$	$Na_{1.16}V_3O_8$	41	32
32519	0.7	$Na_{1.16}V_3O_8$	$Na_5V_{12}O_{32}$	44	26
32520	0.8	$Na_{1.16}V_3O_8$	$Na_{1.16}V_3O_8$, NaV_2O_5	27	18
32521	0.9	$Na_{0.56}V_2O_5$	Tridymite SiO_2, $Na_2V_2O_6$, $NaVO_3$	17	13

Differently than remaining types of alkali-added vanadium oxide catalysts presented in this study, BET surface are of Na/V and Li/V catalysts were decreased less. This is because no melting occurs in these class of alkali additives where etching of silica can be excluded. The only reason behind that is the increased surface crystallinity during reaction as detected by XRD. In both cases, increased phase crystallinity was observed due to the uncompleted phase formation from the synthesis (520°C was low as calcination temperature based on phase diagrams). The propane oxidation conditions acted here as further calcination which yields in increased phase crystallinity. Generally saying, changes occurs in terms of structural and textural which reflects in catalytic properties over Na/V and Li/V catalysts was not that significant as will be seen in K, Rb and Cs containing systems in where melting occurs.

4.3. Silica supported K/V catalysts with various ratios of K: V

Starting from potassium, the impact of melting of alkali-vanadate(s) on the catalytic performance will be introduced in this section. The results of catalytic testing of the silica supported K/V catalysts are shown in Figure 4.6. Product distribution including CO, CO_2. C_2H_4 (2% selectivity), acetone (~10% selectivity), acrolein, and propionaldehyde (both <1% selectivity) and how the selectivity changes upon melting is presented in Figure S2.3.

Under applied reaction conditions between 350 and 520°C, propane conversion increased with increasing temperature for all K/V catalysts until the melting temperatures were reached. For catalysts with K/V=0.3 and K/V=0.4, the increase of conversion was accompanied by the decrease in selectivity to propylene. However, catalysts with K/V≥0.5 showed relatively stable

selectivity to propylene with increasing conversion. At 390°C where all catalysts are solid, catalytic performances were slightly enhanced with increasing K-loading. However, catalysts with K/V=0.5, K/V=0.6, and K/V=0.7 are less selective to propylene as compared to VO_x/SiO_2. Among all, catalyst with K/V=0.3 was found as the most selective to desired product at the same conversion compared to others.

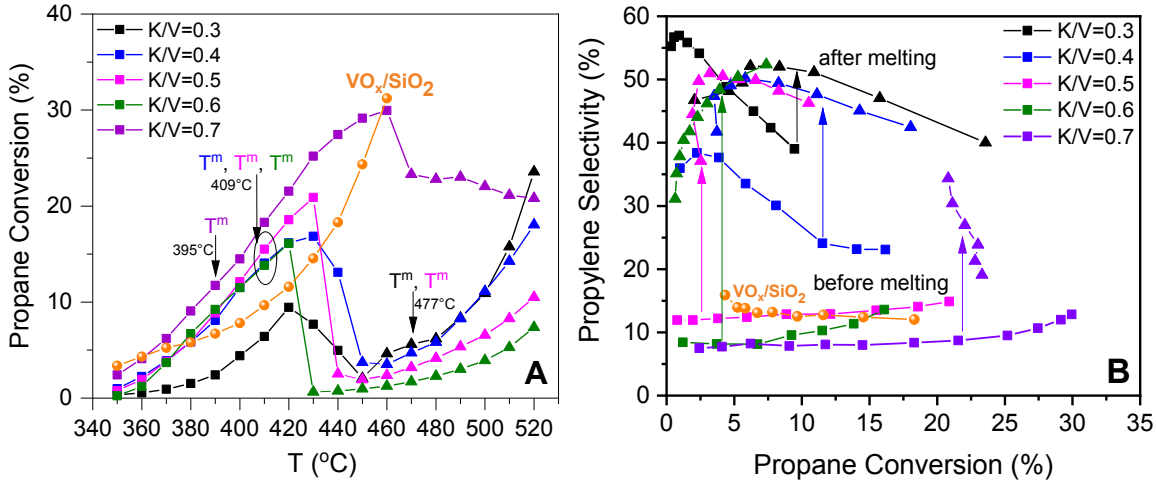

Figure 4.6. (A) Conversion of propane in propane oxidation over silica supported K/V catalysts with increasing temperature, and **(B)** propylene selectivity as a function of propane conversion (■:data before melting temperature of catalysts, ▲:data after melting temperature of catalysts) (Conditions: T=350°C-520°C, feed $C_3H_8/O_2/N_2$=7.5/7.5/85 vol. %, W/F= 1.8 g s ml^{-1}).

Several studies report the poisoning effect of alkali metals on activity by blocking the access of a reacting molecule to the active vanadia centers in oxidation reactions [218, 254, 410, 411]. A.A. Lemonidou *et al.* [273] reported that the addition of potassium with a ratio of K_2O/V_2O_5=0.25 on V/Al_2O_3 (V_2O_5=4 wt. %) catalyst decreases propane conversion. A similar conclusion was observed by A. Klisińska *et al.*[82] over V/Si catalyst (V_2O_5=28.0 wt. %) with K/V ratio of 0.1. This is in agreement with our results with the K/V=0.3 catalyst although our loading of V_2O_5 is different. Overall, the decreasing effect of potassium on activity and increasing effect on selectivity to propylene is still valid when the potassium loading is low (K/V ≤ 0.3).

Table 4.7 summarizes the reactivity and apparent activation energies of catalysts below their respective melting points (at 370°C). The propane consumption rate normalized to vanadium mass (in gr) measured over K/V catalysts differ by order of magnitude. The K/V=0.7 catalyst exhibited the highest consumption rate of propane, and accompanied by the lowest activation energy. The propane consumption rates correlate directly with the K-loading and it decreases

in the following order K/V=0.7 > K/V=0.6 > K/V=0.5 > K/V=0.4 > K/V=0.3. The propylene formation rate was found the highest over K/V=0.4 catalyst among others.

Table 4.7. Consumption rate of propane, activation energy and propylene formation rate measured over K-V/SiO_2 catalysts in the propane oxidation, applying a feed composition of $C_3H_8/O_2/N_2$=7.5/7.5/85 vol. %, and a contact time of 1.8 g s ml^{-1}

Catalyst	$r(C_3H_8)$[a] ($mol.g^{-1}$ $V.s^{-1}$)	Activation energy [b] ($kJ\ mol^{-1}$)	$r(C_3H_6)$[a] ($mol.g^{-1}$ $V.s^{-1}$)
K/V=0.3	3.92	171	2.23
K/V=0.4	15.9	204	6.01
K/V=0.5	17.0	245	2.08
K/V=0.6	18.5	388	1.51
K/V=0.7	33.8	160	2.77
VO_x/SiO_2	19.1	59.0	2.67

[a]At a temperature 370°C (divided by 1E-7)
[b]Calculated in a temperature range between 350°C and 390°C.

First of all, much higher activation energy was found over K-containing catalysts compared to VO_x/SiO_2 (V_2O_5=8.8 wt. %). A theoretical investigation of a silica supported vanadia model catalyst estimates a higher apparent activation energy of 123 kJ/mol [412]. Grüne *et al.* [241] reported experimental apparent activation energies for V/SBA15 catalysts of between 134 and 151 kJ/mol. The changes on activation energies situates differently based on the ratio of two-dimensional polymeric species and three-dimensional bulk-like V_2O_5[241]. In case of two-dimensional vanadium oxide species exist on the surface of silica support, the calculated apparent activation energy was reported as 59 kJ/mol [413] which is consistent with our finding. Apparent activation energies situated in between 160 and 388 kJ/mol. The activation energies measured here are similar for catalysts K/V=0.3 and K/V=0.7. The values decrease in the order K/V=0.6>K/V=0.5>K/V=0.4. Compared to Li, and Na/V catalysts, activity was found higher.

Table 4.8 summarizes the reactivity and apparent activation energies of catalysts above their respective melting point. The expected increase in propane consumption rate was not seen due to the deactivation at specific temperatures. Nonetheless, the propane consumption rate normalized to vanadium content decreases with K loading except for the catalyst with K/V=0.7. Similarly, propylene formation rates also directly correlate with the K-content (except for catalyst with K/V=0.7).

The K/V=0.7 catalyst gives the highest consumption rate of propane and formation rate of propylene. As compared to the temperature between 350 and 390°C, apparent activation

energies calculated here situated in between 109 and 173 kJ/mol and these values decreased in the order K/V=0.3 > K/V=0.6 > K/V=0.4 > K/V=0.5.

Table 4.8. Consumption rate of propane, activation energy and propylene formation rate measured over K-V/SiO_2 catalysts in the propane oxidation, applying a feed composition of $C_3H_8/O_2/N_2$=7.5/7.5/85 vol. %, and a contact time of 1.8 g s ml^{-1}

Catalyst	$r(C_3H_8)$[a] ($mol.g^{-1}$ $V.s^{-1}$)	Activation energy [b] (kJ/mol)	$r(C_3H_6)$[c] ($mol.g^{-1}$ $V.s^{-1}$)
K/V=0.3	19.5	173	9.39
K/V=0.4	14.4	129	6.86
K/V=0.5	10.7	109	5.32
K/V=0.6	6.3	141	2.54
K/V=0.7	162	n.a.	20.9
VO_x/SiO_2	114.0	116.1	11.28

[a]At a temperature 460°C (divided by 1E-7), [c]At a temperature 460°C (divided by 1E-8)
[b]Calculated in a temperature range between 490°C and 520°C.

In general, Figure 4.6 shows an uncommon reactivity profile. The conversion dropped drastically as the melting temperature of catalysts were reached. The conversion was recovered with further temperature increase. The same conversion was achieved at higher temperature. More interestingly, selectivity to propylene was much higher compared to the temperature before activity drops. When selectivity to propylene increased, a decrease in selectivity to CO_2 and CO occurred simultaneously (Figure S2.3). The reason behind this uncommon catalytic profile will be precisely examined in *operando*-DSC part within the concept of melting.

4.3.1. Reproducibility of catalytic activity

Reproducibility of catalytic activity of silica supported K/V catalysts was measured differently than other catalysts. In this case, two temperatures were selected which corresponds to below and above the melting temperatures. These temperatures were 400 and 490°C. After 1st run was completed, catalysts were cooled down to 50°C and propane oxidation were run at 400°C and 490°C, respectively. Figure 4.7 shows the comparison of reactivity data from 1st, 2nd, and 3rd measurement in propane oxidation over silica supported K/V catalysts.

Compared to Li/V and Na/V catalysts, a drastic change in catalytic performance can be seen. For instance, nearly a complete deactivation (96% decrease in propane consumption rate) of K/V=0.6 catalyst was seen after 1st run (400°C). This is due to the blocking of the pores by melt (no porosity in spent catalyst (Figure S2.6)). The decrease in specific surface area right after melting was also measured by stopping the reaction at 420°C in where melting was completed. Melting caused 20% decrease (from 23.6 to 19.1 m^2/g) in BET surface area (Figure S2.7).

However, similar activity and selectivity to propylene were observed at 490°C which is known as a temperature in where homogenous gas-phase reaction takes place more.

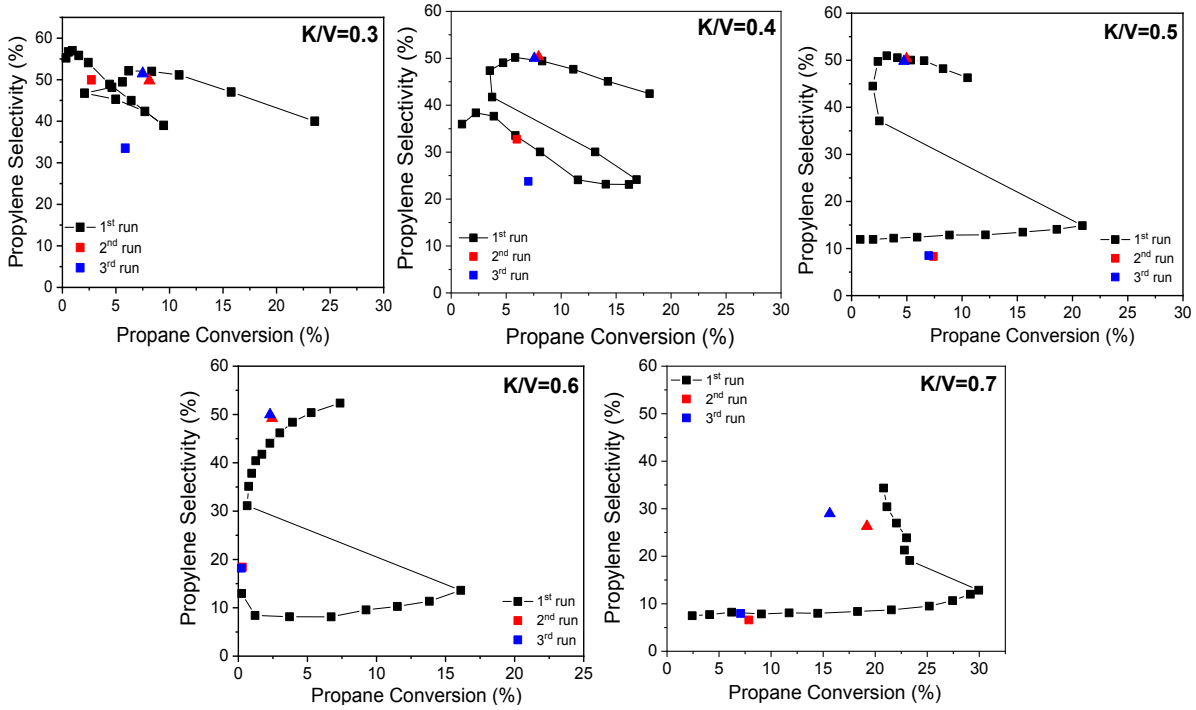

Figure 4.7. Catalytic activity results of silica supported K/V catalysts obtained from 1st, 2nd, and 3rd measurement in propane oxidation reaction (black: 1st run, red: 2nd run, blue: 3rd run)

4.3.2. Properties of spent K/V catalysts

The structural and textural properties of spent silica supported K/V catalysts were analyzed by XRD and BET techniques and compared with fresh K/V catalysts (Table 4.9).

Table 4.9. Properties of spent silica supported K/V catalysts compared to fresh catalysts

ID#	K/V	XRD (fresh)	XRD (spent)	BET (fresh) (m^2/g)	BET (spent) (m^2/g)
29559	0.3	$K_2V_6O_{16}1.5H_2O$	$K_2V_8O_{21}$, unknown	38	10
29560	0.4	$K_3V_5O_{14}$, $K_2V_6O_{16}1.5H_2O$	$K_2V_8O_{21}$, $K_3V_5O_{14}$, *quartz,* opal, cristobalite	33	4
29561	0.5	$K_3V_5O_{14}$ $K_2V_6O_{16}1.5H_2O$	$K_3V_5O_{14}$, KVO_3, opal	34	2
29562	0.6	$K_3V_5O_{14}$	$K_3V_5O_{14}$, $K_{4.2}V_6O_{16.2}0.5H_2O$, opal	24	1.3
29563	0.7	SiO_2 (amorphous)	$K_3V_5O_{14}$, opal	82	3
29564	1	SiO_2 (amorphous)	cristobalite	113	15

After 1 month of stream, catalysts showed significant changes. First, phase change occurred which indicates that potassium-vanadates over silica support are not thermally stable. None of the catalysts showed the same alkali vanadate phase after catalysis. Catalysts with a ratio of potassium to vanadium 0.3 and 0.4 showed potassium octavanadate, $K_2V_8O_{21}$, which was reported in the phase diagram as an expected phase. Catalyst K/V=0.6 which was a phase pure $K_3V_5O_{14}$ showed phase separation and resulted in $K_{4.2}V_6O_{16.2}$ $0.5H_2O$ as a second-phase. After catalysis, silica found in its crystalline forms such as quartz, opal and cristobalite.

For sure after several melting and crystallization cycles, agglomeration and sintering of catalyst particles were expected. BET surface area of catalysts after propane oxidation was found significantly reduced. Pore size distribution analysis of K/V=0.6 (#29562) showed that spent catalyst had nearly no porosity (Figure S2.6). This is simply due to the etching of silica by spreading of potassium.

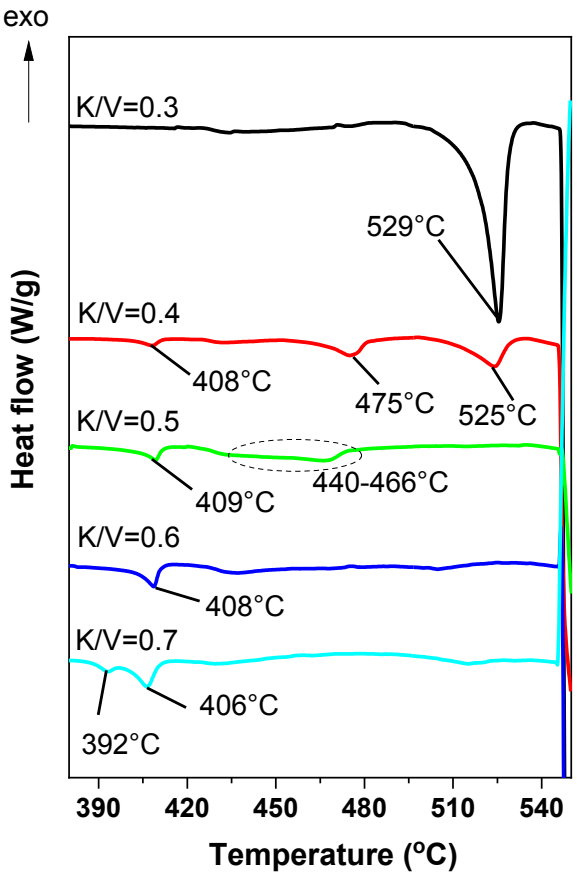

Figure 4.8. DSC profiles of spent K/V catalysts under 21%O_2/ 79% Ar with a flow of 70 ml/min, heating rate: 10 Kpm, cooling rate: 5 Kpm in an alumina crucible with lid

DSC profiles of spent silica supported K/V catalysts are shown in Figure 4.8. Catalyst with a ratio of K/V=0.3 shows melting of the $K_2V_8O_{21}$ [291]. The melting of the $K_3V_5O_{14}$ was

measured at about 410°C for the rest of the catalysts that confirms the existence of $K_3V_5O_{14}$ as detected by XRD. The impurities and/or other existing potassium vanadate phases from the phase separation reflects in an additional melting events in DSC. From our knowledge, we can only confirm the $K_3V_5O_{14}$ (410°C) and $K_2V_8O_{21}$ (529°C) as we measured bulk-materials of these components.

4.4. Silica supported Rb/V catalysts with various ratios of Rb: V

The catalytic performance of silica supported Rb/V catalysts in propane oxidation is shown in Figure 4.9. The major reaction products were C_3H_6, CO and CO_2. C_2H_4 (2% selectivity), acetone (~10% selectivity for Rb/V>0.6), acrolein and propionaldehyde (both <1% selectivity) were not observed in significant amounts (Figure S2.4).

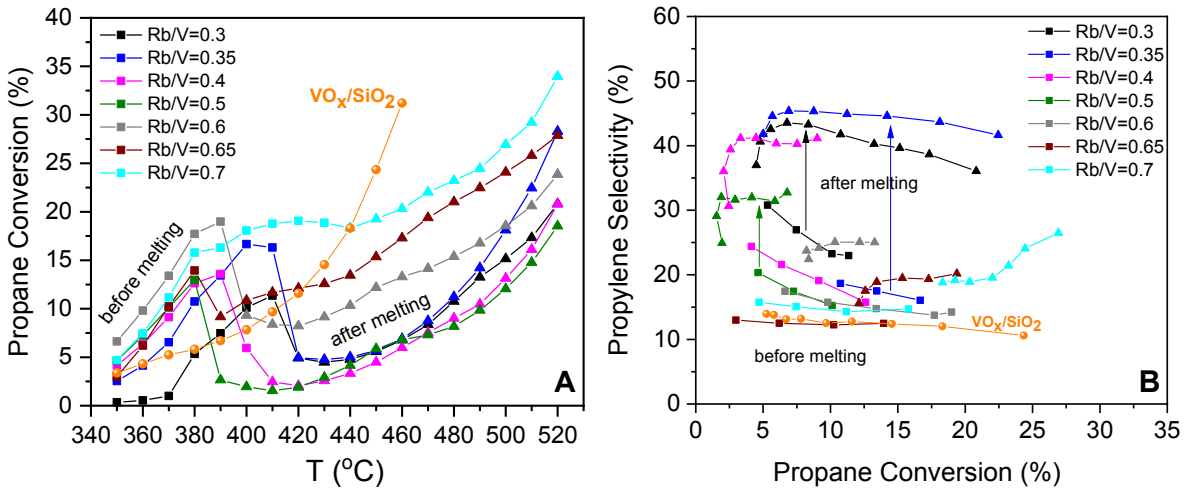

Figure 4.9. (A) Conversion of propane in propane oxidation over silica supported Rb/V catalysts with increasing temperature, and **(B)** propylene selectivity as a function of propane conversion (■:data before melting temperature of catalysts, ▲:data after melting temperature of catalysts) (Conditions: T=350°C-520°C, feed $C_3H_8/O_2/N_2$=7.5/7.5/85 vol. %, W/F= 1.8 g s ml^{-1}).

Silica supported Rb/V catalysts were all active for propane oxidation to propylene in varying degrees. An increase of propane conversion with increasing temperature was obtained for all catalysts until the melting temperatures of rubidium vanadate phases were reached (Figure 4.9A). Increase in conversion was accompanied by the decrease in the selectivity to propylene (Figure 4.9B). However, catalysts with Rb/V ≥ 0.6 demonstrated stable selectivity to propylene (10-20% selectivity at 10% propane conversion) similar to the bare catalyst (VO_x/SiO_2). At 380°C where all catalysts are solid, catalytic performances were enhanced with increasing Rb-loading compared to VO_x/SiO_2 except for Rb/V=0.3. On the other hand, selectivity to propylene decreased with increasing Rb-loading. The Rb/V=0.35 catalyst was found as the most selective

to propylene (47% propylene selectivity at 10% propane conversion) at the same conversion among all.

Table 4.10 summarizes the reactivity and apparent activation energies of catalysts below their respective melting points. The propane consumption rate normalized to vanadium mass (in gr) measured over Rb/V catalysts differ by an order of magnitude. Catalyst Rb/V=0.6 exposes the highest propane consumption rate, combined with the lowest activation energy within RbV catalysts. The propane consumption rate correlates with the Rb-content and it decreases in the order Rb/V=0.6 > Rb/V=0.65 > Rb/V=0.7 > Rb/V=0.5 > Rb/V=0.4 > Rb/V=0.3 > Rb/V=0.2. Catalysts with higher Rb-content were more active as catalysts with higher K-content. However, propylene formation rate increases with the same order.

Table 4.10. Consumption rate of propane, activation energy and propylene formation rate measured over Rb-V/SiO_2 catalysts in the propane oxidation, applying a feed composition of $C_3H_8/O_2/N_2$=7.5/7.5/85 vol. %, and a contact time of 1.8 g s ml^{-1}

Catalyst	$r(C_3H_8)$[a] ($mol.g^{-1}$ $V.s^{-1}$)	Activation energy [b] (kJ/mol)	$r(C_3H_6)$[a] ($mol.g^{-1}$ $V.s^{-1}$)
Rb/V=0.3	4.87	183.9	2.50
Rb/V=0.35	32.5	159.0	9.57
Rb/V=0.4	47.9	132.0	9.15
Rb/V=0.5	55.6	101.6	8.48
Rb/V=0.6	74.9	116.8	11.05
Rb/V=0.65	58.4	139.9	7.16
Rb/V=0.7	68.1	128.7	9.75
VO_x/SiO_2	19.1	59.0	2.67

[a]At a temperature 370°C (divided by 1E-7)
[b]Calculated in a temperature range between 350°C and 380°C.

With further increasing temperature, the conversion drops drastically as melting points are reached. At this point where deactivation occurs due to melting, an enhancement of selectivity to propylene was observed for all Rb/V catalysts. At the same time, selectivity to CO and CO_2 decreased. Here it seems melting appears to play a role which is similar effect observed in the K/V system. Conversion is recovered again with increasing temperature and the same conversion is achieved at higher temperature after melting. Temperatures where activity drop is observed are correlated with the operando DSC measurement (see in Chapter 3).

Table 4.11 summarizes the reactivity and apparent activation energies of catalysts above their respective melting points. The apparent activation energies decreases with increasing Rb content. The propane consumption rate normalized to vanadium content slightly increases with Rb-loading. Compared to blank catalyst, highest Rb content improves the catalytic activity the most. The highest consumption rate was obtained for the Rb/V=0.7 catalyst.

Table 4.11. Consumption rate of propane, activation energy and propylene formation rate measured over Rb-V/SiO_2 catalysts in the propane oxidation, applying a feed composition of $C_3H_8/O_2/N_2$=7.5/7.5/85 vol. %, and a contact time of 1.8 g s ml^{-1}

Catalyst	$r(C_3H_8)$[a] ($mol.g^{-1}$ $V.s^{-1}$)	Activation energy [b] (kJ/mol)	$r(C_3H_6)$[a] ($mol.g^{-1}$ $V.s^{-1}$)
Rb/V=0.3	32.6	113.6	14.2
Rb/V=0.35	34.3	114.4	15.6
Rb/V=0.4	31.4	96.5	12.6
Rb/V=0.5	37.3	84.2	12.2
Rb/V=0.6	74.2	60.0	18.6
Rb/V=0.65	98.7	49.2	19.0
Rb/V=0.7	124.0	33.8	23.4
VO_x/SiO_2	114.0	116.1	11.28

[a]At a temperature 460°C (divided by 1E-7)
[b]Calculated in a temperature range between 450°C and 480°C.

4.4.1. Reproducibility of catalytic activity

The catalyst reproducibility was tested by measuring the propane oxidation second time after complete cool down. Figure 4.10 shows the comparison of reactivity data from 1st and 2nd measurement in propane oxidation over silica supported Rb/V catalysts.

The great impact of melting can be seen on the reactivity profile in the second cycle. Below melting temperature (solid state), catalysts showed lower activity. This indicates that catalyst structure significantly changes upon melting in the first cycle. However after liquefaction, similar selectivity to propylene could be still reachable. This already questions the contribution of the catalyst surface on the performance after melting (*will be discussed further in operando chapter*).

4.4.2. Properties of spent Rb/V catalysts

The spent catalysts were analyzed by XRD and BET and compared with fresh Rb/V catalysts (Table 4.12). No significant change was observed in terms of crystalline phases. However change in intensities of corresponding phases indicates that the concentrations of the phases might be changed. For instance $Rb_3V_5O_{14}$ gave stronger reflection after catalysis in Rb/V=0.4 catalyst. On the other hand, Rb/V=0.65 and Rb/V=0.7 catalysts completely changed and gave no signal beyond amorphous SiO_2. No further crystallization of silica occurred.

As previously seen in K/V catalysts, significant decrease in BET surface areas were expected since all Rb/V catalysts exhibits melting under applied propane oxidation temperature range. After two cycles of propane oxidation which consists of several melting and solidification events, BET surface area of catalysts after propane oxidation was found significantly reduced.

In general, about 70% of the BET surface area of the catalysts was decreased due to melting of rubidium vanadate phase(s). The lowest decrease in BET surface area was obtained for catalyst Rb/V=0.3. DSC profiles of spent silica supported Rb/V catalysts are shown in Figure 4.11.

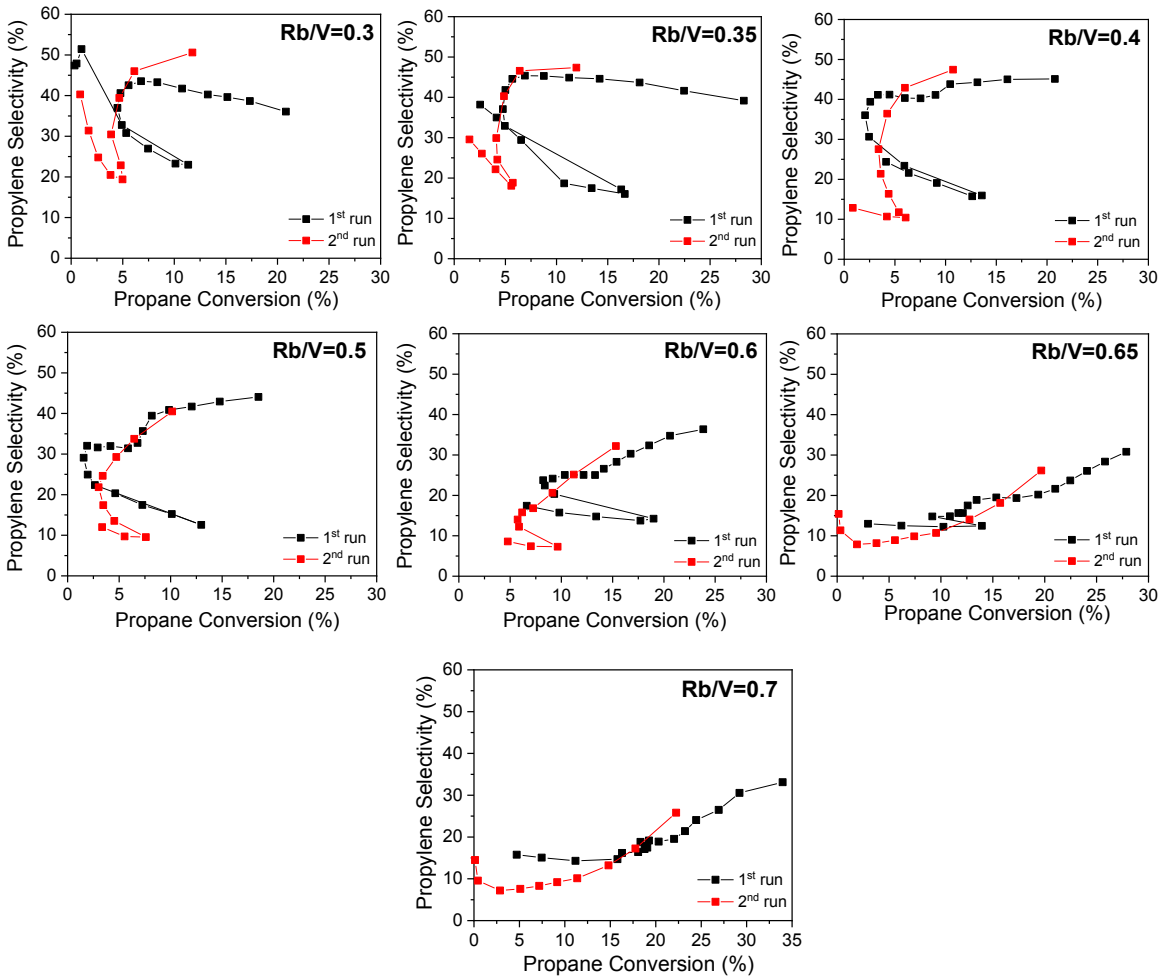

Figure 4.10. Catalytic activity results of silica supported Rb/V catalysts obtained from1st and 2nd measurement in propane oxidation reaction (black: 1st run, red: 2nd run)

First of all, similar melting temperatures were obtained which confirms the XRD findings where no significant phase change occurred. However some exceptions are exist. For instance, the peak at 508°C was found more pronounced for lower Rb-containing of catalysts, *i.e.*, Rb/V=0.3 and Rb/V =0.35 catalysts. In addition, the peak at 442°C disappeared for Rb/V=0.3 catalyst. Since XRD could not detect any new phase, meaning to the formation of some amorphous surface phases after catalysis. The peak at 390°C remained the same and become more pronounced with increasing Rb-content. No melting was observed over Rb/V=0.65 and Rb/V=0.7 catalysts which are in agreement with XRD findings since there is no crystalline phase was detected.

Table 4.12. Properties of spent silica supported Rb/V catalysts as compared to fresh catalysts

ID#	Rb/V	XRD (fresh)	XRD (spent)	BET (fresh) (m^2/g)	BET (spent) (m^2/g)
30765	0.3	$Rb_2V_6O_6$ 1.5H_2O, $Rb_3V_5O_{14}$	$Rb_3V_5O_{14}$	20	15
30766	0.35	$Rb_2V_6O_6$ 1.5H_2O, $Rb_3V_5O_{14}$, $Rb_2V_4O_{11}$,	$Rb_2V_6O_6$ 1.5H_2O, $Rb_3V_5O_{14}$, $Rb_2V_4O_{11}$,	53	15
30767	0.4	$Rb_2V_4O_{11}$, $Rb_3V_5O_{14}$	$Rb_2V_4O_{11}$, $Rb_3V_5O_{14}$	78	20
30768	0.5	$Rb_2V_4O_{11}$, $Rb_3V_5O_{14}$	$Rb_2V_4O_{11}$, $Rb_3V_5O_{14}$	55	20
30770	0.6	$Rb_2V_4O_{11}$, $Rb_3V_5O_{14}$	$Rb_2V_4O_{11}$, $Rb_3V_5O_{14}$	86	24
30771	0.65	$Rb_2V_4O_{11}$	SiO_2 (amorphous)	83	25
30773	0.7	$Rb_2V_4O_{11}$, $Rb_3V_5O_{14}$	SiO_2 (amorphous)	99	27

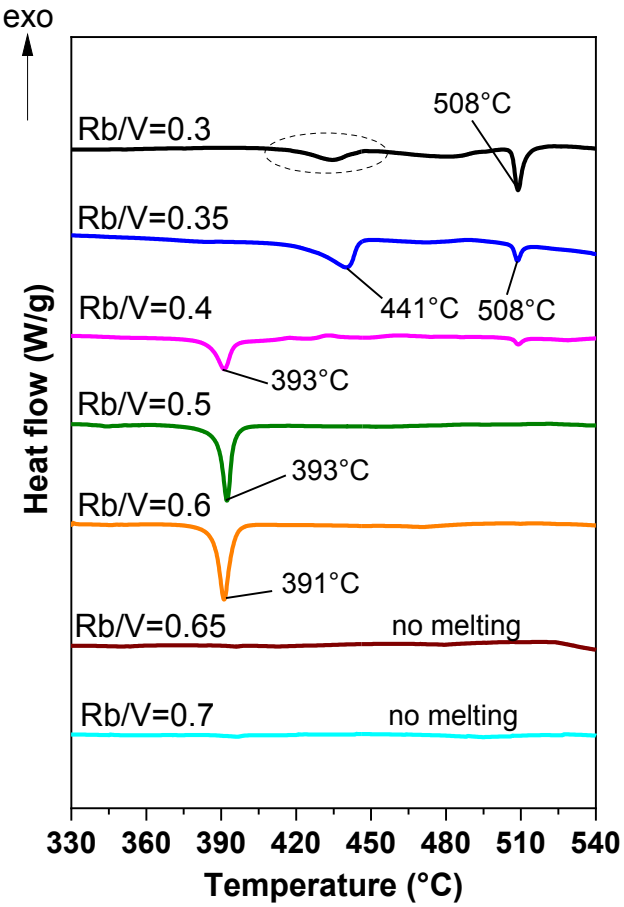

Figure 4.11. DSC profiles of spent Rb/V catalysts under 21%O_2/ 79% Ar with a flow of 70 ml/min, heating rate: 10 Kpm, cooling rate: 5 Kpm in an alumina crucible with lid

4.5. Silica supported Cs/V catalysts with various ratios of Cs: V

The catalytic performance of silica supported Cs/V catalysts were tested in propane oxidation under the same experimental conditions. However, catalysts were found too active with >80% oxygen conversion. Therefore the catalyst mass was reduced and tested again. Propane oxidation was performed with a reaction temperature between 350 and 520°C, in a feed of $C_3H_8/O_2/N_2$=7.5/7.5/85 vol. %, using a catalyst mass of 150 mg, and applying a contact time W/F=0.6 g s ml^{-1} (Figure 4.12). Product distribution of CO and CO_2. C_2H_4 (2% selectivity), acetone (~10% selectivity), acrolein and propionaldehyde (both <1% selectivity) was shown in Figure S2.5.

Silica supported Cs/V catalysts were all active for propane oxidation to propylene in varying degrees based on an alkali content. An increase of propane conversion with increasing temperature was obtained for all catalysts until melting temperatures were reached (Figure 4.12A). Increase in conversion was accompanied by the decrease in the selectivity to propylene (Figure 4.12B). Catalyst which contain the highest Cs- loading (*i.e.* Cs/V=0.6) exhibited constant selectivity to propylene similar to high loaded K- and Rb- catalysts.

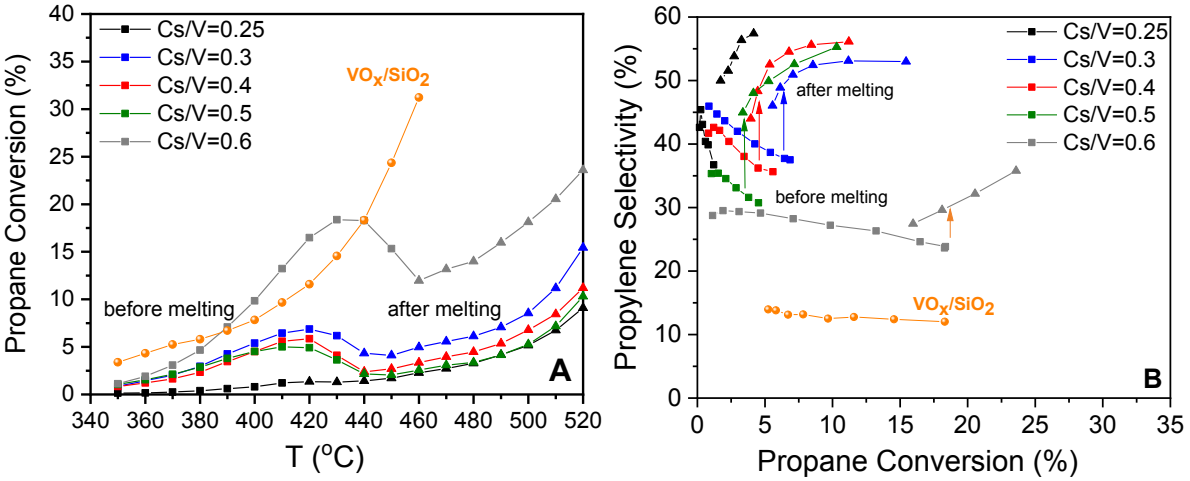

Figure 4.12. (A) Conversion of propane in propane oxidation over silica supported Cs/V catalysts with increasing temperature, and **(B)** propylene selectivity as a function of propane conversion (■:data before melting temperature of catalysts, ▲:data after melting temperature of catalysts) (Conditions: T=350°C-520°C, feed $C_3H_8/O_2/N_2$=7.5/7.5/85 vol. %, W/F= 0.6 g s ml^{-1}).

It is generally seen that Cs-addition lowers the catalytic activity of VO_x/SiO_2 except for the catalyst Cs/V=0.6. At 410°C where all catalysts are solid, catalyst Cs/V=0.6 shows higher conversion than all other catalysts, including VO_x/SiO_2. The Cs/V =0.3 catalyst demonstrated the appreciable conversion and highest selectivity to propylene, and at 410°C a 7% conversion

of propane and 40% selectivity towards propylene was observed. The propylene production for other catalysts were relatively low.

At higher temperature (*i.e.* after melting), activity remained as highest over the highest Cs-containing catalysts and decreases systematically with decreasing Cs-content. This reflected oppositely in the selectivity to propylene in which catalyst Cs/V=0.25 exhibited the highest propylene selectivity (58% selectivity to propylene at 5% propane conversion, at 520°C). After deactivation by crossing melting temperatures, selectivity to propylene over each catalysts were enhanced.

Table 4.13 summarizes the reactivity and apparent activation energies of catalysts below their melting temperatures. Catalyst Cs/V=0.6 exposes the highest propane consumption rate, combined with ac activation energy of 153.6 kJ/mol. The propane consumption rate decreases in the following order Cs/V=0.6 > Cs/V=0.25 > Cs/V=0.3 > Cs/V=0.4 > Cs/V=0.5. Catalysts with higher Cs-content were more active as catalysts with higher K-content. However, propylene formation rate increases with the same order.

Table 4.13. Consumption rate of propane, activation energy and propylene formation rate measured over silica supported Cs/V catalysts in the propane oxidation, applying a feed composition of $C_3H_8/O_2/N_2$=7.5/7.5/85 vol. %, and a contact time of 0.6 g s ml^{-1}

Catalyst	$r(C_3H_8)$[a] ($mol.g^{-1}$ $V.s^{-1}$)	Activation energy [b] (kJ/mol)	$r(C_3H_6)$[a] ($mol.g^{-1}$ $V.s^{-1}$)
Cs/V=0.25	3.51	148.2	1.59
Cs/V=0.3	31.5	126.7	13.7
Cs/V=0.4	25.9	115.9	10.9
Cs/V=0.5	34.0	108.3	11.7
Cs/V=0.6	59.2	153.6	17.3
VO_x/SiO_2	19.1	59.0	2.67

[a]At a temperature 370°C (divided by 1E-7)
[b]Calculated in a temperature range between 350°C and 380°C.

Table 4.14 summarizes the reactivity and apparent activation energies of catalysts above their respective melting temperatures. Apparent activation energies decreased with increasing Cs content. The highest activation energy was found over the catalyst with the lowest Cs-content as 83 kJ/mol (Cs/V=0.25). The propane consumption rate normalized to vanadium content decreases with Cs-loading. Compared to the blank vanadia catalyst, Cs addition always increased the propylene formation rate.

Table 4.14. Consumption rate of propane, activation energy and propylene formation rate measured over silica supported Cs/V catalysts in propane oxidation, applying a feed composition of $C_3H_8/O_2/N_2$=7.5/7.5/85 vol. %, and a contact time of 0.6 g s ml^{-1}

Catalyst	$r(C_3H_8)$[a] ($mol.g^{-1}$ $V.s^{-1}$)	Activation energy [b] (kJ/mol)	$r(C_3H_6)$[a] ($mol.g^{-1}$ $V.s^{-1}$)
Cs/V=0.25	32.6	83.3	16.8
Cs/V=0.3	77.2	79.2	34.1
Cs/V=0.4	52.9	71.3	22.2
Cs/V=0.5	41.3	72.7	15.8
Cs/V=0.6	229.2	45.9	53.0
VO_x/SiO_2	114.0	116.1	11.28

[a]At a temperature 460°C (divided by 1E-7)
[b]Calculated in a temperature range between 450°C and 480°C.

Generally, the conversion decreases as melting temperatures are reached. At this point where deactivation occurs, an enhancement of selectivity towards propylene was observed for all silica supported Cs/V catalysts. Moreover, selectivity to CO and CO_2 decreases. This is a general phenomenon which was observed for K/V and Rb/V catalysts as well. Conversion is recovered with increasing temperature and the same conversion is achieved at higher temperature after melting for all catalysts.

4.5.1. Reproducibility of catalytic activity

The catalyst reproducibility was tested by measuring the propane oxidation second time after complete cool down. Figure 4.12 shows the comparison of reactivity data from the first and second measurements in propane oxidation over silica supported Cs/V catalysts.

Similar to the silica supported K/V and Rb/V catalysts, decrease in activity and selectivity to propylene was obtained for silica supported Cs/V catalysts in the second run of propane oxidation. In a summary, for systems who show melting (K-, Rb-, and Cs- containing silica supported vanadium oxide catalysts), non-reproducible catalytic performance was obtained. This underlines the huge impact of melting on the catalyst dynamics.

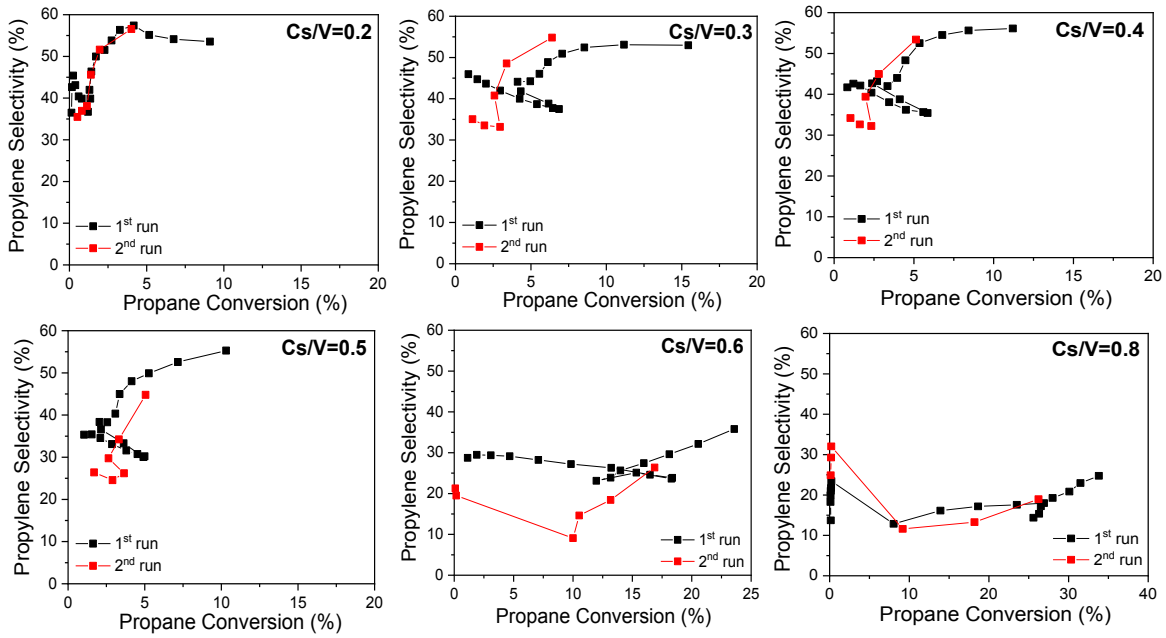

Figure 4.12. Catalytic activity results of silica supported Cs/V catalysts obtained from1st and 2nd measurement in propane oxidation reaction (black: 1st run, red: 2nd run)

4.5.2. Properties of spent Cs/V catalysts

Properties of the spent Cs/V catalysts compared to the fresh Cs/V catalysts are shown in Table 4.15. No change in cesium-vanadate phase was observed but higher crystallinity of it was identified by XRD.

After two times performing the propane oxidation, BET surface areas of catalysts were found to be reduced about 70%, varied between 15-37 m^2/g. The decrease was again due to the etching of silica by spreading of cesium vanadate due to melting. The significant decrease in catalyst porosity can be found in Figure S2.7.

Table 4.15. Properties of spent silica supported Cs/V catalysts compared to fresh catalysts

ID#	Cs/V	XRD (fresh)	XRD (spent)	BET (fresh) (m^2/g)	BET (spent) (m^2/g)
30164	0.25	CsV_2O_5	CsV_2O_5	20	15
30165	0.3	CsV_2O_5	CsV_2O_5	77	19
30166	0.4	CsV_2O_5	CsV_2O_5	89	20
30167	0.5	CsV_2O_5	CsV_2O_5	67	26
30168	0.6	CsV_2O_5	CsV_2O_5	142	35
30169	0.8	CsV_2O_5	CsV_2O_5	139	37
30170	1	SiO_2	SiO_2	108	36

DSC profiles of spent Cs/V catalysts are shown in Figure 4.13. The peak at 430°C become more pronounced (increase in peak area) for catalysts with Cs: V ratio between 0.25 and 0.4 which

supports higher amount of crystalline cesium-vanadate phase. This is in agreement with increased crystallinity of CsV_2O_5 as detected by XRD. Due to the increased amount of this phase, the sharpening of the peak was obtained. For Cs/V =0.5 and Cs/V=0.6 catalyst, the peak at 430°C vanished while the peak at 449°C become sharper. No significant change was observed for Cs/V=0.8 catalysts.

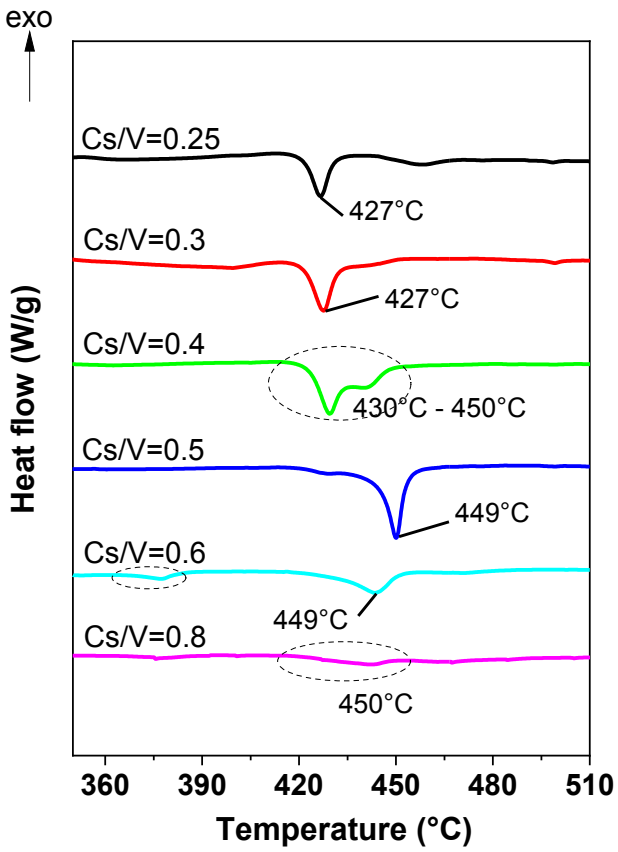

Figure 4.13. DSC profiles of spent Cs/V catalysts under 21%O_2/ 79% Ar with a flow of 70 ml/min, heating rate: 10 Kpm, cooling rate: 5 Kpm in an alumina crucible with lid

4.6. Discussion 1: Comparison of silica supported A/V catalysts with various A: V ratios

As it mentioned before, catalytic performance in the propane oxidation over A/V catalysts with a different ratio of alkali to vanadium was investigated in a temperature between 350°C and 520°C. Since K-, Rb-, and Cs-containing catalysts show melting, the direct comparison regarding to impact of a type of alkali at one temperature would not be a proper way. Thus, two different temperatures were selected and the impact of alkali was evaluated at those temperatures. 370°C was selected where all catalysts are in solid state whereas 460°C was selected as a high temperature. This temperature is above the melting temperatures of the surface alkali-vanadate phases in K-, Rb-, and Cs-containing catalysts.

Figure 4.14 compares the consumption rate of propane normalized to the V content (in *gr*.) for silica supported A/V catalysts with a different ratio of A: V at 370°C and 460°C, respectively. The data presented also can explain how catalytic performance of V/SiO_2 catalyst may vary with the addition of alkali. At low temperature (*i.e.*, 370°C) (Figure 4.14A), the alkali addition may have positive or negative effect depending on the A: V ratio. The presence of Li and Na additives decrease the activity in propane oxidation independently from the alkali loading However, K, Rb and Cs show different effect on activity of V/SiO_2 depending the alkali content. At low loadings of K, Rb, and Cs, the activity is decreased compared to alkali-free VO_x/SiO_2 catalyst similar to Li and Na-containing catalysts. This is an agreement with the literature in where alkali was proposed as poison due to the geometrical blocking the active sites [82, 227]. However, an enhancement in activity can be seen with higher content of K, Rb, and Cs. A maximum in the promoting effect of alkali was roughly found at A: V=1:2.

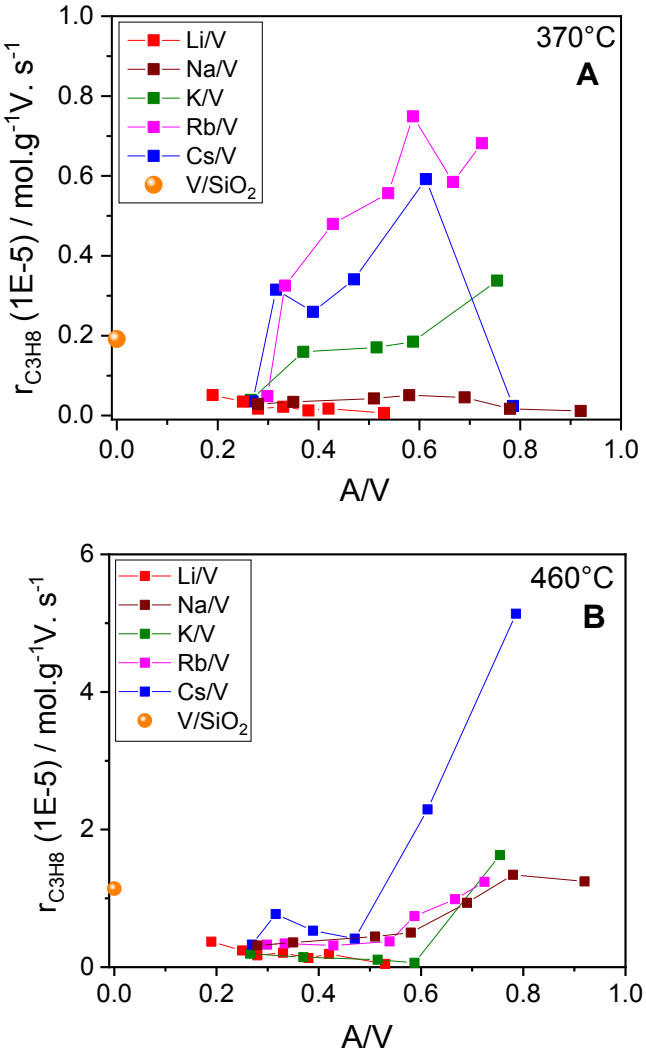

Figure 4.14. Propane consumption rate for A/V catalysts with various A: V ratio. Reaction temperature **(A)** 370°C; **(B)** 460°C

At high temperature (*i.e.*, 460°C) (Figure 4.14B), the situation is inverted. The minimum propane consumption rate was found around A: V =1:2. The propane consumption rates only increased for high alkali content (A/V > 0.5). The most distinct effect was observed by Cs-containing catalyst.

In case of a selectivity to propylene at 5% conversion (Figure 4.15), the alkali addition shows a positive effect as compared to V/SiO_2 catalyst. For all of the catalysts, the selectivity to propylene was improved by alkali addition. The effects of additives on the selectivity were attributed mostly to the change in acid-base properties (decrease in acidity) and the modification on the metal-oxygen bond energy and the type of oxygen species. In terms of acidity, additives with lower electronegativity than that of the main oxide cation decrease the acidity which yields in increase in basicity allows easier desorption of propylene. Electronegativity decreases in the order Li > Na> K = Rb> Cs and Li-containing catalysts yield in higher selectivity to propylene. However, no direct correlation based on electronegativity and selectivity cannot be done for the rest of alkali since it is strongly bounded to the alkali to vanadium ratio. Further studies are necessary to determine metal-oxygen bond energy such as determining work-function, TPR and DFT studies.

Positive effect on selectivity to propylene were not observed when A/V ratios are higher than 0.6 for K-, Rb-, and Cs-containing catalysts. In general, selectivity to propylene decreases with increasing alkali content except for the Li addition. The highest selectivity to propylene was reached at 75% over Li/V= 0.5 catalyst.

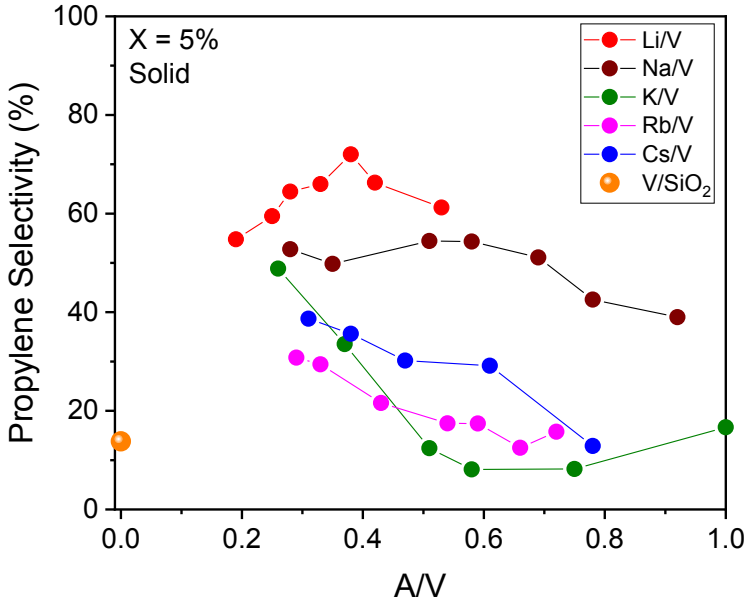

Figure 4.15. Selectivity to propylene at X=5% as a function of A/V ratio

4.7. Discussion 2: Comparison of silica supported A/V catalysts with similar A: V ratios

To compare only the impact of the type of alkali, herein we present the selected silica supported A/V catalysts that contain a similar ratio of alkali to vanadium (~0.5). Table 4.16 summarizes the physical and chemical properties of those selected catalysts. Although the properties presented before, herein the short discussion will be done.

Table 4.16. Chemical composition, phase composition and surface area of silica supported A/V catalysts with similar ratio of A: V

Alkali (A)	A/V	V_2O_5 wt.%	Total loading* wt.%	V (at.%)	A (at.%)	XRD	BET (m^2/g)	DSC (T^{peak},°C) syn air
Li #30072	0.4	5.8	6.2	70	30	$Li_{1.1}V_3O_8$	100	536, 566
Na #30689	0.5	5.4	7.0	65	34	$Na_{1.1}V_3O_8$	55	572
K #28654	0.6	6.4	8.5	62	37	$K_3V_5O_{14}$	24	410
Rb #29680	0.5	5.8	9.0	65	35	$Rb_2V_4O_{11}$, $Rb_3V_5O_{14}$	56	392, 438
Cs #28857	0.5	5.5	9.4	68	32	CsV_2O_5	67	430-450
Reference catalysts								
V/SiO_2	-	8.8	8.8	100	-	V_2O_5	206	667
SiO_2	-	-	-	-	-	SiO_2	285	-

*Analyzed by XRF, based on $A_2O+V_2O_5$

First of all, powder XRD patterns of silica supported A/V catalysts indicated that the catalysts formed some crystalline alkali-vanadate phases (Figure 4.16). For Li- and Na-containing catalysts, alkali trivanadate with low crystallinity was detected by XRD. This was discussed before due to insufficient calcination temperature needed for complete liquefaction. However, in order to follow systematic synthesis protocol, synthesis conditions were not changed. In contrast, crystalline alkali-vanadates were successfully formed over K, Rb, and Cs-containing catalysts. For K/V catalyst, potassium pentavanadate ($K_3V_5O_{14}$)[294] (ICSD No. 24068) was the only crystalline phase detected beyond the amorphous support. A mixture of rubidium-vanadates were identified over Rb/V catalyst. Based on Rietveld refinement, the catalyst contains rubidium tetravanadate (85%) ($Rb_2V_4O_{11}$, ICSD No. 85005)[395] and rubidium pentavanadate (15%) ($Rb_3V_5O_{14}$, ICSD No. 248228)[294, 394]. The crystal structure of CsV_2O_5 (ICSD No. 187267)[414] was refined on the Cs/V catalyst.

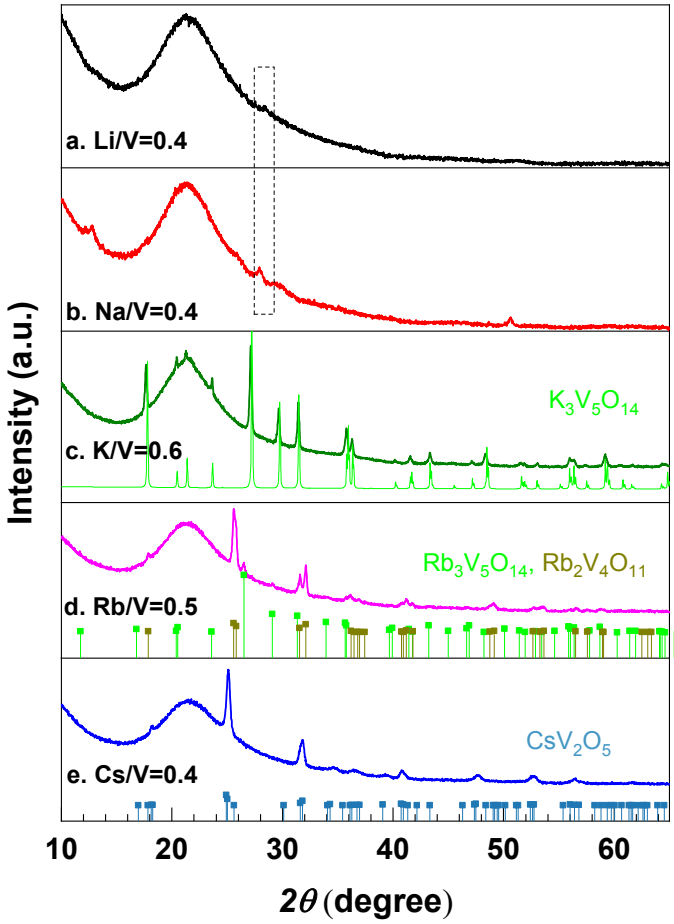

Figure 4.16. XRD of silica supported A/V catalysts; **(a)** Li/V=0.4, **(b)** Na/V=0.4, **(c)** K/V=0.6, **(d)** Rb/V=0.5, **(e)** Cs/V=0.4

The DSC profile of silica supported A/V catalysts are shown in Figure 4.17. Generally, all catalysts show endothermic events during heating. The bare catalyst (V/SiO_2) was heated to higher temperature since V_2O_5 starts to melt down near its melting temperature (~680°C). The silica supported vanadia catalyst has melting temperature at 667°C (T^{peak}). Independently from the type of alkali, addition of alkali decreases the melting temperatures of the catalysts compared to bare catalyst due to the low melting temperature of alkali metal oxides. As it expected, Li and Na –containing catalysts have higher melting temperatures than the temperature applied for propane oxidation (350-520°C). A clear endothermic event at about 570°C is distinguishable for both Li, and Na/V catalysts. Na/V catalysts seems rather more amorphous phase exist than the Li/V catalyst due to the broader shape of endothermicity at 566°C. On the other hand, addition of K, Rb, and Cs results in significantly lower melting temperature compared to the bare catalyst. Melting temperatures decreases from 667°C to the temperature around 400°C. For K, Rb, and Cs/V catalysts, endothermic peaks are located at 409°C, 392°C and 450°C, respectively.

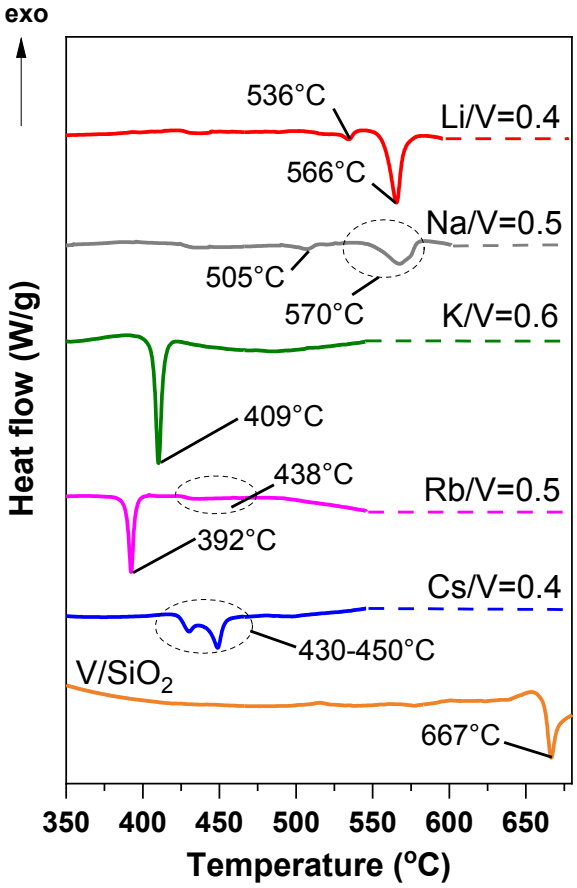

Figure 4.17. DSC profiles of A/V catalysts (A: Li, Na, K, Rb, and Cs) compared to the blank catalyst (i.e. V/SiO_2); 21%O_2 / 79% Ar with a flow of 70 ml min^{-1}, heating rate: 10 Kpm, cooling rate: 5 Kpm in an alumina crucible with lid.

Propane conversion over A/V catalysts as well as over bare catalyst (V/Si) with increasing temperature is shown in Figure 4.18(A) and (B). Based on two different catalytic systems explained above *i.e.*, (i) systems show melting, and (ii) system show no melting, two different reactivity profile was observed. First of all, catalysts were all active for propane oxidation to propylene in varying degrees. Silica supported Li/V and Na/V catalysts are less active compared to bare and other alkali-containing catalysts (Figure 4.18B). More interestingly, within the concept of impact of phase transition on ODP kinetics, system show melting have a general impact on catalyst behavior. For catalysts in which melting occurs, namely, silica supported K/V, Rb/V, and Cs/V, a peculiar activity profile is observed (Figure 4.18A). That means activity drastically decreases at some temperature which is specific for each catalyst. When crossing the temperature where sudden drop in activity occurs, selectivity to propylene increases as shown previously. The most dramatic effect was seen with the catalyst with K-containing catalysts where complete melting of surface phase is expected.

On the other hand, for silica supported Li/V and Na/V catalysts in which no melting occurs during propane oxidation, activity increases with increasing temperature whereas selectivity to propylene decreases with increasing conversion (Figure 4.18B). This is a typical catalytic profile which occurs over many oxidation catalysts.

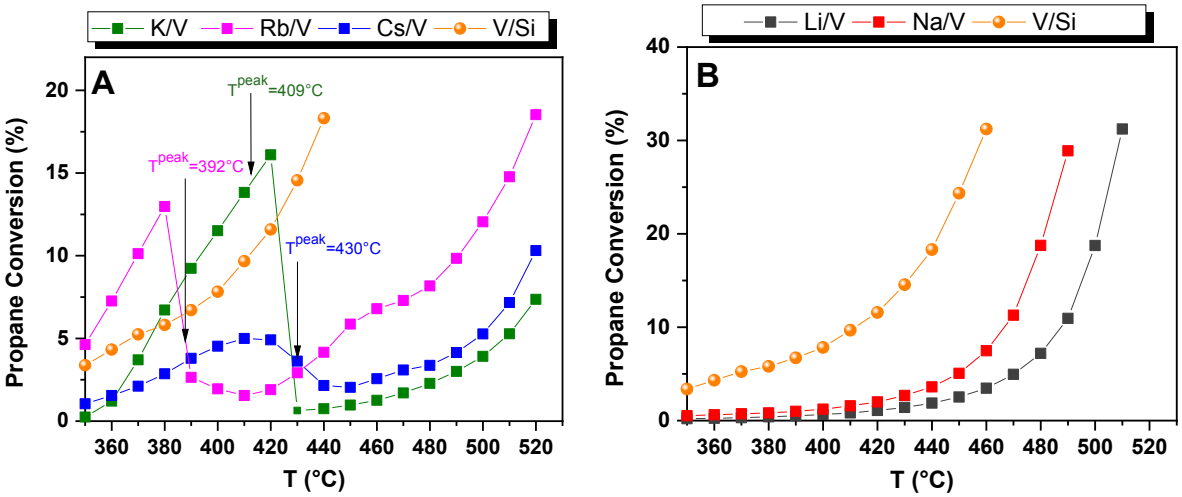

Figure 4.18. (A) Conversion of propane in ODP with increasing temperature over **(A)** catalysts show melting, *i.e.*, K/V, Rb/V, and Cs/V catalysts **(B)** catalysts show no melting, *i.e.*, Li/V, and Na/V, catalysts (Conditions: $C_3H_8/O_2/N_2$=7.5/7.5/85, T=350-520°C, W/F= 1.8 g s ml^{-1})

Comparison of selectivity to propylene at 5% conversion accompanied by temperature for A/V catalysts with similar ratio to A: V is presented in Figure 4.19. Since K, Rb, and Cs catalysts show drop in activity due to expected phase transition, selectivity to propylene at 5% conversion were measured two times, one in solid state (before melting, indicated with *s(solid)*), and the other one is in liquid state (after melting, indicated with *liq. (liquid)*).

With this, it can be understood that 5% propane conversion was reachable after drop in activity with an increase in temperature. Within the whole series, Li/V catalyst displayed the highest selectivity as 72%, this is followed by Na/V catalyst which gives 58% propylene selectivity. However, it must be noted that the temperature was 470°C and 450°C for Li/V and Na/V, respectively which is critical temperature due to the large contributions from homogeneous gas-phase reactions. In case of K, Rb, and Cs/V catalysts, selectivity to propylene varies between 10- 35% in a solid state. In either case, the selectivity to propylene increases after liquefaction. The highest promoting effect of melting was found over K/V catalyst in which selectivity increases from 10% to 50% (450°C). The similar propylene selectivity could be reached at the same conversion over Cs/V catalyst as well after melting.

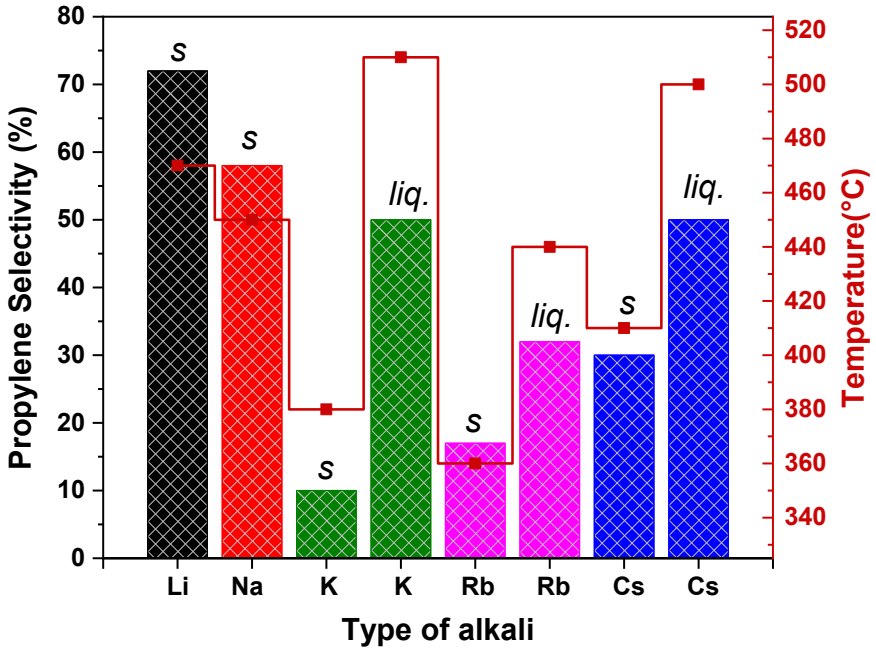

Figure 4.19. Propylene selectivity at 5% propane conversion over A/V catalysts (s: solid, liq: liquid) (Conditions: $C_3H_8/O_2/N_2$=7.5/7.5/85, T=350-520°C, W/F= 1.8 $gsml^{-1}$)

Overall, we summarized the impact of alkali addition on supported vanadia catalyst at the similar A: V ratios. The liquefaction is found to be making the catalyst more selective at high temperature. This is a general phenomenon occurs over catalysts who melt in the applied reaction conditions, *namely* silica supported K, Rb, and for Cs/V catalysts.

Next chapter will be on understanding peculiar catalytic profile (decrease in activity, increase in selectivity to propylene). First of all, it is needed to validate if the drastic change in reactivity is associated with melting. Therefore, operando DSC technique will be introduced. With this, it is aimed to identify endothermicity of melting enveloped with the exothermicity of the reaction. Further role of melting on the reactivity will be examined using surface sensitive spectroscopic techniques in presence of reactive environment.

CHAPTER 5

5. Detailed Characterization under Operando Conditions

This chapter of the thesis presents *operando*-studies including calorimetry, Raman, and NAP-XPS and NEXAFS spectroscopies. Silica supported K/V=0.6 catalyst was studied in detail. The chemical composition, phase composition and melting temperature of the catalyst are shown in Table 5.1.

Table 5.1. Chemical composition, phase composition, surface area, and melting temperature of silica supported K/V=0.6 catalyst

Internal ID	Alkali	A/V	XRD	Total loading* ($A_2O+V_2O_5$) wt.%	BET (m^2/g)	DSC (T^{peak}, °C) synthetic air
#28654	K	0.6	$K_3V_5O_{14}$	8.5	24	410

*Analysed by XRF, based on $A_2O + V_2O_5$

Combining XRD, Raman spectroscopy, SEM and DSC experiments up to now, it can be explicitly deduced that alkali addition at ratio of K:V=0.6 results in a segregated crystalline K-V-O phase, *namely* $K_3V_5O_{14}$, on the catalyst surface which is expected to melt during propane oxidation reaction conditions (T^{peak}= 409°C). At this point, the impact of phase transition meets with catalysis.

First of all, operando DSC was applied to figure out if melting is associated with drastic changes in catalytic properties (*i.e.*, drop in activity and increase in selectivity to propylene). Later on, structural changes of the catalyst due to melting and how these changes affect catalyst performance in propane oxidation reaction were studied by Raman spectroscopy applying two different lasers. Changes in the electronic environment of the vanadium due to melting were analyzed based on the data obtained from NAP-NEXAFS measurements.

Overall, the findings in this chapter demonstrate a comprehensive investigation to uncover structural changes of the catalyst that occur under reaction conditions. Based on this, working catalyst with its active structure will be discussed.

5.1. Operando DSC

5.1.1. Introduction

The noticeable impact of alkali addition on a catalytic profile was observed with catalysts which show melting (*i.e.,* K, Rb and Cs) (Figure 4.18A). Figure 5.1 presents the combined knowledge which consists of melting temperatures of K/V catalysts measured under synthetic air by DSC

(from Figure 3.16) and their propane conversion data (from Figure 4.6). In general, the drop in activity seem to occur at a temperature either lower or higher than the melting temperatures.

For instance, K/V=0.2 catalyst shows melting at 477°C and 525°C but the activity starts decreasing at 420°C. Oppositely for the K/V=0.6 catalyst, activity drops between 430 and 440°C which is higher than the melting temperature of the $K_3V_5O_{14}$ (T^{peak}=412°C). Therefore, temperatures where activity drops cannot be directly associated with the melting temperatures measured by DSC. The same inconsistency was obtained over Rb/V and Cs/V catalysts as well (Figure S3.1)

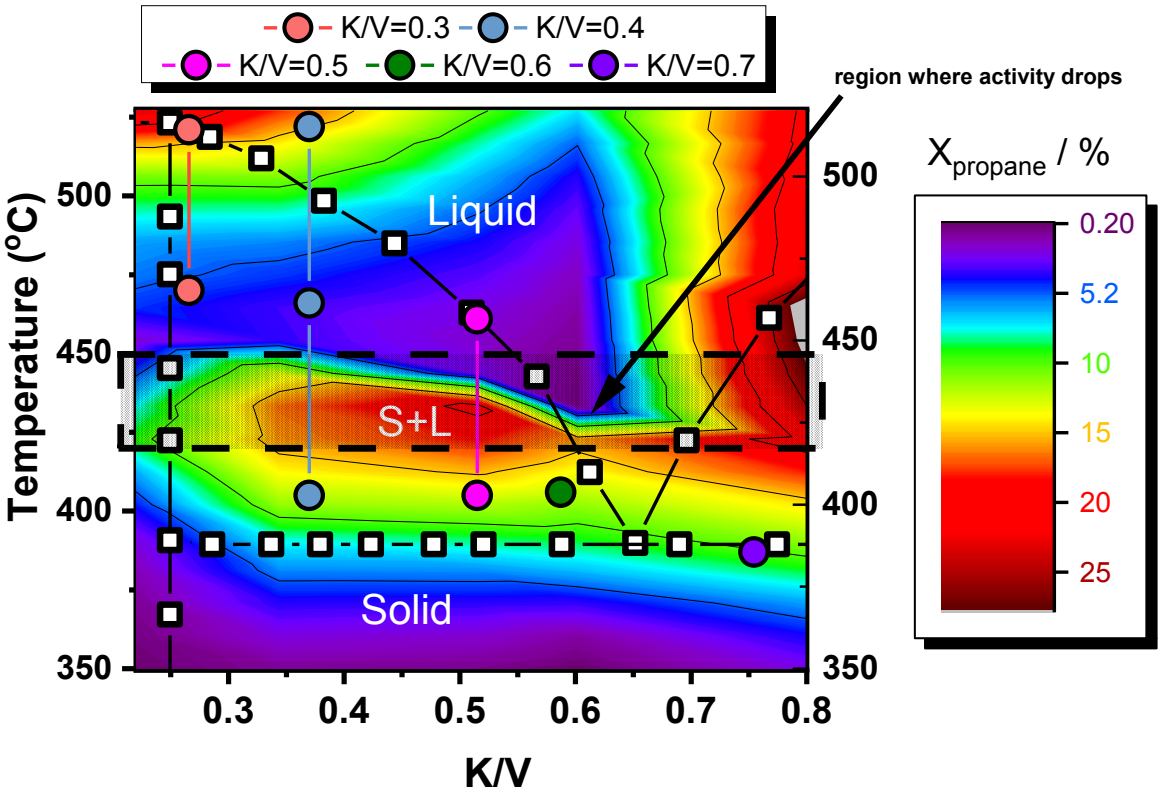

Figure 5.1. A combined phase diagram with measured melting temperatures of K/V catalysts and activity data in propane oxidation (●: melting temperatures of freshly prepared K/V catalysts measured by DSC (from Figure 3.16)

The one possible explanation raised here is that melting temperatures may be affected by the gas atmosphere, and thus melting temperatures measured in synthetic air and in reaction feed are different [292]. In addition, the amount of catalyst used in a reactor is ~30x more than the amount used in DSC. That means the detection of melting impact can be delayed in a reactor due to temperature gradient over the catalyst bed thus the effect might be seen later at higher temperature. In order to precisely find if melting is responsible for drastic changes in catalyst

performance (i.e., activity drops, selectivity to propylene increases), *operando* Differential Scanning Calorimetry (*operando*- DSC) was performed.

5.1.2. Results and Discussion

Figure 5.2 shows the *operando*-DSC of silica supported K/V=0.6 catalyst (Table 5.1) in ODH of propane. The freshly prepared catalyst precursor has melting temperature is at 410°C (T^{onset}=402°C) in a reaction feed which is consistent with the previous measurement in synthetic air (Figure 3.16). However, simultaneous measurement of propane oxidation over freshly prepared catalyst precursor indicated that catalyst shows very low conversion (data in red color in Figure 5.2B) and selectivity to propylene increases with increasing conversion (data in red color in Figure 5.2C). In addition, melting has no impact on catalyst performance.

The low activity could be due to the adsorption of some CO_x species on the surface of the catalyst which is known as general reason for air-sensitive catalysts. At this point, TG-MS analysis supported this in which there was a significant amount of CO_2 released from the surface of freshly prepared catalyst K/V=0.6 already below melting temperature (400°C) (Figure S3.4). Therefore, the catalyst activation ($21O_2/79N_2$, and 520°C, 2 h) prior to reaction which was applied all the catalysts were found highly crucial.

In heat flow plot of activated catalyst (Figure 5.2A), the evolved heat increases with increasing temperature due to the exothermicity of the reaction. Above 400°C, an endothermic trend in heat evolution starts due to the phase transition from solid to liquid. At 409°C, a clear endothermic peak was obtained. This melting significantly affects the catalytic profile. The conversion suddenly drops when endothermicity starts (Figure 5.2B). The drop in activity reflects in selectivity to propylene to increase from 13% to 23% (Figure 5.2C). First of all, the experiment shows that the drastic change in catalytic performance of K/V=0.6 catalyst is associated with melting of the surface K-V-O phase. It cannot be explicitly state that it is the melting of $K_3V_5O_{14}$ since catalyst is always activated prior to the reaction (520°C, $21O_2$/ $79N_2$) in where decomposition must already occur (Figure 3.24A). Nonetheless, this is an excellent confirmation between melting temperature of the K-V-O phase with the temperature where catalytic activity drops. The calculated heat of reaction based on product distribution (see equation 2.7 in section 2.5.1.2.) is very much consistent with the measured heat flow.

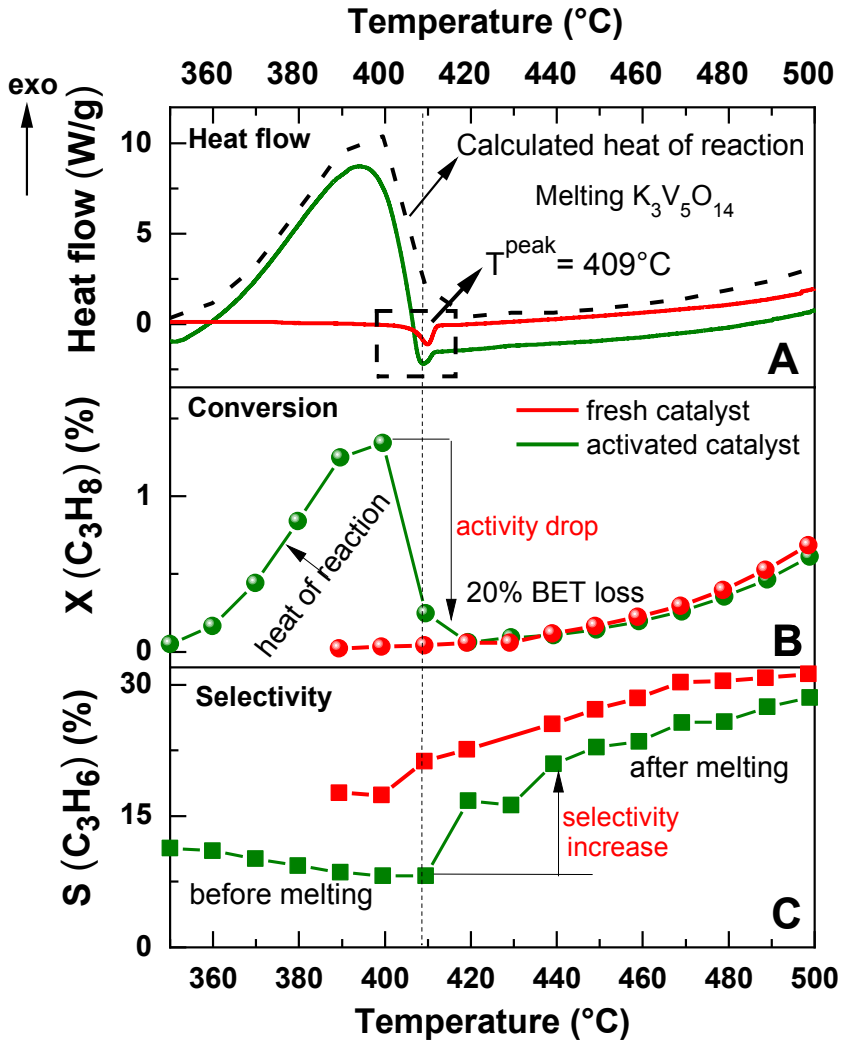

Figure 5.2. *operando*- DSC profile of catalyst K/V=0.6 in propane oxidation (Total flow: 9 ml/min, $C_3H_8/O_2/N_2$=7.5/7.5/85 vol. %, GHSV ≈ 4300 h^{-1}, β=0.42 Kpm, W/F: 0.34 g s ml^{-1}); freshly prepared catalyst precursor (data in red), activated catalyst (data in green)

The analogous behavior was obtained for silica supported Rb/V=0.5 and Cs/V=0.4 catalysts which also show melting under applied reaction conditions (Figure S3.2 and S3.3).

The Rb/V catalyst showed noticeable melting at 393°C under reaction conditions which is followed by drop in activity. The recovery of activity was achieved further at ~ 480°C. The detection of endothermicity in spite of high exothermicity of the Cs/V catalyst due to its high activity was challenging but achieved by lowering the catalyst mass (1/3 of the mass of K/V and Rb/V catalysts). With this, comparable conversion within the series was reached. The broader melting between 430 and 450°C results in a plateau in heat flow rather than an endothermic peak. However the effect of melting observed in catalytic activity as a plateau reflects in an activity not as a drop, but as a plateau. This perfectly confirms that the effect of

melting reflects in a catalytic activity and it is detectable. A slight increase in selectivity to propylene after melting was also observed.

The power of the technique showed that detection of endothermic events in spite of exothermicity of the reaction is possible. Two important results are obtained: (i) The oxygen treatment is needed to make the catalyst active, and the most importantly (ii) the melting of surface alkali-vanadate phase(s) results in decrease in activity and increase in selectivity to propylene. Overall, the impact of melting on reaction is found to be as a general phenomenon for catalysts whose melting temperatures are in applied reaction conditions.

Next section is dedicated to understand how melting cause such drastic change in catalytic activity. Therefore, changes in the surface dynamics of catalyst structure before and after melting under reaction conditions were studied by Raman and NAP-NEXAFS spectroscopies.

5.2. Operando Raman Spectroscopy

5.2.1. Introduction

The Raman experiments under reaction conditions were conducted for silica supported K/V= 0.6 catalyst whose properties described in Table 5.1. First of all, it is crucial to find the right laser wavelength for optimization of results based on sample behaviour. Each different laser wavelength has an impact on experimental capabilities in terms of sensitivity, and spatial resolution. Therefore, multi-laser Raman spectra were taken using available lasers, namely, 266, 355, 442, 457, 488, and 532 nm. Figure 5.3A shows the multi- Raman spectra of silica supported K/V= 0.6 catalyst. 266 nm laser already showed that the catalyst has surface vanadium oxide species whose stretching vibrations are located between 1020- 1060 cm^{-1} [349, 356]. Moreover, 532 nm laser was capable to detect $K_3V_5O_{14}$. This is confirmed by measuring the spectra of support-free $K_3V_5O_{14}$ and calculating the spectra of it by DFT (Figure 5.3B).

Overall, these two lasers which are 266 nm and 532 nm laser were selected for following Raman experiments. However, 266 nm laser caused a severe change on a catalyst structure under propane oxidation environment since the catalyst was highly reducible. Therefore, 266 nm laser was only used to detect changes during catalyst activation under the flow of synthetic air. With this, changes in surface vanadium oxide species due to melting of K-V-O were recorded. Since no laser damage was observed with 532 nm laser, both activation and propane oxidation reaction were performed with 532 nm laser. For both lasers, the catalyst was first pressed under 0.0196 MPa and sieved in a particle size 250-300 μm. Around 20 mg of catalyst was loaded on an alumina bed (baked at 600°C for 2 h) in the sample holder of the Linkam (CCR1000) cell.

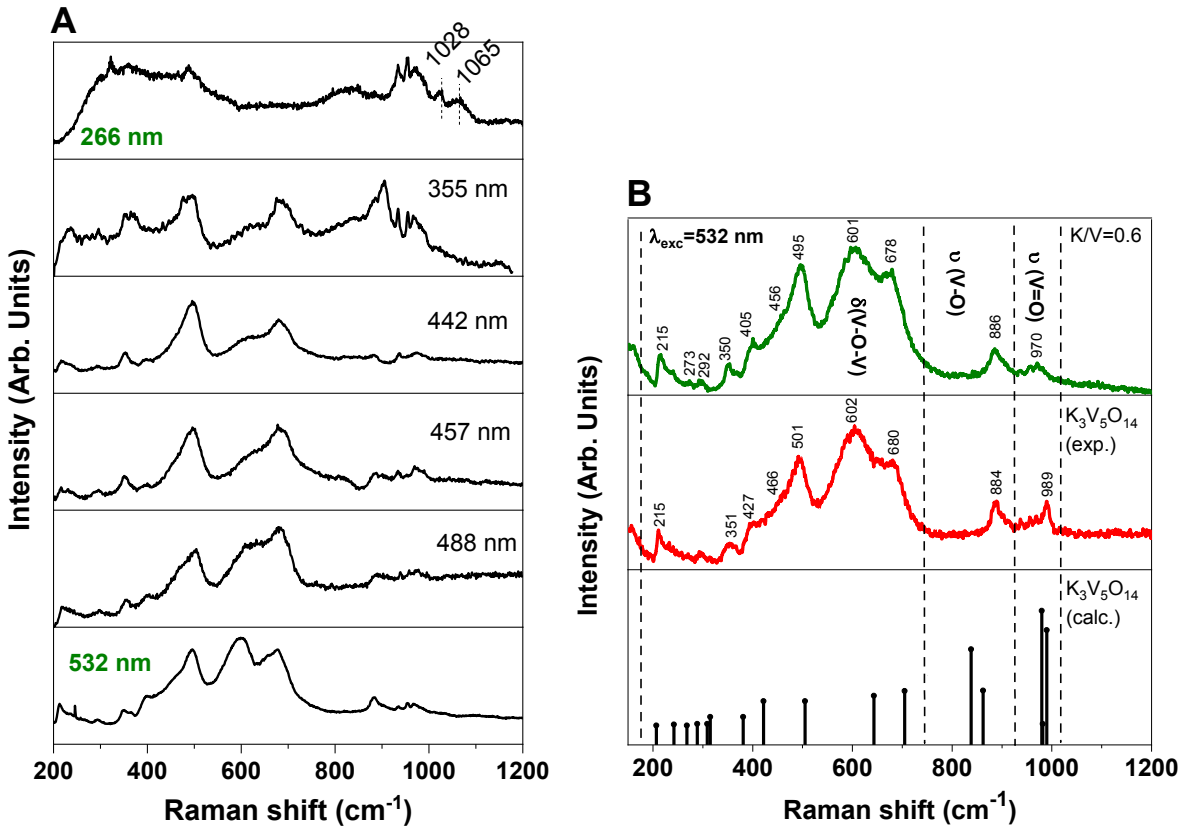

Figure 5.3. (A) Multi-Raman spectra of silica supported K/V=0.6 catalyst, **(B)** The ex-situ Raman spectrum of silica supported K/V=0.6 catalyst compared to experimental and calculated Raman spectra of support-free $K_3V_5O_{14}$ (λ_{exc} = 532 nm)

5.2.2. The deep-ultraviolet laser: 266 nm

The 266 nm laser was used to detect possible structural changes during catalyst activation ($21O_2/79N_2$, 10 mlmin^{-1}, and 520°C). First of all, the measurement with 266 nm laser showed that the K/V=0.6 catalyst has Raman modes at 882, 934, 954, 971, 989, 1020 and 1060 cm^{-1} (Figure 5.4A). By comparing the spectra of K/V=0.6 with the spectra of support-free $K_3V_5O_{14}$ measured by 266 nm laser (Figure S3.5), it can be stated that bands detected at 882, 932, 954 and 989 are resulted from the stretching vibrations of V=O and V-O in VO_4 tetrahedral and VO_5 square pyramids units in $K_3V_5O_{14}$. Additionally, two Raman bands were detected at 1020 and 1061 cm^{-1} at 30°C. The band at 1061 cm^{-1} was previously assigned to silica network TO mode and Si (—O^-)$_2$ and Si—O^- functionalities[335, 415]. However, recent theoretical studies suggest that it indicates V–O–Si stretching mode [351, 356, 416].

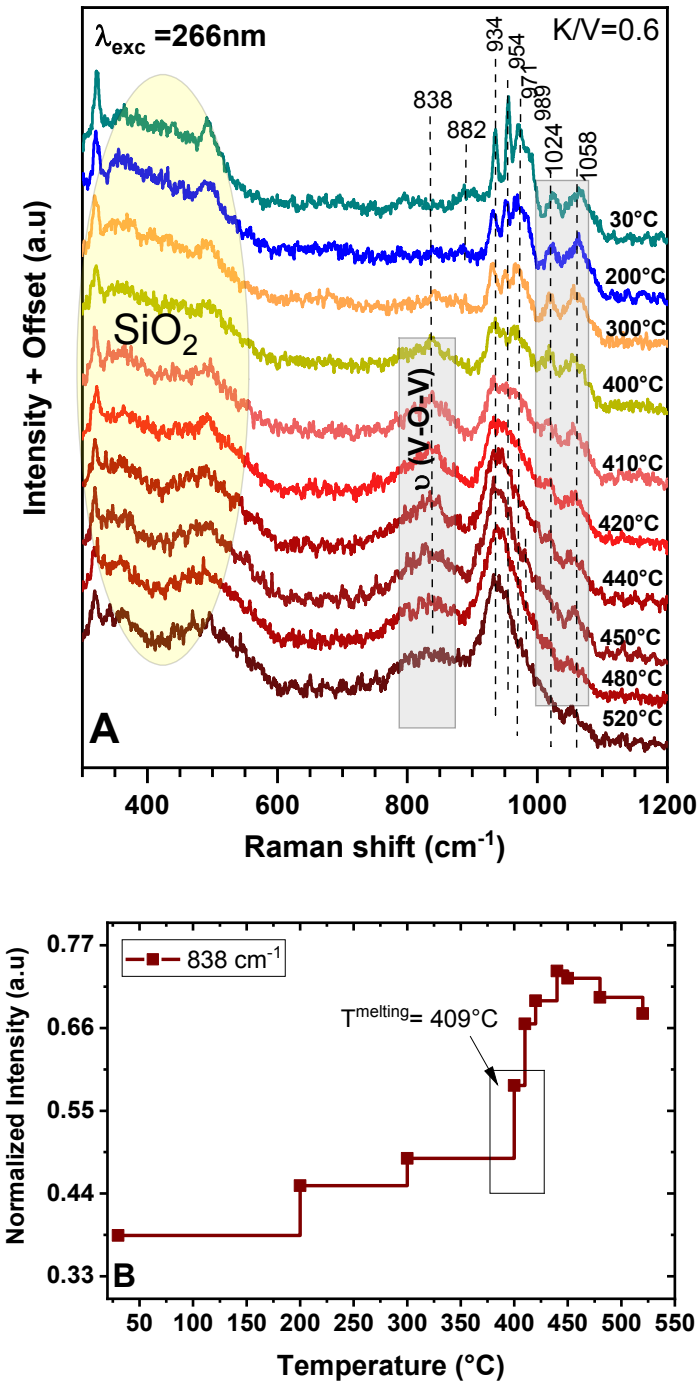

Figure 5.4. (A) In-situ Raman spectra of catalyst K/V=0.6 during activation under synthetic air (λ_{exc}=266 nm, $21O_2/79N_2$ vol. %, 10 mlmin^{-1}), **(B)** a change in the band intensity at 838 cm^{-1} with increasing temperature

In order to make our assignment correct within the controversy in the literature, Raman spectra of hydrated SiO_2 and in-house synthesized VO_x/SiO_2 were measured with 266nm laser (Figure S9). Two bands at 1023 and 1057 cm^{-1} was observed in the visible Raman spectrum of hydrated VO_x/SiO_2 catalyst whereas no band was detected at higher than 1000 cm^{-1} in the spectrum of hydrated SiO_2. Based on these, the band at 1020 and 1063 cm^{-1} were assigned to V═O and

stretching and V–O–Si stretching, respectively. Upon heating in synthetic air, the intensity of bands at 1020 and 1063 cm^{-1} seems decreased, but remained still detectable. At 200°C, a significant change in relative intensity of 954 to 932 and 971 cm^{-1} was detected. With further increase in temperature, bands in range 934-989 cm^{-1} merged together and resulted in a peak centred at 934 cm^{-1}. None of the Raman bands went undergo any frequency shift upon heating.

Other than this, one of the remarkable features occurred before melting was the band found at 838 cm^{-1} at 400°C. This band at 838 cm^{-1} is attributed to the vibrations of V-O-V stretching of surface vanadium oxide species [356]. Since the experiment was measured in situ under the exact same conditions for each temperature, a change in band intensity at 838 cm^{-1} was analysed further (Figure 5.4B). As seen, the band intensity increases upon increasing temperature. The highest increase obtained with melting at 409°C. This explains that melting initiates an oligomerization of monomeric surface vanadium oxide species. This is an exciting finding regarding the description of active species at the surface and the role of melting. Since support-free $K_3V_5O_{14}$ is not active for propane oxidation (Figure 3.31), in-situ formed oligomeric vanadium oxide species *via* melting of surface potassium-vanadate phase(s) during catalyst activation might be the source of catalytic activity. The further proof and discussion regarding this hypothesis will be (re)evaluated based on NAP-NEXAFS spectroscopy findings.

After holding the catalyst 2 h at 520°C under dynamic flow, catalyst were cooled down to room temperature. Figure 5.5 shows that comparison of Raman spectra of K/V=0.6 catalyst before and after activation. The spectra recorded at 30°C after cooled down dominantly features the bands of $K_3V_5O_{14}$ at 882, 934, and 952 cm^{-1}. However, the intensity of the band at 971 cm^{-1} decreased relatively to the band at 952 cm^{-1} which further confirms the incongruent melting of $K_3V_5O_{14}$. The in situ generated band at 838 cm^{-1} remained stable. Overall, beside the structural alteration of $K_3V_5O_{14}$, the major finding of this Raman investigation was discovering in-situ generation of polymeric surface vanadium oxide species upon melting of $K_3V_5O_{14}$.

Normally, after complete cooled down, the reaction was planned to be performed. However as it stated before, 266 nm laser damaged the catalyst under reducing environment ($C_3H_8/O_2/N_2$). This severe change in catalyst structure reflects in dramatically change in the spectra (Figure S3.6.). Therefore, the result obtained with 266 nm laser under propane oxidation environment were excluded.

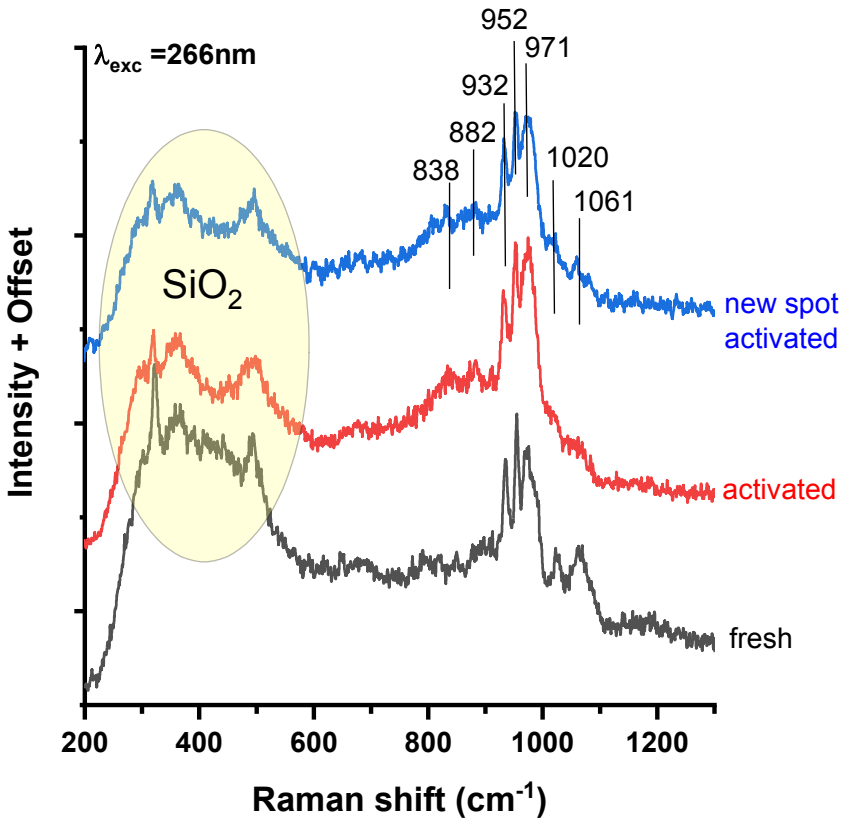

Figure 5.5. In-situ Raman spectra of fresh and activated catalyst K/V=0.6 under oxygen flow at 50°C (λ_{exc} = 266 nm, 21O_2/79N_2 vol. %, 10 mlmin^{-1})

5.2.3. The visible laser: 532 nm

The catalyst K/V=0.6 was first in-situ activated in a flow of static air (21 vol. % O_2, rest Ar) at at 520°C (T^{set}= 494°C) for 2 h. The spectra collected during in -situ activation can be found in Figure S5. After completing the activation, the catalyst was completely cooled down (50°C) under the flow of synthetic air. The spectra were taken from different spots to verify the homogeneity of sample. The spectrum before and after activation can be found in Figure S3.8.

The Raman spectroscopy was performed in propane oxidation with a reaction temperature between 350 and 520°C, in a feed of C_3H_8/O_2/N_2=7.5/7.5/85 vol. %, and applying a contact time W/F= 1.2 g s ml^{-1}. The K/V=0.6 catalyst showed all features corresponding to a support-free $K_3V_5O_{14}$ phase, which were clearly visible at 459, 599, 677, 884, 936, 954, and 968 cm^{-1} at room temperature (Figure 5.6A), and are consistent with XRD data. The assignment of these bands was done based on DFT calculation of $K_3V_5O_{14}$ applying local density approximation (LDA) functional and non-conserving pseudopotentials and based on a measurement of Raman spectra of support-free $K_3V_5O_{14}$ itself (support-free) (see in Figure 5.3B). The strong Raman bands appearing between 200 and 750 cm^{-1} were characterized as bending vibrational modes

whereas the weaker bands between 800 and 970 cm^{-1} were assigned as stretching modes, based on DFT calculation (Table 3.8).

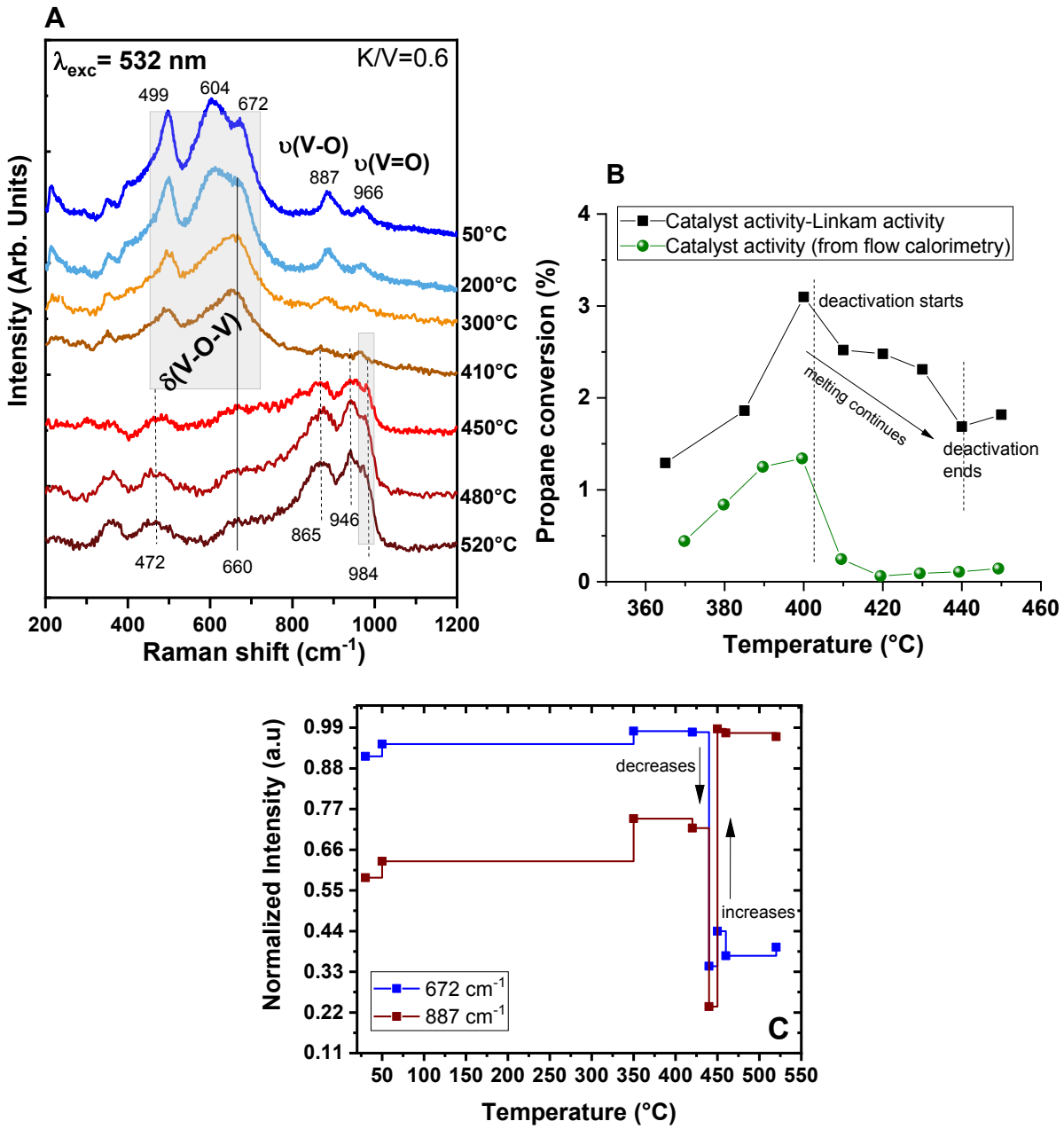

Figure 5.6. (A) Raman spectra of the catalyst K/V=0.6 under reaction conditions (λ_{exc}=532 nm) **(B)** Simultaneously obtained catalytic data of K/V=0.6 in propane oxidation and comparison of catalyst profile with data obtained from flow calorimetry, (C) Changes in band intensity at 672 and 887 cm^{-1}, respectively. (Conditions for Raman: $C_3H_8/O_2/N_2$=7.5/7.5/85 vol. %, F= 1 $mlmin^{-1}$ and contact time W/F= 1.2 g s ml^{-1}; Conditions for flow calorimetry: $C_3H_8/O_2/N_2$=7.5/7.5/85 vol. %, F= 10 $mlmin^{-1}$ and contact time W/F= 0.4 g s ml^{-1})

The most intense bands were observed between 459 and 677 cm^{-1} were assigned as V-O-V bending vibrational modes. Considering the structure of $K_3V_5O_{14}$ (Figure 5.7), the band at 499

cm^{-1} was due to V1-O4-V2 bending whereas the one at 662 cm^{-1} was characteristic of the vibrational bending modes of O3-V2-O4. Furthermore, the Raman band at 887 cm^{-1} was attributed to the vibrational stretching modes of O4-V2-O4 and O4-V1-O4 in the VO_4 tetrahedral units. The weaker band at 936 cm^{-1} was due to stretching modes in VO_4 tetrahedral and VO_5 square pyramids. The other two bands between 954 and 968 was attributed to the V=O stretching vibrational modes.

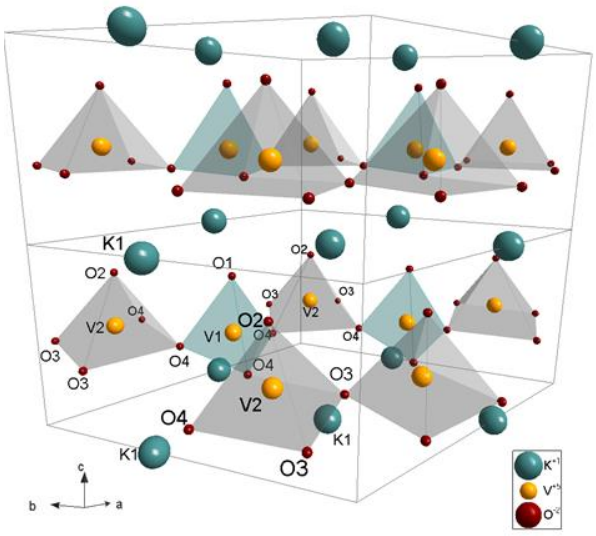

Figure 5.7. Polyhedral diagram of $K_3V_5O_{14}$[291]

By increasing temperature, the feature at 677 cm^{-1} increased relative to 599 cm^{-1} which leads structure alteration. Beside the alteration, decrease in Raman shifts and band broadening were observed. However, a drastic change in the spectra was observed by crossing the melting point. At 450°C, significant loss in V-O-V bending modes (blue in Figure 5.6C) and in vanadyl stretching in VO_x units (brown in Figure 5.6C) could be seen. This is structural relaxation caused by melting of potassium-vanadate phase. Further increase in a temperature to 520°C, the dominancy of two bands at 864, 938 and 975 cm^{-1} was observed which could be evidence of reordering some K-doped and/or un-doped V_xO_y units after V-O-V bond cleavage were broken.

Upon heating, the feature at 677 cm^{-1} increased relative to 599 cm-^{1}, and centered more at 677 cm^{-1}. Beside this, decrease in Raman shifts and band broadening were observed. The more drastic change in the spectra was observed again by crossing the melting temperature (450°C). At 450°C, disappearance of V-O-V bending modes and dominancy of two bands at 864 and 938 cm^{-1} were observed. The intensity of these two bands increased and become more noticeable after melting suggesting the structural rearrangement of vanadium oxide units.

Further increase in a temperature to 520°C shows an enhancement of bands at 494, 650, 865, 946 cm^{-1} and a formation of new band at 984 cm^{-1}. This is similar band as presented before in the in situ melting experiment of support-free $K_3V_5O_{14}$ which were attributed to the formation of bulk-like V_2O_5 or K-distorted V_xO_y species upon melting (see Figure 3.30).

Detecting drop in activity due to melting was challenging due to the high activity of the empty cell itself. Therefore, the activity of empty cell in propane oxidation under same conditions was measured (Figure S3.9) and subtracted from the measurement with the catalyst loaded. With this, the drop in activity was finally detectable. Herein Figure 5.6B shows the activity profile of silica supported K/V=0.6 catalyst (empty cell subtracted) compared to the activity measured by flow calorimetry. Deactivation of the catalyst due to melting starts at 410°C which is expected but the effect of melting continues until 450°C (Figure 5.6B). This delay or longer time of the effect of melting can be explained due to the temperature gradient occurs in the catalyst bed since the thermocouple in the Linkam cell was inserted at the bottom of the sample holder. The melting ended at 450°C followed by disappearing of Raman features at 495, 599, and 677 cm^{-1}. Activity was recovered by enhancement of two bands at about 865, and 946 cm^{-1} and a formation of new band at 984 cm^{-1} upon heating further. The intensity of these three bands increased and become more noticeable after melting. The same initial Raman features were observed after cooling down to 30°C in a reaction mixture (Figure S3.10).

5.2.4. Discussion

Temperature dependent spectra of silica supported K/V=0.6 catalyst were recorded with 266 and 532 nm lasers. The 266 nm laser was used to detect changes in catalyst structure under synthetic air whereas 532 nm laser allowed to be used in both synthetic air and propane oxidation reaction conditions. Based on results presented above, main findings can be reported as a function of the environment and the laser type:

O_2/N_2 environment with laser 266 nm:

- The laser 266 nm detected surface vanadium oxide species whose Raman shifts were at 1020 and 1061 cm^{-1}.
- This finding indicated that silica supported K/V=0.6 catalyst consists of $K_3V_5O_{14}$ and dispersed VO_x species over the support.
- The formation of new band at 838 cm^{-1} ($\nu^{V\text{-}O\text{-}V}$) was observed upon heating in synthetic air. Specifically, the dominancy of 838 cm^{-1} ($\nu^{V\text{-}O\text{-}V}$) become pronounced at temperature where melting starts. This suggests that melting facilitates the formation of polymeric

surface vanadium oxide species. No disappearance of the band at 838 cm^{-1} was observed after complete cooled down in synthetic air.

$C_3H_8/O_2/N_2$ environment with laser 532 nm:

- The laser 532 nm provided an information regarding the alkali-vanadate, *i.e.,* $K_3V_5O_{14}$ phase whose Raman bands were in between 450- 980 cm^{-1}.
- The melting of the $K_3V_5O_{14}$ was detectable. The melting of the phase was completed at 450°C in which V-O-V bonds cleavage (494, 599, and 667 cm^{-1}) was observed. Upon heating to 520°C, Raman bands between about 865 and 946 cm^{-1} become more pronounced and new band at 984 cm^{-1} were formed which was attributed to the formation of bulk-like species.
- Spectral changes in synthetic air and reaction environment were similar. Although significant changes occur before and after each experiment, almost identical spectra was observed at room temperature.

As mentioned before, activity data was simultaneously recorded. After subtracting the empty cell activity, the drop in activity was detectable. At temperatures where activity drops, the decrease in V-O-V bond cleavage of $K_3V_5O_{14}$ structure was found. Activity recovered where bands at 865 and 946 cm^{-1} were enhanced and new band of 984 cm^{-1} were formed as detected by 532 nm laser. Overall, the activated catalyst structure can be drawn as shown in Figure 5.8. Silica supported $K_3V_5O_{14}$ (532 nm laser) and dispersed vanadium oxide species (266 nm laser) takes place in the reaction.

After describing such complexity of catalyst structure, the role of melting on the distribution of surface species needs to be investigated. Next part will be about the possible role of melting of $K_3V_5O_{14}$ by providing demonstration from path-finder experiment. At the end, NAP-NEXAFS spectroscopy experiments will be discussed as a complimentary technique to cross-check Raman spectroscopy findings.

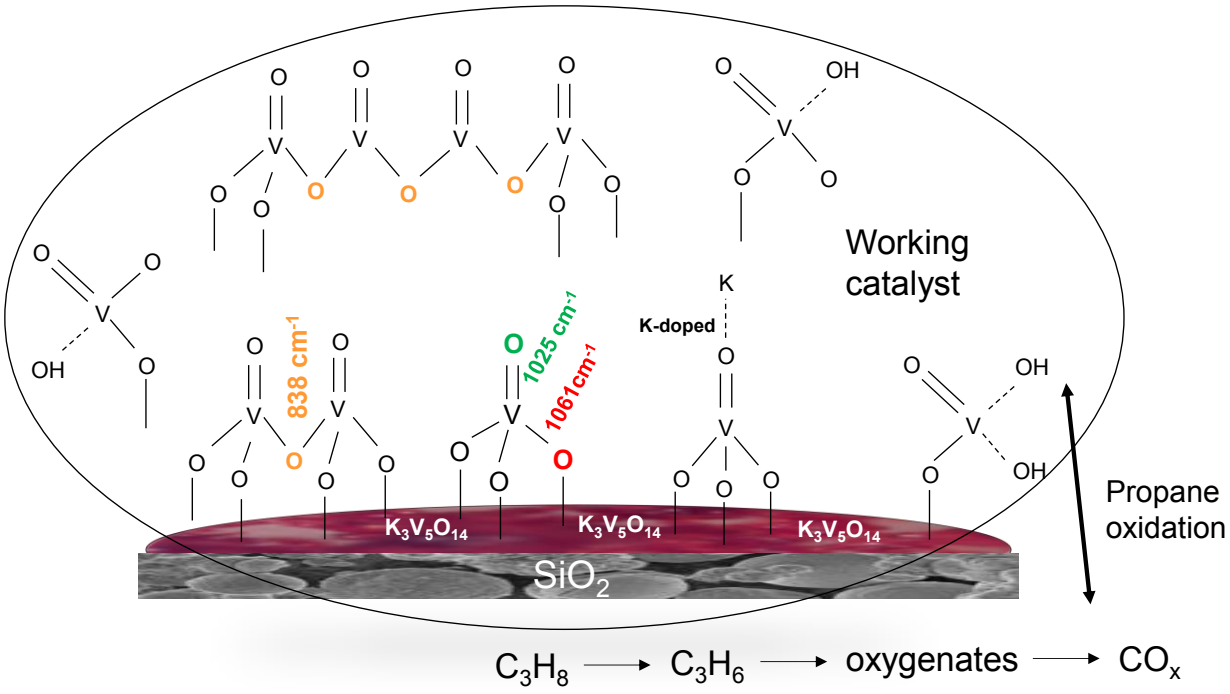

Figure 5.8. Schematic representation of activated silica supported K/V=0.6 catalyst based on Raman findings

5.3. A path-finder experiment: Possible role of melting of $K_3V_5O_{14}$

Raman spectroscopy experiments proofed the existence of $K_3V_5O_{14}$ and the melting of the phase. The behavior of melting previously was defined as wetting based on experiments conducted under light microscope in Harrick cell (Figure 3.25). The inactivity of support-free $K_3V_5O_{14}$ in oxidative dehydrogenation of propane is also known (Figure 3.31). Here once again the comparison between activities of support-free $K_3V_5O_{14}$ and silica supported K/V=0.6 catalyst ($K_3V_5O_{14}$/ SiO_2) (Figure 5.9A) and wetting phenomena on silicon wafer (Figure 5.9B) are shown.

In addition to these findings, 266 nm laser showed the polymeric surface vanadium oxide species formed due to melting. The activity of supported dispersed vanadium oxide species in ODH of propane is known [1] and shown in this study as well (Figure 4.1A). At this point, a questioning on a source of activity and the function of $K_3V_5O_{14}$ raised.

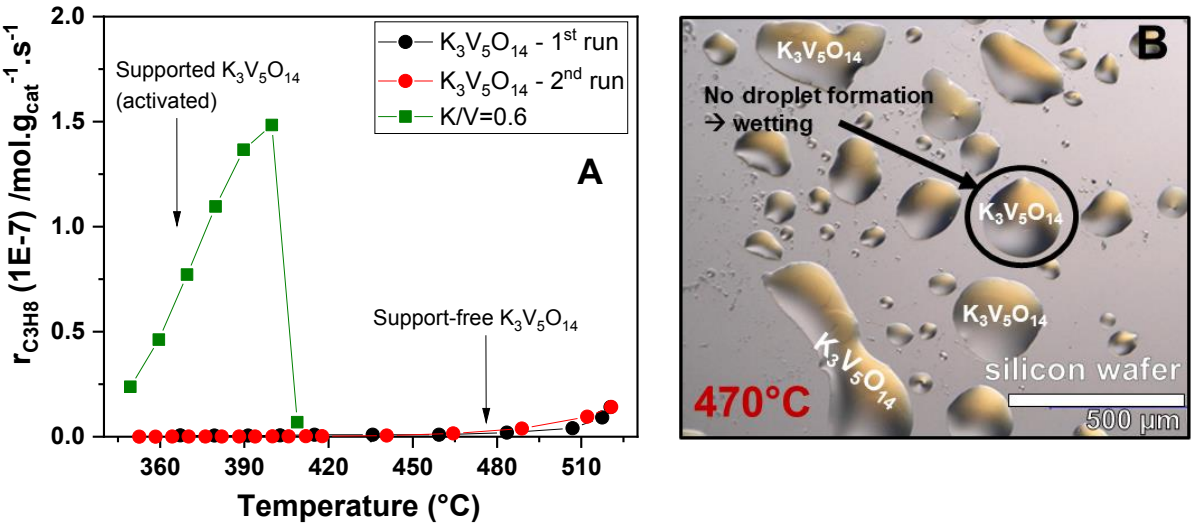

Figure 5.9. (A) Rate of propane consumption with increasing temperature of supported-free $K_3V_5O_{14}$ compared to supported K/V=0.6 catalyst (T=350°C-520°C, feed $C_3H_8/O_2/N_2$=7.5/7.5/85 vol. % W/F=0.9 g s ml^{-1}), **(B)** Optical microscope image of melting of support-free $K_3V_5O_{14}$ on silicon wafer.

Considering the existence of monomeric and polymeric vanadium oxide species and the wetting behavior of the $K_3V_5O_{14}$ together, a path-finder experiment was designed further. The idea was to investigate how melting of $K_3V_5O_{14}$ inhibits the reactivity. If this is a blockage affect by coverage of the active sites by the melt, the same effect must be observed on any active component. To proof that hypothesis, V/SBA-15 (5.6 wt. % V, 2D vanadium oxide species on the surface of mesoporous SBA-15, Internal ID #11713) was selected as an active component [241, 413], and it was placed beneath the bed of $K_3V_5O_{14}$. The quartz wool was placed under

the catalyst bed to protect the system from melting (Figure 5.10). Figure 5.10 shows the exact same catalysis profile which was obtained over supported K/V=0.6 catalyst (see previously in Figure 4.6A). The activity of vanadium oxide specie(s) were inhibited when $K_3V_5O_{14}$ melts. The path-finder experiment result indicates that the mobility of $K_3V_5O_{14}$ due to melting blocks the accessibility of active sites, which yields in a drop in activity. Overall, this experiment allowed us to gain an initial idea on the possible role of molten layer on the activity.

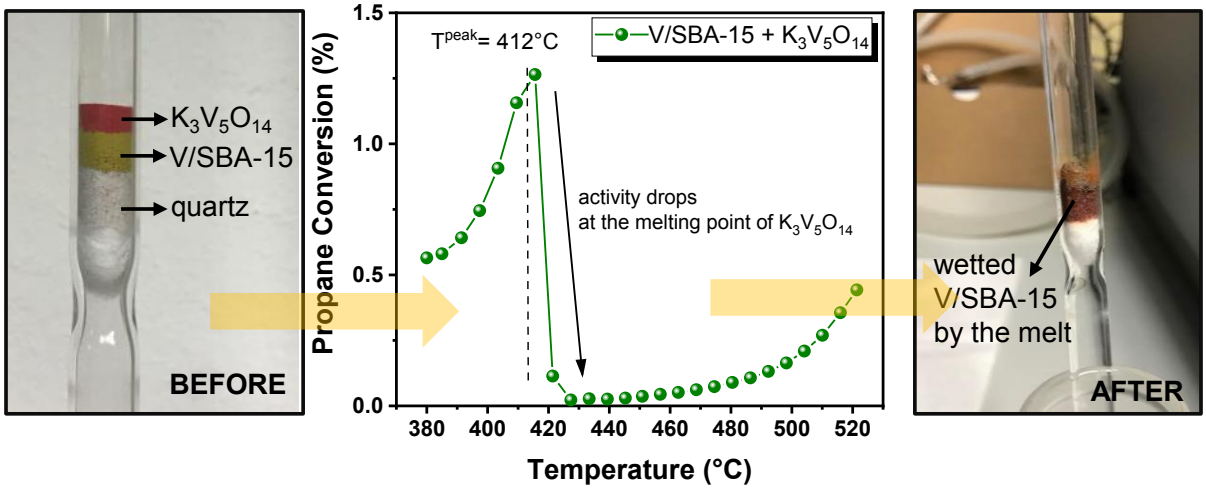

Figure 5.10. A model system: Catalytic performance of V/SBA-15 and $K_3V_5O_{14}$ in propane oxidation (T=350°C-520°C, feed $C_3H_8/O_2/N_2$=7.5/7.5/85, W/F=1.8 g s ml^{-1})

Next, NAP-NEXAFS experiments will be shown and discussed to investigate if the hypothesis built up to now is valid.

5.4. Operando Near-Edge X-ray Absorption Fine Structure (NEXAFS)

5.4.1. Introduction

X-ray absorption spectroscopy (XAS) is used as a probe for unoccupied band structure and local chemical environment of a material[417]. In a simple words, the radiation energy is scanned while the absorption is observed. The sample is irritated with monochromatic X-rays of photon energy *(E_{ph}=hv)* and an electron is excited to an unoccupied state of the atom or to the continuum of states[418]. Based on energy, discrete structures such as X-ray absorption near edge structure (XANES) and the extended x-ray absorption fine structure (EXAFS) can be observed[419]. Near edge X-ray absorption spectroscopy is (NEXAFS) a powerful method due to its atom specificity and it allows to study local (atomistic) and electronic structures of materials by providing information about e.g. valence band, coordination environment, and oxidation state [359]. It is used to make an identification of quantitative structure of the dynamic surface under realistic gas-phase operation conditions [161, 336, 371].

In the present study, the aim with NAP-XPS and NEXAFS technique is to determine structural characterization of alkali-doped silica supported vanadium oxide catalysts. In addition, since there is a phase transition occurs under reaction conditions, the dynamic changes on the electronic structure of the absorbing atom, in this case it is vanadium, during melting is extremely needed to investigate. The experimental protocol was followed by the exact same protocol applied in reactor, Raman and DSC studies. For this, a pressed powder pellet (1 ton, 8 mm diameter) of about 15 mg supported catalysts on a SiC plate and a sapphire sample holder was prepared. The sample was first activated, *i.e.*, heated under dynamic flow (21 O_2, rest N_2) with 10 K/min to 520°C and held there for 2 h. The measurements for propane oxidation were carried out at temperature range between 350 and 520°C and 250 Pa in 1:1 (7.5 $mlmin^{-1}$, 7.5 $mlmin^{-1}$) mixtures of propane and oxygen (C_3H_8/O_2, rest N_2).

NEXAFS measurements were carried out in the total electron yield (TEY) and Auger electron yield mode (AEY, *i.e.*, secondary electrons). AEY was obtained by using the electron spectrometer as a detector to minimize the gas phase to the spectra as explained in detail elsewhere[359]. Simultaneously to the AEY mode, absorption spectra in the TEY mode was also recorded by applying a positively biased wire. TEY signal is also surface sensitive due to the short inelastic mean free path of the emitted photoelectrons however the probing depth of TEY signal is unknown due to the high influence from the low-energy secondary electrons[420].

Kinetic energies were set to 385 eV for K, Rb, and Cs-V-O/SiO_2 while 285 eV for Li-V-O/SiO_2 and 185 eV for Na-V-O/SiO_2 catalystS with a pass energy of 100 eV as X-ray absorption spectroscopy (XAS) detector to minimize contributions from the gas phase spectra. O K-edge spectra of the sample surface were reconstructed applying a correction for the varying photon flux at sample position by using a gas phase O_2 TEY spectrum (Figure S3.11) based on a methodology explained elsewhere[359]. The example of reconstructed spectra for silica supported K/V=0.6 catalyst and SiO_2 can be seen in Figure 5.11.

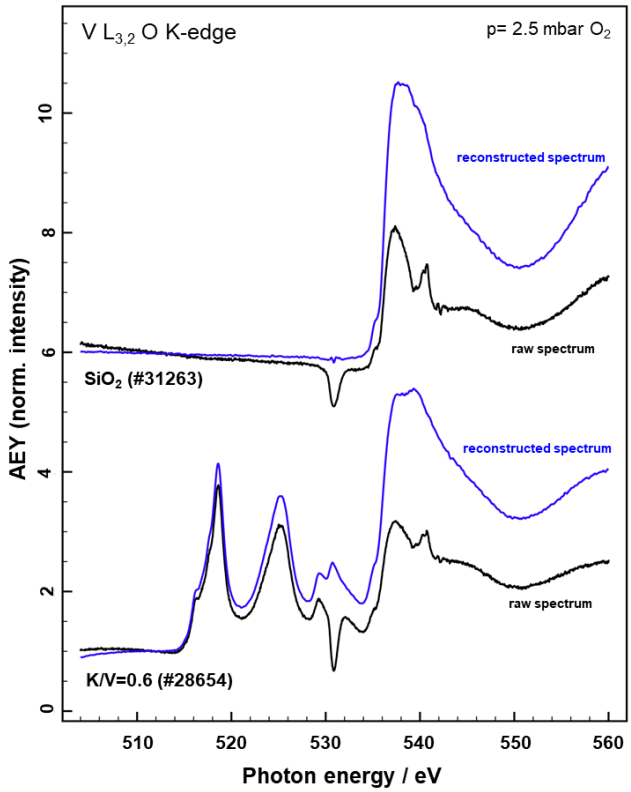

Figure 5.11. Demonstration of the reconstruction of the measured Auger Electron Yield NEXAFS spectrum of silica supported K/V=0.6 catalyst and SiO_2 (Aerosil 300) (provided by M. Hävecker)

Using insulating supports like SiO_2 inhibit the quality spectra due to differential charging. Fortunately, the unfavourable effect of differential charging decreases with increasing temperature. In this work, the loading of vanadium was sufficient to obtain a high quality of NEXAFS spectra.

V L_3 and L_2- X-ray absorption spectra of catalysts were measured in the photon energy range between 512 and 528 eV. The V L_3- edge (corresponding to transition from V 2p to 3d orbitals) is sensitive to changes in the stoichiometry of the vanadium oxide therefore it can be used for identification of coordination environment of vanadium. However V L_2-edge is less important

for the analysis due to its broadened structure along Coster-Kronig decay of the $2p_{1/2}$ hole [375, 376].

The oxygen K-edge (transition from O 1s to O 2p) above 528 eV was also measured. The energy range between 528 and 534 eV are defined by the pecularities of the V-O bonding while resonances at photon energy above ca. 534 eV reflect mainly the O 1s excitations of Si-O-Si bonds [336, 372]. Recent review gives the comprehensive information on oxygen K-edge X-ray absorption spectra of both molecules and solids[377].

The interpretation of the NEXAFS spectrum is challenging. Therefore, NEXAFS of support-free alkali-vanadates were also measured as reference. In addition, fitting of V L-edges was conducted in an ATHENA (Demeter)[293] software.

Si 2p, O 1s and V 2p XPS core level spectra were collected by setting the pass energy of the spectrometer to 20 eV. The excitation energy was 680 eV for O1s/V 2p spectra and 260 eV for Si 2p spectra, respectively. XPS core level spectra of K 2p, Cs 3d, Rb 3d, and Na 2p were also collected with a photon energy of 440, 880, 260, and 180 eV, respectively. Quantitative element abundance of O 1s and the V $2p_{1/2}$ and V $2p_{3/2}$ core levels were determined using atomic subshell photo-ionization cross sections [378, 379]. The peaks were fitted with Gaussian-Lorentzian functions after a Shirley background correction within CASA data analysis software[380]. The total peak areas of the respective core levels after a Shirley background correction were taken for calculation of average oxidation state. For vanadium, the sum of V $2p_{1/2}$ and V $2p_{3/2}$ areas was used. Due to the fact that the silica causes huge differential charging, low temperature NAP-XPS data is not reliable for discussion. However, the NAP-XPS of silica supported A/V catalyst at the highest temperature (520°C) can be discussed and are presented in Figure S4.9.

5.4.2. V $L_{3,2}$-edge and O K-edge of silica supported K/V=0.6 catalyst

The silica supported K/V=0.6 catalyst shows melting under applied propane oxidation reaction conditions and the melting has drastic impact on reactivity. Therefore, major changes in electronic structure of vanadium are expected. V L_3 and L_2-edges of vanadium including compounds exhibit several spectral features in the photon energy range between 512 and 528 eV which is characterized by V2p- V3d electronic transitions [336, 372, 421, 422]. Figure 5.12 **(A)** presents the NEXAFS of K/V=0.6 catalyst during activation in 250 Pa O_2 ($21O_2/79N_2$, 10 ml min^{-1}) between 296°C and 524°C while **(B)** presents the NEXAFS of K/V=0.6 catalyst in

propane oxidation ($C_3H_8/O_2/N_2$=7.5/7.5/85 10 ml min^{-1}) at the same temperature range. V L-edges and O K-edge spectra were presented in both AEY and TEY mode.

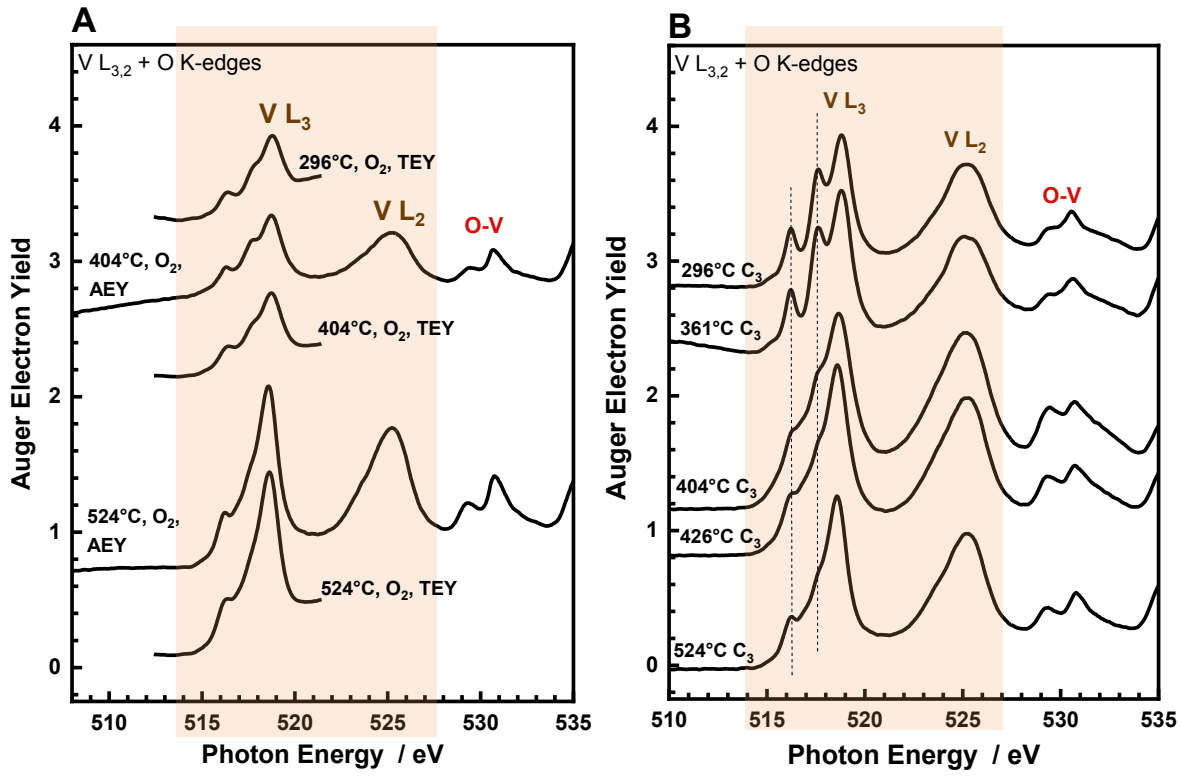

Figure 5.12. (A) V $L_{3,2}$- NEXAFS of silica supported K/V=0.6 under synthetic air during activation (at 250 Pa O_2/N_2=21/79 10 ml min^{-1}) and **(B)** under propane oxidation (at 250 Pa $C_3H_8/O_2/N_2$=7.5/7.5/85 10 ml min^{-1})

Three components of V L_3-edge for K/V=0.6 catalyst were observed in oxygen feed at 404°C (Figure 5.12A) whose resonances are located at ~516.2, ~517.6 and ~518.7 eV. Maganas *et al.*[423], explained that the first two features at lower photon energy arise from the $3d_{xz}$ + $3d_{yz}$ and $3d_{xy}$ components whereas the peak maxima exhibits more of the $3d_{z2}$ of vanadium ions. Upon increasing temperature to the maximum, *i.e.*, 524°C in oxygen feed, two distinct transitions in the VL_3-edge spectra of K/V was observed instead of three absorption features. After activation was completed, catalyst was completely cooled down to 30°C and exposed to the reaction mixture. Figure 5.12B shows the V $L_{3,2}$- and O K-edge NEXAFS of K/V=0.6 catalyst upon heating under propane oxidation conditions. The V L_3-edge spectra of K/V catalyst at 294°C in C_3 environment look more ordered compared to the spectra in O_2 feed. It is highly noticeable that the activated K/V=0.6 sample has three spectral features whose photon energies are at 516.2, 517.6 and 518.7 eV. Compared to the spectrum at 294°C in O_2, no shift was observed in energy positions after activation. When temperature reached above the melting temperature (*i.e.* 410°C), a considerable difference between spectra at 296°C and 426°C was

observed. At 426°C in reaction second absorption shoulder in the photon energy at 517.6 eV disappeared. This dramatic change observed in the V L_3-NEXAFS of K/V=0.6 catalyst proofs the impact on the electronic change in the first coordination shell of vanadium due to the melting of alkali vanadates.

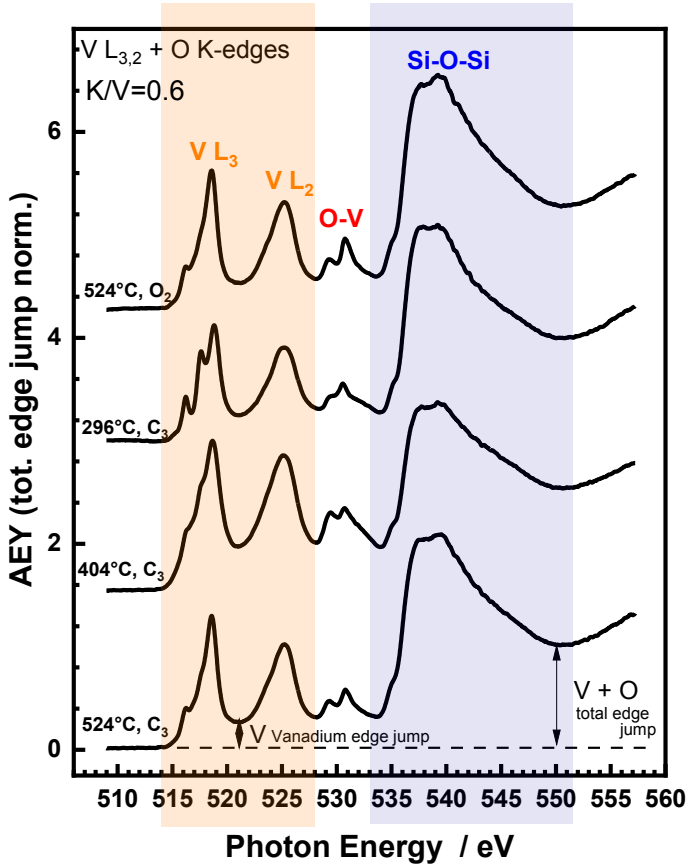

Figure 5.13. The vanadium edge ("V") and the total energy jump ("V+O") in the V L-edge NEXAFS of silica supported K/V=0.6 under different reaction conditions

One of the first approaches on understanding spectral changes might be determining edge-jump ratio of each spectra collected at the same conditions. This is explained by the following. The changes in the X-ray absorption intensity (edge-jump) is proportional to the amount of absorbing atoms. Therefore it can be used to measure elemental abundance [336, 424]. However, in the soft energy range, only relative changes can be evaluated meaning to no absolute abundance can be extracted. Following protocol described by Hävecker *et al.*[336], the quantitative analysis of the XAS edge intensity was performed by comparing the ratio between V-edge and total edge jump. In Figure 5.13, it is shown that the intensity at ~522 eV indicated as "V" after subtracting the pre-edge intensity. This was taken as a measure of V abundance since silica does not show any absorption feature in this energy. Intensity at ~548 eV is defined as the total edge jump that represents vanadium plus all oxygen absorbers. This

is a good measure for V+Si abundance since the majority of oxygen is bound to the non-reducible silica support[336].

The evolution of the vanadium to the total edge jump ratio (V/V+O), related to the V/V+Si abundance is shown in Figure 5.14. Upon heating under propane oxidation reaction conditions, edge jump ratio increased. This suggests an increase in the dispersion of vanadium increases over support. The highest V abundance in the edge jump ratio was reached at 404°C which is the temperature where the effect of melting of $K_3V_5O_{14}$ was seen in V L-NEXAFS. Above melting (404°C), some of the vanadium species was covered and became not further accessible. At this point, quantitative analysis techniques is needed to determine whether the surface was covered by alkali or not *(will be discussed in Section 5.4.3.2.)*. Due to the batch-reactor-like design of the in situ spectroscopy cell, conversion was found very low (<1%) and the impact of melting on activity could not be detected. However, the change in selectivity was still noticeable. Further increase in temperature from 404°C, selectivity to propylene increased (Figure S3.12) supporting the previous findings.

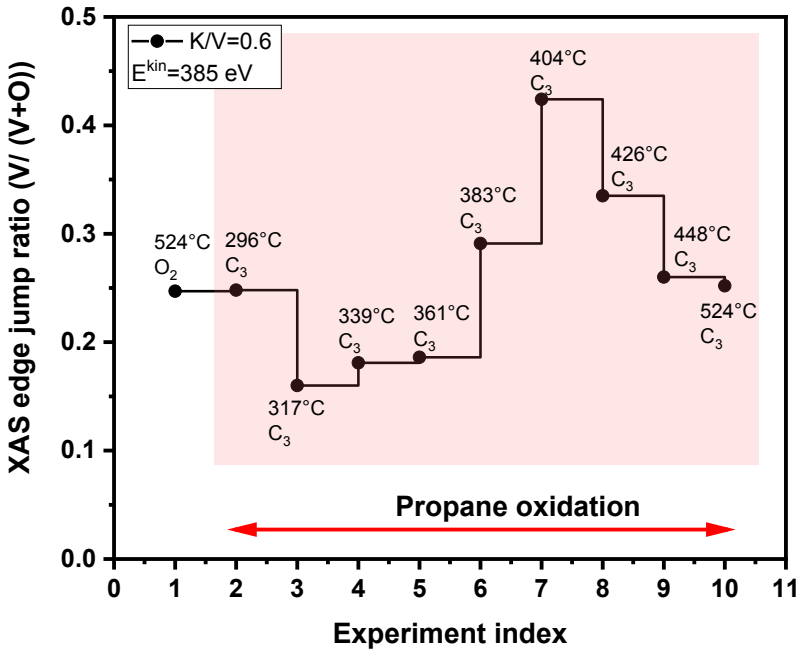

Figure 5.14. The evolution of the V-edge/total edge jump ratio (corresponds to the intensity ratio V/ (V+O)) as indicated in Figure 5.13 for silica supported K/V=0.6 catalyst at different reaction conditions

The evolution of O K-edge spectra of K/V=0.6 catalyst including both activation and propane oxidation is shown in Figure 5.15. The O K-edge of K/V=0.6 in any condition exhibits two main features due to hybridization of O 2p states. The photon energies of these two features are centred at 529.3 eV and 530.8 eV. The intensity of these two resonance at 529.3 eV and 530.8

are significantly enhanced when the catalyst is heated from 404°C to 524°C in O_2. The O K-edge of activated K/V catalyst at 296°C in C_3 resemble the spectra at 404°C in O_2 however the resonance ratio were different. Interestingly, the resonance at 529.3 eV was remarkably enhanced when melting starts at 404°C. This is the considerable change in V-O bonding which shows the structural modifications along melting. The shoulder at 529.3 eV loses its intensity with further increasing the temperature which can be explained due to the re-ordering of the structure after melting was completed.

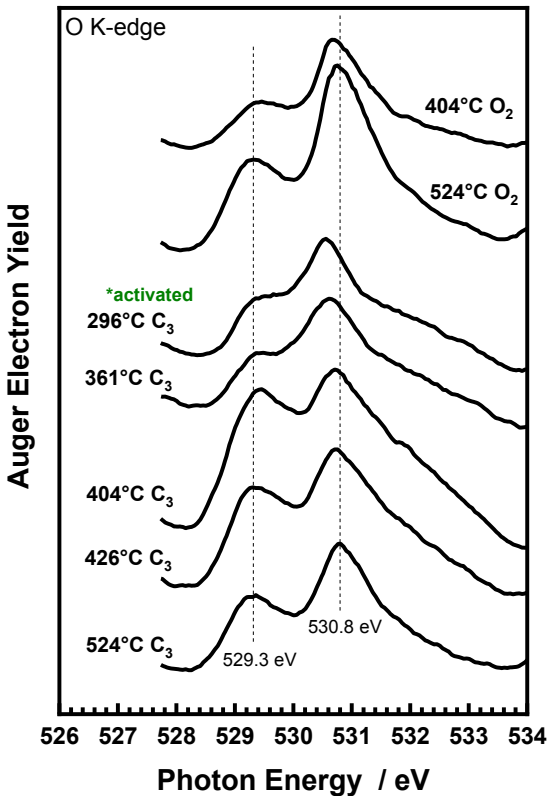

Figure 5.15. The evolution of O K-edge spectra of K/V=0.6 catalyst at different conditions followed by first activation in O_2 (at 250 Pa O_2/N_2=21/79 10 ml min^{-1}) and then propane oxidation reaction (at 250 Pa $C_3H_8/O_2/N_2$=7.5/7.5/85 10 ml min^{-1})

in-situ V2p XP spectra of K/V=0.6 catalyst was analyzed to determine the oxidation state of vanadium (520°C, 250 Pa in propane feed) (Figure S4.9). As mentioned before, due to the high charging at low temperature, only the data at very high temperature was reliable. Two components of V2p (*i.e.* $V2p_{3/2}$ and $V\ 2p_{1/2}$) fitted by Gaussian-Lorentzian functions which represents V^{4+} and V^{5+}. The overall area of V^{4+} and V^{5+}components were analyzed. Two mixed Gaussian-Lorentzian fit profiles centered at 517.5 and 516.5 eV binding energy (BE) were used as V^{5+} and V^{4+} components of $V2p_{3/2}$ core levels. For $V2p_{1/2}$ core levels, two mixed Gaussian-Lorentzian fit profiles centered at 525.0 and 524.0 eV binding energy (BE) were used for V^{5+} and V^{4+} components. The difference between BE of V^{5+} and V^{4+} was 1 eV which is reasonable

compared to the literature[425]. The contribution of V^{4+} was found to be very low in V2p core levels. The abundance of components V^{5+} and V^{4+} and the calculated oxidation state of vanadium can be found in Table 5.2. Table 5.2 shows that the dominancy of V^{5+} species was present after melting (520°C). The oxidation state of vanadium was calculated to be as 4.83 which is in line with the formal oxidation state of vanadium of the phase.

Table 5.2. Abundance of V species determined by XPS

Material	V species	Binding Energy (BE)	Abundance based on fitting model
K/V=0.6	V^{5+}	517.5 ($V2p_{3/2}$) 525.0 ($V2p_{1/2}$)	81.9
	V^{4+}	516.5 ($V2p_{3/2}$) 524.0 ($V2p_{1/2}$)	18.0

5.4.3. Analysis of NEXAFS spectra of silica supported K/V=0.6 catalyst

5.4.3.1. Comparison of the spectra of K/V=0.6 catalyst to the spectra of supported/unsupported vanadium oxide catalysts in the literature

The NEXAFS spectra of K/V=0.6 catalyst were first compared with some supported vanadium oxide catalysts since the spectral shapes very much resemble each other. The spectra of supported vanadium oxide catalysts (V/SBA-15) and V_2O_5 were used from the study done by Hävecker *et. al.*[336]. In that study, V $L_{3,\ 2}$–edge and O K-NEXAFS of dehydrated VO_x/SBA-15 with various vanadia loadings were measured. It was stated that V loadings of 8 wt. % and below on SBA-15 suggests that both monomeric and polymeric species while at V loadings above 12 wt. % some three-dimensional characters to V species were present. Since the melting occurs at 410°C and the spectral shape changes significantly, the spectra before and after melting were separately discussed:

- **Before melting (296°C, propane oxidation feed)**

Figure 5.16 presents the V L_3-edge followed by O K-edge of K/V=0.6 (denoted by KV, taken at 296°C in C_3) compared to supported vanadia catalysts. VO_x/SBA-15 catalysts were designated as 6V-14V which shows vanadia loading in the range 6-8 wt. %[336]. VO_x/SiO_2 catalyst synthesized in this study was also included and denoted by V/Si.

The absorption peaks of V L_3-edge spectra of VO_x/SBA-15 catalysts are in the photon energy range between 512 and 528 eV (Figure 5.16A). The spectral shape of K/V=0.6 catalyst (at 296°C in C3) resemble very much the spectral shape of V L_3-edge of V/SBA-15 and V/Si

catalysts. From this point, the overall spectra of V L_3-edge of alkali catalysts suggests the monomeric/polymeric surface vanadium oxide species might exist in the activated catalyst.

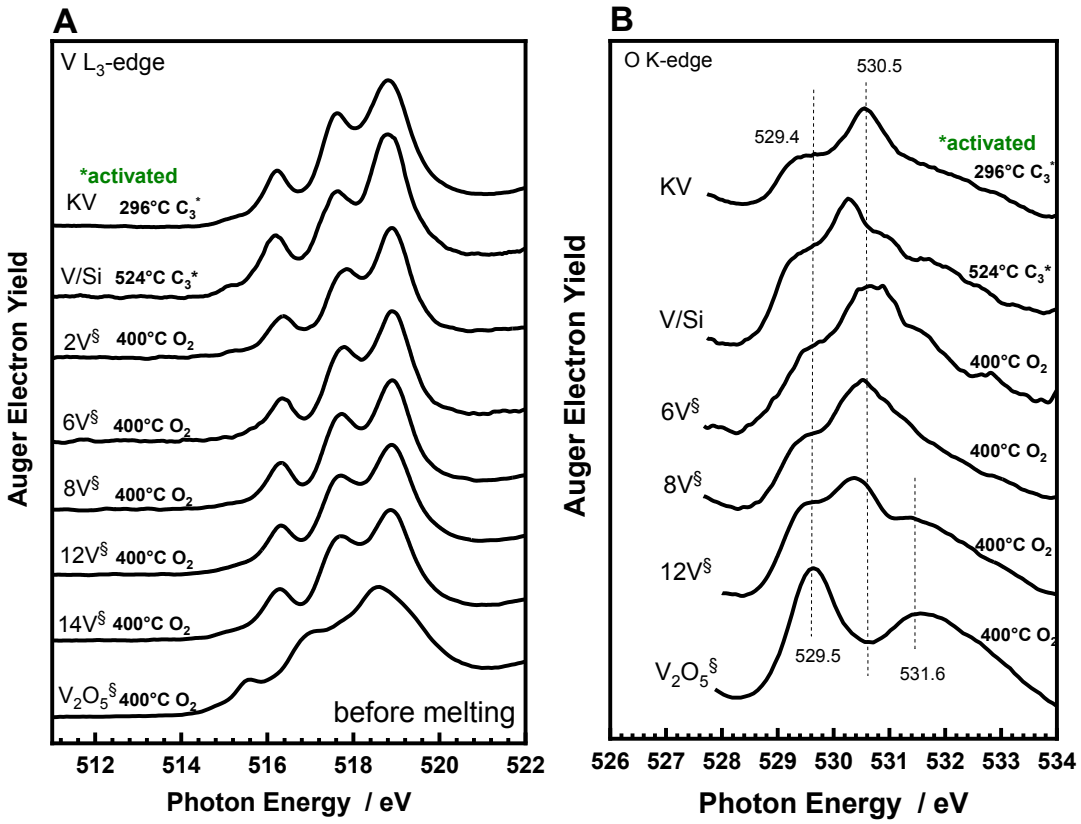

Figure 5.16. (A) V L_3-edge of activated K/V=0.6 catalyst in 250 Pa C_3H_8:O_2 at 296°C (solid state) **(B)** O K-edge of activated K/V=0.6 catalyst at the same condition. A reference spectrum of blank catalyst (*i.e.* V/Si) synthesized in this study (internal ID #28683), V_xO_y/SBA-15 with various vanadium loadings (§)[336] and V_2O_5 powder (§)[336] were shown as well.

The O K-edge feature are in the energy range between 528 and 534 eV (Figure 5.16B). In the O K-edge spectra of 12V, the characteristic feature of V_2O_5 at 529.5 eV is obviously distinguished[336]. Based on vanadia loading, O K-edge looks different which indicates different V-O bonding are exist. The O K –edge of K/V=0.6 catalyst (at 296°C in C_3) is similar to the O K-edge of 8V catalyst. This further supports the monomeric and polymeric vanadium oxide species might exist in the supported K/V=0.6 catalyst. However, the overall spectral shape is still different from the dispersed V_xO_y species.

Moreover, the spectra of K/V=0.6 is quite different than the spectra of V_2O_5 which tells us there is no indication of bulk-like vanadia formation in activated catalyst before melting temperature.

- **After melting (426°C, propane oxidation feed)**

Figure 5.17 **(A)** and **(B)** present the V L_3-edge and O K-edge spectra of K/V=0.6 (denoted by KV, taken at 426°C in C_3) at higher temperature where alkali-vanadate melts. Spectral features and energy positions of K/V=0.6 catalyst were compared with the V L_3-edge and O K-edge of reference compounds, *namely*, V/Si, 6V, 8V, 12V, and V_2O_5.

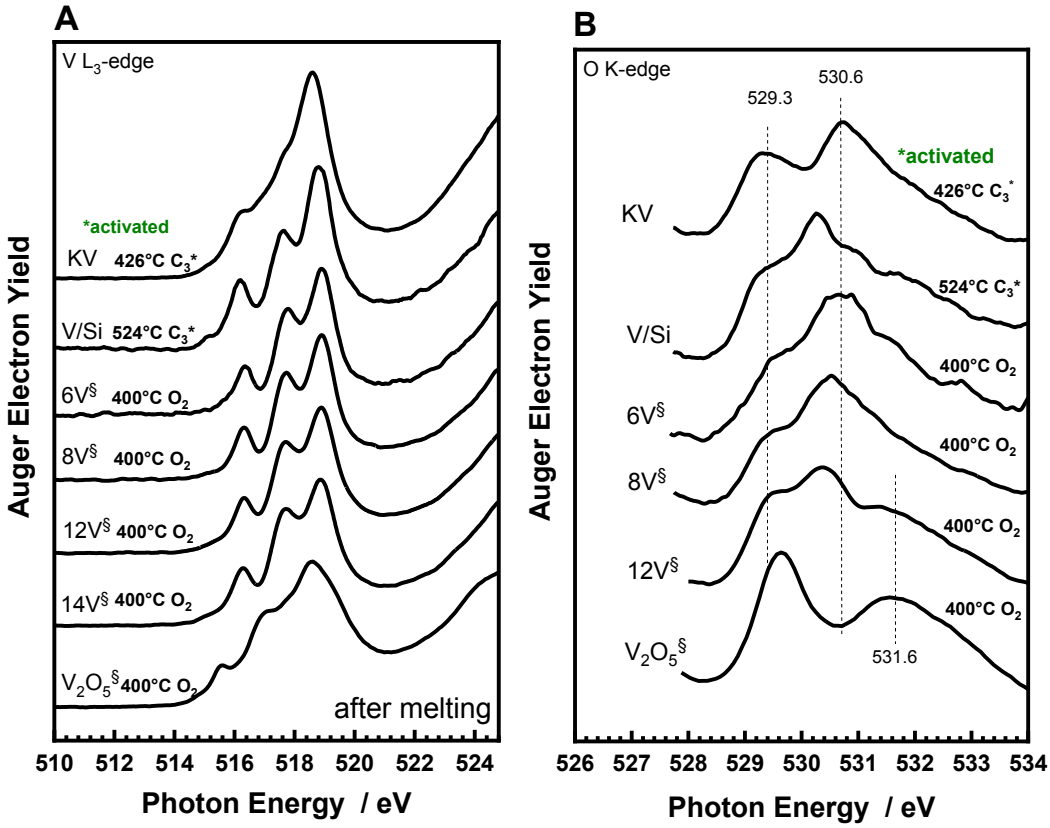

Figure 5.17. (A) V L_3-edge of activated K/V=0.6 catalyst in 250 Pa C_3H_8:O_2 at 426°C (molten state) **(B)** O K-edge of activated K/V=0.6 catalyst at the same condition. A reference spectrum of blank catalyst (*i.e.* V/Si) synthesized in this study (internal ID #28683), V_xO_y/SBA-15 with various vanadium loadings (§)[336] and V_2O_5 powder (§)[336] were shown as well.

Compared to the spectra before melting, the spectral shape of V L-edge of K/V=0.6 catalyst looks different. Obviously the shoulder whose resonance position at 517.5 eV disappeared (Figure 5.17A). One may speculate that it resembles the features of V_2O_5, however the slight difference in energies (~0.5 eV shift in higher energy) must be noted. The O K-edge of K/V=0.6 catalyst show more pronounced shoulder at 529.3 eV (Figure 5.17B) which is a characteristic feature of V_2O_5 might be indicating some three-dimensional vanadia species formed after melting.

According to the comparison between the NEXAFS spectra of silica supported K/V=0.6 catalyst and the supported vanadium oxide species, it is possible to draw general conclusion.

Apparently, the V L_3-edges of silica supported K/V=0.6 catalyst possesses three features at about 516, 517 and 519 eV along with an O K-edge at about 529 and 530 eV evidencing the formation of dispersed vanadium oxide species after catalyst activation. This finding is supporting the findings of Raman spectroscopy in where υ (V-O-V) bridging bond vibrations from the dispersed vanadium oxide species at 838 cm^{-1} was detected with 266 nm laser (see previously in Figure 5.4A).

In a summary, there is a certain change occurred in spectral shape in NEXAFS under reaction conditions, in particular before and after melting. Obviously, electronic structure around the vanadium atom is dramatically affected by the melting phenomenon. However, drawing a conclusion based on these findings is not sufficient. Hence, computational aid which allows quantitative analysis is highly needed. Linear combination analysis will be explained as a next for determining components of V L_3-edge of silica supported K/V=0.6 catalyst by analysing the spectra with reference materials.

5.4.3.2. V L_3-edge fitting of silica supported K/V=0.6 catalyst

NEXAFS of unknown material (especially a mixture) can be analysed by several techniques: (i) Linear Combination analysis[426], (ii) Principal Component Analysis[427], (iii) Multivariate Curve Resolution and Alternating Least-Squares (MCR-ALS)[428], (iv) Differential Data analysis[429], and (v) Machine Learning[430]. Among them, Linear Combination Analysis (LCA) is a useful approach to get reliable and precise information about the components of the unknown material. If the actual catalyst is unknown and it is a mixture of some other materials, the measured spectra of an actual catalyst can be fit with a linear combinations of NEXAFS spectra of known materials and determine the proportion (weighted average of the spectra) of each materials in the actual catalyst.

For this, the NEXAFS of relevant species to the actual catalyst (target) has to be measured. First of all, these species were not decided randomly. ESEM analysis on silica supported K/V=0.6 catalyst suggested that nano-rods with K: V=1:2.5 (at.) were formed upon activation (Figure S1.17). Therefore, support-free KV_3O_8 were first synthesized as a possible decomposition product of $K_3V_5O_{14}$ on supported system and then K-amount systematically reduced to get nonstoichiometric K-V-O compounds. In addition, $K_3V_5O_{14}$ (main phase as detected by XRD and Raman spectroscopy), and some other K-V-O compounds with different coordination environment of vanadium (such as KVO_3, $K_2V_8O_{21}$) as well as supported vanadium oxide species were included in the reference pool.

The support-free K-V-O species used for spectra fitting are shown in Table 5.3. The V L_3-edge NEXAFS of these materials are shown in Figure S3.13.

Table 5.3. K-V-O compounds used for LC fitting of NEXAFS spectra of K/V=0.6 catalyst

Internal ID#	Name (phase detected by XRD)	K/V (at.)$^{\perp}$
32836	$K_{0.75}V_6O_{16} + V_2O_5$	0.09
32835	$K_{0.75}V_6O_6 + K_xV_2O_5$	0.11
33753	$K_{0.71}V_6O_6$	0.12
32841	$K_{0.75}V_6O_6 + V_2O_5$	0.125
32815	$K_xV_6O_{16}, K_xV_2O_5$	0.15
32812	$K_{0.75}V_6O_{16} + K_{0.25}V_2O_5 + KV_3O_8$	0.17
32780	$K_2V_8O_{21} + K_{0.48}V_2O_5$	0.22
32741	$K_2V_8O_{21} + K_{0.25}V_2O_5 + K_xV_2O_5$	0.23
32691	$K_2V_8O_{21} + KV_3O_8$	0.25
29584	$K_2V_8O_{21}$[291]	0.25
32648	$K_2V_8O_{21} + KV_3O_8 + K_2V_6O_{16}.1.5H_2O$	0.27
32008	KV_3O_8	0.33
32579	$K_{0.75}V_6O_{16} + V_2O_5$	0.35
31564	$K_3V_5O_{14}$	0.6
25450	$K_3V_5O_{14}$[291]	0.6
30216	KVO_3*	1

*commercial
$^{\perp}$Analyzed by XRF, based on $A_2O+V_2O_5$

Regarding data treatment and fitting, ATHENA (Demeter)[431] software was used. First, the background subtraction and normalization was performed. The normalization was done at the pre-edge (~ 512 eV) where there is no absorption. Combinatorial approach was used which means total number of references used for each fit kept limited to get an idea which reference spectra might be relevant to the measured spectra. Overall reference pool including supported vanadium oxide catalysts and potassium-vanadates for fitting of silica supported K/V=0.6 catalyst is shown in Figure 5.18.

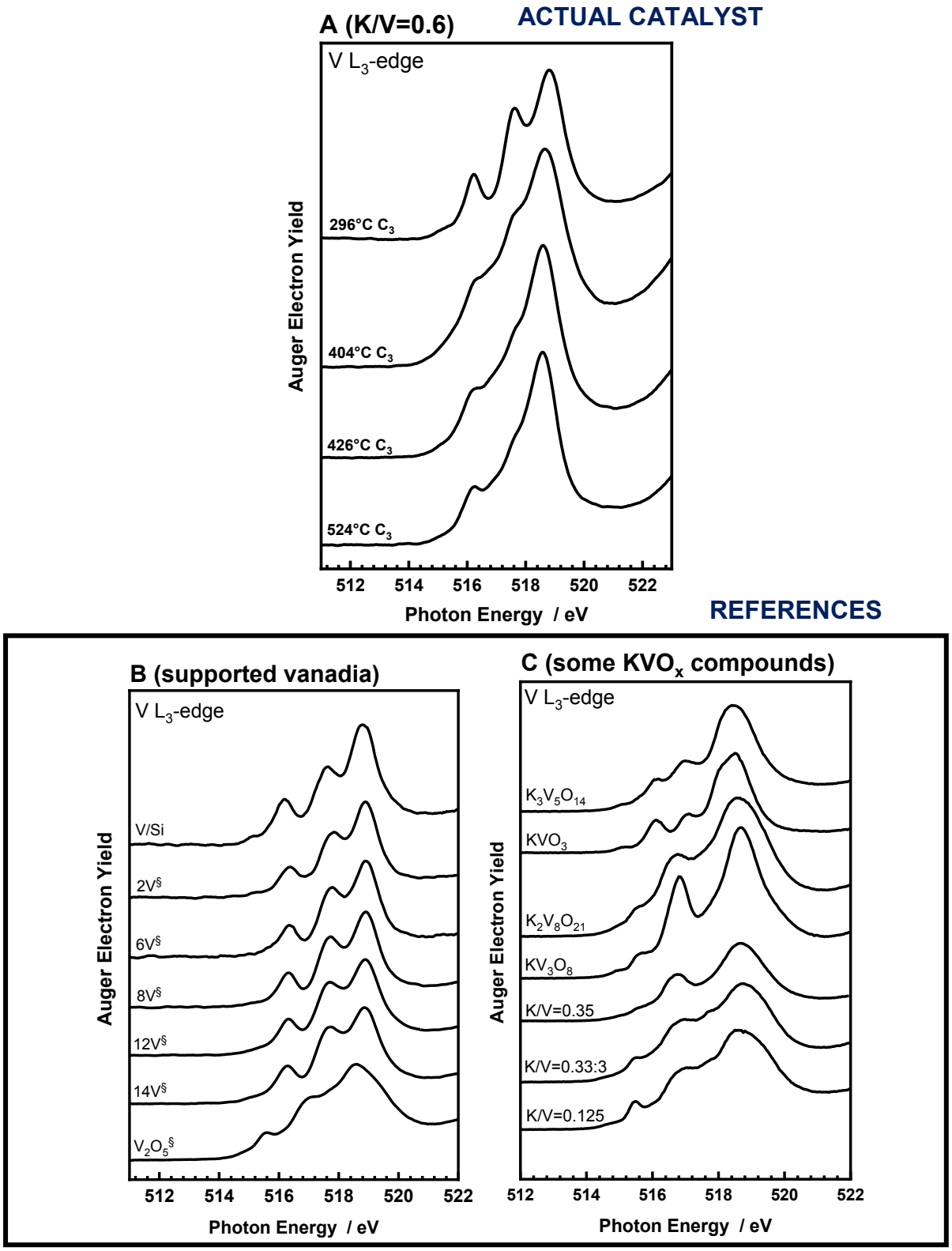

Figure 5.18. (A) V L_3-edge of silica supported K/V=0.6 catalyst activation (at 250 Pa O_2/N_2=21/79 10 ml min^{-1}) and in propane oxidation (at 250 Pa $C_3H_8/O_2/N_2$=7.5/7.5/85 10 ml min^{-1}) and **(B)** V L_3-edge of V/Si synthesized in this study, V_xO_y/SBA-15 with various vanadium loadings (§)[336] and V_2O_5 powder (§)[336] as reference materials, **(C)** V L_3-edge of support-free K-V-O phases synthesized in this study.

Figure 5.19 compares experimentally measured data of V L_3-edge of K/V=0.6 catalyst and the results of the data fitting using reference spectra in the ATHENA software. With the combinatorial approach, the number of references might be relevant were able to be minimized. Here for the silica supported K/V=0.6 catalyst, possible contributions of $8V^{\S}$, $14V^{\S}$, V_2O_5, KV_3O_8, and $K_3V_5O_{14}$ were found.

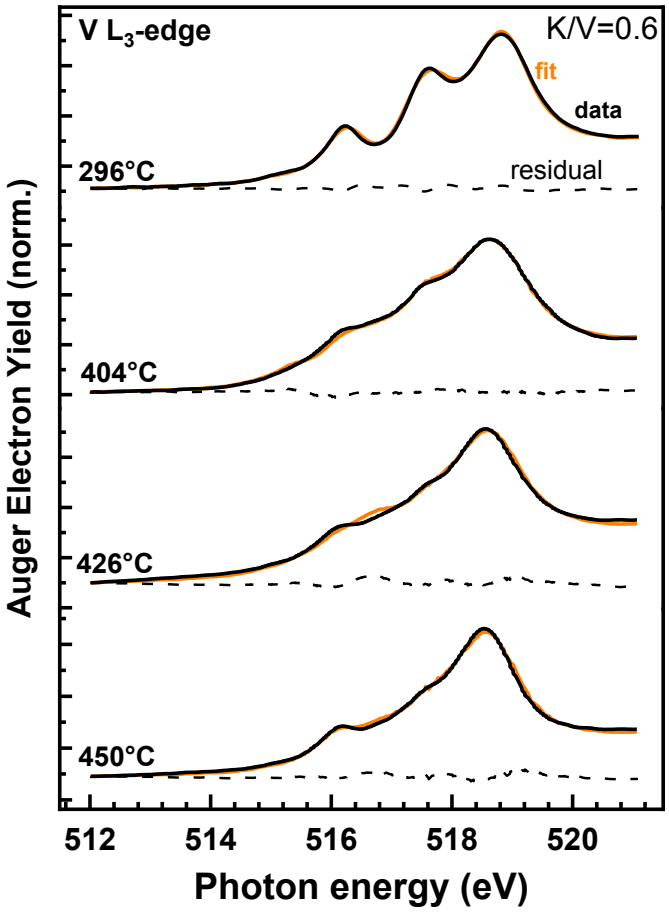

Figure 5.19. Experimental versus fitting curves of V L_3-edge NEXAFS spectra of K/V=0.6 catalyst (activated) in different temperatures during propane oxidation reaction. The experimentally measured data and fitting curves are plotted with solid black and orange line, respectively. The dashed line indicates the residual spectra obtained by subtracting fitting curve from the measured data.

It has to be mentioned that the spectra itself at the liquid state (denoted by KVO_x (liquid)) was also added since there is no V L_3-edge measured in the liquid state exist. In general, NEXAFS of a liquid and a solid is not necessarily very different as in first approximation only the first shell around the absorbing atom (V) is represented. However, due to the random movements and small changes in binding angle and/ or atom distances due to melting of surface K-V-0 phase(s), the resonant structure might be smeared out. This was actually seen in the in-situ Raman of both support-free $K_3V_5O_{14}$ and supported K/V=0.6 ($K_3V_5O_{14}$/ SiO_2). Since the local

structure changes more significantly as the whole compound falls apart, NEXAFS might be completely different. There are also some other examples exist in literature in where the NEXAFS of gas phase, liquid and solid water were compared [432, 433]. Therefore, it was the best strategy to add a spectra measured at 460°C as a reference for liquid state.

Generally speaking, very good agreement between the model and the fit were reached. The fit models provides a weighted average of the spectra using references. The contribution ("weight") of the chosen references to the experimental spectra as obtained by the fit is shown in Figure 5.20. One can see that activated catalyst is a mixture of monomeric/polymeric vanadium oxides species with a small contribution from KV_3O_8. This is contrary with Raman experiments where $K_3V_5O_{14}$ was still detected after activation. At 404°C, a minor contribution of the $K_3V_5O_{14}$ and bulk-like V_2O_5 were obtained. This is the temperature where melting starts and spectral shape changes significantly.

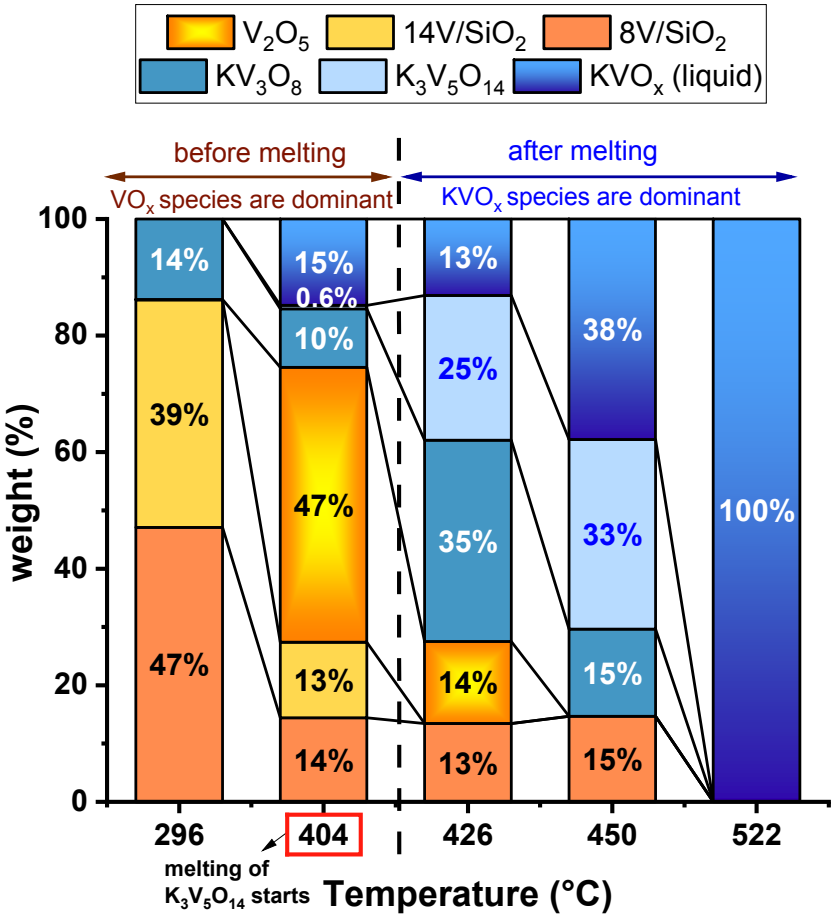

Figure 5.20. Distribution of species over silica supported K/V=0.6 catalyst during propane oxidation reaction as calculated by the fit model using ATHENA program

Upon heating from 404°C to 426°C, weighted average of K-V-O species increases further suggesting that the surface concentration enhanced with the mixture of potassium vanadates

after melting. In other words, K-V-O dominated the surface. It must be reminded that this is where activity drops in catalytic measurement. Simultaneously, contributions from the vanadia species (14V, and 8V) decreases upon dominancy with potassium-vanadates.

5.4.3.3. K $L_{3,2}$ -edge of silica supported K/V=0.6 catalyst

The evolution of K-V-O species during reaction (before and after melting) was shown by fitting procedure above. One way to check if the assignment is correct, is to compare K L-edges of the reference K-V-O compounds with the K L-edge of the main catalyst (the supported K/V=0.6). K $L_{3,2}$-edge electron yield NEXAFS spectra of silica supported K/V=0.6 catalyst under reaction conditions with increasing temperature is shown in Figure S3.14. The energy positions of the K L-edge NEXAFS features of K/V=0.6 are shown in Table 5.4. Typical potassium L-edge values are reported in the literature as 294.6 eV and 297.3 eV attesting to the bonding character[434]. Two distinct peaks between 297 and 300 eV were clearly seen in the K/V=0.6 catalyst. These two peaks are assigned to the potassium L-edge $2p_{3/2}$ and $2p_{1/2}$ levels, respectively and are a clear indication of potassium insertion on the silica supported vanadia system.

Table 5.4. Positions of features measured in in-situ potassium L-edge NEXAFS of K/V=0.6 catalyst during heating in propane oxidation reaction conditions

Temperature (°C)	Band I ($2p_{3/2}$) (eV)	Band II ($2p_{1/2}$) (eV)
340	298.40	-
361	298.35	-
404	297.55	300.05
426	297.30	300.00
450	297.25	299.80
522	297.15	299.75

The in situ experiment of silica supported K/V=0.6 in reaction feed showed observable changes in the positions of K L_3-edge features (Figure 5.21) before and after melting. The K L_3-edge recorded at 361°C shows rather broader shoulder compared to spectra at higher temperatures. Since Auger electrons were collected, this broader feature could result from moving of photoelectron lines through the spectrum while scanning. Therefore it can be concluded that the spectra below melting temperature (*i.e.*, < 404°C) does not contain any significant potassium at the surface layer which is consistent with the fitting of the V L_3-edge into vanadium oxide species rather than K-V-O (see Figure 5.20, 296°C). This is a reliable result

since K L-edge is even more surface sensitive than V L-edge spectra due to the lower kinetic energy of primary Auger electrons.

At 404°C, slight increase in potassium L-edge can be seen along with melting. Further heating from 404°C to 522°C resulted in the L_3 resonance position (~297.5 eV) become more and more pronounced, followed by a slowly shifting in energy to 297.15 eV. This is an indication of potassium enrichment at the surface due to melting which supports the findings from the V L_3-edge fitting.

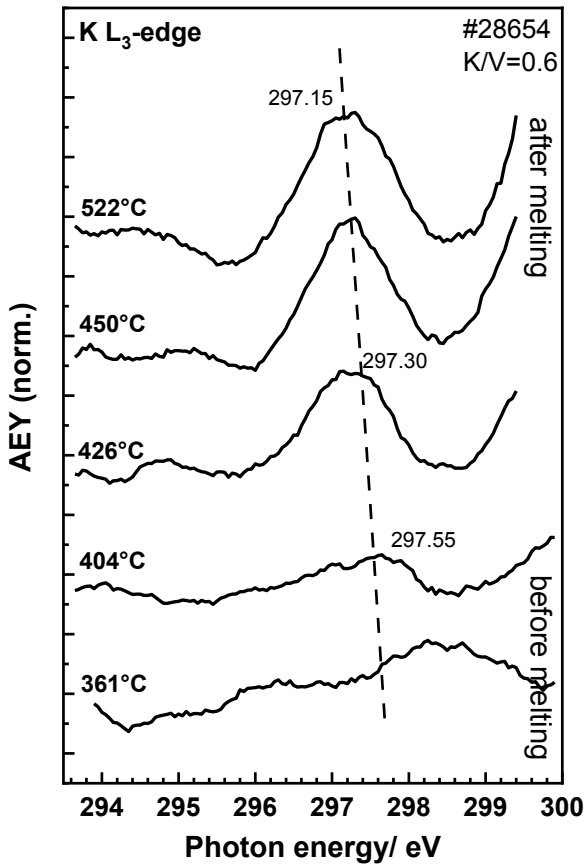

Figure 5.21. *In-situ* K L_3-edge NEXAFS spectra of K/V=0.6 catalyst during heating in reaction atmosphere (at 250 Pa $C_3H_8/O_2/N_2$=7.5/7.5/85 10 ml min^{-1})

Further, the resonance positions of silica supported K/V=0.6 catalyst upon heating was compared with resonance positions of support-free K-V-O references in the K L_3-edge spectra. In situ K L-edge spectra of reference compounds can be found in Figure S3.15.

Herein the K L_3-edge resonance positions are plotted as a function of K: V ratio (at.) (Figure 5.22). The data points related to phase pure K-V-O species are presented in blue whereas the ones of mixtures (nonstoichiometric) are presented in green. The resonance positions of in-situ

K L_3-edge of silica supported K/V=0.6 catalyst are indicated with orange line (obtained from Figure 5.21, *e.g.* 297.55 eV at 404°C).

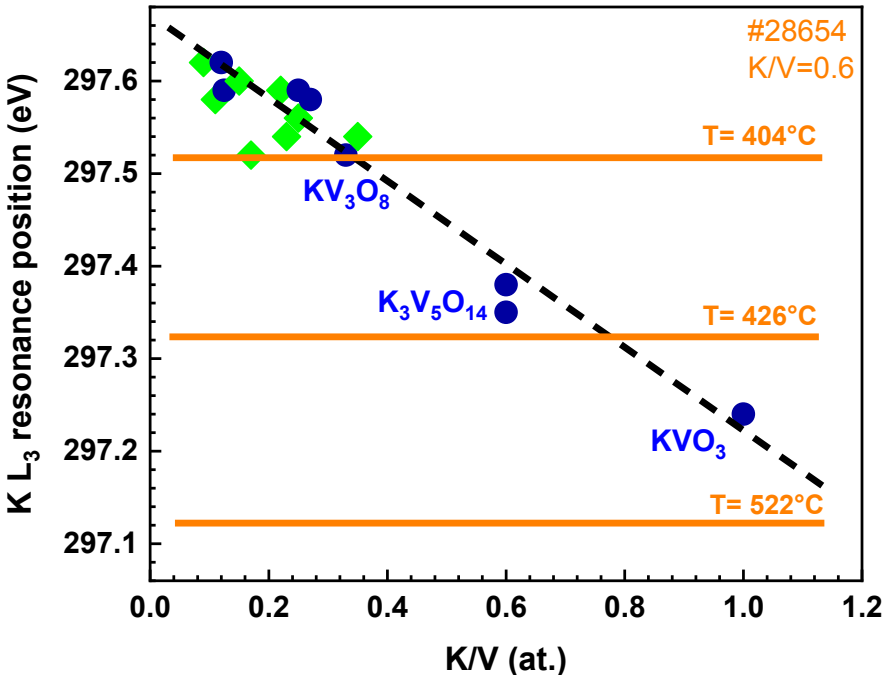

Figure 5.22. K L_3 resonance positions versus K/V ratio (green: mixture of K-V-O phases, blue: phase pure K-V-O phases)

Based on a K L_3 resonance positions analysis, the energy of the resonance position of K/V=0.6 catalyst at 404°C was found as closest to the energy of the resonance position of K/V ratio to 1:3, *namely* the KV_3O_8 phase. The temperature at 426°C (after melting) has K L_3-edge whose resonance position fits to mixture of $K_3V_5O_{14}$ and KVO_3 (closer to one of the $K_3V_5O_{14}$) but not to any of non-stoichiometric K-V-O species. The resonance position shifts to lower, where materials with K: V approaching 1 and better to a mixture of K-V-O. That means the melted phase is rich in potassium which supports wetting phenomena (surface enrichment with potassium) and finally V L-edge findings.

Moreover, the width of the absorption feature can be evaluated beyond energy positions and the width. Generally, energy positions describes the energy difference between two states (initial- final), while area describes transition probability between two states. But the width includes information about crystal quality, and transitional life time. Therefore, in order to the figure out how crystalline our system is, the width of the K L-edge of the actual catalyst can be compared with the width of the reference compounds. As expected, reference compounds, since they are phase pure and support-free, showed narrower width while the compounds with mixture yields in broader in width.

The K L_3-edge of silica supported K/V=0.6 catalyst at 426°C (after melting) seems rather broad (Δ=1.4 eV) compared to references (Δ= ~0.9 eV) (Figure 5.23). This indicates that the material is either less crystalline than reference materials or that one has a mixture of phases (decomposition product of $K_3V_5O_{14}$ + $K_3V_5O_{14}$ itself). Therefore, the melted phase would be characterized by a variety of K-V-O bonding configurations.

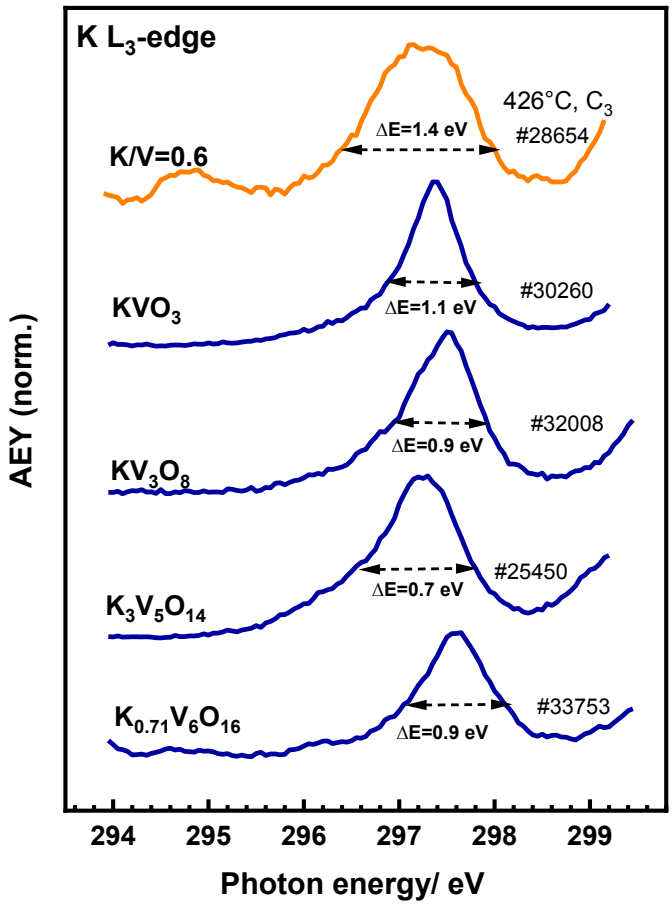

Figure 5.23. K L_3-edge of silica supported K/V=0.6 catalyst (426°C-after melting) and support-free K-V-O reference compounds

5.5. Overall Discussion of Complimentary Techniques: Raman and NAP-NEXAFS Spectroscopy

Investigating geometric and electronic properties are of utmost importance for our fundamental understanding of the behaviour of the catalyst under applied reaction conditions. In order to do this reliably and precisely, so many different tools and techniques developed. Among them, synchrotron based method (*i.e.*, NAP-NEXAFS) have played a prominent role for the exploration of electronic and structural properties of the catalyst[419]. However the NEXAFS alone is not sufficient to make a direct determination of the sample stoichiometry, *i.e.*, it is not a quantitative method. When it comes to a determination of chemical nature on the solid surface, combinatory techniques such as Raman and infrared (IR) spectroscopy techniques are recommended. In this study, we used NEXAFS and Raman spectroscopy as a complimentary techniques for each other. Final discussion will be done by comparing results obtained from these two advanced catalyst characterization techniques.

Figure 5.24 summarizes the most important results obtained from V L-edge and Raman spectroscopy experiments under propane oxidation reaction. Once again, the evolution of V L_3-edge of silica supported K/V=0.6 catalyst under propane oxidation reaction coupled with distribution of species calculated by ATHENA software were shown in Figure 23A. Figure 23B presents temperature-dependent Raman spectroscopy of the catalyst under propane oxidation (λ_{exc}=532 nm) and Raman spectroscopy of relevant reference compounds which were determined by fit model for V L-edges. With this, it is aimed to see if results are consistent.

First of all, Raman spectroscopy experiments allowed us to figure out that the silica supported K/V=0.6 catalyst consists of $K_3V_5O_{14}$ and dispersed vanadium oxide species. More importantly, melting in synthetic air treatment (activation) prior to the reaction caused a formation of polymeric V_xO_y species. In addition, a path-finder experiment showed the wetting phenomena which yielded in a drop in catalytic activity of V/SBA-15 due to the blockage of active centres. With this, the source of catalytic activity and the role of melting were hypothesized.

Due to the fact that the NEXAFS spectroscopy is more surface sensitive technique (Auger yield), V L-edge experiments together with fitting gave more precise information regarding how surface dynamics change under reaction conditions. By combining NEXAFS data and Raman spectroscopy experiments, one can state that there is undoubtedly a change in compositions of surface species with increasing temperature under reaction conditions. The fitting result of the V L_3-edge spectra of the catalyst at 296°C (C_3 feed) suggests the presence of both monomeric and polymeric species (39%=14V/SiO_2 and 47%= 8V/SiO_2) with minor

contribution of KV_3O_8 (14%) (Figure 24B). The Raman spectrum of the catalyst at the same condition (296°C, C_3) resemble the spectra of $K_3V_5O_{14}$ (50°C, O_2) (Figure 5.24C). However, it is not exactly the same spectra. For instance, V-O-V bending modes of $K_3V_5O_{14}$ (603 and 682 cm^{-1}) was not exist in the supported catalyst. Instead, the band at 660 cm^{-1} was detected. By looking at the spectra of KV_3O_8 and the $K_3V_5O_{14}$ at the position 660 cm^{-1}, one can state that the centred peak at 660 cm^{-1} could be due to the mixed potassium vanadates (Figure 5.24D). It is known that the $K_3V_5O_{14}$ must be already decomposed during synthetic air treatment and the possible decomposition product was defined closest as KV_3O_8 (Figure S1.17).

Moreover, 266 nm laser detected the formation of characteristic of V-O-V bonds (838 cm^{-1}, 2-dimensional vanadium oxide oligomers) upon melting. At this point it must be noted that UV lasers are more surface sensitive[435]. Therefore, defining initial catalyst structure as a mixture of monomeric/polymeric vanadium oxide plus potassium vanadate species is convincing. Upon heating, formation of bulk-like vanadia (47%=V_2O_5) species was found by fitting model (Figure 5.24B) In Raman spectroscopy, crystalline V_2O_5 particles exhibits the typical V=O1 mode at 997 cm^{-1} [356, 407, 415]. Here in the Raman spectrum, no significant change was seen with increasing temperature from 404°C to 426°C. However a new mode at 984 cm^{-1} were started forming at 426°C.This can be attributed to the bulk-like vanadia with slight shift in its V=O1 mode due to potassium perturbation[409, 436, 437]. Similarly in our study, some potassium vanadates (compounds (I), (II), and (III)) which includes V_2O_5 as bi-phase exhibited typical V=O mode of bulk V_2O_5 in slightly lower Raman shift compared to bulk V_2O_5 (orange) (Figure 5.24D). Above 426°C, dominancy of $K_3V_5O_{14}$ (25%) and KV_3O_8 (35%) in V L_3-edge of the catalyst was obtained (Figure 5.24B). This is expected since these K-V-O phases melt below 420°C (KV_3O_8 also melts at 418°C). The Raman spectrum of the catalyst *e.g.*, at 450°C completely similar to the spectrum of support-free $K_3V_5O_{14}$ in molten state ($K_3V_5O_{14}$, 410°C O_2, red spectra in Figure 5.24D). Raman modes of KV_3O_8 specifically at 950 and 997 cm^{-1} could be exist in the supported system. However since the amount was expected to be less than 5% (wt. %), the Raman intensity of KV_3O_8 could be very low. Nonetheless, there is a significant enhancement of potassium occurs at the surface.

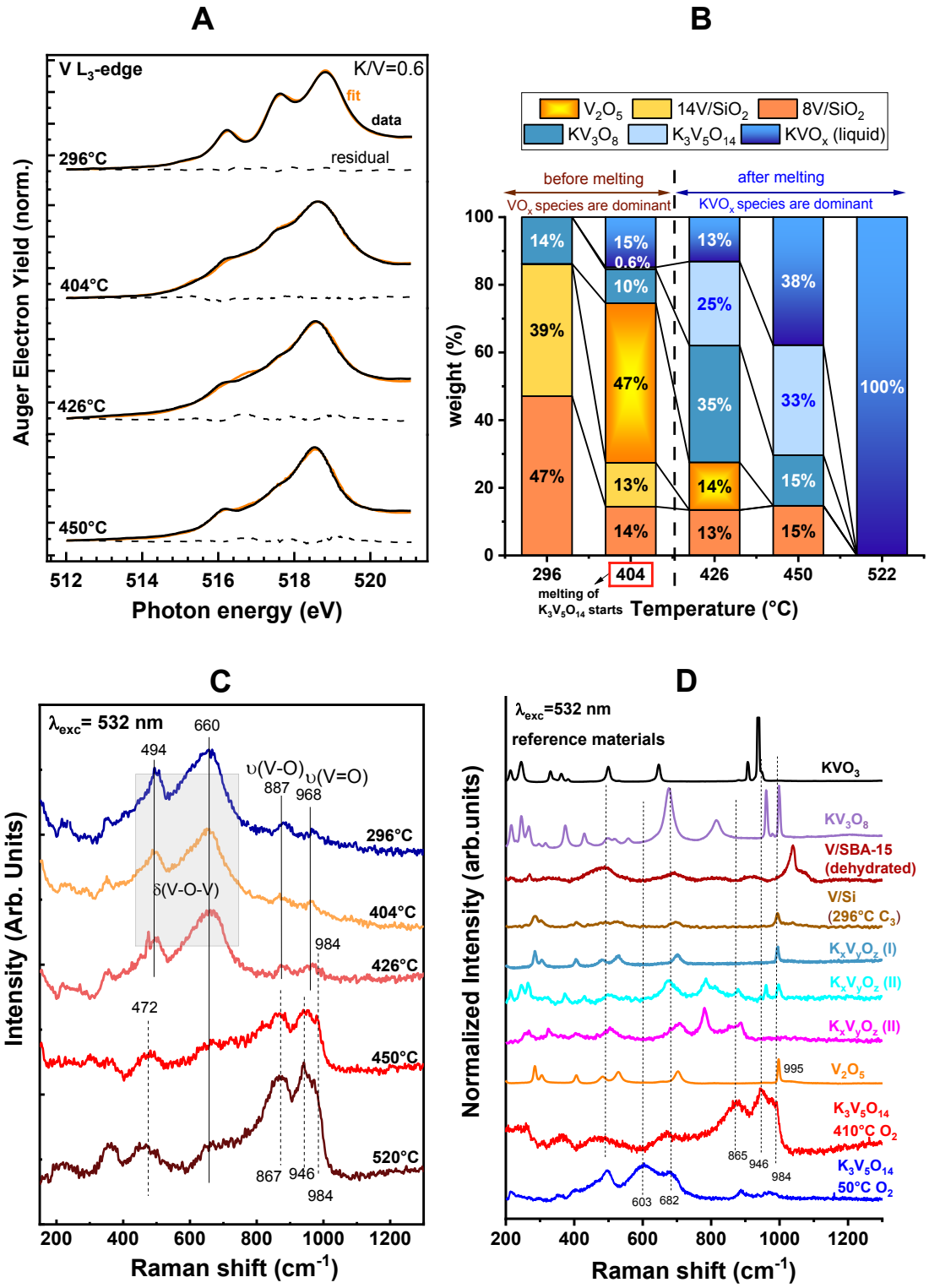

Figure 5.24. (A) V L_3-edge NEXAFS spectra of K/V=0.6 catalyst (experimental vs fit model) **(B)** with fitting results obtained by ATHENA software; **(C)** Raman spectrum of K/V=0.6 catalyst measured at the same temperatures of NEXAFS data and **(D)** Raman spectra of reference compounds (including K-V-O, $K_3V_5O_{14}$, V_2O_5, and V/Si)

Based on all these observations, the catalytic profile of K/V=0.6 catalyst can be finally understood (Figure 5.25). Activated catalyst has much more dispersed vanadia species than $K_3V_5O_{14}$ at the surface. This explained in a way that $K_3V_5O_{14}$ was already melted at the activation step and diffused to the pores and solidifies there upon cooling. At this point, surface sensitive techniques such as NEXAFS could not detect $K_3V_5O_{14}$ anymore but Raman spectroscopy does. The melting of the phase created potassium-deficient vanadates and oligomeric vanadium oxide species due to structural rearrangement. This is the system proposed as active catalyst for propane oxidation.

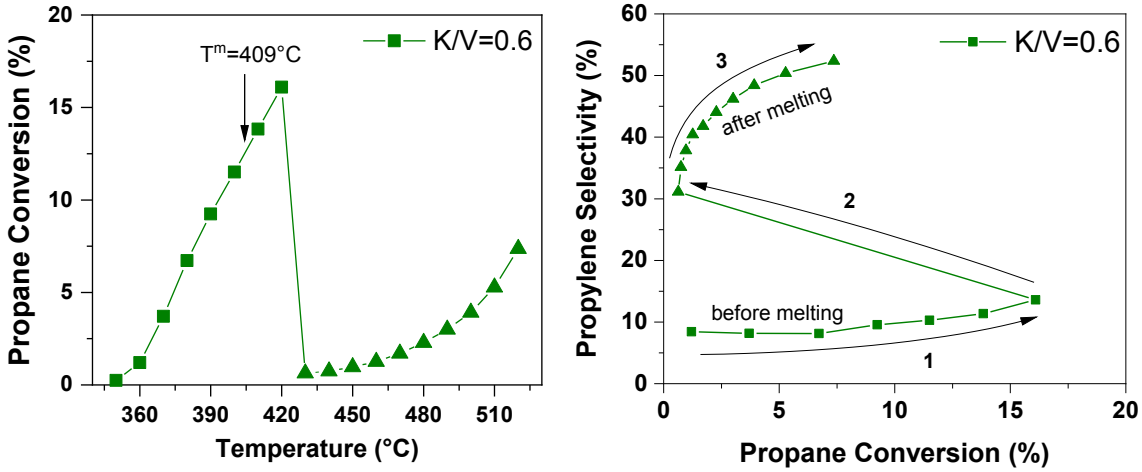

Figure 5.25. Conversion of propane in propane oxidation with increasing temperature, and propylene selectivity as a function of propane conversion (Conditions: T=350°C-520°C, feed $C_3H_8/O_2/N_2$=7.5/7.5/85 vol. %, W/F= 1.8 g s ml^{-1}).

Figure 5.26 shows the proposed representation of silica supported K/V=0.6 catalyst (activated) **before melting** in propane oxidation. The catalyst has activity propane activation due to the existence of supported monomeric/polymeric vanadium oxide species. Upon increasing temperature in propane oxidation, second melting of $K_3V_5O_{14}$ occurs due to the reversible melting of the phase. This leads $K_3V_5O_{14}$ spreads out of the pores and wets the surface. This is the factor which causes a sudden drop in activity by blocking the accessibility of dispersed vanadium oxide species for converting propane to propylene. The increase in selectivity is due to the prevention of consecutive over-oxidation of propylene due to the liquid layer. Proposed representation of silica supported K/V=0.6 catalyst (activated) **after melting** in propane oxidation is shown in Figure 5.27.

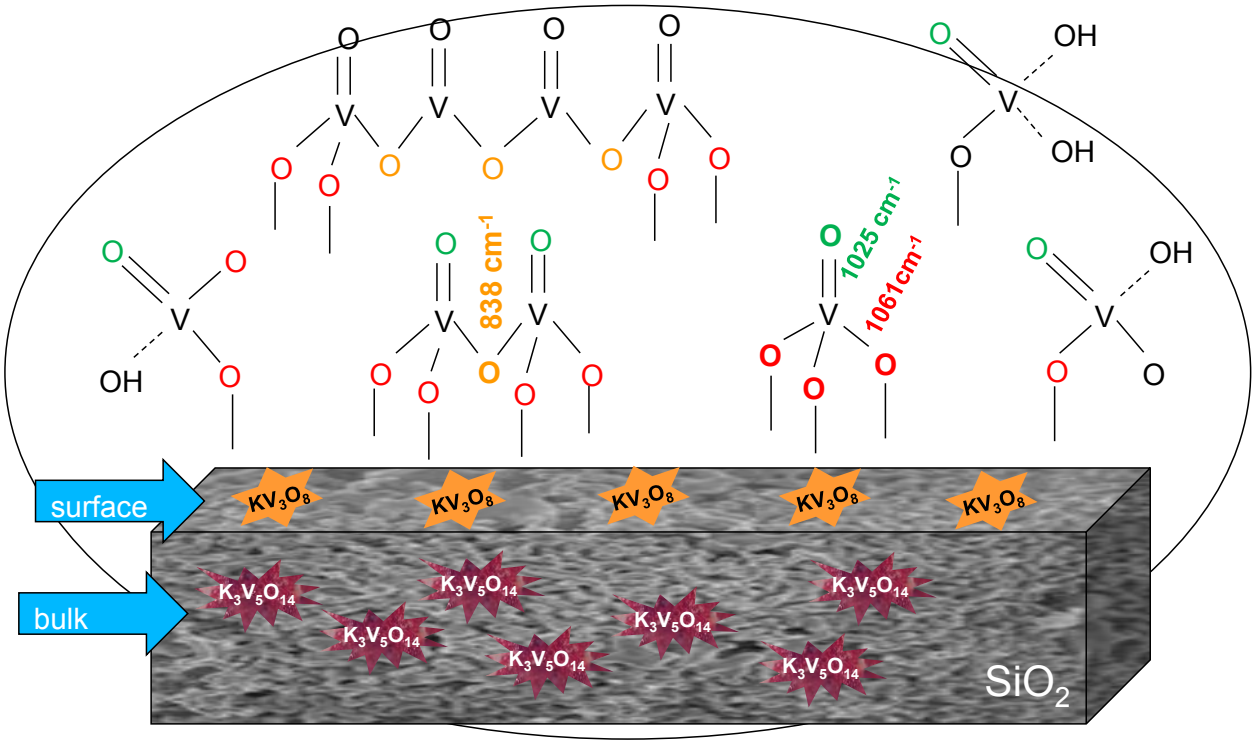

Figure 5.26. Schematic representation of silica supported K/V=0.6 catalyst (activated) **before melting**

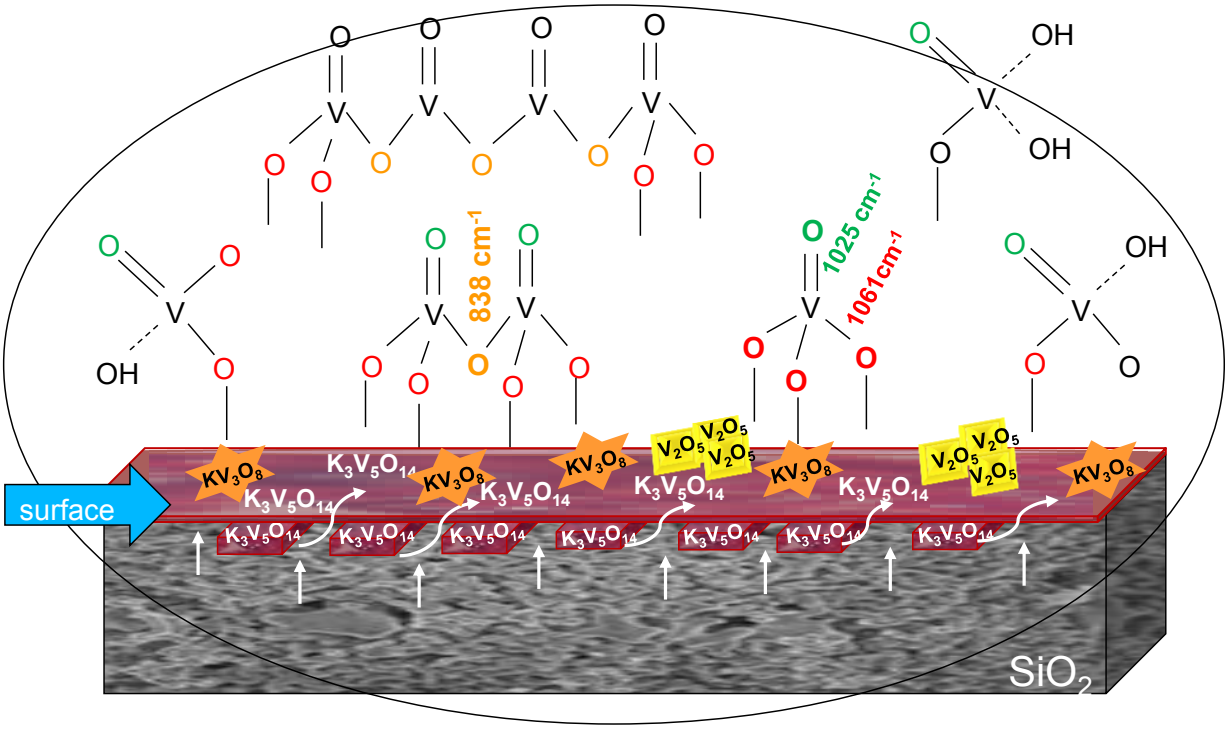

Figure 5.27. Schematic representation of silica supported K/V=0.6 catalyst (activated) **after melting**

Drop in activity and increase in selectivity to propylene was found to be a "general phenomenon" for catalysts who show melting under applied reaction conditions. Based on V $L_{3,2}$-edge measurements for all A/V (A: alkali) with similar A: V ratio, it can be stated that similar changes occurs on the electronic structure on vanadia for catalysts who show melting (K/V, Rb/V, and Cs/V) whereas almost no change occurred for systems who show no melting (Li/V, and Na/V). More information regarding operando V L_3-edge of silica supported A/V (Li, Na, Rb, and Cs) catalysts can be found in Chapter S4.

6. Thesis Summary and Final Conclusion

The impact of alkali addition and the melting behaviour of alkali-vanadate(s) on the surface dynamics on silica supported vanadium oxide catalyst was studied in oxidative dehydrogenation of propane. Li, Na, K, Rb, and Cs additives with a variation of alkali to vanadium ratio between 0.2 and 0.9 (at.) was used. This range was selected in purpose since phase transitions were expected under applied propane oxidation conditions based on phase diagrams. Summary of major findings of the thesis are as follows:

- Independently from the type of alkali, specific surface areas of calcined catalysts were significantly decreased compared to supported vanadium oxide catalyst. The most dramatic effect was found upon potassium addition. The highest surface area was obtained for Li addition and decreases in the order Li > Cs > Rb > Na > K. Within the series of each alkali, those values were found to be varied based on alkali to vanadium ratio.
- Crystalline alkali vanadate phases were formed as detected by XRD. Deviation from the original phase diagram of A_2O-V_2O_5 systems is attributed to the impact of silica on the phase formation. Beyond XRD, ex situ Raman spectroscopy confirmed formation of alkali-vanadate phases. The formation of alkali vanadates in catalysts where K, Rb, and Cs added were distinguishable in SEM images since these phases melts and solidifies on the surface.
- One of the most important characterization methods was thermal analysis (DSC). Alkali addition caused a substantial decrease in melting temperatures compared to the supported vanadia catalyst. The highest melting temperature was obtained for Li≈ Na and decreases in the following order Li≈ Na > Cs> K> Rb.
- The impact of melting of surface alkali-vanadate phases were studied in oxidative dehydrogenation of propane. Li and Na containing catalysts showed no melting whereas K, Rb, and Cs showed melting under applied reaction conditions. This was expected since melting temperatures of Li, and Na containing catalysts were already above the applied reaction temperature range (350-520°C).
- Typical catalytic profile was found for silica supported Li/V and Na/V catalysts, *i.e.*, selectivity to propylene decreased with increasing conversion upon increasing temperature. However peculiar catalytic profile was observed for catalysts which show melting, *namely* silica supported K/V, Rb/V, and Cs/V catalysts. Activity drops, selectivity to propylene increases when melting temperatures were reached.

Higher selectivity to propylene was obtained at the same conversion after liquefaction. This peculiar behaviour was associated with melting of surface A-V-O phases as confirmed by operando DSC experiments.

- Detailed characterization was performed on silica supported K/V=0.6 ($K_3V_5O_{14}/SiO_2$) catalyst to understand the role of melting on the dynamics of surface species which results in drastic change in catalyst performance. For this, support-free $K_3V_5O_{14}$ was deeply studied. The melting of the phase itself on silicon wafer and/or physical mixture with Aerosil 300 proofed that the behaviour of melting is wetting. Moreover, three cycles of heating and cooling experiments with DSC showed that $K_3V_5O_{14}$ melts incongruently. Possible decomposition product was suggested as KV_3O_8 (K: V=1:2.5 at.). However, either $K_3V_5O_{14}$ or KV_3O_8 has no activity in ODH of propane.
- A path-finder experiment using V/SBA-15 and $K_3V_5O_{14}$ successfully worked for understanding the role of melting. It was discovered that melting blocked the accessibility of active sites (*i.e.*, inhibition effect of melting on the activity of vanadia species due to the coverage by the melt) and the same catalysis profile of K/V=0.6 catalyst can be obtained. This experiment provided a basis for understanding on the possible function of the melt.
- Operando Raman spectroscopy of silica supported K/V=0.6 catalyst confirmed the melting and structural alteration of $K_3V_5O_{14}$ (532 nm laser). More interestingly, melting initiated the formation of dispersed oligomeric vanadium oxide species (266 nm laser). Since support-free $K_3V_5O_{14}$ has no activity in ODP the mixture of monomeric/polymeric vanadium oxides were defined as active for propane oxidation.
- NAP-NEXAFS experiments were extremely needed to investigate the dynamic changes on the electronic structure of vanadium under reaction conditions upon melting. Since either Raman spectroscopy or NAP-NEXAFS is not sufficient alone complimentary study using these two advanced techniques was applied.
- The in situ V L_3- edge of K/V=0.6 under ODH of propane (at 250 Pa) showed considerable difference before and after melting temperature of $K_3V_5O_{14}$. It was undoubtedly a change in distribution of species due to melting. Each spectra at different temperature (below and above melting) were analysed by spectra fitting (LCA) using ATHENA (Demeter) software. Results showed that catalyst has much more dispersed mixture of monomeric/oligomeric vanadia species than $K_3V_5O_{14}$ at

the surface which is in agreement with 266 nm laser findings. However minor contributions from $K_3V_5O_{14}$ and KV_3O_8 were also found before melting (<426°C). Upon increasing temperature in propane oxidation, melting of $K_3V_5O_{14}$ occurred as detected an increase in K-enhancement at the surface by K L-edge measurements as well. That means $K_3V_5O_{14}$ wets the surface. This mobility of the melt led a sudden drop in activity by blocking the accessibility of dispersed vanadium oxide species for converting propane to propylene. The significant decrease in porosity due to the blockage by the melt was observed over catalysts which show melting (*e.g.*, see Figure S2.6 and S2.7)

- The increase in selectivity might be related to the prevention of consecutive overoxidation of propylene due to the coverage of active sites by the melt. In addition, the change in reaction network before and after melting by eliminating the unselective reaction pathway occurs. Product distribution analysis supports this in a way a sudden decrease in selectivity to carbon oxides when temperature was above the melting (*e.g.,* see Figure S2.3). Moreover, liquefaction may initiate radicals in which catalyst generates alkyl fragments to produce olefins in the gas phase. A slight increase in selectivity to propylene was also observed over support-free $K_3V_5O_{14}$ when the catalyst was completely molten (Figure S2.9).

Overall, the thesis provided a knowledge on the control of activity and selectivity to propylene upon alkali addition. It is a "general phenomenon" that activity drops and selectivity increases if melting of alkali-vanadate phases occur under applied reaction conditions. Combining powerful characterization techniques such as DSC, Raman, and NAP-NEXAFS spectroscopy under reaction conditions, the impact of melting of surface alkali-vanadate phases on the catalytic activity of vanadium oxide species were unravelled. Most of the alkali-vanadates has no activity in ODH of propane however mobility of these phases due to melting has a great impact on the reaction kinetics. The melting of A-V-O, in which the strain is lost, inhibits the reactivity of surface vanadium oxide species. Therefore the study underlines the importance of the coordination environment of the active phase is a critical issue that needs to be controlled, notably when alkali additives are used.

7. Acknowledgements

This study is based upon collaborative work between Fritz-Haber-Institut der Max-Planck-Gesellschaft (https://www.fhi.mpg.de), BasCat- UniCat BASF Joint Lab https://www.bascat.tu-berlin.de/bascat/menue/bascat) and Technical University Berlin https://www.tu.berlin/en/faculty-ii-mathematics-and-natural-sciences). I appreciate all colleagues at AC department for their help on conducting experiments, training for setups, and as well as for their valuable scientific discussions.

Scientific supports who has a contribution to this PhD work are listed below:

Chemical and Technical Support	Jasmin Allan, Sven Richter, Rania Hanna, Daniel Brennecke, Dr. Gregor Koch, Dr. Pierre Kube
Phase Composition (XRD)	Dr. Frank Girgsdies
Chemical Composition (XRF, ICP-OES)	Dr. Olaf Timpe
Surface area (BET)	Maike Hashagen
Catalyst Morphology (SEM, TEM, ESEM)	Danail Ivanov, Dr. Milivoj Plodinec, Dr. Luis Ernesto Sandoval Diaz, Dr. Gregor Koch, Wiebke Frandsen
Optical Microscope	Danail Ivanov, Dr. Milivoj Plodinec
Thermal Analysis (TG-DTA, DSC)	Jasmin Allan, Dr. Andrey Tarasov
Catalytic Testing and Gas Chromatography	Dr. Pierre Kube
Raman Spectroscopy	Dr. Yuanqing Wang, Dr. Gregory Huff
DFT Calculation (PP&B)	Dr. Yuanqing Wang
X-ray Photoelectron Spectroscopy (XPS)	Dr. Spencer Carey, Dr. Detre Teschner
X-ray Absorption Spectroscopy (NEXAFS)	Dr. Michael Hävecker
Discussions	Dr. Pierre Kube, Dr. Andrey Tarasov, Dr. Gregor Koch, Dr. Yuanqing Wang, Dr. Gregory Huff, Dr. Spencer Carey, and Dr. Michael Hävecker
Writing and Language Support	Dr. Gregory Huff, and Dr. Spencer Carey
Scientific Advisory Board	Dr. Frank Rosowski (BasCat, BASF SE) Dr. Annette Trunschke (FHI) Prof. Robert Schlögl (FHI)

8. Outlook

Based on knowledge gained within this four and half years of PhD study, one could consider to improve some aspects of the project and propose a new study. Suggestions are explained in the following.

8.1. Support Variation

The amount of potassium in the alkali vanadate phase decreases after melting since potassium sinks in the silica. Therefore the sufficient amount of alkali-vanadate could not be reached. The formation of K-silicate was also found by SEM-EDS analysis on glassy molten surface (Figure S19). To overcome with this, support as an insulator such as β-alumina can be evaluated instead of SiO_2 as semi-conductor. As a parallel to this PhD study, potassiuam-containing vanadium oxide on various supports were tested as well. These supports were CeO_2, ZrO_2, TiO_2, BN, δ-alumina, α-alumina, and MgKAl (Puralox). Moreover, β-alumina (2x2 cm, thin-walled ceramic disks from IONOTEC LIMITED, UK) were obtained. After grinding the beta-alumina in a mortar, powder form was obtained. Spray drying and calcination followed by catalytic activity measurements were conducted (synthesized by research intern, Charles Pare (TUM)). To give an idea for future studies, initially obtained catalytic results of potassium-containing vanadia catalysts (fixed K: V at. %) on different supports are shown in Figure 8.1.

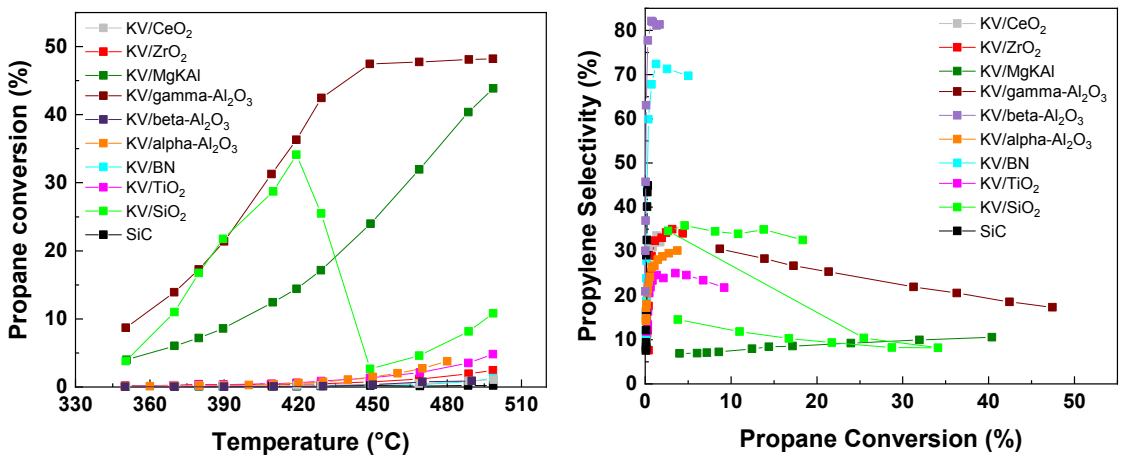

Figure 8.1. Conversion of propane in propane oxidation with increasing temperature, and propylene selectivity as a function of propane conversion (Conditions: T=350°C-520°C, feed $C_3H_8/O_2/N_2$=7.5/7.5/85 vol. %, W/F= 1.8 g s ml^{-1}, 8-fold parallel reactor "Grimsel 2")

Although melting of potassium vanadate occurs on CeO_2, ZrO_2, TiO_2, and α-alumina support, drop in activity was not seen due to the very low conversion. The homogeneous gas-phase

reactions was observed over BN and β-alumina supported catalysts which results more than 70% selectivity to propylene at ~1-2% propane conversion. On the other hand, δ-alumina and MgKAl (Puralox) supports seems promising for further studies.

8.2. Alkali-vanadate(s) as thermal- and electro-catalyst

In this study, the formation of alkali-vanadate phase(s) such as $K_3V_5O_{14}$, $Rb_2V_4O_{11}$, and CsV_2O_5 was detected beyond amorphous SiO_2 by XRD. Vanadates itself have been attractive for rechargeable battery technologies[438]. In the class of alkali metal vanadates, potassium vanadates have been frequently studied as an electrode material [439, 440]. For instance, a remarkable specific capacity which is at about 210 mAh g^{-1} were found for KV_5O_{13} as well as for $K_2V_8O_{21}$ (190 mAh g^{-1}) while the KV_3O_8 (100 mAh g^{-1}) and $K_3V_5O_{14}$ (50 mAh g^{-1}) capacities remained far too low for positive electrodes[439]. A significant improvement of the capacity of KV_3O_8 to 249 mAh g^{-1} were later achieved[441] by ball-mixing of as-received KV_3O_8, which results in particle size reduction with an increase in the surface area from 2.6 m^2g^{-1} to 33.2 m^2g^{-1}. In another study, LiV_3O_8 and NaV_3O_8 resulted in much better electrochemical properties in comparison to KV_3O_8 (potassium trivanadate) [442]. In that case authors postulated the large K ions could hinder some pathways for lithium transferring, resulting in poor electrochemical activity. Therefore, potassium deficient vanadates were suggested as a strategy for Li- ion transfer. With this regard, $K_{0.66}V_3O_8$ were found well-promising with a discharge capacity of 268.9 mAh g^{-1} (reversible capacity of 197.5 mAh g^{-1} after 25 cycles)[442].

In this project, potassium-rich vanadates such as KV_3O_8, $K_3V_5O_{14}$ as well as $K_2V_8O_{21}$ were tested in oxidative dehydrogenation of propane. No catalytic activity was found under applied conditions. On the other hand, potassium-vanadate systems with systematically reduced potassium content were also synthesized. The whole list of reduced potassium-vanadate phase(s) synthesized was presented in Table 5.3. Interestingly, non-stoichiometric phases with reduced potassium content showed higher activity compared to potassium-rich vanadates (Figure 8.2).

Based on discussions and studies above, potassium-rich alkali-metal vanadate systems is proposed to have higher potential to be used as an electrode rather than oxidation catalyst. On the other hand, potassium-deficient systems can be used to study both (thermally and electrochemically) since the impact (improved activity) seems similar. It is agreed that the electrode material for battery systems is still unsatisfactory within the existence research. Therefore, the alkali-vanadates synthesized in this study has been suggested as a basis for

collaboration for possible future project. A reaction which can studied in both electrochemical cell and the plug flow reactor is a must. For instance, performance of potassium-deficient vanadates in CO_2 reduction (e.g. reverse water gas shift reaction and electrochemical CO_2 reduction, CO_2R) can be evaluated as a test reaction.

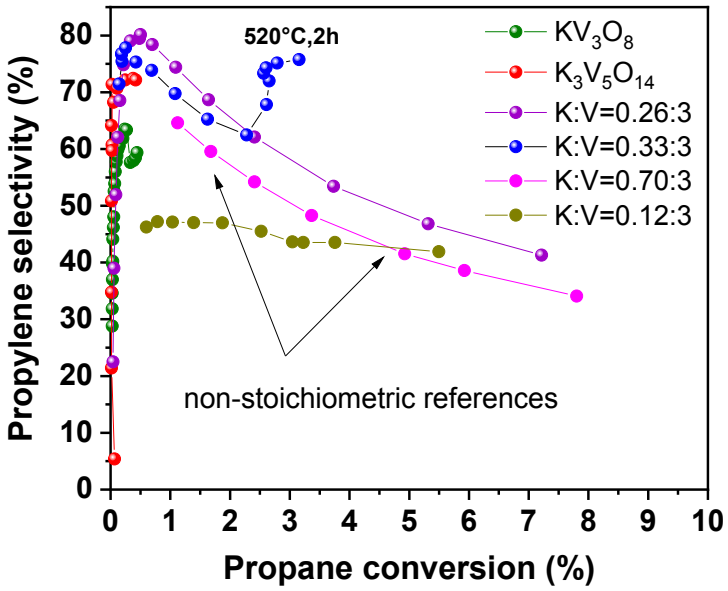

Figure 8.2. Conversion of propane in propane oxidation with increasing temperature, and propylene selectivity as a function of propane conversion over stoichiometric and un-stoichiometric KVO_x catalysts (Conditions: T=350°C-520°C, feed $C_3H_8/O_2/N_2$=7.5/7.5/85 vol. %, W/F= 1.8 g s ml^{-1}

Supporting Information

S1 .Chemical, Morphological, and Thermal Properties of Catalysts

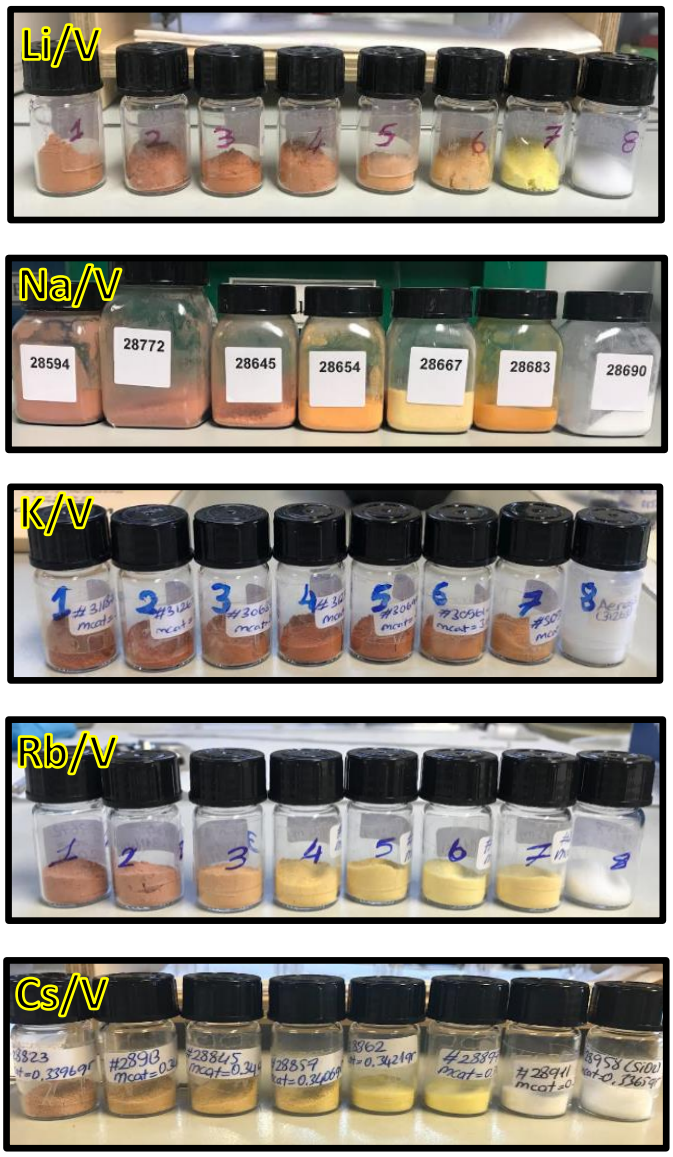

Figure S1.1. Silica supported Li, Na, K, Rb and Cs/V catalysts (color changes from dark salmon to yellow with increasing alkali content from left to right)

Morphology of silica supported Li/V catalysts:

The representative SEM images of silica supported Li/V catalysts with different ratio of Li: V are presented in Figure S1.2.

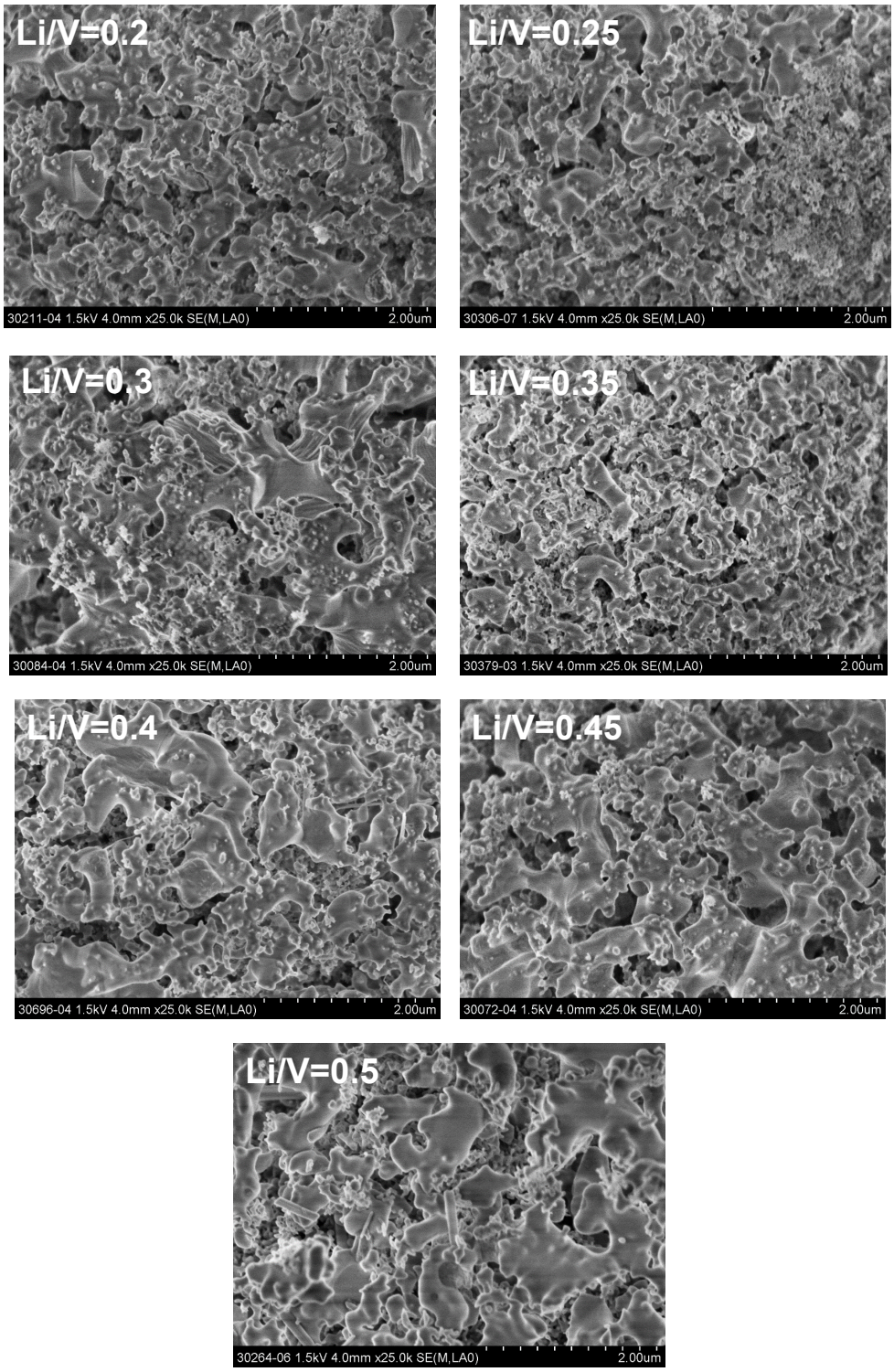

Figure S1.2. SEM images of silica supported Li/V catalysts

Morphology of silica supported Na/V catalysts:

The representative SEM images of silica supported Na/V catalysts with different ratio of Na: V are presented in Figure S1.3.

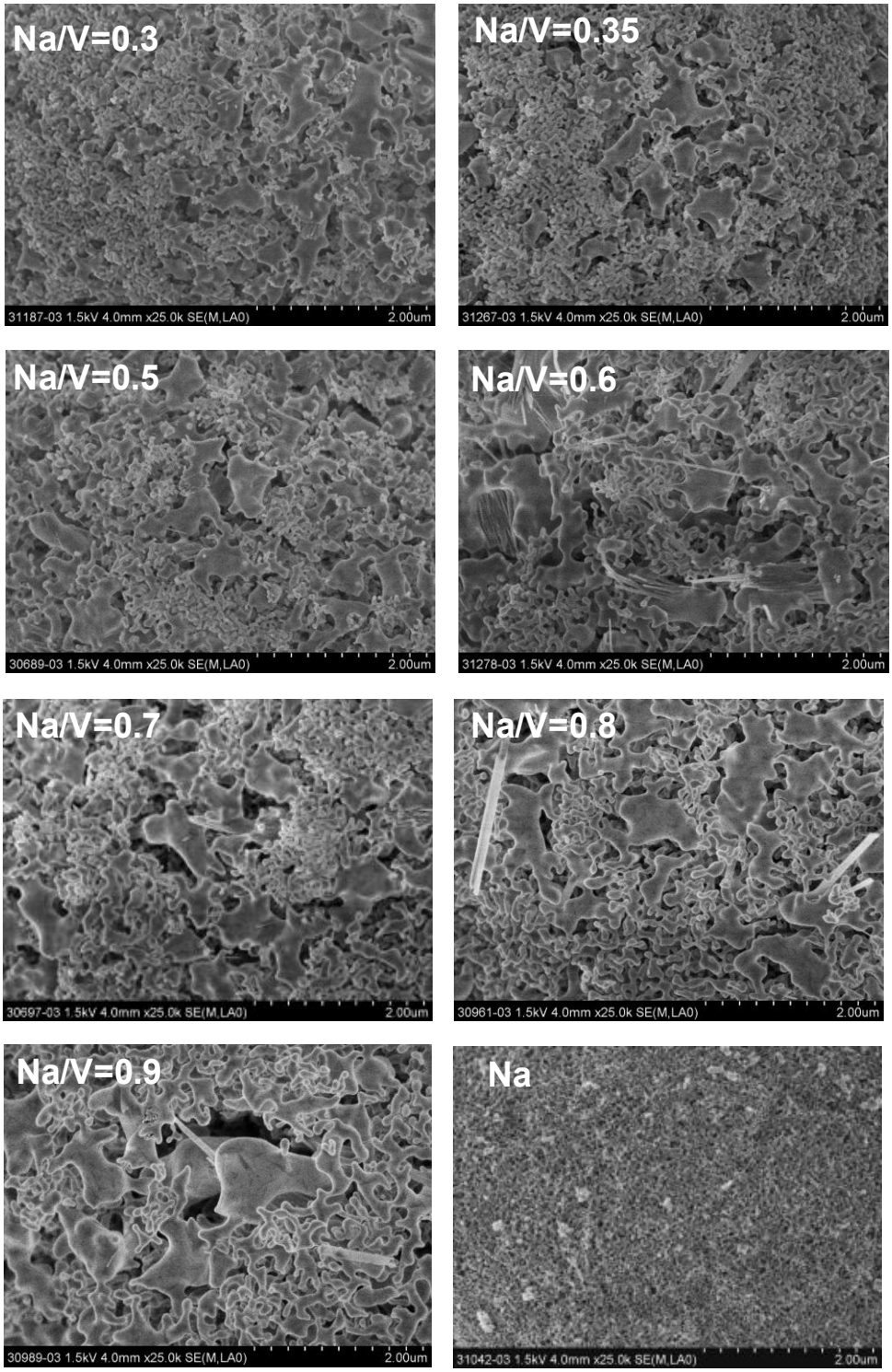

Figure S1.3. SEM images of silica supported Na/V catalysts

Morphology of silica supported K/V catalysts:

The representative SEM images of silica supported K/V catalysts with different ratio of K: V are presented in Figure S1.4.

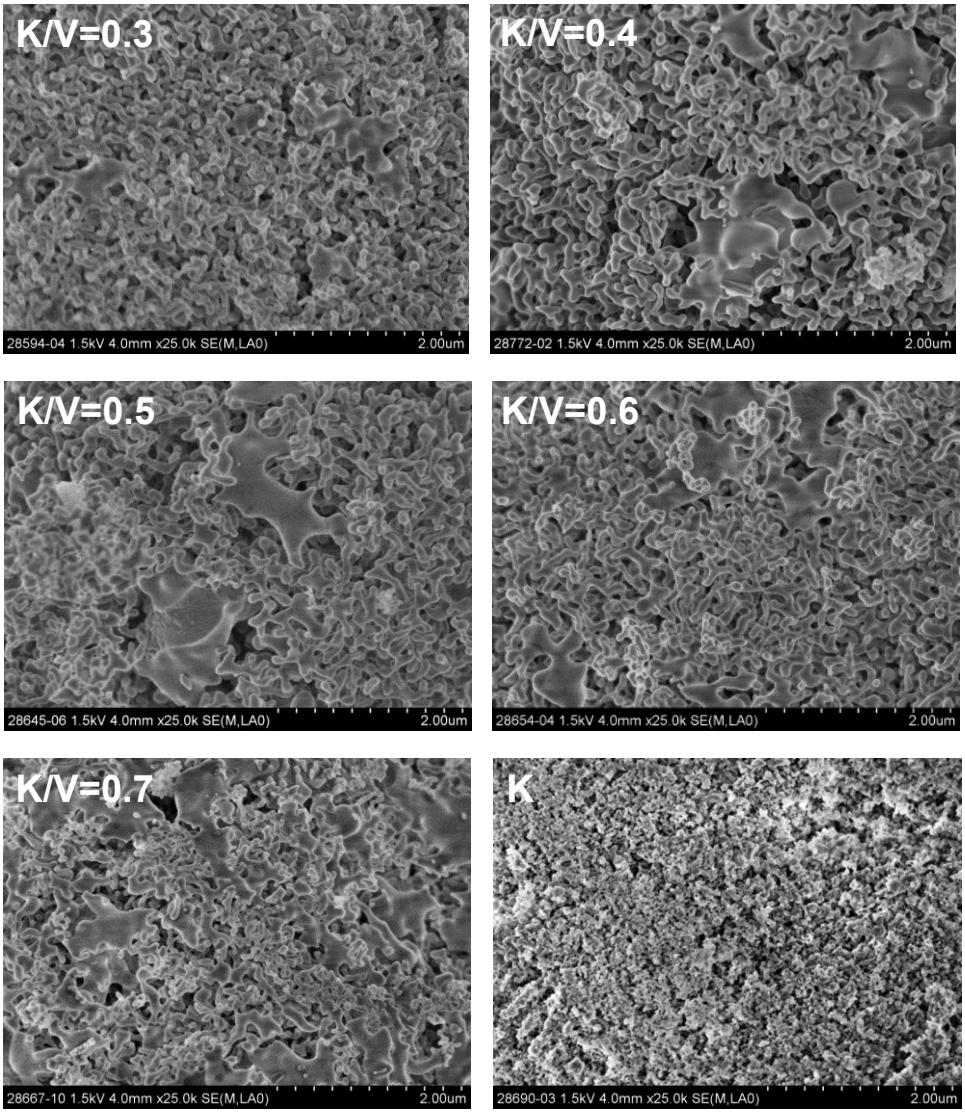

Figure S1.4. SEM images of silica supported K/V catalysts

Morphology of silica supported Rb/V catalysts:

The representative SEM images of silica supported Rb/V catalysts with different ratio of Rb: V are presented in Figure S1.5.

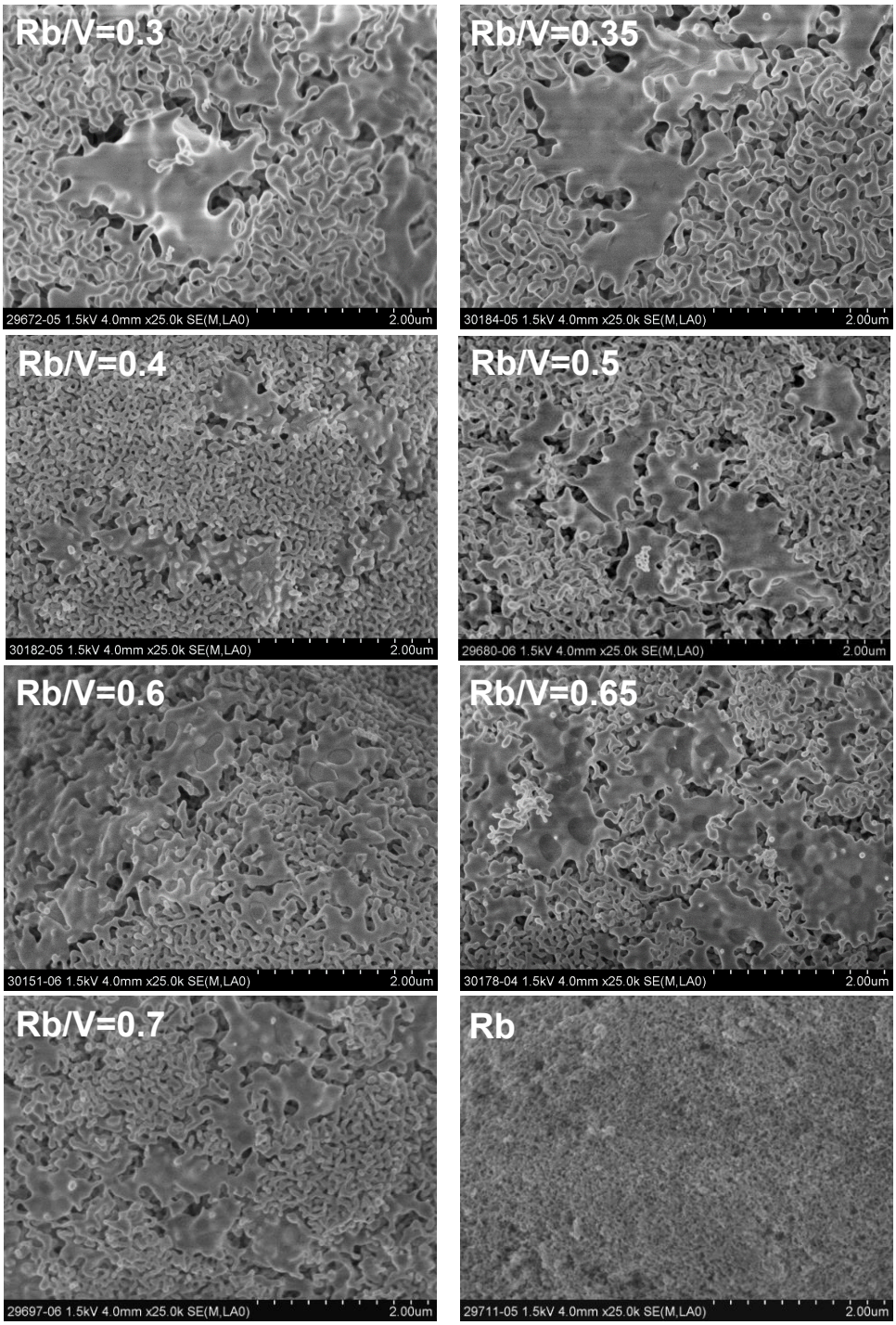

Figure S1.5. SEM images of silica supported Rb/V catalysts

Morphology of silica supported Cs/V catalysts:

The representative SEM images of silica supported Cs/V catalysts with different ratio of Cs: V are presented in Figure S1.6.

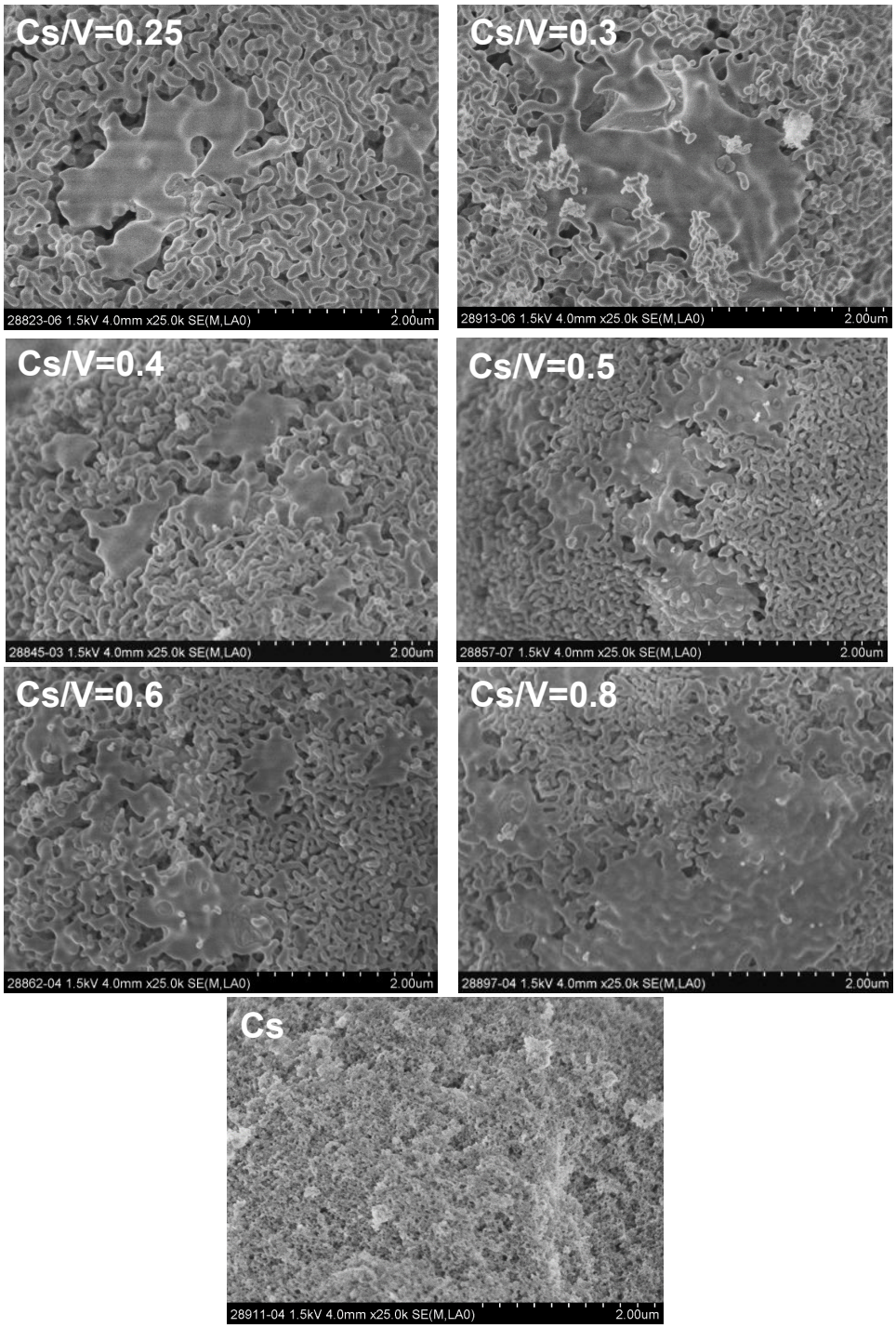

Figure S1.6. SEM images of silica supported Cs/V catalysts

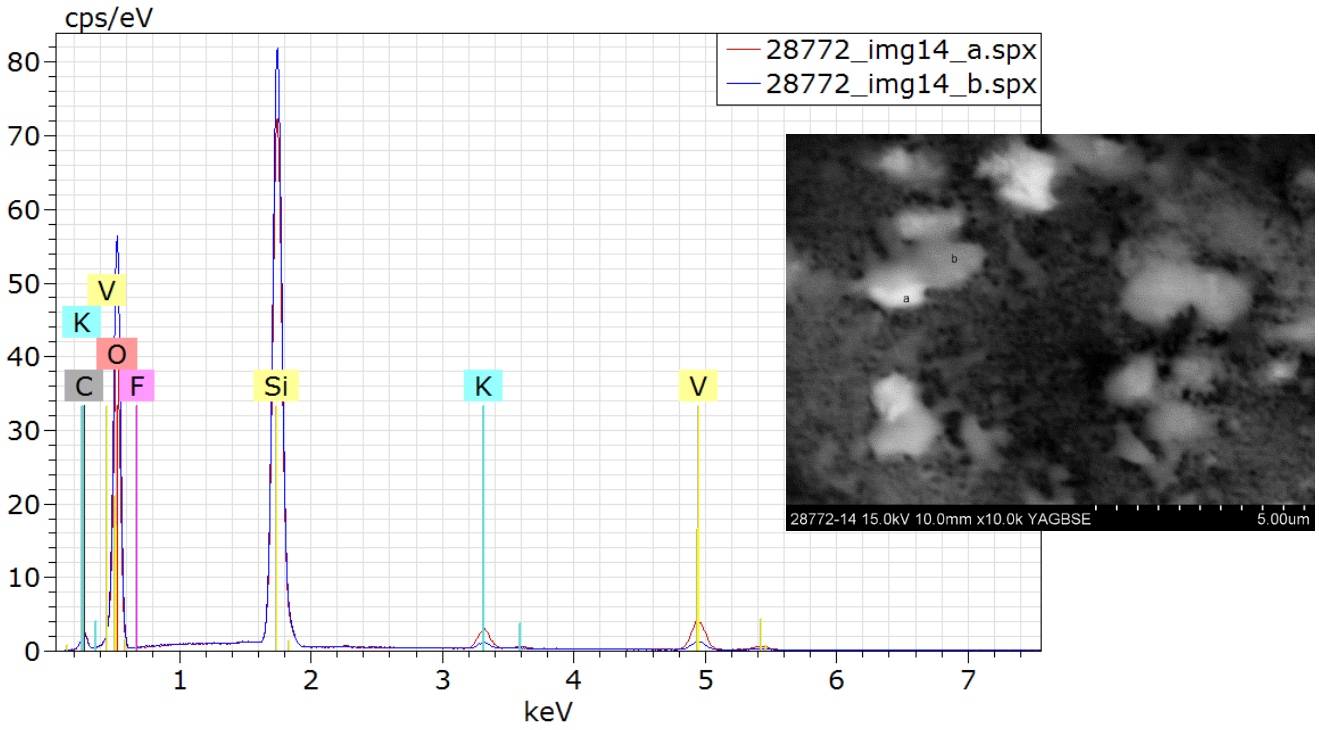

Figure S1.7. SEM image of catalyst K/V=0.4 with YAG-BSE detector (internal ID=#28772)

Thermal behavior of silica supported Li/V catalysts measured by DSC:

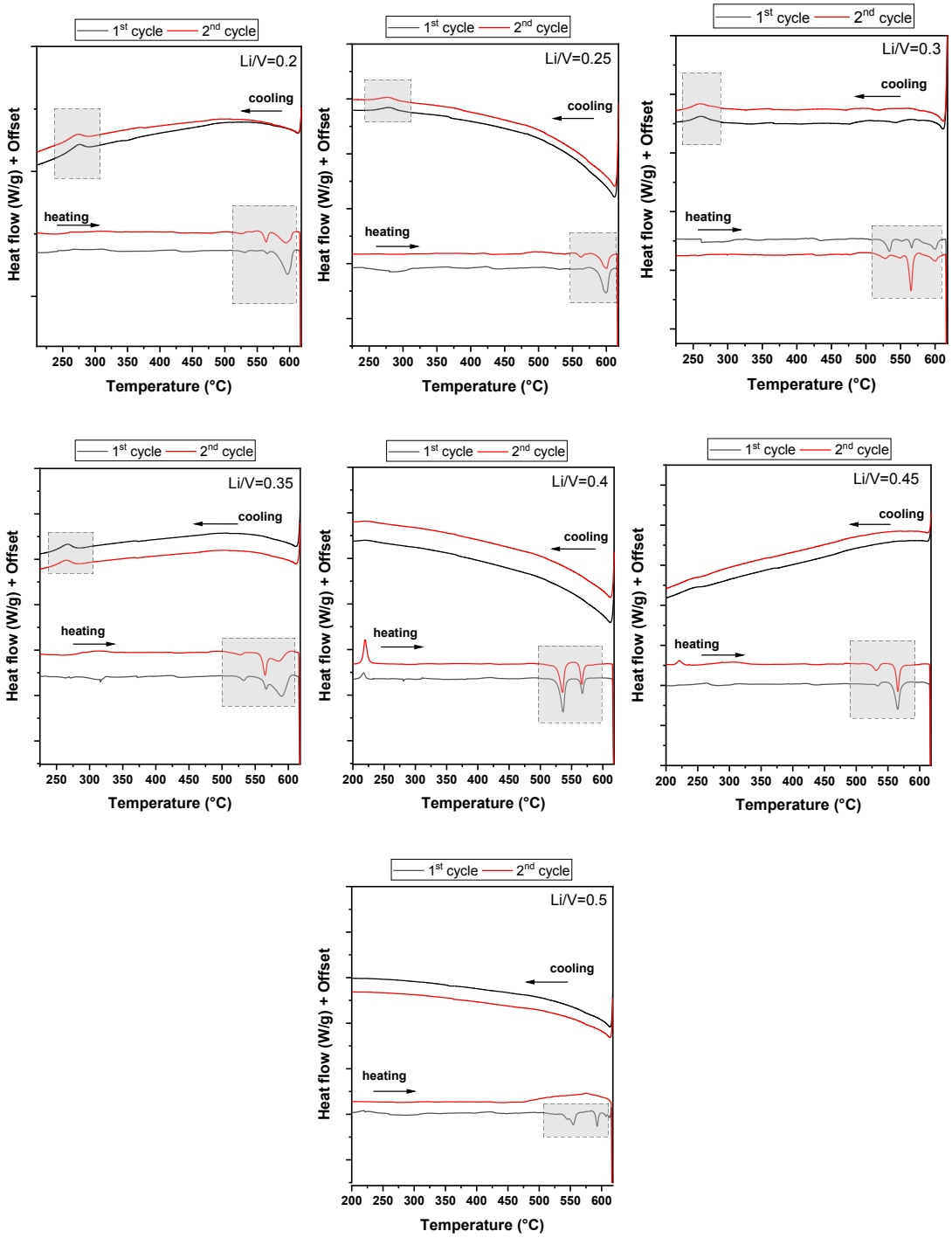

Figure S1.8. DSC profiles of silica supported Li/V catalysts under 21%O_2/ 79% Ar with a flow of 50 ml/min, heating rate: 10 Kpm, cooling rate: 5 Kpm in an alumina crucible with lid. (2 heating and 2 cooling were applied)

Table S 1.1. Peak data of silica supported Li/V catalysts measured by DSC (Figure S1.8)

Li/V	Cycle and peak info		T^{onset} (°C)	T^{peak} (°C)	Peak area (J/g)
0.2	1st cycle	1st peak	528.28	532.20	0.037
		2nd peak	561.09	565.37	0.28
		3rd peak	588.25	597.50	1.97
	2nd cycle	1st peak	513.55	525.69	0.75
		2nd peak	557.10	563.67	2.06
		3rd peak	584.48	596.67	1.73
0.25	1st cycle	1st peak	559.72	565.29	0.13
		2nd peak	591.37	600.07	2.94
	2nd cycle	1st peak	555.55	562.63	0.85
		2nd peak	589.39	600.59	2.95
0.3	1st cycle	1st peak	525.74	533.96	2.17
		2nd peak	562.05	566.11	0.98
		3rd peak	592.38	600.40	1.22
	2nd cycle	1st peak	515.87	527.69	0.88
		2nd peak	559.95	565.28	4.48
		3rd peak	586.39	600.60	0.65
0.35	1st cycle	1st peak	524.3	532.8	1.06
		2nd peak	579.9	591.6	3.18
		3rd peak	562.0	566.2	1.07
	2nd cycle	1st peak	518.6	527.8	0.42
		2nd peak	559.5	564.8	2.68
		3rd peak	575.8	586.5	0.87
0.4	1st peak	1st peak	528.15	536.26	7.57
		2nd peak	563.09	567.11	1.96
	2nd peak	1st peak	527.29	535.31	6.37
		2nd peak	562.09	566.47	2.95
0.45	1st peak	1st peak	529.03	534.70	0.42
		2nd peak	557.52	565.49	7.23
	2nd peak	1st peak	523.28	531.35	2.29
		2nd peak	561.24	565.64	4.45
0.5	1st cycle	1st peak	545.78	554.64	3.37
		2nd peak	589.36	592.79	1.69
	2nd cycle	No melting			

Thermal behavior of silica supported Na/V catalysts measured by DSC:

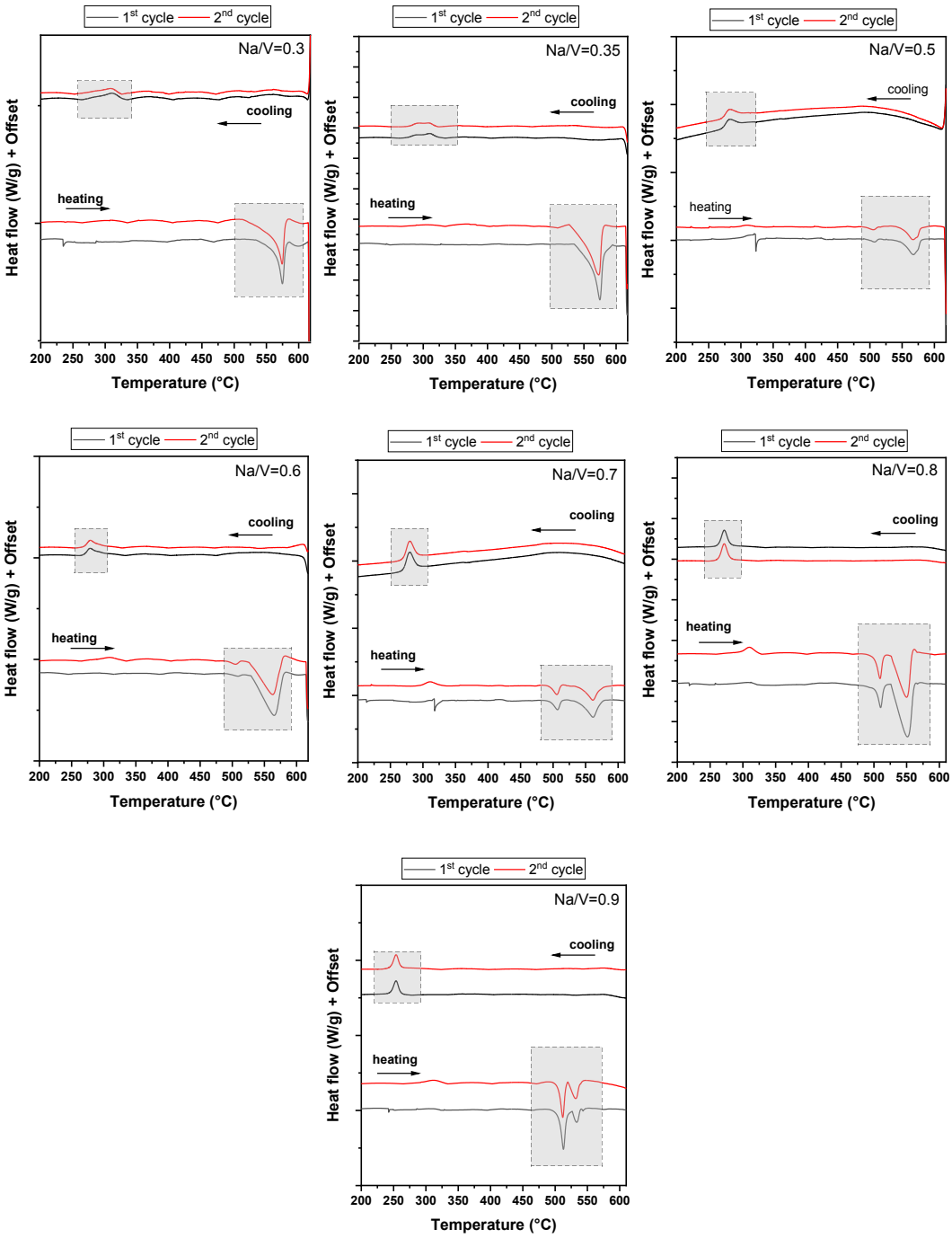

Figure S1.9. DSC profiles of silica supported Na/V catalysts under 21%O2/ 79% Ar with a flow of 50 ml/min, heating rate: 10 Kpm, cooling rate: 5 Kpm in an alumina crucible with lid. (2 heating and 2 cooling were applied)

Table S1.2. Peak data of silica supported Na/V catalysts measured by DSC (Figure S1.9)

Na/V	Cycle and peak info		T^{onset} (°C)	T^{peak} (°C)	Peak area (J/g)
0.3	1st cycle	1st peak	565.06	574.86	11.99
	2nd cycle	1st peak	563.67	574.44	10.88
0.35	1st cycle	1st peak	561.87	574.82	26.53
	2nd cycle	1st peak	550.86	573.20	33.62
0.5	1st cycle	1st peak	499.44	507.62	0.36
		2nd peak	551.13	567.60	4.85
	2nd cycle	1st peak	493.35	505.60	0.60
		2nd peak	551.88	567.41	3.72
0.6	1st cycle	1st peak	531.4	565.8	30.7
	2nd cycle	1st peak	529.9	563.6	24.3
0.7	1st peak	1st peak	494.7	506.9	2.21
		2nd peak	543.5	561.4	4.76
	2nd peak	1st peak	492.8	505.8	2.86
		2nd peak	545.1	561.1	4.27
0.8	1st peak	1st peak	503.6	510.3	3.8
		2nd peak	523.1	551.9	31.0
	2nd peak	1st peak	501.3	509.3	5.9
		2nd peak	531.5	551.0	16.3
0.9	1st cycle	1st peak	503.1	512.8	59.7
	2nd cycle	1st peak	502.3	511.9	52.4

Thermal behavior of silica supported K/V catalysts measured by DSC:

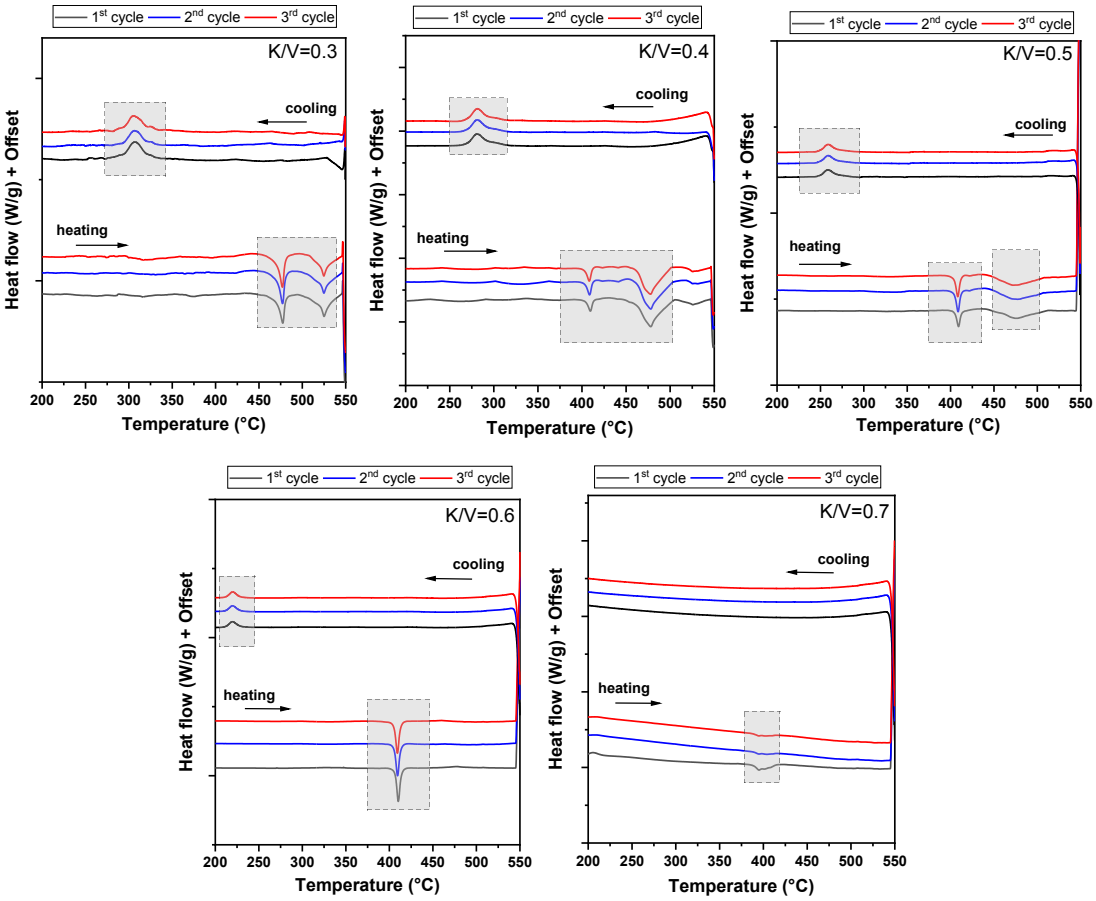

Figure S1.10. DSC profiles of silica supported K/V catalysts under 21%O_2/ 79% Ar with a flow of 50 ml/min, heating rate: 10 Kpm, cooling rate: 5 Kpm in an alumina crucible with lid. (Three heating and three cooling were applied)

Table S1.3. Peak data of silica supported K/V catalysts measured by DSC (Figure S1.10)

K/V	Cycle and peak info		T^{onset} (°C)	T^{peak} (°C)	Peak area (J/g)
0.3	1st cycle	1st peak	470.8	477.5	2.18
		2nd peak	521.0	525.0	0.67
	2nd cycle	1st peak	470.0	477.1	2.15
		2nd peak	519.1	524.8	0.43
	3rd cycle	1st peak	469.9	476.9	2.20
		2nd peak	519.8	524.8	0.79
0.4	1st cycle	1st peak	404.7	409.5	1.35
		2nd peak	466.4	478.0	6.95
	2nd cycle	1st peak	403.5	408.5	1.81
		2nd peak	466.2	478.3	5.56
	3rd cycle	1st peak	403.1	408.2	1.71
		2nd peak	470.5	478.0	5.86
0.5	1st cycle	1st peak	404.75	409.05	3.24
	2nd cycle	1st peak	404.14	408.73	4.70
	3rd cycle	1st peak	403.92	408.23	3.96
0.6	1st cycle	1st peak	406.6	410.2	7.63
	2nd cycle	1st peak	405.5	409.4	7.80
	3rd cycle	1st peak	405.3	409.2	7.46
0.7	1st peak	1st peak	387.2	394.79	3.72
	2nd peak	1st peak	387.12	394.81	0.18
	3rd cycle	1st peak	387.08	394.65	0.60

Thermal behavior of silica supported Rb/V catalysts measured by DSC:

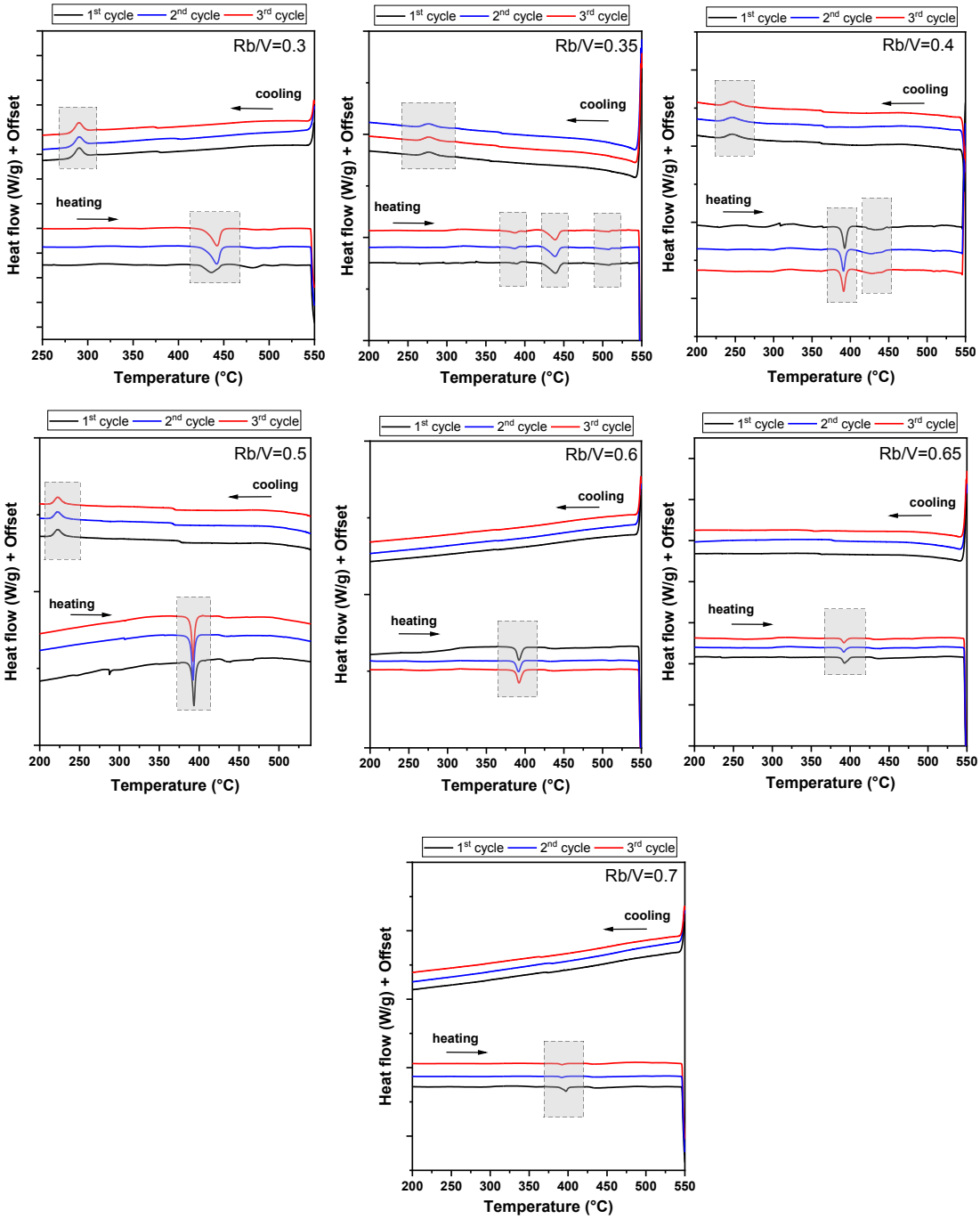

Figure S1.11. DSC profiles of silica supported Rb/V catalysts under 21%O_2/ 79% Ar with a flow of 50 ml/min, heating rate: 10 Kpm, cooling rate: 5 Kpm in an alumina crucible with lid. (Three heating and three cooling were applied)

Table S1.4. Peak data of silica supported Rb/V catalysts measured by DSC (Figure S1.11)

Rb/V	Cycle and peak info		T^{onset} (°C)	T^{peak} (°C)	Peak area (J/g)
0.3	1st cycle	1st peak	422.29	436.05	3.87
		2nd peak	470.16	483.21	0.37
	2nd cycle	1st peak	430.90	442.64	4.76
		2nd peak	474.35	486.18	0.12
	3rd cycle	1st peak	430.22	442.14	5.04
		2nd peak	473.15	483.51	0.13
0.35	1st cycle	1st peak	384.2	389.3	0.48
		2nd peak	425.2	439.3	3.72
		3rd peak	498.8	508.4	0.14
	2nd cycle	1st peak	378.8	387.5	0.41
		2nd peak	422.2	438.8	5.12
		3rd peak	488.8	508.1	0.74
	3rd cycle	1st peak	378.6	386.8	0.41
		2nd peak	424.0	438.3	4.23
		3rd peak	499.5	508.0	0.37
0.4	1st cycle	1st peak	387.60	392.58	2.67
		2nd peak	421.06	431.76	0.28
	2nd cycle	1st peak	386.25	391.21	2.34
		2nd peak	414.15	428.40	0.80
	3rd cycle	1st peak	385.90	391.04	2.34
		2nd peak	413.12	427.06	0.38
0.5	1st cycle	1st peak	389.9	393.3	4.09
	2nd cycle	1st peak	389.1	392.4	4.12
	3rd cycle	1st peak	388.9	392.3	4.16
0.6	1st cycle	1st peak	387.3	392.2	3.50
	2nd cycle	1st peak	386.1	391.5	2.95
	3rd cycle	1st peak	385.8	391.3	2.99
0.65	1st cycle	1st peak	387.85	392.94	1.34
	2nd cycle	1st peak	387.40	392.11	0.84
	3rd cycle	1st peak	387.26	391.94	0.71
0.7	1st peak	1st peak	391.1	397.4	1.39
	2nd peak	1st peak	387.7	392.0	0.32
	3rd cycle	1st peak	387. 0	392.0	0.45

Thermal behavior of silica supported Cs/V catalysts measured by DSC:

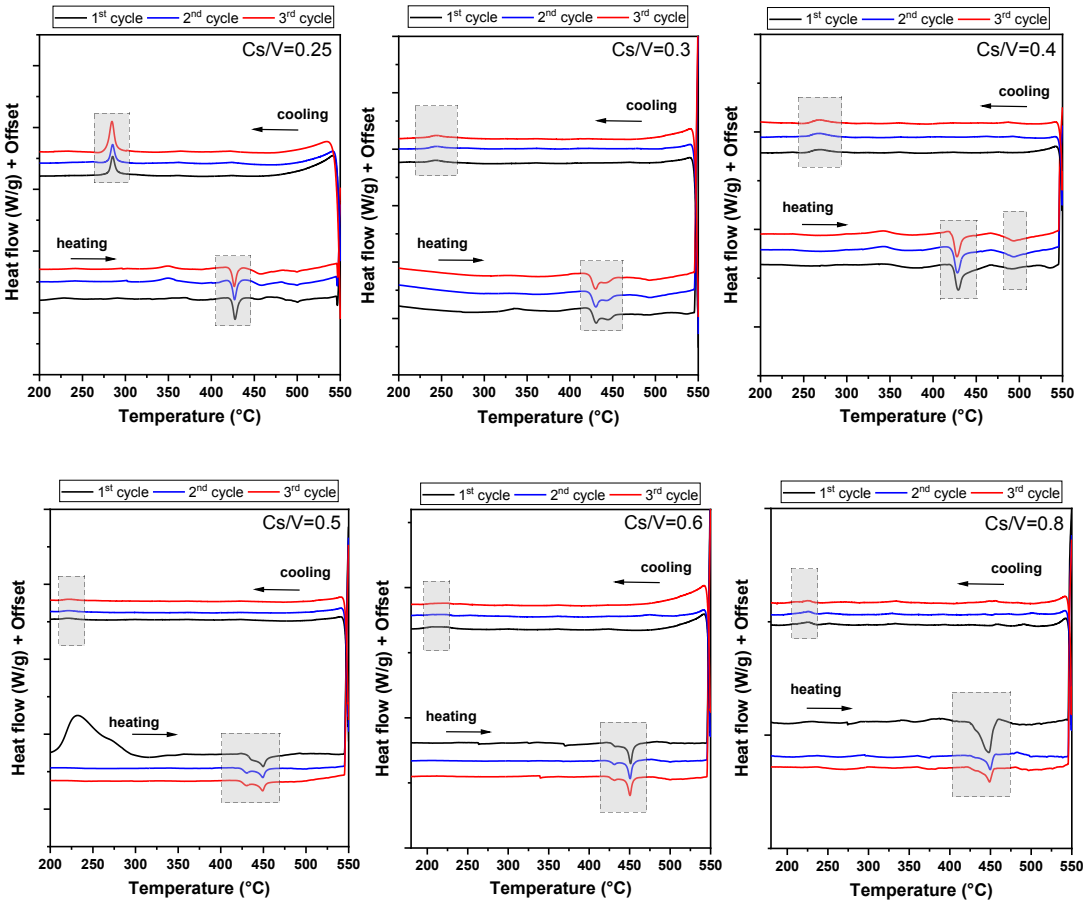

Figure S1.12. DSC profiles of silica supported Cs /V catalysts under 21%O_2/ 79% Ar with a flow of 50 ml/min, heating rate: 10 Kpm, cooling rate: 5 Kpm in an alumina crucible with lid. (Three heating and three cooling were applied)

Table S1.5. Peak data of silica supported Cs/V catalysts measured by DSC (Figure S1.12)

Rb/V	Cycle and peak info		T^{onset} (°C)	T^{peak} (°C)	Peak area (J/g)
0.25	1st cycle	1st peak	423.36	427.66	4.19
	2nd cycle	1st peak	422.78	426.95	2.46
	3rd cycle	1st peak	422.35	426.77	2.36
0.3	1st cycle	1st peak	423.3	428.9	3.20
	2nd cycle	1st peak	422.5	428.0	3.20
	3rd cycle	1st peak	422.2	427.5	2.88
0.4	1st cycle	1st peak	423.8	430.6	5.09
		2nd peak	480.5	493.1	0.25
	2nd cycle	1st peak	423.4	430.4	4.65
		2nd peak	485.3	492.3	0.31
	3rd cycle	1st peak	423.1	429.9	4.16
		2nd peak	486.3	492.3	0.24
0.5	1st cycle	1st peak	430.0	449.6	8.20
	2nd cycle	1st peak	441.6	449.2	4.73
	3rd cycle	1st peak	441.8	449.0	4.14
0.6	1st cycle	1st peak	446.3	451.1	3.94
	2nd cycle	1st peak	446.1	450.6	2.51
	3rd cycle	1st peak	445.3	450.4	3.88
0.8	1st cycle	1st peak	436.4	451.1	0.36
	2nd cycle	1st peak	447.5	451.1	0.065
	3rd cycle	1st peak	433.6	450.6	0.20

Thermal behavior of support-free $K_3V_5O_{14}$ (#31564) measured by DSC:

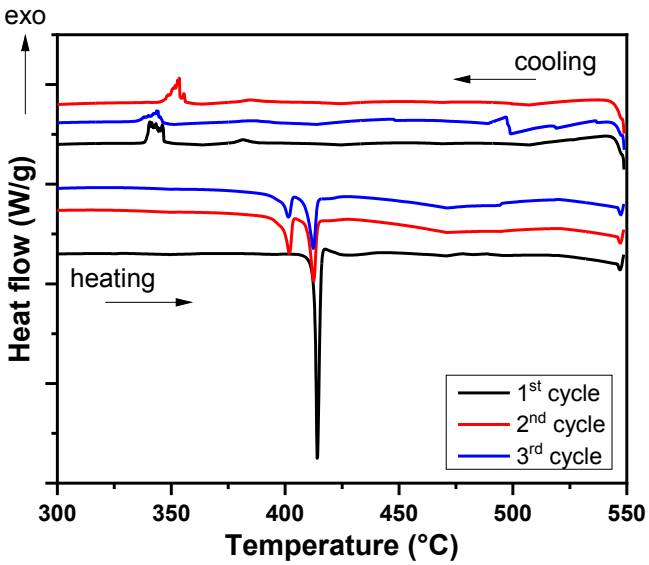

Figure S1.13. DSC profile of support-free $K_3V_5O_{14}$ catalysts under 21%O_2/ 79% Ar with a flow of 50 ml/min, heating rate: 10 Kpm, cooling rate: 5 Kpm in Pt crucible with lid. (Three heating and three cooling were applied)

XRD of spent of support-free $K_3V_5O_{14}$ (#31564) after ODP

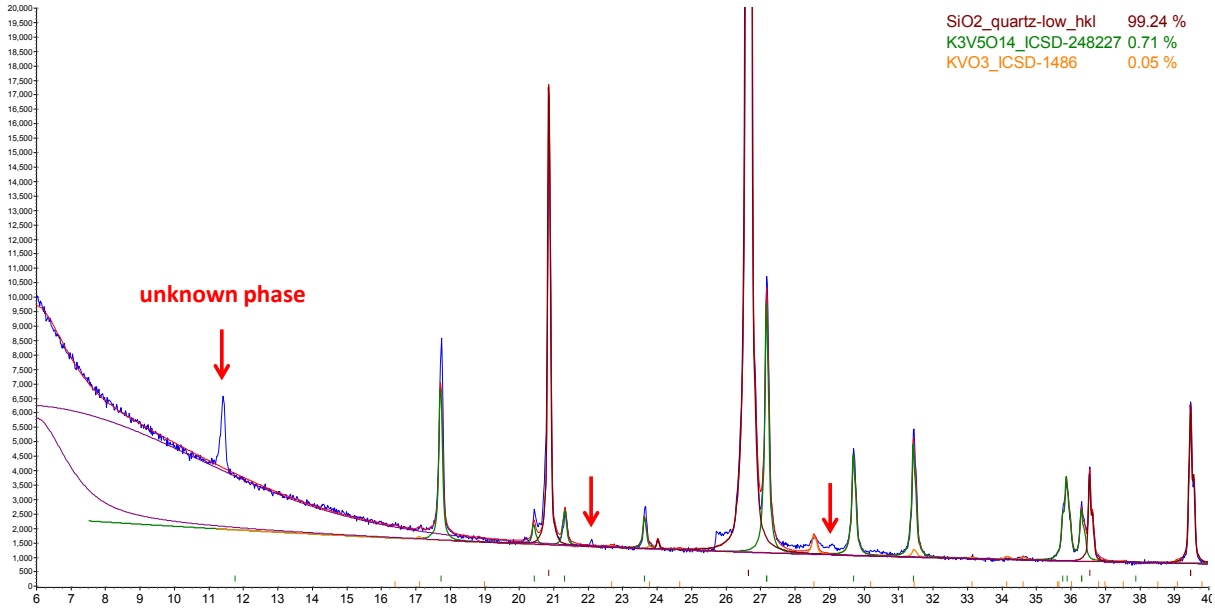

Figure S1.14. XRD pattern of spent of $K_3V_5O_{14}$ after ODP in s single tube reactor

High resolution TEM image of spent K/V=0.6 after activation:

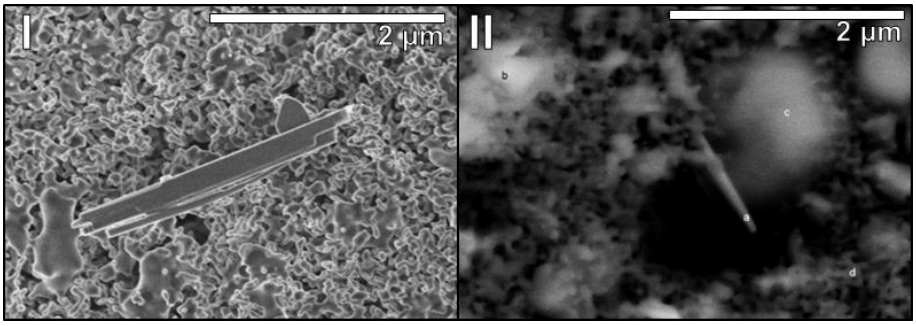

Figure S1.15. Representative ESEM image of silica supported K/V=0.6 catalyst during activation (heating in synthetic air to 520°C, 2.5mbar)

ESEM analysis shows that during heating of catalysts, needle formation occurs (FigureS1.15). In-situ generated needles stayed stable during heating and cooling down to room temperature. EDX analysis on image II showed that the needles contains vanadium and potassium (Figure S1.16). TEM analysis on ESEM samples were not possible because of beam sensitivity of the needles. However, the same needle structure (in a larger diameter) was found in the spent catalyst of K/V=0.6 (internal ID: 29562) from ODH of propane in a reactor. The microstructure of the needles was investigated using high-resolution TEM (HRTEM) and EDX. TEM analysis of the spent catalyst shows the powder consists of nano-needles with different size with high crystallinity. In the images of I-a, and II-a layered structure (nano-sheets) of these nano-needles are seen.

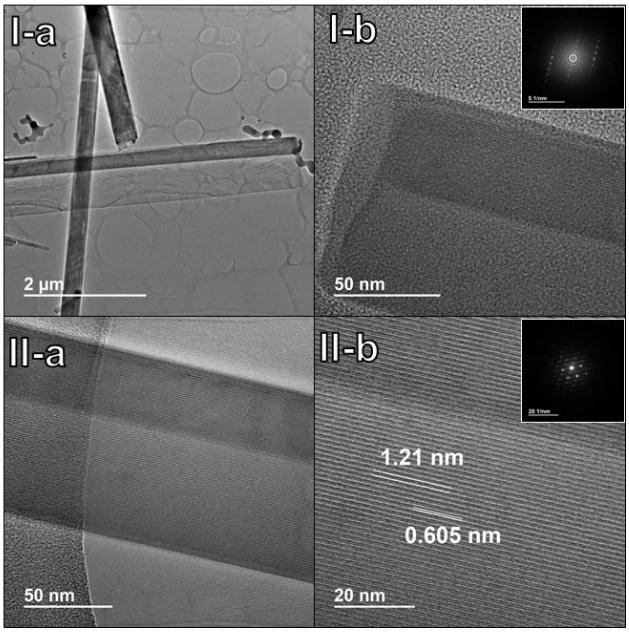

Figure S1.16. Representative HRTEM images of spent K/V=0.6 catalyst after ODH of propane (internal ID: 29562)

Homogeneity of elemental distribution of K, V and O was confirmed using EDX (Figure S15). EDX analysis revealed on a ratio between potassium and vanadium is 1: 2.5 at. % (Figure S16). However, according to the diffraction pattern of these nano-needles observed by electron diffraction, the best fitting was obtained with KV_3O_8 monoclinic structure (Figure 19). This experiment gives a crucial information on formed needles could be a decomposition product (i.e. KV_3O_8) and they are for sure taking place in ODH of propane.

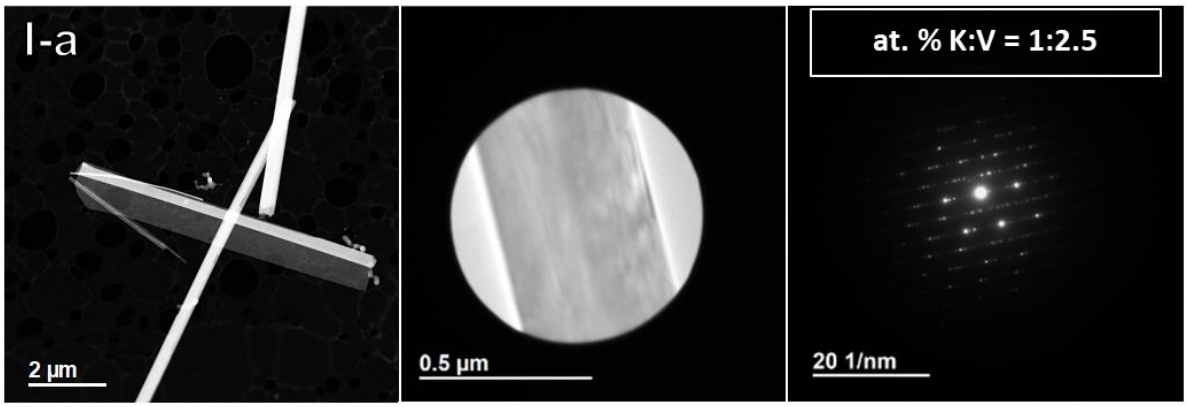

Figure S1.17. Representative HRTEM image and diffraction pattern of nano-needle of spent K/V=0.6 catalyst after ODH of propane (2.5 mbar) (internal ID: 29562)

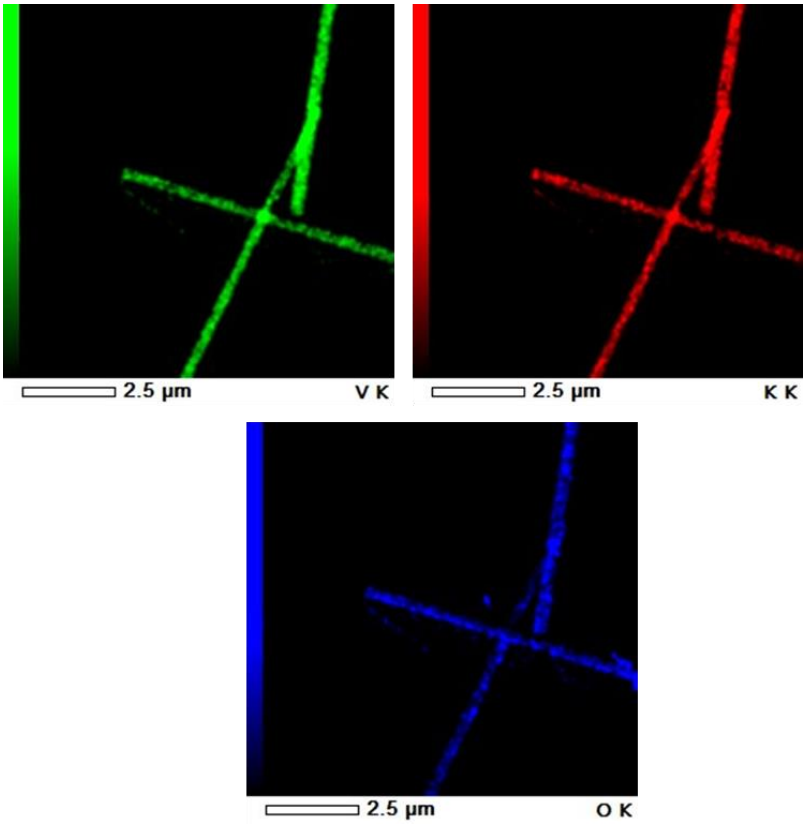

Figure S1.18. EDX image of spent K/V=0.6 catalyst after ODH of propane (2.5mbar) (internal ID: 29562)

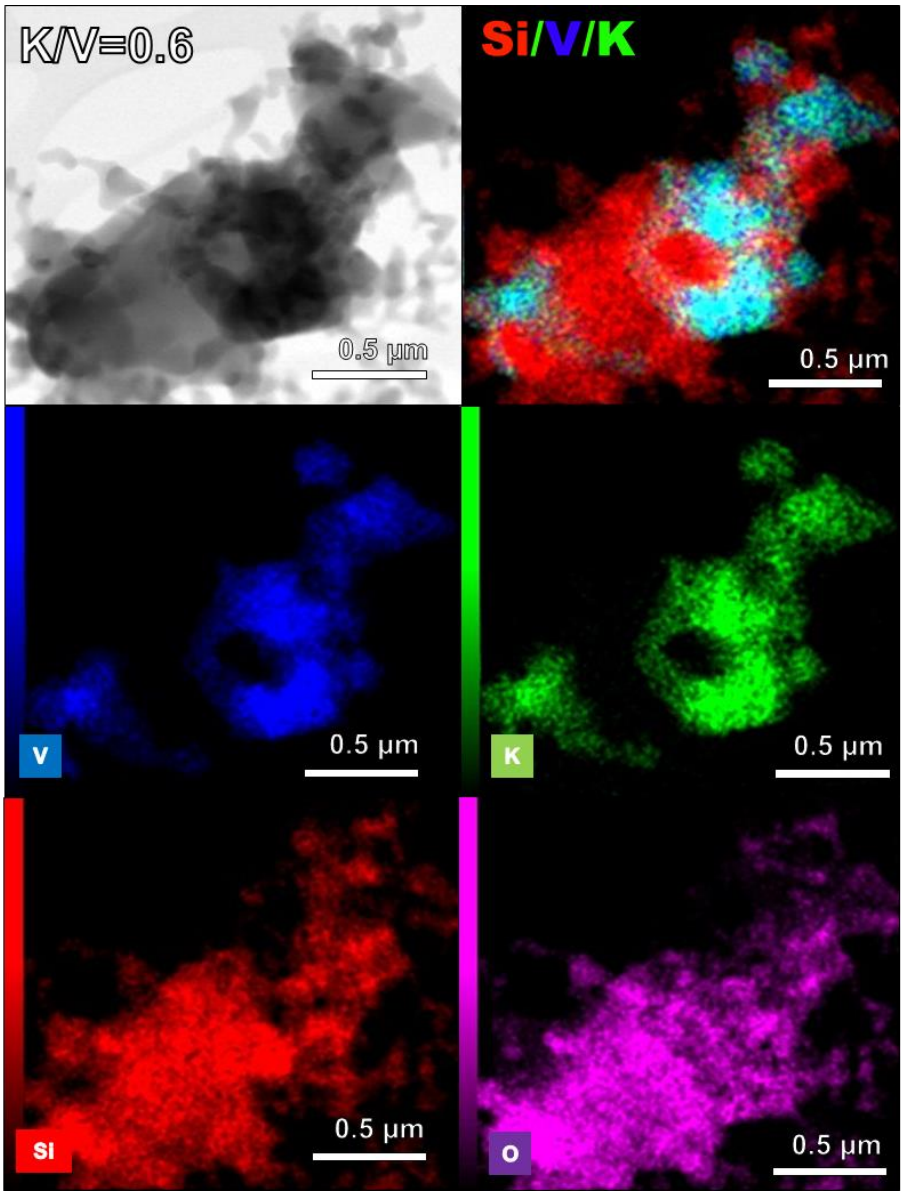

Figure S1.19. SEM-EDS image of silica supported K/V=0.6 catalyst (internal ID: 28654)

S2. Catalytic properties

Product Distribution over silica supported Li/V catalysts in propane oxidation:

Product distribution including CO_2, CO, ethylene, acrolein, acetone and propionaldehyde is seen in Figure S2.1. The amounts of ethylene, acrolein and propionaldehyde were below 2% of the total amounts of products.

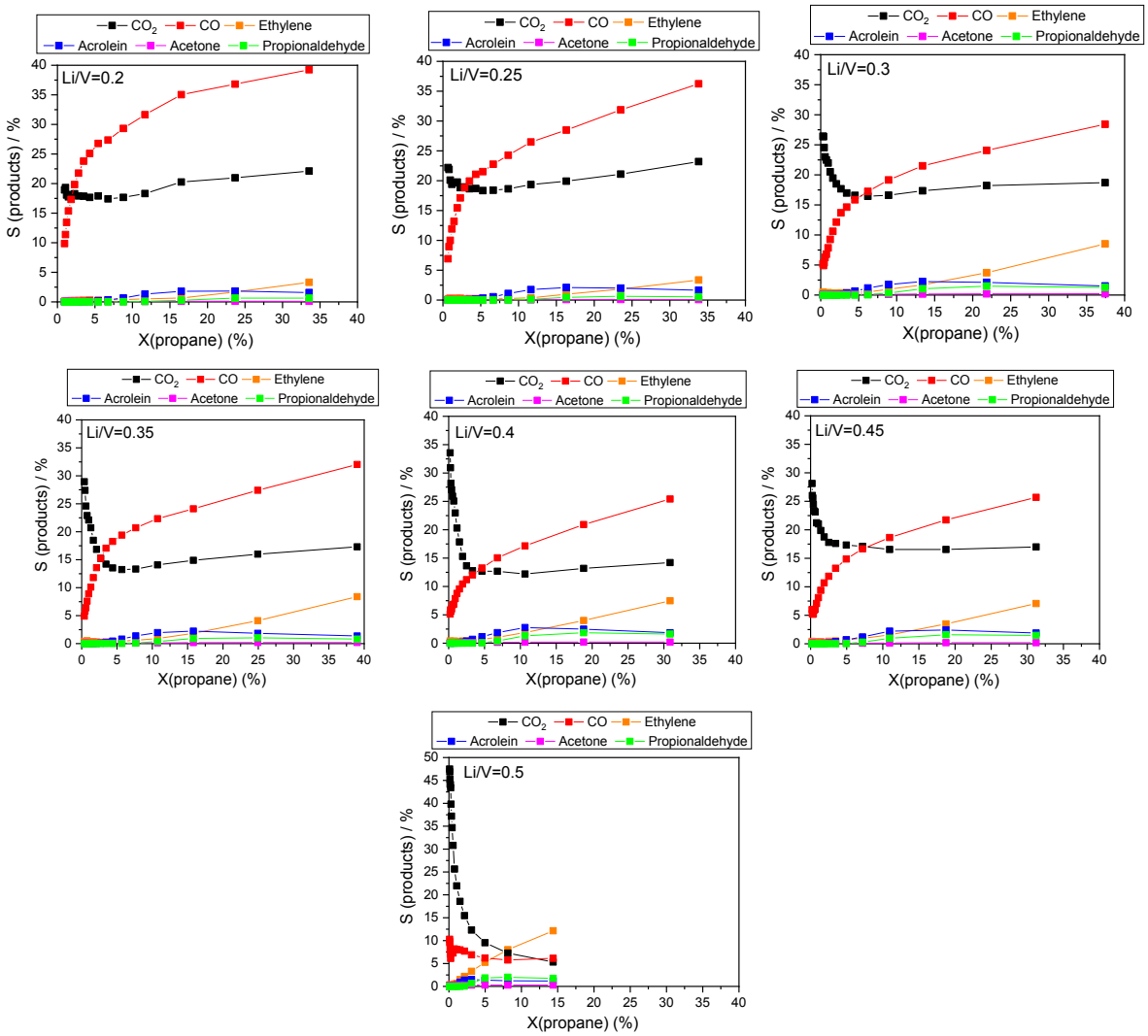

Figure S2.1. Product selectivity as a function of propane conversion over silica supported Li/V catalysts (Products: CO_2, CO, ethylene, acrolein, acetone, propionaldehyde)

Product Distribution over silica supported Na/V catalysts in propane oxidation:

Product distribution including CO_2, CO, ethylene, acrolein, acetone and propionaldehyde is presented in Figure S2.2. The amount of ethylene was always at 10% while acrolein and propionaldehyde were below 2% of the total amounts of products.

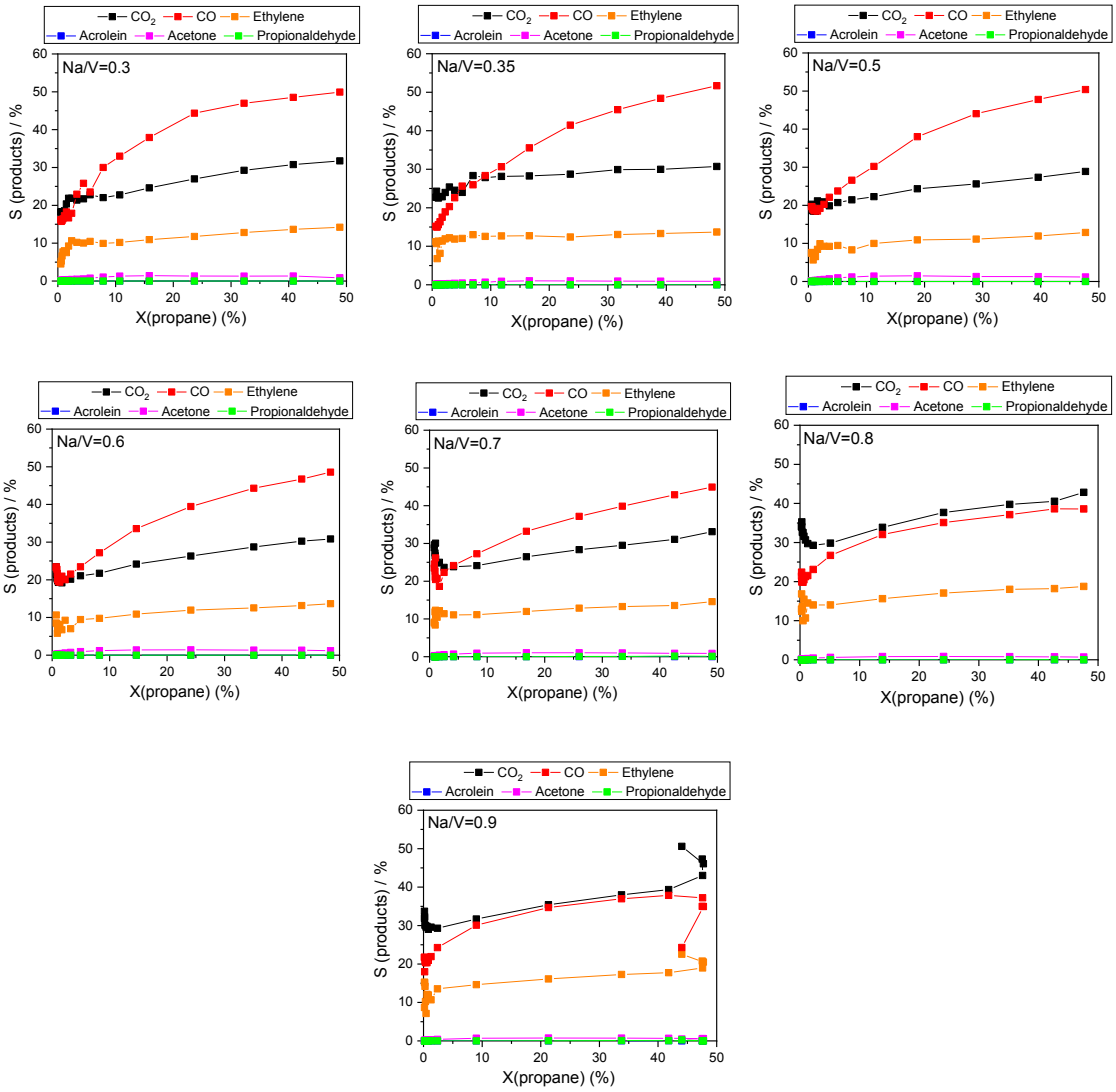

Figure S2.2. Product selectivity as a function of propane conversion over silica supported Na/V catalysts (Products: CO_2, CO, ethylene, acrolein, acetone, propionaldehyde)

Product Distribution over silica supported K/V catalysts in propane oxidation:

Product distribution including CO_2, CO, ethylene, acrolein, acetone and propionaldehyde is presented in Figure S2.3. Due to melting of alkali vanadate phase(s), change in selectivity to each product at specific temperature (melting temperature) can be seen. For instance, selectivity to CO and CO_2 were simultaneously decreased while propylene increases. The amounts of ethylene, acrolein and propionaldehyde were below 2% of the total amounts of products. However, selectivity to acetone was higher with increasing K-content (yielded at about 10% selectivity at 5% conversion).

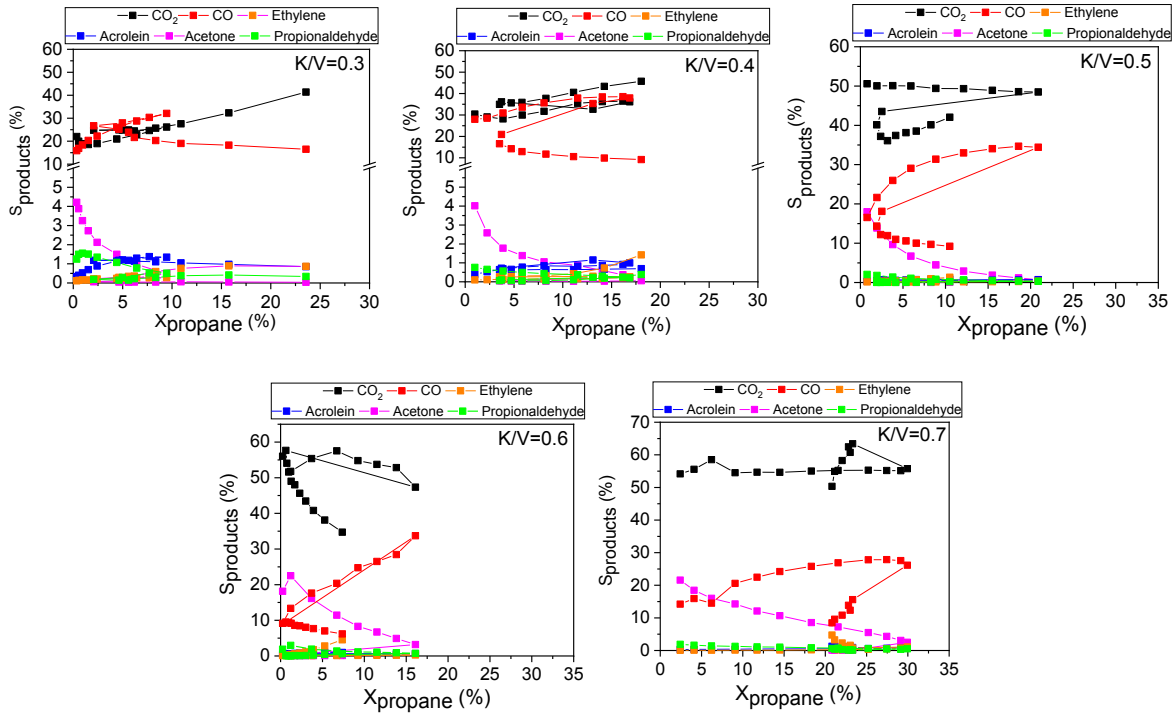

Figure S2.3. Product selectivity as a function of propane conversion over silica supported K/V catalysts (Products: CO_2, CO, ethylene, acrolein, acetone, propionaldehyde)

Product Distribution over silica supported Rb/V catalysts in propane oxidation:

Product distribution including CO_2, CO, ethylene, acrolein, acetone and propionaldehyde is presented in Figure S2.4. Upon crossing melting temperature of rubidium-vanadate phase(s), similar change in product distribution was seen as similar Figure S2.3. The amounts of ethylene, acrolein and propionaldehyde were below 2% of the total amounts of products. Selectivity to acetone was increasing with increasing Rb-content as similarly seen in K-containing catalysts (yielded at about 10% selectivity at 5% conversion).

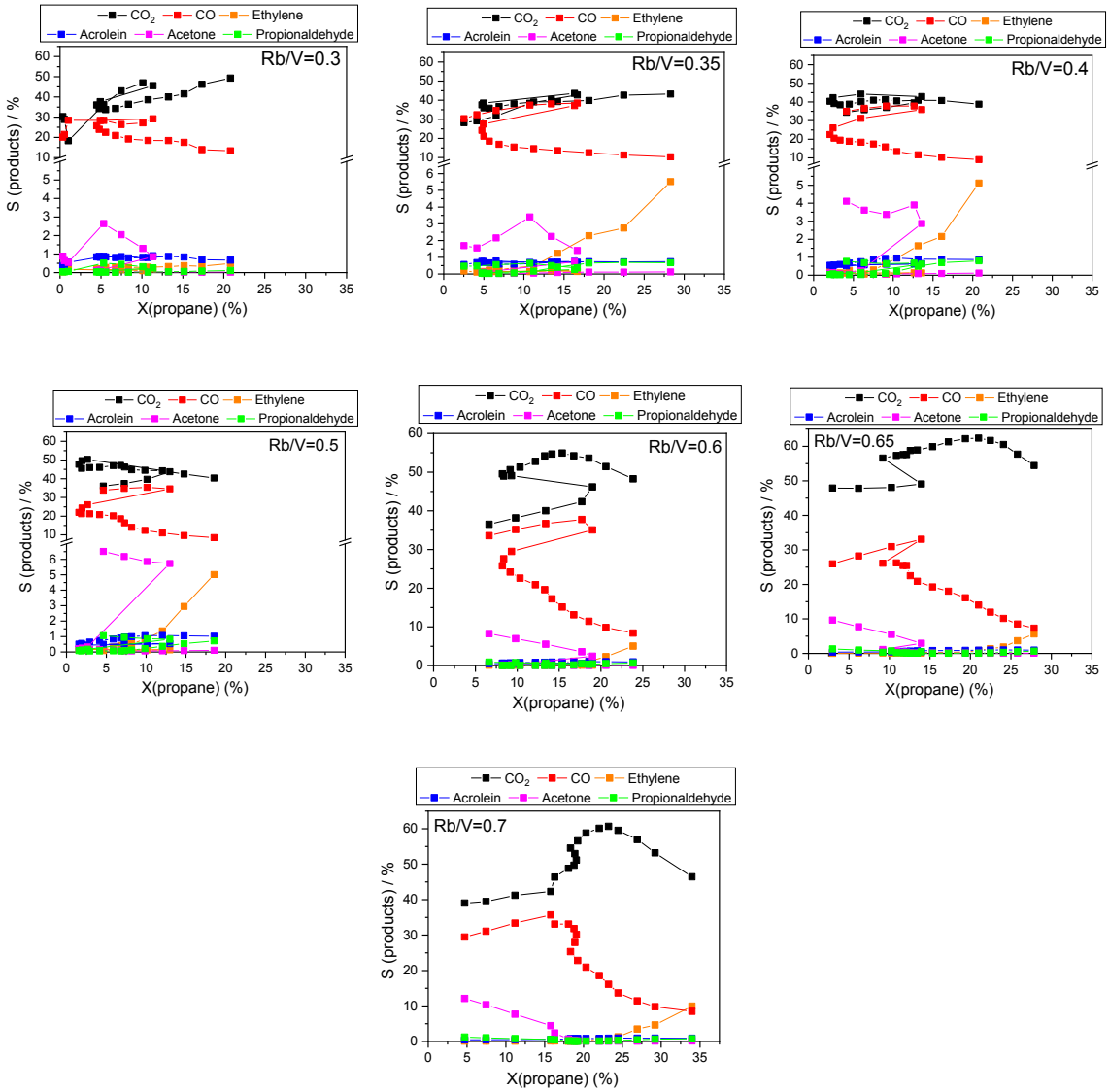

Figure S2.4. Product selectivity as a function of propane conversion over silica supported Rb/V catalysts (Products: CO_2, CO, ethylene, acrolein, acetone, propionaldehyde)

Product Distribution over silica supported Cs/V catalysts in propane oxidation:

Product distribution including CO_2, CO, ethylene, acrolein, acetone and propionaldehyde is presented in Figure S2.5. Upon crossing melting temperature of cesium-vanadate phase(s), similar change in product distribution was seen as similar Figure S2.3 and S2.4. For instance, selectivity to CO and CO_2 were decreased except for the catalysts Cs/V =0.6 in which CO_2 selectivity increased. The amounts of ethylene, acrolein and propionaldehyde were below 2% of the total amounts of products. Selectivity to acetone was increasing with increasing Cs-content as similarly seen in K- and Rb-containing catalysts (yielded at about 10% selectivity at 5% conversion).

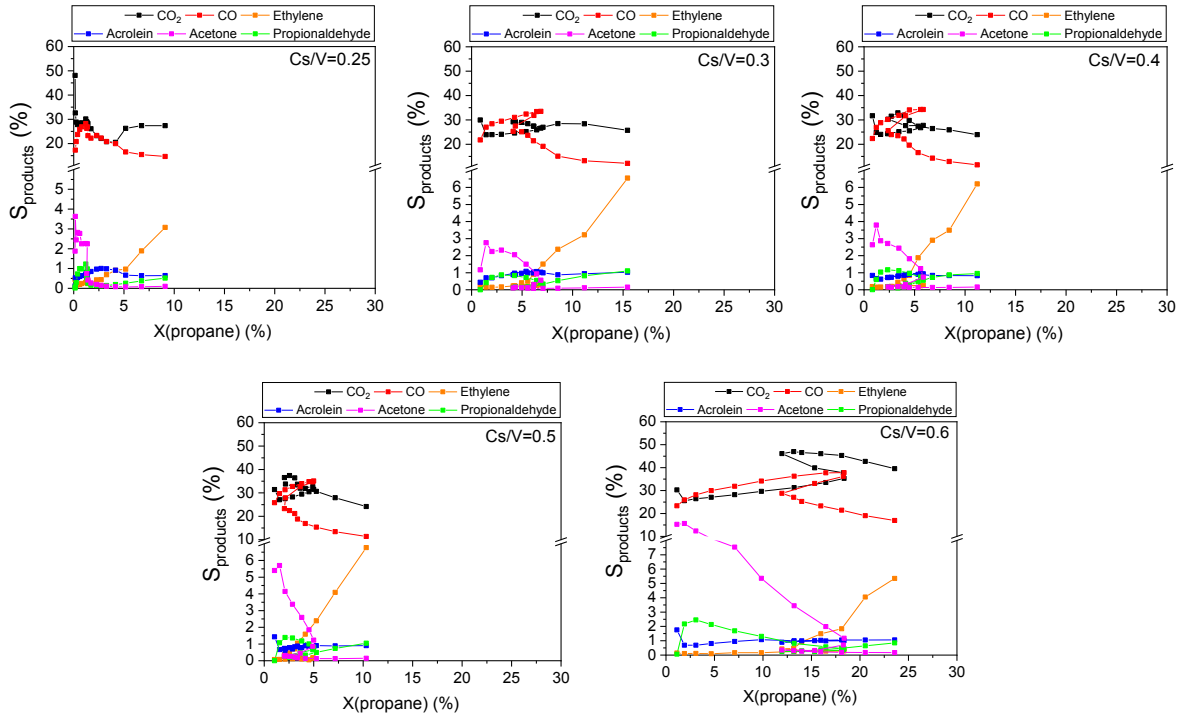

Figure S2.5. Product selectivity as a function of propane conversion over silica supported Cs/V catalysts (Products: CO_2, CO, ethylene, acrolein, acetone, propionaldehyde)

Adsorption-desorption isotherm of silica supported K/V=0.6 catalysts before and after reaction:

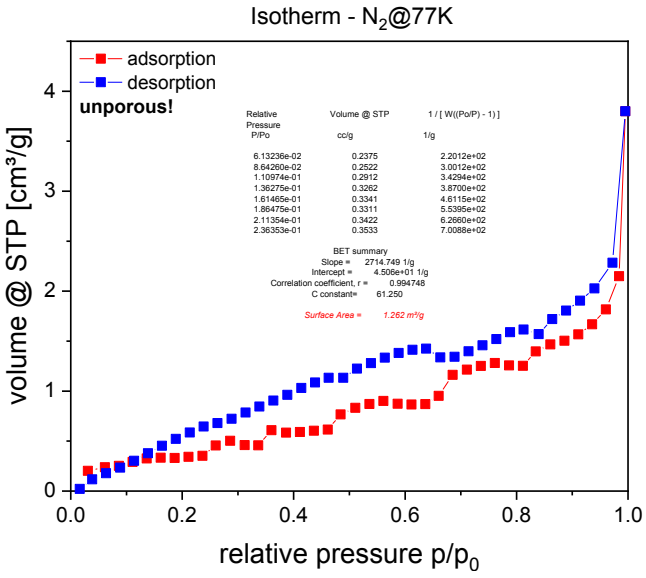

Figure S2.6. Adsorption-desorption isotherms of silica supported catalyst K/V=0.6 after catalysis

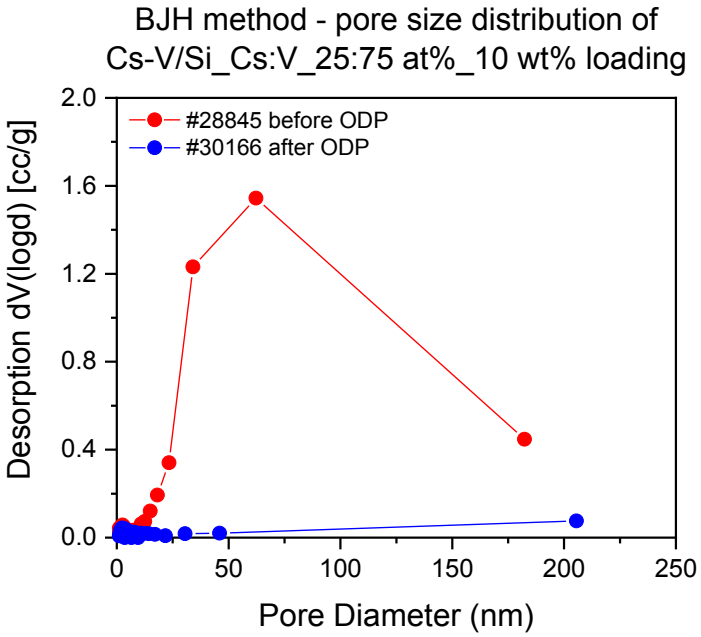

Figure S2.7. Desorption isotherm of silica supported catalyst Cs/V=0.4 before and after catalysis

The change in BET surface area right after activity drop:

To be sure that the activity drop is not directly because of significant change surface area, propane oxidation was again performed in a single tube reactor. For this, K-containing catalyst was used. Drop in activity was observed in a temperature where melting happens (*i.e.* 410°C). After this point, experiment was stopped and the sample was transferred for BET measurement. The BET surface area was found to be decreases from 23.6 to 19.1 m^2/g.

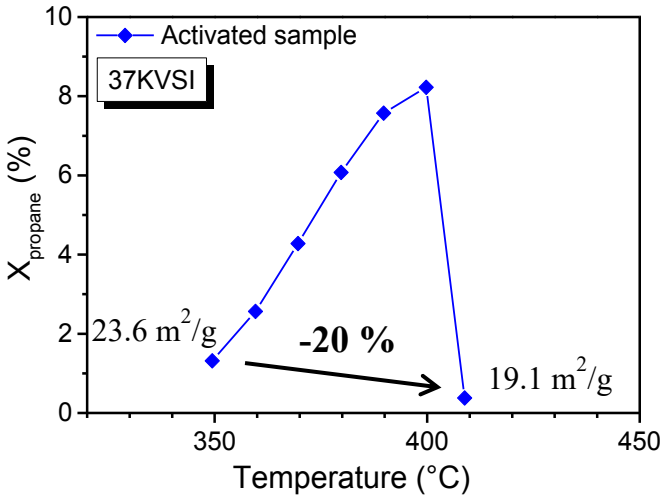

Figure S2.8. Propane oxidation of K/V=0.6 (#28654) in a single tube reactor. (Total flow: 10 ml/min, $C_3H_8/O_2/N_2$=7.5/7.5/85 vol. %, W/F=1.8 g s ml^{-1})

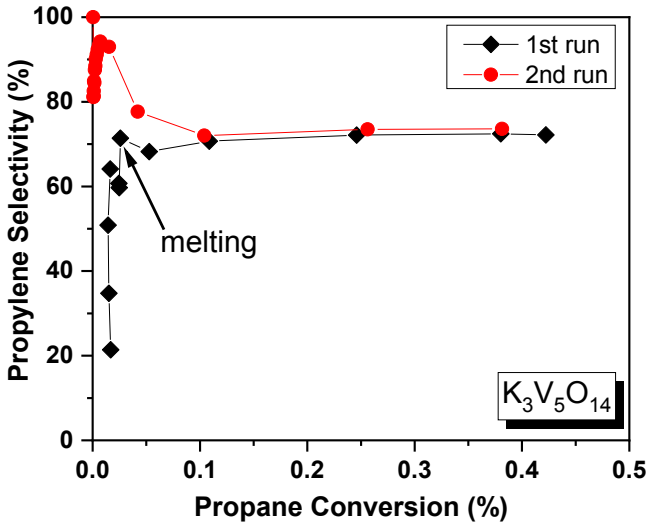

Figure S2.9. Propylene selectivity as a function of propane conversion with increasing temperature (Conditions: T=350°C-520°C, feed $C_3H_8/O_2/N_2$=7.5/7.5/85 vol. %, W/F= 0.9 g s ml^{-1})

S3. Operando Studies

Combined plots of phase diagram and catalysis data:

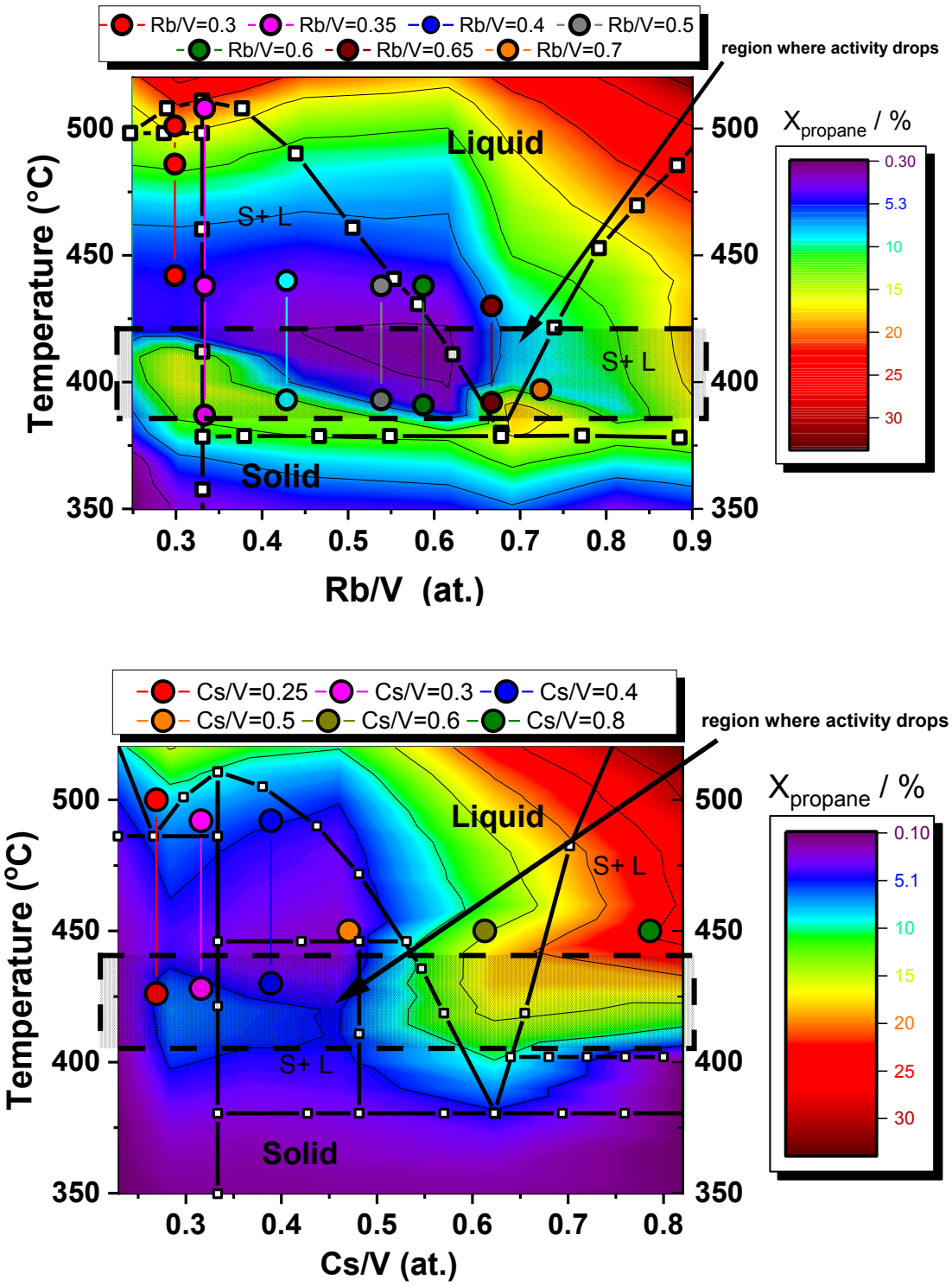

Figure S3.1. A combined phase diagram with measured melting points of Rb/V (top) and Cs/V (bottom) catalysts and activity data in propane oxidation (●: melting points of freshly prepared Rb/V and Cs/V catalysts measured by DSC

Operando-DSC of Rb/V and Cs/V catalysts:

operando- DSC of activated Rb/V=0.5 catalyst is shown in Figure S3.2. The heat evolution increases with increasing temperature during propane oxidation. Calculated heat of reaction based on product distribution is consistent with the measured heat flow. The Rb-vanadate phase/s have noticeable melting at 392°C (T^{peak}). When temperature arise above 380°C, it is seen that activity drops with the onset of melting of the surface phase(s). However, selectivity to propylene enhanced. Activity was later recovered at higher temperature ~ 480°C.

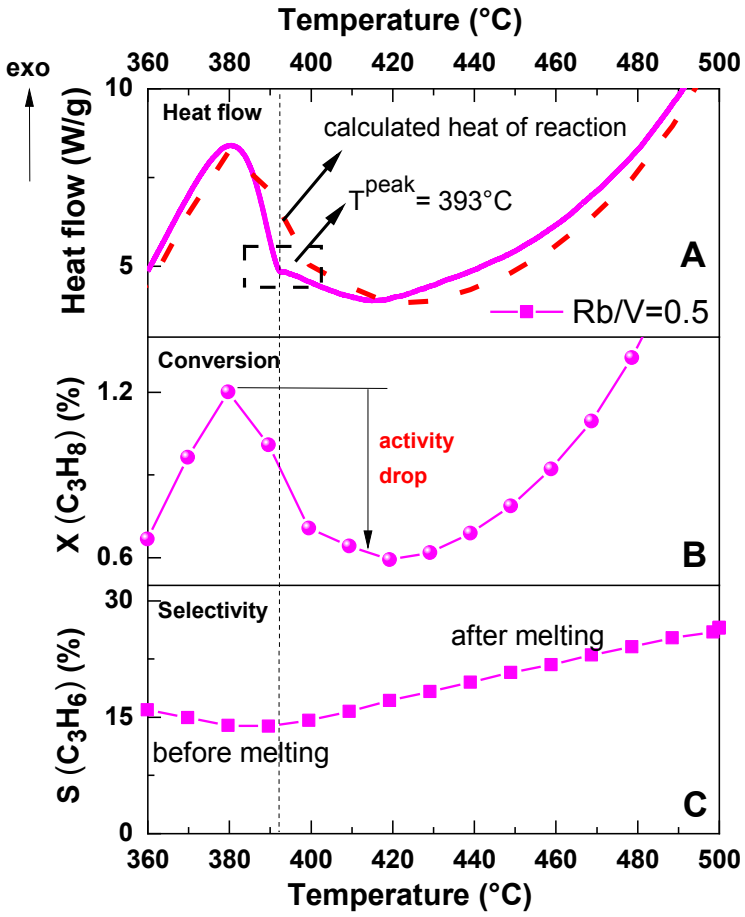

Figure S 3.2. *operando*- DSC profile of catalyst Rb/V=0.5 in propane oxidation (Total flow: 9 ml/min, $C_3H_8/O_2/N_2$=7.5/7.5/85 vol. %, GHSV ≈ 5700 h^{-1}, β=0.42 Kpm, W/F: 0.33 g s ml^{-1})

Figure S3.3 shows the *operando*-DSC profile of activated Cs/V=0.5 catalyst in propane oxidation. Due to the high activity of the catalyst, the contact time is reduced to 1/3 of the measurement protocol. This was similarly done in the catalysis protocol in a reactor as it was mentioned before (see Figure 37). With this, comparable conversion within the selected catalysts were reached. The heat flow increases with increasing temperature. Calculated heat of reaction is very consistent with the measured heat flow. Due to the existence of surface amorphous phase(s), a broad melting between 430 and 450°C was obtained. This resulted in a plateau in both conversion and heat flow plot rather than a drop. Although the impact of melting is less pronounced compared to K/V and Rb/V catalysts, it is still detectable and noticeable. A slight increase in selectivity to propylene was also seen after liquefaction.

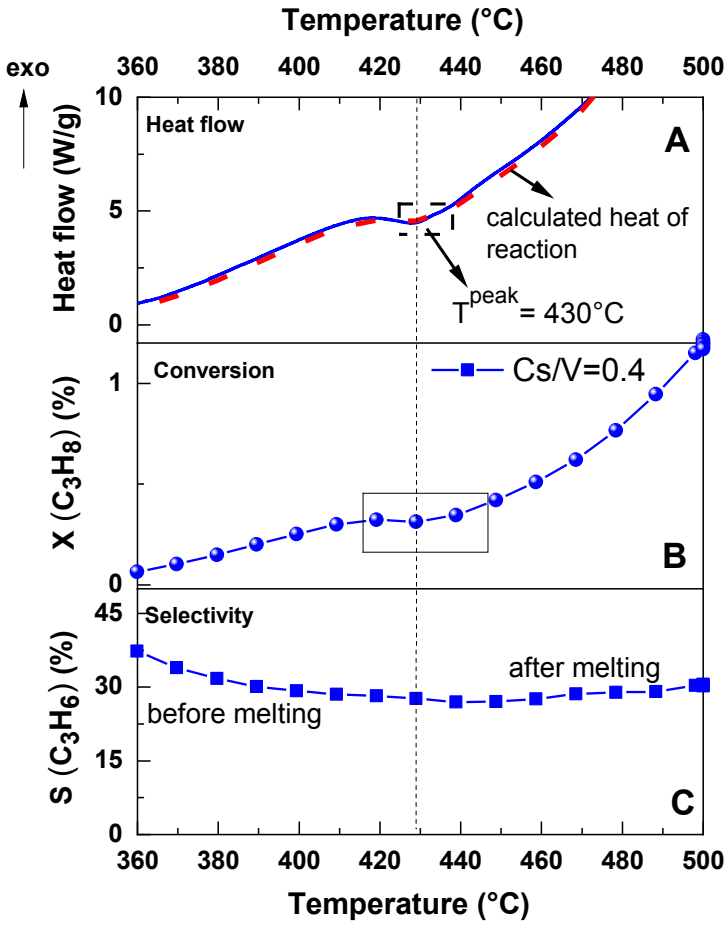

Figure S3.3. *operando*- DSC profile of catalyst Cs/V=0.4 in propane oxidation (Total flow: 9 ml/min, $C_3H_8/O_2/N_2$=7.5/7.5/85 vol. %, GHSV ≈ 5700 h^{-1}, β=0.42 Kpm, W/F: 0.11 g s ml^{-1})

TG-MS-DTA study of silica supported K/V=0.6 catalyst with/without activation:

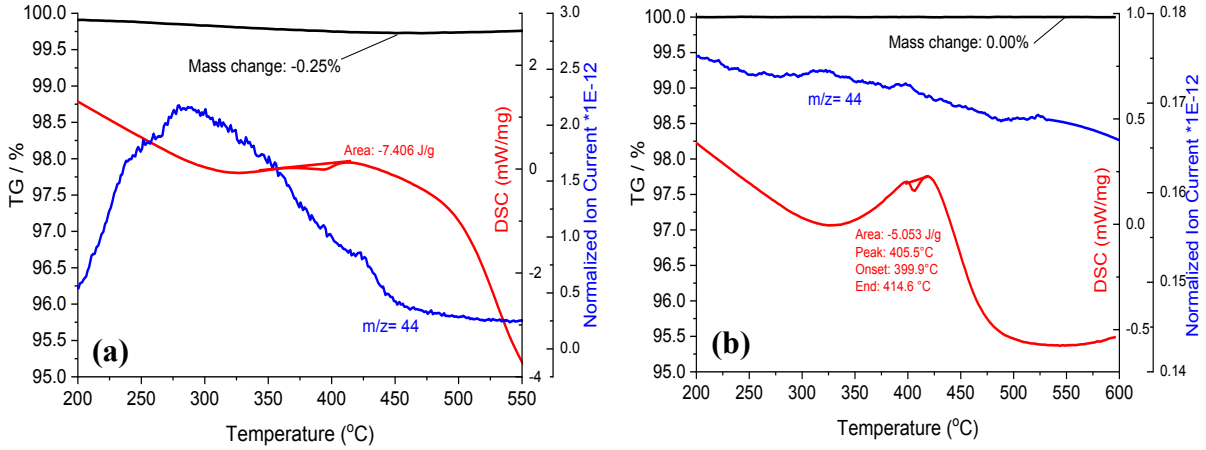

Figure S3.4. TG-MS analysis of K/V=0.6 catalyst in 70 mlmin^{-1} of Ar flow (a) without activation (fresh catalyst) (b) activated in 620°C in syn air

Raman spectrum of silica supported K/V=0.6 compared to some references (266 nm):

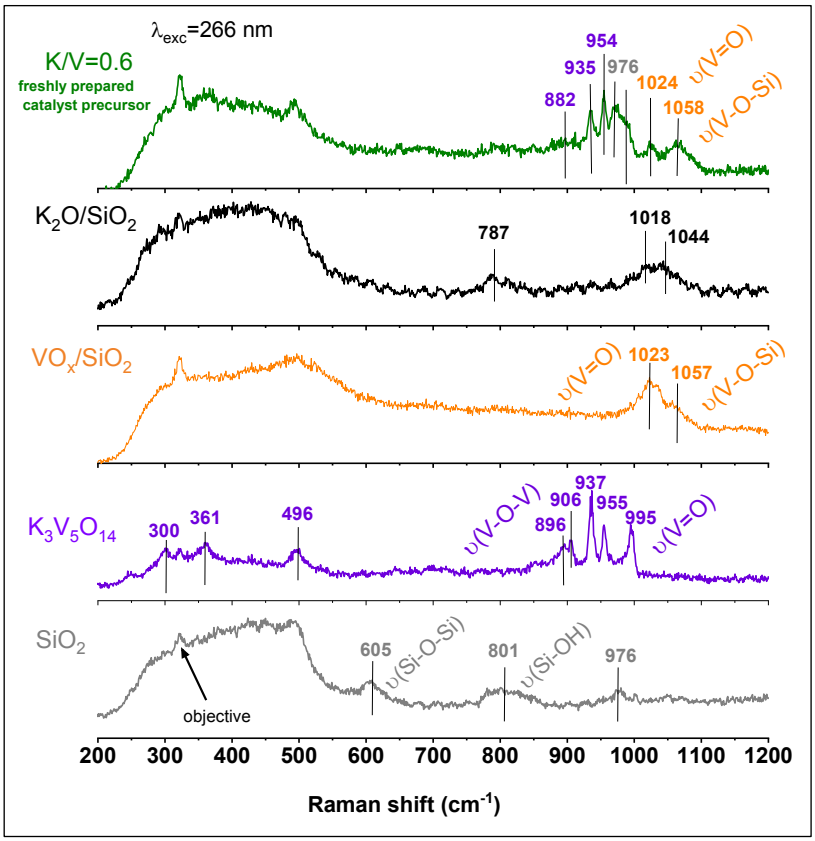

Figure S3.5. The Raman spectrum of silica supported K/V=0.6 catalyst compared to reference catalysts (K_2O/SiO_2, VO_x/SiO_2 and $K_3V_5O_{14}$ were in-house synthesized) (λ_{exc} = 266 nm)

T-dependent Raman spectra of K/V=0.6 catalyst in propane oxidation reaction (266 nm):

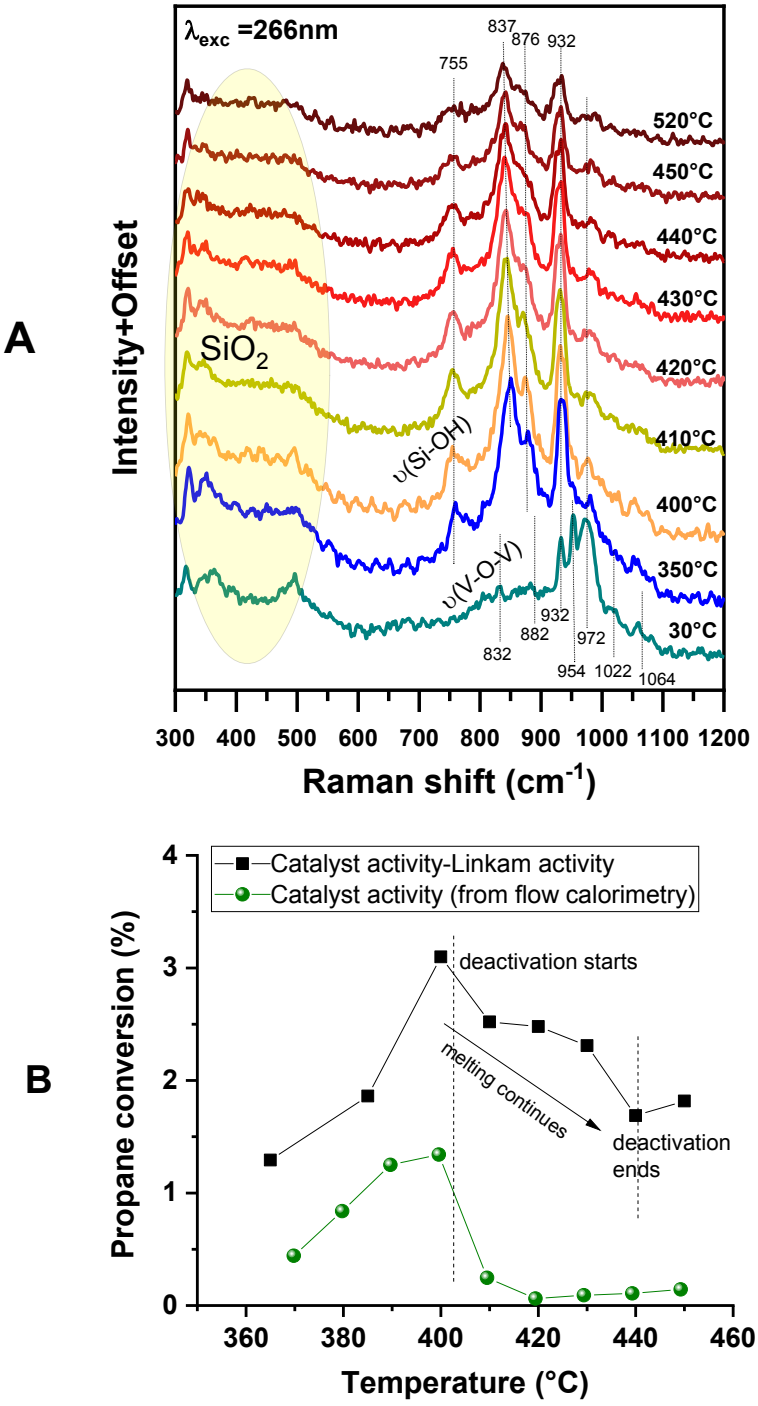

Figure S3.6. (A) Raman spectra of the catalyst K/V=0.6 under reaction conditions (λ_{exc}=266 nm) **(B)** Simultaneously obtained catalytic data of K/V=0.6 in propane oxidation and comparison of catalyst profile with data obtained from flow calorimetry (Conditions for Raman: $C_3H_8/O_2/N_2$=7.5/7.5/85 vol. %, F= 1 mlmin^{-1} and contact time W/F= 1.2 g s ml^{-1}; Conditions for flow calorimetry: $C_3H_8/O_2/N_2$=7.5/7.5/85 vol. %, F= 10 mlmin^{-1} and contact time W/F= 0.4 g s ml^{-1})

Raman spectra of K/V=0.6 catalyst before and after propane oxidation reaction (266 nm):

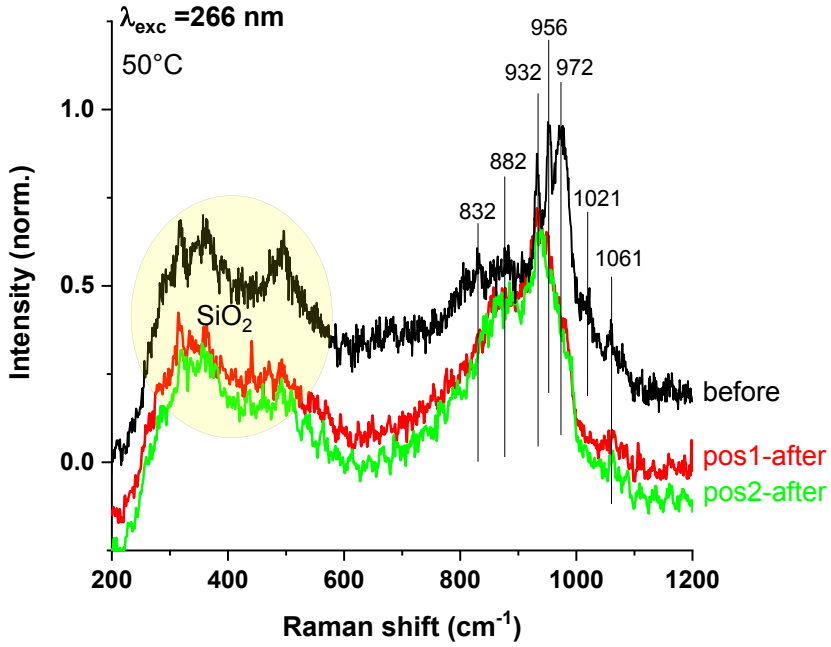

Figure S3.7. The Raman spectra of K/V=0.6 obtained before and after reaction under the flow of air (λ_{exc}=266 nm, C_3H_8: O_2: N_2= 7.5/7.5/85, 1 mlmin^{-1})

Raman spectra of K/V=0.6 catalyst before and after activation (532 nm):

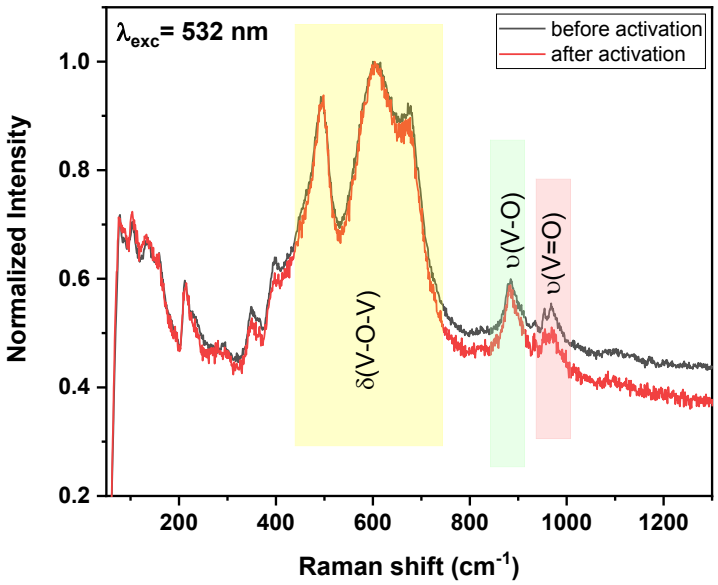

Figure S3.8. The Raman spectra of K/V=0.6 obtained before and after activation under the flow of air (λ_{exc}=532 nm, 21O_2/79N_2, 10 mlmin^{-1})

Empty cell (Linkam CCR100) activity in propane oxidation:

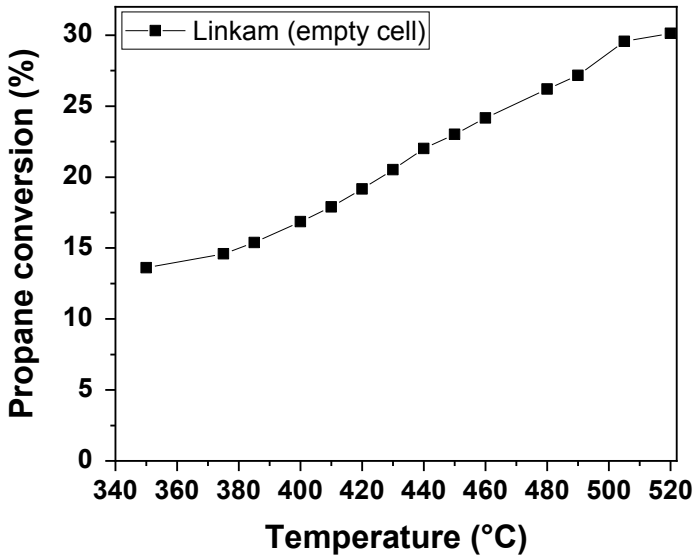

Figure S3.9. Propane conversion measured in empty Linkam cell under the flow of C_3H_8: O_2: N_2= 7.5/7.5/85 with 1 mlmin^{-1})

Raman spectra of K/V=0.6 catalyst before and after reaction (532 nm):

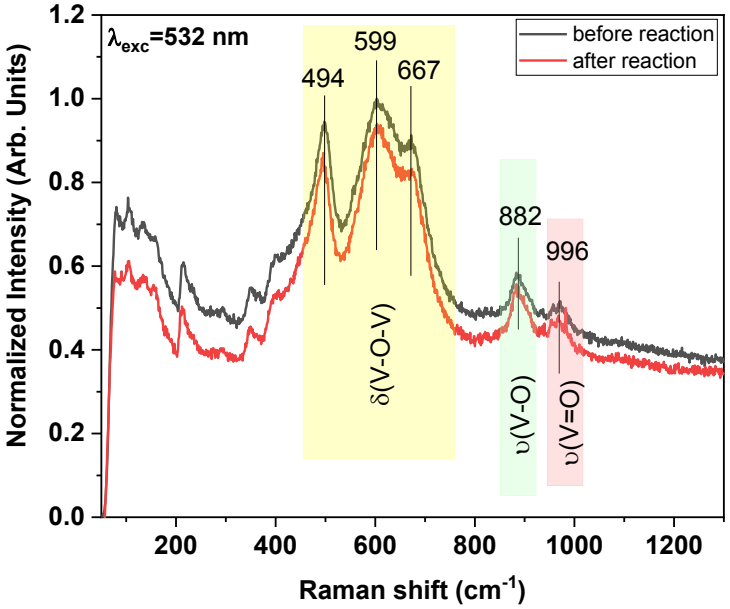

Figure S3.10. The Raman spectra of silica supported K/V=0.6 obtained before and after reaction (λ_{exc}=532 nm, C_3H_8: O_2: N_2= 7.5/7.5/85 vol. %, 1 mlmin^{-1})

The gas phase NEXAFS of O_2:

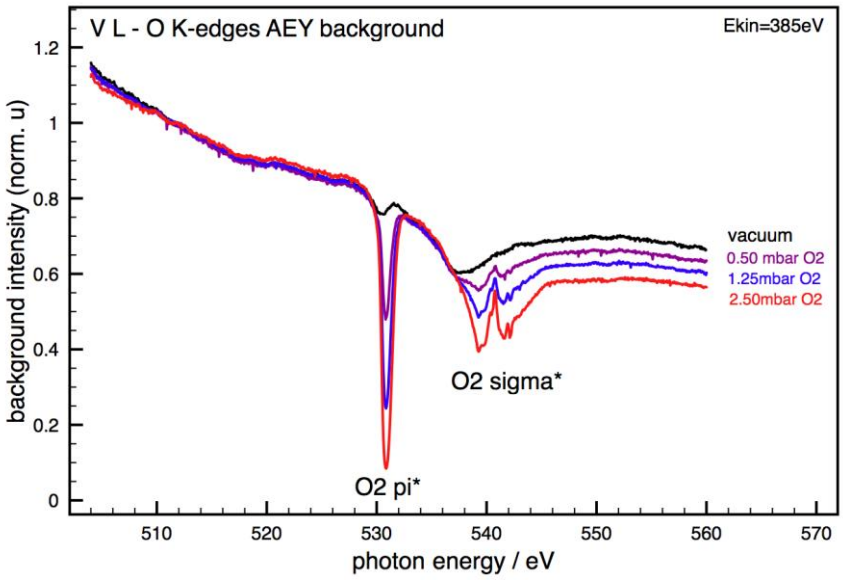

Figure S3.11. The gas phase NEXAFS of O_2 (provided by Michael Hävecker)

Catalytic data of K/V=0.6 catalyst measured in XPS cell:

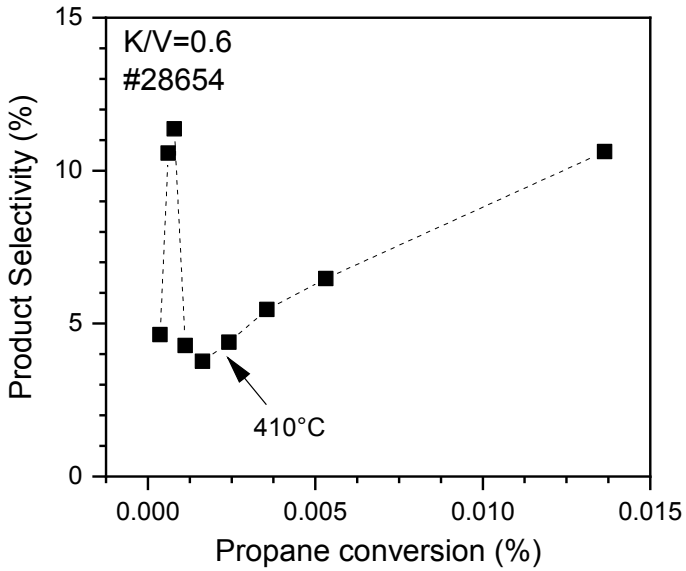

Figure S3.12. Selectivity to propylene versus propane conversion measured in XPS chamber (250 Pa, $C_3H_8/O_2/N_2$=7.5/7.5/85 vol. %, 10 $mlmin^{-1}$)

The in situ NAP-NEXAFS of KVO_x compounds:

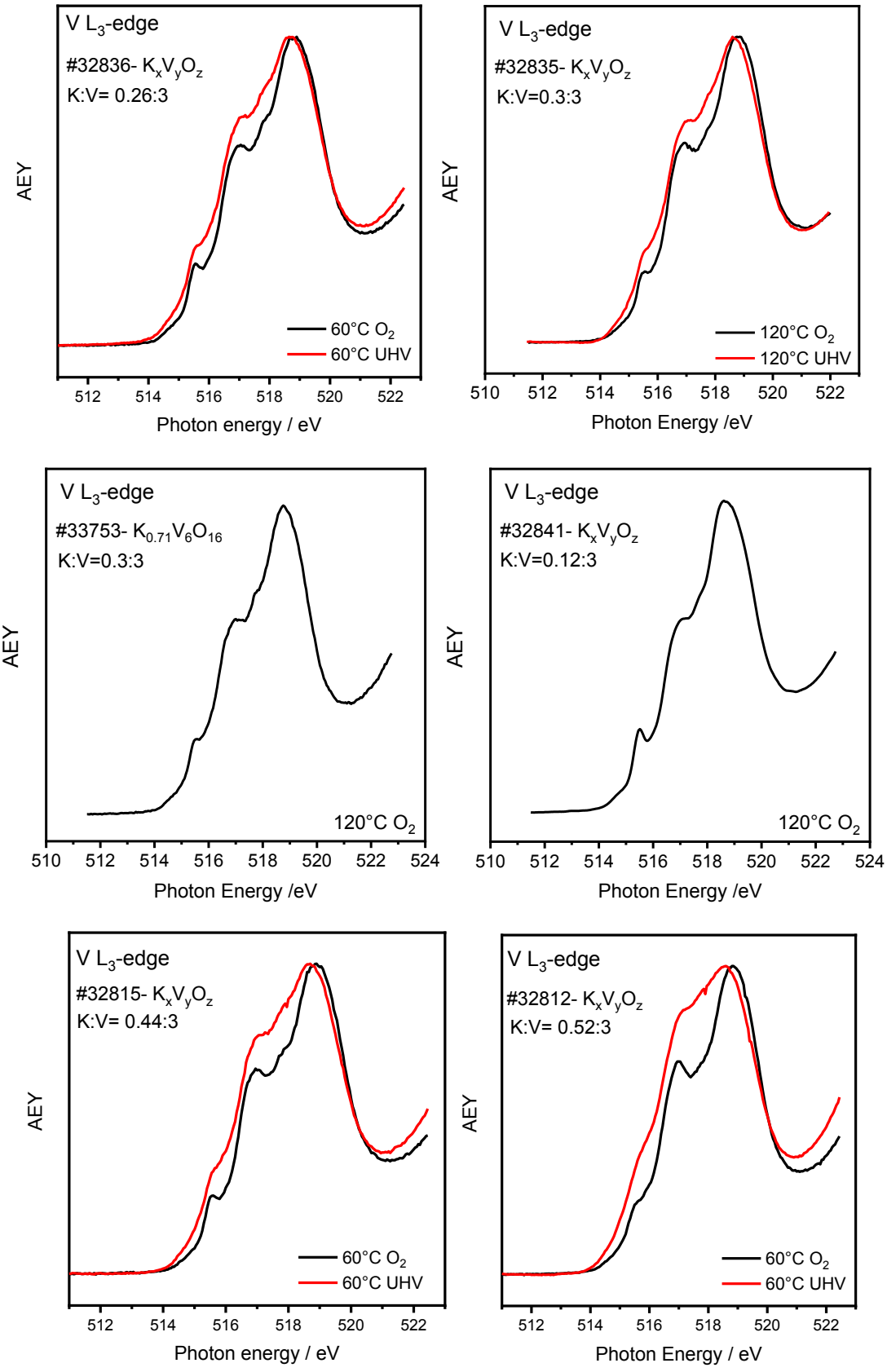

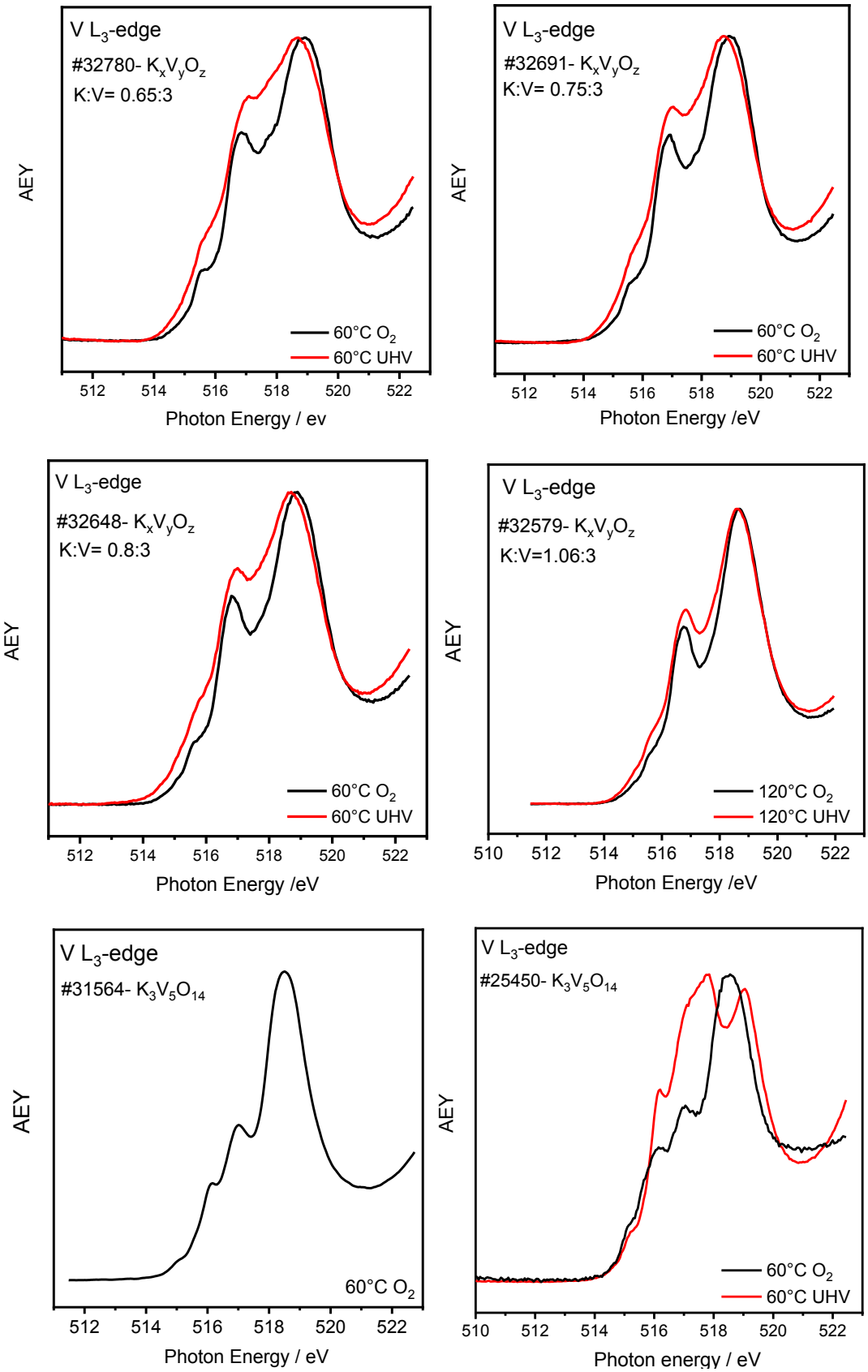
V L3-edge
#32780- KxVyOz
K:V= 0.65:3
AEY
60°C O2
60°C UHV
512 514 516 518 520 522
Photon Energy / ev
V L3-edge
#32691- KxVyOz
K:V= 0.75:3
AEY
60°C O2
60°C UHV
512 514 516 518 520 522
Photon Energy /eV
V L3-edge
#32648- KxVyOz
K:V= 0.8:3
AEY
60°C O2
60°C UHV
512 514 516 518 520 522
Photon Energy /eV
V L3-edge
#32579- KxVyOz
K:V=1.06:3
AEY
120°C O2
120°C UHV
510 512 514 516 518 520 522
Photon Energy /eV
V L3-edge
#31564- K3V5O14
AEY
60°C O2
512 514 516 518 520 522
Photon Energy / eV
V L3-edge
#25450- K3V5O14
AEY
60°C O2
60°C UHV
510 512 514 516 518 520 522
Photon energy / eV

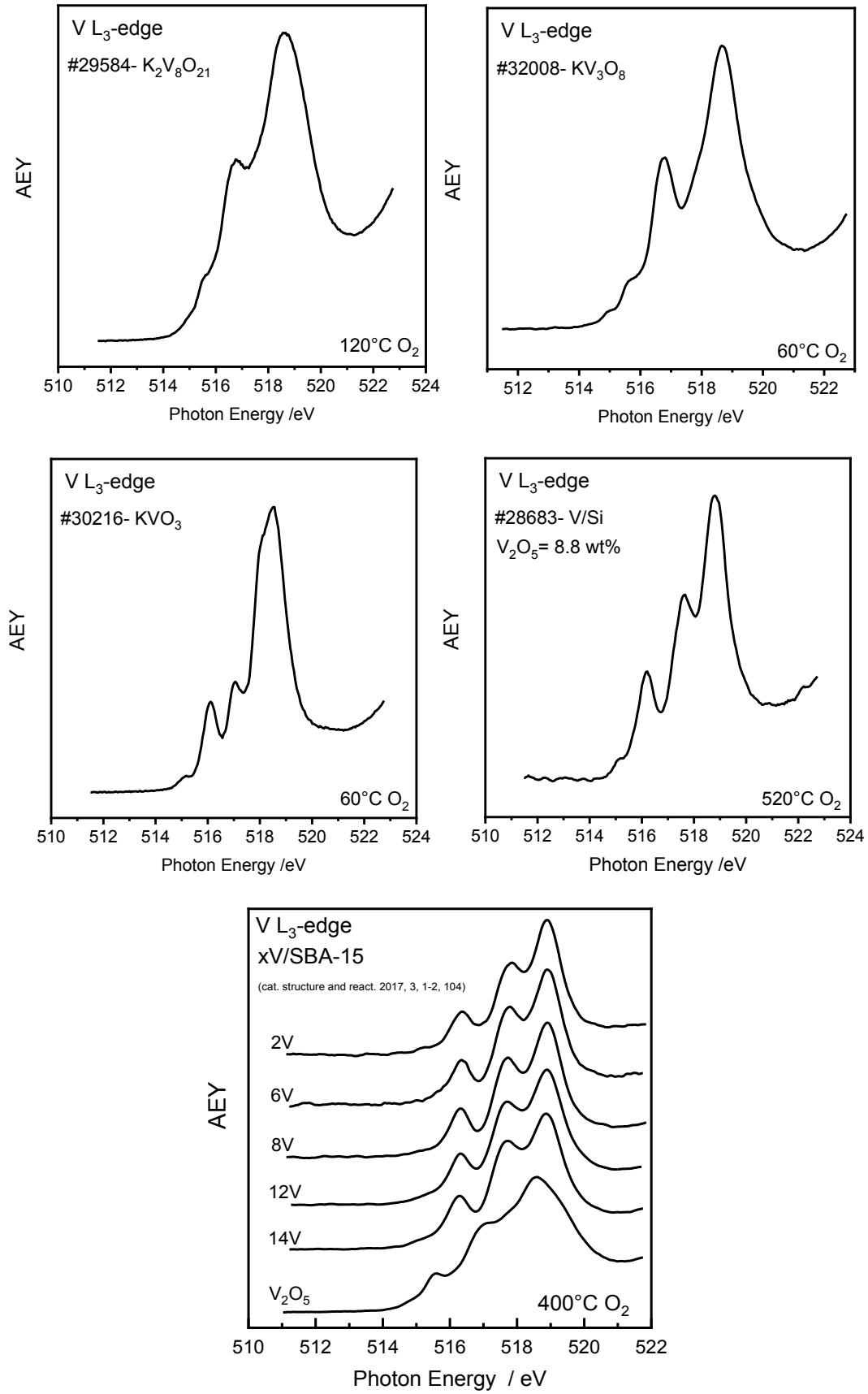

Figure S3.13. In situ NAP-NEXAFS spectra of reference compounds including KVO_x and vanadium oxide catalysts (250 Pa, either O_2 or UHV or both, 10 $mlmin^{-1}$)

In situ K L-edge NEXAFS of silica supported K/V=0.6 catalyst:

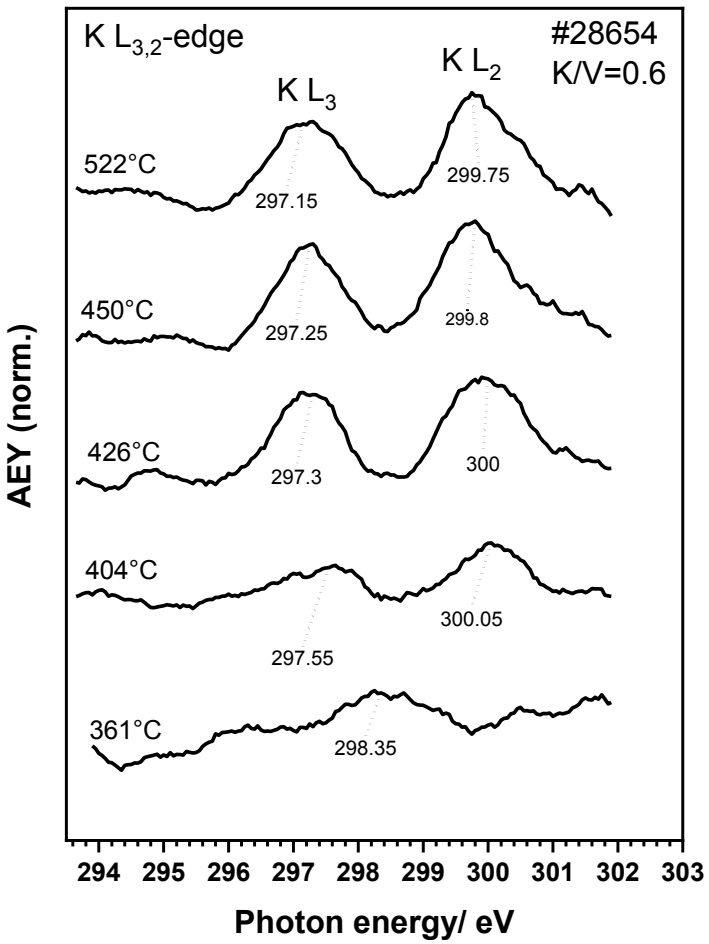

Figure S3.14. In situ K $L_{3,2}$-edge NEXAFS of silica supported K/V=0.6 catalyst measured in propane oxidation reaction conditions (at 250 Pa $C_3H_8/O_2/N_2$=7.5/7.5/85 10 ml min^{-1})

In situ K L-edge NEXAFS of KVO_x compounds:

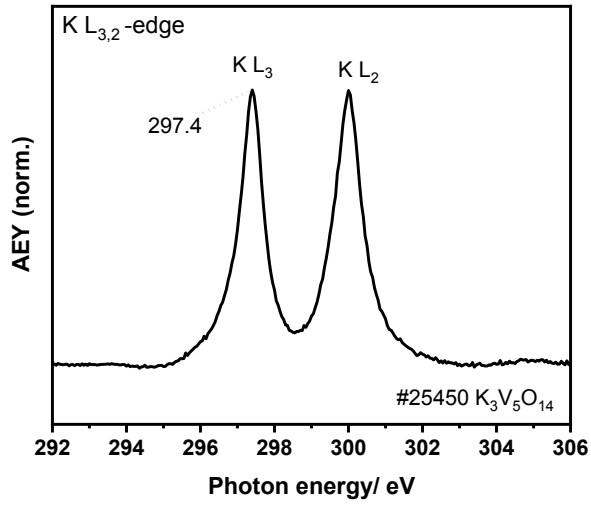

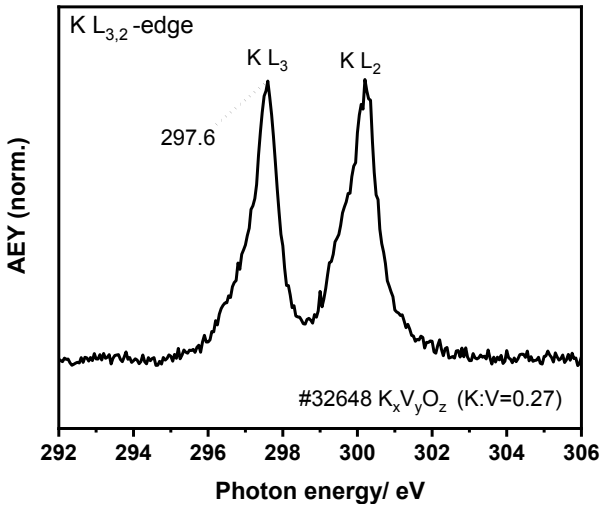

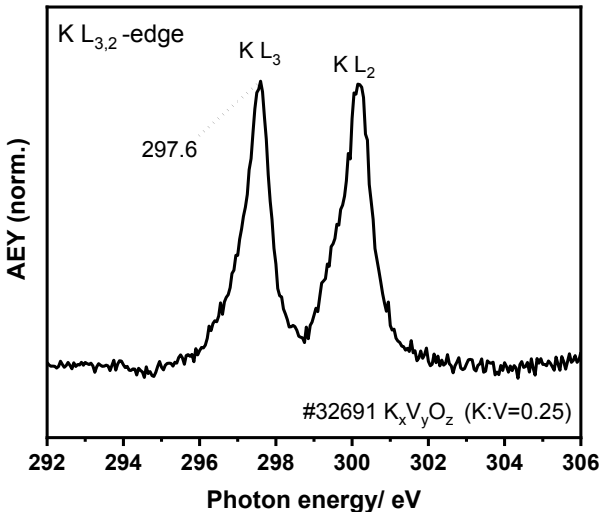

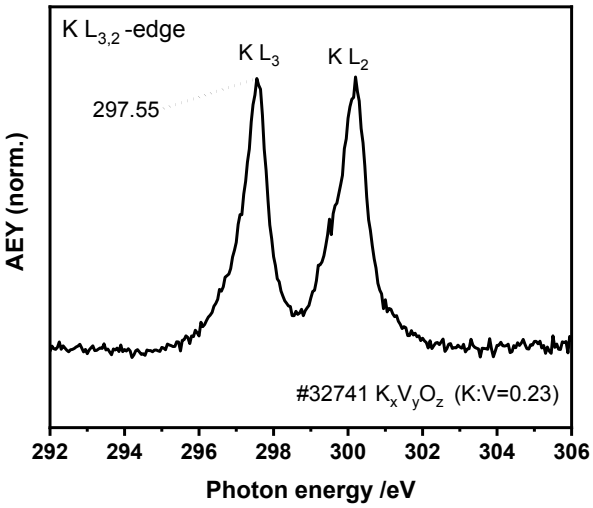

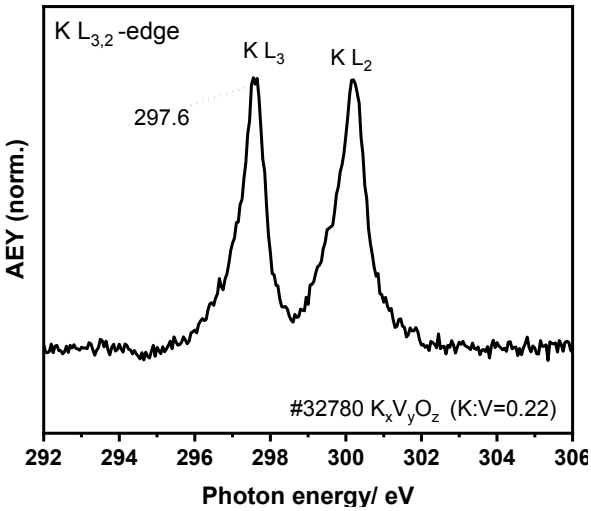

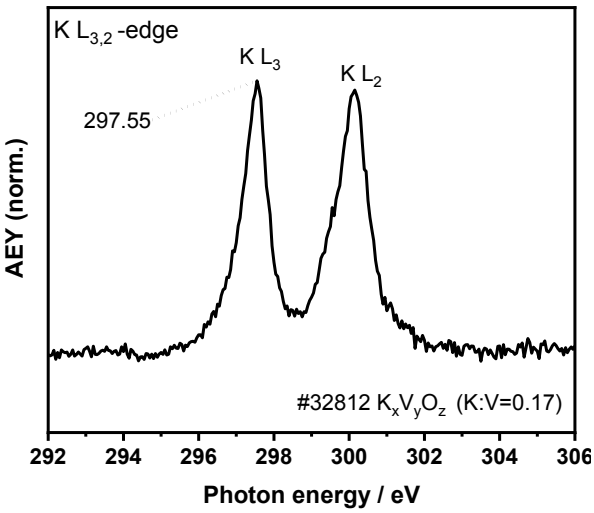

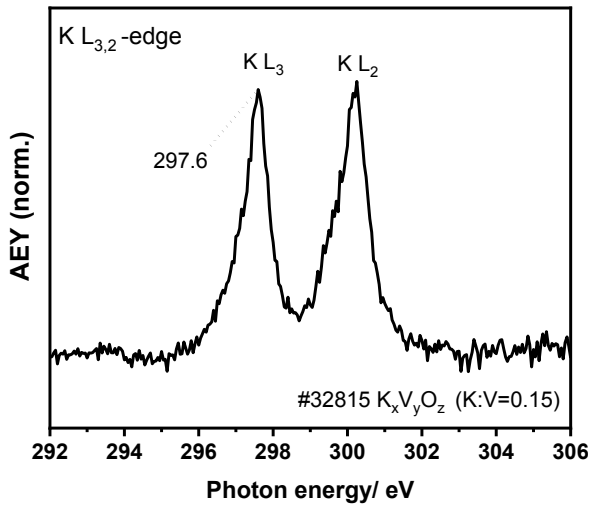
K L3,2 -edge
K L3
K L2
297.6
AEY (norm.)
#32815 KxVyOz (K:V=0.15)
292 294 296 298 300 302 304 306
Photon energy/ eV

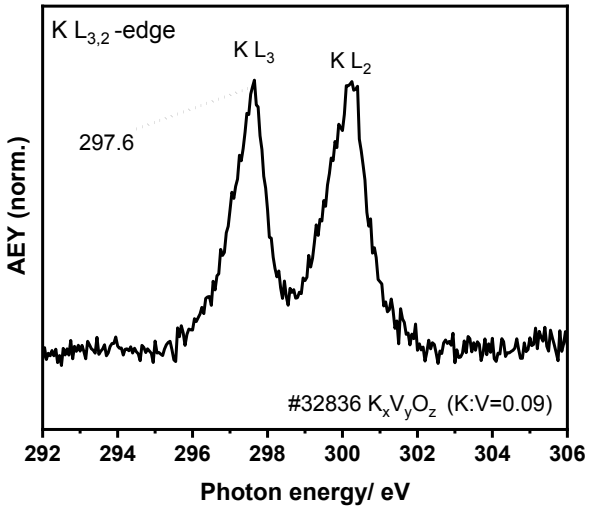
K L3,2 -edge
K L3
K L2
297.6
AEY (norm.)
#32836 KxVyOz (K:V=0.09)
292 294 296 298 300 302 304 306
Photon energy/ eV

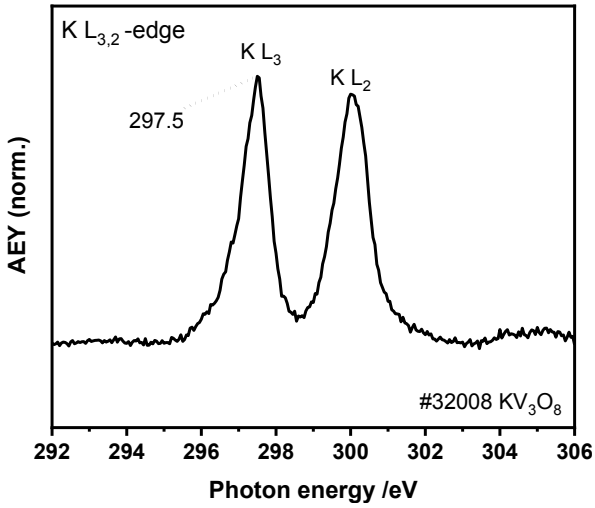
K L3,2 -edge
K L3
K L2
297.5
AEY (norm.)
#32008 KV3O8
292 294 296 298 300 302 304 306
Photon energy /eV

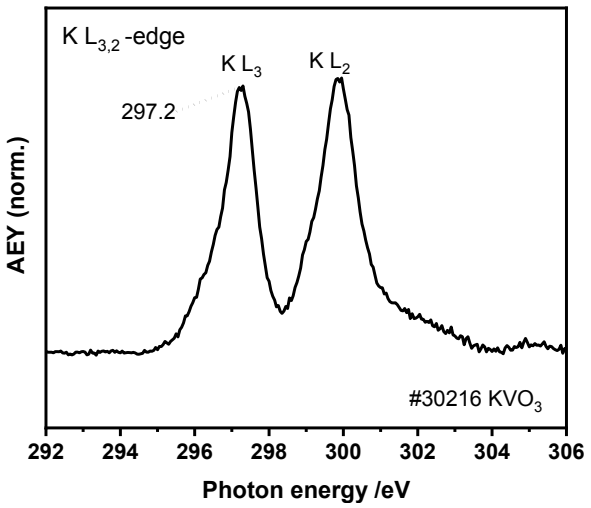
K L3,2 -edge
K L3
K L2
297.2
AEY (norm.)
#30216 KVO3
292 294 296 298 300 302 304 306
Photon energy /eV

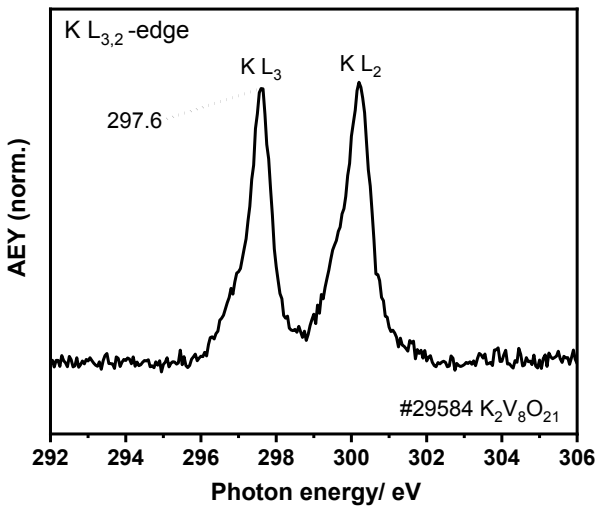
K L3,2 -edge
K L3
K L2
297.6
AEY (norm.)
#29584 K2V8O21
292 294 296 298 300 302 304 306
Photon energy/ eV

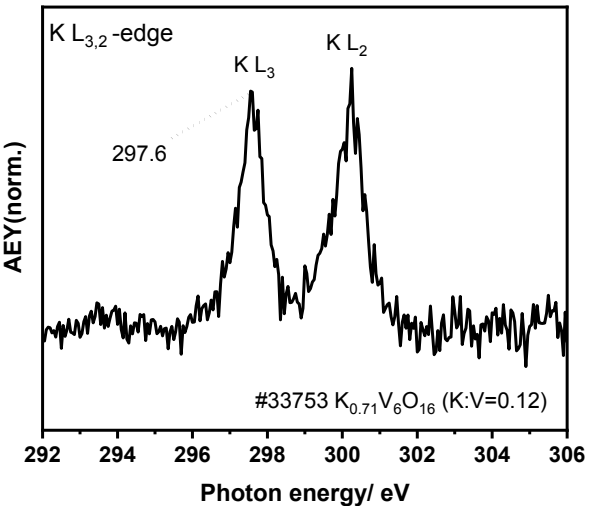
K L3,2 -edge
K L3
K L2
297.6
AEY(norm.)
#33753 K0.71V6O16 (K:V=0.12)
292 294 296 298 300 302 304 306
Photon energy/ eV

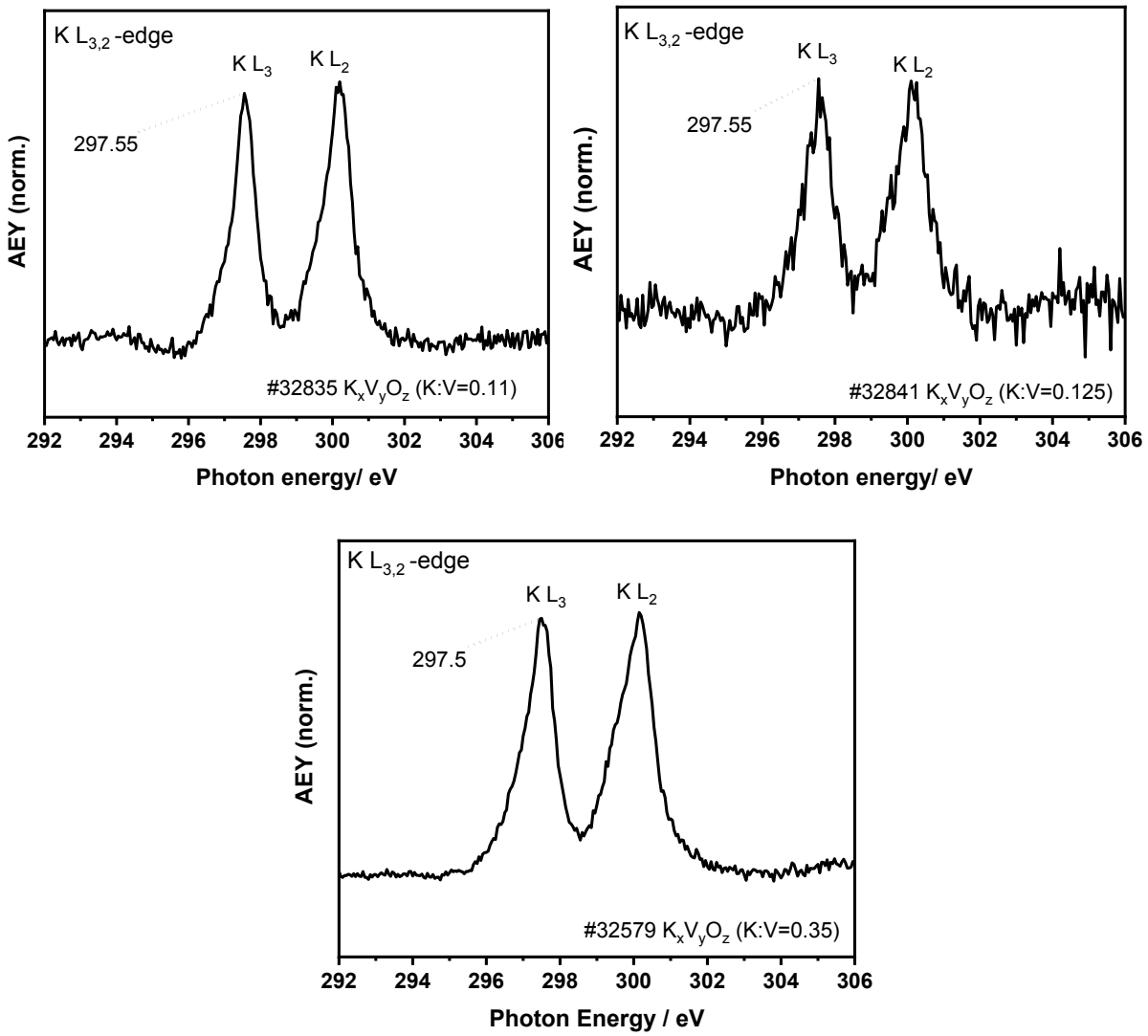

Figure S3.15. In situ K $L_{3,2}$-edge NEXAFS of support-free KVO_x references (at 60°C 250 Pa O_2/N_2=21/79 10 ml min^{-1})

S4. NAP-NEXAFS of silica supported A/V catalysts (A: Li, Na, Rb, and Cs)

V $L_{3,2}$- and O K-edge of Li/V=0.4 catalyst

Silica supported Li/V=0.4 catalyst show no melting in applied propane oxidation conditions. Figure S4.1 presents the V $L_{3,2}$ – (A) and the evolution of O K-edge (B) of Li/V=0.4 catalyst in oxygen and in reaction mixture. V L-edges and O K-edge spectra were presented in the Auger yield (AEY) mode.

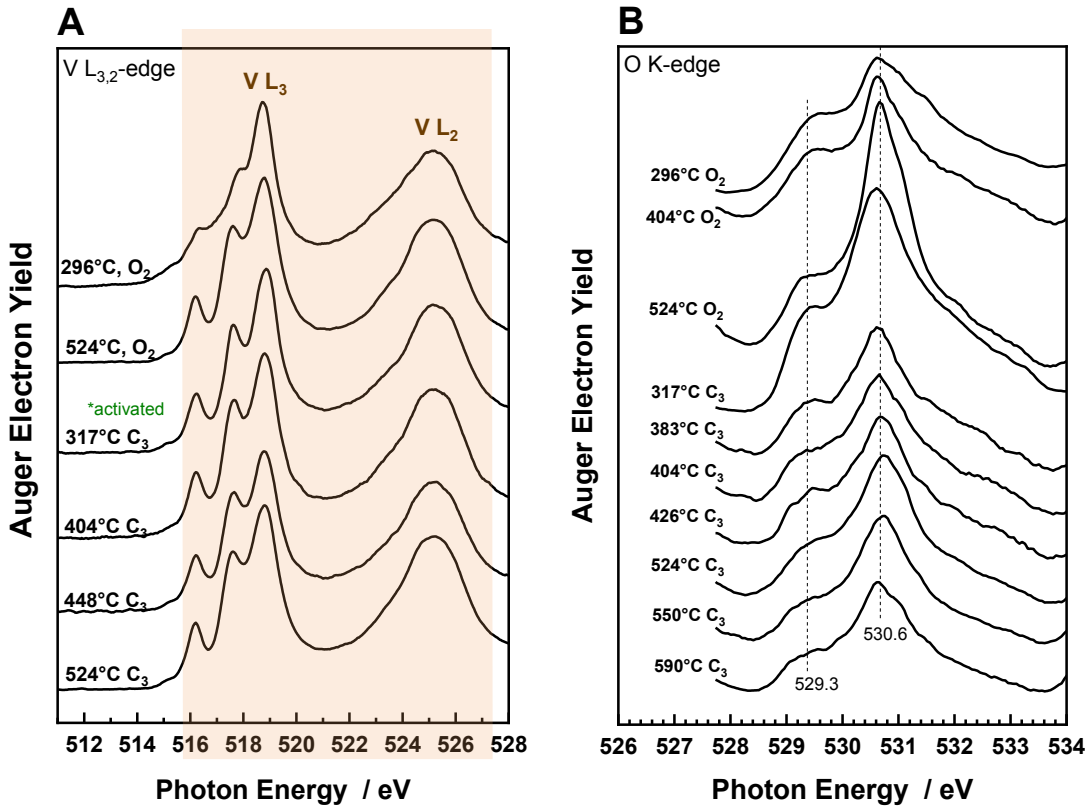

Figure S4.1. **(A)** V $L_{3,2}$- NEXAFS and **(B)** the evolution of O K-edge spectra of silica supported Li/V=0.4 catalyst in activation (at 250 Pa O_2/N_2=21/79 10 ml min^{-1}) and in propane oxidation (at 250 Pa $C_3H_8/O_2/N_2$=7.5/7.5/85 10 ml min^{-1})

In Figure S4.1 (A) there are three shoulders in the V L_3-edge spectra located at ~516.2, ~517.6 and ~518.7 eV. These features did not show any modification upon heating in propane oxidation. V L_3-edges at 524°C in O_2 and in reaction feed (C_3) resemble very much each other. Therefore, it can be stated that the surface state of V_xO_y species has not been altered upon heating as seen in the series of spectra taken during reaction. O K-edge of vanadium containing catalysts represents transitions from O 1s to O 2p. It is a fingerprint for V-O bonds. O K-edge NEXAFS spectra of silica supported Li/V=0.4 catalyst are shown in Figure S4.2 (B). In contrast

to V L_3-edge, O K-NEXAFS spectra show some minor changes. Activated catalyst (at 317°C C_3) has higher resonance intensity compared to the spectra in 296°C in O_2 at phonon energy at 530.6 eV. Moreover, the intensity of the resonance at 529.3 eV is slightly reduced when the catalyst is heated from 380°C to 550°C under reaction conditions. Therefore, structural modification over vanadium oxide species seems occur during reaction.

V $L_{3,2}$- and O K-edge of Na/V=0.5 catalyst:

Na-containing silica supported vanadium oxide catalyst shows no melting behaviour in temperature range where propane oxidation is applied. Figure S4.2 presents the V $L_{3,2}$ – (A) and the evolution of O K-edge (B) of Na/V catalyst in oxygen and in reaction mixture. V L-edges and O K-edge spectra were presented in the AEY mode.

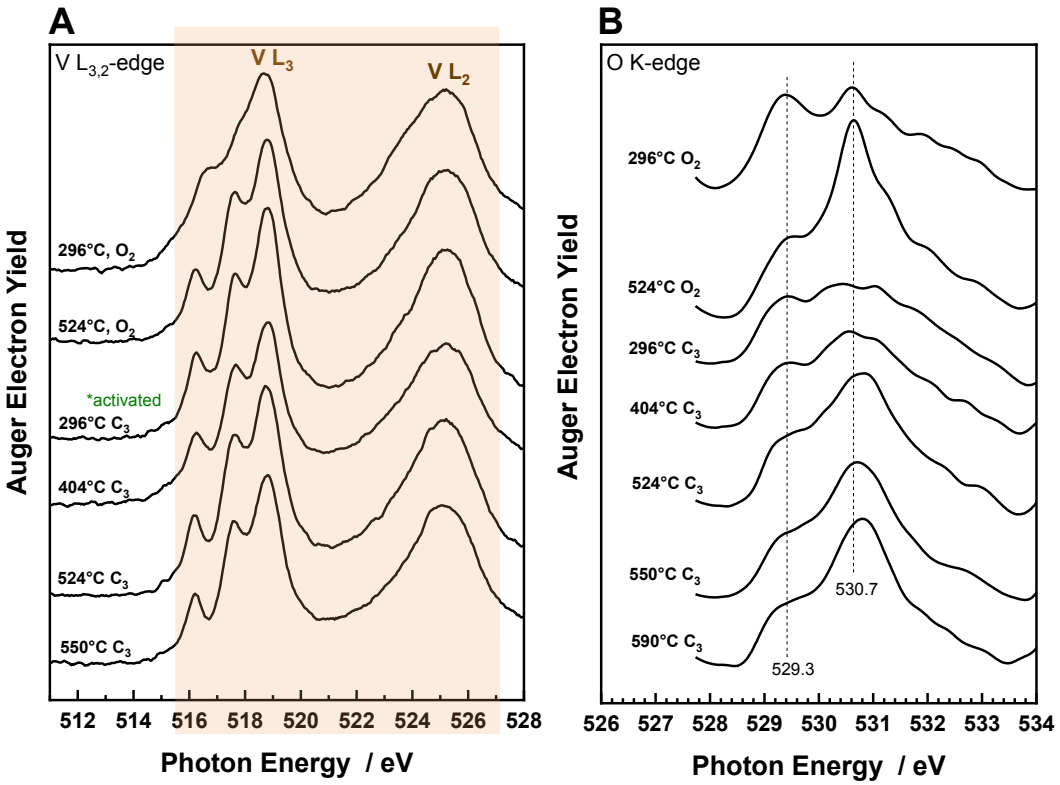

Figure S 4.2. (A) V $L_{3,2}$- NEXAFS and **(B)** the evolution of O K-edge spectra of silica supported Na/V=0.5 catalyst in activation (at 250 Pa O_2/N_2=21/79 10 ml min^{-1}) and in propane oxidation (at 250 Pa $C_3H_8/O_2/N_2$=7.5/7.5/85 10 ml min^{-1})

Similarly in V $L_{3,2}$-edge of Li/V=0.4 catalyst, there is no alteration observed either in the spectral shape or in the energy position of three components of V L_3-edge of Na/V=0.5 catalyst. That means electronic environment of vanadium possesses the same via heating under reaction conditions. On the other hand, O K-edge shows major changes. The one big change occurred with activation. A significant difference between the O K-edges of the catalyst between 296°C

under O_2 and 296°C under reaction feed is present. When temperature increases from 296°C to 550°C under reaction, the strong intensity increase at the onset of the O K-edge at about 530.7 eV.

V L_3-edge fitting of Na/V=0.5 catalyst:

V L_3-edge NEXAFS of silica supported Na/V=0.6 catalyst together with reference compounds is shown in Figure S4.3. Since there is no support-free Na-containing vanadium oxide sample available, the fitting was done using only supported vanadium oxide species. That means the fit model for K/V=0.6 and Na/V=0.5 catalysts are not the same. However, the same approach was applied. For developing the fit model for Na/V catalyst, several V/SBA-15 references with various vanadia loadings were used. Then combinatorial approach which testing all combinations (but limiting the number of references used for each fit) were used to find which spectra might be relevant.

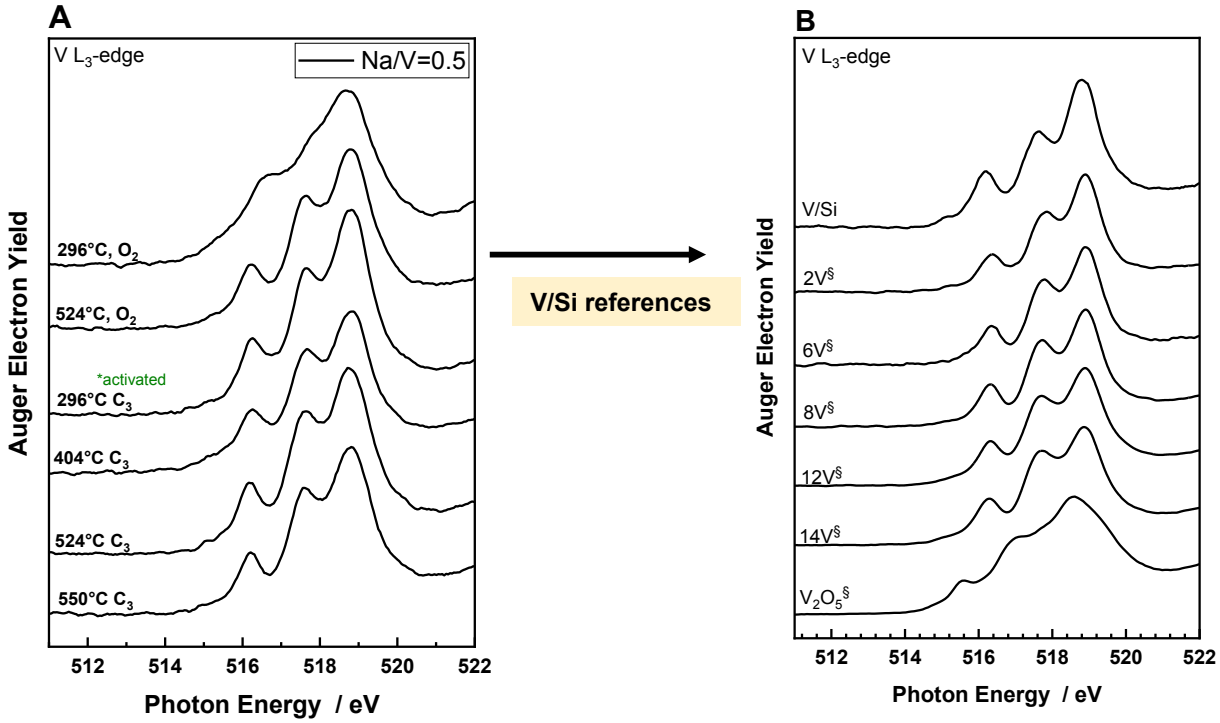

Figure S4.3. (A) V L_3-edge of silica supported Na/V=0.5 catalyst activation (at 250 Pa O_2/N_2=21/79 10 ml min^{-1}) and in propane oxidation (at 250 Pa $C_3H_8/O_2/N_2$=7.5/7.5/85 10 ml min^{-1}) and **(B)** V L_3-edge of V/Si synthesized in this study, V_xO_y/SBA-15 with various vanadium loadings (§)[336] and V_2O_5 powder (§)[336] as reference materials.

After that, the fit model was reduced to a minimum number of spectra (also fix the energy position), and let the final spectra set run through the complete Na/V series for different temperatures. The result of a constrained fit is shown in Figure S4.4. Here for silica supported

Na/V=0.5 catalyst, possible contributions of $8V^{\S}$, $12V^{\S}$, and V_2O_5 were found. It is seen in Figure S4.4 shows that the model fits very well to the measured data. This tells surface vanadium oxide species are dominant in the Na/V=0.5 catalyst. The contribution ("weight") of the chosen references to the experimental spectrum as obtained by the fit is shown in Figure S4.5. One can see that activated Na/V=0.5 catalyst is a mixture of monomeric/polymeric and as well as bulk-like V_2O_5 species. With increasing temperature, the weight of polymeric species ($12V^{\S}$) are increased.

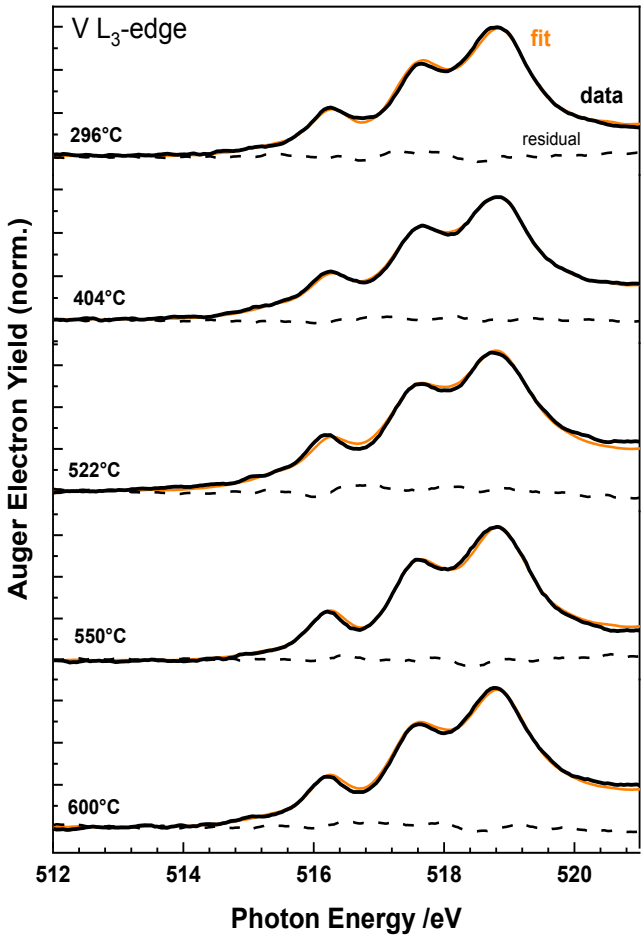

Figure S4.4. Experimental versus fitting curves of V L_3-edge NEXAFS spectra of Na/V=0.5 catalyst (activated) in different temperatures during propane oxidation reaction. The experimentally measured data and fitting curves are plotted with solid black and orange line, respectively. The dashed line indicates the residual spectra obtained by subtracting fitting curve from the measured data.

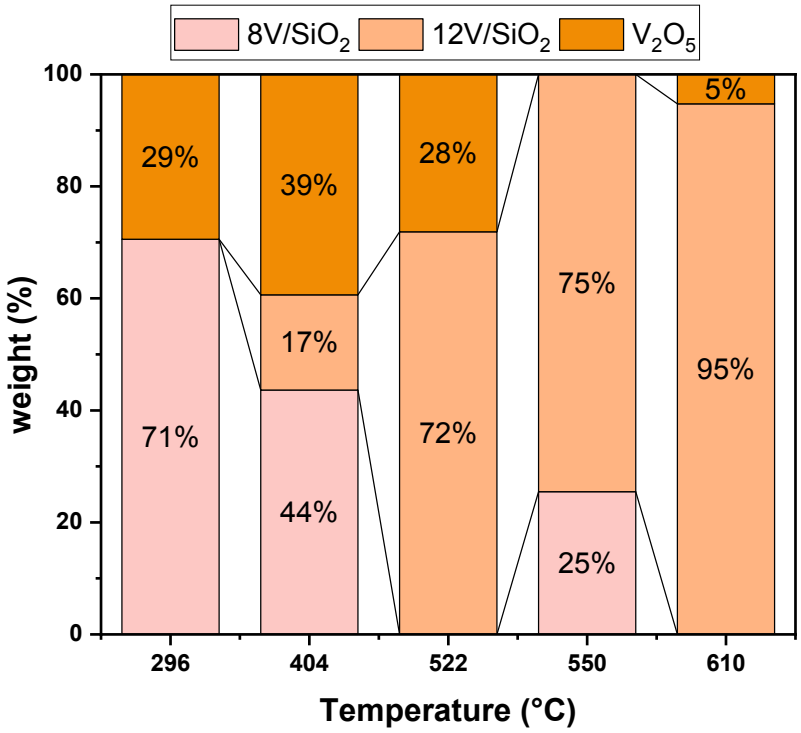

Figure S4.5. Distribution of reference species over silica supported Na/V=0.5 catalyst during propane oxidation reaction as calculated by the fit model using ATHENA program.

V $L_{3,2}$- and O K-edge of Rb/V=0.6 catalyst:

Rb-containing silica supported vanadium oxide catalysts show melting under applied propane oxidation reaction conditions. Figure S4.6 presents the V $L_{3,2}$ – **(A)** in oxygen and in reaction mixture and the evolution of O K-edge **(B)** of Rb/V catalyst in reaction mixture. V L-edges and O K-edge spectra were presented in both AEY and TEY mode.

The V L_3-edge of Rb/V=0.6 shows three distinct features after activation (*i.e.* 296°C in C_3) at ~516.2, ~517.6 and ~518.7 eV as similarly seen in V L-edge of K/V=0.6 catalyst. Resonances at 516.2 and 517.6 eV loses their intensities drastically when temperature raised from 361°C to 404°C. This is occurring at the temperature where Rb/V phase/s melts (T_m=393°C) Again, the significant impact of melting of Rb/V phase on the electronic environment of vanadium is obtained.

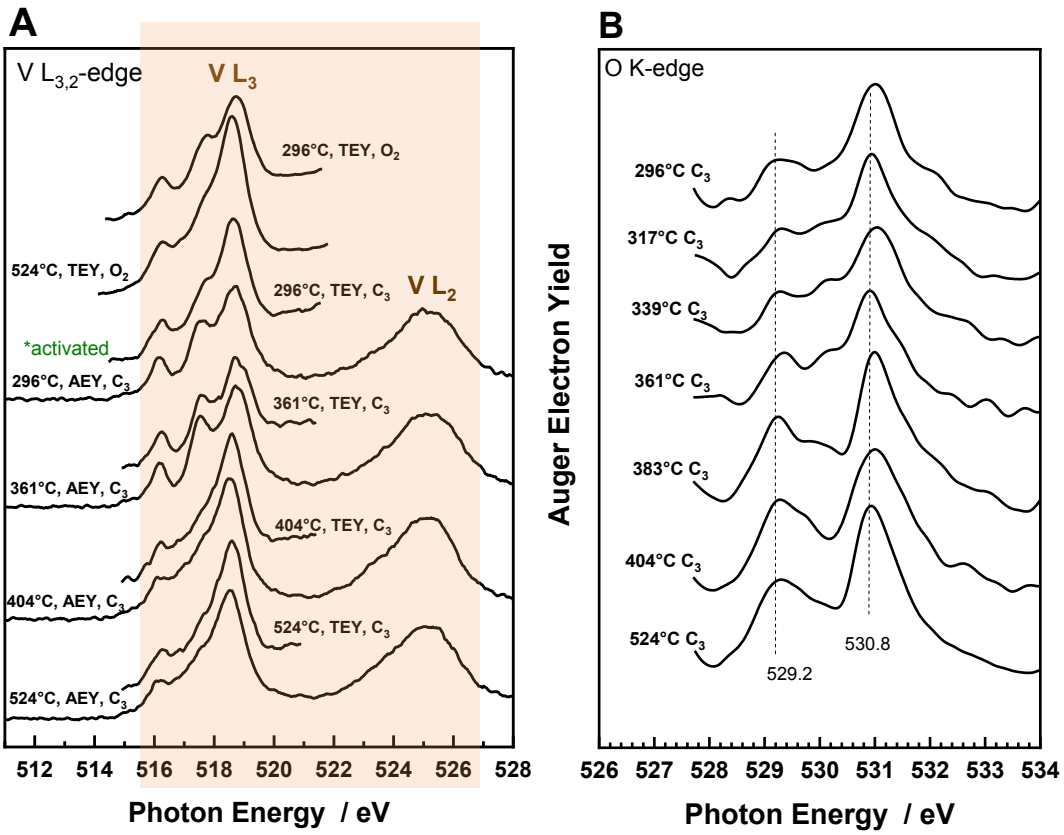

Figure S4.6. (A) V $L_{3,2}$- NEXAFS of silica supported Rb/V=0.6 catalyst in activation (at 250 Pa O_2/N_2=21/79 10 ml min^{-1}) and in propane oxidation (at 250 Pa $C_3H_8/O_2/N_2$=7.5/7.5/85 10 ml min^{-1}) and **(B)** the evolution of O K-edge spectra in propane oxidation (at 250 Pa $C_3H_8/O_2/N_2$=7.5/7.5/85 10 ml min^{-1})

Moreover O K-edge of the catalyst possesses two pronounced shoulder at 529.2 and 530.8 eV. The resonance intensity ratio between two features do not show any change until melting. When temperature is above the melting of the phase in propane oxidation (404°C, C_3), the increase in intensity in both shoulder was recognizable.

V $L_{3,2}$- and O K-edge of Cs/V=0.4 catalyst:

Cs-containing silica supported vanadium oxide catalysts show melting under applied propane oxidation reaction conditions. Figure S4.7 presents the V $L_{3,2}$ – **(A)** in oxygen and in reaction mixture and the evolution of O K-edge **(B)** of Cs/V=0.4 catalyst in reaction mixture. V L-edges and O K-edge spectra were presented in both AEY mode.

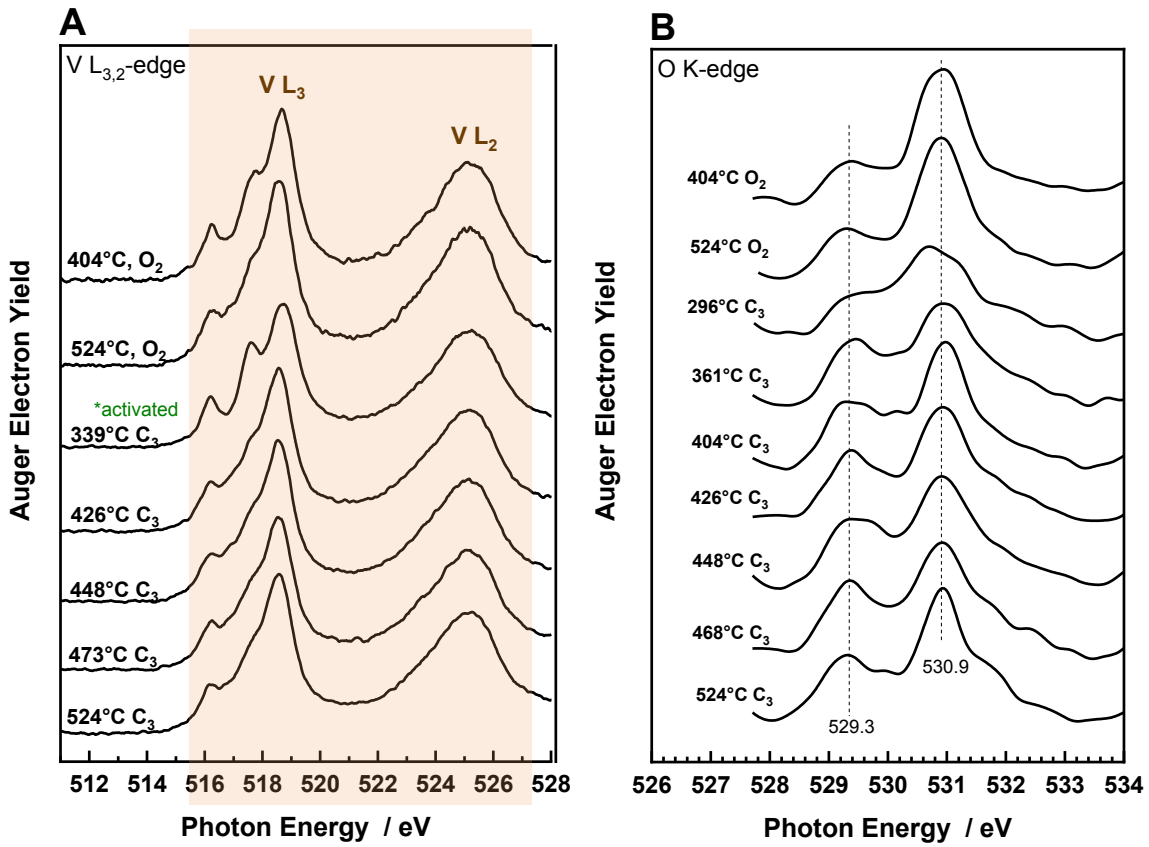

Figure S4.7. (A) V $L_{3,2}$- NEXAFS and **(B)** the evolution of O K-edge spectra of silica supported Cs/V=0.4 catalyst in activation (at 250 Pa O_2/N_2=21/79 10 ml min^{-1}) and in propane oxidation (at 250 Pa $C_3H_8/O_2/N_2$=7.5/7.5/85 10 ml min^{-1})

The V L_3-edge of Cs/V=0.6 shows three distinct absorption features after activation (*i.e.* 339°C in C_3) at ~516.2, ~517.6 and ~518.7 eV as similarly seen in V L-edge of K/V and Rb/V catalysts. Resonances at 516.2 and 517.6 eV loses their intensities drastically when temperature raised from 339°C to 448°C. This is the temperature range where melting of surface Cs/V phase/s occur as determined by DSC (T_m= 430-450°C). The significant impact of melting of Cs/V phase is seen on the electronic environment of vanadium. O K-edge of the catalyst possesses two pronounced shoulder at 529.3 and 530.9 eV. Spectral shape and the intensities of absorption energies of activated catalyst (296°C C_3) is different than the fresh catalyst (404°C O_2). When temperature arises above melting (from 404°C C_3 to 468°C C_3), a strong intensity increase at the onset of the O K-edge at about 529.3 eV is found.

Catalytic performance measured for A/V catalysts in XPS chamber:

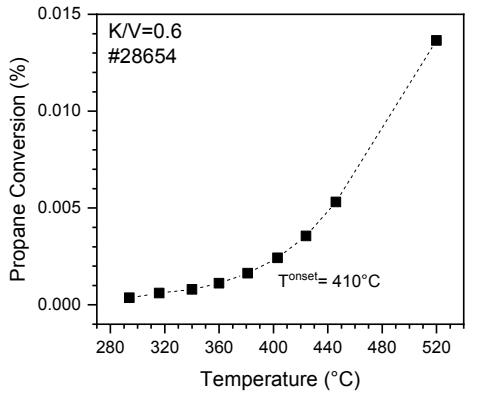

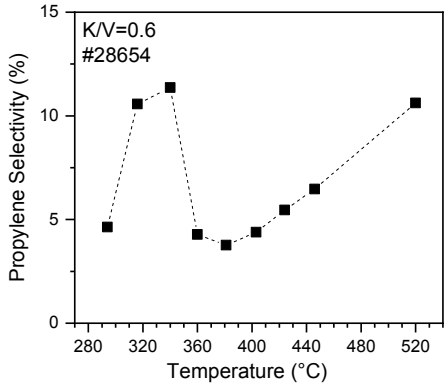

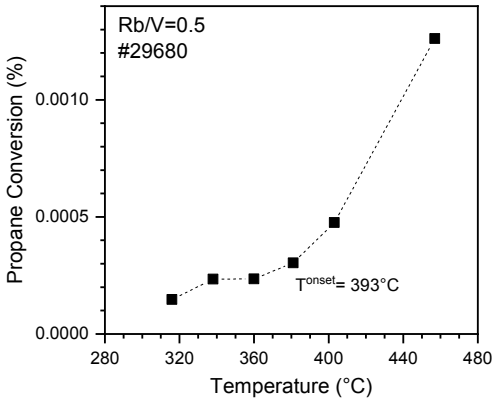

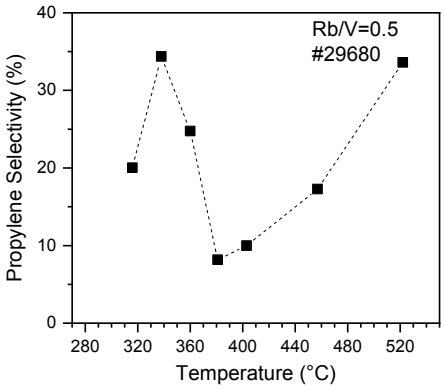

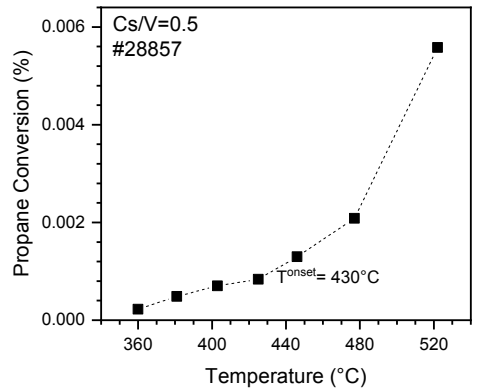

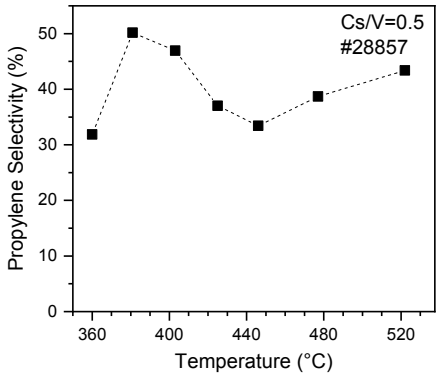

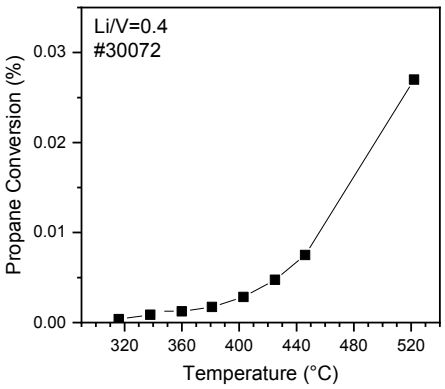

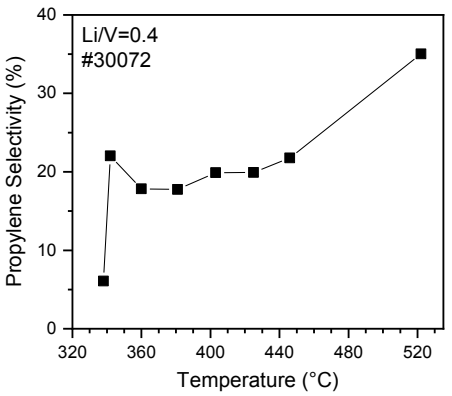

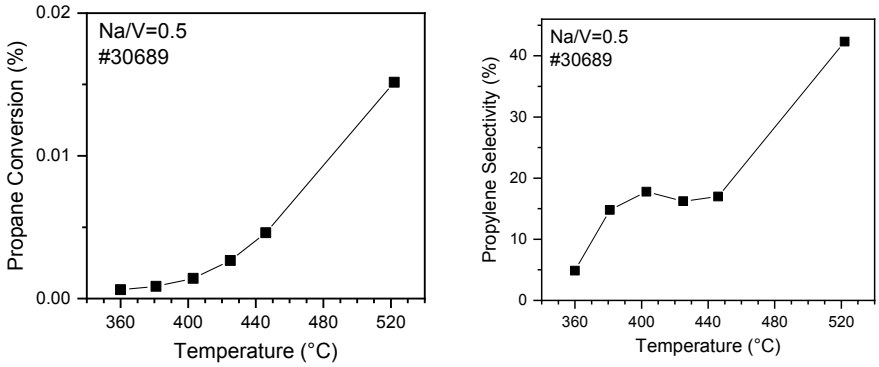

Figure S 4.8. Propane oxidation measured over silica supported A/V catalysts at 250 Pa, with a feed $C_3H_8/O_2/N_2$=7.5/7.5/85 and a total flow of 10 ml min^{-1})

NAP-XPS: only high T (O 1s and V2p) could be analyzed due to differential charging of silica)

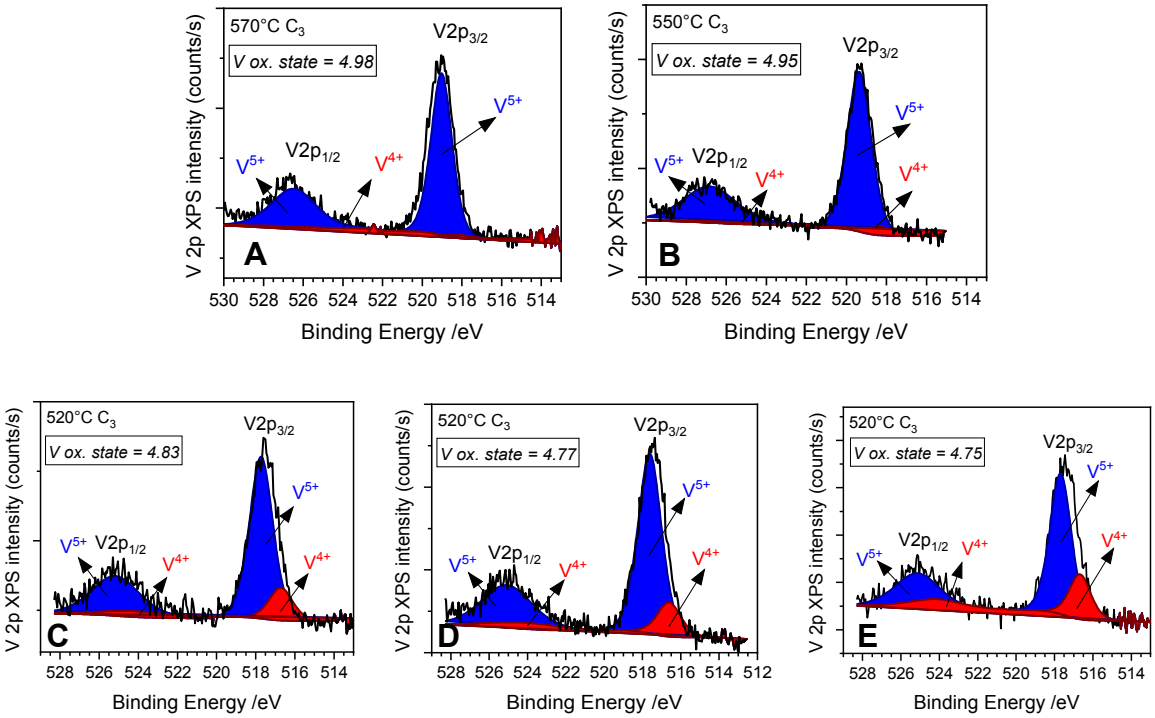

Figure S4.9. V $2p_{3/2}$ XP core level spectra in O_2 of A/V catalysts at 520°C (250Pa in $21O_2$/79Ar) **(A)** Li/V=0.4, **(B)** Na/V=0.5, **(C)** K/V=0.6**, (D)** Rb/V=0.5, **(E)** Cs/V=0.4

Bibliography

[1] C.A. Carrero, R. Schloegl, I.E. Wachs, R. Schomaecker, Critical Literature Review of the Kinetics for the Oxidative Dehydrogenation of Propane over Well-Defined Supported Vanadium Oxide Catalysts, ACS Catalysis, 4 (2014) 3357-3380.
[2] J. Haber, Theoretical Basis of the Activation of C-H Bond in Catalytic Activation and Functionalisation of Light Alkanes, 1st edition ed., Kluwer Academic Publishers, 1998.
[3] R. Schlögl, Heterogeneous Catalysis, Angewandte Chemie International Edition, 54 (2015) 3465-3520.
[4] R. Schlögl, Selective Oxidation: From a Still Immature Technology to the Roots of Catalysis Science, Topics in Catalysis, 59 (2016) 1461-1476.
[5] J. Haber, Fifty years of my romance with vanadium oxide catalysts, Catalysis Today, 142 (2009) 100-113.
[6] I.E. Wachs, Catalysis science of supported vanadium oxide catalysts, Dalton Transactions, 42 (2013) 11762-11769.
[7] B. Grzybowska-Świerkosz, Effect of Additives on the Physicochemical and Catalytic Properties of Oxide Catalysts in Selective Oxidation Reactions, Topics in Catalysis, 21 (2002) 35-46.
[8] R.K. Grasselli, Fundamental Principles of Selective Heterogeneous Oxidation Catalysis, Topics in Catalysis, 21 (2002) 79-88.
[9] G. Bauer, V. Güther, H. Hess, A. Otto, O. Roidl, H. Roller, S. Sattelberger, S. Köther-Becker, T. Beyer, Vanadium and Vanadium Compounds, Ullmann's Encyclopedia of Industrial Chemistry, pp. 1-22.
[10] E. Del Carpio, L. Hernández, C. Ciangherotti, V. Villalobos Coa, L. Jiménez, V. Lubes, G. Lubes, Vanadium: History, chemistry, interactions with α-amino acids and potential therapeutic applications, Coordination Chemistry Reviews, 372 (2018) 117-140.
[11] M. Sutradhar, J.A.L. Da Silva, A.J.L. Pombeiro, Chapter 1 Introduction: Vanadium, Its Compounds and Applications, Vanadium Catalysis, The Royal Society of Chemistry 2021, pp. 1-11.
[12] J.P. Dunn, H.G. Stenger, I.E. Wachs, Oxidation of SO2over Supported Metal Oxide Catalysts, Journal of Catalysis, 181 (1999) 233-243.
[13] A. Bielański, M. Najbar, $V_2O_5 \bullet MoO_3$ catalysts for benzene oxidation, Applied Catalysis A: General, 157 (1997) 223-261.
[14] G.S. Patience, R.E. Bockrath, Butane oxidation process development in a circulating fluidized bed, Applied Catalysis A: General, 376 (2010) 4-12.
[15] U.S. Ozkan, T.A. Harris, B.T. Schilf, The partial oxidation of C_5 hydrocarbons over vanadia-based catalysts, Catalysis Today, 33 (1997) 57-71.
[16] T. Boningari, R. Koirala, P.G. Smirniotis, Low-temperature catalytic reduction of NO by NH_3 over vanadia-based nanoparticles prepared by flame-assisted spray pyrolysis: Influence of various supports, Applied Catalysis B: Environmental, 140-141 (2013) 289-298.
[17] F. Gao, C.H.F. Peden, Recent Progress in Atomic-Level Understanding of Cu/SSZ-13 Selective Catalytic Reduction Catalysts, Catalysts, 8 (2018) 140.
[18] N.-Y. Topsøe, Mechanism of the Selective Catalytic Reduction of Nitric Oxide by Ammonia Elucidated by in Situ On-Line Fourier Transform Infrared Spectroscopy, Science, 265 (1994) 1217-1219.
[19] N.Y. Topsoe, H. Topsoe, J.A. Dumesic, Vanadia/Titania Catalysts for Selective Catalytic Reduction (SCR) of Nitric-Oxide by Ammonia: I. Combined Temperature-Programmed in-Situ FTIR and On-line Mass-Spectroscopy Studies, Journal of Catalysis, 151 (1995) 226-240.
[20] I. Bull, W.-M. Xue, P. Burk, R.S. Boorse, W.M. Jaglowski, G.S. Koermer, A. Moini, J.A. Patchett, J.C. Dettling, M.T. Caudle, Copper CHA zeolite catalysts, BASF Corp, 2008.

[21] Y. Inomata, H. Kubota, S. Hata, E. Kiyonaga, K. Morita, K. Yoshida, N. Sakaguchi, T. Toyao, K.-i. Shimizu, S. Ishikawa, W. Ueda, M. Haruta, T. Murayama, Bulk tungsten-substituted vanadium oxide for low-temperature NOx removal in the presence of water, Nature Communications, 12 (2021) 557.
[22] M. Kramer, M. Schubert, T. Lautensack, T. Hill, R. Korner, F. Rosowski, J. Zuhlke, Catalyst for the oxidation of SO2 to SO3, BASF SE, 2010.
[23] H.K. G. Ertl, J.Weitkamp (Eds.), Handbook of Heterogeneous Catalysis, Wiley-VCH, Weinheim, 1997.
[24] P.M. Lorz, F.K. Towae, W. Enke, R. Jäckh, N. Bhargava, W. Hillesheim, Phthalic Acid and Derivatives, Ullmann's Encyclopedia of Industrial Chemistry.
[25] M.S. Wainwright, N.R. Foster, Catalysts, Kinetics and Reactor Design in Phthalic Anhydride Synthesis, Catalysis Reviews, 19 (1979) 211-292.
[26] Edgar Viktor HUENNEKES, Kevin David BEARD, Petra CORDES, Ruediger WOLFF, J.M. BECKER, SCR Catalysts for the Treatment of an Exhaust Has of a Diesel Engine in: U. States (Ed.), BASF Corporation, 2019.
[27] M. Thiemann, E. Scheibler, K.W. Wiegand, Nitric Acid, Nitrous Acid, and Nitrogen Oxides, Ullmann's Encyclopedia of Industrial Chemistry.
[28] J.C. Védrine, Heterogeneous Partial (amm)Oxidation and Oxidative Dehydrogenation Catalysis on Mixed Metal Oxides, Catalysts, 6 (2016) 22.
[29] K. Karim, E. Mamedov, M.H. Al-Hazmi, A.H. Fakeeha, M.A. Soliman, Y.S. Al-Zeghayer, A.S. Al-Fatish, A.A. Al-Arify, Catalysts for producing acetic acid from ethane oxidation, Saudi Basic Industries Corp, 2000.
[30] G. Tufan, A. Akgerman, Kinetics of benzene oxidation over a vanadium oxide (V_2O_5) catalyst, Industrial & Engineering Chemistry Process Design and Development, 20 (1981) 604-608.
[31] T.Q.P. Quach, D. Rouleau, C. Chavarie, C. Laguerie, Catalytic oxidation of benzene to maleic anhydride in a continuous stirred tank reactor, The Canadian Journal of Chemical Engineering, 56 (1978) 72-78.
[32] K. Lohbeck, H. Haferkorn, W. Fuhrmann, N. Fedtke, Maleic and Fumaric Acids, Ullmann's Encyclopedia of Industrial Chemistry.
[33] N. Ballarini, F. Cavani, C. Cortelli, S. Ligi, F. Pierelli, F. Trifirò, C. Fumagalli, G. Mazzoni, T. Monti, VPO catalyst for n-butane oxidation to maleic anhydride: A goal achieved, or a still open challenge?, Topics in Catalysis, 38 (2006) 147-156.
[34] F. Trifirò, R.K. Grasselli, How the Yield of Maleic Anhydride in n-Butane Oxidation, Using VPO Catalysts, was Improved Over the Years, Topics in Catalysis, 57 (2014) 1188-1195.
[35] G. Mestl, MoVW mixed metal oxides catalysts for acrylic acid production: from industrial catalysts to model studies, Topics in Catalysis, 38 (2006) 69-82.
[36] J.F. Brazdil, J.P. Bartek, US Patent 5 854 172 1998.
[37] J.F. Brazdil, F.A.P. Kobarvkantei, J.P. Padolwski, JP Patent 11033399, 1999.
[38] A.T. Guttman, R.K. Graselli, F.J. Brazdil, US Patents 4 746 641, (1999).
[39] G. Busca, Chapter 11 - Oxidation Catalysts, in: G. Busca (Ed.) Heterogeneous Catalytic Materials, Elsevier, Amsterdam, 2014, pp. 375-419.
[40] K. Miyaki, M. Yanagita, H. Watanabe, T. Karasuda, Catalyst for synthesizing acrylonitrile and process for producing acrylonitrile, Mitsubishi Chemical Corp, 2008.
[41] R. Hugo, S. Jordan, K. Wenz, T. Preiss, A. Weck, Method for Producing Xylenediamine BASF Aktiengesellschaft Ludwigshafen (DE), 2009.
[42] F. Cavalca, P. Beato, J. Hyldtoft, K. Christensen, S. Helveg, Vanadia-Based Catalysts for the Sulfur Dioxide Oxidation Studied In Situ by Transmission Electron Microscopy and Raman Spectroscopy, The Journal of Physical Chemistry C, 121 (2017) 3350-3364.

[43] J.H. Frazer, W.J. Kirkpatrick, A New Mechanism for the Action of the Vanadium Pentoxide-Silica-Alkali Pyrosulfate Catalyst for the Oxidation of Sulfur Dioxide, Journal of the American Chemical Society, 62 (1940) 1659-1660.
[44] A.R. Glueck, C.N. Kenney, The kinetics of the oxidation of sulphur dioxide over molten salts, Chemical Engineering Science, 23 (1968) 1257-1265.
[45] C.N. Kenney, Molten Salt Catalysis of Gas Reactions, Catalysis Reviews, 11 (1975) 197-224.
[46] J. Villadsen, H. Livejerg, Supported Liquid-Phase Catalysts, Catalysis Reviews, 17 (1978) 203-272.
[47] S. Boghosian, R. Fehrmann, N.J. Bjerrum, G.N. Papatheodorou, Formation of crystalline compounds and catalyst deactivation during SO_2 oxidation in $V_2O_5 \bullet M_2S_2O_7$ (M = Na, K, Cs) melts, Journal of Catalysis, 119 (1989) 121-134.
[48] A. Christodoulakis, S. Boghosian, Molecular structure of supported molten salt catalysts for SO2 oxidation, Journal of Catalysis, 215 (2003) 139-150.
[49] P. Mars, J.G.H. Maessen, The mechanism and the kinetics of sulfur dioxide oxidation on catalysts containing vanadium and alkali oxides, Journal of Catalysis, 10 (1968) 1-12.
[50] F.J. Doering, D.A. Berkel, Comparison of kinetic data for KV and CsV sulfuric acid catalysts, Journal of Catalysis, 103 (1987) 126-139.
[51] G. Centi, Vanadyl Pyrophosphate - A Critical Overview, Catalysis Today, 16 (1993) 5-26.
[52] G. Centi, G. Fornasari, F. Trifiro, n-Butane oxidation to maleic anhydride on vanadium-phosphorus oxides: kinetic analysis with a tubular flow stacked-pellet reactor, Industrial & Engineering Chemistry Product Research and Development, 24 (1985) 32-37.
[53] V.V. Guliants, J.B. Benziger, S. Sundaresan, I.E. Wachs, J.M. Jehng, J.E. Roberts, The effect of the phase composition of model VPO catalysts for partial oxidation of n-butane, Catalysis Today, 28 (1996) 275-295.
[54] J. Haber, V.A. Zazhigalov, J. Stoch, L.V. Bogutskaya, I.V. Batcherikova, Mechanochemistry: the activation method of VPO catalysts for n-butane partial oxidation, Catalysis Today, 33 (1997) 39-47.
[55] M. Conte, G. Budroni, J.K. Bartley, S.H. Taylor, A.F. Carley, A. Schmidt, D.M. Murphy, F. Girgsdies, T. Ressler, R. Schlögl, G.J. Hutchings, Chemically Induced Fast Solid-State Transitions of ω-$VOPO_4$ in Vanadium Phosphate Catalysts, Science, 313 (2006) 1270-1273.
[56] G.J. Hutchings, Effect of promoters and reactant concentration on the selective oxidation of n-butane to maleic anhydride using vanadium phosphorus oxide catalysts, Applied Catalysis, 72 (1991) 1-32.
[57] E.M. Boghosian, US Patent 3 862 146, in: I. Standard Oil Co. (Ed.), 1974.
[58] R.L.a.J. Vekemans, US Patent 3 987 063 in: U.C.B. (Ed.), 1976.
[59] V.V. Guliants, J.B. Benziger, S. Sundaresan, I.E. Wachs, A.M. Hirt, Effect of promoters for n-butane oxidation to maleic anhydride over vanadium–phosphorus-oxide catalysts: comparison with supported vanadia catalysts, Catalysis Letters, 62 (1999) 87-91.
[60] S. Irusta, A. Boix, B. Pierini, C. Caspani, J. Petunchi, Effect of Mo on the Active Sites of VPO Catalysts upon the Selective Oxidation of n-Butane, Journal of Catalysis, 187 (1999) 298-310.
[61] B.T. Pierini, E.A. Lombardo, Cr, Mo and W used as VPO promoters in the partial oxidation of n-butane to maleic anhydride, Catalysis Today, 107-108 (2005) 323-329.
[62] B. He, L. Nan, Z. Li, B. Wen, J. Niu, R. Liu, Effect of Mo Species on the Selective Oxidation of n-Butane to Maleic Anhydride over Mo-Promoted VPP, ChemistrySelect, 4 (2019) 662-669.
[63] F. Ivars, L.N. J.M., Lights alkane oxidation:Targets and current challenges, Imperial College Press: London, UK2014.
[64] K. Hamada, S. Komada, US Patent 590 705 2A, Asahi Kasei Group, 1998.
[65] K. Oshama, A. Kayo, T.K. Umezawa, K. Kiyono, I. Sawaki, Synthesis of MoVTe(Sb)-O composite oxide catalyst via reduction of polyoxometalates in an aqueous medium. EP 529 853, 1992.

[66] F. Cavani, N. Ballarini, A. Cericola, Oxidative dehydrogenation of ethane and propane: How far from commercial implementation?, Catalysis Today, 127 (2007) 113-131.
[67] C.A. Gärtner, A.C. van Veen, J.A. Lercher, Oxidative Dehydrogenation of Ethane: Common Principles and Mechanistic Aspects, ChemCatChem, 5 (2013) 3196-3217.
[68] J.M. Lopez Nieto, P. Concepcion, A. Dejoz, H. Knozinger, F. Melo, M.I. Vazquez, Selective oxidation of n-butane and butenes over vanadium-containing catalysts, Journal of Catalysis, 189 (2000) 147-157.
[69] J.M.L. Nieto, The selective oxidative activation of light alkanes. From supported vanadia to multicomponent bulk V-containing catalysts, Topics in Catalysis, 41 (2006) 3-15.
[70] J.C. Védrine, The Role of Redox, Acid-Base and Collective Properties and of Cristalline State of Heterogeneous Catalysts in the Selective Oxidation of Hydrocarbons, Topics in Catalysis, 21 (2002) 97-106.
[71] R. Schlögl, Active Sites for Propane Oxidation: Some Generic Considerations, Topics in Catalysis, 54 (2011) 627-638.
[72] Z. Zhai, X. Wang, R. Licht, A.T. Bell, Selective oxidation and oxidative dehydrogenation of hydrocarbons on bismuth vanadium molybdenum oxide, Journal of Catalysis, 325 (2015) 87-100.
[73] D. Delgado, B. Solsona, A. Ykrelef, A. Rodríguez-Gómez, A. Caballero, E. Rodríguez-Aguado, E. Rodríguez-Castellón, J.M. López Nieto, Redox and Catalytic Properties of Promoted NiO Catalysts for the Oxidative Dehydrogenation of Ethane, The Journal of Physical Chemistry C, 121 (2017) 25132-25142.
[74] E. Heracleous, A.A. Lemonidou, Ni–Nb–O mixed oxides as highly active and selective catalysts for ethene production via ethane oxidative dehydrogenation. Part I: Characterization and catalytic performance, Journal of Catalysis, 237 (2006) 162-174.
[75] E. Heracleous, A.A. Lemonidou, Ni–Me–O mixed metal oxides for the effective oxidative dehydrogenation of ethane to ethylene – Effect of promoting metal Me, Journal of Catalysis, 270 (2010) 67-75.
[76] S. Gaab, J. Find, T.E. Müller, J.A. Lercher, Kinetics and mechanism of the oxidative dehydrogenation of ethane over Li/Dy/Mg/O/(Cl) mixed oxide catalysts, Topics in Catalysis, 46 (2007) 101-110.
[77] L. Ji, J. Liu, X. Chen, M. Li, The oxidative dehydrogenation of ethane over alkali-doped lanthanum-calcium oxide catalysts, Catalysis Letters, 39 (1996) 247-252.
[78] E.M. Kennedy, N.W. Cant, Oxidative dehydrogenation of ethane and the coupling of methane over sodium containing cerium oxides, Applied Catalysis A: General, 87 (1992) 171-183.
[79] E. Morales, J.H. Lunsford, Oxidative dehydrogenation of ethane over a lithium-promoted magnesium oxide catalyst, Journal of Catalysis, 118 (1989) 255-265.
[80] C.P. Kumar, S. Gaab, T.E. Müller, J.A. Lercher, Oxidative Dehydrogenation of Light Alkanes on Supported Molten Alkali Metal Chloride Catalysts, Topics in Catalysis, 50 (2008) 156-167.
[81] T. Blasco, A. Galli, J.M. López Nieto, F. Trifiró, Oxidative Dehydrogenation of Ethane andn-Butane on VO_x/Al_2O_3 Catalysts, Journal of Catalysis, 169 (1997) 203-211.
[82] A. Klisińska, S. Loridant, B. Grzybowska, J. Stoch, I. Gressel, Effect of additives on properties of V_2O_5/SiO_2 and V_2O_5/MgO catalysts: II. Structure and physicochemical properties of the catalysts and their correlations with oxidative dehydrogenation of propane and ethane, Applied Catalysis A: General, 309 (2006) 17-27.
[83] Z. Zhao, Y. Yamada, Y. Teng, A. Ueda, K. Nakagawa, T. Kobayashi, Selective Oxidation of Ethane to Acetaldehyde and Acrolein over Silica-Supported Vanadium Catalysts Using Oxygen as Oxidant, Journal of Catalysis, 190 (2000) 215-227.
[84] Z. Zhao, Y. Yamada, A. Ueda, H. Sakurai, T. Kobayashi, The roles of redox and acid–base properties of silica-supported vanadia catalysts in the selective oxidation of ethane, Catalysis Today, 93-95 (2004) 163-171.

[85] M. Aouine, T. Epicier, J.-M.M. Millet, In Situ Environmental STEM Study of the MoVTe Oxide M1 Phase Catalysts for Ethane Oxidative Dehydrogenation, ACS Catalysis, 6 (2016) 4775-4781.
[86] R. Canioni, C. Marchal-Roch, N. Leclerc-Laronze, M. Haouas, F. Taulèlle, J. Marrot, S. Paul, C. Lamonier, J.-F. Paul, S. Loridant, J.-M.M. Millet, E. Cadot, Selective conversion of {Mo_{132}} Keplerate ion into 4-electron reduced crown-capped Keggin derivative $[Te_5Mo_{15}O_{57}]^{8-}$. A key intermediate to single-phase M1 multielement MoVTeO light-alkanes oxidation catalyst, Chemical Communications, 47 (2011) 6413-6415.
[87] P. Botella, A. Dejoz, M.C. Abello, M.I. Vázquez, L. Arrúa, J.M. López Nieto, Selective oxidation of ethane: Developing an orthorhombic phase in Mo–V–X (X=Nb, Sb, Te) mixed oxides, Catalysis Today, 142 (2009) 272-277.
[88] P. Botella, E. García-González, A. Dejoz, J.M. López Nieto, M.I. Vázquez, J. González-Calbet, Selective oxidative dehydrogenation of ethane on MoVTeNbO mixed metal oxide catalysts, Journal of Catalysis, 225 (2004) 428-438.
[89] R. Burch, R. Swarnakar, Oxidative dehydrogenation of ethane on vanadium-molybdenum oxide and vanadium-niobium-molybdenum oxide catalysts, Applied Catalysis, 70 (1991) 129-148.
[90] S.T. Oyama, G.A. Somorjai, Effect of structure in selective oxide catalysis: oxidation reactions of ethanol and ethane on vanadium oxide, The Journal of Physical Chemistry, 94 (1990) 5022-5028.
[91] C. Carrara, S. Irusta, E. Lombardo, L. Cornaglia, Study of the Co-VPO interaction in promoted n-butane oxidation catalysts, Applied Catalysis A: General, 217 (2001) 275-286.
[92] M. Heenemann, C. Heine, M. Hävecker, A. Trunschke, R. Schlögl, Influence of Steam on a Vanadyl Pyrophosphate Catalyst During Propane Oxidation, The Journal of Physical Chemistry B, 122 (2018) 695-704.
[93] C. Heine, M. Hävecker, E. Stotz, F. Rosowski, A. Knop-Gericke, A. Trunschke, M. Eichelbaum, R. Schlögl, Ambient-Pressure Soft X-ray Absorption Spectroscopy of a Catalyst Surface in Action: Closing the Pressure Gap in the Selective n-Butane Oxidation over Vanadyl Pyrophosphate, The Journal of Physical Chemistry C, 118 (2014) 20405-20412.
[94] C. Schulz, F. Pohl, M. Driess, R. Glaum, F. Rosowski, B. Frank, Selective Oxidation of n-Butane over Vanadium Phosphate Based Catalysts: Reaction Network and Kinetic Analysis, Industrial & Engineering Chemistry Research, 58 (2019) 2492-2502.
[95] M. Eichelbaum, R. Glaum, M. Hävecker, K. Wittich, C. Heine, H. Schwarz, C.-K. Dobner, C. Welker-Nieuwoudt, A. Trunschke, R. Schlögl, Towards Physical Descriptors of Active and Selective Catalysts for the Oxidation of n-Butane to Maleic Anhydride, ChemCatChem, 5 (2013) 2318-2329.
[96] C. Heine, F. Girgsdies, A. Trunschke, R. Schlögl, M. Eichelbaum, The model oxidation catalyst α-V2O5: insights from contactless in situ microwave permittivity and conductivity measurements, Applied Physics A, 112 (2013) 289-296.
[97] A.M. Wernbacher, M. Eichelbaum, T. Risse, S. Cap, A. Trunschke, R. Schlögl, Operando Electrical Conductivity and Complex Permittivity Study on Vanadia Oxidation Catalysts, The Journal of Physical Chemistry C, 123 (2019) 8005-8017.
[98] B. Solsona, J.M. López Nieto, P. Concepción, A. Dejoz, F. Ivars, M.I. Vázquez, Oxidative dehydrogenation of ethane over Ni–W–O mixed metal oxide catalysts, Journal of Catalysis, 280 (2011) 28-39.
[99] P. Concepción, A. Corma, J.M. López Nieto, J. Pérez-Pariente, Selective oxidation of hydrocarbons on V- and/or Co-containing aluminophosphate (MeAPO-5) using molecular oxygen, Applied Catalysis A: General, 143 (1996) 17-28.
[100] P. Concepción, J.M. López Nieto, J. Pérez-Pariente, Oxidative dehydrogenation of ethane on a magnesium-vanadium aluminophosphate (MgVAPO-5) catalyst, Catalysis Letters, 28 (1994) 9-15.
[101] J.M.L. Nieto, P. Botella, M.I. Vázquez, A. Dejoz, The selective oxidative dehydrogenation of ethane over hydrothermally synthesised MoVTeNb catalysts, Chemical Communications, (2002) 1906-1907.

[102] H.X. Dai, C.F. Ng, C.T. Au, Perovskite-Type Halo-oxide $La_{1-x}Sr_xFeO^{3-\delta}X^{\sigma}$ (X=F, Cl) Catalysts Selective for the Oxidation of Ethane to Ethene, Journal of Catalysis, 189 (2000) 52-62.
[103] P. Botella, A. Dejoz, J.M. López Nieto, P. Concepción, M.I. Vázquez, Selective oxidative dehydrogenation of ethane over MoVSbO mixed oxide catalysts, Applied Catalysis A: General, 298 (2006) 16-23.
[104] S. Ishikawa, W. Ueda, Microporous crystalline Mo–V mixed oxides for selective oxidations, Catalysis Science & Technology, 6 (2016) 617-629.
[105] A. Beretta, P. Forzatti, E. Ranzi, Production of Olefins via Oxidative Dehydrogenation of Propane in Autothermal Conditions, Journal of Catalysis, 184 (1999) 469-478.
[106] A. Galli, J.M. López Nieto, A. Dejoz, M.I. Vazquez, The effect of potassium on the selective oxidation ofn-butane and ethane over Al_2O_3-supported vanadia catalysts, Catalysis Letters, 34 (1995) 51-58.
[107] S. Benomar, A. Chieregato, A. Masso, M.D. Soriano, J.A. Vidal-Moya, T. Blasco, R. Issaadi, J.M. López Nieto, Al_2O_3-Supported W–V–O bronze catalysts for oxidative dehydrogenation of ethane, Catalysis Science & Technology, 10 (2020) 8064-8076.
[108] M. Soliman, Y. Al-Zeghayer, A.S. Al-Awadi, S. Al-Mayman, Economics of Acetic Acid Production by Partial Oxidation of Ethane, APCBEE Procedia, 3 (2012) 200-208.
[109] N.F. Chen, K. Oshihara, W. Ueda, Selective oxidation of ethane over hydrothermally synthesized Mo–V–Al–Ti oxide catalyst, Catalysis Today, 64 (2001) 121-128.
[110] X. Li, E. Iglesia, Support and promoter effects in the selective oxidation of ethane to acetic acid catalyzed by Mo-V-Nb oxides, Applied Catalysis A: General, 334 (2008) 339-347.
[111] J.H. Holles, C.J. Dillon, J.A. Labinger, M.E. Davis, A substrate-versatile catalyst for the selective oxidation of light alkanes: I. Reactivity, Journal of Catalysis, 218 (2003) 42-53.
[112] A. Erdöhelyi, F. Solymosi, Partial oxidation of ethane over KVO_3/SiO_2 and potassium promoted V_2O_5/SiO_2 catalysts, Applied Catalysis, 39 (1988) L11-L14.
[113] A. Erdöhelyi, F. Solymosi, Oxidation of ethane over silica-supported alkali metal vanadate catalysts, Journal of Catalysis, 129 (1991) 497-510.
[114] Z. Zhao, T. Kobayashi, Partial oxidation of ethane into acetaldehyde and acrolein by oxygen over silica-supported bismuth catalysts, Applied Catalysis A: General, 207 (2001) 139-149.
[115] E.V. Kondratenko, O. Ovsitser, J. Radnik, M. Schneider, R. Kraehnert, U. Dingerdissen, Influence of reaction conditions on catalyst composition and selective/non-selective reaction pathways of the ODP reaction over V_2O_3, VO_2 and V_2O_5 with O_2 and N_2O, Applied Catalysis A: General, 319 (2007) 98-110.
[116] L. Liu, X. Han, J. Zhou, M. Zhang, M. Wu, K. Fang, Oxidative dehydrogenation of propane over three-dimensionally ordered macroporous VMgO catalysts with different vanadium doping, Journal of Porous Materials, 25 (2018) 955-963.
[117] L. Balderas-Tapia, J.A. Wang, I. Hernández-Pérez, G.G. Aguilar-Ríos, P. Schacht, Physicochemical and textural characterization of vanadium–magnesium mixed oxides, Materials Letters, 58 (2004) 3034-3039.
[118] A. Walter, Spectroscopic and catalytic investigations of VxOy/SBA-15 and magnesium vanadate model catalysts for selective propene oxidation, Technische Universität Berlin, Fakultät II - Mathematik und Naturwissenschaften10.14279/depositonce-3046, 2011.
[119] S. Zhang, H. Liu, Insights into the structural requirements for oxidative dehydrogenation of propane on crystalline Mg-V-O catalysts, Applied Catalysis A: General, 568 (2018) 1-10.
[120] J.A. Valverde, A. Echavarría, J.-G. Eon, A.C. Faro, L.A. Palacio, V–Mg–Al catalyst from hydrotalcite for the oxidative dehydrogenation of propane, Reaction Kinetics, Mechanisms and Catalysis, 111 (2014) 679-696.
[121] E.V. Kondratenko, O.V. Buyevskaya, M. Baerns, Characterisation of vanadium-oxide-based catalysts for the oxidative dehydrogenation of propane to propene, Topics in Catalysis, 15 (2001) 175-180.

[122] Z. Zhao, X. Gao, I.E. Wachs, Comparative Study of Bulk and Supported V−Mo−Te−Nb−O Mixed Metal Oxide Catalysts for Oxidative Dehydrogenation of Propane to Propylene, The Journal of Physical Chemistry B, 107 (2003) 6333-6342.
[123] R. Dula, K. Wcisło, J. Stoch, B. Grzybowska, E.M. Serwicka, F. Kooli, K. Bahranowski, A. Gaweł, Layered double hydroxide-derived vanadium catalysts for oxidative dehydrogenation of propane: Influence of interlayer-doping versus layer-doping, Applied Catalysis A: General, 230 (2002) 281-291.
[124] S. Blanco, S.R.G. Carrazán, V. Rives, Oxidative dehydrogenation of propane on Mg-V-Al mixed oxides, Applied Catalysis A: General, 342 (2008) 93-98.
[125] T. Katou, D. Vitry, W. Ueda, Structure dependency of Mo-V-O-based complex oxide catalysts in the oxidations of hydrocarbons, Catalysis Today, 91-92 (2004) 237-240.
[126] M. De, D. Kunzru, Oxidative Dehydrogenation of Propane on V_2O_5/ZrO_2 Catalyst, Catalysis Letters, 96 (2004) 33-42.
[127] J.B. Stelzer, J. Caro, M. Fait, Oxidative dehydrogenation of propane on TiO_2 supported antimony oxide/vanadia catalysts, Catalysis Communications, 6 (2005) 1-5.
[128] S.A. D'Ippolito, M.A. Bañares, J.L.G. Fierro, C.L. Pieck, Propane Oxidative Dehydrogenation on V–Sb/ZrO2 Catalysts, Catalysis Letters, 122 (2008) 252-258.
[129] L. Yuan, S. Bhatt, G. Beaucage, V.V. Guliants, S. Mamedov, R.S. Soman, Novel Mesoporous Mixed Nb−M (M = V, Mo, and Sb) Oxides for Oxidative Dehydrogenation of Propane, The Journal of Physical Chemistry B, 109 (2005) 23250-23254.
[130] M.I. Khan, K. Aydemir, M.R.H. Siddiqui, A.A. Alwarthan, C.L. Marshall, Oxidative Dehydrogenation Properties of Novel Nanostructured Polyoxovanadate Based Materials, Catalysis Letters, 141 (2011) 538-543.
[131] M. Sun, J. Zhang, C. Cao, Q. Zhang, Y. Wang, H. Wan, Significant effect of acidity on catalytic behaviors of Cs-substituted polyoxometalates for oxidative dehydrogenation of propane, Applied Catalysis A: General, 349 (2008) 212-221.
[132] A.C. Sanfiz, T.W. Hansen, D. Teschner, P. Schnörch, F. Girgsdies, A. Trunschke, R. Schlögl, M.H. Looi, S.B.A. Hamid, Dynamics of the MoVTeNb Oxide M1 Phase in Propane Oxidation, The Journal of Physical Chemistry C, 114 (2010) 1912-1921.
[133] V.V. Guliants, R. Bhandari, J.N. Al-Saeedi, V.K. Vasudevan, R.S. Soman, O. Guerrero-Pérez, M.A. Bañares, Bulk mixed Mo–V–Te–O catalysts for propane oxidation to acrylic acid, Applied Catalysis A: General, 274 (2004) 123-132.
[134] W. Ueda, D. Vitry, T. Katou, Structural organization of catalytic functions in Mo-based oxides for propane selective oxidation, Catalysis Today, 96 (2004) 235-240.
[135] K. Amakawa, Y.V. Kolen'ko, A. Villa, M.E. Schuster, L.-I. Csepei, G. Weinberg, S. Wrabetz, R. Naumann d'Alnoncourt, F. Girgsdies, L. Prati, R. Schlögl, A. Trunschke, Multifunctionality of Crystalline MoV(TeNb) M1 Oxide Catalysts in Selective Oxidation of Propane and Benzyl Alcohol, ACS Catalysis, 3 (2013) 1103-1113.
[136] D. Vitry, Y. Morikawa, J.L. Dubois, W. Ueda, Mo-V-Te-(Nb)-O mixed metal oxides prepared by hydrothermal synthesis for catalytic selective oxidations of propane and propene to acrylic acid, Applied Catalysis A: General, 251 (2003) 411-424.
[137] H. Tsuji, K. Oshima, Y. Koyasu, Synthesis of Molybdenum and Vanadium-Based Mixed Oxide Catalysts with Metastable Structure: Easy Access to the $MoVNbTe(Sb)O_x$ Catalytically Active Structure Using Reductant and Oxoacid, Chemistry of Materials, 15 (2003) 2112-2114.
[138] S. Albonetti, G. Blanchard, P. Burattin, F. Cavani, S. Masetti, F. Trifirò, Propane ammoxidation to acrylonitrile over a tin-based mixed-oxide catalyst, Catalysis Today, 42 (1998) 283-295.
[139] E. Arcozzi, N. Ballarini, F. Cavani, M. Cimini, C. Lucarelli, F. Trifirò, P. Delichere, J.-M.M. Millet, P. Marion, The control of catalytic performance of rutile-type Sn/V/Nb/Sb mixed oxides, catalysts for propane ammoxidation to acrylonitrile, Catalysis Today, 138 (2008) 97-103.

[140] N. Ballarini, F. Cavani, S. Di Memmo, F. Zappoli, P. Marion, The role of Sb and Nb in rutile-type Sn/V/Nb/Sb mixed oxides, catalysts for propane ammoxidation to acrylonitrile, Catalysis Today, 141 (2009) 264-270.
[141] N. Ballarini, F. Cavani, D. Ghisletti, R. Catani, U. Cornaro, Cr/V/Sb mixed oxide catalysts for the ammoxidation of propane to acrylonitrile: Part I: Nature of the V species, Catalysis Today, 78 (2003) 237-245.
[142] A.A. Lemonidou, G.J. Tjatjopoulos, I.A. Vasalos, Investigations on the oxidative dehydrogenation of n-butane over VMgO-type catalysts, Catalysis Today, 45 (1998) 65-71.
[143] J. Rischard, C. Antinori, L. Maier, O. Deutschmann, Oxidative dehydrogenation of n-butane to butadiene with Mo-V-MgO catalysts in a two-zone fluidized bed reactor, Applied Catalysis A: General, 511 (2016) 23-30.
[144] O. Rubio, J. Herguido, M. Menéndez, Oxidative dehydrogenation of n-butane on V/MgO catalysts—kinetic study in anaerobic conditions, Chemical Engineering Science, 58 (2003) 4619-4627.
[145] A.P.S. Dias, L.D. Dimitrov, M.C.-R. Oliveira, R. Zăvoianu, A. Fernandes, M.F. Portela, Oxidative dehydrogenation of butane over substoichiometric magnesium vanadate catalysts prepared by citrate route, Journal of Non-Crystalline Solids, 356 (2010) 1488-1497.
[146] X. Liu, L. Duan, W. Yang, X. Zhu, Oxidative dehydrogenation of n-butane to butenes on Mo-doped VMgO catalysts, RSC Advances, 7 (2017) 34131-34137.
[147] R.G. Rizayev, R.M. Talyshinskii, J.M. Seifullayeva, E.M. Guseinova, Y.A. Panteleyeva, E.A. Mamedov, Oxidative Dehydrogenation of The C_4-C_5 Paraffins Over Vanadium-Containing Oxide Catalysts, in: V.C. Corberán, S.V. Bellón (Eds.) Studies in Surface Science and Catalysis, Elsevier 1994, pp. 125-132.
[148] L.M. Cam, N.D. Huyen, N.N. Ha, Oxidative Dehydrogenation of n-Butane over LaV Catalysts Supported on TiO_2, Journal of Chemistry, 2013 (2013) 868906.
[149] N. Madaan, R. Haufe, N.R. Shiju, G. Rothenberg, Oxidative Dehydrogenation of n-Butane: Activity and Kinetics Over VO_x/Al_2O_3 Catalysts, Topics in Catalysis, 57 (2014) 1400-1406.
[150] B. Solsona, F. Ivars, P. Concepcion, J.M. Lopez Nieto, Selective oxidation of n-butane over MoV-containing oxidic bronze catalysts, Journal of Catalysis, 250 (2007) 128-138.
[151] P. Nagaraju, N. Lingaiah, P.S. Sai Prasad, V. Narayana Kalevaru, A. Martin, Preparation, characterization and catalytic properties of promoted vanadium phosphate catalysts, Catalysis Communications, 9 (2008) 2449-2454.
[152] G.J. Hutchings, Vanadium phosphate: a new look at the active components of catalysts for the oxidation of butane to maleic anhydride, Journal of Materials Chemistry, 14 (2004) 3385-3395.
[153] F. Cavani, F. Trifirò, The oxidative dehydrogenation of ethane and propane as an alternative way for the production of light olefins, Catalysis Today, 24 (1995) 307-313.
[154] M. Machli, E. Heracleous, A.A. Lemonidou, Effect of Mg addition on the catalytic performance of V-based catalysts in oxidative dehydrogenation of propane, Applied Catalysis A: General, 236 (2002) 23-34.
[155] T. Ushikubo, H.Nakamura, Y.Koyasu, S.Wajiki, in: U. Patent (Ed.), assigned to Mitsubishi, 1995.
[156] M. Baca, A. Pigamo, J.L. Dubois, J.M.M. Millet, Propane Oxidation on MoVTeNbO Mixed Oxide Catalysts: Study of the Phase Composition of Active and Selective Catalysts, Topics in Catalysis, 23 (2003) 39-46.
[157] P. Kube, B. Frank, R. Schlögl, A. Trunschke, Isotope Studies in Oxidation of Propane over Vanadium Oxide, ChemCatChem, 9 (2017) 3446-3455.
[158] A. Tompos, M. Sanchez-Sanchez, L. Végvári, G.P. Szijjártó, J.L. Margitfalvi, A. Trunschke, R. Schlögl, K. Wanninger, G. Mestl, Combinatorial optimization and synthesis of multiple promoted MoVNbTe catalysts for oxidation of propane to acrylic acid, Catalysis Today, 363 (2021) 45-54.

[159] A. Trunschke, J. Noack, S. Trojanov, F. Girgsdies, T. Lunkenbein, V. Pfeifer, M. Hävecker, P. Kube, C. Sprung, F. Rosowski, R. Schlögl, The Impact of the Bulk Structure on Surface Dynamics of Complex Mo–V-based Oxide Catalysts, ACS Catalysis, 7 (2017) 3061-3071.
[160] X. Li, D.J. Buttrey, D.A. Blom, T. Vogt, Improvement of the Structural Model for the M1 Phase Mo–V–Nb–Te–O Propane (Amm)oxidation Catalyst, Topics in Catalysis, 54 (2011) 614.
[161] M. Hävecker, S. Wrabetz, J. Kröhnert, L.-I. Csepei, R. Naumann d'Alnoncourt, Y.V. Kolen'ko, F. Girgsdies, R. Schlögl, A. Trunschke, Surface chemistry of phase-pure M1 MoVTeNb oxide during operation in selective oxidation of propane to acrylic acid, Journal of Catalysis, 285 (2012) 48-60.
[162] A. Chieregato, J.M. López Nieto, F. Cavani, Mixed-oxide catalysts with vanadium as the key element for gas-phase reactions, Coordination Chemistry Reviews, 301–302 (2015) 3-23.
[163] D. Melzer, G. Mestl, K. Wanninger, A. Jentys, M. Sanchez-Sanchez, J.A. Lercher, On the Promoting Effects of Te and Nb in the Activity and Selectivity of M1 MoV-Oxides for Ethane Oxidative Dehydrogenation, Topics in Catalysis, 63 (2020) 1754-1764.
[164] W.o. Science, http://apps.webofknowledge.com/.
[165] J.S. Plotkin, The changing dynamics of olefin supply/demand, Catalysis Today, 106 (2005) 10-14.
[166] H. Zimmermann, Propene, Ullmann's Encyclopedia of Industrial Chemistry, pp. 00-00.
[167] U.o. York, The Essential Chemical Online: Propene, http://www.essentialchemicalindustry.org/chemicals/propene.html, accessed June 6, 2021.
[168] U. Olsbye, S. Svelle, M. Bjørgen, P. Beato, T.V.W. Janssens, F. Joensen, S. Bordiga, K.P. Lillerud, Conversion of Methanol to Hydrocarbons: How Zeolite Cavity and Pore Size Controls Product Selectivity, Angewandte Chemie International Edition, 51 (2012) 5810-5831.
[169] Propane Dehydrogenation (High Performance CATOFIN Catalysts), https://www.clariant.com/en/Business-Units/Catalysts/Petrochemical-and-Refining-Catalysts/On_Purpose_Propylene/CATOFIN-Technology, accessed June 16, 2021.
[170] J.J.H.B. Sattler, J. Ruiz-Martinez, E. Santillan-Jimenez, B.M. Weckhuysen, Catalytic Dehydrogenation of Light Alkanes on Metals and Metal Oxides, Chemical Reviews, 114 (2014) 10613-10653.
[171] S. Lwin, I.E. Wachs, Olefin Metathesis by Supported Metal Oxide Catalysts, ACS Catalysis, 4 (2014) 2505-2520.
[172] P. Castro-Fernández, D. Mance, C. Liu, I.B. Moroz, P.M. Abdala, E.A. Pidko, C. Copéret, A. Fedorov, C.R. Müller, Propane Dehydrogenation on $G_{a2}O_3$-Based Catalysts: Contrasting Performance with Coordination Environment and Acidity of Surface Sites, ACS Catalysis, 11 (2021) 907-924.
[173] G. Liu, Z.-J. Zhao, T. Wu, L. Zeng, J. Gong, Nature of the Active Sites of VO_x/Al_2O_3 Catalysts for Propane Dehydrogenation, ACS Catalysis, 6 (2016) 5207-5214.
[174] S. Tan, L.B. Gil, N. Subramanian, D.S. Sholl, S. Nair, C.W. Jones, J.S. Moore, Y. Liu, R.S. Dixit, J.G. Pendergast, Catalytic propane dehydrogenation over In_2O_3–Ga_2O_3 mixed oxides, Applied Catalysis A: General, 498 (2015) 167-175.
[175] V.J. Cybulskis, S.U. Pradhan, J.J. Lovón-Quintana, A.S. Hock, B. Hu, G. Zhang, W.N. Delgass, F.H. Ribeiro, J.T. Miller, The Nature of the Isolated Gallium Active Center for Propane Dehydrogenation on Ga/SiO2, Catalysis Letters, 147 (2017) 1252-1262.
[176] K. Fukudome, T. Suzuki, Highly Selective Oxidative Dehydrogenation of Propane to Propylene over VOx–SiO2 Catalysts, Catalysis Surveys from Asia, 19 (2015) 172-187.
[177] B. Schimmoeller, Y. Jiang, S.E. Pratsinis, A. Baiker, Structure of flame-made vanadia/silica and catalytic behavior in the oxidative dehydrogenation of propane, Journal of Catalysis, 274 (2010) 64-75.
[178] E.D. Sushchenko, T.S. Kharlamova, T.I. Izaak, O.V. Vodyankina, Supported MgO–V2O5/Al2O3 catalysts for oxidative propane dehydration: Effect of the molar Mg : V ratio on the phase composition and catalytic properties of samples, Kinetics and Catalysis, 58 (2017) 630-641.

[179] I. Rossetti, G.F. Mancini, P. Ghigna, M. Scavini, M. Piumetti, B. Bonelli, F. Cavani, A. Comite, Spectroscopic Enlightening of the Local Structure Of VOX Active Sites in Catalysts for the Odh of Propane, The Journal of Physical Chemistry C, 116 (2012) 22386-22398.
[180] H. Tian, E.I. Ross, I.E. Wachs, Quantitative Determination of the Speciation of Surface Vanadium Oxides and Their Catalytic Activity, The Journal of Physical Chemistry B, 110 (2006) 9593-9600.
[181] I.E. Wachs, The generality of surface vanadium oxide phases in mixed oxide catalysts, Applied Catalysis A: General, 391 (2011) 36-42.
[182] E.V. Kondratenko, N. Steinfeldt, M. Baerns, Transient and steady state investigation of selective and non-selective reaction pathways in the oxidative dehydrogenation of propane over supported vanadia catalysts, Physical Chemistry Chemical Physics, 8 (2006) 1624-1633.
[183] D. Maganas, A. Trunschke, R. Schlögl, F. Neese, A unified view on heterogeneous and homogeneous catalysts through a combination of spectroscopy and quantum chemistry, Faraday Discussions, 188 (2016) 181-197.
[184] A. Dinse, S. Khennache, B. Frank, C. Hess, R. Herbert, S. Wrabetz, R. Schlögl, R. Schomäcker, Oxidative dehydrogenation of propane on silica (SBA-15) supported vanadia catalysts: A kinetic investigation, Journal of Molecular Catalysis A: Chemical, 307 (2009) 43-50.
[185] J.T. Grant, C.A. Carrero, A.M. Love, R. Verel, I. Hermans, Enhanced Two-Dimensional Dispersion of Group V Metal Oxides on Silica, ACS Catalysis, 5 (2015) 5787-5793.
[186] M.D. Argyle, K. Chen, A.T. Bell, E. Iglesia, Ethane Oxidative Dehydrogenation Pathways on Vanadium Oxide Catalysts, The Journal of Physical Chemistry B, 106 (2002) 5421-5427.
[187] J.T. Grant, J.M. Venegas, W.P. McDermott, I. Hermans, Aerobic Oxidations of Light Alkanes over Solid Metal Oxide Catalysts, Chemical Reviews, 118 (2018) 2769-2815.
[188] F. Klose, T. Wolff, H. Lorenz, A. Seidel-Morgenstern, Y. Suchorski, M. Piórkowska, H. Weiss, Active species on γ-alumina-supported vanadia catalysts: Nature and reducibility, Journal of Catalysis, 247 (2007) 176-193.
[189] Z. Wu, H.-S. Kim, P.C. Stair, S. Rugmini, S.D. Jackson, On the Structure of Vanadium Oxide Supported on Aluminas: UV and Visible Raman Spectroscopy, UV−Visible Diffuse Reflectance Spectroscopy, and Temperature-Programmed Reduction Studies, The Journal of Physical Chemistry B, 109 (2005) 2793-2800.
[190] Y. Gambo, S. Adamu, A.A. Abdulrasheed, R.A. Lucky, M.S. Ba-Shammakh, M.M. Hossain, Catalyst design and tuning for oxidative dehydrogenation of propane – A review, Applied Catalysis A: General, 609 (2021) 117914.
[191] A. Corma, J.M. López-Nieto, N. Paredes, M. Pérez, Y. Shen, H. Cao, S.L. Suib, Oxidative Dehydrogenation Of Propane Over Supported-Vanadium Oxide Catalysts, in: P. Ruiz, B. Delmon (Eds.) Studies in Surface Science and Catalysis, Elsevier 1992, pp. 213-220.
[192] J.M. López Nieto, R. Coenraads, A. Dejoz, M.I. Vazquez, The role of metal oxides as promoters of $V_2O_5/\gamma\text{-}Al_2O_3$ catalysts in the oxidative dehydrogenation of propane, in: R.K. Grasselli, S.T. Oyama, A.M. Gaffney, J.E. Lyons (Eds.) Studies in Surface Science and Catalysis, Elsevier 1997, pp. 443-452.
[193] G. Mul, M.A. Bañares, G. Garcia Cortéz, B. van der Linden, S.J. Khatib, J.A. Moulijn, MultiTRACK and operando Raman-GC study of oxidative dehydrogenation of propane over alumina-supported vanadium oxide catalysts, Physical Chemistry Chemical Physics, 5 (2003) 4378-4383.
[194] B. Olthof, A. Khodakov, A.T. Bell, E. Iglesia, Effects of Support Composition and Pretreatment Conditions on the Structure of Vanadia Dispersed on SiO_2, Al_2O_3, TiO_2, ZrO_2, and HfO_2, The Journal of Physical Chemistry B, 104 (2000) 1516-1528.
[195] C. Resini, T. Montanari, G. Busca, J.-M. Jehng, I.E. Wachs, Comparison of alcohol and alkane oxidative dehydrogenation reactions over supported vanadium oxide catalysts: in situ infrared, Raman and UV–vis spectroscopic studies of surface alkoxide intermediates and of their surface chemistry, Catalysis Today, 99 (2005) 105-114.

[196] K. Chen, A.T. Bell, E. Iglesia, The Relationship between the Electronic and Redox Properties of Dispersed Metal Oxides and Their Turnover Rates in Oxidative Dehydrogenation Reactions, Journal of Catalysis, 209 (2002) 35-42.
[197] W. Daniell, A. Ponchel, S. Kuba, F. Anderle, T. Weingand, D.H. Gregory, H. Knözinger, Characterization and Catalytic Behavior of VO_x-CeO_2 Catalysts for the Oxidative Dehydrogenation of Propane, Topics in Catalysis, 20 (2002) 65-74.
[198] R. Grabowski, J. Słoczyński, Kinetics of oxidative dehydrogenation of propane and ethane on VO_x/SiO_2 pure and with potassium additive, Chemical Engineering and Processing: Process Intensification, 44 (2005) 1082-1093.
[199] J. Liu, F. Mohamed, J. Sauer, Selective oxidation of propene by vanadium oxide monomers supported on silica, Journal of Catalysis, 317 (2014) 75-82.
[200] M. Nadjafi, P.M. Abdala, R. Verel, D. Hosseini, O.V. Safonova, A. Fedorov, C.R. Müller, Reducibility and Dispersion Influence the Activity in Silica-Supported Vanadium-Based Catalysts for the Oxidative Dehydrogenation of Propane: The Case of Sodium Decavanadate, ACS Catalysis, 10 (2020) 2314-2321.
[201] C. Xiong, S. Chen, P. Yang, S. Zha, Z.-J. Zhao, J. Gong, Structure–Performance Relationships for Propane Dehydrogenation over Aluminum Supported Vanadium Oxide, ACS Catalysis, 9 (2019) 5816-5827.
[202] M. Zboray, A.T. Bell, E. Iglesia, Role of C−H Bond Strength in the Rate and Selectivity of Oxidative Dehydrogenation of Alkanes, The Journal of Physical Chemistry C, 113 (2009) 12380-12386.
[203] S. Barman, N. Maity, K. Bhatte, S. Ould-Chikh, O. Dachwald, C. Haeßner, Y. Saih, E. Abou-Hamad, I. Llorens, J.-L. Hazemann, K. Köhler, V. D' Elia, J.-M. Basset, Single-Site VO_x Moieties Generated on Silica by Surface Organometallic Chemistry: A Way To Enhance the Catalytic Activity in the Oxidative Dehydrogenation of Propane, ACS Catalysis, 6 (2016) 5908-5921.
[204] H. Zhang, S. Cao, Y. Zou, Y.-M. Wang, X. Zhou, Y. Shen, X. Zheng, Highly efficient V–Sb–O/SiO2 catalyst with Sb atom-isolated VO_x species for oxidative dehydrogenation of propane to propene, Catalysis Communications, 45 (2014) 158-161.
[205] M.O. Guerrero-Pérez, T. Kim, M.A. Bañares, I.E. Wachs, Nature of Catalytic Active Sites for Sb−V−O Mixed Metal Oxides, The Journal of Physical Chemistry C, 112 (2008) 16858-16863.
[206] I.E. Wachs, C.A. Roberts, Monitoring surface metal oxide catalytic active sites with Raman spectroscopy, Chemical Society Reviews, 39 (2010) 5002-5017.
[207] T. Fu, Y. Wang, A. Wernbacher, R. Schlögl, A. Trunschke, Single-Site Vanadyl Species Isolated within Molybdenum Oxide Monolayers in Propane Oxidation, ACS Catalysis, 9 (2019) 4875-4886.
[208] C. Carrero, M. Kauer, A. Dinse, T. Wolfram, N. Hamilton, A. Trunschke, R. Schlögl, R. Schomäcker, High performance (VO_x)n–(TiO_x)m/SBA-15 catalysts for the oxidative dehydrogenation of propane, Catalysis Science & Technology, 4 (2014) 786-794.
[209] N. Hamilton, T. Wolfram, G. Tzolova Müller, M. Hävecker, J. Kröhnert, C. Carrero, R. Schomäcker, A. Trunschke, R. Schlögl, Topology of silica supported vanadium–titanium oxide catalysts for oxidative dehydrogenation of propane, Catalysis Science & Technology, 2 (2012) 1346-1359.
[210] E.V. Kondratenko, A. Brückner, On the nature and reactivity of active oxygen species formed from O_2 and N_2O on VO_x/MCM-41 used for oxidative dehydrogenation of propane, Journal of Catalysis, 274 (2010) 111-116.
[211] E.V. Kondratenko, M. Cherian, M. Baerns, D. Su, R. Schlögl, X. Wang, I.E. Wachs, Oxidative dehydrogenation of propane over V/MCM-41 catalysts: comparison of O_2 and N_2O as oxidants, Journal of Catalysis, 234 (2005) 131-142.
[212] Y.-M. Liu, W.-L. Feng, T.-C. Li, H.-Y. He, W.-L. Dai, W. Huang, Y. Cao, K.-N. Fan, Structure and catalytic properties of vanadium oxide supported on mesocellulous silica foams (MCF) for the oxidative dehydrogenation of propane to propylene, Journal of Catalysis, 239 (2006) 125-136.

[213] U. Rodemerck, M. Stoyanova, E.V. Kondratenko, D. Linke, Influence of the kind of VOx structures in VO_x/MCM-41 on activity, selectivity and stability in dehydrogenation of propane and isobutane, Journal of Catalysis, 352 (2017) 256-263.
[214] H. Kazerooni, J. Towfighi Darian, Y. Mortazavi, A.A. Khadadadi, R. Asadi, Titania-Supported Vanadium Oxide Synthesis by Atomic Layer Deposition and Its Application for Low-Temperature Oxidative Dehydrogenation of Propane, Catalysis Letters, 150 (2020) 2807-2822.
[215] A. Essakhi, A. Löfberg, S. Paul, P. Supiot, B. Mutel, V. Le Courtois, E. Bordes-Richard, From Materials Science to Catalysis: Influence of the Coating of 2D- and 3D-Inserts on the Catalytic Behaviour of VO_x/TiO_2 in Oxidative Dehydrogenation of Propane, Topics in Catalysis, 54 (2011) 698-707.
[216] A. Löfberg, T. Giornelli, S. Paul, E. Bordes-Richard, Catalytic coatings for structured supports and reactors: VO_x/TiO_2 catalyst coated on stainless steel in the oxidative dehydrogenation of propane, Applied Catalysis A: General, 391 (2011) 43-51.
[217] M. Machli, A.A. Lemonidou, Optimization of V_2O_5–MgO/TiO_2 catalyst for the oxidativedehydrogenation of propane effect of magnesia loading and preparation procedure, Catalysis Letters, 99 (2005) 221-230.
[218] R. Grabowski, B. Grzybowska, K. Samson, J. Słoczyński, J. Stoch, K. Wcisło, Effect of alkaline promoters on catalytic activity of V_2O_5/TiO_2 and MoO_3/TiO_2 catalysts in oxidative dehydrogenation of propane and in isopropanol decomposition, Applied Catalysis A: General, 125 (1995) 129-144.
[219] M. Kazemeini, M. Nikkah, M. Fattahi, L. Vafajoo, Physicochemical Properties and Catalytic Performances of Nanostructured V_2O_5 over TiO_2 and γ-Al_2O_3 for Oxidative Dehydrogenation of Propane, Chemical and Biochemical Engineering Quarterly, 30 (2016) 9-18.
[220] J.T. Grant, A.M. Love, C.A. Carrero, F. Huang, J. Panger, R. Verel, I. Hermans, Improved Supported Metal Oxides for the Oxidative Dehydrogenation of Propane, Topics in Catalysis, 59 (2016) 1545-1553.
[221] O. Ovsitser, R. Schomaecker, E.V. Kondratenko, T. Wolfram, A. Trunschke, Highly selective and stable propane dehydrogenation to propene over dispersed VO_x-species under oxygen-free and oxygen-lean conditions, Catalysis Today, 192 (2012) 16-19.
[222] O. Ovsitser, E.V. Kondratenko, Similarity and differences in the oxidative dehydrogenation of C2–C4 alkanes over nano-sized VO_x species using N_2O and O_2, Catalysis Today, 142 (2009) 138-142.
[223] O.V. Buyevskaya, A. Brückner, E.V. Kondratenko, D. Wolf, M. Baerns, Fundamental and combinatorial approaches in the search for and optimisation of catalytic materials for the oxidative dehydrogenation of propane to propene, Catalysis Today, 67 (2001) 369-378.
[224] S.A. Karakoulia, K.S. Triantafyllidis, A.A. Lemonidou, Preparation and characterization of vanadia catalysts supported on non-porous, microporous and mesoporous silicates for oxidative dehydrogenation of propane (ODP), Microporous and Mesoporous Materials, 110 (2008) 157-166.
[225] G. Mitran, R. Ahmed, E. Iro, S. Hajimirzaee, S. Hodgson, A. Urdă, M. Olea, I.-C. Marcu, Propane oxidative dehydrogenation over VO_x/SBA-15 catalysts, Catalysis Today, 306 (2018) 260-267.
[226] W. Ruettinger, A. Benderly, S. Han, X. Shen, Y. Ding, S.L. Suib, Influence of Support Surface Area and Niobium Addition on the Reactivity of Vanadium Catalysts for Propane Oxidative Dehydrogenation, Catalysis Letters, 141 (2011) 15-21.
[227] A.A. Lemonidou, L. Nalbandian, I.A. Vasalos, Oxidative dehydrogenation of propane over vanadium oxide based catalysts - Effect of support and alkali promoter, Catalysis Today, 61 (2000) 333-341.
[228] M.P. Casaletto, G. Landi, L. Lisi, P. Patrono, F. Pinzari, Effect of the support on the catalytic properties of vanadyl phosphate in the oxidative dehydrogenation of propane, Journal of Molecular Catalysis A: Chemical, 329 (2010) 50-56.

[229] M. Høj, A.D. Jensen, J.-D. Grunwaldt, Structure of alumina supported vanadia catalysts for oxidative dehydrogenation of propane prepared by flame spray pyrolysis, Applied Catalysis A: General, 451 (2013) 207-215.
[230] B. Mitra, I.E. Wachs, G. Deo, Promotion of the propane ODH reaction over supported V_2O_5/Al_2O_3 catalyst with secondary surface metal oxide additives, Journal of Catalysis, 240 (2006) 151-159.
[231] J. Guo, X. Li, Y. Tang, J. Zhang, Effect of Vanadium Oxides Composition Loaded on γAl2O3 Catalyst for Oxidative Dehydrogenation of Propane to Propylene, Chemistry Select, 4 (2019) 13576-13581.
[232] T. Kharlamova, E. Sushchenko, T. Izaak, O. Vodyankina, Phase composition, structural peculiarities and catalytic properties of supported $MgO\text{-}V_2O_5/Al_2O_3$ catalysts for oxidative dehydrogenation of propane: Insight into formation of surface Mg-V-O phase, Catalysis Today, 278 (2016) 174-184.
[233] M.A. Bañares, S.J. Khatib, Structure–activity relationships in alumina-supported molybdena–vanadia catalysts for propane oxidative dehydrogenation, Catalysis Today, 96 (2004) 251-257.
[234] A. Klisinska, K. Samson, I. Gressel, B. Grzybowska, Effect of additives on properties of V_2O_5/SiO_2 and V_2O_5/MgO catalysts: I. Oxidative dehydrogenation of propane and ethane, Applied Catalysis A: General, 309 (2006) 10-16.
[235] M. Fattahi, M. Kazemeini, F. Khorasheh, A.M. Rashidi, Morphological investigations of nanostructured V2O5 over graphene used for the ODHP reaction: from synthesis to physiochemical evaluations, Catalysis Science & Technology, 5 (2015) 910-924.
[236] V.J.M. Ferreira Neto, T.d.S.B. Costa, A.L.L. Magalhães, A.B. Gaspar, P.G. Pries de Oliveira, F.M.T. Mendes, Propane oxidation by vanadium supported on activated carbon from sugarcane straw, Molecular Catalysis, 458 (2018) 317-325.
[237] I.V. Mishakov, A.A. Vedyagin, A.F. Bedilo, V.I. Zaikovskii, K.J. Klabunde, Aerogel VO_x/MgO catalysts for oxidative dehydrogenation of propane, Catalysis Today, 144 (2009) 278-284.
[238] S. Dźwigaj, I. Gressel, B. Grzybowska, K. Samson, Oxidative dehydrogenation of propane on VSiβ catalysts, Catalysis Today, 114 (2006) 237-241.
[239] A.Z. Varzaneh, M.S. Moghaddam, J.T. Darian, Oxidative dehydrogenation of propane over vanadium catalyst supported on nano-HZSM-5, Petroleum Chemistry, 58 (2018) 13-21.
[240] M. Fattahi, M. Kazemeini, F. Khorasheh, A. Rashidi, Kinetic modeling of oxidative dehydrogenation of propane (ODHP) over a vanadium–graphene catalyst: Application of the DOE and ANN methodologies, Journal of Industrial and Engineering Chemistry, 20 (2014) 2236-2247.
[241] P. Gruene, T. Wolfram, K. Pelzer, R. Schlögl, A. Trunschke, Role of dispersion of vanadia on SBA-15 in the oxidative dehydrogenation of propane, Catalysis Today, 157 (2010) 137-142.
[242] R. Chlosta, G. Tzolova-Müller, R. Schlögl, C. Hess, Nature of dispersed vanadium oxide: influence of the silica support structure and synthesis methods, Catalysis Science & Technology, 1 (2011) 1175-1181.
[243] T. Blasco, J.M.L. Nieto, Oxidative dyhydrogenation of short chain alkanes on supported vanadium oxide catalysts, Applied Catalysis A: General, 157 (1997) 117-142.
[244] A.A. Lemonidou, L. Nalbandian, I.A. Vasalos, Oxidative dehydrogenation of propane over vanadium oxide based catalysts: Effect of support and alkali promoter, Catalysis Today, 61 (2000) 333-341.
[245] M.V. Martínez-Huerta, X. Gao, H. Tian, I.E. Wachs, J.L.G. Fierro, M.A. Bañares, Oxidative dehydrogenation of ethane to ethylene over alumina-supported vanadium oxide catalysts: Relationship between molecular structures and chemical reactivity, Catalysis Today, 118 (2006) 279-287.
[246] X. Gao, M.A. Bañares, I.E. Wachs, Ethane and n-Butane Oxidation over Supported Vanadium Oxide Catalysts: An in Situ UV–Visible Diffuse Reflectance Spectroscopic Investigation, Journal of Catalysis, 188 (1999) 325-331.

[247] X. Gao, S.R. Bare, B.M. Weckhuysen, I.E. Wachs, In Situ Spectroscopic Investigation of Molecular Structures of Highly Dispersed Vanadium Oxide on Silica under Various Conditions, The Journal of Physical Chemistry B, 102 (1998) 10842-10852.
[248] S. Rostom, H. de Lasa, Propane Oxidative Dehydrogenation on Vanadium-Based Catalysts under Oxygen-Free Atmospheres, Catalysts, 10 (2020) 418.
[249] G.G. Cortez, J.L.G. Fierro, M.A. Banares, Role of potassium on the structure and activity of alumina-supported vanadium oxide catalysts for propane oxidative dehydrogenation, Catalysis Today, 78 (2003) 219-228.
[250] D. Courcot, A. Ponchel, B. Grzybowska, Y. Barbaux, M. Rigole, M. Guelton, J.P. Bonnelle, Effect of the sequence of potassium introduction to V_2O_5/TiO_2 catalysts on their physicochemical properties and catalytic performance in oxidative dehydrogenation of propane, Catalysis Today, 33 (1997) 109-118.
[251] Q. Liu, M. Luo, Z. Zhao, L. Guo, Effect of Potassium on the Structure, Physic-Chemical and Catalytic Properties of Vanadium-Incorporated Mesoporous Catalysts for the Oxidative Dehydrogenation of Propane, Catalysis Letters, 149 (2019) 1345-1358.
[252] I.A. Bakare, S. Adamu, M. Qamaruddin, S.A. Al-Bogami, S. Al-Ghamdi, M.M. Hossain, Oxidative Dehydrogenation of Propane to Propylene over VO_x on Mixed θ-Al_2O_3/Alkaline Earth Metal Oxide Supports, Industrial & Engineering Chemistry Research, 58 (2019) 10785-10792.
[253] S. Rostom, H.I. de Lasa, Propane Oxidative Dehydrogenation Using Consecutive Feed Injections and Fluidizable $VO_x/\gamma Al_2O_3$ and $VO_x/ZrO_2–\gamma Al_2O_3$ Catalysts, Industrial & Engineering Chemistry Research, 56 (2017) 13109-13124.
[254] K. Chen, A.T. Bell, E. Iglesia, Kinetics and Mechanism of Oxidative Dehydrogenation of Propane on Vanadium, Molybdenum, and Tungsten Oxides, The Journal of Physical Chemistry B, 104 (2000) 1292-1299.
[255] R. Grabowski, Kinetics of Oxidative Dehydrogenation of C_2-C_3 Alkanes on Oxide Catalysts, Catalysis Reviews, 48 (2006) 199-268.
[256] J. Haber, M. Witko, Oxidation catalysis—electronic theory revisited, Journal of Catalysis, 216 (2003) 416-424.
[257] S. Albonetti, F. Cavani, F. TrifirÒ, Key Aspects of Catalyst Design for the Selective Oxidation of Paraffins, Catalysis Reviews, 38 (1996) 413-438.
[258] V. Fleischer, R. Steuer, S. Parishan, R. Schomäcker, Investigation of the surface reaction network of the oxidative coupling of methane over $Na_2WO_4/Mn/SiO_2$ catalyst by temperature programmed and dynamic experiments, Journal of Catalysis, 341 (2016) 91-103.
[259] E.V. Kondratenko, M. Baerns, Catalytic oxidative dehydrogenation of propane in the presence of O_2 and N_2O—the role of vanadia distribution and oxidant activation, Applied Catalysis A: General, 222 (2001) 133-143.
[260] T. Otroshchenko, G. Jiang, V.A. Kondratenko, U. Rodemerck, E.V. Kondratenko, Current status and perspectives in oxidative, non-oxidative and CO2-mediated dehydrogenation of propane and isobutane over metal oxide catalysts, Chemical Society Reviews, 50 (2021) 473-527.
[261] A. Klisińska, A. Haras, K. Samson, M. Witko, B. Grzybowska, Effect of additives on properties of vanadia-based catalysts for oxidative dehydrogenation of propane: Experimental and quantum chemical studies, Journal of Molecular Catalysis A: Chemical, 210 (2004) 87-92.
[262] D. Courcot, B. Grzybowska, Y. Barbaux, M. Rigole, A. Ponchel, M. Guelton, Effect of potassium addition to the TiO_2 support on the structure of V_2O_5/TiO_2 and its catalytic properties in the oxidative dehydrogenation of propane, Journal of the Chemical Society, Faraday Transactions, 92 (1996) 1609-1617.
[263] C. Resini, M. Panizza, L. Arrighi, S. Sechi, G. Busca, R. Miglio, S. Rossini, A study of the reaction pathway upon propane oxidation over $V–K/Al_2O_3$ catalysts, Chemical Engineering Journal, 89 (2002) 75-87.

[264] R. Grabowski, Kinetics of the oxidative dehydrogenation of propane on vanadia/titania catalysts, pure and doped with rubidium, Applied Catalysis A: General, 270 (2004) 37-47.
[265] R. Grabowski, B. Grzybowska, A. Kozłowska, J. Słoczyński, K. Wcisło, Y. Barbaux, Effect of alkali metals additives to V_2O_5/TiO_2 catalyst on physicochemical properties and catalytic performance in oxidative dehydrogenation of propane, Topics in Catalysis, 3 (1996) 277-288.
[266] M. Calatayud, C. Minot, Effect of Alkali Doping on a V_2O_5/TiO_2 Catalyst from Periodic DFT Calculations, The Journal of Physical Chemistry C, 111 (2007) 6411-6417.
[267] Y. Li, Z. Wei, J. Sun, F. Gao, C.H.F. Peden, Y. Wang, Effect of Sodium on the Catalytic Properties of VO_x/CeO_2 Catalysts for Oxidative Dehydrogenation of Methanol, The Journal of Physical Chemistry C, 117 (2013) 5722-5729.
[268] A.L. Kustov, S.B. Rasmussen, R. Fehrmann, P. Simonsen, Activity and deactivation of sulphated TiO_2- and ZrO_2-based V, Cu, and Fe oxide catalysts for NO abatement in alkali containing flue gases, Applied Catalysis B: Environmental, 76 (2007) 9-14.
[269] J.M. López Nieto, P. Concepción, A. Dejoz, F. Melo, H. Knözinger, M.I. Vázquez, Oxidative dehydrogenation of n-butane and 1-butene on undoped and K-doped VOx/Al2O3 catalysts, Catalysis Today, 61 (2000) 361-367.
[270] L. Lietti, P. Forzatti, G. Ramis, G. Busca, F. Bregani, Potassium doping of vanadia/titania de-NOxing catalysts: Surface characterisation and reactivity study, Applied Catalysis B: Environmental, 3 (1993) 13-35.
[271] G.K. Boreskov, A.A. Ivanov, O.M. Ilyinich, V.G. Ponomareva, Influence of alkaline promoters on the selectivity of vanadium catalysts in the oxidation of o-xylene to phthalic anhydride, Reaction Kinetics and Catalysis Letters, 3 (1975) 1-8.
[272] A. Klisińska, K. Samson, I. Gressel, B. Grzybowska, Effect of additives on properties of V_2O_5/SiO_2 and V_2O_5/MgO catalysts: I. Oxidative dehydrogenation of propane and ethane, Applied Catalysis A: General, 309 (2006) 10-16.
[273] A.A. Lemonidou, L. Nalbandian, I.A. Vasalos, Oxidative dehydrogenation of propane over vanadium oxide based catalysts: Effect of support and alkali promoter, Catalysis Today, 61 (2000) 333-341.
[274] L. Balderas-Tapia, I. Hernández-Pérez, P. Schacht, I.R. Córdova, G.G. Aguilar-Ríos, Influence of reducibility of vanadium–magnesium mixed oxides on the oxidative dehydrogenation of propane, Catalysis Today, 107-108 (2005) 371-376.
[275] M.A. Bañares, M.V. Martínez-Huerta, X. Gao, J.L.G. Fierro, I.E. Wachs, Dynamic behavior of supported vanadia catalysts in the selective oxidation of ethane: In situ Raman, UV–Vis DRS and reactivity studies, Catalysis Today, 61 (2000) 295-301.
[276] B. Beck, M. Harth, N.G. Hamilton, C. Carrero, J.J. Uhlrich, A. Trunschke, S. Shaikhutdinov, H. Schubert, H.-J. Freund, R. Schlögl, J. Sauer, R. Schomäcker, Partial oxidation of ethanol on vanadia catalysts on supporting oxides with different redox properties compared to propane, Journal of Catalysis, 296 (2012) 120-131.
[277] J.M. Kanervo, M.E. Harlin, A.O.I. Krause, M.A. Bañares, Characterisation of alumina-supported vanadium oxide catalysts by kinetic analysis of H2-TPR data, Catalysis Today, 78 (2003) 171-180.
[278] V.D.N. Nguyen, D. Yun, N. Sakulchaicharoen, J.E. Herrera, The Reducibility and Cluster Size of Vanadium Oxide as Potential Descriptors of Its Catalytic Activity in the Partial Oxidation of Ethanol, International Journal of Chemical Reactor Engineering, 16 (2018).
[279] V. Brázdová, M.V. Ganduglia-Pirovano, J. Sauer, Vanadium Oxides on Aluminum Oxide Supports. 2. Structure, Vibrational Properties, and Reducibility of V_2O_5 Clusters on α-Al_2O_3(0001), The Journal of Physical Chemistry B, 109 (2005) 23532-23542.
[280] T.K. Todorova, M.V. Ganduglia-Pirovano, J. Sauer, Vanadium Oxides on Aluminum Oxide Supports. 1. Surface Termination and Reducibility of Vanadia Films on α-Al_2O_3(0001), The Journal of Physical Chemistry B, 109 (2005) 23523-23531.

[281] S. Besselmann, C. Freitag, O. Hinrichsen, M. Muhler, Temperature-programmed reduction and oxidation experiments with V_2O_5/TiO_2 catalysts, Physical Chemistry Chemical Physics, 3 (2001) 4633-4638.
[282] A. Dinse, B. Frank, C. Hess, D. Habel, R. Schomäcker, Oxidative dehydrogenation of propane over low-loaded vanadia catalysts: Impact of the support material on kinetics and selectivity, Journal of Molecular Catalysis A: Chemical, 289 (2008) 28-37.
[283] A. Gervasini, P. Carniti, J. Keränen, L. Niinistö, A. Auroux, Surface characteristics and activity in selective oxidation of o-xylene of supported V2O5 catalysts prepared by standard impregnation and atomic layer deposition, Catalysis Today, 96 (2004) 187-194.
[284] J.K. Nørskov, P. Stoltze, Theoretical aspects of surface reactions, Surface Science, 189-190 (1987) 91-105.
[285] Chapter 6 Adsorption of Gases On Surfaces Modified By Alkali Metals, in: M.P. Kiskinova (Ed.) Studies in Surface Science and Catalysis, Elsevier 1991, pp. 169-283.
[286] A.P.E. York, A. Brückner, G.-U. Wolf, P.-M. Wilde, M. Meisel, Further studies of the active phase in Cs-doped Fe–V–oxide catalysts, Chemical Communications, (1996) 239-240.
[287] L.Y. Margolis, A.A. Firsova, Modification of catalysts, International Reviews in Physical Chemistry, 8 (1989) 1-20.
[288] T. Kobayashi, Selective oxidation of light alkanes to aldehydes over silica catalysts supporting mononuclear active sites - acrolein formation from ethane, Catalysis Today, 71 (2001) 69-76.
[289] Z. Zhao, Y. Yamada, A. Ueda, H. Sakurai, T. Kobayashi, Oxidation of ethane into acetaldehyde and acrolein over silica containing cesium and a very small amount of additives, Applied Catalysis A: General, 196 (2000) 37-42.
[290] Z. Zhao, J. Liu, A.J. Duan, C.M. Xu, T. Kobayashi, I.E. Wachs, Effects of alkali metal cations on the structures, physico-chemical properties and catalytic behaviors of silica-supported vanadium oxide catalysts for the selective oxidation of ethane and the complete oxidation of diesel soot, Topics in Catalysis, 38 (2006) 309-325.
[291] H. Ahi, Supported Liquid Phase Catalysts, PhD Thesis, Technische Universität Berlin, Fritz-Haber-Institut der MPG, Berlin Germany (2017).
[292] S.J. Schneider, C.L. McDaniel, Effect of Environment Upon the Melting Point of Al(2)O(3), J Res Natl Bur Stand A Phys Chem, 71a (1967) 317-333.
[293] B. Ravel, M. Newville, ATHENA, ARTEMIS, HEPHAESTUS: data analysis for X-ray absorption spectroscopy using IFEFFIT, Journal of Synchrotron Radiation 12 (2005) 537-541.
[294] J. Yeon, S.-H. Kim, P.S. Halasyamani, $A_3V_5O_{14}$ (A = K+, Rb+, or Tl+), New Polar Oxides with a Tetragonal Tungsten Bronze Related Structural Topology: Synthesis, Structure, and Functional Properties, Inorganic Chemistry, 49 (2010) 6986-6993.
[295] B. Feng, D. Sun, H. Wang, S. Tan, H. Zhang, A Simple Method for the Synthesis of $KV_3O_8.0.42H_2O$, Int. J. Electrochem. Sci., 8 (2013) 1095-1102.
[296] P. Kube, Comparison of alkane activation over supported and bulk transition metal oxide catalysts and transition metal free carbon nano structures, Fakultät II – Mathematik und Naturwissenschaften der Technischen Universität Berlin, Technischen Universität Berlin, https://depositonce.tu-berlin.de/bitstream/11303/8171/4/kube_pierre.pdf, 2018.
[297] B. Wunderlich, U. Gaur, Differential Scanning Calorimetry of Flexible, Linear Macromolecules, Polymer Characterization, AMERICAN CHEMICAL SOCIETY1983, pp. 195-208.
[298] R. Haines PJ, M, Wilburn FW, Differential thermal analysis and differential scanning calorimetry, The Netherlands: Elsevier Science B.V., 1998.
[299] C.S.T. Chang, J. Banhart, Low-Temperature Differential Scanning Calorimetry of an Al-Mg-Si Alloy, Metallurgical and Materials Transactions A, 42 (2011) 1960-1964.

[300] Z. Li, Y. Zhang, X. Jing, Y. Zhang, L. Chang, Insight into the intrinsic reaction of brown coal oxidation at low temperature: Differential scanning calorimetry study, Fuel Processing Technology, 147 (2016) 64-70.
[301] Z. Zhang, D. Fouchard, J.R. Rea, Differential scanning calorimetry material studies: implications for the safety of lithium-ion cells, Journal of Power Sources, 70 (1998) 16-20.
[302] T. Takkawatakarn, S. Praserthdam, S. Wannakao, J. Panpranot, P. Praserthdam, Identification of extremely hard coke generation by low-temperature reaction on tungsten catalysts via Operando and in situ techniques, Scientific Reports, 11 (2021) 8071.
[303] P. Gill, T.T. Moghadam, B. Ranjbar, Differential scanning calorimetry techniques: applications in biology and nanoscience, J Biomol Tech, 21 (2010) 167-193.
[304] J.M. Sturtevant, Biochemical Applications of Differential Scanning Calorimetry, Annual Review of Physical Chemistry, 38 (1987) 463-488.
[305] P.K. LeMaire, R. Speel, R. Ruotolo, Extended Electrical Transport Measurements on the Mixed Conductor Ag_3CS_2, Journal of The Electrochemical Society, 148 (2001) E237.
[306] P.C. Weber, F.R. Salemme, Applications of calorimetric methods to drug discovery and the study of protein interactions, Curr Opin Struct Biol, 13 (2003) 115-121.
[307] A.F. Barnes, M.J. Hardy, T.J. Lever, A review of the applications of thermal methods within the pharmaceutical industry, Journal of Thermal Analysis, 40 (1993) 499-509.
[308] P. Aggarwal, D. Dollimore, Degradation of starchy food material by thermal analysis, Thermochimica Acta, 357-358 (2000) 57-63.
[309] D.R. L., Differential Scanning Calorimetry, in: E. Patent (Ed.), 2001.
[310] C. McGregor, M.H. Saunders, G. Buckton, R.D. Saklatvala, The use of high-speed differential scanning calorimetry (Hyper-DSC™) to study the thermal properties of carbamazepine polymorphs, Thermochimica Acta, 417 (2004) 231-237.
[311] D.R. L., Infrared Heated Differential Scanning Calorimetry, in: W. Patent (Ed.), 2008.
[312] B.J.F. Plotnikov V. V., Brandts J. M., Pressure Perturbation Calorimetry Instruments and Methods, in: U. Patent (Ed.), 2004.
[313] G.W.H. Höhne, W. Hemminger, H.-J. Flammersheim, Differential Scanning Calorimetry, Springer-Verlag Berlin Heidelberg1996.
[314] H.K.D.H. Bhadesia, Differential Scanning Calorimetry, University of Cambridge, Materials Science & Metallurgy, www.msm.cam.ac.uk/phasetrans/2002/Thermal2.pdf.
[315] K. Lukas, P.K. LeMaire, Differential scanning calorimetry: Fundamental overview, Resonance, 14 (2009) 807-817.
[316] E.J.P. Calvet, Calorimeter, in: U. States (Ed.) United StatesUnited States, 1962.
[317] S.K. Technologies, https://setaramsolutions.com/app/uploads/sites/2/2020/09/Family-brochure-EN-CALVET.pdf.
[318] H.P. E. Calvet, H. A. Skinner, Recent Progress in Microcalorimetry, Pergamon Press, Oxford, 1963.
[319] S.K. Technologies, https://setaramsolutions.com/, https://setaramsolutions.com/.
[320] A. Tarasov, Operando Thermal Analysis, http://www.fhi-berlin.mpg.de/acnew/department/pages/teaching/pages/teaching__wintersemester__2017_2018/andrey_tarasov__in-situ_ta__171208.pdf, FHI Berlin, 2017.
[321] M. Sinev, V. Bychkov, High-temperature differential scanning in situ calorimetric study of the mechanism of catalytic processes, Kinetics and Catalysis, 40 (1999) 819-835.
[322] Sir C. V. Raman, F.R.S, Nature, 143 (1939) 326-326.
[323] R. Baddour-Hadjean, J.-P. Pereira-Ramos, Raman Microspectrometry Applied to the Study of Electrode Materials for Lithium Batteries, Chemical Reviews, 110 (2010) 1278-1319.
[324] C. Hess, New advances in using Raman spectroscopy for the characterization of catalysts and catalytic reactions, Chemical Society Reviews, 50 (2021) 3519-3564.

[325] R.R. Jones, D.C. Hooper, L. Zhang, D. Wolverson, V.K. Valev, Raman Techniques: Fundamentals and Frontiers, Nanoscale Research Letters, 14 (2019) 231.
[326] B.J.B. J. G. Grasselli, Analytical Raman Spectroscopy, John Wiley & Sons, UK, 1991.
[327] L. Bellot-Gurlet, F.-X.L. Bourdonnec, G. Poupeau, S. Dubernet, Raman micro-spectroscopy of western Mediterranean obsidian glass: one step towards provenance studies?, Journal of Raman Spectroscopy, 35 (2004) 671-677.
[328] I. Reiche, S. Pages-Camagna, L. Lambacher, In situ Raman spectroscopic investigations of the adorning gemstones on the reliquary Heinrich's Cross from the treasury of Basel Cathedral, Journal of Raman Spectroscopy, 35 (2004) 719-725.
[329] D. Liu, H. Ai, J. Li, M. Fang, M. Chen, D. Liu, X. Du, P. Zhou, F. Li, K.H. Lo, Y. Tang, S. Chen, L. Wang, G. Xing, H. Pan, Surface Reconstruction and Phase Transition on Vanadium–Cobalt–Iron Trimetal Nitrides to Form Active Oxyhydroxide for Enhanced Electrocatalytic Water Oxidation, Advanced Energy Materials, 10 (2020) 2002464.
[330] F. Ureña-Begara, A. Crunteanu, J.-P. Raskin, Raman and XPS characterization of vanadium oxide thin films with temperature, Applied Surface Science, 403 (2017) 717-727.
[331] M.O. Guerrero-Pérez, M.A. Bañares, From conventional in situ to operando studies in Raman spectroscopy, Catalysis Today, 113 (2006) 48-57.
[332] B.M. Weckhuysen, D.E. Keller, Chemistry, spectroscopy and the role of supported vanadium oxides in heterogeneous catalysis, Catalysis Today, 78 (2003) 25-46.
[333] E. Stavitski, B.M. Weckhuysen, Infrared and Raman imaging of heterogeneous catalysts, Chemical Society Reviews, 39 (2010) 4615-4625.
[334] I.E. Wachs, In situ Raman spectroscopy studies of catalysts, Topics in Catalysis, 8 (1999) 57-63.
[335] E.L. Lee, I.E. Wachs, In Situ Spectroscopic Investigation of the Molecular and Electronic Structures of Si_{O2} Supported Surface Metal Oxides, The Journal of Physical Chemistry C, 111 (2007) 14410-14425.
[336] M. Hävecker, P. Düngen, S. Buller, A. Knop-Gericke, A. Trunschke, R. Schlögl, Restructuring of silica supported vanadia during propane oxidative dehydrogenation studied by combined synchrotron radiation based in situ soft X-ray absorption and photoemission, Catalysis, Structure & Reactivity, 3 (2017) 104-111.
[337] E.L. Lee, I.E. Wachs, In Situ Raman Spectroscopy of SiO_2-Supported Transition Metal Oxide Catalysts: An Isotopic 18O−16O Exchange Study, The Journal of Physical Chemistry C, 112 (2008) 6487-6498.
[338] P. Waleska, S. Rupp, C. Hess, Operando Multiwavelength and Time-Resolved Raman Spectroscopy: Structural Dynamics of a Supported Vanadia Catalyst at Work, The Journal of Physical Chemistry C, 122 (2018) 3386-3400.
[339] I.E. Wachs, M. Bañares, In Situ and Operando Raman Spectroscopy of Oxidation Catalysts, Handbook of Advanced Methods and Processes in Oxidation Catalysis, pp. 420-446.
[340] M.J. Werny, Y. Wang, F. Girgsdies, R. Schlögl, A. Trunschke, Fluctuating Storage of the Active Phase in a Mn-Na_2WO_4/SiO_2 Catalyst for the Oxidative Coupling of Methane, Angewandte Chemie International Edition, 59 (2020) 14921-14926.
[341] A. Celaya Sanfiz, T.W. Hansen, F. Girgsdies, O. Timpe, E. Rödel, T. Ressler, A. Trunschke, R. Schlögl, Preparation of Phase-Pure M1 MoVTeNb Oxide Catalysts by Hydrothermal Synthesis—Influence of Reaction Parameters on Structure and Morphology, Topics in Catalysis, 50 (2008) 19.
[342] A. Kubas, J. Noak, A. Trunschke, R. Schlögl, F. Neese, D. Maganas, A combined experimental and theoretical spectroscopic protocol for determination of the structure of heterogeneous catalysts: developing the information content of the resonance Raman spectra of M1 MoVOx, Chemical Science, 8 (2017) 6338-6353.
[343] J. A.Lercher, A. Jentys, Introduction to zeolite Molecular Sieves, 3rd revised edition ed., Elsevier B.V., 2007.

[344] P.R. Carey, Raman spectroscopy in enzymology: the first 25 years, Journal of Raman Spectroscopy, 29 (1998) 7-14.
[345] C.A. Carrero, C.J. Keturakis, A. Orrego, R. Schomäcker, I.E. Wachs, Anomalous reactivity of supported V_2O_5 nanoparticles for propane oxidative dehydrogenation: influence of the vanadium oxide precursor, Dalton Transactions, 42 (2013) 12644-12653.
[346] G.G. Cortez, M.A. Bañares, A Raman Spectroscopy Study of Alumina-Supported Vanadium Oxide Catalyst during Propane Oxidative Dehydrogenation with Online Activity Measurement, Journal of Catalysis, 209 (2002) 197-201.
[347] A.H.S. Kootenaei, J. Towfighi, A. Khodadadi, Y. Mortazavi, Characterization and Deactivation Study of Mixed Vanadium and Potassium Oxide Supported on Microemulsion-Mediated Titania Nanoparticles as Catalyst in Oxidative Dehydrogenation of Propane, International Journal of Chemical Reactor Engineering, 13 (2015) 9-19.
[348] Y.-M. Liu, Y. Cao, N. Yi, W.-L. Feng, W.-L. Dai, S.-R. Yan, H.-Y. He, K.-N. Fan, Vanadium oxide supported on mesoporous SBA-15 as highly selective catalysts in the oxidative dehydrogenation of propane, Journal of Catalysis, 224 (2004) 417-428.
[349] Z. Wu, S. Dai, S.H. Overbury, Multiwavelength Raman Spectroscopic Study of Silica-Supported Vanadium Oxide Catalysts, The Journal of Physical Chemistry C, 114 (2010) 412-422.
[350] M.A. Bañares, I.E. Wachs, Molecular structures of supported metal oxide catalysts under different environments, Journal of Raman Spectroscopy, 33 (2002) 359-380.
[351] J. Döbler, M. Pritzsche, J. Sauer, Vibrations of Silica Supported Vanadia: Variation with Particle Size and Local Surface Structure, The Journal of Physical Chemistry C, 113 (2009) 12454-12464.
[352] C. Moisii, L.J. van de Burgt, A.E. Stiegman, Resonance Raman Spectroscopy of Discrete Silica-Supported Vanadium Oxide, Chemistry of Materials, 20 (2008) 3927-3935.
[353] G.T. Went, S.T. Oyama, A.T. Bell, Laser Raman spectroscopy of supported vanadium oxide catalysts, The Journal of Physical Chemistry, 94 (1990) 4240-4246.
[354] O.L.J. Gijzeman, J.N.J. van Lingen, J.H. van Lenthe, S.J. Tinnemans, D.E. Keller, B.M. Weckhuysen, A new model for the molecular structure of supported vanadium oxide catalysts, Chemical Physics Letters, 397 (2004) 277-281.
[355] D.E. Keller, T. Visser, F. Soulimani, D.C. Koningsberger, B.M. Weckhuysen, Hydration effects on the molecular structure of silica-supported vanadium oxide catalysts: A combined IR, Raman, UV–vis and EXAFS study, Vibrational Spectroscopy, 43 (2007) 140-151.
[356] N. Magg, B. Immaraporn, J.B. Giorgi, T. Schroeder, M. Bäumer, J. Döbler, Z. Wu, E. Kondratenko, M. Cherian, M. Baerns, P.C. Stair, J. Sauer, H.-J. Freund, Vibrational spectra of alumina- and silica-supported vanadia revisited: An experimental and theoretical model catalyst study, Journal of Catalysis, 226 (2004) 88-100.
[357] Y. Wang, Commercial cells in-situ multiwavelength Raman spectroscopic system, Lecture Series, Fritz Haber Instititue of the Max Planck Society, Berlin 2019.
[358] A.M. Venezia, X-ray photoelectron spectroscopy (XPS) for catalysts characterization, Catalysis Today, 77 (2003) 359-370.
[359] M. Hävecker, M. Cavalleri, R. Herbert, R. Follath, A. Knop-Gericke, C. Hess, K. Hermann, R. Schlögl, Methodology for the structural characterisation of Vx Oy species supported on silica under reaction conditions by means of in situ O K-edge X-ray absorption spectroscopy, physica status solidi (b), 246 (2009) 1459-1469.
[360] R. Toyoshima, H. Kondoh, In-situobservations of catalytic surface reactions with soft x-rays under working conditions, Journal of Physics: Condensed Matter, 27 (2015) 083003.
[361] A. Knop-Gericke, M. Hävecker, T. Neisius, T. Schedel-Niedrig, New experimental technique: X-ray absorption spectroscopy detector for in situ studies in the soft X-ray range (250 eV $\leqslant$ hv $\leqslant$ 1000 eV) under reaction conditions, Nuclear Instruments and Methods in Physics Research Section A: Accelerators, Spectrometers, Detectors and Associated Equipment, 406 (1998) 311-322.

[362] D.F. Ogletree, H. Bluhm, G. Lebedev, C.S. Fadley, Z. Hussain, M. Salmeron, A differentially pumped electrostatic lens system for photoemission studies in the millibar range, Review of Scientific Instruments, 73 (2002) 3872-3877.
[363] T. Engel, G. Ertl, A molecular beam investigation of the catalytic oxidation of CO on Pd (111), The Journal of Chemical Physics, 69 (1978) 1267-1281.
[364] R. Vakili, E.K. Gibson, S. Chansai, S. Xu, N. Al-Janabi, P.P. Wells, C. Hardacre, A. Walton, X. Fan, Understanding the CO Oxidation on Pt Nanoparticles Supported on MOFs by Operando XPS, ChemCatChem, 10 (2018) 4238-4242.
[365] S.L. Bergman, J. Granestrand, Y. Tang, R.S. París, M. Nilsson, F.F. Tao, C. Tang, S.J. Pennycook, L.J. Pettersson, S.L. Bernasek, In-situ characterization by Near-Ambient Pressure XPS of the catalytically active phase of Pt/Al_2O_3 during NO and CO oxidation, Applied Catalysis B: Environmental, 220 (2018) 506-511.
[366] V.I. Bukhtiyarov, A.I. Nizovskii, H. Bluhm, M. Hävecker, E. Kleimenov, A. Knop-Gericke, R. Schlögl, Combined in situ XPS and PTRMS study of ethylene epoxidation over silver, Journal of Catalysis, 238 (2006) 260-269.
[367] D. Teschner, J. Borsodi, A. Wootsch, Z. Révay, M. Hävecker, A. Knop-Gericke, S.D. Jackson, R. Schlögl, The Roles of Subsurface Carbon and Hydrogen in Palladium-Catalyzed Alkyne Hydrogenation, Science, 320 (2008) 86-89.
[368] A. Knop-Gericke, M. Hävecker, T. Schedel-Niedrig, R. Schlögl, Characterisation of active phases of a copper catalyst for methanol oxidation under reaction conditions: an in situ X-ray absorption spectroscopy study in the soft energy range, Topics in Catalysis, 15 (2001) 27-34.
[369] J.-J. Velasco-Vélez, L.J. Falling, D. Bernsmeier, M.J. Sear, P.C.J. Clark, T.-S. Chan, E. Stotz, M. Hävecker, R. Kraehnert, A. Knop-Gericke, C.-H. Chuang, D.E. Starr, M. Favaro, R.V. Mom, A comparative study of electrochemical cells for in situ x-ray spectroscopies in the soft and tender x-ray range, Journal of Physics D: Applied Physics, 54 (2021) 124003.
[370] C. Heine, M. Hävecker, A. Trunschke, R. Schlögl, M. Eichelbaum, The impact of steam on the electronic structure of the selective propane oxidation catalyst MoVTeNb oxide (orthorhombic M1 phase), Physical Chemistry Chemical Physics, 17 (2015) 8983-8993.
[371] M. Hävecker, R.W. Mayer, A. Knop-Gericke, H. Bluhm, E. Kleimenov, A. Liskowski, D. Su, R. Follath, F.G. Requejo, D.F. Ogletree, M. Salmeron, J.A. Lopez-Sanchez, J.K. Bartley, G.J. Hutchings, R. Schlögl, In Situ Investigation of the Nature of the Active Surface of a Vanadyl Pyrophosphate Catalyst during n-Butane Oxidation to Maleic Anhydride, The Journal of Physical Chemistry B, 107 (2003) 4587-4596.
[372] M. Cavalleri, K. Hermann, A. Knop-Gericke, M. Hävecker, R. Herbert, C. Hess, A. Oestereich, J. Döbler, R. Schlögl, Analysis of silica-supported vanadia by X-ray absorption spectroscopy: Combined theoretical and experimental studies, Journal of Catalysis, 262 (2009) 215-223.
[373] I. Muylaert, P. Van Der Voort, Supported vanadium oxide in heterogeneous catalysis: elucidating the structure–activity relationship with spectroscopy, Physical Chemistry Chemical Physics, 11 (2009) 2826-2832.
[374] E.S. M. Hävecker, M. Gorgoi, St. Hendel, A. Knop-Gericke, R. Schlögl, New facilities BElChem and CAT@EMIL dedicated to ambient pressure X-ray electron spectroscopy put into operation at HZB/BESSY, http://www.fhi-berlin.mpg.de/acnew/groups/electronicstructure/pages/research/pages/electronicstructure_group__research_projects__New_facilites_BELChem_and_CAT@EMIL_dedicated_to_ambient_pressure_X-ray_electron_spectroscopy_put_into_operation_at_BESSY.pdf.
[375] B.T. Thole, G. van der Laan, J.C. Fuggle, G.A. Sawatzky, R.C. Karnatak, J.M. Esteva, 3d x-ray-absorption lines and the $3d^9 4f^{n+1}$ multiplets of the lanthanides, Physical Review B, 32 (1985) 5107-5118.
[376] J. Zaanen, G.A. Sawatzky, Strong interference between decay channels and valence-electron rearrangements in core-hole spectroscopy, Physical Review B, 33 (1986) 8074-8083.

[377] F. Frati, M.O.J.Y. Hunault, F.M.F. de Groot, Oxygen K-edge X-ray Absorption Spectra, Chemical Reviews, 120 (2020) 4056-4110.
[378] D.E. Parry, Atomic calculation of photoionization cross-sections and asymmetry parameters J.-J. YEH, Published by Gordon and Breach, Langhorne PA, 1993 ISBN 2-88124-585-4 Price $125 (*$65), £82 (*£42), ECU 104 (*ECU 54) (*Special price for individuals who order direct from the publisher), Rapid Communications in Mass Spectrometry, 8 (1994) 579-579.
[379] J.J. Yeh, I. Lindau, Atomic subshell photoionization cross sections and asymmetry parameters: 1 ⩽ Z ⩽ 103, Atomic Data and Nuclear Data Tables, 32 (1985) 1-155.
[380] F. N., www.casaxps.com.
[381] I.E. Wachs, B.M. Weckhuysen, Structure and reactivity of surface vanadium oxide species on oxide supports, Applied Catalysis A: General, 157 (1997) 67-90.
[382] G. Centi, Nature of active layer in vanadium oxide supported on titanium oxide and control of its reactivity in the selective oxidation and ammoxidation of alkylaromatics, Applied Catalysis A: General, 147 (1996) 267-298.
[383] C. Hess, U. Wild, R. Schlögl, The mechanism for the controlled synthesis of highly dispersed vanadia supported on silica SBA-15, Microporous and Mesoporous Materials, 95 (2006) 339-349.
[384] A. Reisman, J. Mineo, COMPOUND REPETITION IN OXIDE-OXIDE INTERACTIONS: THE SYSTEM Li_2O-V_2O_5, The Journal of Physical Chemistry, 66 (1962) 1181-1185.
[385] N. Wang , Z. Cao, Review of the phase diagram and thermodynamic data of Na_2O-V_2O_5 and CaO-V_2O_5 systems, Highlights of Sciencepaper Online, 9 (2016) 101-110.
[386] F. Holtzberg, A. Reisman, M. Berry, M. Berkenblit, Reactions of the Group VB Pentoxides with Alkali Oxides and Carbonates. II. Phase Diagram of the System K_2CO_3-V_2O_5, Journal of the American Chemical Society, 78 (1956) 1536-1540.
[387] I.N. Belyaev, T.G. Golovanova, Equilibrium Diagram of the Cs_2CO_3(Cs_2O)-V_2O_5 system, Russian Journal of Inorganic Chemistry, 9 (1964) 228-229.
[388] I.N. Belyaev, T.G. Golovanova, Diagram for the system Rb_2O-V_2O_5, Izv. Vyssh. Uehebn. Zaved Tsvetn. Metall., 7 (1964) 117-120.
[389] S. Jouanneau, A. Le Gal La Salle, A. Verbaere, D. Guyomard, M. Deschamps, S. Lascaud, New alkaline earth substituted lithium trivanadates: synthesis, characterization and lithium insertion behavior, Journal of Materials Chemistry, 13 (2003) 1827-1834.
[390] H.T. Evans, A.M. Brusewitz, CRYSTAL-STRUCTURE OF POTASSIUM PENTAVANADATE, Acta Chemica Scandinavica, 48 (1994) 533-536.
[391] A.P. Tyutyunnik, V.G. Zubkov, V.N. Krasil'nikov, G. Svensson, M.J. Sayagués, Crystal structure of K2V8O21 and Tl2V8O21, Solid State Sciences, 7 (2005) 37-43.
[392] X. Kong, Z. Guo, P. Wen, J. Huang, L. Cao, L. Yin, J. Li, Q. Feng, Controllable synthesis and morphology evolution from two-dimensions to one-dimension of layered $K_2V_6O_{16}{\cdot}nH_2O$, CrystEngComm, 17 (2015) 3777-3782.
[393] J. Tudo, B. Jolibois, Study on System Rb_2O-V_2O_4-V_2O_5, Comptes Rendus Hebdomadaires Des Seances De L Academie Des Sciences Serie C, 273 (1971) 1526-&.
[394] J. Pan, Y. Li, Y. Cui, L. Zhao, X. Li, L. Han, Synthesis, crystal structure and nonlinear optical property of Rb3V5O14, Journal of Solid State Chemistry, 183 (2010) 2759-2762.
[395] Y. Oka, F. Saito, T. Yao, N. Yamamoto, Crystal Structure of $Cs_2V_4O_{11}$ with Unusual V–O Coordinations, Journal of Solid State Chemistry, 134 (1997) 52-58.
[396] K. Waltersson, B. Forslund, A refinement of the crystal structure of CsV_2O_5, Acta Cryst., B33 (1977) 789-793.
[397] R. Herbert, D. Wang, R. Schomäcker, R. Schlögl, C. Hess, Stabilization of Mesoporous Silica SBA-15 by Surface Functionalization, ChemPhysChem, 10 (2009) 2230-2233.

[398] R.J. Chimentão, J.E. Herrera, J.H. Kwak, F. Medina, Y. Wang, C.H.F. Peden, Oxidation of ethanol to acetaldehyde over Na-promoted vanadium oxide catalysts, Applied Catalysis A: General, 332 (2007) 263-272.
[399] Z. Zhao, L. Jian, A. Duan, X. Chunming, T. Kobayashi, I. Wachs, Effects of alkali metal cations on the structures, physico-chemical properties and catalytic behaviors of silica-supported vanadium oxide catalysts for the selective oxidation of ethane and the complete oxidation of diesel soot, Topics in Catalysis, 38 (2006) 309-325.
[400] N.N.M. Zorkipli, M.Z. Yahaya, N.A. Salleh, A. Purwanto, S. Kheawhom, N.H.M. Kaus, A.A. Mohamad, Synthesis and electrochemical performance of LiV_3O_8/graphene for aqueous lithium batteries, Ionics, 26 (2020) 2277-2292.
[401] Z.V. Popović, M.J. Konstantinović, R. Gajić, V.N. Popov, M. Isobe, Y. Ueda, V.V. Moshchalkov, Phonon dynamics in AV_2O_5 (A=Na,Ca,Mg,Cs) oxides, Physical Review B, 65 (2002) 184303.
[402] V.N. Krasil'nikov, L.A. Perelyaeva, I.V. Baklanova, L.Y. Buldakova, M.Y. Yanchenko, Synthesis and properties of $M_2V_8O_{21}$ (M = K, Tl) octavanadates and $K_{2-x}Tl_xV_8O_{21}$ ($0 \le x \le 2$) solid solutions, Russian Journal of Inorganic Chemistry, 54 (2009) 1537.
[403] K. Gáplovská, Ľ. ŽÚrková, Thermal properties of pentavanadates, Journal of thermal analysis, 20 (1981) 463-469.
[404] Ľ. Žúrková, V. Suchá, K. Gáplovská, Study of solid-phase reaction of RbNO3 with V2O5, Journal of thermal analysis, 20 (1981) 17-21.
[405] G. Li, G. Su, X. Zhuang, Z. Li, Y. He, Characterization and properties of a new IR nonlinear optical crystal: $K_3V_5O_{14}$, Optical Materials, 27 (2004) 539-542.
[406] Raman High Temperature Reaction Chamber, https://www.harricksci.com/ftir/accessories/group/Raman-High-Temperature-Reaction-Chamber.
[407] S.T. Oyama, G.T. Went, K.B. Lewis, A.T. Bell, G.A. Somorjai, Oxygen chemisorption and laser Raman spectroscopy of unsupported and silica-supported vanadium oxide catalysts, The Journal of Physical Chemistry, 93 (1989) 6786-6790.
[408] D.A. Bulushev, L. Kiwi-Minsker, V.I. Zaikovskii, O.B. Lapina, A.A. Ivanov, S.I. Reshetnikov, A. Renken, Effect of potassium doping on the structural and catalytic properties of V/Ti-oxide in selective toluene oxidation, Applied Catalysis A: General, 202 (2000) 243-250.
[409] H. Si-Ahmed, M. Calatayud, C. Minot, E.L. Diz, A.E. Lewandowska, M.A. Bañares, Combining theoretical description with experimental in situ studies on the effect of potassium on the structure and reactivity of titania-supported vanadium oxide catalyst, Catalysis Today, 126 (2007) 96-102.
[410] G. Centi, G. Golinelli, G. Busca, Modification of the surface pathways in alkane oxidation by selective doping of Broensted acid sites of vanadyl pyrophosphate, The Journal of Physical Chemistry, 94 (1990) 6813-6819.
[411] Z. Zhu, Z. Liu, S. Liu, H. Niu, A novel carbon-supported vanadium oxide catalyst for NO reduction with NH3 at low temperatures, Applied Catalysis B: Environmental, 23 (1999) L229-L233.
[412] X. Rozanska, R. Fortrie, J. Sauer, Oxidative Dehydrogenation of Propane by Monomeric Vanadium Oxide Sites on Silica Support, The Journal of Physical Chemistry C, 111 (2007) 6041-6050.
[413] P. Kube, B. Frank, S. Wrabetz, J. Kröhnert, M. Hävecker, J. Velasco-Vélez, J. Noack, R. Schlögl, A. Trunschke, Functional Analysis of Catalysts for Lower Alkane Oxidation, ChemCatChem, 9 (2017) 573-585.
[414] H. Luo, J. Pan, B. Lou, Y. Li, X. Li, L. Han, Synthesis, crystal structure and nonlinear optical property of CsV_2O_5, Inorganic Chemistry Communications, 27 (2013) 79-81.
[415] S. Xie, E. Iglesia, A.T. Bell, Effects of Hydration and Dehydration on the Structure of Silica-Supported Vanadia Species, Langmuir, 16 (2000) 7162-7167.
[416] S. Guimond, M. Abu Haija, S. Kaya, J. Lu, J. Weissenrieder, S. Shaikhutdinov, H. Kuhlenbeck, H.J. Freund, J. Döbler, J. Sauer, Vanadium oxide surfaces and supported vanadium oxide nanoparticles, Topics in Catalysis, 38 (2006) 117-125.

[417] J. Evans, Basis of XAFS, X-Ray Absorption Spectroscopy for the Chemical and Materials Sciences2018, pp. 9-32.
[418] J.J. Velasco-Vélez, Soft X-ray Absorption Spectroscopy at the Solid-Gas Interface, Ambient Pressure Spectroscopy in Complex Chemical Environments, American Chemical Society 2021, pp. 93-118.
[419] F. Meirer, B.M. Weckhuysen, Spatial and temporal exploration of heterogeneous catalysts with synchrotron radiation, Nature Reviews Materials, 3 (2018) 324-340.
[420] A. Erbil, G.S. Cargill Iii, R. Frahm, R.F. Boehme, Total-electron-yield current measurements for near-surface extended x-ray-absorption fine structure, Physical Review B, 37 (1988) 2450-2464.
[421] D. Collison, C. David Garner, J. Grigg, C. M. McGrath, J. Frederick W. Mosselmans, E. Pidcock, M. D. Roper, J. M. W. Seddon, E. Sinn, P. A. Tasker, G. Thornton, J. F. Walsh, N. A. Young, X-Ray absorption fine structure study of the bound state electronic transitions at the vanadium K and L edges in low symmetry, molecular, vanadium-(IV) and -(V) complexes with oxyoxime and oxyoximate ligands‡, Journal of the Chemical Society, Dalton Transactions, (1998) 2199-2204.
[422] D. Maganas, M. Roemelt, T. Weyhermüller, R. Blume, M. Hävecker, A. Knop-Gericke, S. DeBeer, R. Schlögl, F. Neese, L-edge X-ray absorption study of mononuclear vanadium complexes and spectral predictions using a restricted open shell configuration interaction ansatz, Physical Chemistry Chemical Physics, 16 (2014) 264-276.
[423] D. Maganas, M. Roemelt, M. Hävecker, A. Trunschke, A. Knop-Gericke, R. Schlögl, F. Neese, First principles calculations of the structure and V L-edge X-ray absorption spectra of V2O5 using local pair natural orbital coupled cluster theory and spin–orbit coupled configuration interaction approaches, Physical Chemistry Chemical Physics, 15 (2013) 7260-7276.
[424] S. J., NEXAFS Spectroscopy, Springer, Berlin, 1993.
[425] G. Silversmit, D. Depla, H. Poelman, G.B. Marin, R. De Gryse, Determination of the V2p XPS binding energies for different vanadium oxidation states (V5+ to V0+), Journal of Electron Spectroscopy and Related Phenomena, 135 (2004) 167-175.
[426] J.A. Rodriguez, J.C. Hanson, A.I. Frenkel, J.Y. Kim, M. Pérez, Experimental and Theoretical Studies on the Reaction of H2 with NiO: Role of O Vacancies and Mechanism for Oxide Reduction, Journal of the American Chemical Society, 124 (2002) 346-354.
[427] Q. Wang, J.C. Hanson, A.I. Frenkel, Solving the structure of reaction intermediates by time-resolved synchrotron x-ray absorption spectroscopy, The Journal of Chemical Physics, 129 (2008) 234502.
[428] A. Halder, C. Lenardi, J. Timoshenko, A. Mravak, B. Yang, L.K. Kolipaka, C. Piazzoni, S. Seifert, V. Bonačić-Koutecký, A.I. Frenkel, P. Milani, S. Vajda, CO2 Methanation on Cu-Cluster Decorated Zirconia Supports with Different Morphology: A Combined Experimental In Situ GIXANES/GISAXS, Ex Situ XPS and Theoretical DFT Study, ACS Catalysis, 11 (2021) 6210-6224.
[429] C.S. Spanjers, T.P. Senftle, A.C.T. van Duin, M.J. Janik, A.I. Frenkel, R.M. Rioux, Illuminating surface atoms in nanoclusters by differential X-ray absorption spectroscopy, Physical Chemistry Chemical Physics, 16 (2014) 26528-26538.
[430] Y. Liu, N. Marcella, J. Timoshenko, A. Halder, B. Yang, L. Kolipaka, M.J. Pellin, S. Seifert, S. Vajda, P. Liu, A.I. Frenkel, Mapping XANES spectra on structural descriptors of copper oxide clusters using supervised machine learning, The Journal of Chemical Physics, 151 (2019) 164201.
[431] B. Ravel, M. Newville, ATHENA, ARTEMIS, HEPHAESTUS: data analysis for X-ray absorption spectroscopy using IFEFFIT, Journal of Synchrotron Radiation, 12 (2005) 537-541.
[432] A. Nilsson, D. Nordlund, I. Waluyo, N. Huang, H. Ogasawara, S. Kaya, U. Bergmann, L.Å. Näslund, H. Öström, P. Wernet, K.J. Andersson, T. Schiros, L.G.M. Pettersson, X-ray absorption spectroscopy and X-ray Raman scattering of water and ice; an experimental view, Journal of Electron Spectroscopy and Related Phenomena, 177 (2010) 99-129.

[433] M. Leetmaa, M.P. Ljungberg, A. Lyubartsev, A. Nilsson, L.G.M. Pettersson, Theoretical approximations to X-ray absorption spectroscopy of liquid water and ice, Journal of Electron Spectroscopy and Related Phenomena, 177 (2010) 135-157.
[434] A.J. Nelson, T. van Buuren, E. Miller, T.A. Land, C. Bostedt, N. Franco, P.K. Whitman, P.A. Baisden, L.J. Terminello, T.A. Callcott, X-ray absorption analysis of KDP optics, Journal of Electron Spectroscopy and Related Phenomena, 114-116 (2001) 873-878.
[435] H. Harima, Raman scattering characterization on SiC, Microelectron. Eng., 83 (2006) 126–129.
[436] D.A. Bulushev, F. Rainone, L. Kiwi-Minsker, A. Renken, Influence of Potassium Doping on the Formation of Vanadia Species in V/Ti Oxide Catalysts, Langmuir, 17 (2001) 5276-5282.
[437] A. Held, J. Kowalska-Kuś, K. Nowińska, K. Góra-Marek, Potassium-modified silica-supported vanadium oxide catalysts applied for propene epoxidation, Journal of Catalysis, 347 (2017) 21-35.
[438] H. Chen, S. Cheng, D. Chen, Y. Jiang, E.H. Ang, W. Liu, Y. Feng, X. Rui, Y. Yu, Vanadate-based electrodes for rechargeable batteries, Materials Chemistry Frontiers, 5 (2021) 1585-1609.
[439] V. Manev, A. Momchilov, A. Nassalevska, G. Pistoia, M. Pasquali, Potassium vanadates — promising materials for secondary lithium batteries, Journal of Power Sources, 44 (1993) 561-568.
[440] P. Hao, T. Zhu, Q. Su, J. Lin, R. Cui, X. Cao, Y. Wang, A. Pan, Electrospun Single Crystalline Fork-Like $K_2V_8O_{21}$ as High-Performance Cathode Materials for Lithium-Ion Batteries, Frontiers in Chemistry, 6 (2018).
[441] H.J. Kim, J.H. Jo, J.U. Choi, N. Voronina, S.-T. Myung, KV_3O_8 with a large interlayer as a viable cathode material for zinc-ion batteries, Journal of Power Sources, 478 (2020) 229072.
[442] X. Huang, B. Dai, G. Xu, X. He, S. Zhou, Y. Chen, B. Liu, Potassium Vanadate Nanobelt as a High-Capacity Cathode Material for Li-ion Battery, Int. J. Electrochem. Sci., 9 (2014) 6640-6667.

Information about the author

Personal Information

Name/ Surname	Ezgi Erdem

Education

10/2017-06/2022	PhD candidate (Dr.-Ing.) Fritz Haber Institute of the Max Planck Society, Berlin DE Department of Inorganic Chemistry
07/2017	Master of Science (M.Sc.) in Chemical Engineering Koc University, Istanbul TR
06/2014	Bachelor of Science (B.Sc.) in Chemical Engineering Yildiz Technical University, Istanbul TR

Teaching/ Mentoring and Work Experience

12/2021-2022	Research Assistant Supervised a MSc student from Technische Universität München
07/2015-2017	Research and Teaching Assistant Koc University, Istanbul TR
01/2012-2013	Student Assistant Yildiz Technical University, Istanbul TR
06/2012	Chemical Laboratory Internship Institute of Chemistry, Marmara Research Center (MAM) The Scientific and Technological Research Council of Turkey (TUBITAK), Kocaeli TR
06/2013	Process Engineering Internship PETKIM Petrochemical Inc. (Chlor-alkali plant), Izmir TR

Courses

04/2022	HZB Bessy Photon School (1 week) Humbolt-Universität zu Berlin
11/2019	Autumn School (Institute für Physik and IRIS Adlershof, Humboldt-Universität zu Berlin) (4D- STEM, TEM data analysis, EELS-EDX at JEOL ARM)
09/2014	Kaplan International Language Schools, Washington DC, USA

List of Publications

1 Erdem, E.; Kube, P., Tarasov, A., Wang, Y, Rosowski, F.; Schlögl, R.; Trunschke, A. A peculiar catalytic behavior of supported potassium-vanadate in propane oxidation, *in preparation (Angewandte Chemie, Communication, #51183)*

2 Erdem, E.; Kube, P., Tarasov, A., Wang, Y, Rosowski, F.; Schlögl, R.; Trunschke, A. The general impact of alkali-vanadate phase(s) on supported vanadia species in propane oxidation reaction, *in preparation (research article, #51679)*

3 Erdem, E.; Kube, P., Tarasov, A., Wang, Y., Carey, S., Hävecker, M., Rosowski, F.; Schlögl, R.; Trunschke, A.
The role of melting on the surface dynamics of supported vanadia studied with in situ techniques, *in preparation (research article, #51680)*

4 Erdem, E.; Ahi, H., Wang, Y., Rosowski, F.; Schlögl, R.; Trunschke, A
$K_3V_5O_{14}$: Synthesis, properties and functionality in propane oxidation, *in preparation (research article, #50981).*

Honors and Awards

Graduate Fellowship	The Scientific and Technological Research Council of Turkey (TUBITAK), TR
Poster Prize	Koc University TUPRAS Energy Center (KUTEM), Istanbul TR "Nanoalloys of Pt electrocatalysts for PEMFC for electricity production"
High honored student ranking	Chemical engineering (B.Sc.) (GPA: 3.52/4.00) Yildiz Technical University, Istanbul TR

List of Oral Presentations

05/2022	The 27th North American Catalysis Society Meeting (NAM 27), New York, USA "The role of melting in SiO_2-supported alkali-vanadate catalysts for propane oxidation reaction"
06/2021	Soapbox Science Berlin, Berlin Central Station (public talk) "Catalysis: An essential pillar of nature and chemical industry"

List of Poster Presentations

03/2021 — 54th German Catalysis Meeting (Jahrestreffen Deutscher Katalytiker) "The impact of phase transition of alkali-vanadate phase on the activity of vanadium oxide species for propane oxidation" (#50839)

03/2020 — 53th German Catalysis Meeting (Jahrestreffen Deutscher Katalytiker) "The effect of phase transition of alkali added supported vanadium oxide catalysts in propane oxidation" (#48572)

11/2019 — Supported Liquid Phase Catalysts for Oxidative Dehydrogenation of Propane, Fachbeirat 2019, FHI Berlin (#48613)

03/2019 — 52th German Catalysis Meeting (Jahrestreffen Deutscher Katalytiker) "Supported liquid phase catalysts for oxidative dehydrogenation of light alkanes" (#46969)

06/2019 — BASF Project Days, Ludwigshafen
"Oxide Catalysts for C-H activation"

08/2018 — 14th European Congress on Catalysis, EuropaCat 2019
"Supported liquid phase catalysts for oxidative dehydrogenation of light alkanes" (#48030)

List of PhD Day and Oxide Day Talks

03/2021 — Oxide Day
Operando NEXAFS and XPS study on A-V-O/SiO_2 catalysts (A: Li, Na-, K-, Rb-, and Cs-) (#50844)

09/2020 — Oxide Day
Structure and reactivity of silica supported K-V-O catalyst studied by operando Raman spectroscopy (#49950)

05/2020 — PhD Day
Following structural changes of a working catalyst *"silica supported alkali vanadate"* with in situ techniques (#50951)

10/2019 — PhD Day
Alkali-added supported vanadia catalysts for propane oxidation: Insights into the melting phenomenon of potassium vanadate (#48462)

08/2019	Oxide Day K-added supported vanadia catalyst for propane oxidation: Some insights into melting and wetting (#48060)
05/2019	PhD Day Influence of alkali additives on phase composition and catalytic properties of supported vanadium oxide catalysts (#47371)
11/2018	PhD Day Investigation of supported liquid phase catalysts for oxidative dehydrogenation of light alkanes (#46111)
10/2018	Oxide Day Investigation of supported liquid phase catalysts for oxidative dehydrogenation of light alkanes (#43879)